

NASA CR-65375

STUDY OF METEOROID IMPACT
INTO ABLATIVE HEAT SHIELD MATERIALS

FINAL REPORT

Prepared by

RESEARCH AND TECHNOLOGY LABORATORIES
SPACE SYSTEMS DIVISION
AVCO CORPORATION
Lowell, Massachusetts

AVSSD-0002-66-RR
Contract NAS 9-3404

by

R. R. McMath
R. F. Suitor
L. L. Lander
E. Langberg

GPO PRICE \$ _____

CFSTI PRICE(S) \$ _____

Hard copy (HC) 7.09

Microfiche (MF) 2.00

April 1966

ff 653 July 65

Prepared for

NASA MANNED SPACECRAFT CENTER
Houston, Texas

N66 27310

FACILITY FORM 602

(ACCESSION NUMBER)

409

(PAGES)

CR-65375
(NASA CR OR TMX OR AD NUMBER)

(THRU)

1

(CODE)

32
(CATEGORY)

STUDY OF METEOROID IMPACT INTO ABLATIVE HEAT SHIELD MATERIALS

FINAL REPORT

Prepared by

RESEARCH AND TECHNOLOGY LABORATORIES
SPACE SYSTEMS DIVISION
[REDACTED] COPY [REDACTED]
AVCO CORPORATION
Lowell, Massachusetts

[REDACTED] FT. WORTH TEXAS
[REDACTED] AVSCOR 0002-66-RR
[REDACTED] Contract NAS 9-3404

by

R. R. McMath
R. F. Suitor
L. L. Lander
E. Langberg

April 1966

Prepared for

NASA MANNED SPACECRAFT CENTER
Houston, Texas

ABSTRACT

27310

Meteoroid impact damage to Apollo and Gemini heat shield material has been experimentally and analytically studied. Hypervelocity impact tests were performed on these materials both in honeycomb and as tiles at room temperature and at temperatures down to -250°F . Projectiles of aluminum and Delrin were used to investigate the effect that changing projectile density would have on impact damage. Impact velocities varied from 3 km/sec to 8 km/sec.

The data from this extensive parametric study were treated with a regression analysis on the 7094 computer to determine the best curve fit to the data. Combined with an analysis of the hypervelocity impact process in these materials, this resulted in equations that permit prediction of impact damage to these heat shields.

CONTENTS

1.0 Summary	1
2.0 Introduction	2
3.0 Experimental Program	4
3.1 Hypervelocity Experiments	4
3.2 Measurement of Impact Damage	10
3.3 Analysis of Error	12
4.0 Material Testing	15
4.1 Introduction	15
4.2 Mechanical Properties of Targets	15
4.2.1 Description of Experimental Facilities	15
4.2.2 Discussion of Analytical Techniques	20
4.2.3 Mechanical Properties of Sylgard 325 Tile	24
4.2.4 Mechanical Properties of Avcoat 5026 Tile	37
4.3 Thermal Properties	45
4.4 Properties of Projectiles	56
5.0 Impact Test Results and Analysis	62
5.1 Introduction	62
5.2 Data Presentation and Analysis	67
5.2.1 Crater Volume	73
5.2.2 Crater Diameter	75
5.2.3 Damage Diameter (Spall Diameter)	75
5.2.4 Penetration	76
5.2.5 Total Damage Depth	77
5.2.6 Effects of Projectile Variation	78
5.2.7 Effect of the Presence of Honeycomb	79
5.2.8 Effect of Temperature Variation	81
6.0 Scaling	84
6.1 Introduction	84
6.2 Scaling Principles	85
6.2.1 Applicability of Late Stage Equivalence	85
6.2.2 Scaling Crater Geometry	87

CONTENTS (Concl'd)

6. 2. 3	Scaling of Spall and Other Damage	88
6. 2. 4	Scaling in Honeycomb	89
6. 3	Scaling Results to Meteoritic Velocities	89
6. 3. 1	Scaling for Penetration and Crater Diameter	89
6. 3. 2	Scaling for Spall Diameter	99
6. 3. 3	Scaling for Total Damage Depth	101
6. 4	Expected Variations	101
7. 0	Conclusions	103
8. 0	References	105

Appendixes

A.	Data Reduction Program	107
B.	Analysis of the Exploding Foil Process	131
C.	Heat Shield Impact Data	163
D.	Crater Parameters versus Velocity	175
E.	Crater Parameters versus Momentum	223
F.	Crater Parameters versus Energy	271
G.	Selected Data Plots	319
H.	Regression Forms	375

ILLUSTRATIONS

Figure 1	Avco SSD Terminal Ballistic Laboratory	5
2	.22 Caliber Light Gas Gun.....	6
3	Target Tank	6
4a	Target Instrumented with Thermocouples	8
4b	Target in Cooling Box.....	8
5	1/16-Inch Projectile and .22 Caliber Sabot	9
6a	Crater Diameter Measurement.....	11
6b	Spall Diameter Measurement.....	11
6c	Crater Depth Measurement	11
6d	Crater Volume Measurement.....	11
7	High Speed Tensile and Fatigue Tester	16
8	High Speed Tensile and Fatigue Tester with Environmental Chamber.....	17
9	Typical Trace of Load and Strain Versus Time.....	19
10	Tensile Strength of Epoxolite 5403 Versus Time at Various Temperatures	21
11	Master Curve of Tensile Strength of Epoxolite 5403 Versus Reduced Time.....	22
12	Shift Factor for Epoxolite 5403	23
13	Tensile Strength of DC 325 Versus Time at Various Temperatures	26
14	Master Curve of Tensile Strength Versus Reduced Time	27
15	Shift Factors for DC 325 Materials	28
16	Tensile Strength of DC 325 Tile Versus Time at Various Temperatures (Extrapolated Curves).....	30

ILLUSTRATIONS (Cont'd)

Figure 17	Compressive Strength of DC 325 Honeycomb Versus Time at Various Temperatures	31
18	Master Curves of Shear Strength of DC 325 Tile and Honeycomb Materials Versus Reduced Time	34
19	Master Curve of Penetration Force in DC 325 Tile Versus Reduced Time	36
20	Tensile Strength of Avcoat 5026 Tile Versus Time at Various Temperatures	39
21	Master Curve of Compression Strength of Avcoat 5026 Time Versus Time	42
22	Master Curve of Compression Strength of Avcoat 5026 Honeycomb Versus Reduced Time	43
23	Shift Factor for Avcoat 5026 Tile and Honeycomb Materials	44
24	Master Curve of Shear Strength of Avcoat 5026 Tile and Honeycomb Versus Reduced Time	48
25	Master Curve of Penetration Force in Avcoat 5026 Tile and Honeycomb Versus Reduced Velocity	50
26	Schematic of Thermal Conductivity Apparatus	51
27	Schematic of Arrangement of Semi-automatic Low Temperature Guarded Hot Plate	53
28	Schematic of Furnace Calorimeter Specific Heat Set	55
29	Thermal Conductivity of DC 325 Materials Versus Temperatures	57
30	Thermal Conductivity of Avcoat 5026 Materials Versus Temperature	58
31	Enthalpy-Temperature Curves for DC 325 Materials	59
32	Enthalpy-Temperature Curves for Avcoat 5026 Materials ...	60

ILLUSTRATIONS (Concl'd)

Figure 33	Impact Damage to Avcoat 5026-39 at Various Velocities.....	63
34	Impact Damage to Sylgard 325 at Various Velocities.....	64
35a	A Sylgard Honeycomb Showing Popped Cells	65
35b	Deep Penetrations into Sylgard Honeycomb	65
36	Temperature Effect on Impact-Sylgard Tile.....	66
37	Deep Penetrations into Avcoat.....	66
38	Initial Impact Pressures, Aluminum on Avcoat.....	70
39	Initial Impact Pressures, Aluminum on Dow Sylgard 325.....	70
40	Effect of Structure Material on Crater Boundaries.....	81
41	Cratering Efficiency in Avcoat 5026.....	90
42	Cratering Efficiency in Dow Sylgard 325 at RT.....	91
43	Cratering Efficiency in Dow Sylgard 325 at -150°F	92
44	Cratering Efficiency in Dow Sylgard at -250°F	93
45	Scaling of Crater Parameters for Avcoat 5026 Tile.....	95
46	Scaling of Crater Parameters for Avcoat 5026 Honeycomb....	96
47	Scaling of Crater Parameters in Dow Sylgard 325, Tile and Honeycomb at Room Temperature.....	97
48	Scaling of Crater Parameters in Dow Sylgard 325, Tile and Honeycomb at Low Temperatures	98

TABLES

Table	I	Error in Crater Measurement	13
	II	Tensile Properties of Sylgard-325 Tile	25
	III	Compression Properties of Sylgard-325 Honeycomb	32
	IV	Shear Properties of Sylgard-325 Tile Material	33
	V	Shear Properties of Sylgard-325 Honeycomb	33
	VI	Penetration Force in Sylgard-325 Tile	35
	VII	Tensile Properties of Avcoat 5026 Tile	38
	VIII	Compression Properties of Avcoat 5026 Tile	40
	IX	Compression Properties of Avcoat 5026 Honeycomb	41
	X	Shear Properties of Avcoat 5026 Tile	46
	XI	Shear Properties of Avcoat 5026 Honeycomb	47
	XII	Penetration Test, Avcoat 5026 Tile	49
	XIII	Penetration Test, Avcoat 5026 Honeycomb	49
	XIV	Properties of Aluminum and Delrin Projectiles	61
	XV	Cratering Efficiency for Avcoat 5026	73
	XVI	Cratering Efficiency for Sylgard 325	74
	XVII	Total Damage Depth/Crater Penetration	78
	XVIII	Materials Properties of the Targets	83
	XIX	Spall Diameter/Mean Crater Radius for Sylgard Tile	100
	XX	Spall Diameter/Mean Crater Radius for Sylgard Honeycomb	100
	XXI	Spall Diameter/Mean Crater Radius for Avcoat	101

SYMBOLS

C	Constant
d	crater diameter
d_s	spall diameter
D	projectile diameter
\bar{D}	diameter of sphere of same material and equal mass as the projectile
H_t	used to denote some strength property of the target
l	$(pr^2)^{1/3}$, mean crater radius
L	projectile length
m	porosity, (ρ_n/ρ) , ρ_n density of normally dense material
p	penetration
p_m	maximum damage depth
p_s	spall depth
p^*	$(l/\bar{D})(\rho_t/\rho_p)^{1/3}$
P	pressure
r	crater radius
T	temperature
u_1	shock velocity
u_2	particle velocity behind shock
v	crater volume
V	projectile velocity
x	used to denote a linear crater parameter
ρ_p	projectile density

SYMBOLS (Concl'd)

ρ_t	target density
E	energy
M	momentum
α	late stage equivalence velocity exponent
τ	time
K	shift factor

NOTE: For a discussion of the system of units, see page 3.

1.0 SUMMARY

Hypervelocity impact tests of Apollo and Gemini heat shield materials (Avcoat-5026 and Sylgard 325 respectively) were made with varying conditions of velocity, temperature, heat shield structure, and projectile to provide engineering data for predictions of meteoroid damage. Impact velocities were varied from 3 km/sec to 8 km/sec. Target temperatures were -250°F, -150°F and room temperature.

These experiments show that for a high-strength projectile into a low-density target the transition into the hypervelocity region occurs at a very high velocity. For an aluminum projectile impacting an Avcoat target, an impact at 8.2 km/sec is probably still in the transition region.

Experimentally there was no enhancement of penetration due to the honeycomb structure that could not be accounted for by material changes between the tile and the honeycomb filler. The honeycomb, however, did inhibit the very large spall area in the Sylgard material at -250°F. All other effects were minor.

The effects of target temperature on the extent of the impact damage were negligible in the Avcoat but quite pronounced in the Sylgard 325. These effects can be explained qualitatively by changes in the materials properties of Sylgard at very low temperatures. The Sylgard exhibited typical rubbery behavior at room temperature with deep puncture penetrations at low velocities and profuse cracking of the crater walls at higher velocities. At -150 and -250°F, the Sylgard behaved like a brittle material with more uniform cratering.

Extensive materials properties tests were performed at various temperatures and with various strain rates. An attempt has been made to relate these tests to the prediction of hypervelocity impact damage. For these materials, there does not appear to be any standard laboratory material test that provides enough information to predict hypervelocity impact damage quantitatively. The standard laboratory tests do permit some qualitative conclusions as to trends that the damage will follow (such as the temperature effect on Sylgard).

A study of the theory of hypervelocity impact, and an analysis of the experimental data, has resulted in the conclusion that the principle of late stage equivalence^{1, 2} can be successfully applied to scale the results of this study to meteoritic velocities. On this basis, the following relationship predicts the penetration in the hypervelocity region:

$$\frac{P}{D} = C \left(\frac{\rho_p}{\rho_t} \right)^{1/3} v^{0.58}$$

where the constant C is determined for each individual material from hypervelocity impact tests.

2.0 INTRODUCTION

The intelligent design of space vehicles requires an accurate estimate of the meteoroid hazard. If a meteoroid shield is needed, its weight can be a significant fraction of the total vehicle weight. Therefore, the more exactly the hazard can be specified, the better the design can provide the adequate protection at minimum weight.

To accurately assess the meteoroid hazard, one must know first the properties of the meteoroid and frequency of encounter. NASA has been vigorously pursuing flight programs to obtain this information. Also required is knowledge of the impact damage meteoroids will cause when they hit a space vehicle. This damage may take several critical forms, one of which is sufficient damage to the heat shield so that it will not protect the vehicle during reentry into the earth's atmosphere. The purpose of this program was to provide enough information about meteoroid impact damage to low-density heat shield materials to determine the degree of protection, if any, the heat shield of the reentry capsule will require. Very little experimental data exist on hypervelocity impact into heat shield materials.¹ This is especially true of the low-density materials such as those used on the Gemini vehicles and to be used on Apollo. The experimental phase of this program was a parametric study to provide sufficient data on impact damage into these materials to permit damage predictions and extrapolations to higher velocities.

The materials considered were the Gemini material, Dow Corning Sylgard 325, in cast tile and fiberglass honeycomb, and the Apollo material, Avcoat 5026-39, gunned into fiberglass honeycomb and cast into tile.

Impacts were made into these materials at velocities varying from 2.4 km/sec to 8 km/sec with 1/16-inch diameter aluminum and Delrin projectiles. Each of the four types of target was impacted at three temperatures: room temperature, -150° F, and -250° F.

The resultant impacts were carefully measured for total penetration, crater diameter, volume of material removed, spall diameter and spall depth. These data, along with the projectile parameters (such as velocity, energy and momentum) were then analyzed by a linear regression analysis programmed to be run on an IBM 7094-computer. The computer program was written to accept and plot all the data, and apply the curves with a "least squares" fit. From these data and the analysis of the phenomena of hypervelocity impact, equations were derived for predicting the damage to Sylgard 325 and Avcoat 5026-39 from a meteoroid impact.

In addition to the impact testing, research was conducted into the physical and thermal properties of these materials. This information was studied in conjunction with impact results to find a correlation between them. A high-strain rate penetrometer test comes closest to simulating hypervelocity impact. Applying

the principle of temperature-strain rate superposition, it is possible to produce curves which indicate the trends that the hypervelocity penetration will take in these materials at various temperatures. It has not been possible, however, to obtain a direct numerical prediction of penetration from these materials properties.

From the limited number of materials tested it appears that similar penetration formulas may hold for other materials of this general type. To determine the constants in the equation, however, it is still necessary to conduct hypervelocity impacts at one condition to fix one point on the curve. From this one experimentally-determined point it is possible to extrapolate to other velocities and projectile densities.

Data have been expressed in various units, largely for numerical and physical convenience. Though cgs units are used generally, the data in Appendix C and the Materials Testing Section are reported in the units in which the measurements were originally made. Other deviations used throughout the report are: energy, expressed in joules; temperature, reported as °F; and velocity, reported as kilometers per second.

3.0 EXPERIMENTAL PROGRAM

3.1 HYPERVELOCITY EXPERIMENTS

The hypervelocity impact experiments conducted on this program were performed in the Avco Space Systems Division Terminal Ballistics Laboratory (see Figure 1). These experiments used the .22 caliber shock compression light gas gun shown in Figure 2.

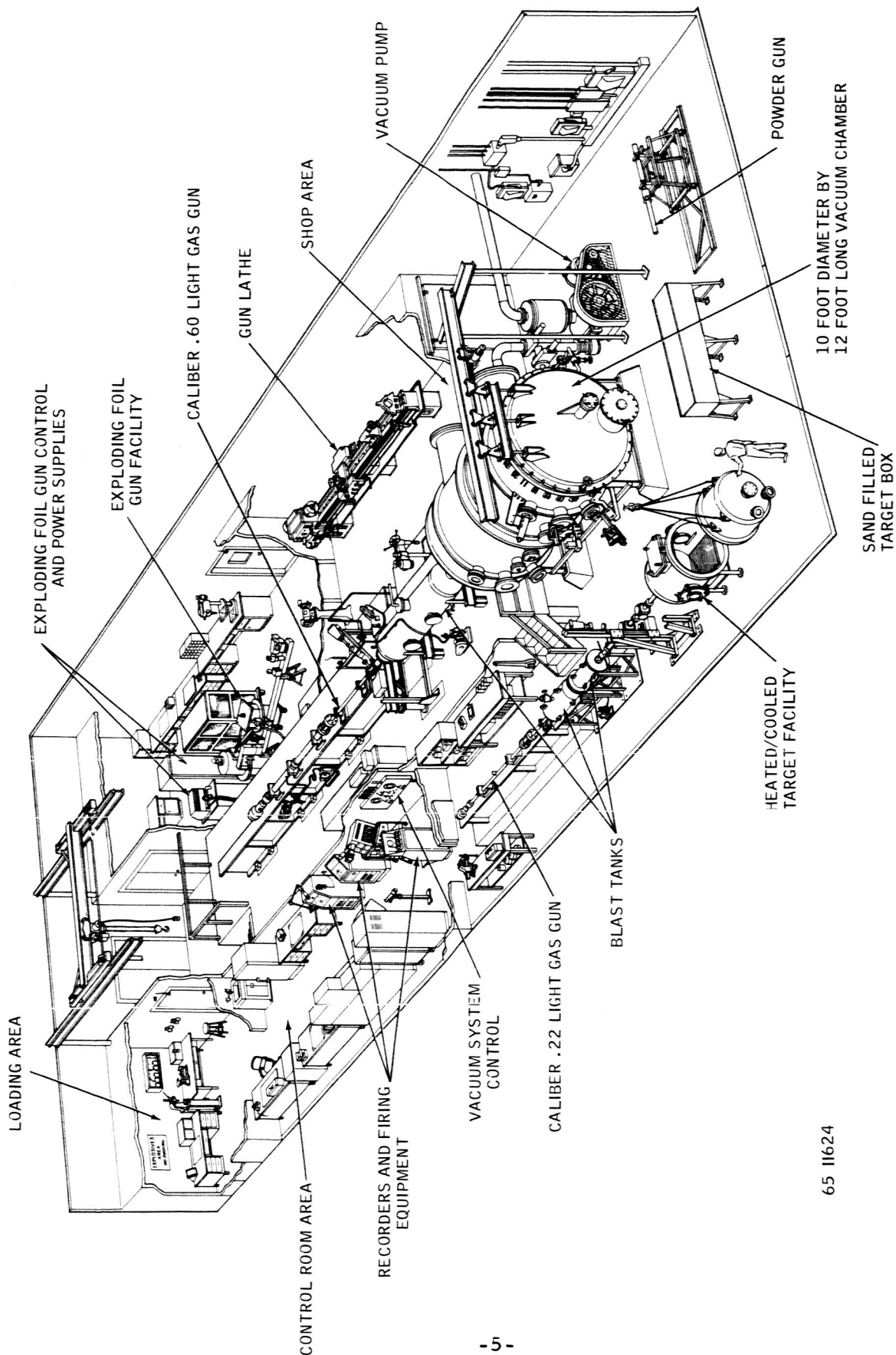
In the impact test phase of this program, a total of 484 light gas gun shots were made. These shots resulted in 288 documented data points. A good data point is defined as one in which a good velocity measurement was taken, an intact projectile was photographed at both light stations, and a clean impact resulted with no debris hitting the target in the vicinity of the crater.

The test program originally called for velocities up to 12 km/sec where all impacts over 9 Km/sec were to be made on a best effort basis using an exploding foil hypervelocity accelerator. At the time this program began, Avco was operating such an accelerator at velocities of the order of 9 km/sec. It was felt that since this system was under continual development, these velocities would increase to at least 12 km/sec during the course of the contract. When these expectations did not materialize a close analysis of the exploding foil system was undertaken by Dr. Edwin Langberg. His main conclusion showed that the mylar projectile could not stand the violent acceleration necessary to achieve velocities over 9 km/sec. A summary of this analysis is given in Appendix B of this report. This analysis agrees very closely with the experimental results.

A survey of the other exploding foil facilities in this country^{1, 2} indicated that all were experiencing particle breakup at velocities over about 9 km/sec. To date no one has been successful in accelerating single projectiles to much higher velocities with an exploding foil gun.

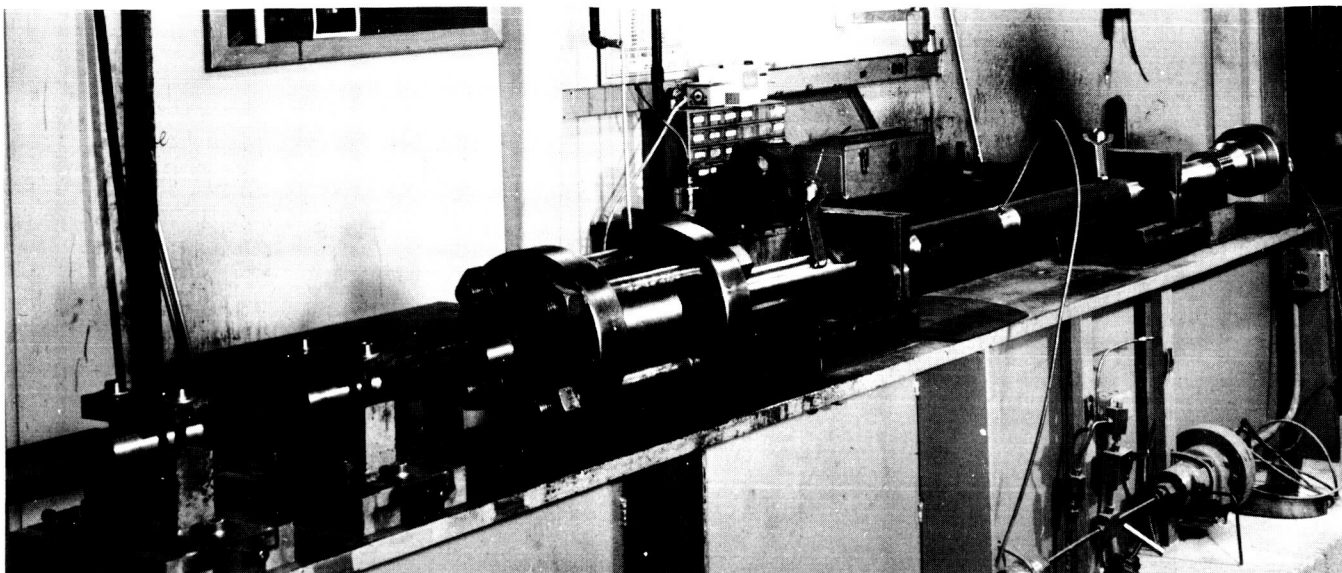
On the basis of Avco's extensive experimentation and analysis, together with experience at other laboratories, it was agreed to drop the exploding foil gun from the program and substitute additional light gas gun shots at the highest velocity obtainable. At the high end of the curve these increase the confidence level by giving enough data for a reasonable statistical fit.

The heat shield targets that were impacted in this program were 6 x 6 x 1 inches, large enough to be considered semi-infinite compared to the size of the projectile and its velocity. Each target consisted of the ablator attached to a 0.064-inch thick aluminum backplate to simulate the spacecraft structure. The backplate acoustically terminated the ablator in such a way as to allow the shock wave from the impact to reflect and contribute to the cratering or spall as it would in a real situation. The Sylgard 325 appeared to be cast directly onto the backup and was self adhering while the Avcoat material was bonded to the backup with HT424, a commercial epoxy manufactured by Bloomingdale Rubber Company, a Division



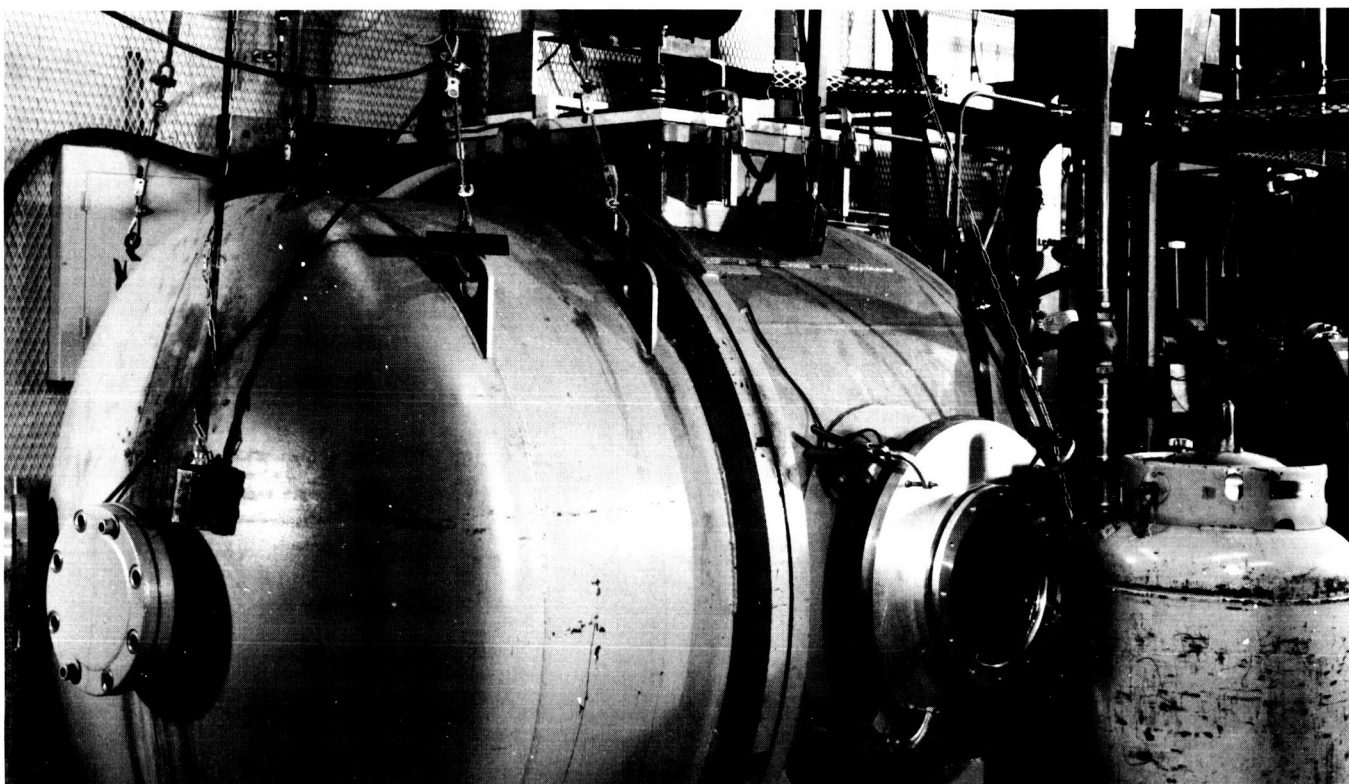
65 11624

Figure 1 AVCO/SSD TERMINAL BALLISTIC LABORATORY



26-1829

FIGURE 2. .22 CALIBER LIGHT GAS GUN



26-1830

FIGURE 3 TARGET TANK

of American Cyanimide. The test samples of the Sylgard Gemini material were fabricated by McDonnell Aircraft to guarantee that they were made to the same specifications as the operational material. The Avcoat Apollo material was fabricated by Avco/SSD to the Apollo operational specifications.

The projectile materials used for these tests were 2017-T3 aluminum and Delrin. Both types of projectile were 1/16-inch in diameter. The aluminum projectiles weighed 5.8 mg and the Delrin projectiles weighed 3 mg. The aluminum had a density of 2.8 gms/cc and the Delrin, a density of 1.43 gms/cc. This projectile density variation of a factor of 2 provided a good range in this parameter.

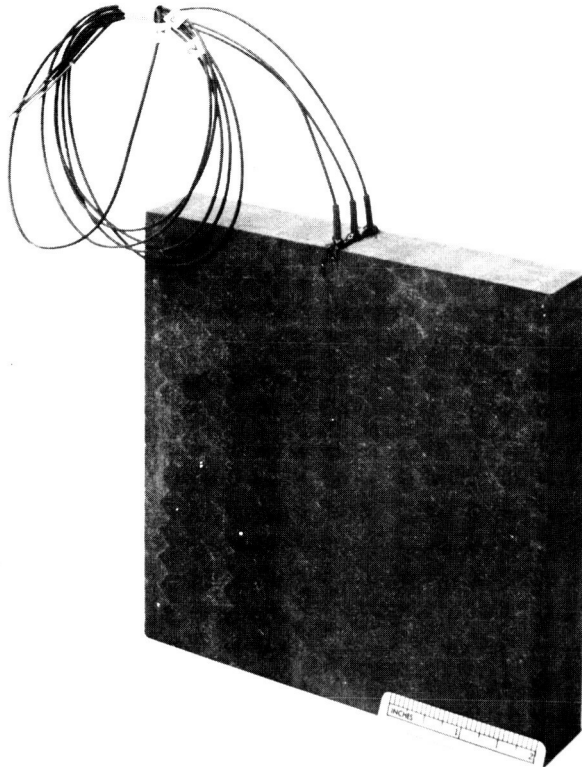
The targets were impacted at three temperatures, -250°F, -150°F, and room temperature, and at impact velocities varying from 3 km/sec to 8 km/sec.

The procedure followed in all the tests was identical except for the target cooling. The following discussion of the sequence of events for a cold shot will cover the entire procedure.

The target sample was instrumented with three iron-constantan thermocouples as shown in Figure 4a. They were placed as follows: 1/16-inch from the front-face, in the center of the ablator and 1/16-inch from the bond at the backface of the target. The target was then placed in the cooling box shown in figure 4b and clamped in place. Liquid nitrogen was then circulated through the cooling coils until all of the thermocouples stabilized at the test temperature desired. The output from all three thermocouples was continuously recorded on an Offner 6-channel recorder. For the target temperature of -250°F, it was necessary to cascade liquid nitrogen over the target and cooling box. Once the target was at temperature, the cooling coils would hold it there.

While the target was being cooled and the temperature stabilized by valving the liquid nitrogen, the light gas gun was loaded and readied to fire. A photograph of the light gas gun and range used in the tests is shown in Figure 2. The spherical projectile was first fitted into a sabot as shown in Figure 5. This sabot was machined to fit tightly into the light gas gun barrel. The sabot sealed the gas pressure behind it and protected the projectile from the hot propellant gas, barrel erosion and deformation during launch. After leaving the barrel, the sabot was separated by the aerodynamic forces acting on it in such a way as to let the projectile fly free without disturbing its trajectory. The range pressure was maintained at 50 mm pressure to furnish the aerodynamic drag for good sabot separation. This pressure was low enough so that no appreciable ablation of the projectile occurred before impact. After the sabot separated, the projectile passed through a 1/2-inch hole in a stop ring used to catch the sabot pieces.

The remainder of the range consisted of 1) a light screen which started a time interval counter and triggered a Kerr cell shadowgraph camera to photograph the projectile, 2) a second light screen which stopped the counter and triggered the second Kerr cell shadowgraph, 3) the target tank (Figure 3) where the



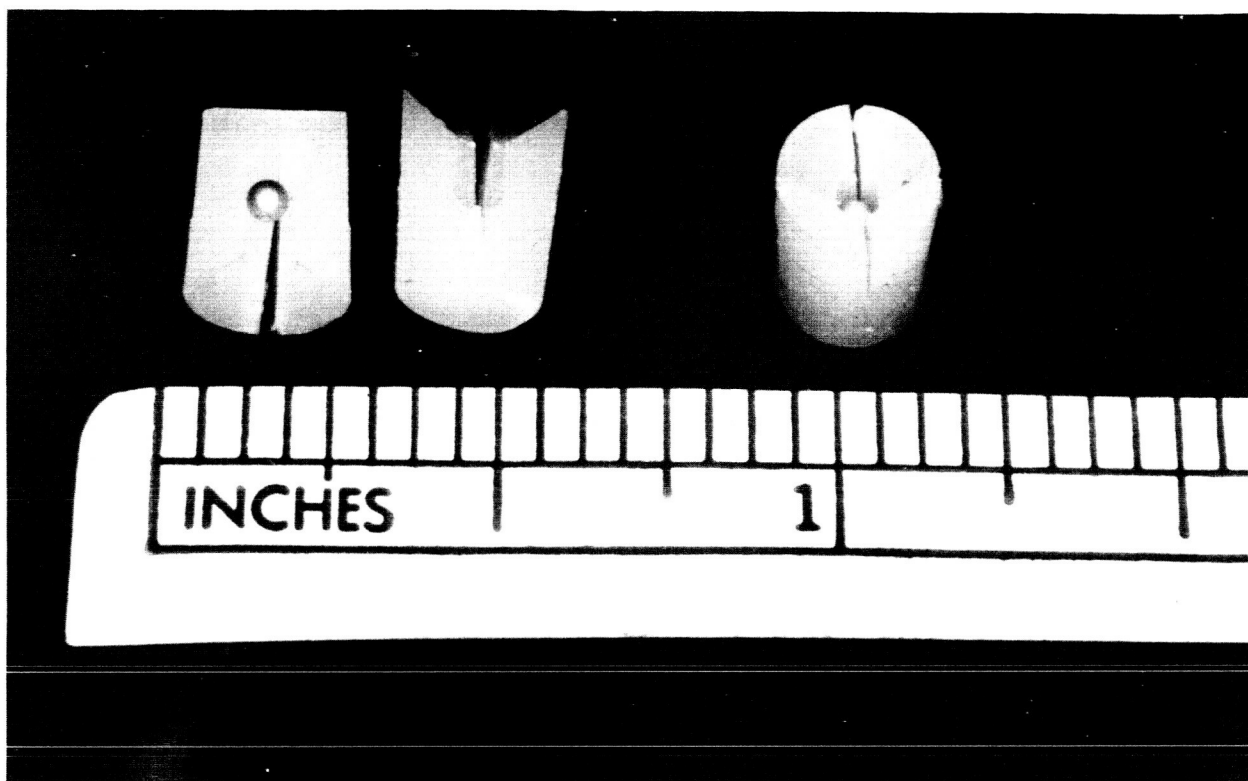
26-1831

FIGURE 4A TARGET INSTRUMENTED WITH THERMOCOUPLES



26-1832

FIGURE 4B TARGET IN COOLING BOX



26-1819

FIGURE 5 1/16 INCH PROJECTILE AND .22 CALIBER SABOT

projectile impacted the target. Each shadowgraph contained a fiducial line. The distance between the fiducials was known to be within ($\pm .020$ inch). The counter reading and the projectile position in relation to the fiducial permitted calculation of the projectile velocity within ± 1 percent. The target tank was evacuated to the same pressure as the range. This also minimized the heat loss from the cold targets and allowed them to come to equilibrium at the test temperature desired.

3.2 MEASUREMENT OF IMPACT DAMAGE

The problem of characterization of impact damage is particularly difficult in the target materials used in this program because the Avcoat is non-homogeneous and brittle while the Sylgard is rubbery. Both materials tend to produce irregular, rough craters compared to metallic targets. The following is a description of exactly how these craters were measured:

Crater Diameter

A Starrett small hole gage was inserted in the crater and adjusted to fit. The diameter was then measured on a micrometer. Three readings were taken, then averaged. Figure 6a shows the small hole gage in use.

Spall Diameter

When spall was reasonably round, three diameter readings were made at different points using vernier calipers and then averaged. Figure 6b shows this operation.

If spall was irregular, a long and short dimension was measured using vernier calipers.

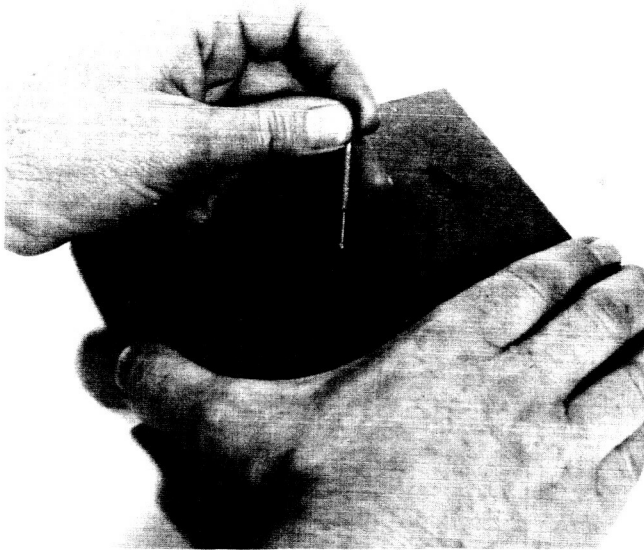
Crater Depth

A Starrett depth indicator was used to measure crater depth. Three readings were taken, then averaged. Figure 6c shows a target being measured with this setup.

All the Sylgard targets and the Avcoat targets impacted at low velocities were sectioned through the center of the crater and remeasured for penetration using the vernier calipers. This was necessary because in many cases in the Sylgard, the crater had closed up at the surface to the extent that the micrometer probe would not penetrate and in all cases a simple depth of crater reading was not indicative of maximum damage depth.

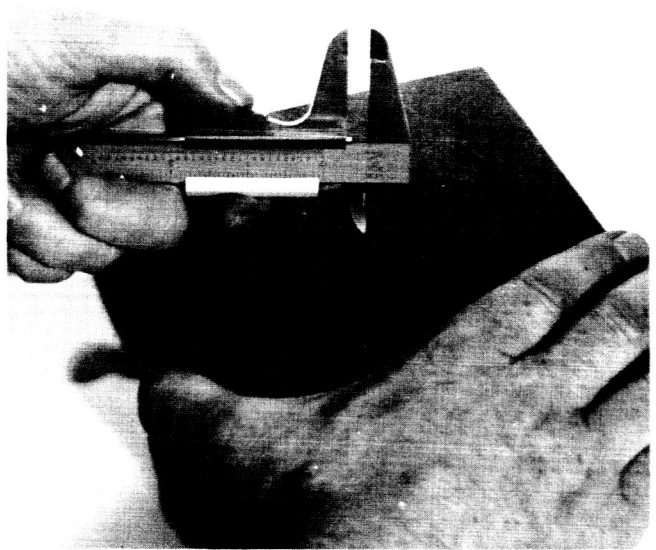
Spall Depth

Same method as crater depth.



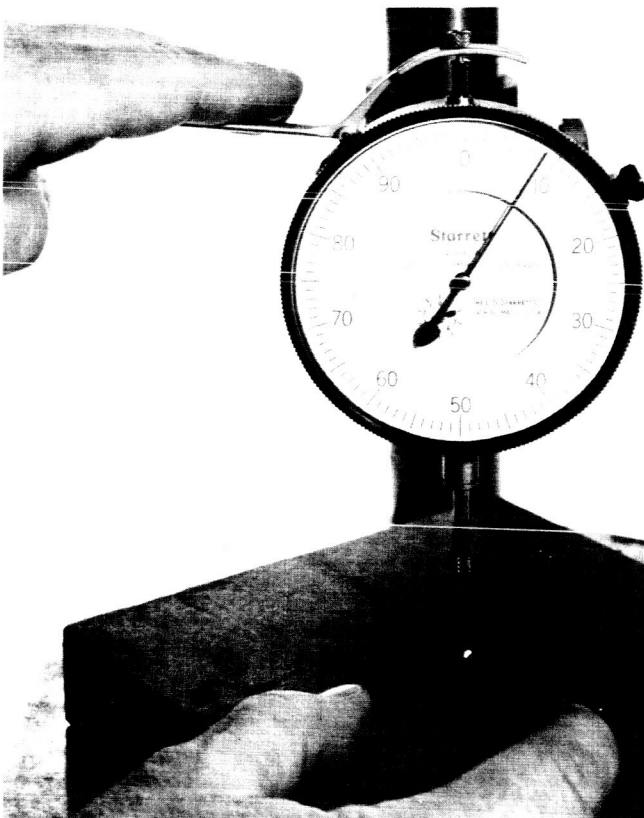
26-1820

FIGURE 6A. CRATER DIAMETER MEASUREMENT



26-1821

FIGURE 6B. SPALL DIAMETER MEASUREMENT



26-1823

FIGURE 6D. CRATER VOLUME MEASUREMENT



26-1822

FIGURE 6C. CRATER DEPTH MEASUREMENT

Total Damage Volume

The crater was sprayed lightly with clear lacquer to seal it. Using a mixture of 50 percent glycerine and 50 percent water, the crater was filled and then blown out with air. This was done to "pre-wet" the crater, thereby eliminating the meniscus when the actual measurement was made.

A micrometer burette was filled with the above mixture and the indicator set at "0". The crater was then filled, making sure the liquid was level with the surrounding area of the target. The burette was read to indicate exactly how much liquid was left in the instrument. Figure 6d illustrates the technique used in this measurement. The micrometer burette is calibrated in 0.001 cc and can be interpolated to 0.0001 cc.

3.3 ANALYSIS OF ERROR

Analysis of the physical errors involved in the conduct of the hypervelocity impact experiments show that the target material properties contribute the largest source of error. Of the four target materials tested, the Sylgard 325 tile has the most reproducible properties. Its density is uniform and it is a homogeneous material. Scatter is produced, however, by the randomness with which the rubbery material responds to shearing and tensile forces. This scatter is further accentuated by the fiberglass structure in the Sylgard honeycomb targets. In these impacts, the projectile might impact on a honeycomb wall or in the center of a cell, (with the small cell size of this honeycomb, most of the impacts involved more than one cell). In addition to this, the strain in the bond between the Sylgard and the fiberglass was added at low temperatures. All of these items tend to produce an impact condition that is different for each shot.

The Avcoat material is basically nonhomogeneous, being made of randomly-oriented chopped silica fibers and phenolic microballoons in a phenolic resin binder. The response of this material to impact damage is small compared to its structure and tends to be more random than for similar damage into a uniform homogeneous material. The density of this material may also vary between targets. A random sampling of the density showed variation of ± 2.5 percent. There were undoubtedly individual targets where this variation was larger.

The Avcoat honeycomb exhibits the greatest scatter due to material properties. In the Avcoat honeycomb, the density can vary as much as 12 percent and still be within specifications. Since each cell is a separate entity, it is possible for adjacent cells to show this variation. Short of weighing each individual cell, there is no way of defining the density of an individual cell. Since in the Avcoat most of the craters made were small enough to be contained primarily in one cell, the target material was basically undefined. This was also true of the other material properties on an individual cell basis in the Avcoat honeycomb. The location of an impact in relation to the honeycomb structure also influenced crater size and shape. This also contributed to the data scatter.

Another property of the material which could affect the impact data scatter is the temperature effect. The laboratory materials tests show that the physical properties of Avcoat are largely unaffected by temperature: consequently, slight variations in test temperature should not materially contribute to the data scatter. The Sylgard, being a rubbery material, does go through a transition to a brittle material as it is cooled. However, the effect of a few degrees temperature variation on this material at the test temperature of -150°F would introduce negligible scatter in the results. The target temperature was stabilized so that all three thermocouples were normally within $\pm 10^{\circ}\text{F}$ of the test temperature.

It has also been observed that the properties of Avcoat change somewhat under prolonged exposure to vacuum. In these experiments the target was not in a vacuum environment for more than an hour, but it is possible that some outgassing did occur.

The experimental parameters are quite well defined. The mass of the projectile will vary about ± 1 percent and the velocity is measured to ± 1 percent.

The actual measurement of the impact damage involves two sources of error. First, since many of the craters are of irregular shape, the crater diameter and spall diameter becomes largely a matter of judgement. The criterion used has been to take an average diameter equivalent to a circle of equal area.

The second source of scatter is the human error in the measurement itself. To define this aspect of the analysis the craters in a representative Sylgard and Avcoat tile were measured several times by the same technician who measured all of the craters. The deviation in the various measurements is shown in Table I.

TABLE I
ERROR IN CRATER MEASUREMENT

	Sylgard 325	Avcoat 5026-39
Crater Diameter	± 3 percent	± 1 percent
Spall Diameter	± 1.5	± 2.5
Penetration Depth	± 3	± 1.5
Spall Depth	± 5	± 5
Volume	± 6	$\pm .5$
Total Damage Depth	± 2.5	± 2.5

It can be seen that the measurement variation in the Sylgard is a little larger than in the Avcoat. This is due to the irregular appearance of the crater interior and to the rubbery behavior of the material being measured. The error in the spall depth is large because the spall depths were of the order of 0.005 -inch and a 0.001 - inch variation in reading represents a large error.

There are many significant errors involved in the acquisition of hypervelocity impact damage data in the general class of low density, nonhomogeneous ablative materials used as targets in this program. However, from the preceeding discussion of the sources of errors, it would appear that they are independent. Thus, while any one data point may be subject to large error, the data taken as a whole and fitted to curves by the computer should yield substantially correct results.

4.0 MATERIALS TESTING

4.1 INTRODUCTION

The purpose of the materials testing portion of this contract was to measure certain mechanical, thermal and analytical properties of the target materials in the hope of correlating these properties with hypervelocity impact damage.

Tensile, compressive and shear properties were measured over 3 to 4 orders of magnitude in strain rate and at temperatures from 80°F to -260°F. Measurements of the retarding force on a 0.0625 inch diameter pin penetrating the surface of the targets were made at various velocities over the same temperature range. A description of the test facilities, test results, and analytical approaches used to analyze the data are given in Section 4.2.

The thermal properties measured were thermal conductivity and specific heat. These properties were measured at temperatures from 250°F to -250°F. The experimental facilities and test data are discussed in Section 4.3.

Section 4.4 is devoted to presenting the properties of the projectiles. The data presented in this section are handbook properties supplied by the vendors.

4.2 MECHANICAL PROPERTIES OF TARGETS

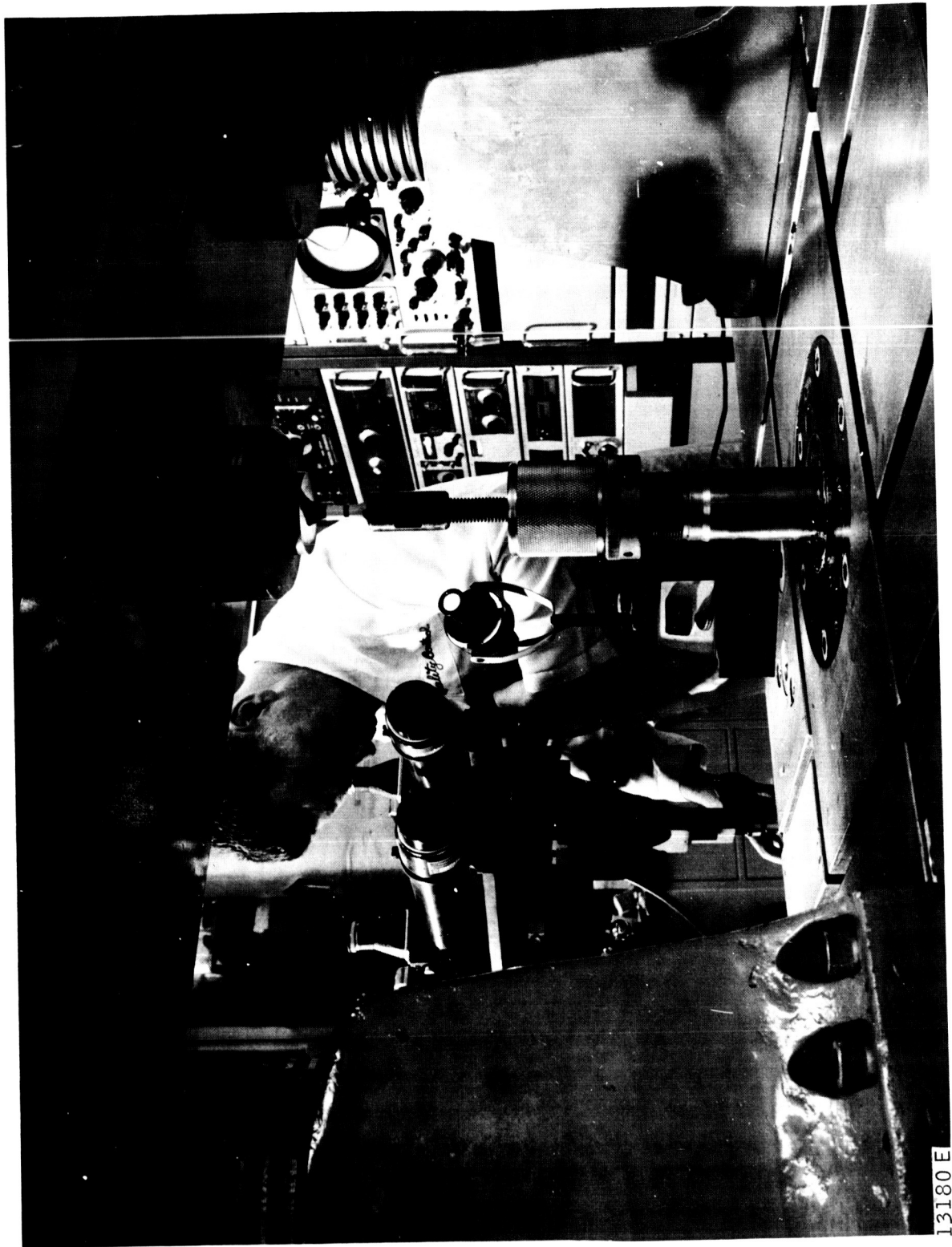
The mechanical properties measurements were carried out on a dynamic mechanical test facility built around a high-speed tensile and fatigue tester (Figures 7 and 8). The capabilities of this facility are:

4.2.1 Description of Experimental Facilities

Conventional engineering properties of metallic and nonmetallic materials in tension, compression, shear, and flexure can be measured at strain rates from less than 1×10^{-3} in/in-min to 1×10^4 in/in-min. Fatigue properties of materials can be measured at frequencies from 10^{-3} cps to 10^3 cps at either constant strain or load amplitudes with a variety of waveforms.

Associated instrumentation permits the measurement of dynamic load and strain imposed on the test sample; therefore, the phase angle between load and strain, due to hysteresis under cyclic loading, can be measured. Thus, the dynamic damping characteristics of a material can be determined as a function of strain, frequency, and temperature.

All these tests may be performed at temperatures from -260°F to 1000°F.



13180 E

Figure 7 HIGH SPEED TENSILE AND FATIGUE TESTER

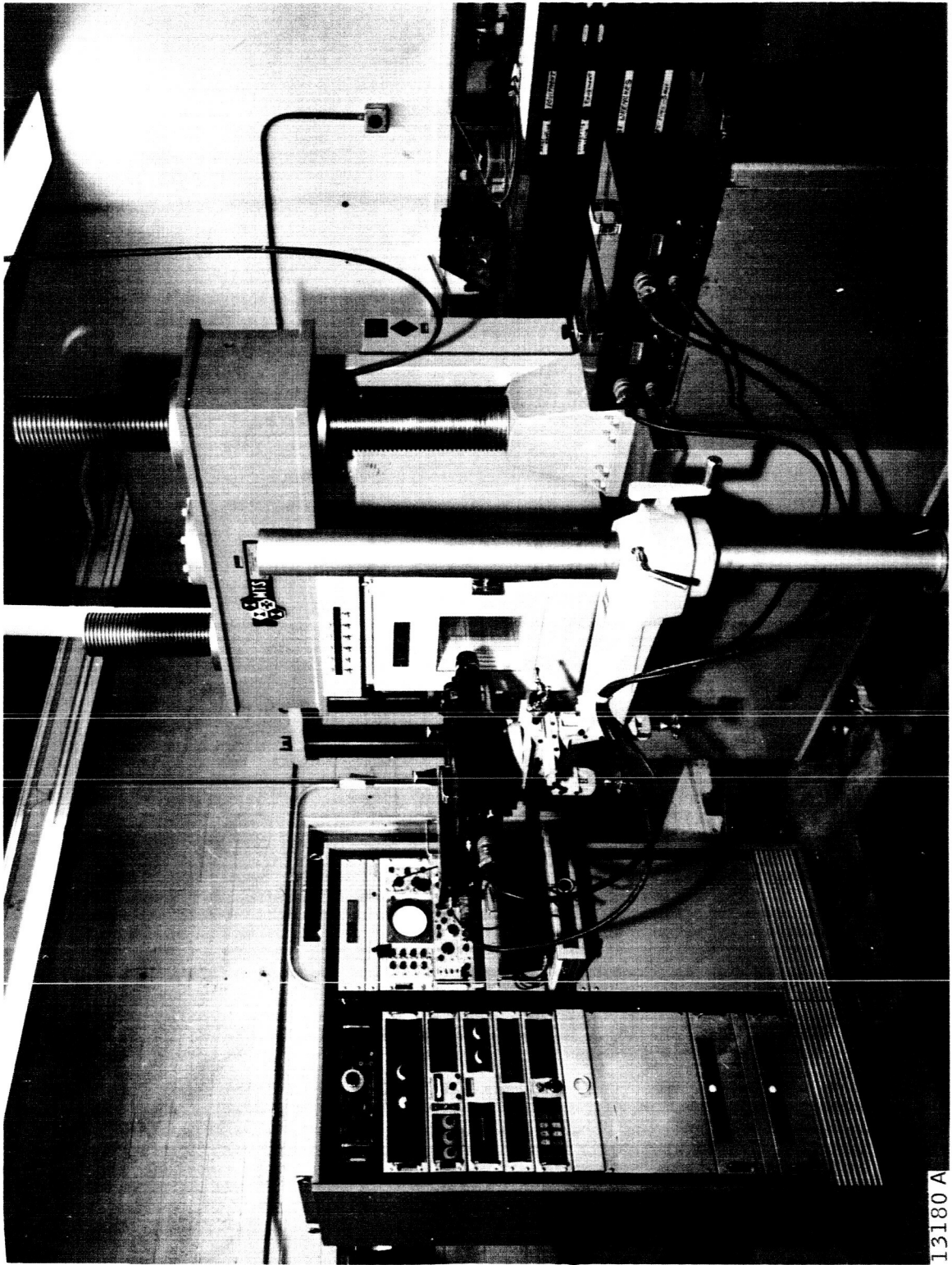


Figure 8 HIGH SPEED TENSILE AND FATIGUE TESTER WITH ENVIRONMENTAL CHAMBER

The high speed tensile and fatigue tester uses a closed-loop controlled hydraulic ram capable of velocities up to 700 in/min. with a 10,000-pound force. The ram has a full stroke of 5 inches of controlled travel. The ram is capable of higher velocities at full-load capacity but the amount of closed loop control begins to fall off and the ram motion approaches an open loop operation with the associated tendency for the ram to slow down when loading the specimen. However, velocities up to 18,000 in/min have been obtained with 10,000-pound force on the ram when testing an aluminum specimen. The associated change in the velocity of the ram was only about 10 percent (i.e., the velocity of the ram dropped from 18,000 to 16,000 in/min throughout the duration of the test. Performance surpasses the present tentative ASTM specification in high-speed testing (tentative method of test for tensile properties of plastics at high straining rates D-2289-64T).

Under closed-loop control three separate modes of control are available: loading rate, ram velocity, or strain rates as measured directly on the test specimen.

Strain gages of various types are used mainly for measuring the strain in hard brittle materials. For low modulus or highly ductile materials, strain may also be measured directly on the specimen using two electro-optical trackers (Optron model No. 680). This particular system is capable of measuring strain at strain rates up to 120,000 in/in-min. Unlike strain gages or L.V.D.T. strain followers, this strain-measuring system is not in contact with the specimen; hence, its accuracy is not affected by temperature or strain rate.

The Avco high-speed tensile and fatigue machine is equipped with a Missimer's temperature chamber (model FTI-3.2-300 1,000), shown in Figure 8, which operates at temperatures from -300°F to +1000°F. Other cryostats or furnaces are available for testing at temperatures at either end of the range of the Missimer's chamber.

During a test, all pertinent data parameters versus time are recorded using a Tektronix Model 565 Oscilloscope and camera. A typical trace of load and strain versus time is shown in Figure 9. Data in this format are reduced to punch card format by means of a Benson-Lehner Oscar Model J Reader and an analog to digital converter. Each punch card obtained from a given photograph contains the time value and the corresponding stress and strain levels as well as pertinent facts identifying both the test specimen and test conditions. These punched card decks (12 to 15 cards per photograph) then serve as input to a computer program which, by use of the SC4020 Computer Recorder made by Stromberg-Carlson, gives an output in the form of a conventional stress-strain diagram labeled with the pertinent specimen and test parameter data as well as coordinate identification.

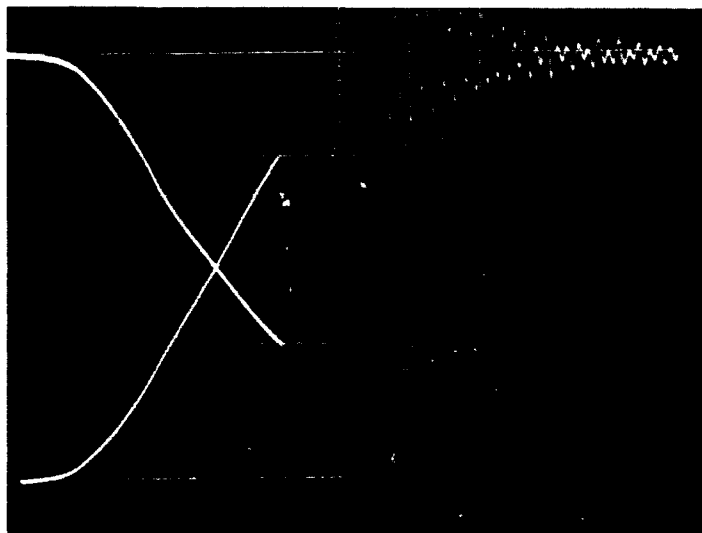
Work Request No.
66371

Material Designation
PO7651

Vendor
Lycoming

Part No.
TC 208

Specimen No.
57



Type Test	Tensile x	Compression 0
Direction	circumferential	
Area	0.127	

Load Scale	500	lbs./cm	Strain rate	1.63	in./in.-sec
Time Scale	2×10^{-3}	sec/cm	Maximum Load	2,070	lb.
Strain Scale	2000×10^{-6}	cm	Maximum Strain	0.0091	in/in
Test Temperature	80	°F			
Bar Design	TS- 142				

Comments:

A-5 gages - specimen broke outside gages.
65-3291

Figure 9 TYPICAL TRACE OF LOAD AND STRAIN VERSUS TIME

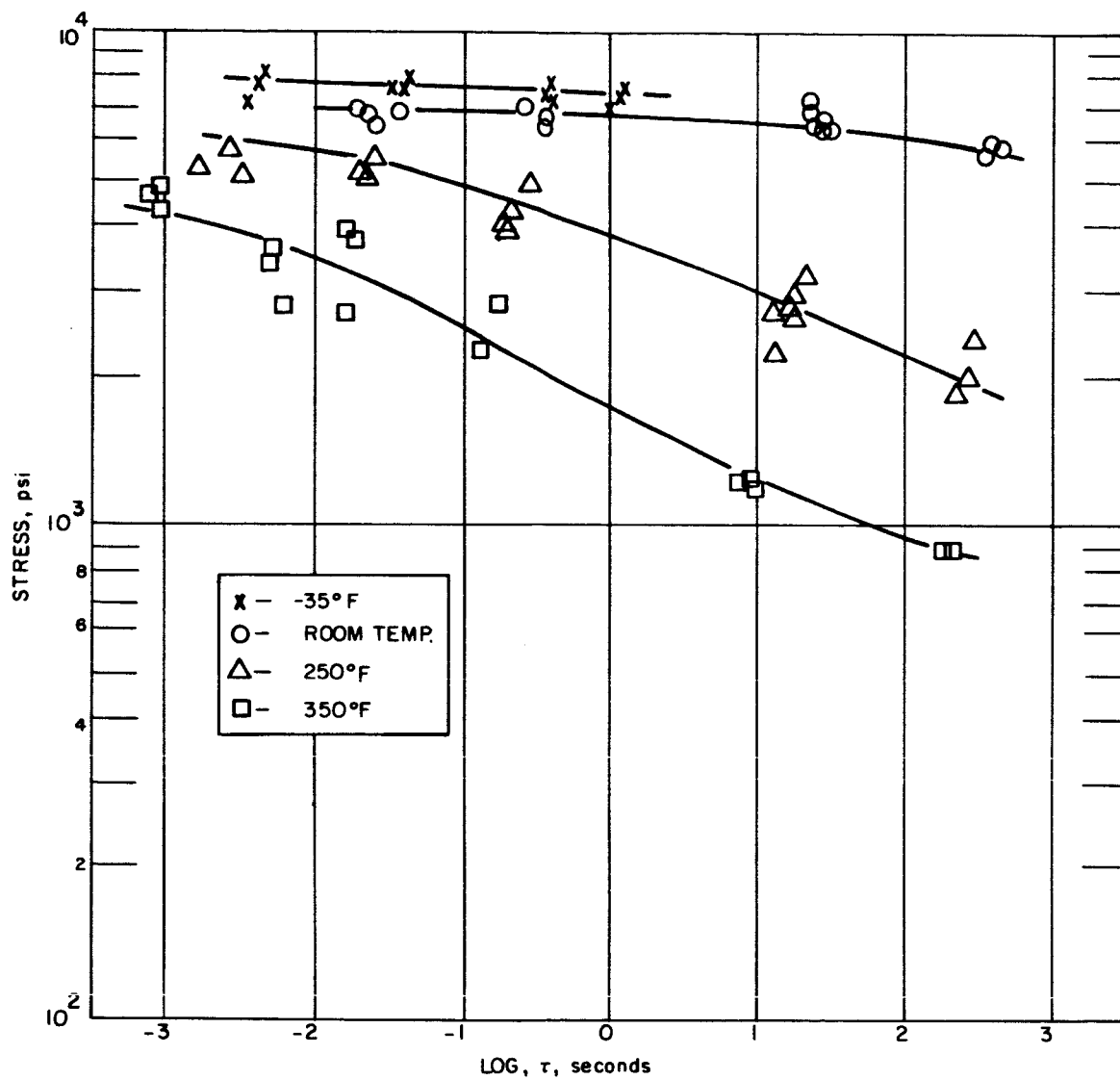
4.2.2 Discussion of Analytical Techniques

As pointed out in Section 4.2.1 above, the high-speed tensile and fatigue machine has a maximum ram velocity of 18,000 inches-min. This enables one to subject materials to strain rates in excess of 10^4 in/in-min or impacts at velocities up to 25 ft/sec. However, for many materials the maximum strain rate or impact velocity is limited to rates from 1 to 2 orders of magnitude lower because of limitations in load cell response. The natural frequency of the load cell should be such that at least 10 cycles will transpire within the test period. The natural frequency of the load cell in the high-speed tester is 7.5×10^4 cps; with the addition of grips, fixtures, etc., the natural frequency may drop to 10^4 cps. This limitation requires that the test periods be greater than 5×10^{-4} seconds. In this program it was desired that material properties in the time range of 10^{-4} to 10^{-5} second be measured. This corresponds to velocities which are three to four orders of magnitude higher than can be obtained experimentally with the above facility. The principle of time-temperature superposition may be used to obtain estimates of mechanical properties at time periods or strain rates not obtainable with conventional high strain rate machines. This approach has been used by Avco with considerable success on various Air Force Programs on a wide variety of materials.

The principle of time-temperature was discovered simultaneously by Ferry⁴, Leaderman⁵, and Tobolsky⁶, each of whom did major work in establishing the validity and scope of the principle. This principle is based on the hypothesis that the rate sensitivity of a material is a thermodynamic property. Hence, the rate sensitivity of a material at one temperature is the same as its rate sensitivity at another temperature over a different time scale (see Figure 10). Figure 10 is a log-log plot of tensile strength versus τ , where τ is the duration of test in seconds.

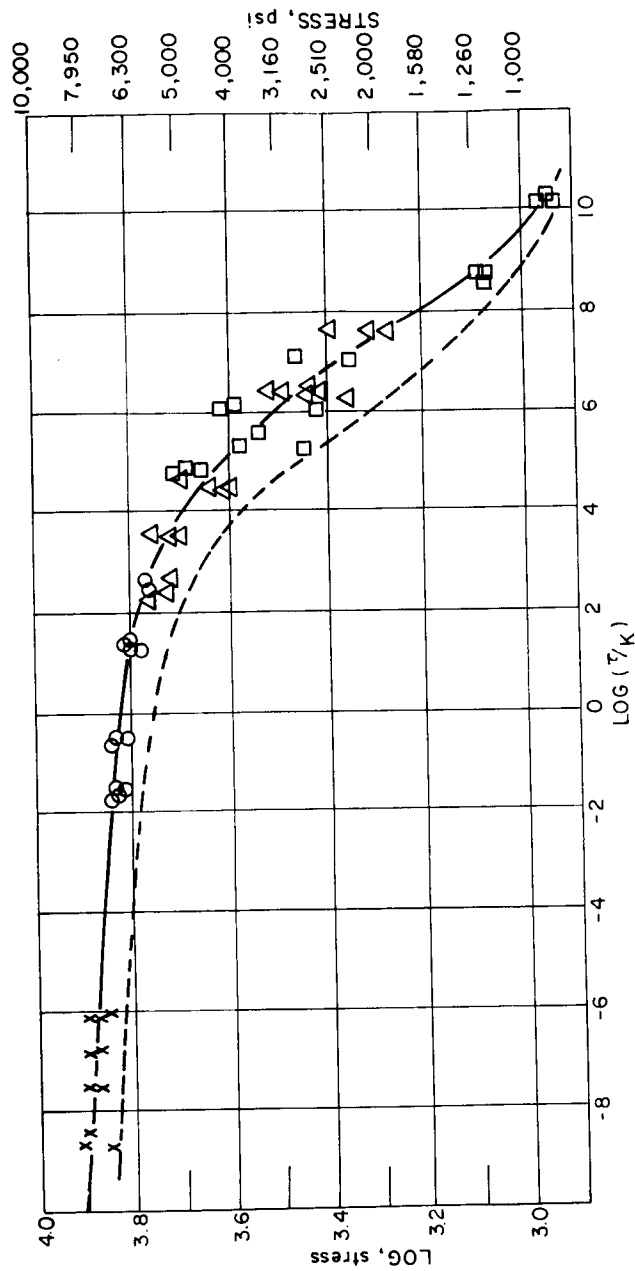
Here it is seen that the tensile strength at 250°F over the time scale from 10^{-1} to 10^2 seconds is the same as its strength at 350°F in the time scale from 10^{-3} to 10^0 seconds. The time-temperature superposition principle may be used to construct a "master curve" relating tensile strength of the Epoxolite 5403 over a much larger time scale than is obtainable in a practical laboratory experiment. Figure 11 is the master curve constructed from the data depicted in Figure 10. Figure 11 is a log-log plot of tensile strength versus τ/k , where "k" is the amount the data had to be shifted along the time axis to obtain the superimposed master curve. Figure 12 is a plot of the shift factor ($1/k$) versus the reciprocal of absolute temperature ($1/T$) which was used in the construction of the master curve in Figure 11.

Room temperature was chosen arbitrarily as the reference temperature for the master curve shown in Figure 11. By definition, then, "k" equals to one and the value of (τ/k) equals (τ) . The master curve in Figure 10,



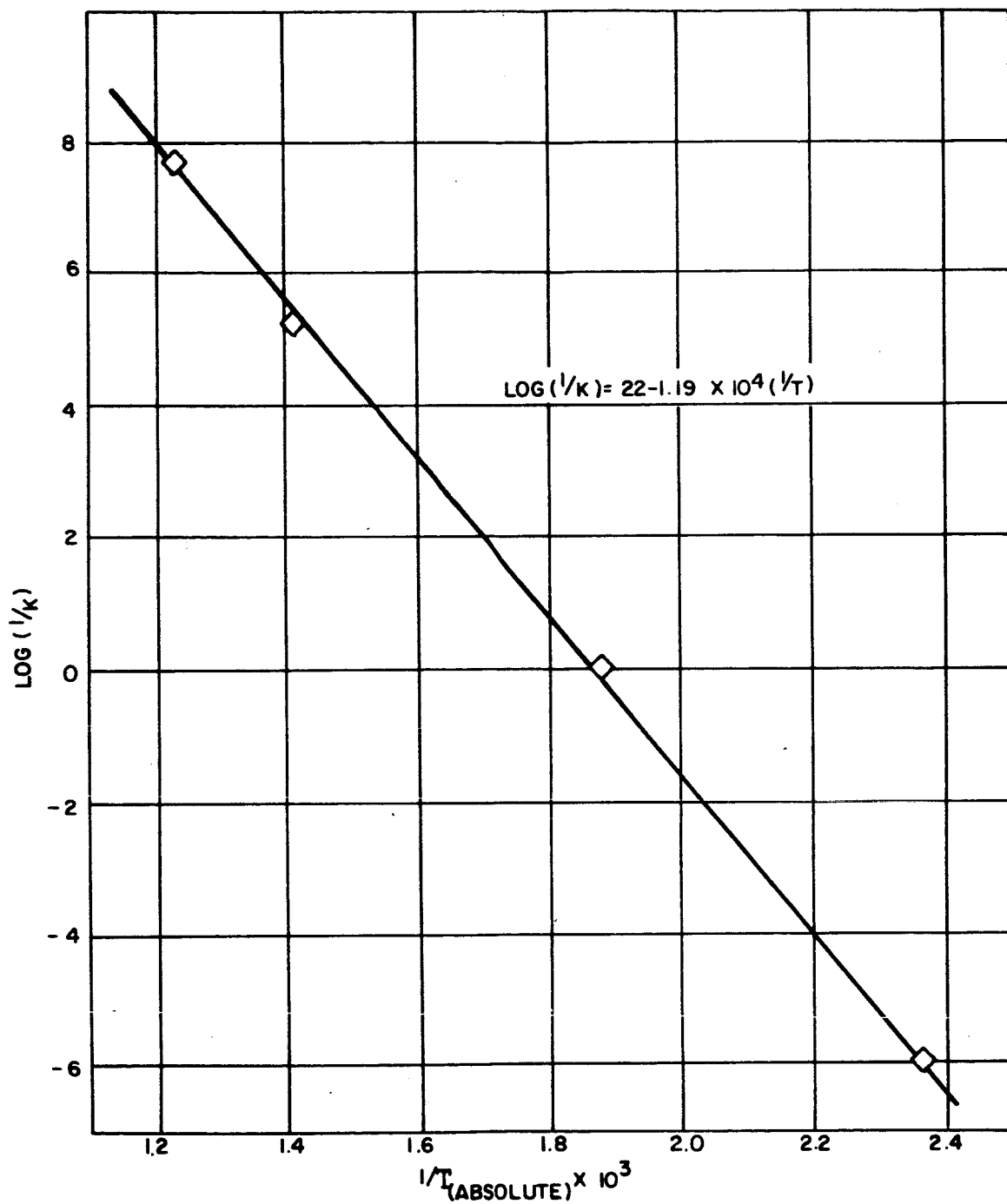
86-1441

Figure 10 TENSILE STRENGTH OF EPOXOLITE 5403 VERSUS TIME
AT VARIOUS TEMPERATURES



86-1442

Figure 11 MASTER CURVE OF TENSILE STRENGTH OF EPOXOLITE 5403
VERSUS REDUCED TIME



86-1443

Figure 12 SHIFT FACTOR FOR EPOXOLITE 5403

therefore, provides an estimate of the tensile strength of Epoxolite 5403 for test times ranging from 10^{-8} to 10^{10} seconds.

It must be emphasized that the principle of time temperature superposition is an analytical approach based on certain thermodynamic assumptions, and, therefore, can be considered absolute only over that time scale where it can be verified experimentally. For instance, it has not yet been experimentally verified that the tensile strength of the Epoxolite 5403 at -35°F is, in fact, indicative of its strength at room temperature in the time range from 10^{-8} to 10^{-6} seconds.

The mechanical properties of Epoxolite 5403 are of no importance to this program but are included here for the purpose of illustrating the application of time-temperature superposition.

4.2.3 Mechanical Properties of Sylgard 325

Tensile tests were performed on the Sylgard 325 tile at strain rates ranging from 0.06 to 600 in/in-min at temperatures from 80°F to -260°F . These data are tabulated in Table II. Figure 13 is a log-log plot of tensile strength versus time at various temperatures (Note: each data point represents one test). These data are presented as a function of time (the duration of test) because of the difficulty involved in defining an effective strain rate associated with a hypervelocity impact. It will be noted that tests were performed at several intermediate temperatures which were not of direct interest to this program. At these temperatures behavior was determined to establish the shape of the shift factor-temperature relationship.

Figure 14 is the "master curve" which was constructed using the principle of time-temperature superposition. It is a log-log plot of tensile strength versus reduced time (τ/k), where τ is time and ($1/k$) is the shift factor. Figure 15 is a plot of $\log(1/k)$ versus the reciprocal of absolute temperature ($1/T$) used to construct Figure 14. It will be noted that there are two distinct slopes or activation energies associated with this material.

The transition in the shift factor-temperature curve is in the region of -50°F to -100°F . This agrees well with transitions found in thermal expansion curves. If in fact, there is a phase change in this temperature range, one would expect to observe different activation energies associated with each phase.

If room temperature (80°F) is chosen as the reference temperature for the master curve in Figure 14, then ($1/k$) equals one, and the value of (τ/k) equals τ . For room temperature then, the curve in Figure 14 covers the time scale from 10^2 down to 10^{-26} seconds. As demonstrated earlier, this is an analytical approach and the validity of extrapolating down to 10^{-26} seconds is questionable. At present however, we are interested in materials

TABLE II
TENSILE PROPERTIES OF SYLGARD-325 TILE

Specimen No.	Test temperature (°F)	Total test time (seconds)	Strain rate (in/in min)	Total strain (in/in)	Ultimate stress (psi)	Specimen No.	Test temperature (°F)	Total test time (seconds)	Strain rate (in/in min)	Total strain (in/in)	Ultimate stress (psi)
1	80	160	0.065	0.623	297	26	-125	85	0.48	0.635	734
2	80	106	-	0.630	313	28	-125	1.2	11.1	0.285	1095
4	80	120	0.306	0.693	313	29	-125	0.155	72	0.277	1219
3	80	5.5	-	0.624	383	30	-125	0.016	564	0.230	1484
6	80	5.2	7.4	1.054	453						
5	80	0.54	-	0.760	477	34	-150	26	0.58	0.258	1070
7	80	0.50	80	0.895	484	33	-150	5.0	7.0	-	1156+
8	80	0.063	440	0.800	570	32	-150	0.07	36.0	0.087	2080
						31	-150	0.014	423	0.116	1719
14	-30	138	0.375	1.060	398						
13	-30	146	-	0.720	383	50	-200	10.1	0.13	0.023	4150
12	-30	5.1	7.5	0.749	625	41	-200	9.6	0.16	0.033	3420
11	-30	0.51	68	0.698	719	40	-200	8.5	-	-	4000
10	-30	0.07	480	0.528	852	44	-200	0.30	3.0	0.0214	4480
9	-30	0.067	520	0.632	813	42	-200	0.044	28	0.0204	6400
						45	-200	0.033	46	0.0245	3320
15	-100	156	0.30	-	688	46	-200	0.030	24	0.0164	5040
17	-100	7.0	18	1.410	781	52	-200	0.006	210	0.0176	6560
21	-100	0.62	-	0.945	852						
22	-100	0.58	90	1.085	836	59	-260	10.8	0.075	0.0139	6560
19	-100	0.062	480	1.380	953	60	-260	0.35	2.0	0.0130	6080
						49	-260	0.035	18	0.0134	5920
25	-115	93	0.53	0.895	684	51	-260	0.030	20	0.0139	6400
24	-115	5.1	9.15	0.940	852	48	-260	0.0048	152	0.0121	6400
23	-115	0.46	97.2	0.800	945						
20	-115	0.052	600	0.800	1030						

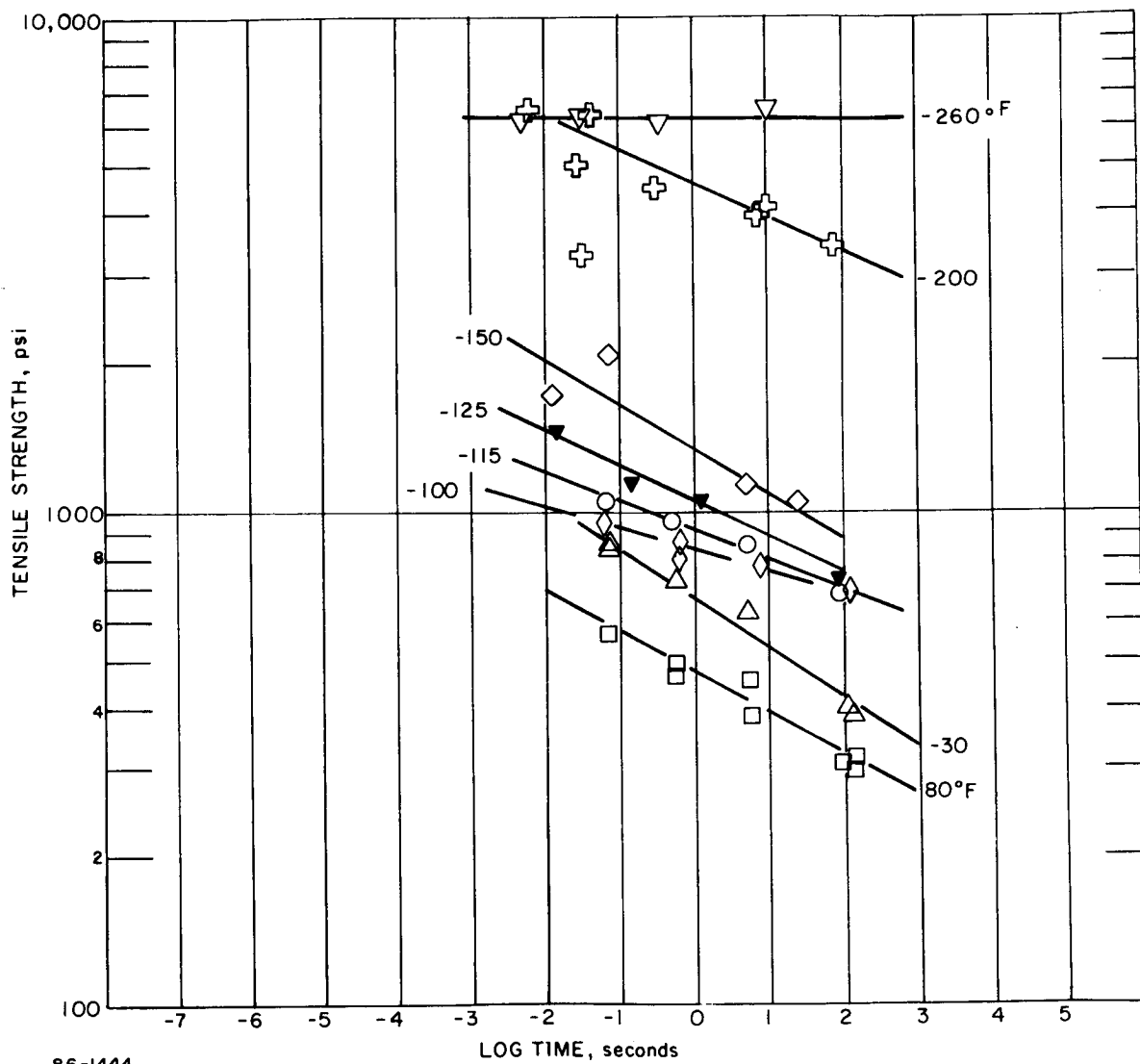
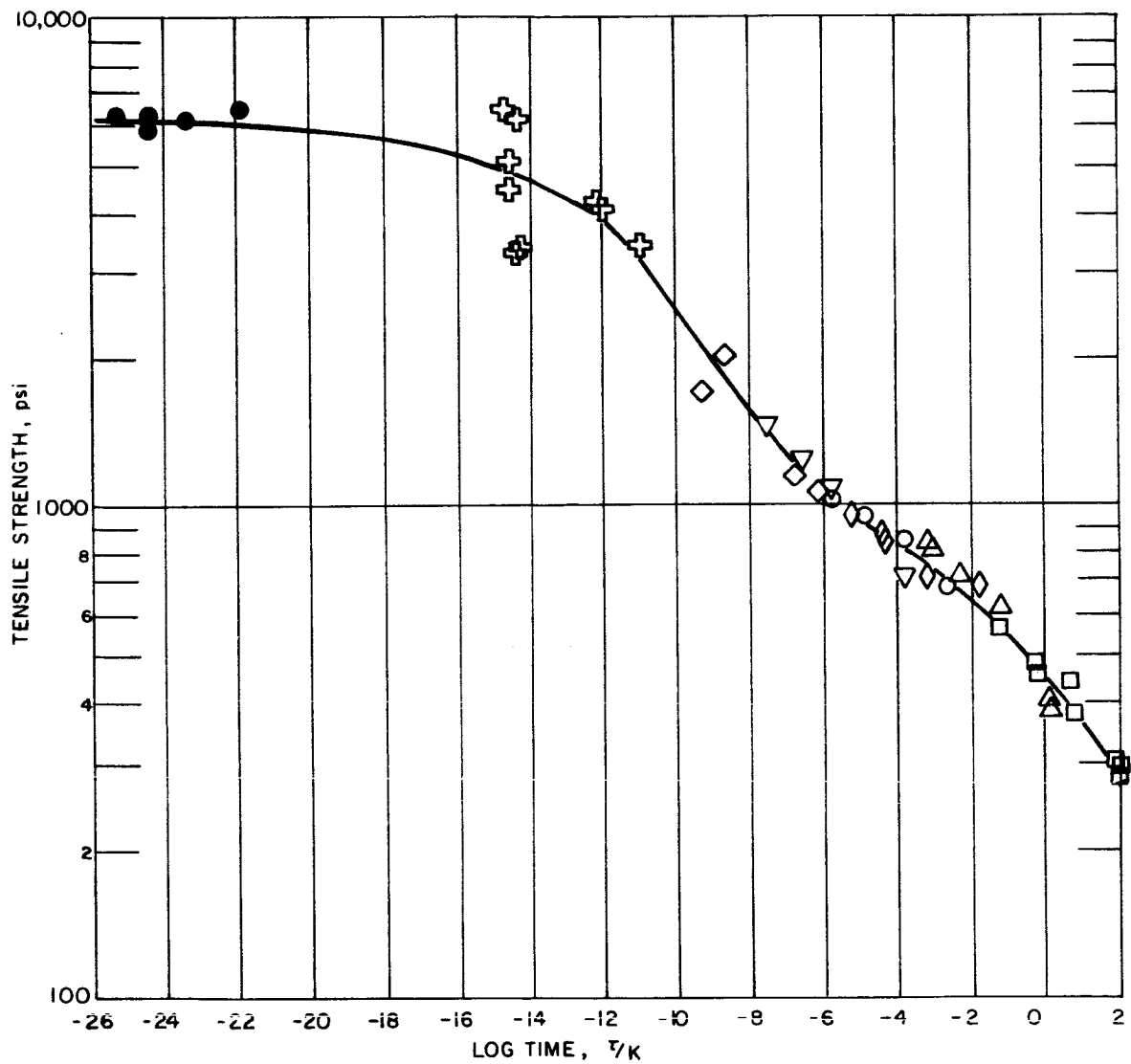


Figure 13 TENSILE STRENGTH OF DC 325 VERSUS TIME AT VARIOUS TEMPERATURES



86-1445

Figure 14 MASTER CURVE OF TENSILE STRENGTH VERSUS REDUCED TIME

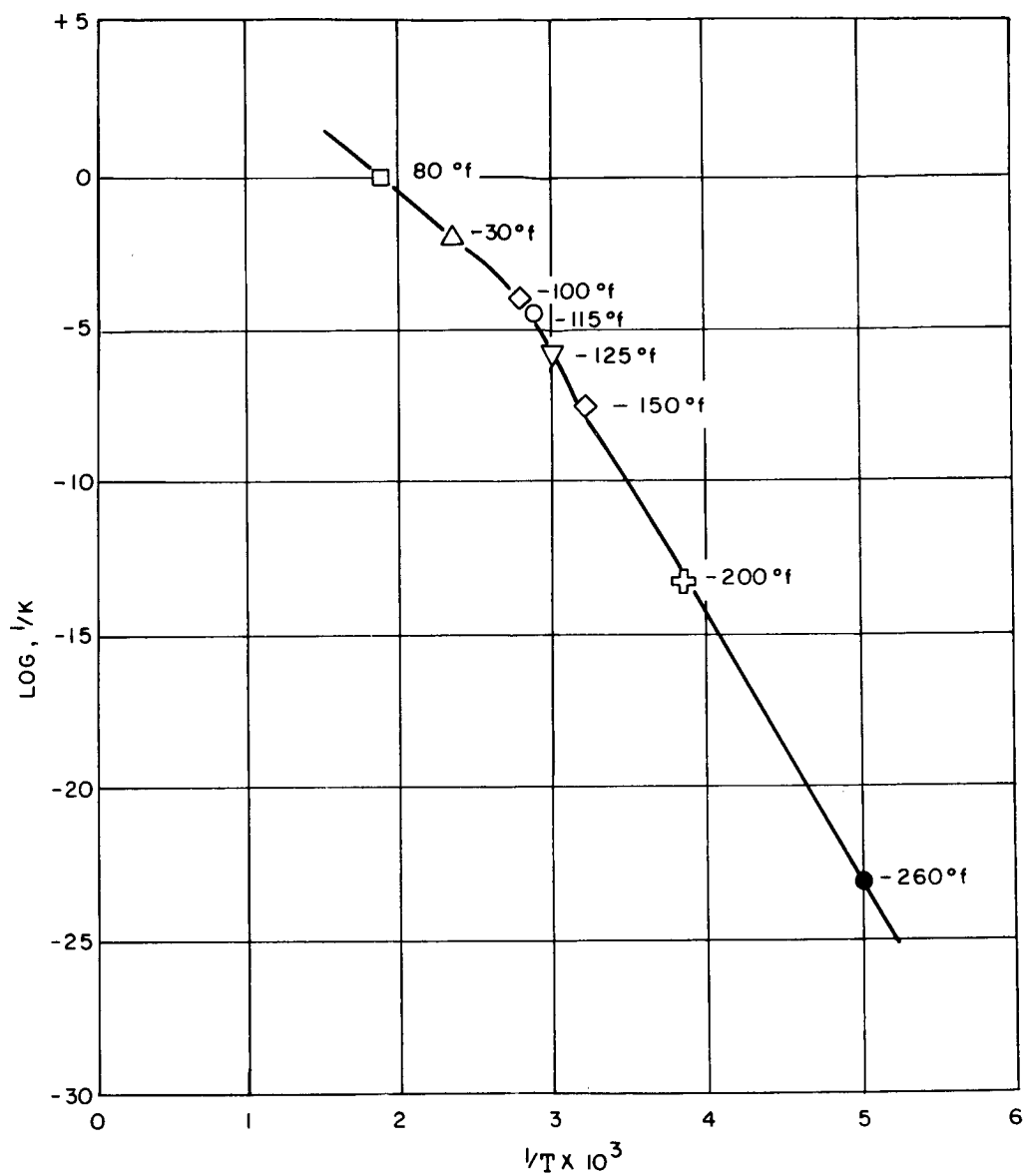


Figure 15 SHIFT FACTORS FOR DC 325 MATERIALS

response in the time scale of 10^{-5} to 10^{-4} . The value of tensile strength is on the order of 900 psi. Referring to Figure 15, we see that the value for $\log (1/k)$ at -150°F is -7.5 . The value of $\log (\tau/k)$ for times in the range of 10^{-5} to 10^{-4} seconds is then -12.5 to -11.5 .

Figure 16 is a log-log plot of tensile strength versus time at 80°F , -150°F , -260°F . The curves drawn through the data points are based on the curve established in the master curve of Figure 14. The curves have been extrapolated into the time range of interest (10^{-5} to 10^{-4} seconds).

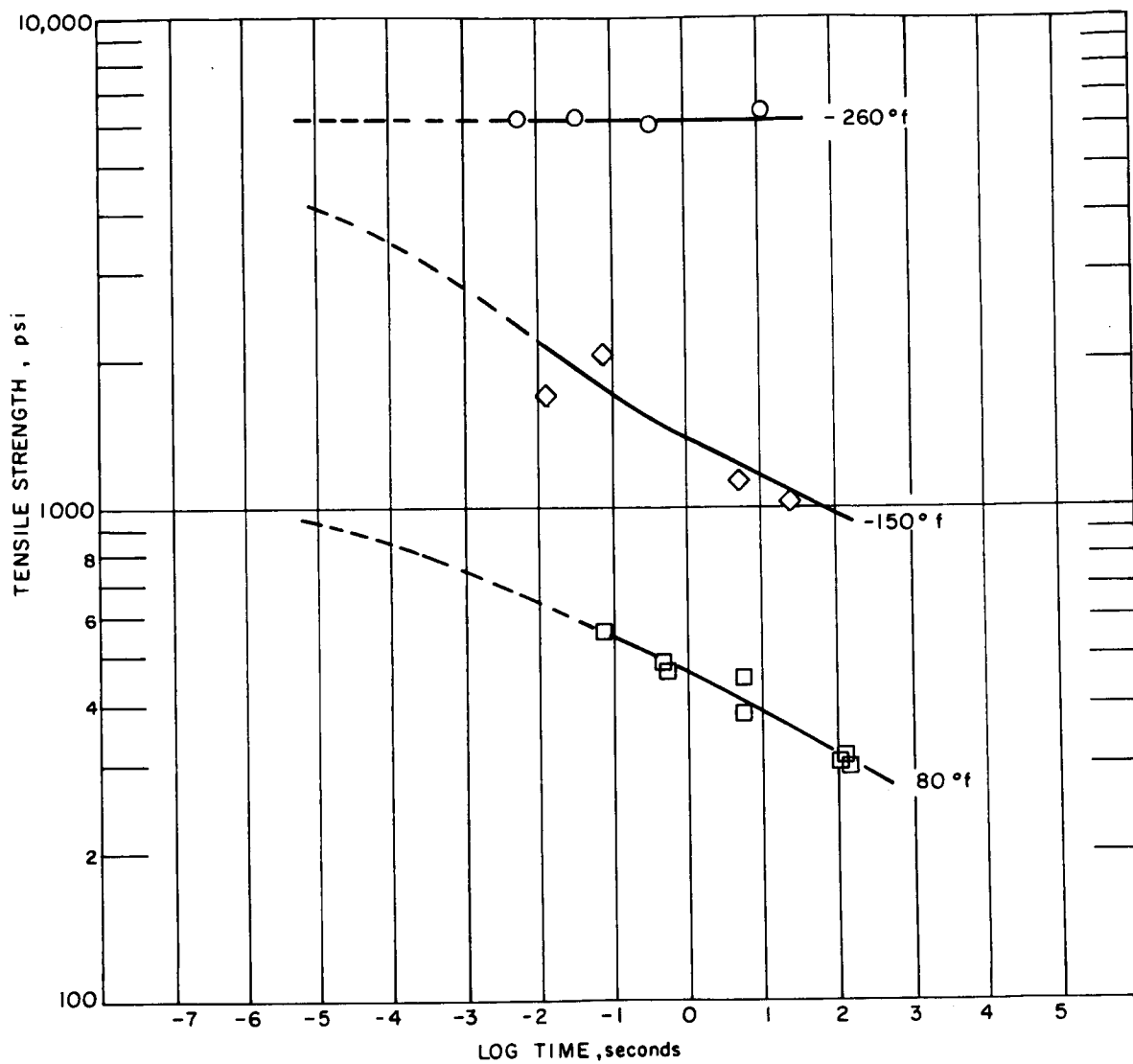
In attempts to obtain tensile data on the Sylgard 325 honeycomb material considerable difficulty was encountered. The main problem was to arrive at a specimen design which would work. No data were obtained on any of the specimens tested.

Compression tests were performed on Sylgard 325 tile materials at various strain rates and temperatures. Very little sense could be made of the data. There was no compression failure at room temperature until bottoming out occurred (i.e., greater than 50 percent compression). There may have been significant size effects.

Compression tests were also performed on the Sylgard 325 honeycomb material. This material failed in compression at fairly moderate strain levels (less than 25 percent) and the mode of failure is probably the buckling of the honeycomb wall. The significance of this failure mode in hypervelocity impact is questionable. The data obtained are tabulated in Table III. Figure 17 is a log-log plot of compressive strength of the Sylgard 325 versus time at various temperatures.

Core shear tests were performed at various loading rates and temperatures on both the Sylgard 325 tile and honeycomb materials. These data are tabulated in Tables IV and V. Figure 18 is a plot of the master curves for both the tile and honeycomb materials (Note: the strength scales are separated). The general shape of the "master" shear strength time curve for the tile material is essentially the same as that observed for the tensile strength. The shear strength of the honeycomb material definitely falls off at the low temperature end. This may be a manifestation of high thermal stresses resulting from the mismatch in thermal expansion coefficients between the fiberglass honeycomb and the Sylgard 325 filler. Based on this observation, one might expect to see delamination of the Sylgard 325 pencils when impacted at temperatures of -200°F and below.

Penetration tests were performed using a 1/16-inch diameter steel pin with a hemispherical head. These tests were performed at various velocities and at temperatures ranging from 80°F to -260°F . Table VI is a tabulation of maximum force required to penetrate the surface of the Sylgard 325 tile material. Figure 19 is the master curve relating penetration force to



86-1447

Figure 16 TENSILE STRENGTH OF DC 325 TILE VERSUS TIME AT VARIOUS TEMPERATURES (EXTRAPOLATED CURVES)

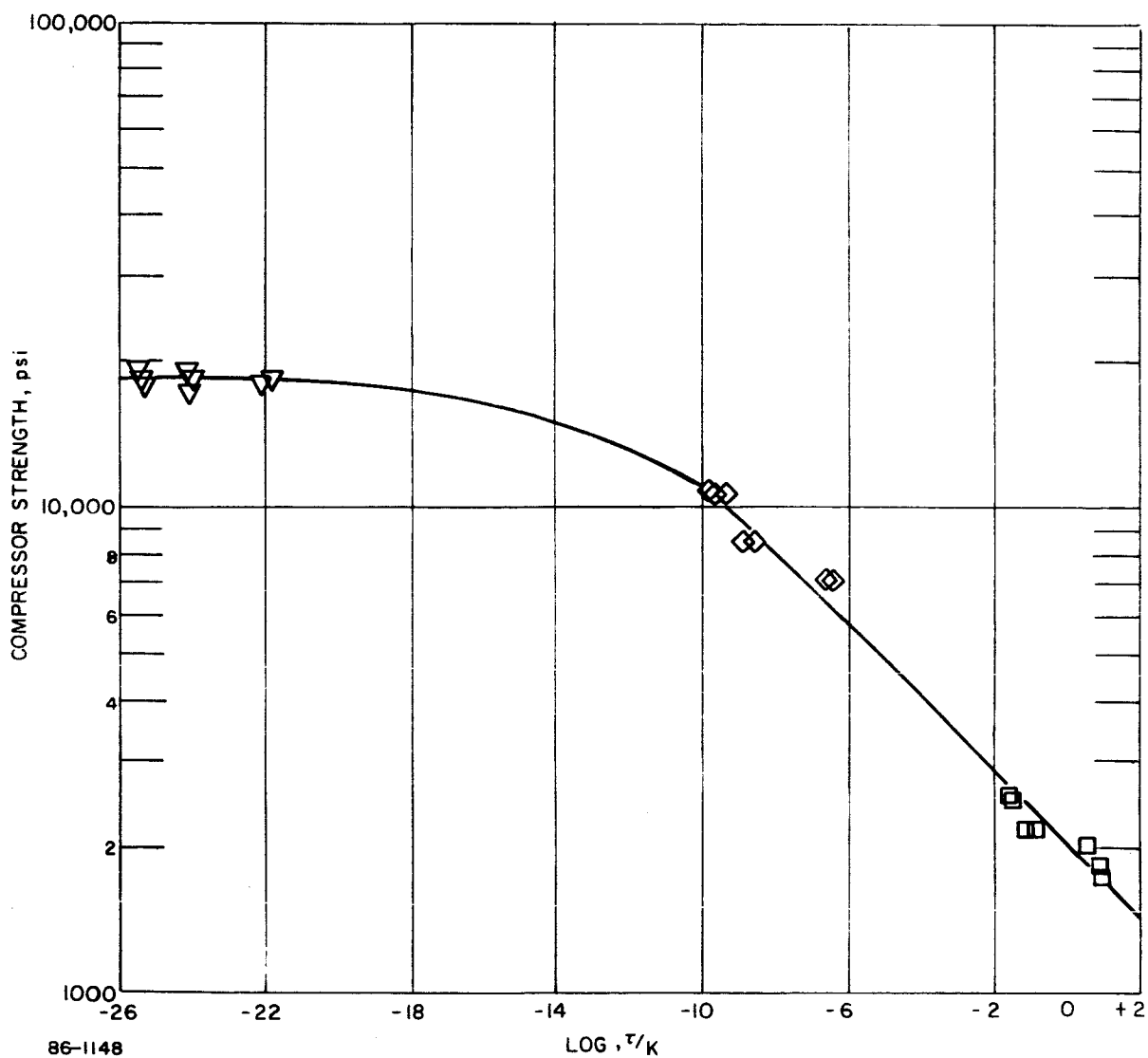


Figure 17 COMPRESSIVE STRENGTH OF DC 325 HONEYCOMB VERSUS TIME
AT VARIOUS TEMPERATURES

TABLE III
COMPRESSION PROPERTIES OF
SYLGARD-325 HONEYCOMB

Specimen No.	Test Temperature (° F)	Total Test Time (Seconds)	Strain Rate	Compression Strength (psi)
36	80	7.0	0.10	1720
18	80	6.4	0.117	1860
33	80	0.080	10.1	2140
19	80	0.086	10.2	2140
30	80	5.9	.21	2000
20	80	0.0014	752	2520
15	80	0.0017	720	2560
12	-150	7.8	0.169	7000
29	-150	8.0	0.180	7000
5	-150	0.145	14.5	8400
28	-150	0.148	14.6	8400
32	-150	0.0038	1050	10600
9	-150	0.0035	1140	10600
17	-150	0.0042	1140	10800
25	-250	18.5	0.116	18,400
D	-250	18.0	0.123	18,400
13	-250	0.195	11.2	19,600
C	-250	0.191	11.5	17,200
22	-250	0.176	11.5	18,000
11	-250	0.187	11.6	18,800
10	-250	0.0056	665	18,600
31	-250	0.0045	665	18,200
2	-250	0.0047	685	19,200

TABLE IV

SHEAR PROPERTIES OF
SYLGARD-325 HONEYCOMB

Test temp. (° F)	Test Time (seconds)	Shear stress (psi)	Test time (seconds)	Shear stress (psi)	Test time (seconds)	Shear stress (psi)	Test time (seconds)	Shear stress (psi)
80	45	420	2.9	490	0.21	500	0.024	500
-30	48	520	2.1	610	0.21	590	0.022	700
-100	35	800	1.9	790	0.22	880	0.018	1070
-115	36	1120	2.0	1420	0.16	1140	0.022	1980
-125	33	1090	1.9	1740	0.15	1270	0.020	1910
-150	37	1810	1.6	1970	0.13	1650	0.012	2140
-200	39	1810	1.2	1380	0.17	2350	0.013	1510
-260	24	810	2.8	1460	0.11	1390	0.012	1090
								560
								730
								1240
								1900
								1810
								2440
								2530
								1540

TABLE V

SHEAR PROPERTIES OF
SYLGARD-325

Test temp. (° F)	Test time (seconds)	Shear stress (psi)	Test time (seconds)	Shear stress (psi)	Test time (seconds)	Shear stress (psi)	Test time (seconds)	Shear stress (psi)
-80	124	250	6.4	320	0.79	370	0.088	440
-30	140	360	6.8	450	0.72	500	0.076	600
-100	114	600	6.8	710	0.72	750	0.076	840
-115	120	1120	5.8	1180	0.61	1360	0.060	1450
-125	136	1190	5.0	1310	0.48	1280	0.050	1560
-150	92	1400	6.4	1470	0.70	1310	0.036	2020
-200	41	3980	1.9	4300	0.23	4530	0.022	4430
-260	50	6340	6.1	6150	0.23	5790	0.026	4980
								500
								660
								1080
								1400
								1740
								2120
								4030
								4860

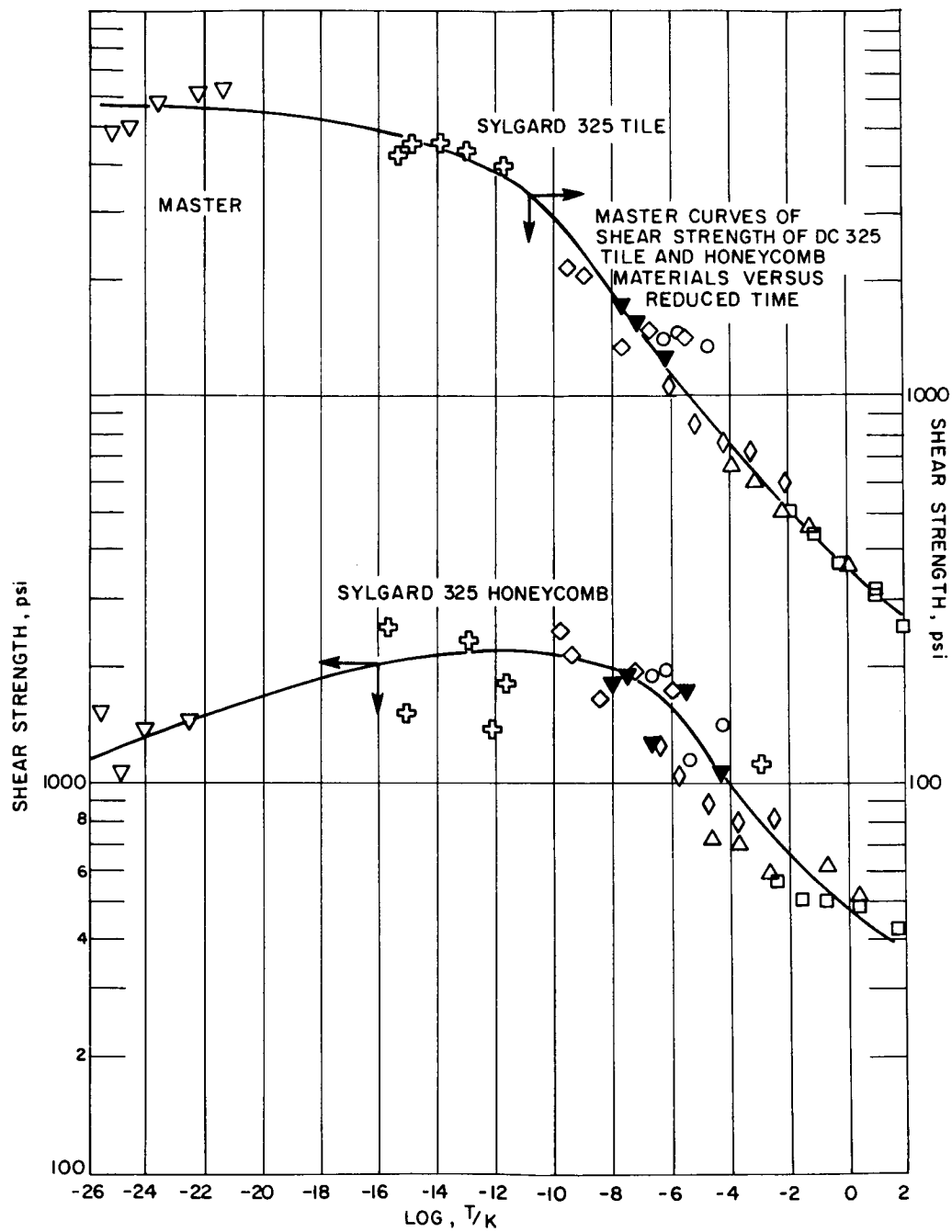
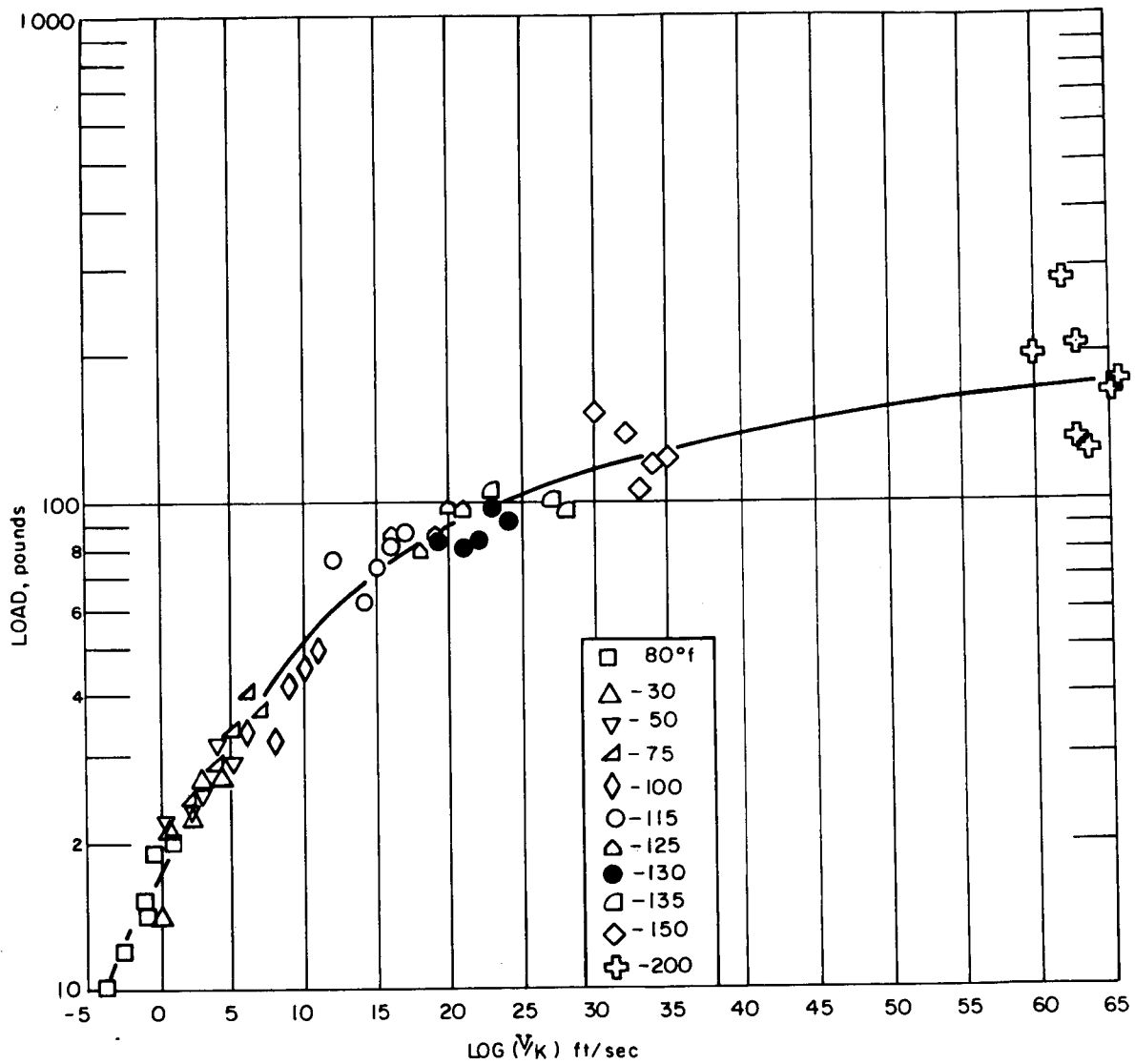


Figure 18 MASTER CURVES OF SHEAR STRENGTH OF DC 325 TILE AND HONEYCOMB MATERIALS VERSUS REDUCED TIME

TABLE VI
PENETRATION FORCE IN
SYLGARD-325 TILE

Velocity	Test Temperature (°F)											
	75	-30	-50	-75	-100	-115	-125	-130	-135	-150	-200	-260
ft/sec												
0.00014	10	14	22	24	34	76	85	84	106	151	200	-
0.00023	-	-	-	-	-	-	-	-	-	-	280	-
0.0038	12	21	23	28	32	62	79	80	-	138	208	-
0.0080	-	-	-	-	-	-	-	-	-	-	132	235
0.017	15	-	-	-	-	-	-	-	-	-	-	-
0.046	14	22	25	34	42	73	85	82	-	105	-	-
0.058	-	-	-	-	-	-	-	-	-	-	128	200
0.46	19	27	32	41	45	81	98	96	101	120	168	-
0.70	-	-	-	-	-	-	-	-	-	-	111	158
6.7	20	27	29	37	48	85	96	91	97	122	141	-



86-1450

Figure 19 MASTER CURVE OF PENETRATION FORCE IN DC 325 TILE
VERSUS REDUCED TIME

velocity. This is a log-log plot of penetration force versus velocity. Using room temperature as the reference temperature the velocity ranges from 10^{-5} to $10^{6.5}$ ft/sec. The "limit" of this extrapolation is obviously ridiculous but in the range of velocities of interest, 10^4 ft/sec, the extrapolation is believed to be quite good. From the master curve in Figure 19, the estimated penetration force at 10^4 ft/sec at room temperature is on the order of 30 pounds, at -150° it is 115 pounds, at -250° it is on the order of 200 pounds.

The test matrix followed in this program was not complete in that not all tests were performed on both the Sylgard 325 tile and honeycomb materials. There was also very little redundancy or replication of tests to determine material variable. However, some general conclusions can be drawn.

First, all the data indicate that the predicted properties in the time or velocity range of interest at -150°F and -260°F are about the same and are quite different than those predicted for room temperature. This appears to agree well with the observed trends in the hypervelocity impact tests.

There would also appear to be little difference between the tile and honeycomb materials except at the low temperatures. Here the honeycomb material appears to be weaker than the tile. This may be the result of residual stresses resulting from differences in thermal expansion coefficients.

4.2.4 Mechanical Properties of Avcoat 5026 Materials

Tensile tests were performed on the Avcoat 5026 tile material at various strain rates and temperatures. These data are tabulated in Table VII, and depicted graphically in Figure 20. As can be seen, all the data are about the same level and the scatter is such that one could not delineate any temperature or rate sensitivity.

The same specimen configuration problem existed with the Avcoat 5026 honeycomb as was experienced with the Sylgard 325 honeycomb. Suitable tensile specimens were obtained for Avcoat 5026 honeycomb material in the plane of the material, though not for the radial direction which was of interest here.

Compression tests were performed at various strain rates and temperatures for both the 5026 tile and honeycomb material. These data are tabulated in Tables VIII and IX. "Master curves" have been constructed of compressive strength versus time for both materials and are shown in Figures 21 and 22. The plot of $\log(1/k)$ versus the reciprocal of the absolute temperature used in the construction of these curves is shown in Figure 23.

TABLE VII
TENSILE PROPERTIES OF
AVCOAT 5026 TILE

Test temp. (° F)	Total test time (seconds)	Ultimate stress (psi)	Test temp. (° F)	Total test time (seconds)	Ultimate stress (psi)
80	0.005	1640	-150	0.004	1470
80	0.004	1460	-150	0.034	1630
80	0.015	1650	-150	0.25	1530
80	0.14	1570	-150	0.31	1490
80	1.9	1410	-150	2.7	1380
80	20.2	1360	-150	21	1650
80	21.6	1450			
-30	0.0057	1530	-200	0.0046	1720
-30	0.005	1650	-200	0.037	1540
-30	0.015	1810	-200	0.045	1540
-30	0.038	1530	-200	0.3	1520
-30	0.044	1670	-200	2.7	1240
-30	0.35	1380	-200	14.2	1180
-30	1.7	1470			
-30	3.0	1540			
-30	16.5	1630			
-30	14.6	1310			
-100	0.0044	1270	-260	0.034	1540
-100	0.040	1580	-260	0.38	1990
-100	0.3	1520	-260	0.34	1700
-100	23	1760	-260	4.0	1560
-100	25	1740	-260	16	1880

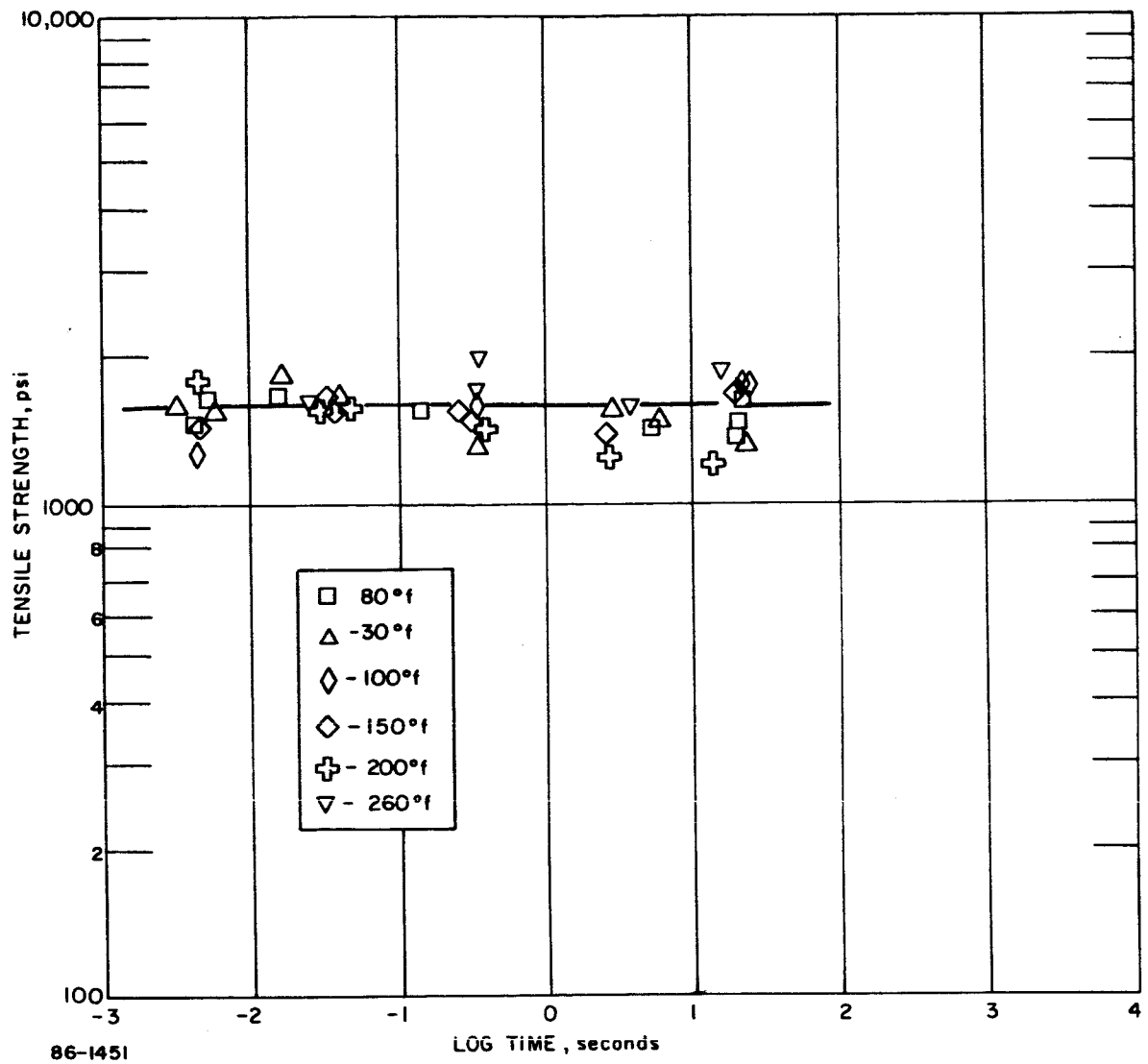


Figure 20 TENSILE STRENGTH OF AVCOAT 5026 TILE VERSUS TIME
AT VARIOUS TEMPERATURES

TABLE VIII

COMPRESSION PROPERTIES OF AVCOAT 5026 TILE

Test temp (°F)	Total test time (seconds)	Compression strength (psi)	Test temp. (°F)	Total test time (seconds)	Compression strength (psi)
80	0.0002	2700	-150	0.0019	3270
80	0.0003	3100	-150	0.033	3340
80	0.0003	2800	-150	0.049	2880
80	0.0022	2300	-150	0.035	3500
80	0.0020	2100	-150	0.045	3200
80	0.0020	2200			
80	0.021	1700	-250	0.0003	4730
80	0.021	1900	-250	0.0002	4600
80	0.022	1700	-250	0.0002	4500
			-250	0.0027	4000
			-250	0.0018	4200
-150	0.0004	5000	-250	0.0021	4400
-150	0.0002	4770	-250	0.0017	4300
-150	0.0005	4100	-250	0.038	4000
-150	0.0001	5140	-250	0.045	4050
-150	0.0040	3670	-250	0.042	4100
-150	0.0049	3600	-250	0.037	4000
-150	0.0035	3670			

TABLE IX

COMPRESSION PROPERTIES OF AVCOAT 5026 HONEYCOMB

Test temp.. (° F)	Total test (seconds)	Comp. strength (psi)	Test temp.. (° F)	Total test (seconds)	Comp. strength (psi)
80	0.0003	3830	-150	0.064	4700
80	0.0003	3800	-150	0.052	5000
80	0.00043	2800	-150	0.048	4700
80	0.012	3200	-150	0.064	4600
80	0.019	3400			
80	0.028	3600	-250	0.0005	6300
80	0.27	3000	-250	0.0007	5300
			-250	0.0004	4900
-150	0.0003	5600	-250	0.0040	6100
-150	0.0004	5100	-250	0.0047	5700
-150	0.0008	4200	-250	0.0020	4500
-150	0.0003	5200	-250	0.0021	5400
-150	0.0044	3700	-250	0.0032	4800
-150	0.0054	4700	-250	0.0033	4700
-150	0.0047	4100	-250	0.054	2900
-150	0.0052	4100	-250	0.048	5700
			-250	0.053	5500
			-250	0.053	5600

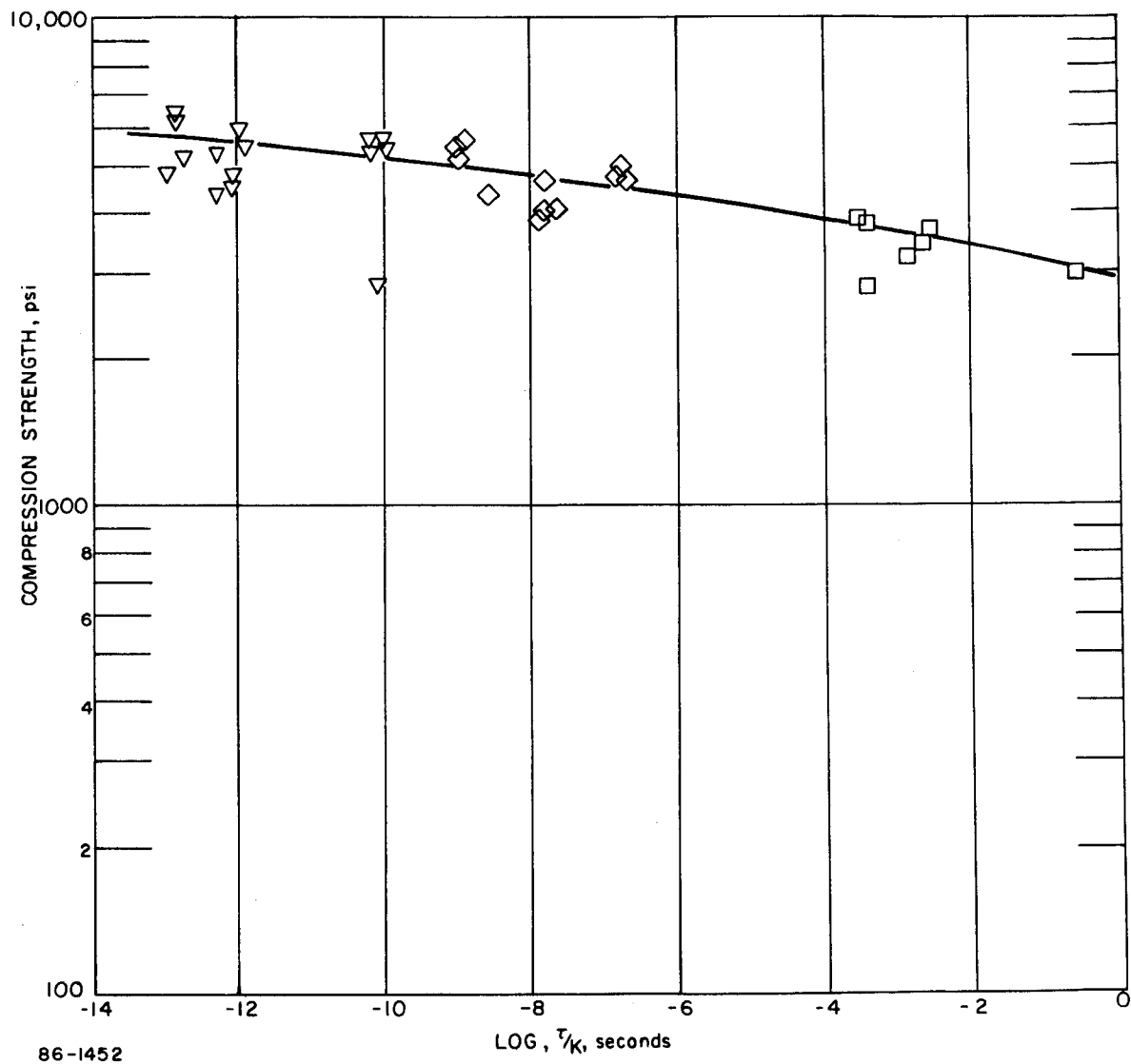


Figure 21 MASTER CURVE OF COMPRESSION STRENGTH OF AVCOAT 5026
TIME VERSUS TIME

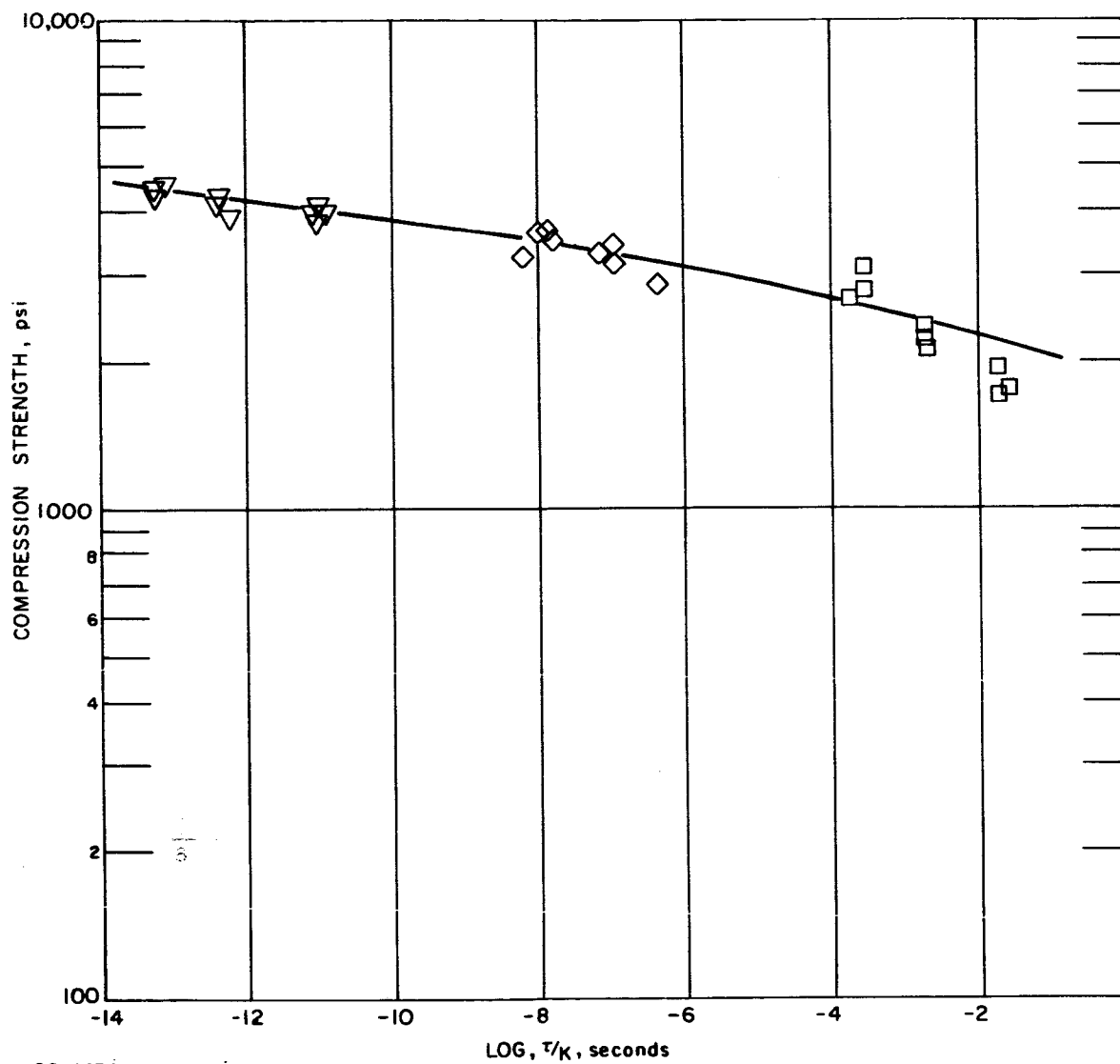
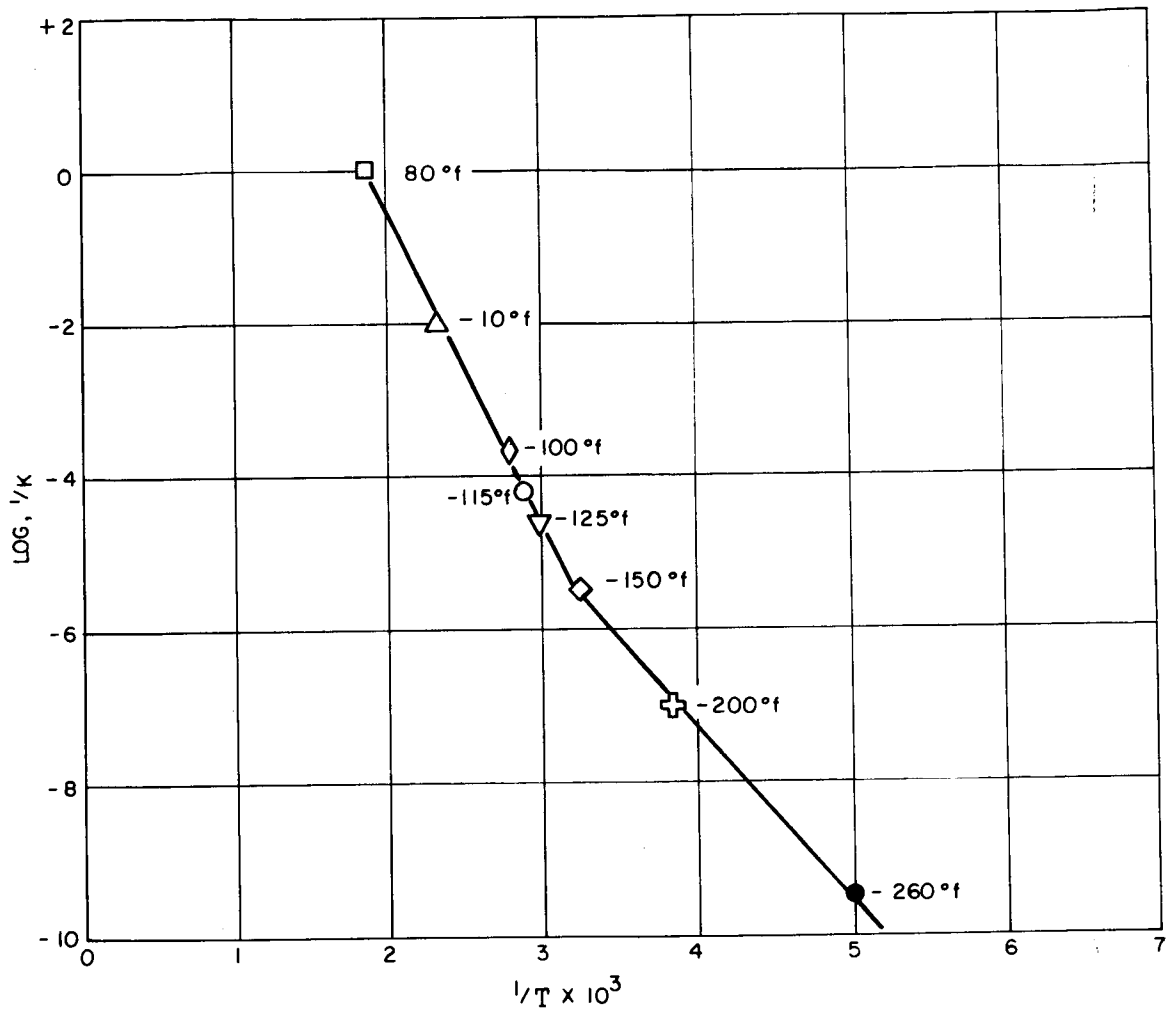


Figure 22 MASTER CURVE OF COMPRESSION STRENGTH OF AVCOAT 5026 HONEYCOMB VERSUS REDUCED TIME



86-1454

Figure 23 SHIFT FACTOR FOR AVCOAT 5026 TILE AND HONEYCOMB MATERIALS

One would expect the honeycomb to measurably increase the compressive strength; however, the compression strength for the two materials do not appear to be significantly different. This would indicate that the Avcoat 5026 filler in the honeycomb is weaker than in the tile. This is borne out in the shear and penetration tests discussed below.

Core shear tests were performed on both the Avcoat 5026 tile and honeycomb materials at various loading rates and temperatures. These data are tabulated in Tables X and XI. The master curves for both materials are shown in Figure 24. Here it is seen that the shear strength of the two materials varies in about the same manner. However, the strength of the tile materials is 2.5 to 3 times as much as the honeycomb material.

The shift factor-temperature relationship used to construct the curves in Figure 24 is the same as that used for the compression data.

Penetration tests similar to those run on the Sylgard 325 were performed on the Avcoat 5026 tile material. These data are tabulated in Table XII. The master curve constructed from these data is shown in Figure 25. For purposes of comparison, some limited data obtained on Avcoat 5026 honeycomb are included (Table XIII). Again it can be seen that the penetration force for the 5026 tile is on the order of 1.5 times that of the honeycomb material.

Both Avcoat 5026 materials exhibited relatively little rate or temperature sensitivity. One would expect, therefore, that temperature would not play a significant role in hypervelocity damage level. However, a comparison of the properties of the tile and honeycomb materials indicates that the honeycomb material is weaker. One would expect that the honeycomb itself is contributing to the strength of the composite. This, in turn, indicates that the pencils of 5026 within the honeycomb are even weaker than the measured properties indicated. Carrying this to the next step, one would expect that the damage due to hypervelocity impact would be higher than the measured differences in properties would indicate.

4.3 THERMAL PROPERTIES

The "guarded hot plate" technique of determining thermal conductivity, an ASTM-accepted test, was used for the measurements in this study.

The test can be best described by reference to Figure 26. The apparatus in the figure is identified as the "G" apparatus and illustrates general technique. With this type of apparatus, the heat flow proceeds from both faces of the disc-shaped main heater axially through two specimens on opposite sides to the cooler plates. The main heater, which also serves as a calorimeter, is the central element of the heater-specimen-cooler arrangement. The thermal conductivity is calculated from the measurement of main heater input "q", the specimen face area A, the length of path of heat flow (thickness) L, and the

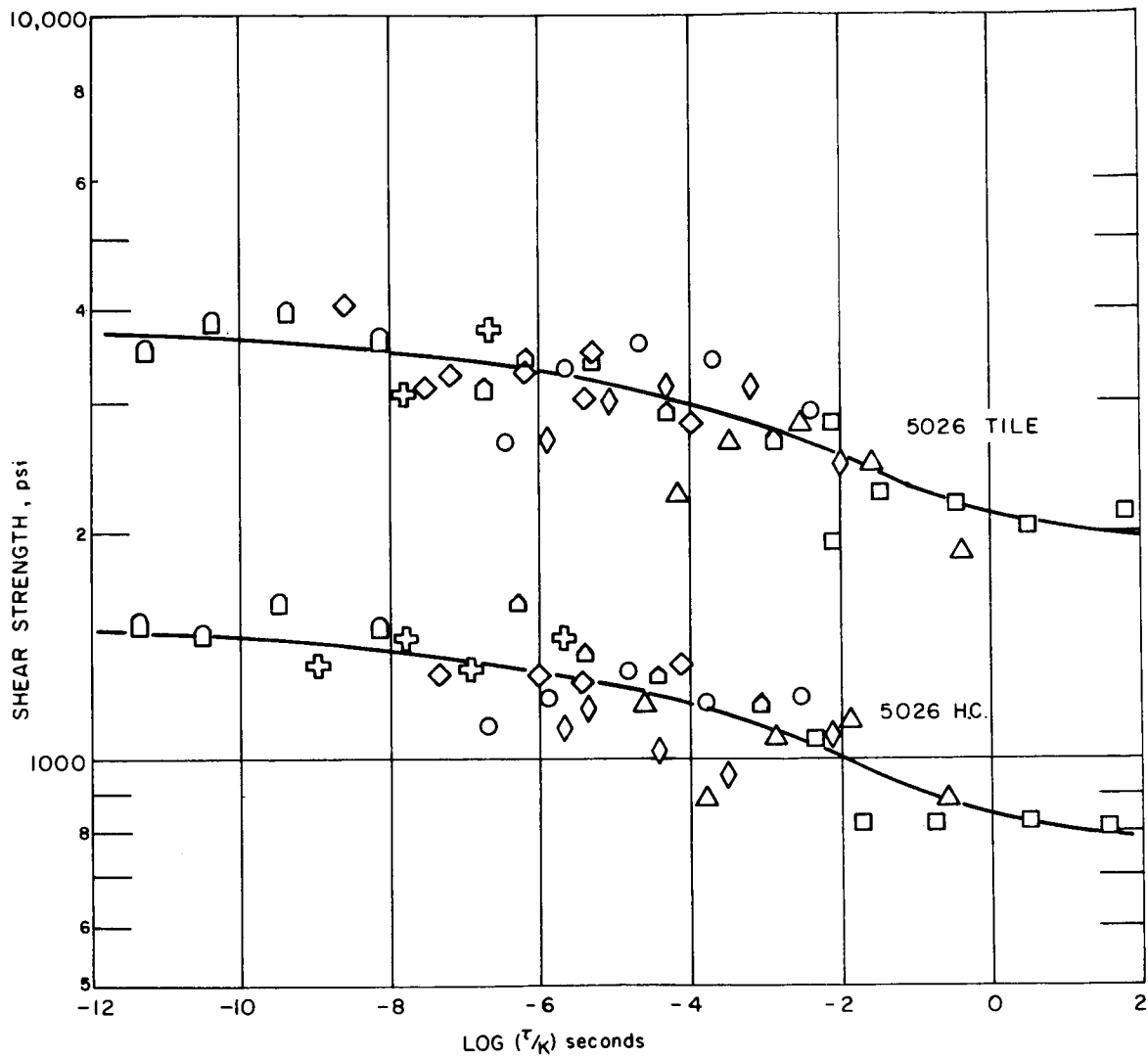
TABLE X

SHEAR PROPERTIES OF AVCOAT 5026 TILE

Test temp. (°F)	Test Time (seconds)	Shear stress (psi)	Test Time (seconds)	Shear stress (psi)	Test Time (seconds)	Shear stress (psi)	Test Time (seconds)	Shear stress (psi)	Test Time (seconds)	Shear stress (psi)
75	60	2110	3.0	2010	0.35	2200			0.0080	2810
-30	52	1880	2.8	2470	0.29	2830	0.032	2270	0.0064	1950
-100	44	2490	2.8	3140	0.26	3140	0.030	2640	0.0064	2260
-115	64	2950	2.9	3450	0.30	3620	0.032	3000	0.0057	2660
-125	46	2670	2.0	2900	0.22	3390	0.033	3340	0.0054	2660
-150	33	2810	1.6	3460	0.20	3390	0.023	3480	0.0070	3080
-200	38	3030	1.9	3710	0.16	3080	0.021	3280	0.0065	3120
-260	35	3580	1.8	3940	0.16	3810	0.24	4050	0.0085	3620
							0.020	3440	0.0075	3170

TABLE XI
SHEAR PROPERTIES OF AVCOAT 5026 HONEYCOMB

Test temp. (°F)	Test Time (seconds)	Shear Stress (psi)	Test Time (seconds)	Shear Stress (psi)	Test Time (seconds)	Shear Stress (psi)	Test Time (seconds)	Shear Stress (psi)
75	45	810	3.0	830	0.155	810	0.017	820
-30	31	870	1.7	1110	0.170	1040	0.016	880
-100	28	1080	1.2	950	0.140	1030	0.016	1150
-115	33	1210	1.9	1190	0.210	1310	0.0175	1200
-125	36	1180	1.5	1270	0.150	1380	0.017	1610
-150	25	1360	1.1	1270	0.270	1290	0.014	1290
-200	23	1470	1.2	1310	0.160	1450	0.011	1330
-260	27	1470	1.3	1600	0.110	1450	0.015	1590
								1120
								1150
								1250
								1180
								1360
								1290
								1630
								1360



86-1455

Figure 24 MASTER CURVE OF SHEAR STRENGTH OF AVCOAT 5026 TILE AND HONEYCOMB VERSUS REDUCED TIME

TABLE XII

PENETRATION TEST, AVCOAT 5026 TILE

Velocity	Test Temperature (°F)							
Ft/sec	75	-30	-100	-115	-125	-150	-200	-260
0.0002	--	76	100	101	110	110	136	139
0.00023	49 53	--	---	---	---	---	---	---
0.0044	--	80	98	103	101	110	122	153
0.0080	54	--	--	---	---	---	---	---
0.045	--	79	100	105	109	112	115 122	148
0.058	65	--	---	---	---	---	---	---
0.44	--	86	99	107	100	112	120	143
0.7	68	--	--	---	---	---	---	---

TABLE XIII

PENETRATION TEST, AVCOAT 5026 HONEYCOMB

Velocity	Test Temperature (°F)	
Ft/sec	80	-150
0.0013	--	66
0.0013	--	63
0.0018	33	--
0.0018	33	--
0.032	--	65
0.032	--	61
0.045	35	--
0.045	35	--
0.8	34	64
0.8	44	57
0.8	37	--
9.5	34	5.5
9.5	37	5.5

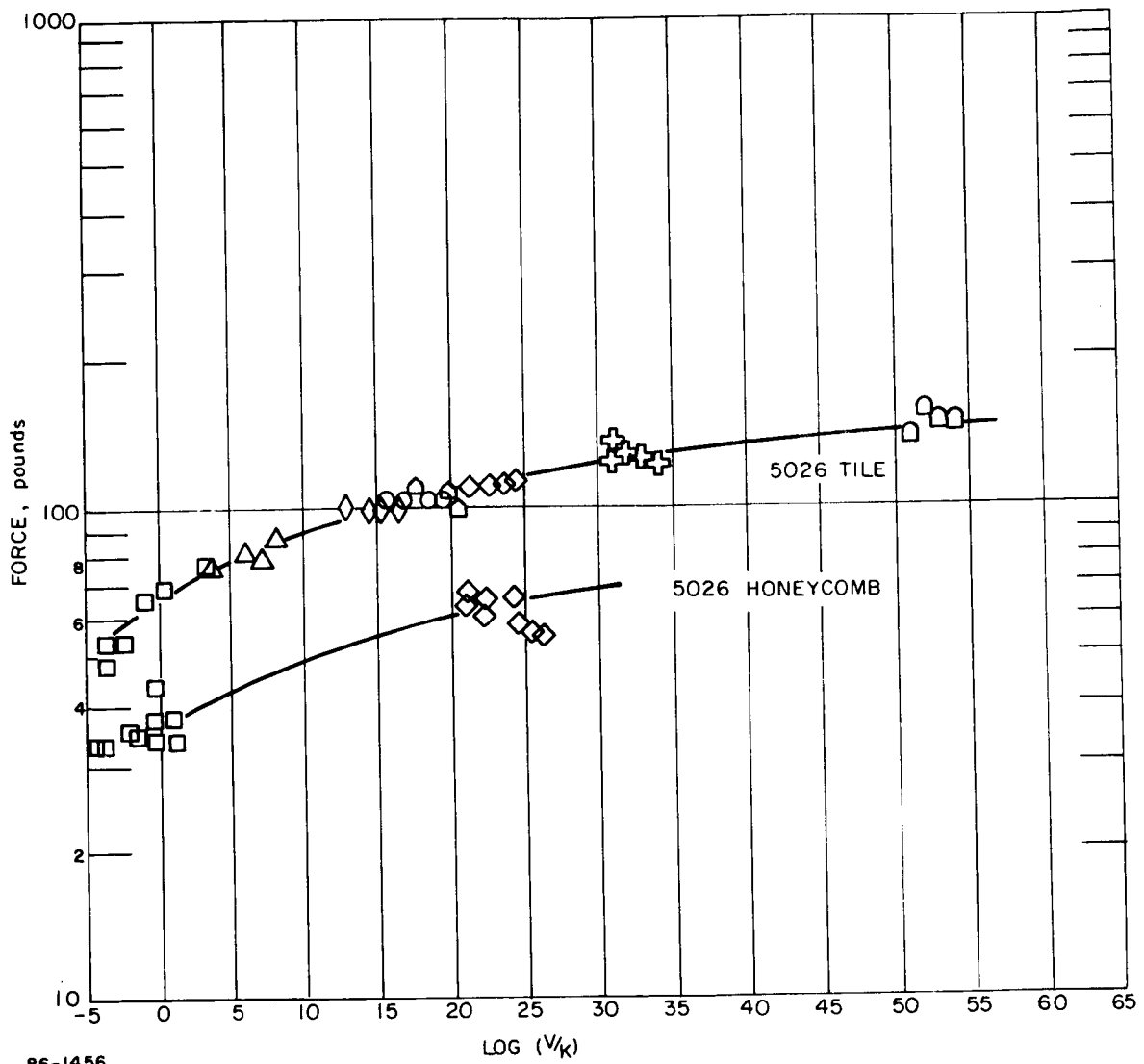


Figure 25 MASTER CURVE OF PENETRATION FORCE IN AVCOAT 5026 TILE AND HONEYCOMB VERSUS REDUCED VELOCITY

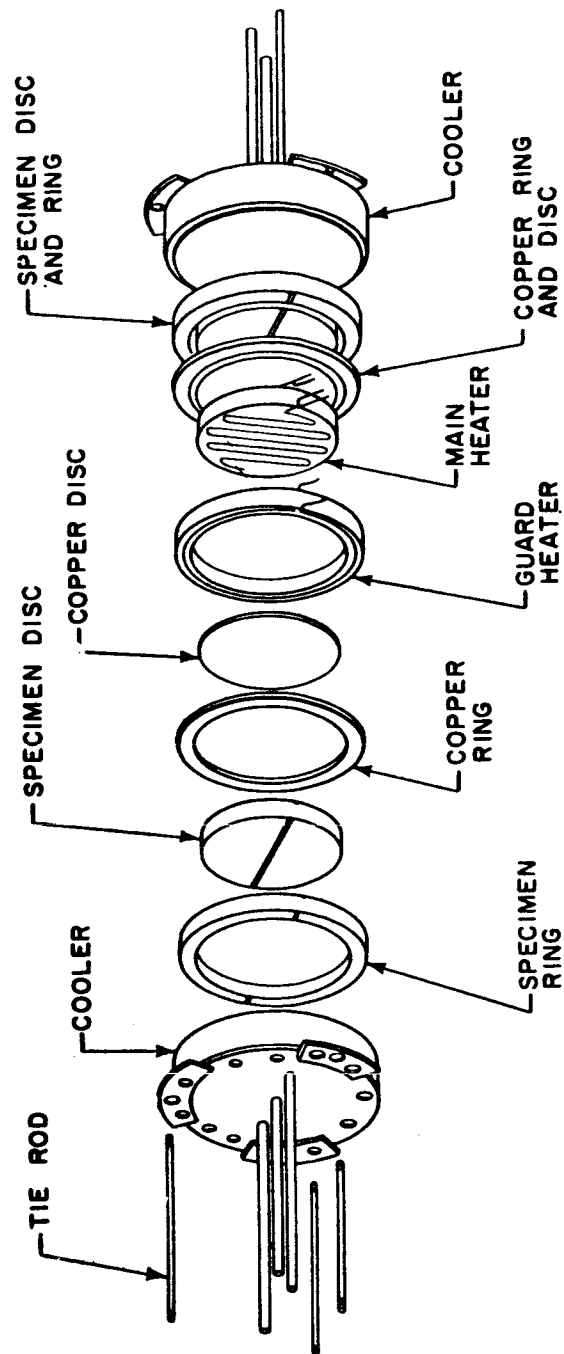


Figure 26 SCHEMATIC OF THERMAL CONDUCTIVITY APPARATUS

61-2020

temperature drop across the specimen ($t_1 - t_2$, where t_1 = hot surface temperature and t_2 = cold surface temperature). The relationship used is

$$K = \frac{qL}{A(t_1 - t_2)}$$

Common to the several designs used at Avco is the provision of a flat, ring-shaped guard heater encircling the main heater and of the same thickness as the heater. Radial heat flow from the main heater is minimized by adjusting the guard heater input for a minimum temperature difference between these two heaters as monitored by a differential thermocouple bridging the gap between them.

At least three determinations (4 preferably) are made on each specimen at mean temperatures within the practical operating limits of the material. For any test, the temperature difference across the specimen is not less than 40° F.

The heating element of the central heater is supplied with electrical energy regulated to give the desired temperature gradient through the specimen and held constant within ± 1 percent.

The cooling units are so adjusted that the temperature drops through the two test specimens do not differ by more than 1 percent.

After steady state has been reached, the test continues with the necessary observations being made to determine temperature difference, center-to-guard balance, and heat input with successive observations made over a period of 3 hours. Thermal conductivity values that are constant to within 3 percent were obtained by use of the technique described above.

With the exception of actual sample loading and final calculations, the entire process is automatically controlled at all temperature levels.

The guarded hot-plate technique has been extended to low-temperature measurements by means of a relatively minor modification of the test apparatus described previously. The auxiliary heater-cooler arrangement was replaced with a constant-level, low-temperature liquid reservoir. The apparatus for low-temperature measurements is shown schematically in Figure 27. The change provides a refractory guarded hot plate to a metal face guarded hot plate with modified cooler assemblies. For low-temperature tests, the faces of the specimens were instrumented. Thin insulating mats were interposed between the heater plates and the specimens to electrically insulate the thermocouples and assist in obtaining the desired temperature differential across the specimen. A variety of cooling fluids were used in the end-plate reservoirs and the electrical power to the main heater to provide incremental thermal conductivity measurements from a -250° F temperature to room temperature.

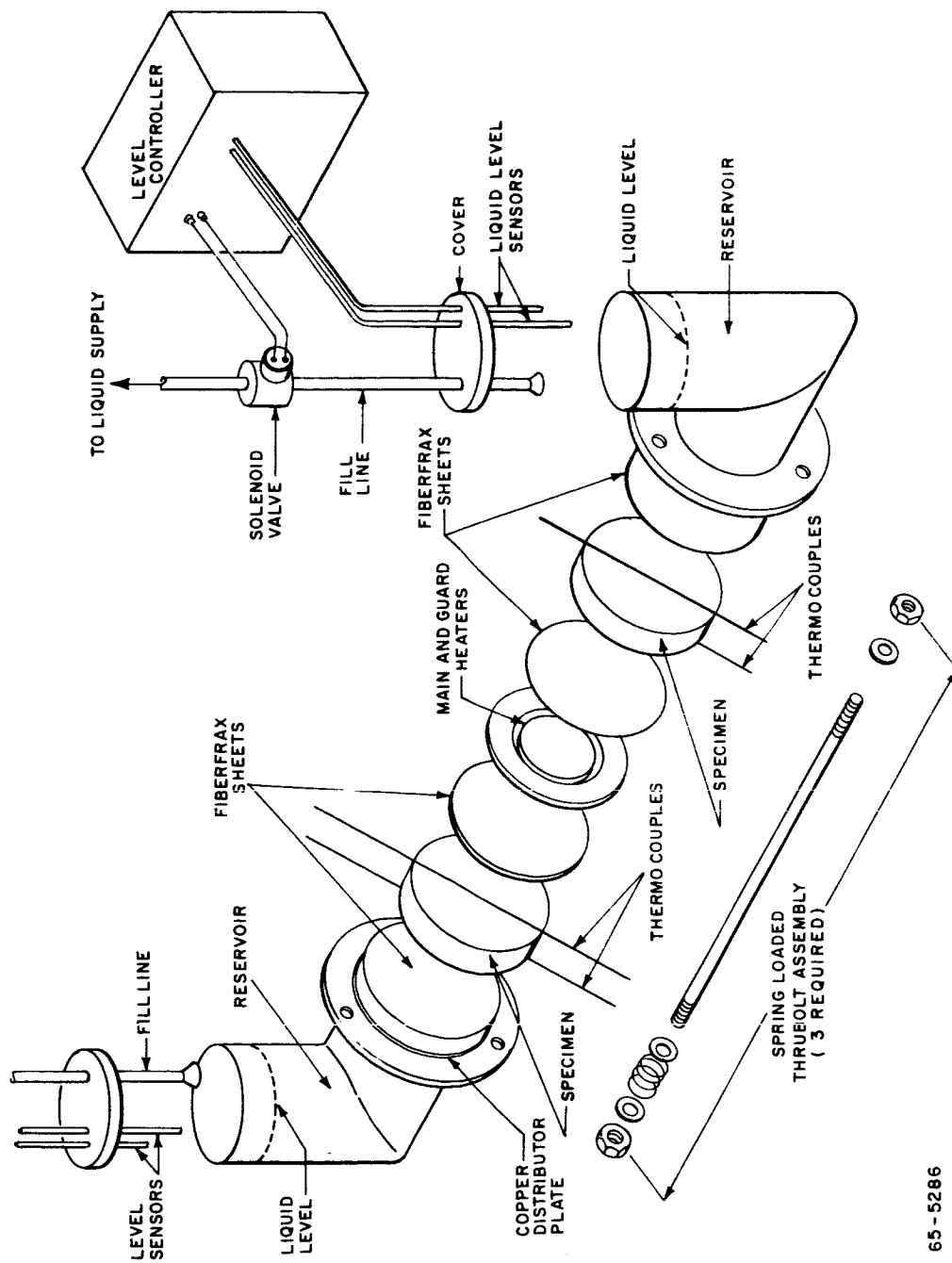


Figure 27 SCHEMATIC OF ARRANGEMENT OF SEMI-AUTOMATIC LOW TEMPERATURE GUARDED HOT PLATE

65-5286

In a procedure similar to that used in the automatic guarded hot-plate control system, the radial heat transfer was monitored and automatically controlled to assure unidirectional heat flow.

For measurement at the very low mean temperatures, liquid nitrogen was used in the cooling reservoirs. To insure a uniform temperature distribution over the cold plate face it is required that the horizontal portion of the reservoir be completely filled at all times. To accomplish this requirement automatically, two controllers were used to maintain a constant level. The level controllers consist of two thermistors located at vertical positions. The thermistor signals are used to maintain the fluid level at the thermistor separation by operating through a controller, a solenoid valve which supplies a cooling liquid supply from reservoirs or tanks.

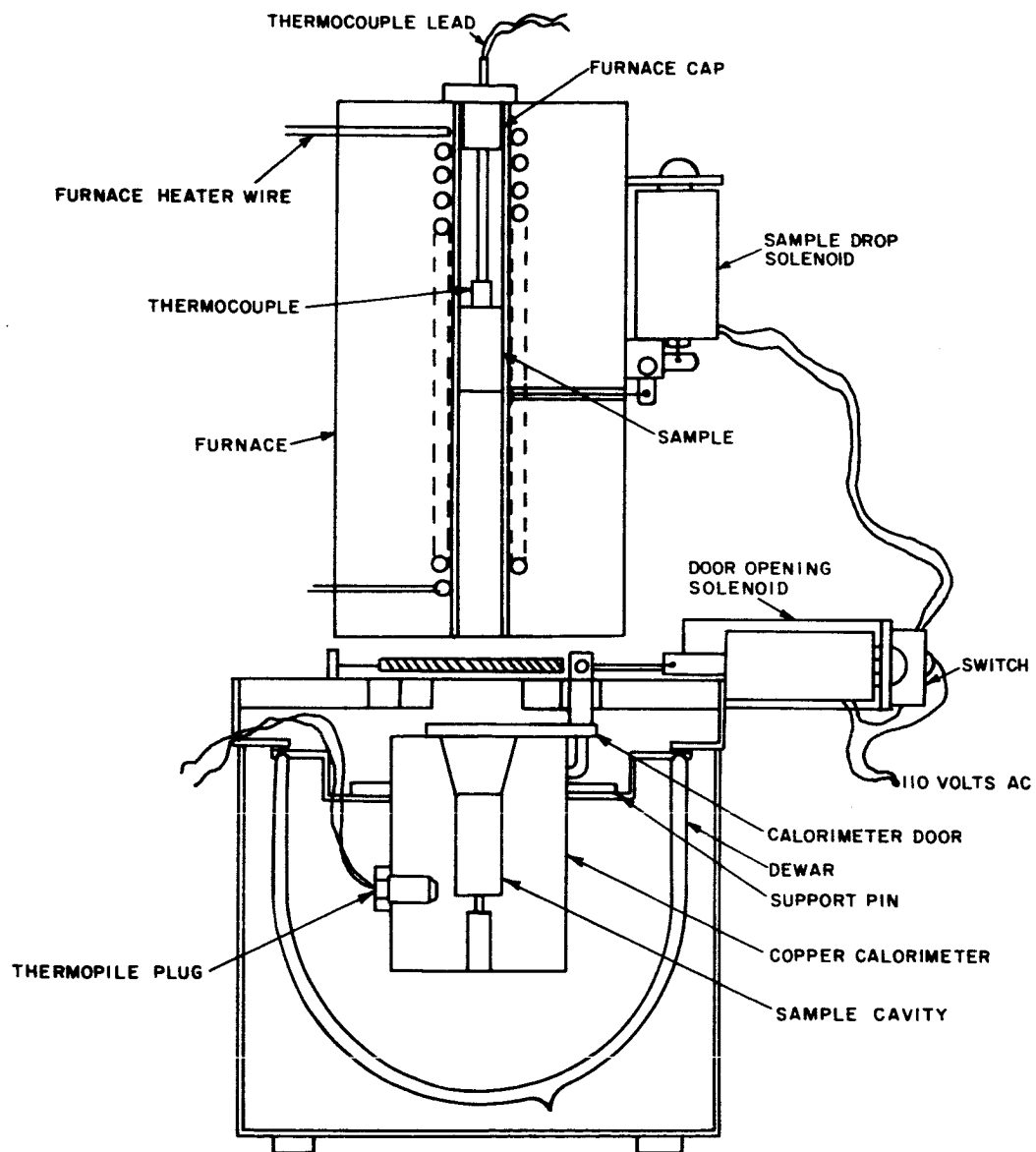
Intermediate data points were obtained by using liquid-solid combinations, such as alcohol and dry ice or crushed ice and water. The use of various cooling fluids and combinations was chosen rather than using one fluid and increasing the heater power. This technique provides small temperature increments and avoids the necessity of forcing excessive temperature gradients in order to obtain several mean temperature levels.

The method of mixtures is used in measuring specific heat. In this method, as the experiment is usually performed, a sample of the material under investigation is heated or supercooled and then lowered into a vessel of water or copper. A copper vessel was selected, since it provides repeatable data and avoids the need for frequent corrections due to losses associated with the use of water. The heat lost or gained by the specimen is set equal to the heat lost or gained by the rest of the system. If the unknown quantity in the heat balance is the specific heat of the specimen, c_p , this may readily be obtained.

The experimental arrangement is illustrated in Figure 28. If, for example, a specimen at the temperature of the furnace t_f is lowered into a copper slug which is equipped with a temperature-measuring device, the temperature of the copper and its contents rises from an initial temperature t_i to a final temperature t_f . From a heat balance, the equation

$$C_{PX} (t_f - t_F) = (C_{PC} + C_{PT}) (t_F - T_I)$$

is obtained, in which C signifies thermal capacity and the subscripts X , C , and T , refer to the specimen, copper, and temperature device, respectively. A calibration check is obtained by measuring the specific heat of synthetic sapphire at regular periodic intervals. Synthetic sapphire is used for calibration on the basis of NBS recommendations. It is well suited as a standard for the calibration of calorimeters.



65-5427

Figure 28 SCHEMATIC OF FURNACE CALORIMETER SPECIFIC HEAT SET

Modification of the illustrated apparatus allows specific heat measurements to be made at low temperatures. This modification involves replacing the furnace assembly with a cryogenic container from which the supercooled sample is lowered.

For a nonuniform rise, graphical methods may be used. Where most Avco measurements concern insulating materials the first condition is most prevalent. In this case, the procedure justification is based upon Newton's law of cooling which states that if the difference in temperature is not large, the rate of cooling of a body is proportional to the difference in temperature between the body and its surrounding. Multiplication of any given time interval by the corresponding rate of cooling gives the temperature loss during the interval.

It is estimated that the methods using this procedure have an accuracy of ± 8 percent; with extra precaution, the accuracy can be improved to ± 4 percent.

Thermal conductivity of both of the Sylgard and Avcoat materials were measured at temperatures of 250, -150 and -250°F. Plots of thermal conductivity versus temperature are presented in Figures 29 and 30.

Enthalpy-temperature curves were determined on all four target materials over the temperature range from 250°F to -250°F. The resulting enthalpy-temperature curves are shown in Figures 31 and 32.

4.4 PROPERTIES OF PROJECTILES

The mechanical and thermal properties of the aluminum and Delrin projectiles are presented in Table XIV. These data were obtained from vendor handbooks.

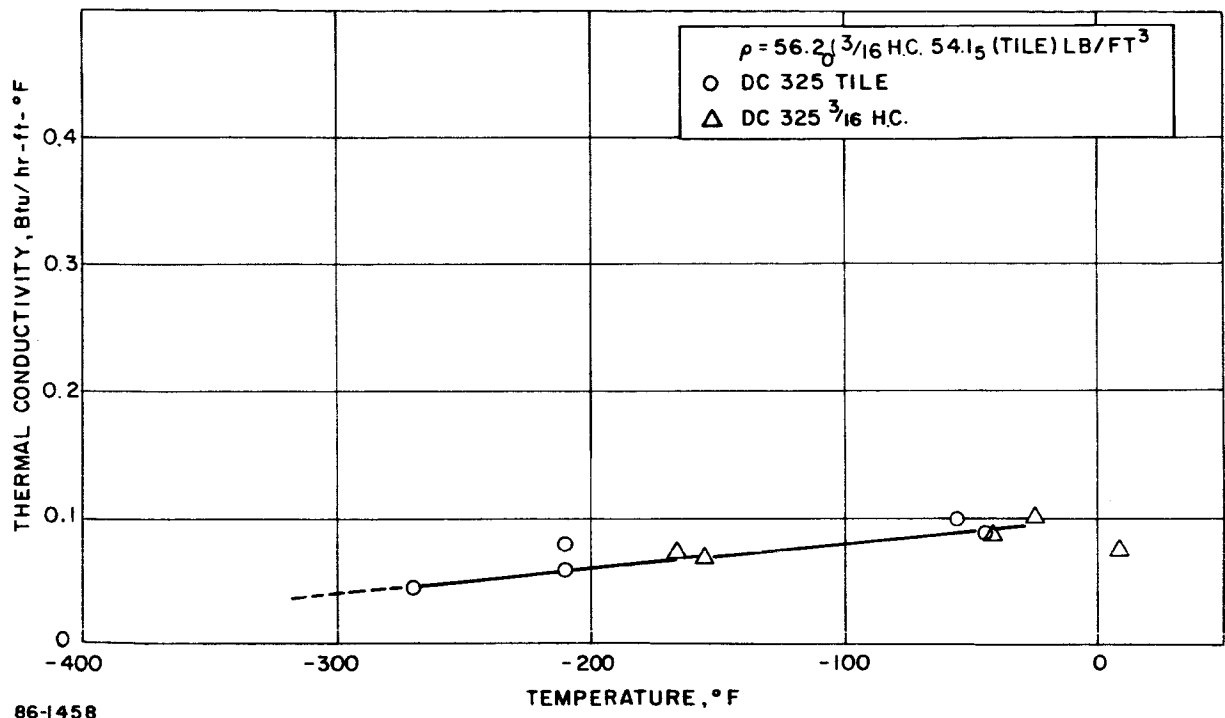


Figure 29 THERMAL CONDUCTIVITY OF DC 325 MATERIALS VERSUS TEMPERATURES

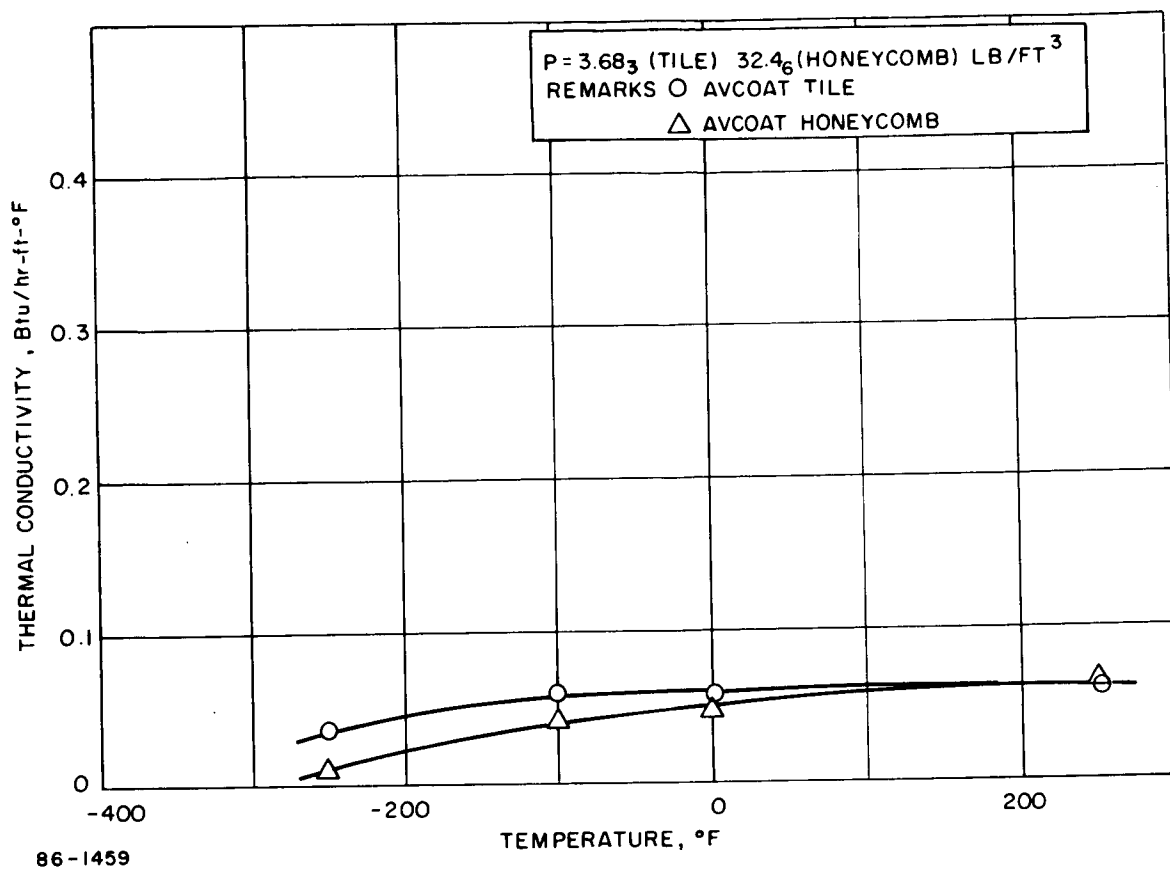
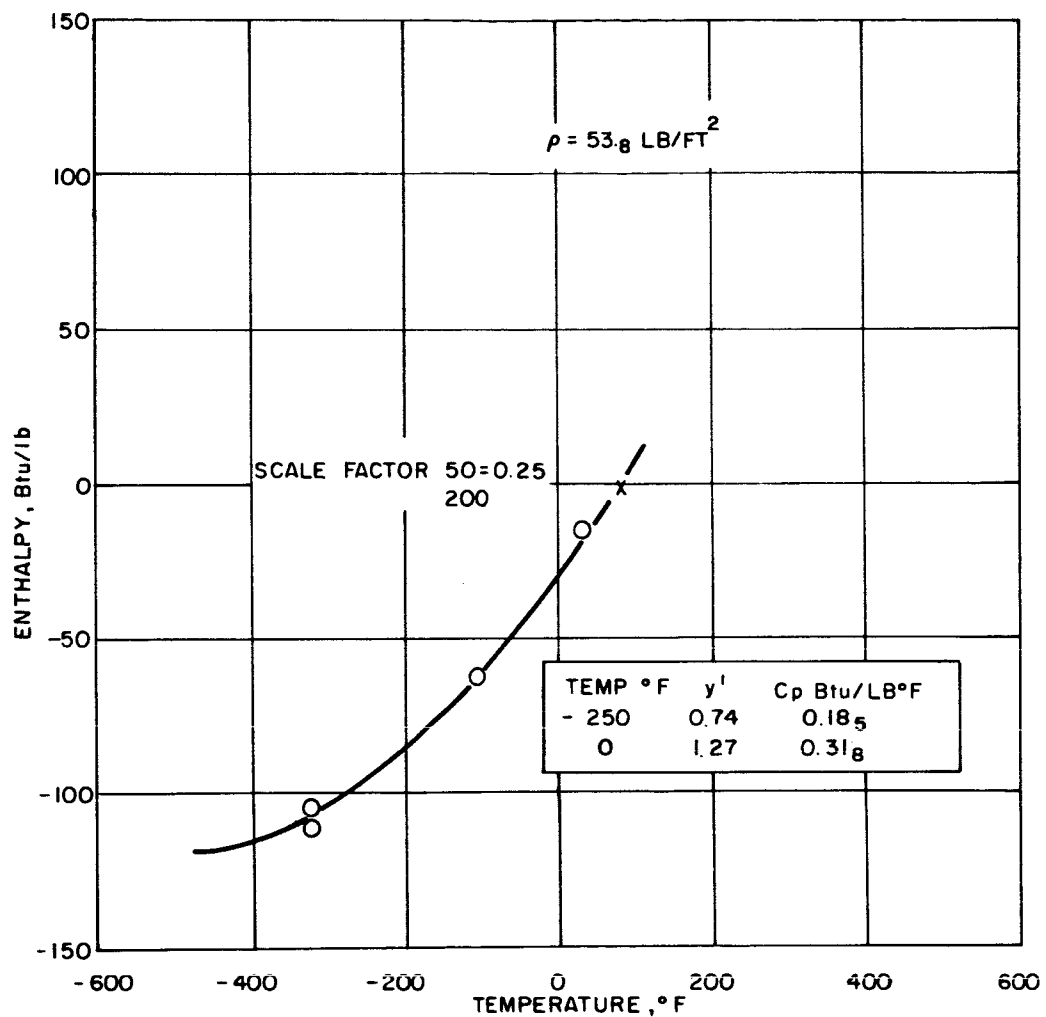
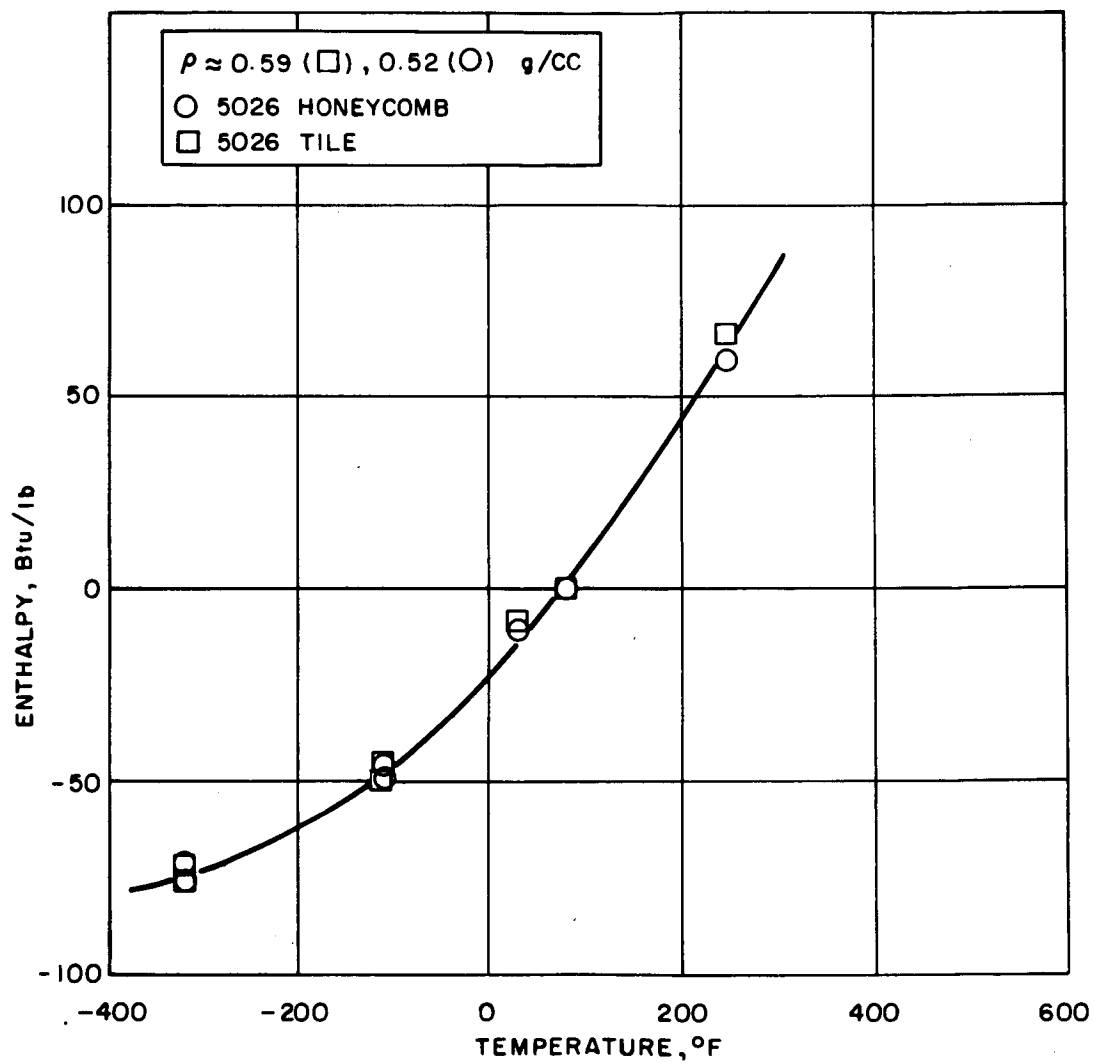


Figure 30 THERMAL CONDUCTIVITY OF AVCOAT 5026 MATERIALS
VERSUS TEMPERATURE



86-1460

Figure 31 ENTHALPY-TEMPERATURE CURVES FOR DC 325 MATERIALS



86-1461

Figure 32 ENTHALPY-TEMPERATURE CURVES FOR AVCOAT 5026 MATERIALS

TABLE XIV
PROPERTIES OF ALUMINUM AND DELRIN PROJECTILES

Material	Tensile Strength (psi)	Total Strain (1/1)	Compression Strength (psi)	Shear Strength (psi)	Poisson's Ratio	Specific Heat (Btu/lb/°F)	Thermal Conductivity (Btu/hr/sq. ft/°F)	Melting Point (°F)	Density (9 ms/cc)
2017-T4 Aluminum	62,000	0.23	---	38,000	0.27	0.22	99.4	955	2.79
Delrin	10,000	----	18,000	9500	0.35	0.405	0.182	347	1.43

5.0 IMPACT TEST RESULTS AND ANALYSIS

5.1 INTRODUCTION

The data for this program are given in the appendixes. The data are tabulated in Appendix C. Linear plots of the data versus velocity, momentum and energy are given in Appendixes D, E and F, respectively.

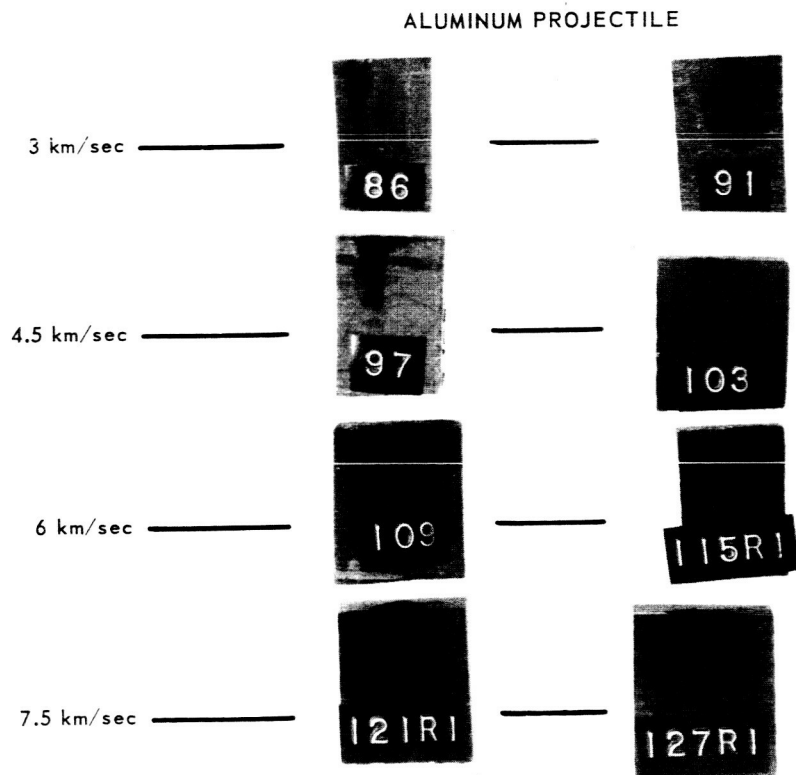
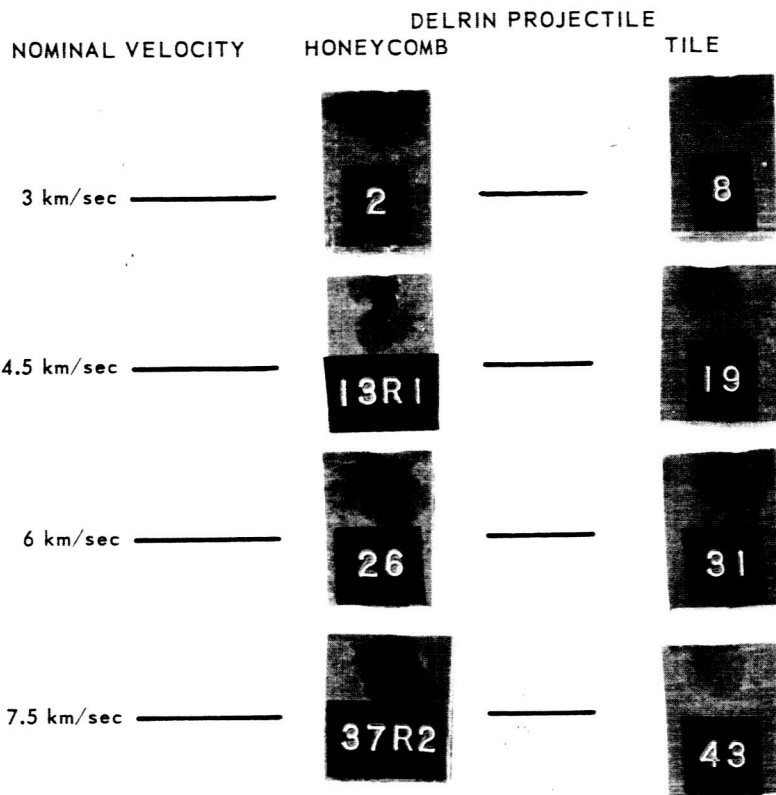
Photographs of typical craters are shown in Figures 33 through 37. Figure 33 shows a series of impacts into Avcoat 5026 at room temperature. Since there is no significant variation in test results with temperature for impact on Avcoat 5026, these can be regarded as typical for all temperatures.

The upper samples are for Delrin projectile impact, the lower are for aluminum projectile impact. Honeycomb targets are on the left, tile targets are on the right. In each group, the impact velocity increases with increasing number, and samples of the velocity range from 3 to 7.6 km/sec are shown. A similar display is given for room temperature Dow Sylgard 325 targets in Figure 34. In the Sylgard, however, temperature variation is quite important; (see Figure 36).

These three figures show the principal features of the impact results. The impacts in Avcoat 5026 are deep and relatively narrow. The crater geometry is not hemispherical at any velocity. At low velocities for aluminum projectile impacts, the projectile is not shattered, but penetrates deeply into the material. Two of the more pathological instances of this type of penetration are shown in Figure 37. Here the projectile although deformed, is intact and is lodged at the bottom of a deep crater whose diameter corresponds to that of the projectile. These figures indicate that the Avcoat resin expanded into the region behind the projectile during the last stages of impact. There is no feature of the material just above the lodged projectile that, to the naked eye, distinguishes it from the undisturbed Avcoat 5026.

At higher impact velocities, the projectile is shattered and the crater, diameter/penetration ratio increases, but remains less than the value of 2 obtained for a hemispherical crater. (see samples 43 and 127 RI in Figure 33).

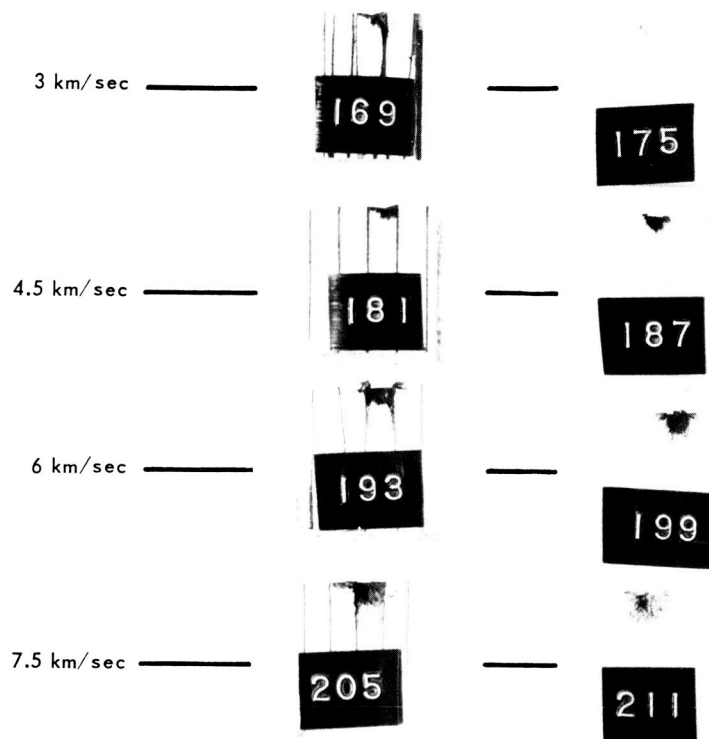
Figure 36 shows the typical effects of sample temperature on the final crater characteristics in Sylgard. Sample 295 was at room temperature. The extensive cracking of the crater walls is typical of impact craters into targets at this temperature. Sample 297 RI was at -150°F at impact; sample 300 was at -250°F at impact. The principal difference between the two low temperatures is that the front surface spall at -250°F is much more extensive than at -150°F . Neither of the low temperature craters shows the extensive cracking typical of craters formed in room temperature material.



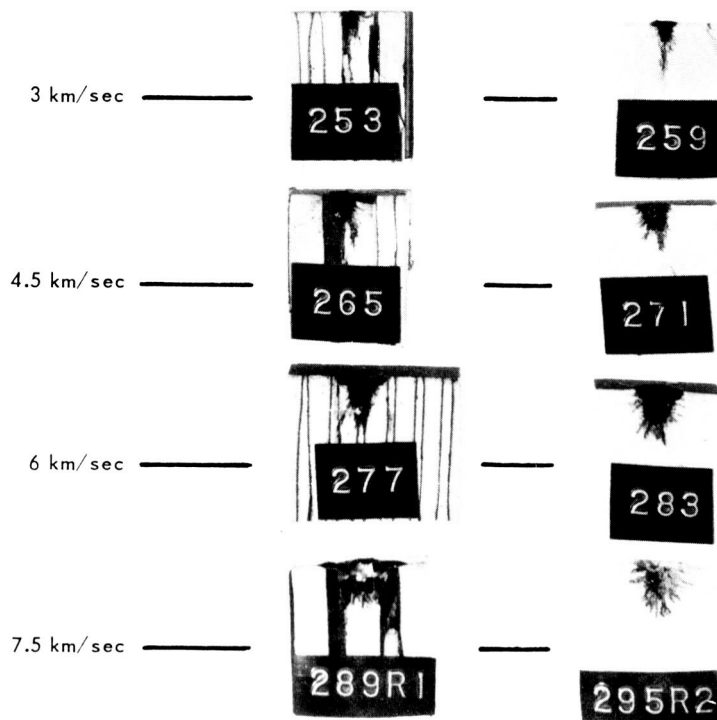
26-1824

FIGURE 33 IMPACT DAMAGE TO SYLGARD 325 AT VARIOUS VELOCITIES

NOMINAL VELOCITY DELRIN PROJECTILE
HONEYCOMB TILE

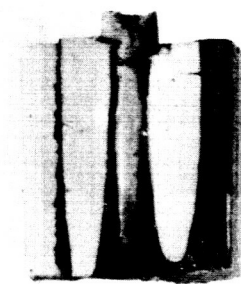


ALUMINUM PROJECTILE



26-1818

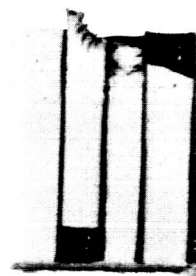
FIGURE 34 IMPACT DAMAGE TO AVCOAT 5026-39 AT VARIOUS VELOCITIES



197



257



294

26-1827

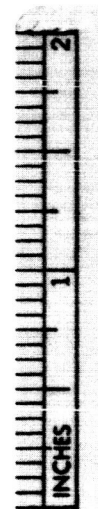
FIGURE 35A SYLGARD HONEYCOMB SHOWING POPPED CELLS



279

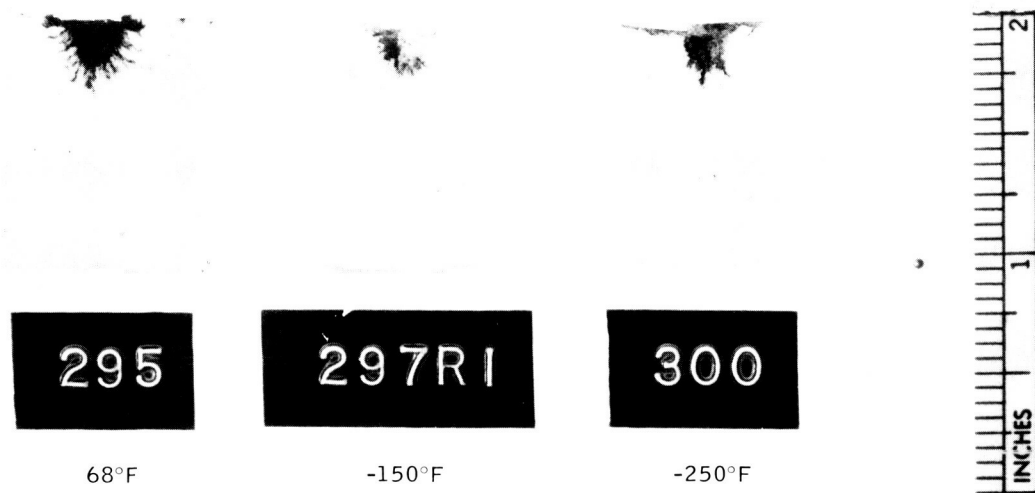


289



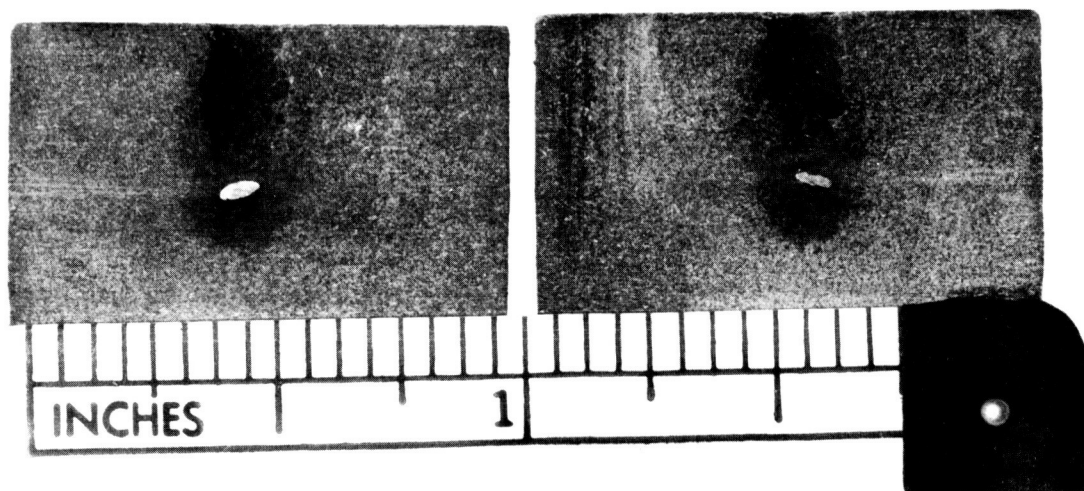
26-1828

FIGURE 35B DEEP PENETRATIONS INTO SYLGARD HONEYCOMB



26-1825

FIGURE 36 TEMPERATURE EFFECT ON IMPACT SYLGARD TILE



26-1826

FIGURE 37 DEEP PENETRATIONS INTO AVCOAT

Some of the impacts into the Sylgard 325 material produced unusual penetrations worthy of notice. Specimens 279 and 289 in Figure 35b show examples of very deep penetration by a piece of the projectile. Apparently the impact pressure at these velocities was not high enough to completely shatter the projectile. As a result some of the projectile material was slowed down sufficiently to survive the impact and go on penetrating as a low velocity slug. The fact that this phenomenon was not observed at the highest impact velocities tends to confirm the interpretation given above.

The deepest of these penetrations occurred when the penetrating slug intersected a honeycomb wall. In this case, the slug turned and followed the wall. Apparently, there was much less resistance to breaking the bond than to penetrating the Sylgard material itself.

There was another failure mode peculiar to the Sylgard 325 Honeycomb at -250°F . In some of these targets, complete cells adjacent to the impact point were debonded from the honeycomb and the backup and lifted out of the honeycomb structure a few mils. Some of these samples, numbers 197, 257, and 294, shown in Figure 35a. The Sylgard pencils are entirely debonded and can easily be pulled free with the fingers. In some cases, they can be vibrated out by inverting the piece and tapping it. Possibly this type of failure is due to the differential coefficient of thermal expansion between the fiberglass in the honeycomb and the Sylgard 325 filler.

The coefficient of thermal expansion of Sylgard is much greater than the honeycomb so the bond is highly stressed at -250°F . When the shock wave from the impact further loads the bond, it breaks, allowing the Sylgard to contract. The reflected shock from the backup plate then lifts the freed Sylgard filler out of the honeycomb as observed.

5.2 DATA PRESENTATION AND ANALYSIS

The data for this program are graphically presented in basic form in Appendixes D, E, and F. The data are plotted versus velocity, momentum and energy in Appendixes D, E, and F respectively. In each case, straight lines have been fitted to the data, and all data points have been considered. For penetration of aluminum projectiles into the Sylgard material, a broken straight line was used for a fit. The momentum and velocity plots are similar with the following exception:

In the velocity plots for Avcoat, straight lines are fitted separately to the data taken at the three temperatures, whereas in the momentum plots only one line is fitted to the data. By comparing a velocity plot with the corresponding

momentum plot, it can be seen that Avcoat shows no significant variation with temperature. Some of the parameters are plotted again in Appendix G. For the plots in this Appendix, those points which appeared to be in excessive error in the previous plots were removed from the regressions. This point will be discussed in more detail below. Log plots of the crater diameter, penetration, and damage diameter are presented. The latter may be either spall diameter or crater diameter. Also, crater volume is again plotted versus energy in Appendix G.

Almost all of the data have good linear fits. The outstanding exception is the penetration by the aluminum projectiles (see Figures D-17, -18, -21, and 22). For impact upon the Sylgard material, there is a definite penetration minimum at a velocity of about 4 km/sec (Figures D-17, -18). Penetration into the Avcoat material is essentially constant for velocities less than 6 km/sec, but seems to rise with higher velocities. This behavior can be related to the properties of the targets and to effects characteristic of velocities below the hypervelocity region. At low velocities the projectile retains its physical integrity. As the velocity of impact is raised, the projectile becomes more and more deformed, if ductile, but still retains its physical integrity. At still higher velocities, the deceleration pressures that occur during the initial phases of impact completely break up the projectile. If this breakup is complete enough, the later stages of impact will not depend significantly on the strength properties of the projectile. For the purposes of this report, "hypervelocity impact" will be used to describe impact at velocities sufficiently high that the strength properties of the projectile will have insignificant effect on the damage caused by the projectile. The velocity range over which the projectile is partially, but not completely, broken up is called "the transition region". Herrmann and Jones¹⁰ reserved "hypervelocity impact" for velocities above which target strength has insignificant effects on the observed effects. However, since there are both theoretical^{11, 12} and experimental^{13, 14} reasons for believing that such a range may be imaginary, the definitions given will be used.

Still the definitions are still not precise. In practice, the region of smooth variation of penetration with velocity ($p = KV^n$, where n is less than 1), will be called the "hypervelocity region". There is a low velocity region where penetration varies as V^2 , and an intermediate region termed the "transition region". The observed effects in the transition region depend upon the target and projectile materials. If the projectile is ductile with a yield strength not much greater than the target strength, the penetration variation with velocity goes smoothly through the transition region. If the projectile is much stronger than the target, however, penetration may increase very slowly through the transition region, or decrease with increasing velocity. Several examples of effects in this region are given in Reference 10. Both types of behavior occurred in this study. Compared to the Sylgard and Avcoat, aluminum is a dense, high-strength material, and the behavior of the penetration versus velocity is characteristic of the transition region of a high-strength material for aluminum on

Avcoat for V less than 6 km/sec and for aluminum on Sylgard for V less than 4 km/sec. Delrin, on the other hand, is a ductile projectile, and the penetration versus velocity curve would be expected to vary smoothly through the transition region. Actually it is difficult to test this assertion, because it is not known how much of the transition region for Delrin is covered by the experimental velocity range.

By definition, the transition region is characteristic of the pressures required to break up the projectile. This assertion can be tested with the data accumulated in this program. The impact pressures during the initial phases of impact when one-dimensional geometry is a reasonable assumption can be easily calculated from the Hugoniot of the materials involved. The Hugoniot relates the thermodynamic conditions behind a shock wave to those in front of the wave. It can be expressed in several equivalent ways: those that are useful here are pressure as a function of the particle velocity behind the shock wave and shock velocity as a function of the particle velocity behind the shock wave. The fact that Hugoniot are not available for the Avcoat 5026 and the Sylgard 325 represents only a minor inconvenience, since for estimation purposes reasonable assumptions can be made. Figures 38 and 39 show estimated Hugoniot for the Avcoat 5026 and the Dow Sylgard 325 respectively plotted as pressure versus particle velocity. The estimated part of the Hugoniot is the dependence of the particle velocity behind the shock on the velocity of the shock itself. This dependence is linear over the velocity range of interest, and varies slightly; the values given are representative. Nevertheless, the values are just rough estimates and should not be used for any purpose more detailed than the present one.

The sum of the particle velocity behind the shock propagating into the projectile and the particle velocity behind the shock propagating into the target must equal the projectile velocity during the initial phases of impact where one dimensional geometry is a reasonable assumption. Hence, in Figures 38 and 39, the aluminum Hugoniot is superimposed on the estimated heat shield Hugoniot, so that the sum of the particle velocities to the point of intersection is the projectile velocity at the end of the transition region. It can be seen that the initial pressure generated in the projectile at this point by impacts on either material is 0.2 megabar, and is comparable to pressures created in aluminum projectiles at the beginning of the hypervelocity region for impacts in other materials (as collected, for instance, in Reference 10). The pertinent relationships that were used are:

$$P = 0.01 \rho u_1 u_2$$

where

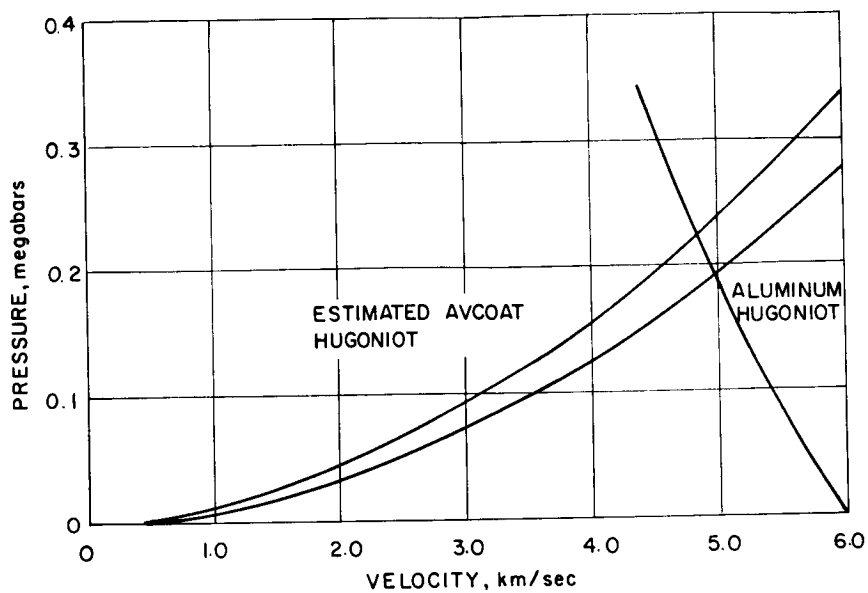
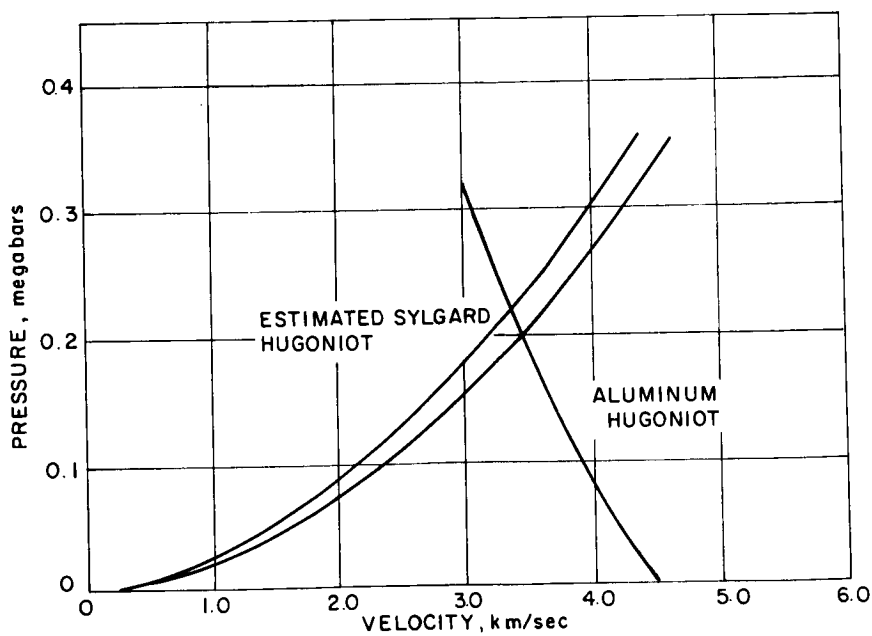


Figure 38 INITIAL IMPACT PRESSURES, ALUMINUM ON AVCOAT



86-1466

Figure 39 INITIAL IMPACT PRESSURES, ALUMINUM ON DOW SYLGARD 325

P = pressure in megabars

ρ = initial density in gm/cc

u_1 = shock velocity, in km/sec

u_2 = particle velocity behind the shock in km/sec

and the assumed relationships between u_1 and u_2 are:

upper Sylgard curve $u_1 = 1.7u_2 + 1.4$ km/sec

$\rho = 0.91$ gm/cc

lower Sylgard curve $u_1 = 1.4u_2 + 0.8$ km/sec

$\rho = 0.86$ gm/cc

upper Avcoat curve $u_1 = 1.7u_2 + 1.0$ km/sec

$\rho = 0.59$ gm/cc

lower Avcoat curve $u_1 = 1.4u_2 + 0.4$ km/sec

$\rho = 0.52$ gm/cc

These suffice to give P as a function of u_2 for the Hugoniot curves in Figures 38 and 39 which represent graphical solutions to the simultaneous equations:

$$P_{\text{projectile}} = P_{\text{target}}$$

$$u_{2\text{target}} + u_{2\text{projectile}} = V, \text{ impact velocity}$$

In the following sections, various features of the results are discussed. In general, numbers given are taken from functions fitted by the regression program described in Appendix A. The actual form of regression used is given in the caption of each Figure in Appendixes D-G. The RMS (root mean square) deviation of the data from the fit is also given with the caption, and occasionally in the text. For linear plots this parameter is given in the units of the dependent variable; for log plots, it is given in percent of the independent variable. If two parameters are measured for the i^{th} data point of N total data points, say X_i and Y_i and a function of the form $Y = f(X)$ is fitted to the data, the RMS deviation, σ of the data from the fit is:

$$\sigma = \sum_i^N [Y_i - f(X_i)]^2 / (N-1)$$

In the curves shown in Appendixes D-G, the curve shown is that function of the form given that minimizes σ .

Some of the regressions could not be meaningfully plotted because of the number of independent variables included in the form of the regression. Those that gave meaningful results are listed in Appendix H, along with a listing of some of the forms used in the regressions.

Log plots are given for several parameters, and a fit of the form

$$P/D = A V^k$$

is obtained.

In the data fits illustrated in Appendix G, data points that produced results which were inconsistent with the rest of the data were discarded. In each case, the numbers that were omitted are listed in the caption. The criterion for omission was a 3σ or more deviation from the fit.

In a study such as the present one this practice has its pitfalls. When deciding whether to remove "bad data" one should consider the physical reasons for the abnormal deviation. For essentially every case in the present study the most tenable reason for an abnormal deviation of the data would be a local deviation of material properties. This is due to the lack of uniformity characteristic of these materials, a point already discussed.

Removal of "bad" points has some justification, in that such points have an inordinate effect on the curve fit (especially on the slope). Thus, in an attempt to study the average properties of the material such a practice is useful. Experimental scatter is due primarily to the properties of the materials; and, although straightlines will be given in Section 6.0 for scaling to meteoritic velocities, there is a characteristic scatter about the mean behavior. Most of the data points omitted gave damage values that deviated above the mean.

5.2.1 Crater Volume

Volume versus energy plots are presented in Figures F-33 to 40 and again in Figures G-38 to 52, with exceptional points removed. All of the plots are straight-line fits, but there are differences in the restrictions placed on the Y-axis intercept. In particular the following options were tried in these G plots: The straight line was required to pass through the origin; there was no restriction on the intercept. For Sylgard, which had a different fit for each temperature, the intercept was allowed to be different from zero, but was required to be the same for all three temperatures. For Avcoat, requiring the curve to pass through the origin was found to give a good fit. The two pairs of plots, (Figures G47 and 8 and G50 and 1) show the same data with the first regression allowed to pass through the origin, while the second is unrestricted. The difference is small enough so that, over the experimental range the crater volume increases proportionally to the projectile energy for Avcoat 5026 tile and honeycomb materials. The slopes of the curves are given in Table XV. The estimated standard error due to data scatter is $\pm .00013$ cc/joule.

TABLE XV

CRATERING EFFICIENCY FOR AVCOAT 5026
(Crater Volume per Projectile Energy in cc/joule)

Projectile	Tile	Honeycomb
Aluminum	0.00266	0.00433
Delrin	0.00278	0.00536

The variation between the numbers for the different projectiles on the Avcoat tile is not significant. The variation for the projectile material on honeycomb targets is significant and may be due to the fact that the honeycomb structure is more likely to restrict the volume of the larger craters. In that case, Figure G49 should show data above the curve in the 70 to 80 joule range. This effect is not seen.

The volume/energy ratios at the higher velocities are shown for the Sylgard material in Table XVI. The estimated standard error due to data scatter is $\pm .00007$ cc/joule.

TABLE XVI

CRATERING EFFICIENCY FOR SYLGARD 325

(Crater Volume per Projectile Energy in cc/joule)

Projectile	Temp.	Tile	Honeycomb
Aluminum	RT	0.00083	0.00096
	-150° F	0.00055	0.00085
	-250° F	0.00134	0.00086
Delrin	RT	0.00079	0.00097
	-150° F	0.00059	0.00081
	-250° F	0.00116	0.00088

For the Sylgard material, the variation between the RT and low temperature impacts is discussed elsewhere. The two low temperatures show similar effects. The principal exception is that the spall formed at -250° F is much more extensive than at -150° F. This difference accounts for the volume/energy ratio difference between the two low temperatures, and for the large change in the volume/energy ratio between tile and honeycomb at -250° F, since the honeycomb material tends to reduce the amount of spall formed at -250° F. For the other two temperatures, the volume tends to increase slightly and probably represents the tendency for failure to follow the honeycomb walls in the Sylgard honeycomb material.

In the volume/energy plots for the Sylgard material, forcing the curve to pass through the origin results in a very bad fit at low velocities. Fits requiring the curve to pass through the origin and fits that do not restrict the intercept are shown in figures G38 through G46. Nonetheless, over the greater part of the velocity range, volume increases proportionally to the projectile energy in a way that does not depend significantly on the projectile material and only to a secondary extent on the presence or absence of honeycomb structure.

5.2.2 Crater Diameter

Log plots of crater diameter in Sylgard targets are shown in figures G13 to G20. One value of the slope seems to fit the data well: G14 and G17 show fits in which the slope is allowed to vary with the temperature. Overall, the diameter varies as $V^{0.908}$ in Sylgard. The crater diameters for the two low temperatures are comparable and are smaller than the room temperature diameters by an average factor of 1.21. The honeycomb decreases the diameter by an average amount of 5 percent. The diameter increases with the projectile density by a factor equivalent to $(\rho_p)^{0.382}$. The RMS deviation from this fit is 13 percent.

Similar plots for Avcoat are shown in Figures G21 to G26. The overall regression gives a velocity dependence of $V^{0.921}$, shows an enhancement of the crater diameter of 9 percent in the honeycomb, shows a projectile dependence equivalent to $(\rho_p)^{0.232}$, and has an RMS deviation of 9 percent from this fit.

5.2.3 Damage Diameter (Spall Diameter)

Log plots of damage diameter (spall diameter or crater diameter) are given in Figures G1 and G12. The variation in slope with temperature for the Sylgard targets did not seem significant. Figures G2 and G5 are included as examples of plots with this variation allowed, but in the other two plots the slope is required to be the same for all temperatures. There are several interesting features to these plots. One is the fact that the effect of honeycomb on the impacts at -250°F is quite different than on the impacts at other temperatures. There is a 25 percent reduction in damage diameter due to the honeycomb at -250°F for both projectile types. For the other two temperatures, the damage diameter is about 25 percent greater in Sylgard honeycomb for the aluminum projectile impacts, and remains about the same in both target structures for the Delrin projectile impacts. The effect at -250°F seems to be due to the fact that the large spall which occurs in the Sylgard tile at -250°F is inhibited by the honeycomb structure. This effect is also noticeable in the variation of the total crater volume with target structure at -250°F . The variation of damage diameter with velocity for impacts with the aluminum projectile is as $V^{1.1}$ whereas the variation for impacts with Delrin projectile is as $V^{0.73}$. The effect of projectile variation is hard to determine because of the difference in other variations, but is about equivalent to $(\rho_p)^{0.35}$. For impacts on Avcoat, the temperature complications do not occur and it is possible to run a general correlation which gives a damage diameter velocity dependence of $V^{1.33}$, a projectile dependence equivalent to $(\rho_p)^{0.139}$, and essentially no variation with structure. The standard deviation from this fit is 16 percent.

5.2.4 Penetration

Log plots of penetration are presented in Figures G27-G37. Since the bulk of the aluminum on Avcoat data was dominated by phenomena not expected to persist to meteoritic velocities, it was not plotted in this form. For the Delrin data, the variation of penetration with velocity goes as $v^{0.51}$ and the penetration is increased in the honeycomb by a factor of 1.32. A regression was run that essentially compared the high velocity aluminum projectile data with the high velocity Delrin data was run; it gave a penetration variation with respect to projectile density of $(\rho_p)^{0.554}$ and a honeycomb enhancement factor of 1.30.

For the penetration into Sylgard targets, the variation of slope (i.e., $\partial \log \frac{P}{D} / \partial \log v$) with temperature may be significant. This variation was not allowed for the aluminum projectile data because the combination of the short velocity range above the transition region and the large scatter in the data produced slope values that are physically meaningless. The variation of slope with temperature was allowed in the Delrin projectile data, and is the second of the pair of plots in each case (in the first of the pair, slope variation was not allowed). The Delrin data is summarized in Figure G-34. The distance between a pair of parallel lines represents the effect of honeycomb; it can be seen to be negligible. The three pairs of lines represent the different temperatures, and go up in order of temperature. It can be seen that the difference between the temperatures decreases as the velocity increases and material strength effects become relatively less important. For Figure G34, the standard deviation from the fit is 22 percent. This is primarily due to scatter in the honeycomb data. A fit which includes all of the Delrin data except for the low velocity aluminum impacts gives an average penetration variation with velocity as $v^{0.953}$, a projectile density dependence equivalent to $(\rho_p)^{0.794}$ and a (negligible) honeycomb enhancement of 3 percent.

5.2.5 Total Damage Depth

No log plots were run for total damage depth in the Sylgard material. Linear plots versus projectile energy are given in Figures D41-D44.

The total damage depth is an important parameter, but the presence of several competing phenomena makes interpretation of the data difficult. Damage below the crater penetration is caused by low velocity, deep penetration of small particles of aluminum projectiles, cracking of the crater walls, and the propagation of failure along honeycomb walls.

The first effect, deep penetration by small aluminum particles, is an extension of the transition region in the Sylgard. The 4 to 7 km/sec can be regarded as still in the transition region (although the projectile is broken up, the breakup is not complete; also, perhaps because of local variations in projectile or in target materials, some of these particles retain their integrity and puncture the material). This effect is appreciable only in the room temperature material, and is due to the resiliency of the material at this temperature. The cracking of the crater walls is another phenomenon that occurs only in impacts on Sylgard at room temperature. This effect also is due to the resiliency of the material at this temperature. During the cratering process, the material is compressed and pushed radially outward. Because of the large amount of compression the room temperature Sylgard can withstand, tensile hoop stresses are induced and the material at the crater walls fails in tension. Then the compressed material expands, leaving the crater walls with cracks comparable in length to the radius of the crater.

Failure along the honeycomb walls occurs at all temperatures, but is most noticeable at the lower temperatures. In part this may be because the other two effects are reduced; certainly, however the difference in material properties at lower temperatures is significant. For instance, the complete debonding of honeycomb cells occurred only at -250°F. Deep penetration by small projectile pieces also occurred in the honeycomb material. Apparently, the projectile fragment finds less resistance when traveling along the bond between the honeycomb structure and the Sylgard 325 filler.

The deep penetration by aluminum fragments into room temperature Sylgard material is peculiar to the material properties characteristic of the rubber and to impact velocities sufficiently low that the projectile is not completely pulverized. The data show that this type of penetration decreases with velocity. It is expected that this phenomenon will not occur at meteoritic velocities.

The cracking is characteristic of the mode of crater formation in room temperature Sylgard material and can be expected to occur at all velocities, and to scale as other linear dimensions of the crater (see Section VI on scaling).

The ratio of total damage depth to crater penetration at the high velocity end of the experimental range is given in Table XVII.

TABLE XVII
TOTAL DAMAGE DEPTH/CRATER PENETRATION

Projectile	Temperature	Sylgard 325 Tile	Honeycomb
Aluminum	RT	1.48	1.74
	-150° F	1.35	1.82
	-250° F	1.26	1.15
Delrin	RT	1.59	2.00
	-150° F	1.23	1.59
	-250° F	1.20	1.51

The honeycomb material shows considerable variation. The tile material, which does not have the complication of honeycomb debonding, shows a consistent total damage depth/penetration enhancement for the RT material by an average factor of 1.54 and for the other two temperatures by an average factor of 1.25.

When the Avcoat craters were split for photographic purposes, it was found that, at the lowest velocities, damage had occurred below the depth measured as the crater penetration. Two examples are shown in Figure 37, and the maximum penetration is listed under "Total Damage Depth" in Appendix C when it was greater than the penetration. This is not a hyper-velocity phenomenon, and no attempts were made to include this parameter in any correlation.

5.2.6 Effects of Projectile Variation

The effects of varying the projectile material are best considered in light of the volume/energy relationships. Tables XV and XVI on pages 73 and 74 indicated that there is no significant variation in this ratio with projectile material. This result is expected -- in general, cratering efficiency does not depend strongly on projectile material. Thus, projectile effects on other parameters

can be related to a changing of crater geometry. In particular, a dense projectile can be expected to form a crater deeper and less wide than would a projectile of the same mass but with lower density.

This effect can be expected to diminish at higher velocities, as will be discussed in Section VI on scaling. Since volume varies linearly with the mass, if the crater had the same shape for all projectile densities, a linear parameter, such as p , should vary as $\rho_p^{1/3}$. However, at the velocities attainable experimentally, the depth/width ratio of the crater increases with increasing projectile density. Hence, at the velocities of this study, penetration can be expected to vary as ρ_p^a . The crater diameter can be expected to vary as ρ_p^{-b} where $a > 1/3 < b$, and where $1/3$ is the value to be expected if the crater remained hemispherical for all projectile densities. The data fits give $a = 0.554$ for Avcoat and $a = 0.794$ for Sylgard, $b = 0.232$ for Avcoat and $b = 0.384$ for Sylgard.

The numbers given for the Sylgard material are influenced by other factors in the regression, apparently, because the crater volume dependence on energy implies that $a + 2b = 1$, which is inconsistent with the value of $a + 2b = 1.56$ obtained above. Figures 47 and 48 in Section VI indicate that the Sylgard data have the correct dependence, since the Delrin crater radius data lie above the aluminum data (this would not be if b were actually greater than $1/3$). The Avcoat values for a and b are consistent with the requirement $a + 2b = 1$.

5.2.7 Effect of the Presence of Honeycomb

For quite different reasons, results of impacts on both target materials studied are quite different in the honeycomb than in the tile materials.

Penetration is much deeper in the Avcoat 5026 honeycomb than in the tile. The appearance of the craters is very much the same, however (see Figure 33). It is only when the crater becomes of the order of the cell size that the presence of the honeycomb appears to have much effect. The major difference in penetration observed (penetration in the honeycomb is a factor of 1.3 times that in the tile) is due to a difference in the manufacture of the two types of targets. The effect of this difference can be seen by comparing the strength properties given in Table XVIII. The shear strength for the honeycomb is only 40 percent that of the tile; the penetration force measured in the Avcoat 5026 honeycomb is only 70 percent of that measured in the Avcoat tile. Comparison of the compressive strength is not meaningful because the macroscopic resistance of the honeycomb structure dominates the results on that material (see Paragraph 4.2.4).

Previous correlations on target strengths indicated a linear crater parameter dependence proportional to $(\rho_t H_t)^{-1/3}$.

Using the shear strength for H_t would give

$$\frac{(\rho_t H_t)_{H.C.}^{-1/3}}{(\rho_t H_t)_{tile}^{-1/3}} = 1.41$$

using the penetration resistance for H_t would give

$$\frac{(\rho_t H_t)_{H.C.}^{-1/3}}{(\rho_t H_t)_{tile}^{-1/3}} = 1.19$$

These two values bracket the observed factor increase (1.3) in penetration mentioned above. Thus the difference between honeycomb and tile targets in Avcoat 5026 can be ascribed to material differences. The data do not determine whether there are differences due to the structure, but visual inspection indicates that any such effect is small.

With the Dow Sylgard 325 material the situation is quite different. Figures 34, 35 and 36 prove that the presence of honeycomb has a significant effect on the damage caused by hypervelocity impact. However, examination of the data shows the effect of honeycomb on crater diameter and crater penetration is negligible. Consideration of the spall diameter shows that the presence of honeycomb inhibits the formation of the large spall characteristics of impacts into materials at -250°F . Actually, the principal effects of the honeycomb structure on impacts in Sylgard are on the total damage depth and on the honeycomb bond. At -250°F there is a tendency for one or more cells to completely debond as illustrated in Figure 35a. At all temperatures, there is a tendency for debonding to occur and for penetration to follow the honeycomb walls, as illustrated in the two samples in Figure 35b. Examination of the total damage depth data indicates that in Sylgard 325 total damage depth in the honeycomb structure is, on the average about 1.3 times that in the tile targets for similar conditions.

Not all of the effects of the honeycomb structure are well represented graphically, as the photographs indicate. One point that must be considered when attempting to scale these results is the relation of the extent of a feature of interest to the characteristic size of the honeycomb. It is reasonable to assume that, for craters small with respect to the honeycomb dimensions and far from the honeycomb walls, the behavior observed will

not be significantly different than for the corresponding tile material (except, of course, when the tile is a different material, as in the case for the Avcoat targets).

In the present study, the craters produced in the Sylgard material had spall damage over several honeycomb cells for the higher velocities. In the Avcoat material, the crater diameter approached the diameter of the honeycomb cells for the higher velocities. Occasionally a projectile struck on or very near to a structure wall.

This means that there are two more variables of importance in the honeycomb impacts: the size of the damage in terms of the honeycomb spacing, and the point of impact in relation to the honeycomb structure.

This latter variable, the point of impact, could not be controlled and represents a source of experimental uncertainty that serves to increase the scatter of the data observed in the honeycomb targets. Only qualitative estimates of the effect of this variable can be given. However, based on observations of the craters, the following generalizations can be made.

As might be expected, the honeycomb structure in general is less damaged than is the heat shield material, and bare honeycomb is often noticed in craters that include part of the structure.

The honeycomb inhibits the growth of the crater. This not surprising, since the structure presents a region of different shock propagation properties, with the result that some energy is reflected which would otherwise be transmitted. This effect results in a tendency for crater boundaries to appear to "grow" or "shrink" to fit the honeycomb boundaries. This effect, illustrated in Figure 40, occurs in both Avcoat and Sylgard materials.

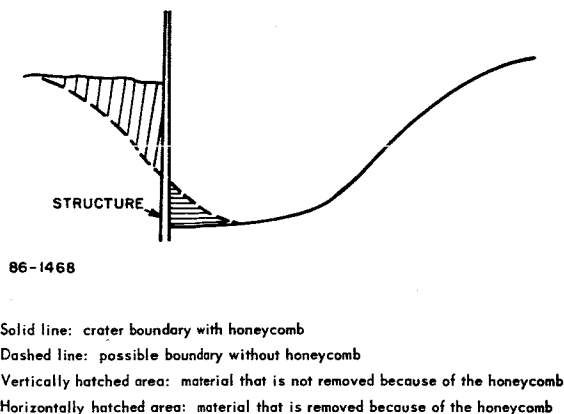


Figure 40 EFFECT OF STRUCTURE MATERIAL ON CRATER BOUNDARIES

In the Sylgard material, the honeycomb - heat shield bond is vulnerable, especially at low temperatures, and debonding occurs outside the crater region, as mentioned earlier.

5.2.8 Effects of Temperature Variation

The effect on crater parameters due to the variation of the initial temperature is due to the change in material properties at the different temperatures. Table XVIII shows that the properties of Avcoat do not change markedly with temperature. Since previous correlations indicate that linear crater parameters would depend on the cube root of a pertinent strength property, it is not surprising that no significant temperature effect was observed in the Avcoat 5026 material. Table XVIII shows that it is no surprise that the results of impacting Dow Sylgard 325 do vary with temperature. Sylgard at room temperature is quite different from Sylgard at low temperatures. The room temperature Sylgard is rubbery, resilient and weak while the low temperature Sylgard is brittle and an order of magnitude stronger than the room temperature material. The results of the impacts reflect these differences. The profuse and deep cracking observed in the craters made in the room temperature material occurs because of the tensile stresses resulting from the large amount of strain that this material will support. (The outward radial compression produced during the impacting process resulted in high tensile hoop stresses, with the result that the crater walls failed in tension, then expanded again to the configuration shown in Figure 36.) The small-particle puncture phenomenon that was observed in the 4 to 7 km/sec velocity range is also peculiar to the room temperature material.

Impacts on the Sylgard at the two low temperatures were very much the same, with one exception. Spall at -250°F was much larger than at -150°F , and probably accounts for the difference in crater volume observed between the impacts at the two temperatures. This excess spall is largely inhibited in the honeycomb material.

TABLE XVIII

MATERIAL PROPERTIES OF THE TARGETS*

		Tensile Strength (psi)	Total Strain (percent)	Compressive Strength (psi)	Shear Strength (psi)	Penetration Force (pounds)	Density (lb/ft ³)
Avcoat 5026 Honeycomb	RT	--	---	2800	1200	50	33
	-150°F	--	---	3800	1400	80	
	-250°F	--	---	4600	1500	90	
Avcoat 5026 Tile	RT	1500	0.9	3900	3000	75	37
	-150°F	1600	0.4	4800	3600	115	
	-250°F	1800	0.4	6200	3800	130	
Sylgard 325 Honeycomb	RT	--	---	--	800	--	56.5
	-150°F	--	---	--	2100	--	
	-250°F	--	---	--	1000	--	
Sylgard 325 Tile	RT	900	40	--	800	28	54.0
	-150°F	6000	1.6	--	5300	140	
	-250°F	6500	1.3	--	6500	200	

*These properties were taken from the tests described in Section 4.0. Using the principle of time-temperature superposition, properties were chosen that would be characteristic of a time scale between 10⁻⁵ and 10⁻⁴ seconds. This represents the time scale in which the crater boundaries are formed and during which the material properties should have their most significant effects.

6.0 SCALING

6.1 INTRODUCTION

Because laboratory experiments at meteoritic velocities for projectile masses of interest seem out of the question in the immediate future, an important question is whether or not impacts at experimentally attainable velocities can be scaled to meteoritic velocities and if so, how. Several plausible relationships have been proposed, but the strongest principle proposed to date seems to be the principle of "late-stage equivalence", which has been extensively investigated by Walsh¹¹ and Riney¹². This principle will be used in this section in conjunction with the experimental results described in the previous section to estimate the results to be expected from meteoroid impact.

The principle of "late-stage equivalence" does not attempt to surmount the problem of strength effects, but tries to avoid it. It asserts that the solutions to two different impact conditions become asymptotically the same and approach each other, while the pressure wave is still strong compared to material strengths. In particular, if the parameter mV^{3a} is kept constant, the pressure profile as a function of time, the total radial momentum as a function of time, and the total axial momentum as a function of time become asymptotically identical and converge within times comparable to that required for the formation of the crater. One can then argue that since these quantities become nearly the same, any subsequent damage will be essentially the same in all cases. This principle then provides a basis for scaling results of impacts at experimental velocities to results of impacts at meteoritic velocities for identical projectile-target combinations. In particular, since the linear dimensions of the crater are observed to scale as $m^{1/3}$, the velocity dependence is simply V^a . The constant a can be expected to be a function of velocity and of the materials considered. Walsh found values of a to range between $0.56 < a < 0.59$; however, for velocities just slightly above the material sonic velocity, a was higher (about 0.6) and that the equivalence was not good. He gives a "best value" of $a = 0.58$. Riney considered values of a of 0.66 and 0.33 and found $a = 0.66$ to give good equivalence, while $a = 0.33$ gave no equivalence. The velocities Riney considered were at the low end of the range considered by Walsh; basis of comparison was somewhat different. These points--in addition to the fact that Riney apparently did not search for an a which would give the best equivalence--account, perhaps, for the difference in the results.

In addition to the studies described, both Walsh and Riney studied the effect of projectile density and of moderate changes of projectile geometry. They found that the principal parameter was the mass of the projectile. Increasing the density of the projectile or its length to diameter ratio would apparently increase the depth of penetration somewhat, but the effect was small and it decreased with the velocity of impact. However, correlations at experimental velocities show a crater geometry dependence on ρ_p and give a penetration dependence of $\rho_p^{2/3}$ rather than the $\rho_p^{1/3}$ dependence found above.

6.2 SCALING PRINCIPLES

It is proposed to use the principle of late-stage equivalence to scale the results of this study to meteoritic velocities. There are several points which must be considered before applying this principle.

6.2.1 Applicability of Late-Stage Equivalence

One important question is whether or not the experimental velocities attained are sufficiently high that late-stage equivalence will hold. This question is difficult to answer. One reason for the success of the late-stage equivalence principle is the fact that at high pressures the equations of state for most materials approach the same form. This is especially true for the metals for which the bulk of the investigation has been conducted. The equations of state for the target materials of this study might not converge to a common form as rapidly as do those of the metals (if, indeed, they converge at all). Moreover, as was shown in paragraph 5.2, the impact pressures that were achieved in this study are lower than those achieved at these velocities for normally dense materials because of the low density of the target materials. Short of measuring the equations of state for these materials, it is impossible to satisfactorily answer the question of whether late-stage equivalence can be justifiably applied to scaling this data.

Nonetheless, the principle of late-stage equivalence will be used because it represents the current best estimate and because reasonable alternatives are not very different. A reasonable alternative in the lower part of the hypervelocity region is energy scaling, which asserts that the damage produced by two impacts will be the same if the projectile energy is the same in both cases. This can be regarded as a "maximal" scaling principle, since it asserts that the efficiency of converting energy to damage remains the same for all velocities. Actually, one would expect that the entropy increase associated with the strong shocks created at high velocities would result in a decrease of cratering efficiency or damage-creating efficiency with velocity. In essence, one expects an "over-kill" and loss of efficiency near the point of impact for hypervelocity impacts. Another scaling principle that has been proposed is momentum scaling; damage will be the same in two impacts if the projectile momentum is the same in both cases (For a review and bibliography of the energy scaling - momentum scaling arguments - see Reference 10). A more reasonable assumption might be that the damage would be the same in two impacts if the momentum transferred to the target were the same in both cases. The calculations by Walsh and Johnson¹¹ showed that because of the ejecta from the forming crater, a momentum greater than the initial projectile momentum was imparted to the target in an amount such that the principle of equal damage for equal momentum transfer turns out to be identical to the principle of late-stage equivalence.

Furthermore, correlations of hypervelocity impact in the experimental velocity range show either energy scaling¹⁰ or scaling agreeing with that predicted by late-stage equivalence.¹⁵ (In Reference 10, Herrmann and Jones give energy scaling correlations and a logarithmic correlation. However, in the experimentally attainable hypervelocity region, the logarithmic correlation agrees closely with the energy scaling correlations and with those obtained in Reference 15. Over the short velocity range that this represents, there is little or no significant difference among the three approaches.)

Based on the points mentioned above, and on the fact that Walsh and Johnson¹¹ found α to increase slightly for lower velocities, the following assumptions seem reasonable and will be used:

- a. Late-stage equivalence will hold for all target materials for sufficiently high impact velocities.
- b. The radius of a crater for like material impact will always increase with velocity faster than predicted by late-stage equivalence. This premise is based on the fact that the radius starts out increasing faster than predicted by late-stage equivalence; the behavior is expected to converge to that predicted by late-stage equivalence, and there is no physical reason to expect a crossover.
- c. The equations of state of the target materials of this study are sufficiently similar to those studied by Walsh and Johnson that $\alpha = 0.58$ is a good representation over the meteoritic velocity range.

The velocity dependence that has been postulated is

$$r = KV^{0.58}$$

The "maximal" behavior expected is

$$r = KV^{2/3}$$

The meteoritic velocity range extends only a factor of 10 above the experimental range. The difference in the above two expressions over a factor of 10 is 20 percent.

In the graphs of the scaled results to be presented, the use of $\alpha = 0.58$ will be presented as a "best estimate" of the expected results. A dashed line representing energy scaling will be presented as a "maximal estimate" of expected results.

6.2.2 Scaling of Crater Geometry

The work done by Walsh¹¹ and Riney¹² indicates a hemispherical crater at hypervelocities, and little or no dependence of crater geometry on projectile geometry. The results of the present study show a crater geometry that is deeper than it is wide, and a dependence of penetration on projectile density as well as on projectile mass. Some reasonable means of joining these two types of behavior must be assumed.

One basic principle that seems to be fairly well supported is that crater volume is insensitive to projectile density changes and to geometry changes. This is, of course, a result of late-stage equivalence scaling. Experimental results vary. A recent correlation¹⁸ of metal-metal impacts gives a volume dependence on projectile density of $\rho_p^{0.345}$ (with a linear scaling with mass removed). Another recent study¹⁴ reports no projectile density effect. In the present study, the density of the projectiles varied by a factor (1.43:2.79) of nearly 2. The difference in cratering efficiency observed between the projectiles was not significant, but it should be noted that the Delrin spheres showed the highest cratering efficiency. It is extremely unlikely that the actual behavior in the present study involves a strong dependence of volume on projectile density, which the chance distribution of data scatter has made to seem smaller.

It is necessary to consider how the shape of the crater will change with velocity. Late-stage equivalence scaling indicates that the shape will become independent of projectile density and hence probably hemispherical. Just how this convergence depends on velocity has not been determined theoretically or experimentally.

It is possible to argue qualitatively that the difference between penetration and crater radius will not grow at hypervelocities. As the projectile velocity is increased, the resulting increase in crater dimensions is due primarily to the fact that the region of highly compressed material that is formed after impact has been increased in volume and pressure. It is the expansion of this region that causes further cratering. The pressure of course is isotropic; hence the argument that $p - r$ should not increase with increasing velocity. In actuality, because of the free boundary at the surface, $p - r$ probably decreases and becomes negative. However, the conservative assumption would be that $p - r$ remains constant. This assumption still provides that the crater geometry will approach a hemisphere at high velocities.

Combining the points made in the preceding section leads to the following assumptions which will be used in scaling:

- a. Crater volume will depend only on $mV^{3a} = mV^{1.74}$

b. $pr^2 = l^3$ will depend only on mV^{3a}

c. $p - r$ will remain constant

The first two assumptions are not quite as equivalent as they might appear. First, because of the unevenness of the crater walls, the volume of an

ellipsoidal crater, in general, would not be $V = \frac{2\pi}{3} pr^2$. Secondly, the

volume in the front surface spall is an appreciable part of the total volume. The first assumption, then, involves extending the crater volume dependence to the spall volume. There is some justification for this; it will be shown that the spall dimensions; hence the spall volume will also scale as mV^{3a} .

6.2.3 Scaling Spall and Other Damage

In the present study, the data indicated that the dimensions of the actual crater were not always the parameters of greatest concern. At the highest velocities there was appreciable front surface spall; also the Sylgard material showed damage below the crater penetration, especially for targets impacted at room temperature.

To scale the spall phenomena, the dimensional analysis developed by Walsh and Johnson¹¹ will be assumed to apply. They assume that the equation of state can be characterized by two parameters, ρ_0 , the initial density, and c_0 , the velocity of sound in the undisturbed material.

It is assumed that two similar parameters will suffice to characterize the high pressure behavior of these targets, say ρ_0 and c_1 , where ρ_0 is as before, but, because the targets are underdense, c_1 may not be the velocity of sound in the undisturbed material. The solutions to an impact are expressible in nondimensional form; in particular, the pressure is expressed as:

$$p = \rho_0 V^2 f \left(\frac{\vec{r}}{\bar{D}}, \frac{tV}{\bar{D}}, \frac{V}{c_1} \right)$$

where \vec{r} is a position in the target and \bar{D} is a characteristic dimension of the projectile. The point is that pressure is a function of position measured in terms of the characteristic dimension of the projectile. If it is now assumed that the spall boundary is determined by the presence of a tensile wave of a certain strength, then it can be seen that the spall boundary will scale with the dimension of the projectile, which means that it will scale as $m^{1/3}V^a$ in the velocity range where late-stage equivalence applies.

A similar assumption can be made for the cracking observed in the room temperature Sylgard. If it is assumed that the boundary of the cracking is determined by the locus of tensile stress of a certain level, then this phenomenon, too, can be scaled as $m^{1/3}v^a$.

The phenomenon of deep penetration by small projectile particles, whether of the puncture nature or of the honeycomb debonding nature, is not expected to occur at meteoritic velocities.

6.2.4 Scaling in Honeycomb

The scaling of the results observed in the honeycomb materials involves another dimension -- there is a characteristic length for honeycomb materials, the characteristic dimension of the cell.

It may be that late-stage equivalence will obtain -- especially if the dimensions of the projectile are small compared to the honeycomb dimensions. However, all that this principle states is that the results will be the same if mv^{3a} is the same. For a homogeneous material a scaling of linear dimensions with $m^{1/3}$ is a good assumption. For the honeycomb targets such an assumption is unjustified. Hence the scaling in the next section can be used for final craters of the order of the craters obtained in this study. For smaller craters, tile relationships can be used. (These were not significantly different from the honeycomb relationships for Sylgard; the differences in Avcoat could be accounted for by material property differences.) These scaling relationships cannot be safely used for crater dimensions large compared to honeycomb spacing.

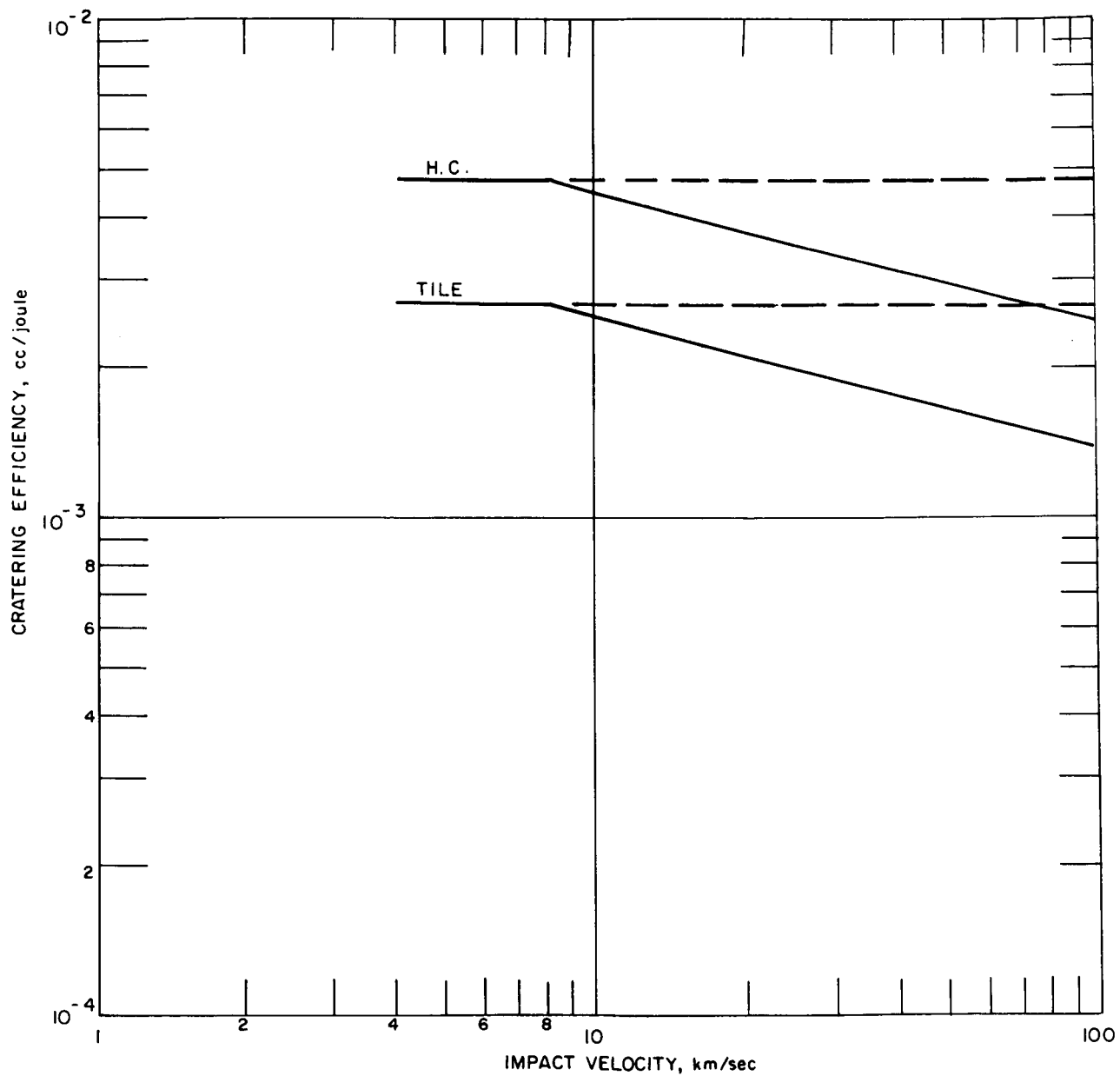
These comments apply in particular to the phenomenon of debonding that occurred in the Sylgard when impacted at -250°F . It is anticipated that similar behavior will occur if a meteoroid with the same mv^{3a} as produced the debonding were to strike a similar target in space. However, the present study does not give information with which to estimate damage that might occur from impact by meteoroids with larger mv^{3a} .

6.3 SCALING RESULTS TO METEORITIC VELOCITIES

Here, the principles presented in the previous sections will be applied to scale the results of the impacts made in the course of this study to estimate results expected from impacts at meteoritic velocities.

6.3.1 Scaling for Penetration and Crater Diameter

In Figures 41 through 44, crater volume scaling relationships are presented. In each case, the horizontal line represents the approximately constant cratering efficiency observed in this study. The $mv^{1.74}$ scaling is assumed



86-1469

Figure 41 CRATERING EFFICIENCY IN AVCOAT 5026

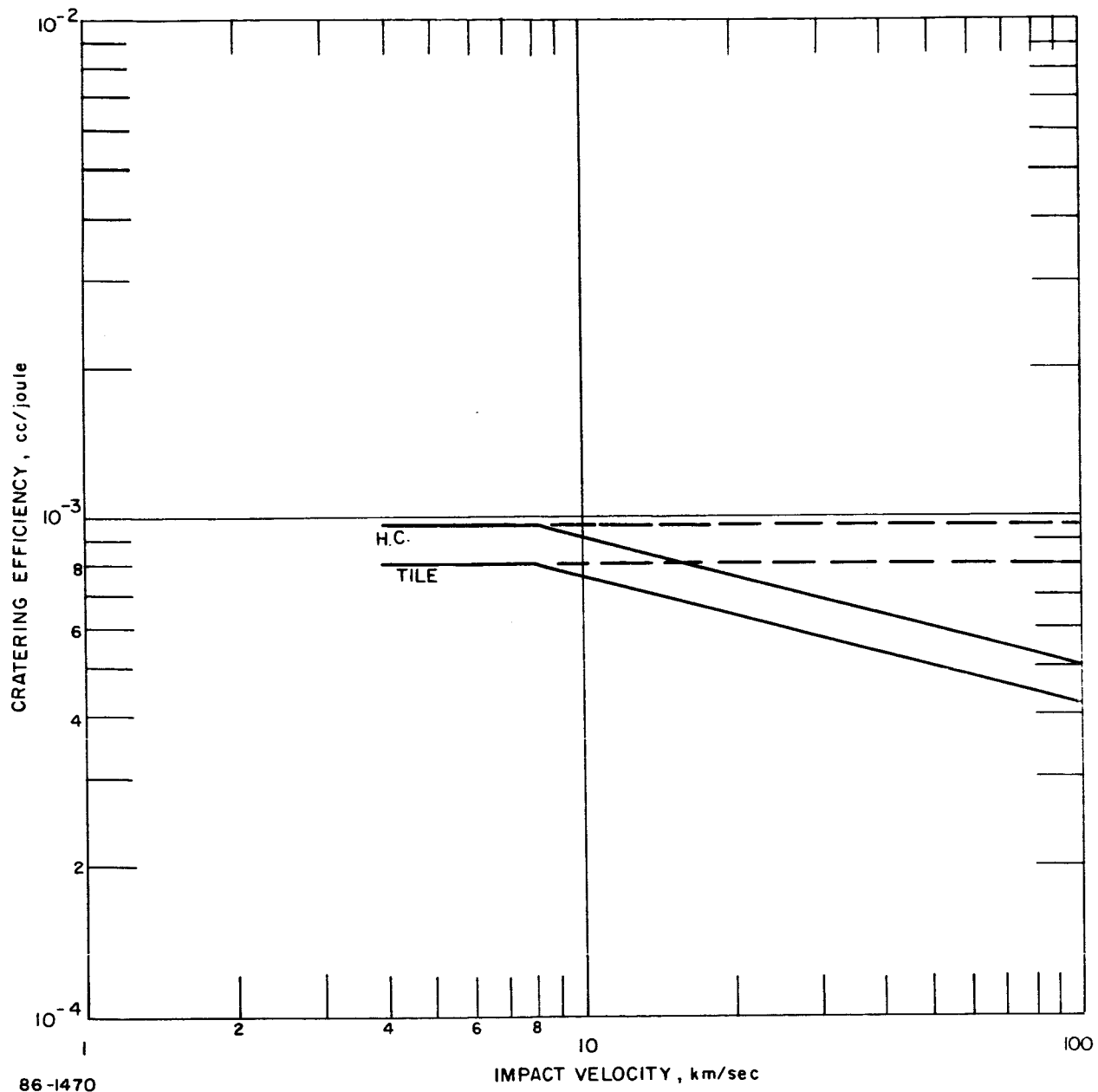
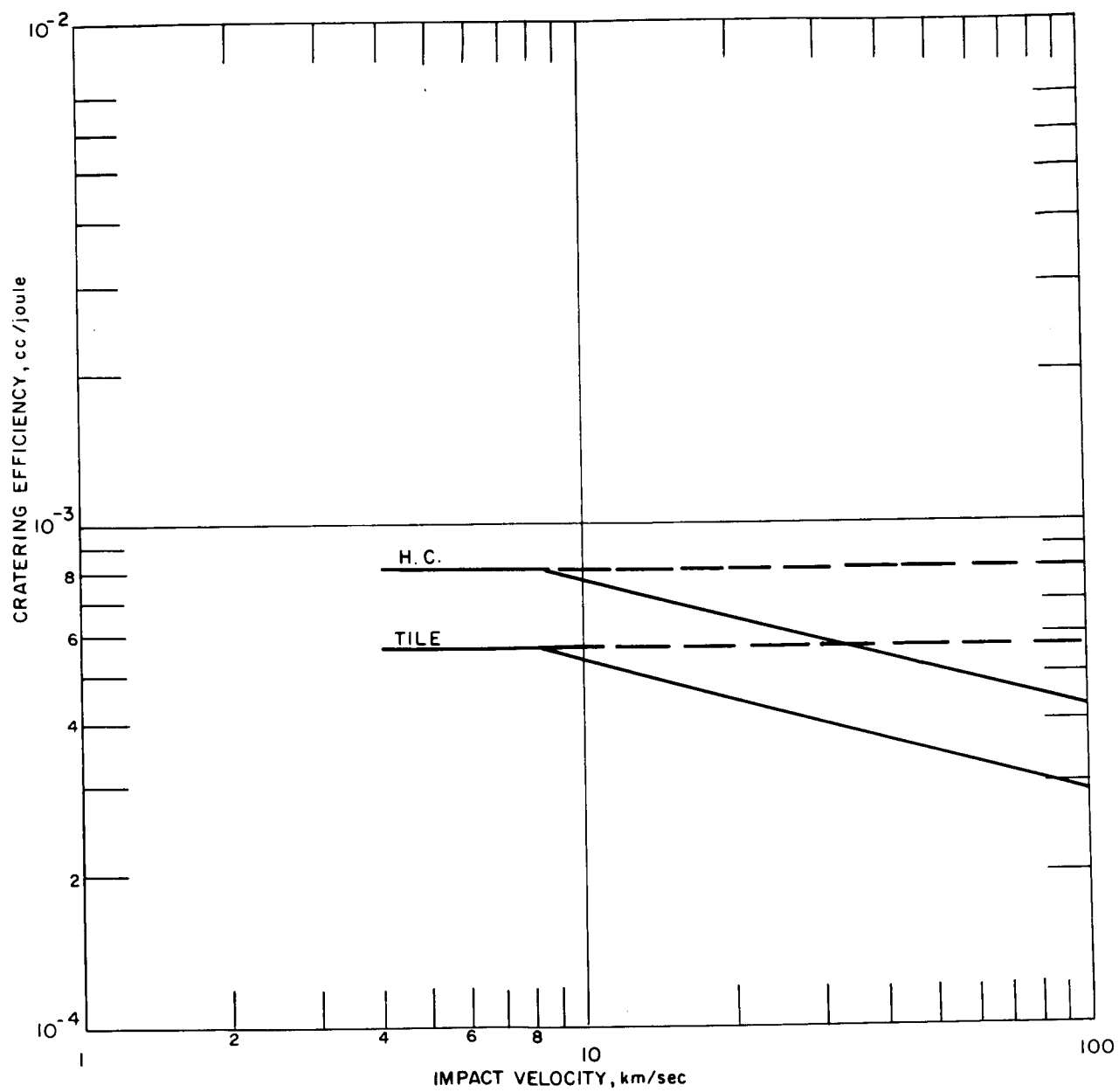


Figure 42 CRATERING EFFICIENCY IN DOW SYLGARD 325 AT RT



86-1471

Figure 43 CRATERING EFFICIENCY IN DOW SYLGARD 325 AT -150°F

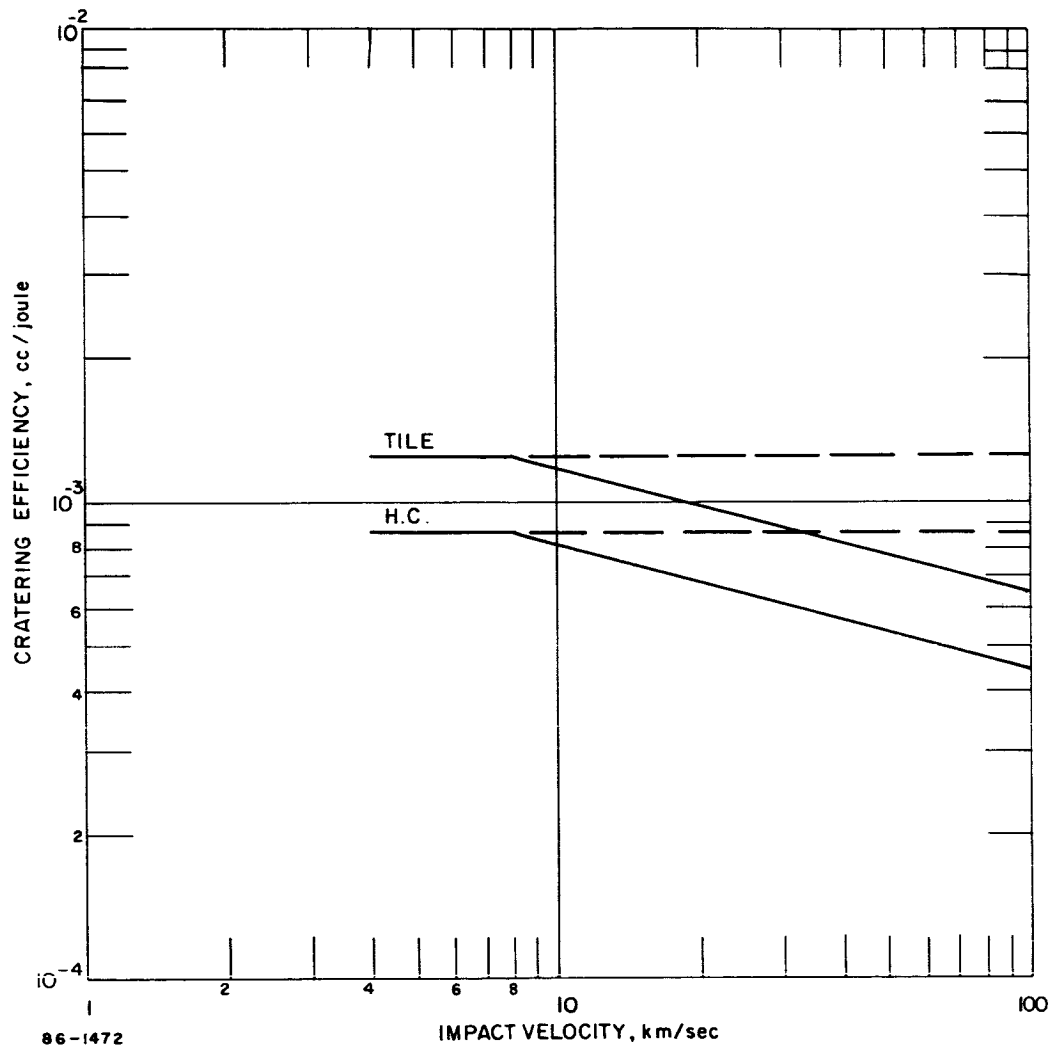


Figure 44 CRATERING EFFICIENCY IN DOW SYLGARD AT -250°F

to start at 8 km/sec at that velocity the cratering efficiency begins to decrease as $v^{-0.26}$. The horizontal line is continued in dashed form to represent a maximal estimate as discussed in Paragraph 6.2.1.

In Figures 45 through 48, scaling is given for linear crater dimensions. The vertical axis is given as:

$$p^* = \frac{l(\rho_t)^{1/3}}{\bar{D}(\rho_p)^{1/3}}$$

where

$$l = (pr^2)^{1/3}$$

and \bar{D} is the diameter of the sphere that is mass equivalent to the projectile. (Note that if the crater walls were smooth, as in craters in ductile metals, l would be the radius of a hemisphere of volume equal to the crater volume. However, this relationship would not necessarily hold for craters with very uneven walls, as were observed in the present study, or for craters with spall.) It is not necessary to include the target density in the parameter, p^* ; this is done just to make p^* dimensionless.

According to the predictions of late-stage equivalence, $p^* = kv^{0.58}$, where k is a function of the target material only. The data indicated that four groups had significantly different crater diameter and penetration. These are: Avcoat tile, Avcoat honeycomb, room temperature Sylgard (both structures) and low temperature Sylgard (both structures). In Figures 45 through 48, the fits to the crater diameter and penetration data are plotted for $3 < v < 8$ km/sec. At $v = 8$, l is computed as $(pr^2)^{1/3}$, and is assumed to vary as $v^{0.58}$ for higher velocities. (A dashed line which varies as $v^{2/3}$ is included as a maximal estimate.)

If the scaling relationships used here are correct, l computed from the Delrin projectile impacts should agree with the l computed for the aluminum impacts. Within the accuracy of the data, this agreement is obtained.

(Note that the slopes of the data curves do not agree with those of the scaled curves. The phenomena determining the experimental slopes are not expected to persist to meteoritic velocities; hence it was necessary to determine velocity behavior for these velocities by theoretical means.)

It would be desirable to be able to express $p - r$ in terms of the projectile and target densities. The first step is to try to express $p - r$ in terms of (ρ_p/ρ_t) . This turns out to be impossible. Some other parameter is important. A possible candidate for this other parameter could possibly be the porosity of the target materials, since the crater penetration/crater

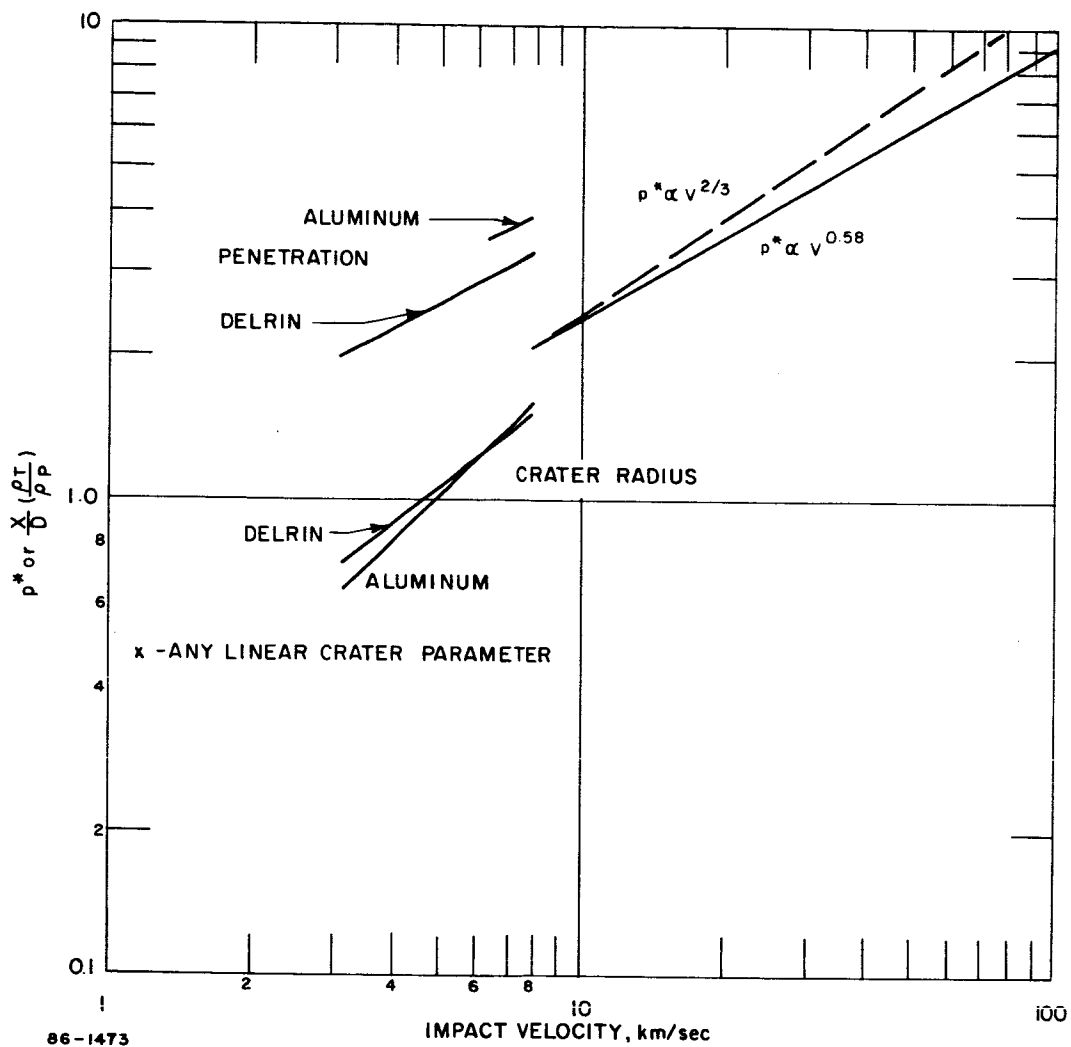
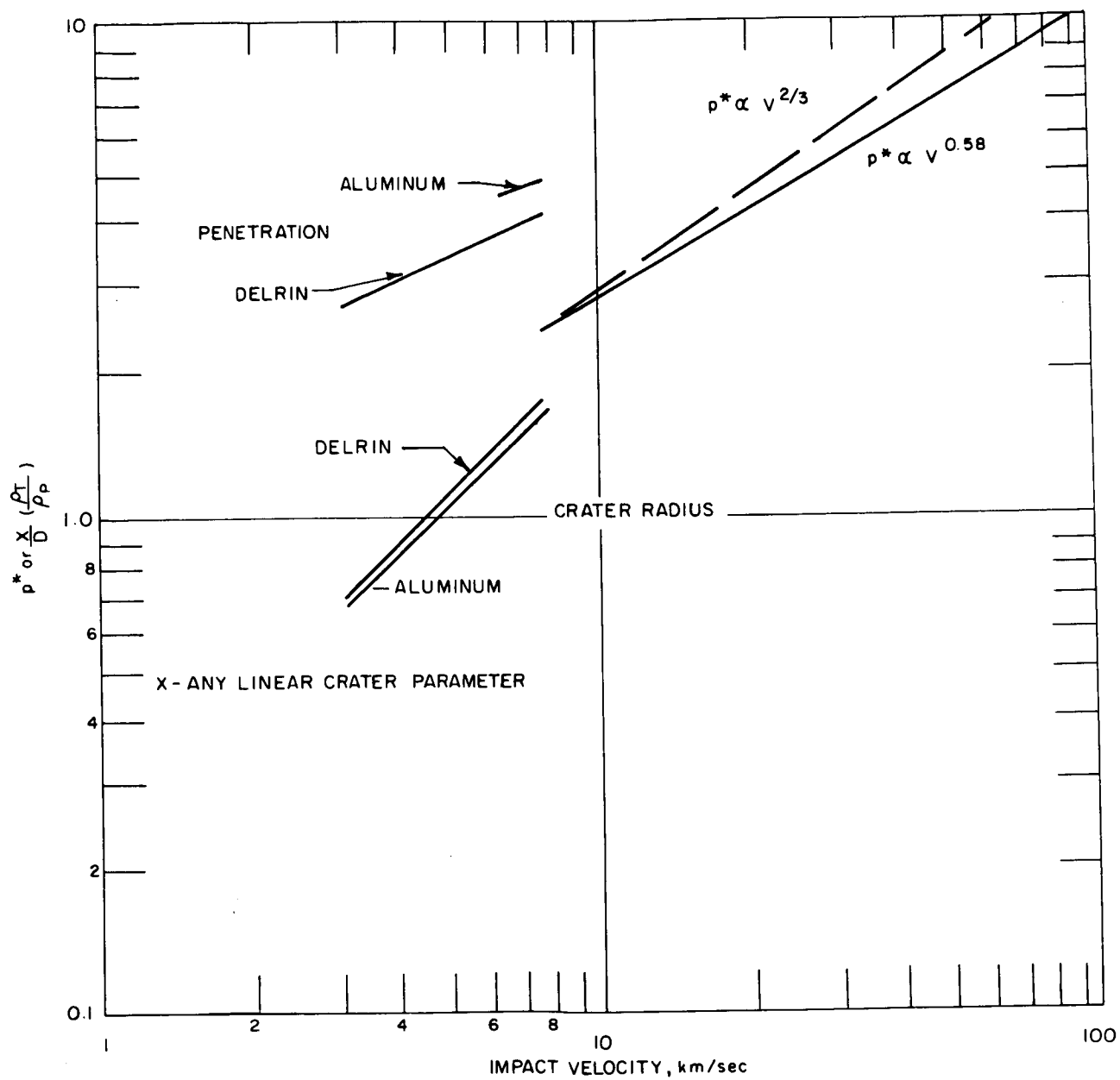
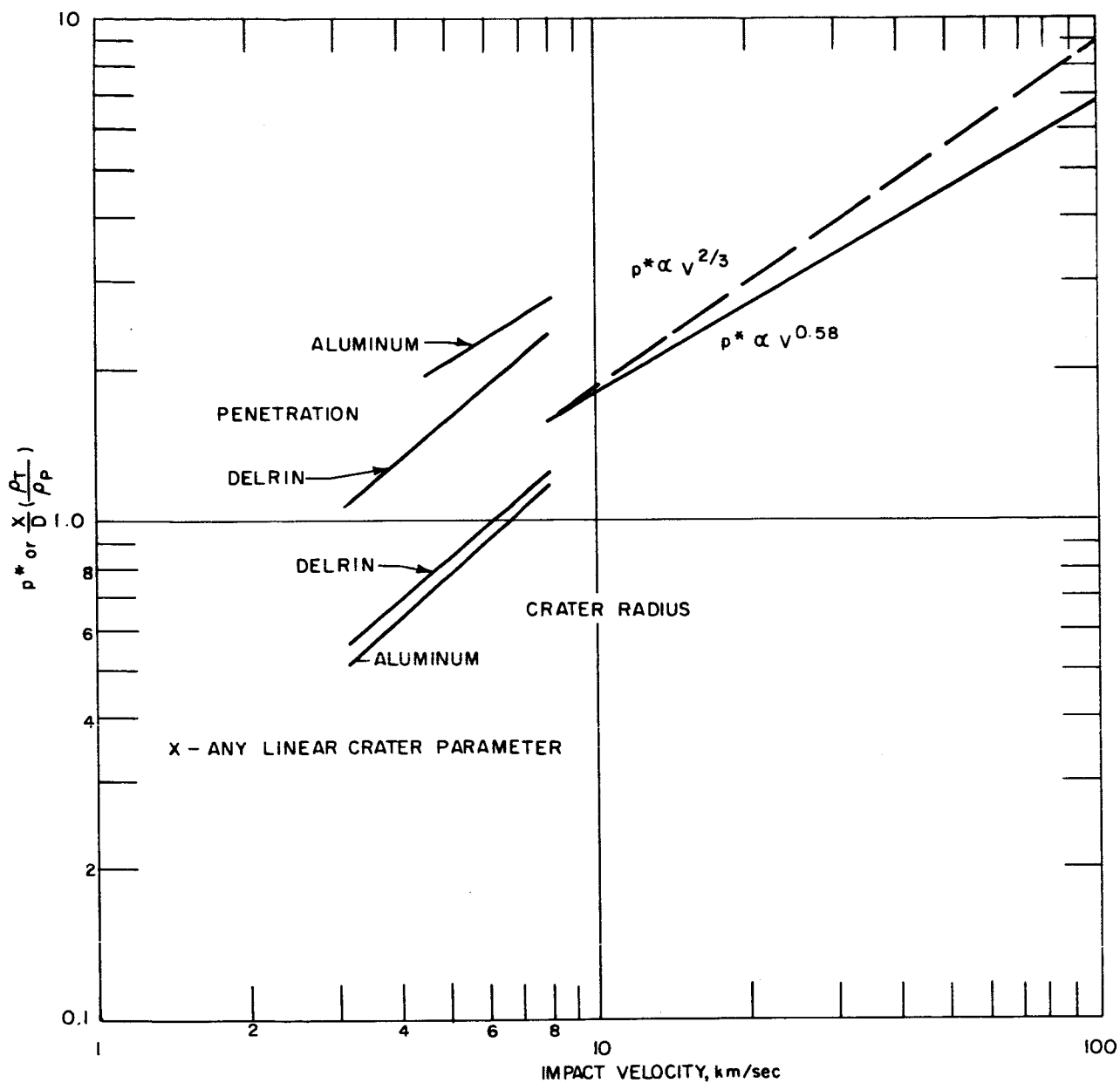


Figure 45 SCALING OF CRATER PARAMETERS FOR AVCOAT 5026 TILE



86-1474

Figure 46 SCALING OF CRATER PARAMETERS FOR AVCOAT 5026 HONEYCOMB



86-1475

Figure 47 SCALING OF CRATER PARAMETERS IN DOW SYLGARD 325, TILE AND HONEYCOMB AT ROOM TEMPERATURE

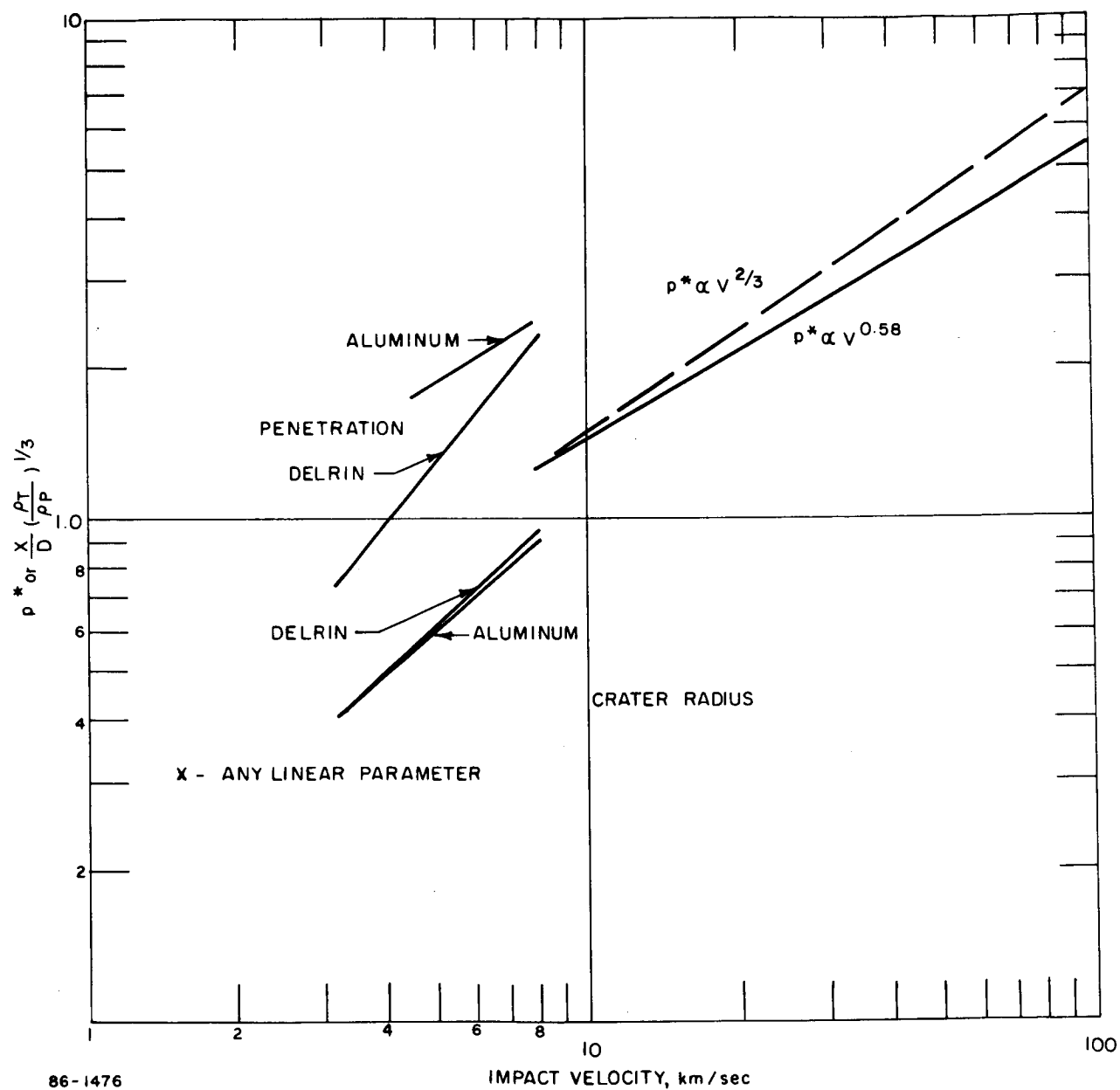


Figure 48 SCALING OF CRATER PARAMETERS IN DOW SYLGARD 325, TILE AND HONEYCOMB AT LOW TEMPERATURES

diameter ratios are much higher in these targets than are observed in normally dense targets, with comparable values of (ρ_p / ρ_t) . (Porosity, m , is the ratio of the density of the normally dense material to the density of the actual material.)

One difficulty in using the porosity is the fact that the density of the normally dense materials is not available. Avcoat 5026 is known to have a normal density of about 1.3 gm/cc. The Sylgard material is composed of material of normal density of 1.04 plus glass micro balloons. These micro balloons are made of a material with a density of 2.5 gm/cc; this material comprises 0.24 to 0.29 of the volume of the micro balloon.¹⁹ Hence, its normal density can be estimated to be from 1.3 to 1.6 gm/cc.

An attempt was made to fit the data to the form

$$\frac{p-r}{D} = m^k \left(\frac{\rho_p}{\rho_t} \right)^{1/2} - 1$$

This form has the following advantages:

- a. It goes to zero for like material impact.
- b. It has the correct density dependence for the crater geometry effects for long rod impact using the predictions of simple jet theory.

A reasonable fit at $V = 8$ km/sec was found with the form

$$\frac{p-r}{D} = m \left(\frac{\rho_p}{\rho_t} \right)^{1/2} - 1$$

The assumption that this value would remain constant for higher velocities

is expected to overestimate $\frac{p-r}{D}$ at higher velocities. This relation

should be useful for interpolation; since it has no theoretical basis, however, it should not be used for extrapolation.

6.3.2 Scaling for Spall Diameter

The ratio of spall diameter to l in the Sylgard tile material is not significantly different for impacts into targets at room temperature and at -150° (see Table XIX). For impacts on targets at -250°F , the spall is much larger. According to the scaling principle given in Paragraph 6.2.3, this ratio can be assumed to be independent of velocity.

TABLE XIX

SPALL DIAMETER/MEAN CRATER RADIUS FOR SYLGARD TILE

Temperature	RT	-150°F	-250°F
d_s/l	2.56	2.56	4.88

The situation is quite different for impacts in the honeycomb Sylgard targets, and represents a case where the characteristic size of the honeycomb cell is affecting the results. The spall for the aluminum projectile impacts is much larger than for the Delrin projectile impacts, and the difference between the spall at -250°F and other temperatures is suppressed. It is postulated that the difference in projectile mass was such that for the Delrin projectile there was an average tendency for the spall to be stopped by a particular honeycomb boundary, whereas for the aluminum projectile the spall would pass that boundary and be stopped at the next. Thus, there was a quantization effect which obscured the normal variation observed in the tile. The actual ratios observed are given in Table XX.

TABLE XX

SPALL DIAMETER/MEAN CRATER RADIUS FOR SYLGARD HONEYCOMB

Projectile \ Temperature	RT	-150°F	-250°F
Aluminum	3.34	3.34	4.08
Delrin	2.58	2.58	3.60

Again, the difference between targets impacted at room temperature and those impacted at -150°F was not significant, and the numbers for those cases represent average values. Note that the ratio for the Delrin projectile for the two higher temperatures is not significantly different from the values observed in the tile, whereas the aluminum projectile impacts into honeycomb targets give a much greater ratio at these temperatures. Note that the ratio for -250°F is much lower for impact into honeycomb than for impact into tile targets.

The same behavior is observed in reverse for the Avcoat material:

TABLE XXI

SPALL DIAMETER/MEAN CRATER RADIUS FOR AVCOAT

Combination	d_s/d
Avcoat Tile	2.38
Delrin on H. C.	2.24
Aluminum on H. C.	1.92

Here the spall diameter is reduced for aluminum impacts, but increased for Delrin impacts by the effect of the honeycomb structure. The spall diameter is about the same for aluminum and Delrin impacts of the same velocity of impact into the honeycomb, but the dependence of l on projectile mass results in the effective decrease of the ratio for aluminum impacts. In this case the spall diameters produced by the Delrin and aluminum impacts are kept to the same size by the effect of the honeycomb structure.

6.3.3 Scaling for Total Damage Depth

The only total damage depth phenomenon that is expected to persist to meteoritic velocities is the crater wall cracking observed in room temperature Sylgard targets. The ratio of total damage depth to the mean crater radius is

$$pm/l = 2.45$$

6.4 EXPECTED VARIATIONS

In applying these scaling relations, deviations from physical reality will occur for causes which may be separated into three distinct groups:

1. There are errors in the theoretical formulation of the scaling relations.
2. The scaling relation has an associated experimental uncertainty.
3. The physical situation, i. e., the cratering phenomenon, has an intrinsic uncertainty not expressed in the scaling relation.

The scaling relations given represent expected mean values. Groups 1 and 2 above represent uncertainties or errors in these mean values. Group 3 represents a variation of a particular physical situation from the mean.

It is difficult to assess the amount of error of Group 1. There were several assumptions made in arriving at the scaling relations used. Furthermore, the scaling is an extrapolation and is suspect on general principle. One estimate of the possible error is the "maximal" curve given. The crater geometry assumption that $p - r$ is constant is conservative; $p - r$ should decrease with increasing velocity.

The experimental error is more easily assessed. The scale factor for each curve is determined by an averaging operation involving approximately 30 points, each with an intrinsic deviation of approximately 15 percent. If one were sure that all of these points physically had the same mean, then the uncertainty would be approximately 15 percent $\sqrt{30}$ or about 3 percent. Actually different groups of data (data for targets at different temperature or with or without honeycomb) were combined because there was no significant difference between them. However, for each group individually, the level of significance is approximately 5 percent; this latter figure is representative of the experimental uncertainty in the scaling factors. There may also be systematic error resulting from measurement techniques and instruments. A likely source of significant systematic deviation would be that due to definition of crater parameters which, because of their irregularity, are ambiguous. Another possible source of systematic error would be projectile mass loss.

The deviation from the mean to be expected in practice due to the nature of the materials is the most easily estimated, for the RMS deviations for the fits can be used. An average value of the RMS scatter is 15 percent.

7.0 CONCLUSIONS

The results of this program have characterized the damage to be expected when Apollo and Gemini heat shield materials are impacted at hypervelocities.

Impacts into Avcoat 5026 produce craters typical of brittle materials. Due to the porosity of the material, craters have extraordinarily large penetration to crater diameter ratios, and for impacts by aluminum projectiles, transition to hypervelocity behavior occurs at the relatively high velocity of 7 km/ μ sec.

The Avcoat 5026 was tested over a range of temperature from -250°F at room temperature. Over this range, there was no significant temperature effect in the damage produced by hypervelocity impacts.

Over this same range, the Sylgard 325 material showed significant temperature changes in response to impact. Craters produced in room temperature targets had walls which were severely cracked, and which illustrated the large strains which this rubbery material will sustain. Craters formed in targets at temperatures of -150°F and -250°F were typical of craters formed in brittle materials and did not evidence this cracking. Targets impacted while at -250°F showed significantly more surface spall than did the other targets.

The transition region for impacts by aluminum projectiles persisted until the relatively high velocity of 4.5 km/sec was reached. At velocities up to about 6 km/sec, a puncture phenomenon was observed in the targets impacted at room temperature. This phenomenon, characteristic of the transition region, involved the deep penetration of the target by small particles of the projectile.

The craters produced in honeycomb materials were quite different in appearance than those produced in tile. The heat shield material was more susceptible to damage than the honeycomb structure, and crater boundaries were obviously affected by the presence of the structure. Nonetheless, there was no significant difference in the mean crater parameters for impacts into tile or honeycomb that could not be readily explained by material differences.

One significant difference between impacts into tile and honeycomb targets in the Sylgard 325 materials was the tendency of cells of the honeycomb to debond when impacted while at a temperature of -250°F. Complete debonding of one or more cells occurred in several instances for impacts into targets at this temperature; this property was not observed in targets impacted at higher temperatures.

Extensive materials testing has been performed on the target materials. The principle of time-temperature superposition has been applied to relate temperature variations to strain rate variations.

The results of the materials tests have been related to the cratering effects observed. The changes with temperature observed in the materials properties of Avcoat 5026 were small. The materials properties of Sylgard 325 showed a transition from rubbery to brittle material between -50 °F and -100 °F.

The results of this study have been scaled to meteoritic velocities using the principle of late stage equivalence.¹¹ For hemispherical craters, the following relationships predict the crater penetration:

$$\text{Avcoat 5026 tile} \quad p/\bar{D} = 0.624 (\rho_p/\rho_t)^{1/3} v^{0.58}$$

$$\text{Avcoat 5026 honeycomb} \quad p/\bar{D} = 0.705 (\rho_p/\rho_t)^{1/3} v^{0.58}$$

$$\text{Sylgard 325 (room temperature)} \quad p/\bar{D} = 0.473 (\rho_p/\rho_t)^{1/3} v^{0.58}$$

$$\text{Sylgard 325 (-150 °F, -250 °F)} \quad p/\bar{D} = 0.379 (\rho_p/\rho_t)^{1/3} v^{0.58}$$

\bar{D} = diameter of projectile mass equivalent sphere

v = velocity in km/sec

where, in general: the crater will not be hemispherical, but will approach a hemispherical geometry at high velocities. For an underdense material such as Avcoat, there may be appreciable deviation from hemisphericity throughout the meteoritic velocity region. This effect may be calculated by assuming (where l is the penetration in a hemispherical crater):

$$pr^2 = l^3$$

$$\frac{p-r}{\bar{D}} = m(\rho_p/\rho_t)^{1/2} - 1$$

This is a conservative prediction in that the actual deviation from a hemisphere will be less than or equal to that predicted.

REFERENCES

1. Jones, A. H., J.F. Polhemus, W. Herrmann, Survey of Hypervelocity Impact Information II, Addendum, MIT ASRL Report 99-2, Dec. 1963.
2. Private Communication with E. Alfaro, NASA Langley Research Laboratory.
3. Private Communication with A. K. Hopkins, Physics Branch, ASD, Wright Patterson AFB.
4. Leaderman, Elastic and Creep Properties of Filamentous Materials, Textile Foundation, Washington, D.C., 1943.
5. Ferry, J.D., Journal of Chem. Soc. 72, 3746, 1950.
6. Tobolsky, A. V., R.D. Andrews, J. Chem. Phys. 13, 3, 1945.
7. Williams, M.L., R.R. Landel, J. D. Ferry, J. Chem. Soc, 77, 3701, 1955.
8. Erich, F.R., Rheology, Volumes 1, 2, and 3, Academic Press Inc., New York, 1956.
9. Alfrey, T. Mechanical Prop. of High Polymers, Interscience Pub. Inc., 1948.
10. Herrmann, W. and A. H. Jones, Survey of Hypervelocity Impact Information, MIT ASRL Report 99-1 September 1962.
11. Walsh, J. M., and W. E. Johnson, On the Theory of Hypervelocity Impact, Seventh Hypervelocity Impact Symposium, Vol. II, Martin Co., Orlando, Fla., February 1965.
12. Riney, T.D., and J. F. Heyda, Hypervelocity Impact Calculations, Seventh Hypervelocity Impact Symposium, Vol. II, Martin Co., Orlando, Fla., February 1965.
13. Kinecke, J.H., Jr. and L.G. Richards, Influence of Target Strength on Hypervelocity Crater Formation in Aluminum, Sixth Symposium on Hypervelocity Impact, Vol. II Part 2, Firestone Tire and Rubber Co., August 1963.
14. Halperson, S.M. Comparisons Between Hydrodynamic Theory and Impact Experiments, Seventh Hypervelocity Impact Symposium, Vol. V, Martin Co., Orlando, Fla., February 1965.

REFERENCES (Concl'd)

15. Allison, F. E., Mechanics of Hypervelocity Impact, Seventh Hypervelocity Impact Symposium, Vol. V., Martin Co., Orlando, Fla. February 1965.
16. Christman, D.R., A. B. Wensel, and J. W. Gehring, Penetration Mechanisms of High Velocity Rods, Seventh Hypervelocity Impact Symposium, Vol. VI., Martin Co., Orlando, Fla. February 1965.
17. Bjork, R. L., Effect of Meteoroid Impact on Steel and Aluminum in Space., RAND Corp., Santa Monica, Calif., P-1662.
18. Sorensen, N.R., Systematic Investigation of Crater Formation in Metals, Seventh Hypervelocity Impact Symposium, Vol. VI, Martin Co., Orlando, Fla., February 1965.
19. Whipple, C. L. Dow Corning Corp., Midland Mich., personal communication.

APPENDIX A
DATA REDUCTION PROGRAM

A.1 INTRODUCTION

The purpose of this program is to fit the data obtained in this study to a specified form by a least-squares method, and to plot the data points and the computed function that is fitted to the data. Of particular interest are the features of the program that permit flexibility in specifying the form of the regression on the data to be included in a particular program. This program was written in FORTRAN IV by John Oliver of the Mathematics Department. The bulk of the program is applicable to any installation which can process FORTRAN IV, (that part which applies to the curve plotting, however, is not generally applicable).

A.2 METHOD

In this program the data fitted to a function by linear regression. A form is chosen from the function. For example

$$p = a_1 + a_2 V + a_3 T + a_4 T^2$$

where a_1, a_2, \dots, a_4 are unknown coefficients. The only restriction on the form is that it be linear in the coefficients, i. e. of the form:

$$p = a_1 f_1(\text{variables}) + a_2 f_2(\text{variables}) + \dots$$

and that the number of unknown coefficients be less than or equal to 10. The last is an arbitrary restriction that could be relaxed if necessary.

A fit that includes products can be performed by fitting logarithms:

$$\log_{10} \left(\frac{p}{d} \right) = a_1 + a_2 \log_{10} V + a_3 \log_{10} \left(\frac{\rho_p}{\rho_t} \right)$$

gives a fit of the form

$$\frac{p}{d} = 10^{a_1} V^{a_2} \left(\frac{\rho_p}{\rho_t} \right)^{a_3}$$

In more general notation, the form of the regression is (using the symbols used in the FORTRAN program):

$$F(v) = \sum_{n=1}^{NROW} a_n \text{AMAT}_n(v) \quad NROW < \quad NROW \leq 10$$

where $F(v)$ is some function of the variables, and each of the $AMAT_n(v)$ is some function of the variables. The constants, a_n , are to be determined by requiring that

$$\sum_{i=1}^{NCOL} \left(F(v_i) - \sum_{n=1}^{NROW} a_n AMAT_n(v_i) \right)^2 = SIG$$

be minimal, where the sum over i is the sum over all the $NCOL$ data points that are included in the regression.

In words, a fit is determined which minimizes the sum or squares of the deviations of the data from the fitted curve.

If SIG is minimal, then

$$\frac{\partial SIG}{\partial a_K} = 0$$

since we can vary SIG by varying a_K

$$\frac{\partial SIG}{\partial a_K} = \sum_{i=1}^{NCOL} \left[AMAT_K(v_i) \left(F(v_i) - \sum_{n=1}^{NROW} a_n AMAT_n(v_i) \right) \right] = 0$$

If there are $NROW$ unknown coefficients, the above procedure gives $NROW$ linear equations in $NROW$ unknowns which are solved by standard methods to give the a_K .

The program performs the regression and prints out the computed coefficients and the RMS (root mean square) deviation, σ . ($\sigma = \sqrt{SIG/NCOL - 1}$ where $NCOL$ is the number of data points included in the regression.)

A.3 INPUT

Any number of data points up to 250 may be read in for one regression. Each data point can have up to 14 variables. The first six variables are considered as independent variables and may be used to specify data to be skipped. The last eight variables are considered dependent. The specification of independent and dependent does not restrict the form of the regression but does affect the processing of the data in a way to be discussed below.

A subroutine which defines the form of the regression must be included. This subroutine is named `DEFINE` and is included in the listing. The subroutine, `DEFINE`, computes $F(v_i)$ and $AMAT_n(v_i)$. In addition, it defines the variables to be plotted on the axes of the plots. $F(v)$ is taken as the vertical axis. The

horizontal axis can be anything, but usually one of the AMAT's is chosen.

The rest of the input consists of control cards which specify the data to be used in a regression of the form given in DEFINE. This information gives the number of terms (AMAT's) to be included in the regression, the values of independent variables to be skipped, the captions for the axes of the plots, and those dependent variables for which the regression is to be run.

A.3.1 Input details

a. Data

The data is in a FORTRAN IV namelist format. One data point is read at a time. Fourteen variables are expected per data point. The first six are treated as independent; they can be used for specifying data to be skipped. The last eight are treated as dependent; they will be checked for missing data. The variables which were used in this study were:

Variable Number	Interpretation	FORTTRAN Symbol	Code
1	Identification number	AID(), XX(1,)	1. Identification: Given as a number with a decimal part to identify a repeat. For example, shot number 120 would be given as 120.00, whereas 120 R 2 would be 120.02. 2. Material code: 1 if the target material were Avcoat, 2 if it were Sylgard. 3. Structure code: 1 if the target were tile, 2 if it were honey-comb. 4. Temperature: in degrees Fahrenheit. 5. Projectile code: 1 if the projectile were aluminum, 2 if it were Delrin. 6. Velocity in ft/sec: the dependent variables were given in the units reported in Appendix C, cc for volume, inches for the rest.
2	Material code	FMAT(), XX(2,)	
3	Structure code	STRUG(), XX(3,)	
4	Temperature	TEMP(), XX(4,)	
5	Projectile code	PROJ(), XX(5,)	
6	Velocity of impact	VEL(), XX(6,)	
7	Spall diameter	DD(1,)	
8	Crater diameter	DD(2,)	
9	Penetration	DD(3,)	
10	Spall depth	DD(4,)	
11	Total damage depth	DD(5,)	
12	Crater volume	DD(6,)	
13, 14	Not used	DD(7,), DD(8,)	

The actual format used is shown; it could be changed within the limits set by namelist format restrictions. Except for the plotting routine, which subroutines are peculiar to the Avco installation, there is no identification of the variables in the program, so the order may be changed, or this program can be applied to an entirely different problem.

The first data entry on the last data card must be 999.99.

b. Control card

This card is also in namelist format. NROW is the number of terms to be used in the regression. ISKIP is the code giving information about data to be skipped. There are six values, one for each of the six independent variables. A negative integer means that the corresponding variable will not be used for skipping data. A zero means that a range of the variable will be skipped. A positive integer, n means that n specific values will be skipped.

c. Caption cards

The next three cards have data in columns 1 -54 which are reproduced on the captions of the plots. The title is first, followed by the x-axis caption, with the y axis caption last.

d. The next cards specify the skipping values, SKIP.

The numbers are written with a decimal point. For every ISKIP of zero, there must be two SKIP cards, one for the lower end of the range, and one for the upper. For each ISKIP of n there must be n cards, giving the n specific values of the variable to be skipped. These must be given in the same order as the numbers appeared in ISKIP.

e. The use card

This card is in namelist format. Eight integers are expected. For any integer, K , not equal to zero, but $K \leq 8$, the K^{th} dependent variable will be included in the regression.

For the last control card, make NROW greater than 10. This will terminate execution of the program and return control to the system monitor.

A.4 PROGRAM FLOW DESCRIPTION

A.4.1 Read in data and store independent variables in X and dependent variables in D. Total number of data points is KSTORE.

A.4.2 Read in control data which gives:

- a. Number of terms to be used in the regression called NROW.
- b. The independent variables to be used in skipping. Skipping can be over a range of variables or can be any number of specific values. This information is stored in ISKIP and SKIP.

A.4.3 Select all data not to be skipped.

A.4.4 Read in the use card. This card specifies the dependent variables to be used in the regression. The information is stored as NUSE.

A.4.5 For each dependent variable, in turn

- a. Remove any points for which dependent variable data is missing. Store the rest in XX (independent variables) and DD (dependent variables). The number of data points left is NCOL.
- b. Call subroutine DEFINE. This subroutine defines the $AMAT_n(v_i)$ and $F(v_i)$.
- c. Construct the vector E

$$E = \begin{pmatrix} e_1 \\ e_2 \\ \vdots \end{pmatrix}$$

$$e_k = \sum_{i \text{ data points}} F(v_i) AMAT_k(v_i)$$

- d. Construct the matrix, D

$$D = \begin{pmatrix} d_{11} & d_{12} & \cdots \\ d_{21} & d_{22} & \cdots \end{pmatrix}$$

$$d_{kj} = \sum_{i=1}^{NCOL} AMAT_k(v_i) AMAT_j(v_i)$$

Let the vector A be

$$A = \begin{pmatrix} a_1 \\ a_2 \\ \vdots \end{pmatrix}$$

The problem to be solved can be expressed in matrix notation.

$$D A = E$$

The solution is

$$A = D^{-1} E$$

Consequently, the next step is

e. Call MATXIN, a subroutine which computes D^{-1} from D

f. Compute $D^{-1} E$

$$g. \text{ Compute } \sigma = \sqrt{\frac{\sum_{i=1}^{NCOL} (F(v_i) - \sum_{n=1}^{NROW} a_n \text{AMAT}_n(v_i))^2}{NCOL-1}}$$

h. Print results and repeat for all specified cases.

A.5 SUBROUTINE DEFINE

A listing of subroutine DEFINE is included in this appendix. The FORTRAN statements immediately preceding the statement with statement number 2, define the AMAT's, which are the terms included in the regression. For example, a constant is included in the regression. Hence the first statement might be:

$$\text{AMAT}(1, K) = 1.0$$

If a term linear in velocity were desired, the next term might be:

$$\text{AMAT}(2, K) = \text{VEL}(K)$$

Other terms can be defined as desired. This subroutine has storage in common with the main program. The symbols as used are shown below. In general, (those symbols marked "no" should not be used.)

	<u>Symbol</u>	<u>Interpretation</u>
no	X (KI, J)*	Independent variable
	AID (JI)	Identification number XX(1, JI)
	FMAT (JI)	Material code, XX(2, JI)
	STRUC (JI)	Structure code, XX(3, JI)
	TEMP (JI)	Temperature, °F, XX(4, JI)
	PROJ (JI)	Projectile code XX(5, JI)
	VEL (JI)	Velocity in ft/sec XX(6, JI)
no	D (J)	Dependent variable
	NUSE (N)	Current dependent variable in the regression
	Y (JI)	DD (NUSE (N), JI)
no	U (I, L)	Element of D or D ⁻¹ depending on stage of computation
	AMAT (I, JI)	The I th term in the regression
no	A(I)	Coefficient of I th term in the regression.
no	Z (JI)	Value computed from fitted curve
no	G (I)	Vector in matrix equation, called E in previous sections
	XX (KI, JI)	Independent variable
	DD (KI, JI)	Dependent variable
	F (JI)	Dependent function, to be defined
	NROW	Number of terms included in regression
	NCOL	Number of data points included in regression
no	SKIP (N, J)	Skipping values
no	DUMMY (K)	Last data point
no	ISKIP (N)	Skipping values
	PLX (JI)	Independent function, to be defined.

* K as a subscript will refer to the Kth (of 14) variable, KI will be the KIth (of 6) independent variable, KD will be the KDth (of 8) dependent variable, J will be the Jth data point, JI will be the JIth of the data points included in the regression. In the actual program dummy subscripts, usually K, are used.

The FORTRAN statements immediately preceding the statement with statement number, 3, define F, which is the function of the dependent variable, and PLX, which will be the x-axis function.

F is usually defined in terms of Y, which is the dependent variable for which the regression is being run. For example, a linear fit might be:

$$F(K) = Y(K)$$

or a log fit might be

$$F(K) = A \log_{10}(Y(K))$$

PLX is usually defined in terms of the velocity. For example, in a linear fit,

$$PLX(K) = VEL(K)$$

or, in a log fit,

$$PLX(K) = A \log_{10}(VEL(K))$$

A. 6 USE OF THE PROGRAM

In practice, in using the method given in this appendix, several precautions must be observed. The equations used tacitly assume that all the error is in the dependent quantity, $F(v)$. In actuality, there will be experimental errors in the independent quantities also, and sometimes the difference in the fit can be appreciable. In the present study the dependent variables, which are various crater parameters, have much greater uncertainties associated with them than do the independent variables, projectile velocity and type, target material and temperature. Thus, use of the regression method described in the present study is justifiable on this point.

There is also a tacit assumption that the source of error (i. e., deviation from the fit) is random and is constant over the range of independent variable. If this is not true, data points in regions of larger inherent error are weighted more heavily in the regression than is their fair share. (This occurred in the present study but was not serious.) The assumption of constant error is best for the log plots since this is equivalent to assuming that the error is a constant percentage. Actually, the error is probably well represented by a sum of a percentage plus a constant, but the percentage dominates over the experimental velocity range.

The value of σ is both a measure of the experimental scatter in the data and the goodness of the fit. The scatter can be reduced by using a more general form for the regression; indeed, an infinite number of curves could be drawn that would pass exactly through all of the data points. The choice of the form of

the regression is thus a matter of judgment and depends on physical considerations. There are statistical considerations that can be used, but these also involve assumptions the validity of which is a matter of judgment.

The forms of the regressions given here are linear in the terms that are functions of velocity (such as $\log(v)$, or energy, etc.). Actually, the mean curve that represents the variation of the parameters with velocity probably is curvilinear rather than straight. However, the scatter in the data is such that attempts to determine the curvature would be meaningless. Values of the slope obtained are not very accurate. Consider, for instance, a crater parameter, l , which in reality,

$$l = KV^{0.7}$$

The velocity varies only by a factor of 2.5. A reasonable value for the scatter in l is 15 percent. Assume the curve is not affected by temperature. Then there are six points at the upper end and six at the lower. Thus the error at the upper end is $\sim 15\%\sqrt{6}$, which combined with a like error at the lower end gives $15\%\sqrt{3}$ for a standard error in vertical change over a velocity change of 2.5, which results in an uncertainty of 22 percent over a velocity change by a factor of 10. Expressed another way, the standard error to be expected in the value of a slope is about ± 0.1 , which is quite appreciable compared to the 0.7 slope expected. When the slope can be expected to vary with temperature, the situation is worse. Consequently, in the scaling section, the only numbers really used for scaling were the average values at the high end of the velocity range; the values obtained for slopes were not used at all.

A.7 LISTING OF THE PROGRAMS USED IN THIS STUDY

```

$J0B          *2121  LEAST
$IBFTC LEAST  LIST
      DIMENSION X(6,250),AID(250),FMAT(250),STRUC(250),TEMP(250),PR0J(25
      10),VEL(250),D(8,250),T(9),NUSE(8),Y(250),U(10,10),AMAT(10,250),
      2A(10),Z(250),G(10),XX(6,250),F(250),DD(8,250),DUMMY(14),ISKIP(6),
      3ISKIP1(6),SKIP(6,250),PLX(250),TX(9),TY(9),ICPL0T(250),
      4FP(100),ZP(100),PLXP(100),MGM(6)
      COMMON X,AID,FMAT,STRUC,TEMP,PR0J,VEL,D, NUSE,Y,U,AMAT,A,Z,G,XX,
      1DD,F,NR0W,NC0L,SKIP,DUMMY,ISKIP,ISKIP1,PLX
      NAMELIST/NAMC0N/NR0W,ISKIP
      NAMELIST/NAMUSE/NUSE
      NAMELIST/NAMDUM/DUMMY
      CALL IDV(84H 80X Z330-SUIT0R HEAT SHIELD IMPACT DATA
      1 ,6H 2121 )
      MGM(1)=19
      MGM(2)=38
      MGM(3)=63
      MGM(4)=16
      MGM(5)=55
      MGM(6)=44
      1 WRITE(6,1000)
1000 FORMAT(1H1)
      K=1
      2 READ(5,NAMDUM)
      IF(DUMMY(1).EQ.999.99)G0 T0 31
      D0 51 J=1,6
      51 X(J,K)=DUMMY(J)
      D0 52 J=1,8
      52 D(J,K)=DUMMY(J+6)
      K=K+1
      G0 T0 2
      31 KST0RE=K-1
C THIS COMPLETES READING IN ALL THE DATA. NOW CHECK FOR DATA T0 BE
C SKIPPED
C IF ISKIP LT 0, ALL DATA WILL BE USED
C IF ISKIP =0,ALL DATA BETWEEN SKIP(1) AND SKIP(2)(INCLUSIVE) WILL
C BE SKIPPED.
C IF ISKIP GT 0,DATA=SKIP WILL BE SKIPPED. IN THIS CASE,ISKIP=NUMBER
C OF DATA SETS T0 BE SKIPPED
      20 READ(5,NAMC0N)
      IF(NR0W.GT.10)G0 T0 501
      READ(5,1050)T
      READ(5,1050)TX
      READ(5,1050)TY
1050 FORMAT(9A6)
      D0 53 L=1,6
      ISKIP1(L)=ISKIP(L)
      IF(ISKIP(L).LT.0)G0 T0 53
      IF(ISKIP(L).EQ.0)ISKIP1(L)=2
      N=ISKIP1(L)
      D0 21 J=1,N
      READ(5,1021)SKIP(L,J)
1021 FORMAT(F10.2)
      21 CONTINUE

```

```

53 CONTINUE
25 J=1
   D0 30 K=1,KSTORE
   D0 54 L=1,6
   IF(ISKIP(L).LT.0)G0 T0 54
   IF(ISKIP(L).EQ.0)G0 T0 27
   IF(ISKIP(L).GT.0)G0 T0 28
27 IF(X(L,K).LT.SKIP(L,1))G0 T0 54
   IF(X(L,K).GT.SKIP(L,2))G0 T0 54
   G0 T0 30
28 N=ISKIP(L)
   D0 29 M=1,N
   IF(X(L,K).EQ.SKIP(L,M))G0 T0 30
29 CONTINUE
54 CONTINUE
26 D0 32 L=1,6
32 XX(L,J)=X(L,K)
   D0 33 L=1,8
33 DD(L,J)=D(L,K)
   J=J+1
30 CONTINUE
   JSTORE=J-1
   WRITE(6,1022)KSTORE
1022 FORMAT(1H0 10X,I5,28H DATA SETS HAVE BEEN READ IN)
   WRITE(6,1023)JSTORE
1023 FORMAT(1H 10X,I5,34H DATA SETS WILL BE USED IN FITTING)
   WRITE(6,1024)NR0W
1024 FORMAT(1H 10X,I5,32H COEFFICIENTS WILL BE DETERMINED)
   D0 55 J=1,6
   IF(ISKIP(J).LT.0)G0 T0 55
   WRITE(6,1025)J
1025 FORMAT(1H0 15X,26H SKIPPING WAS DONE WITH THE,I3,21H INDEPENDENT VAR
11ABLE)
   WRITE(6,1026)ISKIP(J)
1026 FORMAT(1H 15X,9H ISKIP WAS,I5)
   WRITE(6,1027)
1027 FORMAT(1H 15X,24H THE SKIPPING VALUES WERE)
   N=ISKIP(J)
   D0 35 M=1,N
   WRITE(6,1028)M,SKIP(J,M)
1028 FORMAT(1H 20X,5H SKIP(,I3,1H),F12.2)
35 CONTINUE
55 CONTINUE
C THE DATA IS NOW SET UP IN XX AND DD MATRICES
34 NC0L=JSTORE
   READ(5,NAMUSE)
   D0 500 J=1,8
   IF(NUSE(J).EQ.0)G0 T0 500
   L=NUSE(J)
   N=1
   D0 36 K=1,JSTORE
   Y(N)=DD(L,K)
   IF(Y(N).EQ.0.)G0 T0 36
   AID(N)=XX(1,K)
   FMAT(N)=XX(2,K)
   STRUC(N)=XX(3,K)
   TEMP(N)=XX(4,K)
   PROJ(N)=XX(5,K)
   VEL(N)=XX(6,K)
   KPL=0

```

```

      IF(STRUC(N).EQ.2.)KPL=3
      IF(TEMP(N).GT.0.)ICPLØT(N)=1+KPL
      IF(TEMP(N).LE.0.)ICPLØT(N)=2+KPL
      IF(TEMP(N).LT.(-200.))ICPLØT(N)=3+KPL
      N=N+1
36  CØNTINUE
      NCØL=N-1
      CALL DEFINE
      DØ 37 K=1,NRØW
      G(K)=0.
      DØ 38 L=1,NCØL
38  G(K)=G(K)+F(L)*AMAT(K,L)
37  CØNTINUE
      DØ 39 K=1,NRØW
      DØ 40 K1=1,NRØW
      U(K,K1)=0.
      DØ 41 L=1,NCØL
41  U(K,K1)=U(K,K1)+AMAT(K,L)*AMAT(K1,L)
40  CØNTINUE
39  CØNTINUE
      CALL MATXIN(U,NRØW,10,INDEX,DET)
      IF(INDEX.EQ.1)GØ TØ 50
      WRITE(6,1040)J
1040 FØRMAT(1HØ 10X,47HTRØUBLE INVERTING MATRIX FØR DEPENDENT VARIABLE,
      1I3)
      GØ TØ 500
50  DØ 42 K=1,NRØW
      A(K)=0.
      DØ 43 L=1,NRØW
43  A(K)=A(K)+G(L)*U(L,K)
42  CØNTINUE
      DØ 44 L=1,NCØL
      Z(L)=0.
      DØ 45 K=1,NRØW
45  Z(L)=Z(L)+A(K)*AMAT(K,L)
44  CØNTINUE
      SIG=0.
      DØ 46 L=1,NCØL
46  SIG=SIG+(F(L)-Z(L))*2
      ANCØL=NCØL-1
      SIG=SIG/ANCØL
      WRITE(6,1045)J,NCØL
1045 FØRMAT(1H/// 10X,31HSØLUTION FØR DEPENDENT VARIABLE,13,6H USING,14
      1,7H PØINTS)
      DØ 47 K=1,NRØW
      WRITE(6,1046)K,A(K)
1046 FØRMAT(1H 15X,2HA(,12,1H),5X,E12.5)
47  CØNTINUE
      WRITE(6,1047)SIG
1047 FØRMAT(1H 10X,29HSQUARE ØF STANDARD DEVIATION=,E12.5)
70  XL=100000.
      XU=-100000.
      YL=100000.
      YU=-100000.
      DØ 71 L=1,NCØL
      IF(Z(L).LT.YL)YL=Z(L)
      IF(Z(L).GT.YU)YU=Z(L)
      IF(PLX(L).LT.XL)XL=PLX(L)
      IF(PLX(L).GT.XU)XU=PLX(L)
71  CØNTINUE

```

```

DØ 72 L=1,NCØL
IF(F(L).LT.YL)YL=F(L)
IF(F(L).GT.YU)YU=F(L)
72 CØNTINUE
NF=1
DØ 80 L=1,6
KK=1
DØ 81 LL=1,NCØL
IF(ICPLØT(LL).NE.L)GØ TØ 81
FP(KK)=F(LL)
ZP(KK)=Z(LL)
PLXP(KK)=PLX(LL)
KK=KK+1
81 CØNTINUE
NCØLP=KK-1
IF(NCØLP.EQ.Ø)GØ TØ 80
NC=MGM(L)
CALL AICRT3(Ø,Ø,PLXP,FP,NCØLP,1,1,1,NC,T,TX,TY,NF,1,16.Ø,16.Ø,2,
1XL,XU,2,YL,YU)
NF=2
CALL AICRT3(Ø,Ø,PLXP,ZP,NCØLP,1,2,2,42,T,TX,TY,2,1,16.Ø,16.Ø,2,XL,
1XU,2,YL,YU)
80 CØNTINUE
500 CØNTINUE
WRITE(6,1048)
1048 FØRMAT(1H1)
GØ TØ 20
501 CALL EXIT
STØP
END

```

```

$JØB          *2121 MATXN
$IBFTC MATXN  LIST
SUBROUTINE MATXIN (A, NZ, MAXZ, INDEX, DET)
C   THIS SUBROUTINE WILL INVERT ANY MATRIX (MAXIMUM ORDER OF 40) BY A
C   MODIFIED GAUSS-ELIMINATION METHOD.
C   A = THE INPUT MATRIX AS WELL AS THE OUTPUT MATRIX.
C   NZ = THE ORDER OF MATRIX A.
C   MAXZ = THE MAXIMUM ORDER DIMENSIONED IN THE CALLING PROGRAM.
C   INDEX = 1 IF THE INVERSE IS FOUND.
C           = 2 IF THE INPUT MATRIX IS SINGULAR.
C           = 3 IF MACHINE ERROR OCCURRED. IF PROGRAMMER WISHES TO LOOP
C           BACK FOR ANOTHER TRY, BE SURE TO RESET THE INPUT MATRIX.
C   DET = THE DETERMINANT OF THE INPUT MATRIX.
C   MATRIX A IS DUMMY DIMENSIONED. THIS SUBROUTINE REFERS TO IT AS A
C   SINGLE DIMENSIONED VARIABLE BY FINDING THE PROPER SUBSCRIPT.
C   DIMENSION A(2),KØL(101),RØW(101)
      N=NZ
      MAX=MAXZ
      DET=1.0
      KØL(1)=1
      DØ 10 I=2,N
        KØL(I)=KØL(I-1)+1
10  CØNTINUE
      DØ 120 K=1,N
        L=N-K+1
        M=KØL(1)
        J=1
        IF(N-K) 190,60,20
20  AMPY= ABS(A(1))
      DØ 40 I=2,L
        IF(AMPY- ABS(A(I))) 30,40,40
30  J=I
        AMPY= ABS(A(I))
        M=KØL(I)
40  CØNTINUE
        IF(KØL(1)-M) 50,60,50
50  DET= -DET
        KØL(J)=KØL(1)
        KØL(1)=M
60  IF(A(J)) 70,200,70
70  AMPY=A(J)
        DET=DET*AMPY
        DØ 80 I=2,N
          IS=(I-1)*MAX+J
          RØW(I-1)=A(IS)/AMPY
          IC=(I-2)*MAX
          IS=IC+J
          IT=IC+1
          A(IS)=A(IT)
80  CØNTINUE
        RØW(N)=1.0/AMPY
        IC=(N-1)*MAX
        IS=IC+J
        IT=IC+1

```



```

      A(IS)=A(IT)
      DØ 100 I=2,N
      AMPY=A(I)
      DØ 90 J=2,N
      IS=(J-2)*MAX+I-1
      IT=(J-1)*MAX+I
      A(IS)=A(IT)-AMPY*RØW(J-1)
90  CØNTINUE
      IS=(N-1)*MAX+I-1
      A(IS)= -AMPY*RØW(N)
100 CØNTINUE
      DØ 110 J=1,N
      KØL(J)=KØL(J+1)
      IS=(J-1)*MAX+N
      A(IS)=RØW(J)
110 CØNTINUE
      KØL(N)=M
120 CØNTINUE
      DØ 170 K=1,N
      IF(KØL(K)-K) 190,170,130
130 DØ 160 I=K,N
      IF(KØL(I)-K) 190,140,160
140 DØ 150 J=1,N
      IS=(I-1)*MAX+J
      IT=(K-1)*MAX+J
      RØW(1)=A(IS)
      A(IS)=A(IT)
      A(IT)=RØW(1)
150 CØNTINUE
      M=KØL(K)
      KØL(K)=KØL(I)
      KØL(I)=M
      GØ TØ 170
160 CØNTINUE
      INDEX=3
      GØ TØ 180
170 CØNTINUE
      INDEX=1
180 RETURN
190 INDEX=3
      GØ TØ 180
200 INDEX=2
      GØ TØ 180
      END

```

THE LISTING OF THE DATA INPUT CARDS USED IN THE PROGRAM FOLLOWS

```

$NAMDUM DUMMY=001.00,1,2,+072,2,09568,.0001,.0000,.2040,.0001,.2110,.0488,2*0$
$NAMDUM DUMMY=002.00,1,2,+072,2,10225,.0001,.1030,.2150,.0001,.2400,.0374,2*0$
$NAMDUM DUMMY=003.00,1,2,-148,2,11098,.0001,.1390,.2340,.0001,.2370,.0682,2*0$
$NAMDUM DUMMY=004.00,1,2,-145,2,09960,.0001,.1390,.2240,.0001,.2240,.0533,2*0$
$NAMDUM DUMMY=005.00,1,2,-258,2,09133,.0001,.1090,.2380,.0001,.2430,.0427,2*0$
$NAMDUM DUMMY=006.00,1,2,-250,2,09726,.1301,.1040,.2560,.0201,.2240,.0678,2*0$
$NAMDUM DUMMY=007.00,1,1,+084,2,09029,.0001,.0960,.1460,.0001,.1620,.0114,2*0$
$NAMDUM DUMMY=007.01,1,1,+079,2,07143,.0001,.0800,.0980,.0001,.0000,.0087,2*0$
$NAMDUM DUMMY=008.00,1,1,+078,2,10624,.0001,.1270,.1950,.0001,.1970,.0388,2*0$
$NAMDUM DUMMY=009.00,1,1,-147,2,08127,.0001,.1090,.1670,.0001,.1740,.0147,2*0$
$NAMDUM DUMMY=010.00,1,1,-155,2,08564,.0001,.1110,.1290,.0001,.1870,.0200,2*0$
$NAMDUM DUMMY=011.00,1,1,-250,2,10283,.1600,.1500,.1950,.0200,.1950,.0594,2*0$
$NAMDUM DUMMY=012.00,1,1,-248,2,09653,.0001,.1220,.1590,.0001,.1590,.0366,2*0$
$NAMDUM DUMMY=013.00,1,2,+067,2,17495,.2800,.1830,.3860,.0300,.0000,.2970,2*0$
$NAMDUM DUMMY=013.01,1,2,+078,2,14881,.2100,.1440,.3010,.0600,.0000,.0970,2*0$
$NAMDUM DUMMY=014.00,1,2,+067,2,17773,.3100,.2230,.3220,.0500,.0000,.3530,2*0$
$NAMDUM DUMMY=015.00,1,2,-152,2,15346,.2200,.1720,.2920,.0200,.0000,.1560,2*0$
$NAMDUM DUMMY=016.00,1,2,-146,2,15276,.2600,.2050,.2500,.0200,.0000,.1220,2*0$
$NAMDUM DUMMY=017.00,1,2,-250,2,15491,.2500,.1610,.3040,.0200,.0000,.1290,2*0$
$NAMDUM DUMMY=018.00,1,2,-246,2,14893,.2600,.1940,.2640,.0500,.0000,.1430,2*0$
$NAMDUM DUMMY=019.00,1,1,+075,2,14558,.2400,.1510,.2100,.0200,.0000,.0770,2*0$
$NAMDUM DUMMY=019.01,1,1,+075,2,12626,.1700,.1370,.1880,.0200,.0000,.0550,2*0$
$NAMDUM DUMMY=020.00,1,1,+070,2,15123,.2200,.1650,.2060,.0200,.0000,.0730,2*0$
$NAMDUM DUMMY=021.00,1,1,-163,2,16019,.2300,.1760,.2080,.0200,.0000,.0800,2*0$
$NAMDUM DUMMY=022.00,1,1,-141,2,14674,.1900,.1540,.2140,.0200,.0000,.0690,2*0$
$NAMDUM DUMMY=023.00,1,1,-250,2,13528,.1600,.1550,.2060,.0001,.0000,.0720,2*0$
$NAMDUM DUMMY=024.00,1,1,-241,2,13624,.2600,.1790,.2200,.0200,.0000,.0303,2*0$
$NAMDUM DUMMY=025.00,1,2,+070,2,18552,.2600,.2030,.2880,.0200,.0000,.2940,2*0$
$NAMDUM DUMMY=026.00,1,2,+070,2,18590,.2700,.2230,.2840,.0300,.0000,.2940,2*0$
$NAMDUM DUMMY=027.00,1,2,-152,2,21604,.3700,.2470,.3050,.1000,.0000,.4240,2*0$
$NAMDUM DUMMY=028.00,1,2,-151,2,21176,.3000,.2350,.3190,.0600,.0000,.2510,2*0$
$NAMDUM DUMMY=029.00,1,2,-253,2,22311,.4300,.2120,.3010,.1000,.0000,.4100,2*0$
$NAMDUM DUMMY=030.00,1,2,-249,2,21705,.3300,.1920,.3150,.0300,.0000,.3020,2*0$
$NAMDUM DUMMY=031.00,1,1,+070,2,19171,.2000,.1800,.2100,.0100,.0000,.0920,2*0$
$NAMDUM DUMMY=031.01,1,1,+080,2,21219,.3300,.2120,.2530,.0400,.0000,.2830,2*0$
$NAMDUM DUMMY=032.00,1,1,+065,2,22296,.4100,.2420,.2530,.0500,.0000,.2310,2*0$
$NAMDUM DUMMY=032.01,1,1,+070,2,21818,.2900,.2120,.2140,.0500,.0000,.2100,2*0$
$NAMDUM DUMMY=032.02,1,1,+075,2,19081,.2400,.2000,.2420,.0100,.0000,.1050,2*0$
$NAMDUM DUMMY=033.00,1,1,-149,2,21898,.3900,.2330,.2960,.0500,.0000,.3700,2*0$
$NAMDUM DUMMY=033.02,1,1,-146,2,22184,.3800,.2270,.2530,.0400,.0000,.1830,2*0$
$NAMDUM DUMMY=034.00,1,1,-158,2,21345,.4200,.2250,.2050,.0500,.0000,.2180,2*0$
$NAMDUM DUMMY=035.00,1,1,-254,2,20621,.2800,.1940,.2200,.0200,.0000,.1150,2*0$
$NAMDUM DUMMY=036.00,1,1,-246,2,21012,.3100,.2250,.2650,.0300,.0000,.2960,2*0$
$NAMDUM DUMMY=037.00,1,2,+065,2,22885,.4100,.2820,.3310,.0800,.0000,.4950,2*0$
$NAMDUM DUMMY=037.01,1,2,+072,2,23698,.3750,.2600,.3120,.0300,.0000,.3180,2*0$
$NAMDUM DUMMY=037.02,1,2,+070,2,22957,.3600,.2740,.3190,.0400,.0000,.4160,2*0$
$NAMDUM DUMMY=037.03,1,2,+075,2,22764,.3700,.2000,.4040,.0900,.0000,.3420,2*0$
$NAMDUM DUMMY=038.00,1,2,+065,2,23396,.3700,.2430,.3450,.1200,.0000,.4060,2*0$
$NAMDUM DUMMY=038.01,1,2,+073,2,22691,.3900,.2890,.3220,.0300,.0000,.3950,2*0$
$NAMDUM DUMMY=038.02,1,2,+072,2,23310,.4600,.3000,.3930,.0800,.0000,.4630,2*0$
$NAMDUM DUMMY=039.00,1,2,-150,2,25082,.3800,.2540,.3460,.0300,.0000,.3810,2*0$
$NAMDUM DUMMY=040.00,1,2,-146,2,23466,.4200,.2950,.3600,.0800,.0000,.4610,2*0$
$NAMDUM DUMMY=041.00,1,2,-255,2,23584,.3901,.2830,.3210,.0800,.0000,.3950,2*0$

```

\$NAMSDUM DUMMY=041.01,1,2,-250,2,23912,.4000,.2820,.3490,.0700,.0000,.3920,2*0\$
 \$NAMSDUM DUMMY=042.00,1,2,-253,2,23607,.4100,.2930,.3400,.0600,.0000,.3870,2*0\$
 \$NAMSDUM DUMMY=042.01,1,2,-250,2,24613,.4300,.2700,.3610,.0600,.0000,.5140,2*0\$
 \$NAMSDUM DUMMY=042.02,1,2,-250,2,23540,.4350,.2840,.3560,.0800,.0000,.4160,2*0\$
 \$NAMSDUM DUMMY=043.00,1,1,+072,2,23641,.3400,.2200,.2370,.0300,.0000,.1730,2*0\$
 \$NAMSDUM DUMMY=043.01,1,1,+073,2,23148,.4390,.2650,.2840,.0500,.0000,.2710,2*0\$
 \$NAMSDUM DUMMY=044.00,1,1,+070,2,22763,.4300,.2430,.2600,.0700,.0000,.2260,2*0\$
 \$NAMSDUM DUMMY=044.01,1,1,+075,2,24154,.3450,.2400,.2670,.0500,.0000,.1430,2*0\$
 \$NAMSDUM DUMMY=044.02,1,1,+077,2,23431,.3650,.2650,.2750,.0500,.0000,.0000,2*0\$
 \$NAMSDUM DUMMY=044.03,1,1,+072,2,23757,.4400,.2420,.2640,.0400,.0000,.2030,2*0\$
 \$NAMSDUM DUMMY=045.00,1,1,-151,2,24170,.3600,.2240,.2470,.0400,.0000,.3160,2*0\$
 \$NAMSDUM DUMMY=046.00,1,1,-150,2,23085,.3300,.2110,.2310,.0500,.0000,.1460,2*0\$
 \$NAMSDUM DUMMY=047.00,1,1,-255,2,23231,.3200,.2390,.2440,.0400,.0000,.2030,2*0\$
 \$NAMSDUM DUMMY=047.01,1,1,-250,2,23981,.4000,.2690,.2790,.0400,.0000,.2620,2*0\$
 \$NAMSDUM DUMMY=048.00,1,1,-250,2,24582,.4300,.2490,.2870,.0600,.0000,.2710,2*0\$
 \$NAMSDUM DUMMY=085.00,1,2,+068,1,08859,.0001,.1270,.3630,.0001,.4290,.0700,2*0\$
 \$NAMSDUM DUMMY=086.00,1,2,+068,1,09375,.0001,.1160,.4760,.0001,.5550,.0550,2*0\$
 \$NAMSDUM DUMMY=087.00,1,2,-144,1,08321,.0001,.1360,.4930,.0001,.4830,.0650,2*0\$
 \$NAMSDUM DUMMY=088.00,1,2,-142,1,11775,.0001,.1420,.4420,.0001,.4890,.1300,2*0\$
 \$NAMSDUM DUMMY=089.00,1,2,-241,1,09910,.0001,.1130,.5570,.0001,.6140,.1200,2*0\$
 \$NAMSDUM DUMMY=090.00,1,2,-240,1,09939,.0001,.1490,.4300,.0001,.4750,.1550,2*0\$
 \$NAMSDUM DUMMY=091.00,1,1,+068,1,09203,.0001,.1100,.3480,.0001,.3870,.0550,2*0\$
 \$NAMSDUM DUMMY=092.00,1,1,+068,1,08441,.0001,.1050,.3790,.0001,.4170,.0500,2*0\$
 \$NAMSDUM DUMMY=093.00,1,1,-160,1,08616,.0001,.1160,.2930,.0001,.3450,.0500,2*0\$
 \$NAMSDUM DUMMY=094.00,1,1,-148,1,08653,.0001,.0990,.3140,.0001,.3150,.0400,2*0\$
 \$NAMSDUM DUMMY=095.00,1,1,-220,1,08630,.0001,.1110,.3410,.0001,.4100,.0650,2*0\$
 \$NAMSDUM DUMMY=096.00,1,1,-250,1,08653,.0001,.1260,.2800,.0001,.3690,.0600,2*0\$
 \$NAMSDUM DUMMY=097.00,1,2,+068,1,14847,.0001,.1920,.4560,.0001,.0000,.2100,2*0\$
 \$NAMSDUM DUMMY=098.00,1,2,+068,1,14232,.0001,.1750,.4060,.0001,.0000,.1700,2*0\$
 \$NAMSDUM DUMMY=099.00,1,2,-145,1,15051,.0001,.2170,.3790,.0001,.0000,.2200,2*0\$
 \$NAMSDUM DUMMY=100.00,1,2,-140,1,15278,.0001,.1970,.4040,.0001,.0000,.2600,2*0\$
 \$NAMSDUM DUMMY=101.00,1,2,-241,1,15385,.3100,.2020,.4640,.0400,.0000,.2700,2*0\$
 \$NAMSDUM DUMMY=102.00,1,2,-247,1,14829,.3170,.2320,.4030,.0700,.0000,.3100,2*0\$
 \$NAMSDUM DUMMY=103.00,1,1,+068,1,15924,.0001,.2270,.3750,.0001,.0000,.2400,2*0\$
 \$NAMSDUM DUMMY=104.00,1,1,+068,1,14107,.0001,.1640,.3180,.0001,.0000,.1000,2*0\$
 \$NAMSDUM DUMMY=105.00,1,1,-150,1,15189,.0001,.1880,.3610,.0001,.0000,.1700,2*0\$
 \$NAMSDUM DUMMY=106.00,1,1,-150,1,14350,.0001,.1740,.2820,.0001,.0000,.1050,2*0\$
 \$NAMSDUM DUMMY=107.00,1,1,-243,1,15178,.0001,.2140,.3890,.0001,.0000,.2500,2*0\$
 \$NAMSDUM DUMMY=108.00,1,1,-243,1,13345,.0001,.1450,.2970,.0001,.0000,.0800,2*0\$
 \$NAMSDUM DUMMY=109.00,1,2,+068,1,19450,.0001,.2630,.4020,.0001,.0000,.3700,2*0\$
 \$NAMSDUM DUMMY=110.00,1,2,+068,1,21182,.3750,.2830,.4250,.0700,.0000,.4600,2*0\$
 \$NAMSDUM DUMMY=110.01,1,2,+068,1,18400,.4200,.2960,.4810,.0400,.0000,.4400,2*0\$
 \$NAMSDUM DUMMY=110.02,1,2,+068,1,19802,.3900,.2890,.4820,.0700,.0000,.4500,2*0\$
 \$NAMSDUM DUMMY=110.03,1,2,+068,1,20325,.3700,.2740,.5020,.0500,.0000,.3400,2*0\$
 \$NAMSDUM DUMMY=110.04,1,2,+068,1,19639,.4780,.0000,.4380,.0670,.0000,.4600,2*0\$
 \$NAMSDUM DUMMY=110.05,1,2,+068,1,19438,.3900,.2810,.4260,.0200,.0000,.3300,2*0\$
 \$NAMSDUM DUMMY=110.06,1,2,+068,1,19760,.3800,.2760,.3980,.0750,.0000,.3500,2*0\$
 \$NAMSDUM DUMMY=110.07,1,2,+068,1,19546,.3700,.2510,.4940,.0520,.0000,.3600,2*0\$
 \$NAMSDUM DUMMY=110.08,1,2,+068,1,20379,.3900,.3020,.5540,.0750,.0000,.6100,2*0\$
 \$NAMSDUM DUMMY=110.09,1,2,+068,1,19755,.4000,.3100,.5780,.0400,.0000,.6100,2*0\$
 \$NAMSDUM DUMMY=110.10,1,2,+075,1,19146,.3100,.2410,.4220,.0500,.0000,.4230,2*0\$
 \$NAMSDUM DUMMY=110.11,1,2,+077,1,18462,.2900,.2370,.3750,.0500,.0000,.3720,2*0\$
 \$NAMSDUM DUMMY=111.00,1,2,-150,1,21909,.4200,.2770,.4900,.0480,.0000,.5000,2*0\$
 \$NAMSDUM DUMMY=112.00,1,2,-158,1,21713,.3901,.3060,.5040,.0830,.0000,.5100,2*0\$
 \$NAMSDUM DUMMY=113.00,1,2,-246,1,19801,.0001,.2690,.3800,.0001,.0000,.5000,2*0\$
 \$NAMSDUM DUMMY=114.00,1,2,-241,1,19845,.3901,.3160,.4700,.0560,.0000,.5400,2*0\$
 \$NAMSDUM DUMMY=115.00,1,1,+068,1,17862,.0001,.2350,.3380,.0001,.0000,.2300,2*0\$
 \$NAMSDUM DUMMY=115.01,1,1,+068,1,19410,.4340,.2570,.3790,.0800,.0000,.3700,2*0\$
 \$NAMSDUM DUMMY=116.00,1,1,+068,1,19254,.0001,.3330,.4440,.0001,.0000,.5400,2*0\$
 \$NAMSDUM DUMMY=116.01,1,1,+068,1,19410,.3700,.2530,.3670,.0550,.0000,.2300,2*0\$

\$NAMQDUM DUMMY=116.02,1,1,+068,1,19247,.3370,.2250,.2630,.0440,.0000,.1600,2*0\$
 \$NAMQDUM DUMMY=116.03,1,1,+068,1,19773,.3590,.2250,.2770,.0590,.0000,.1700,2*0\$
 \$NAMQDUM DUMMY=116.04,1,1,+068,1,20000,.4200,.2630,.3270,.0680,.0000,.2300,2*0\$
 \$NAMQDUM DUMMY=116.05,1,1,+068,1,20497,.3600,.2400,.3870,.0640,.0000,.2400,2*0\$
 \$NAMQDUM DUMMY=116.06,1,1,+068,1,19218,.3460,.2250,.3910,.1450,.0000,.3100,2*0\$
 \$NAMQDUM DUMMY=116.07,1,1,+068,1,19187,.4100,.2400,.3510,.0520,.0000,.2100,2*0\$
 \$NAMQDUM DUMMY=116.08,1,1,+068,1,19440,.4400,.2490,.3050,.0400,.0000,.2500,2*0\$
 \$NAMQDUM DUMMY=116.09,1,1,+068,1,18400,.3600,.2260,.3240,.0350,.0000,.2100,2*0\$
 \$NAMQDUM DUMMY=117.00,1,1,-147,1,20040,.5380,.2580,.2950,.0680,.0000,.2800,2*0\$
 \$NAMQDUM DUMMY=118.00,1,1,-149,1,20826,.4300,.2750,.3310,.0600,.0000,.3100,2*0\$
 \$NAMQDUM DUMMY=119.00,1,1,-241,1,19320,.4150,.2610,.3530,.0490,.0000,.3200,2*0\$
 \$NAMQDUM DUMMY=120.00,1,1,-241,1,20163,.3200,.2420,.3090,.0001,.0000,.2100,2*0\$
 \$NAMQDUM DUMMY=121.00,1,2,+071,1,23483,.3600,.2900,.4700,.0001,.0000,.6100,2*0\$
 \$NAMQDUM DUMMY=121.01,1,2,+070,1,26448,.4700,.3440,.4880,.0900,.0000,.8840,2*0\$
 \$NAMQDUM DUMMY=121.03,1,2,+075,1,22599,.3850,.2970,.4880,.1000,.0000,.6240,2*0\$
 \$NAMQDUM DUMMY=122.00,1,2,+068,1,23828,.5000,.3200,.6050,.1200,.0000,.7000,2*0\$
 \$NAMQDUM DUMMY=122.01,1,2,+068,1,23652,.0001,.3670,.5930,.0001,.0000,.9470,2*0\$
 \$NAMQDUM DUMMY=122.02,1,2,+073,1,24510,.0001,.3450,.5460,.0001,.0000,.8410,2*0\$
 \$NAMQDUM DUMMY=123.00,1,2,-150,1,23835,.5100,.2700,.4660,.1400,.0000,.5500,2*0\$
 \$NAMQDUM DUMMY=124.00,1,2,-150,1,22762,.4600,.3240,.5260,.1000,.0000,.6900,2*0\$
 \$NAMQDUM DUMMY=124.01,1,2,-150,1,23464,.4400,.2960,.5300,.1000,.0000,.7780,2*0\$
 \$NAMQDUM DUMMY=124.02,1,2,-150,1,24618,.4750,.3290,.4520,.0700,.0000,.7010,2*0\$
 \$NAMQDUM DUMMY=125.00,1,2,-250,1,23297,.3400,.3090,.4920,.0001,.0000,.6590,2*0\$
 \$NAMQDUM DUMMY=125.01,1,2,-250,1,24492,.4900,.2910,.5410,.1000,.0000,.7780,2*0\$
 \$NAMQDUM DUMMY=126.00,1,2,-250,1,25249,.3400,.3200,.4430,.0600,.0000,.6470,2*0\$
 \$NAMQDUM DUMMY=126.01,1,2,-250,1,23667,.2950,.2910,.4300,.0800,.0000,.5570,2*0\$
 \$NAMQDUM DUMMY=127.00,1,1,+070,1,22928,.4100,.2900,.3910,.0650,.0000,.3900,2*0\$
 \$NAMQDUM DUMMY=127.01,1,1,+071,1,24950,.4300,.2940,.3680,.0300,.0000,.4690,2*0\$
 \$NAMQDUM DUMMY=127.02,1,1,+073,1,24759,.4400,.2750,.4060,.0600,.0000,.3780,2*0\$
 \$NAMQDUM DUMMY=127.03,1,1,+077,1,23732,.0000,.2880,.3720,.0300,.0000,.0000,2*0\$
 \$NAMQDUM DUMMY=128.00,1,1,+070,1,23232,.4050,.2730,.3680,.0600,.0000,.3800,2*0\$
 \$NAMQDUM DUMMY=128.01,1,1,+068,1,22532,.5100,.2980,.3660,.0400,.0000,.4330,2*0\$
 \$NAMQDUM DUMMY=128.02,1,1,+073,1,25815,.5100,.2850,.3720,.0500,.0000,.4360,2*0\$
 \$NAMQDUM DUMMY=129.00,1,1,-150,1,24169,.4500,.2820,.4300,.0600,.0000,.4400,2*0\$
 \$NAMQDUM DUMMY=130.00,1,1,-150,1,22522,.3600,.2710,.3420,.0500,.0000,.3100,2*0\$
 \$NAMQDUM DUMMY=130.01,1,1,-147,1,23474,.3600,.3040,.4160,.0600,.0000,.4760,2*0\$
 \$NAMQDUM DUMMY=130.02,1,1,-150,1,23721,.5000,.3050,.3630,.0500,.0000,.4920,2*0\$
 \$NAMQDUM DUMMY=130.03,1,1,-150,1,25225,.4700,.2870,.3890,.0600,.0000,.4170,2*0\$
 \$NAMQDUM DUMMY=131.00,1,1,-250,1,22980,.2800,.2780,.4240,.0400,.0000,.4310,2*0\$
 \$NAMQDUM DUMMY=131.01,1,1,-250,1,24938,.4700,.3450,.3880,.0800,.0000,.5860,2*0\$
 \$NAMQDUM DUMMY=131.02,1,1,-250,1,26408,.4550,.3040,.3610,.0600,.0000,.4590,2*0\$
 \$NAMQDUM DUMMY=132.00,1,1,-248,1,23784,.5300,.3140,.4670,.0800,.0000,.7820,2*0\$
 \$NAMQDUM DUMMY=169.00,2,2,+066,2,11369,.2001,.0810,.0950,.0400,.2040,.0174,2*0\$
 \$NAMQDUM DUMMY=170.00,2,2,+080,2,10460,.1300,.0660,.0860,.0200,.1110,.0100,2*0\$
 \$NAMQDUM DUMMY=171.00,2,2,-149,2,10436,.1300,.0650,.0530,.0200,.0940,.0060,2*0\$
 \$NAMQDUM DUMMY=171.01,2,2,-150,2,07520,.1100,.0390,.0510,.0001,.1180,.0050,2*0\$
 \$NAMQDUM DUMMY=171.02,2,2,-150,2,11478,.1500,.0520,.0380,.0001,.0900,.0074,2*0\$
 \$NAMQDUM DUMMY=172.00,2,2,-150,2,09494,.1200,.0500,.0610,.0100,.0970,.0060,2*0\$
 \$NAMQDUM DUMMY=173.00,2,2,-256,2,10333,.1800,.0700,.0720,.0400,.1520,.0100,2*0\$
 \$NAMQDUM DUMMY=174.00,2,2,-249,2,09739,.1700,.0570,.0200,.0200,.0740,.0110,2*0\$
 \$NAMQDUM DUMMY=175.00,2,1,+075,2,10209,.1500,.0450,.0750,.0000,.1320,.0090,2*0\$
 \$NAMQDUM DUMMY=176.00,2,1,+080,2,10606,.1200,.0590,.0840,.0200,.1080,.0110,2*0\$
 \$NAMQDUM DUMMY=177.00,2,1,-149,2,10269,.1900,.0840,.0660,.0200,.0950,.0060,2*0\$
 \$NAMQDUM DUMMY=178.00,2,1,-147,2,11667,.1200,.0640,.0580,.0200,.1010,.0050,2*0\$
 \$NAMQDUM DUMMY=179.00,2,1,-248,2,09892,.2500,.0590,.0510,.0200,.0720,.0150,2*0\$
 \$NAMQDUM DUMMY=180.00,2,1,-248,2,09924,.1800,.0660,.0510,.0200,.0800,.0090,2*0\$
 \$NAMQDUM DUMMY=181.00,2,2,+075,2,14105,.2001,.0780,.0540,.0300,.1390,.0140,2*0\$
 \$NAMQDUM DUMMY=182.00,2,2,+082,2,15430,.2001,.1010,.1240,.0500,.1830,.0340,2*0\$
 \$NAMQDUM DUMMY=183.00,2,2,-153,2,15286,.1900,.0810,.1190,.0300,.2050,.0240,2*0\$
 \$NAMQDUM DUMMY=184.00,2,2,-153,2,15458,.1900,.0840,.1160,.0500,.1860,.0200,2*0\$

\$NAMDUM DUMMY=185.00,2,2,-247,2,15613,.3000,.0860,.0950,.0400,.1210,.0320,2*0\$
 \$NAMDUM DUMMY=186.00,2,2,-247,2,15864,.2500,.0900,.1110,.0300,.1970,.0300,2*0\$
 \$NAMDUM DUMMY=187.00,2,1,+080,2,13505,.1500,.0910,.0650,.0000,.1660,.0090,2*0\$
 \$NAMDUM DUMMY=188.00,2,1,+078,2,15477,.1800,.1000,.1130,.0200,.2020,.0130,2*0\$
 \$NAMDUM DUMMY=189.00,2,1,-153,2,15170,.1500,.0910,.0940,.0200,.1410,.0110,2*0\$
 \$NAMDUM DUMMY=190.00,2,1,-153,2,15576,.1700,.0920,.0880,.0200,.1310,.0130,2*0\$
 \$NAMDUM DUMMY=191.00,2,1,-247,2,15695,.2500,.0950,.0970,.0300,.1080,.0240,2*0\$
 \$NAMDUM DUMMY=192.00,2,1,-254,2,14697,.2800,.0790,.0900,.0300,.1080,.0430,2*0\$
 \$NAMDUM DUMMY=193.00,2,2,+067,2,21392,.2832,.1390,.1350,.0600,.3020,.0690,2*0\$
 \$NAMDUM DUMMY=193.01,2,2,+075,2,20829,.2500,.1390,.1420,.0300,.2400,.0450,2*0\$
 \$NAMDUM DUMMY=194.00,2,2,+067,2,21183,.2001,.1550,.1630,.0700,.5340,.0620,2*0\$
 \$NAMDUM DUMMY=195.00,2,2,-151,2,20587,.2300,.1150,.1380,.0800,.1900,.0440,2*0\$
 \$NAMDUM DUMMY=196.00,2,2,-156,2,20516,.2800,.1070,.1540,.0900,.2150,.0630,2*0\$
 \$NAMDUM DUMMY=197.00,2,2,-253,2,22184,.2900,.1100,.0620,.0300,.0620,.0570,2*0\$
 \$NAMDUM DUMMY=197.01,2,2,-250,2,18942,.3150,.1120,.1070,.0300,.1370,.0420,2*0\$
 \$NAMDUM DUMMY=198.00,2,2,-253,2,19927,.2800,.0900,.1080,.0600,.2550,.0420,2*0\$
 \$NAMDUM DUMMY=198.01,2,2,-250,2,22211,.4200,.1290,.1300,.0300,.1740,.0820,2*0\$
 \$NAMDUM DUMMY=198.02,2,2,-250,2,20858,.2100,.0810,.0900,.0500,.2470,.0360,2*0\$
 \$NAMDUM DUMMY=199.00,2,1,+070,2,19552,.2200,.1370,.1380,.0300,.1900,.0400,2*0\$
 \$NAMDUM DUMMY=200.00,2,1,+070,2,19873,.2500,.1470,.1440,.0500,.2050,.0480,2*0\$
 \$NAMDUM DUMMY=201.00,2,1,-151,2,21615,.2700,.1210,.1170,.0500,.1400,.0390,2*0\$
 \$NAMDUM DUMMY=202.00,2,1,-150,2,20652,.2200,.1240,.1090,.0400,.1550,.0290,2*0\$
 \$NAMDUM DUMMY=203.00,2,1,-253,2,20411,.3700,.1150,.1100,.0300,.1140,.0510,2*0\$
 \$NAMDUM DUMMY=204.00,2,1,-266,2,19483,.3600,.1190,.1110,.0400,.1300,.0550,2*0\$
 \$NAMDUM DUMMY=205.00,2,2,+067,2,24080,.2600,.1510,.1670,.0700,.3200,.0730,2*0\$
 \$NAMDUM DUMMY=206.00,2,2,+070,2,23793,.2832,.1570,.1480,.0700,.3010,.0850,2*0\$
 \$NAMDUM DUMMY=207.00,2,2,-142,2,24025,.2300,.1180,.1680,.0600,.2900,.0590,2*0\$
 \$NAMDUM DUMMY=207.01,2,2,-150,2,23142,.2300,.1250,.1180,.0300,.2410,.0630,2*0\$
 \$NAMDUM DUMMY=208.00,2,2,-153,2,23979,.2001,.1020,.1580,.1450,.1820,.0590,2*0\$
 \$NAMDUM DUMMY=209.00,2,2,-252,2,23609,.3600,.1250,.0960,.0500,.2530,.0780,2*0\$
 \$NAMDUM DUMMY=209.01,2,2,-250,2,24762,.3470,.0000,.2910,.1100,.4480,.3070,2*0\$
 \$NAMDUM DUMMY=209.02,2,2,-250,2,23307,.3600,.1660,.1280,.0300,.1470,.0710,2*0\$
 \$NAMDUM DUMMY=210.00,2,2,-250,2,23970,.2900,.1130,.0740,.0100,.1950,.0500,2*0\$
 \$NAMDUM DUMMY=211.00,2,1,+075,2,22520,.2700,.1500,.1540,.0400,.2650,.0620,2*0\$
 \$NAMDUM DUMMY=211.01,2,1,+070,2,23485,.2700,.1380,.1610,.0300,.2480,.0660,2*0\$
 \$NAMDUM DUMMY=211.02,2,1,+075,2,23310,.2700,.1510,.1270,.0300,.2320,.0650,2*0\$
 \$NAMDUM DUMMY=211.03,2,1,+072,2,24123,.2800,.1410,.1540,.0300,.3160,.0550,2*0\$
 \$NAMDUM DUMMY=211.04,2,1,+073,2,23696,.2900,.1550,.1490,.0400,.2390,.0620,2*0\$
 \$NAMDUM DUMMY=212.00,2,1,+080,2,24011,.2600,.1490,.1580,.0400,.2150,.0520,2*0\$
 \$NAMDUM DUMMY=212.01,2,1,+070,2,23298,.3000,.1480,.1530,.0400,.2310,.0660,2*0\$
 \$NAMDUM DUMMY=213.00,2,1,-153,2,23981,.2200,.1220,.1350,.0300,.1880,.0350,2*0\$
 \$NAMDUM DUMMY=213.01,2,1,-150,2,22534,.2200,.1240,.1280,.0400,.1590,.0510,2*0\$
 \$NAMDUM DUMMY=214.00,2,1,-150,2,23496,.2400,.1250,.1360,.0500,.1520,.0420,2*0\$
 \$NAMDUM DUMMY=214.01,2,1,-150,2,25769,.2900,.1500,.1450,.0300,.1790,.0640,2*0\$
 \$NAMDUM DUMMY=215.00,2,1,-255,2,25640,.4600,.1240,.1330,.0500,.1600,.1100,2*0\$
 \$NAMDUM DUMMY=216.00,2,1,-254,2,23023,.3300,.1220,.1270,.0400,.1730,.0820,2*0\$
 \$NAMDUM DUMMY=216.01,2,1,-250,2,23928,.3750,.1310,.1400,.0400,.1670,.1120,2*0\$
 \$NAMDUM DUMMY=216.02,2,1,-250,2,24655,.4100,.1500,.1520,.0400,.1870,.0950,2*0\$
 \$NAMDUM DUMMY=253.00,2,2,+068,1,09784,.1200,.0800,.3040,.0500,.3040,.0010,2*0\$
 \$NAMDUM DUMMY=254.00,2,2,+068,1,09649,.1200,.0770,.3090,.0500,.4550,.0010,2*0\$
 \$NAMDUM DUMMY=255.00,2,2,-153,1,09868,.0930,.0750,.2730,.0000,.2730,.0010,2*0\$
 \$NAMDUM DUMMY=256.00,2,2,-152,1,10351,.1700,.0700,.2300,.0200,.2300,.0010,2*0\$
 \$NAMDUM DUMMY=257.00,2,2,-256,1,09718,.1800,.0500,.2120,.0550,.2120,.0010,2*0\$
 \$NAMDUM DUMMY=258.00,2,2,-256,1,10980,.1420,.0790,.2610,.0300,.2610,.0010,2*0\$
 \$NAMDUM DUMMY=259.00,2,1,+068,1,10123,.1570,.0920,.3320,.0400,.3320,.0010,2*0\$
 \$NAMDUM DUMMY=260.00,2,1,+068,1,09930,.1440,.1020,.3380,.0500,.3380,.0010,2*0\$
 \$NAMDUM DUMMY=261.00,2,1,-153,1,09720,.0900,.0700,.2330,.0300,.2330,.0010,2*0\$
 \$NAMDUM DUMMY=262.00,2,1,-151,1,10801,.1020,.0750,.2240,.0300,.2440,.0010,2*0\$
 \$NAMDUM DUMMY=263.00,2,1,-242,1,10769,.2400,.0990,.1700,.0350,.1700,.0010,2*0\$
 \$NAMDUM DUMMY=264.00,2,1,-242,1,10166,.2200,.0750,.1980,.0300,.1980,.0010,2*0\$

\$NAMDUM DUMMY=265.00,2,2,+068,1,13287,.2001,.1180,.1600,.0600,.3480,.0450,2*0\$
 \$NAMDUM DUMMY=265.01,2,2,+070,1,16694,.3350,.1220,.1590,.0600,.1590,.0680,2*0\$
 \$NAMDUM DUMMY=266.00,2,2,+068,1,13968,.2300,.1400,.1670,.0680,.3520,.0500,2*0\$
 \$NAMDUM DUMMY=267.00,2,2,-148,1,13470,.2001,.1020,.1710,.0620,.2420,.0300,2*0\$
 \$NAMDUM DUMMY=268.00,2,2,-148,1,13269,.2001,.1180,.1520,.0800,.2140,.0300,2*0\$
 \$NAMDUM DUMMY=269.00,2,2,-240,1,13932,.2001,.0810,.1350,.0550,.2330,.0010,2*0\$
 \$NAMDUM DUMMY=270.00,2,2,-248,1,13725,.2450,.0900,.1290,.0570,.2590,.0010,2*0\$
 \$NAMDUM DUMMY=271.00,2,1,+068,1,14286,.2130,.1150,.1600,.0300,.3160,.0300,2*0\$
 \$NAMDUM DUMMY=272.00,2,1,+068,1,14344,.2130,.1210,.1570,.0300,.3110,.0300,2*0\$
 \$NAMDUM DUMMY=273.00,2,1,-145,1,13935,.1500,.0980,.1520,.0200,.1970,.0200,2*0\$
 \$NAMDUM DUMMY=274.00,2,1,-150,1,14181,.1540,.0960,.1550,.0200,.2020,.0200,2*0\$
 \$NAMDUM DUMMY=275.00,2,1,-240,1,14067,.3800,.0990,.1560,.0550,.2000,.0700,2*0\$
 \$NAMDUM DUMMY=276.00,2,1,-255,1,14308,.3700,.0980,.1520,.0600,.1740,.0600,2*0\$
 \$NAMDUM DUMMY=277.00,2,2,+068,1,20080,.3473,.1540,.2040,.0850,.3200,.1200,2*0\$
 \$NAMDUM DUMMY=278.00,2,2,+068,1,19246,.3473,.1510,.2250,.0800,.4300,.1200,2*0\$
 \$NAMDUM DUMMY=279.00,2,2,-150,1,20112,.2001,.1570,.2240,.0600,.7200,.1000,2*0\$
 \$NAMDUM DUMMY=280.00,2,2,-152,1,20112,.2832,.1500,.2300,.1100,.3550,.0600,2*0\$
 \$NAMDUM DUMMY=280.01,2,2,-150,1,21320,.4004,.2060,.2800,.1100,.4780,.2400,2*0\$
 \$NAMDUM DUMMY=281.00,2,2,-253,1,20439,.4100,.1180,.2270,.0940,.3200,.1100,2*0\$
 \$NAMDUM DUMMY=282.00,2,2,-250,1,19465,.3830,.1230,.2020,.0730,.3350,.1200,2*0\$
 \$NAMDUM DUMMY=283.00,2,1,+068,1,21645,.2850,.1600,.2200,.0300,.3550,.0800,2*0\$
 \$NAMDUM DUMMY=283.01,2,1,+066,1,21244,.3100,.1850,.1980,.0400,.3320,.0900,2*0\$
 \$NAMDUM DUMMY=283.02,2,1,+070,1,21276,.2800,.1750,.2210,.0400,.3820,.1990,2*0\$
 \$NAMDUM DUMMY=284.00,2,1,+068,1,19259,.3200,.1790,.2170,.0600,.3080,.1100,2*0\$
 \$NAMDUM DUMMY=284.01,2,1,+068,1,18933,.2200,.1730,.2100,.0300,.3870,.0600,2*0\$
 \$NAMDUM DUMMY=284.02,2,1,+068,1,19410,.2300,.1740,.1920,.0300,.3100,.0600,2*0\$
 \$NAMDUM DUMMY=284.03,2,1,+068,1,19547,.2600,.1700,.2160,.0300,.4160,.0700,2*0\$
 \$NAMDUM DUMMY=284.04,2,1,+068,1,20490,.2600,.1800,.2120,.0300,.3370,.0600,2*0\$
 \$NAMDUM DUMMY=284.05,2,1,+068,1,21050,.3250,.2070,.2340,.0300,.3180,.1200,2*0\$
 \$NAMDUM DUMMY=285.00,2,1,-148,1,19184,.2340,.1350,.1880,.0600,.2570,.0550,2*0\$
 \$NAMDUM DUMMY=286.00,2,1,-149,1,18807,.1940,.1370,.1820,.0600,.2500,.0500,2*0\$
 \$NAMDUM DUMMY=287.00,2,1,-255,1,18755,.4500,.1490,.1910,.0580,.2180,.1200,2*0\$
 \$NAMDUM DUMMY=288.00,2,1,-245,1,19887,.5660,.1570,.2130,.0770,.2710,.1700,2*0\$
 \$NAMDUM DUMMY=289.00,2,2,+064,1,22302,.3473,.1970,.2520,.0600,.6700,.1300,2*0\$
 \$NAMDUM DUMMY=289.01,2,2,+073,1,25493,.5500,.2250,.2360,.0900,.4190,.3340,2*0\$
 \$NAMDUM DUMMY=289.02,2,2,+072,1,23912,.4000,.2000,.2240,.0800,.4560,.2830,2*0\$
 \$NAMDUM DUMMY=290.00,2,2,+064,1,24510,.4485,.1900,.2340,.0800,.4200,.1600,2*0\$
 \$NAMDUM DUMMY=290.01,2,2,+077,1,23100,.5450,.2250,.2090,.0800,.3350,.2770,2*0\$
 \$NAMDUM DUMMY=291.00,2,2,-148,1,23759,.3473,.1700,.2460,.2000,.4100,.1360,2*0\$
 \$NAMDUM DUMMY=292.00,2,2,-150,1,22670,.3500,.1650,.2100,.1000,.2250,.1030,2*0\$
 \$NAMDUM DUMMY=292.01,2,2,-150,1,24919,.3000,.1410,.2020,.0600,.4000,.1490,2*0\$
 \$NAMDUM DUMMY=293.00,2,2,-252,1,23896,.3473,.1470,.2620,.1100,.3070,.1580,2*0\$
 \$NAMDUM DUMMY=293.01,2,2,-250,1,25030,.4050,.1200,.1530,.0500,.2370,.1020,2*0\$
 \$NAMDUM DUMMY=294.00,2,2,-251,1,23481,.4485,.1240,.1020,.2700,.2410,.3230,2*0\$
 \$NAMDUM DUMMY=295.00,2,1,+072,1,22917,.3500,.2050,.2090,.0450,.2850,.1600,2*0\$
 \$NAMDUM DUMMY=295.01,2,1,+077,1,23254,.3600,.1780,.2380,.0600,.3810,.1190,2*0\$
 \$NAMDUM DUMMY=295.02,2,1,+073,1,24753,.3300,.1700,.2000,.0400,.3500,.1010,2*0\$
 \$NAMDUM DUMMY=296.00,2,1,+064,1,25252,.3650,.2060,.2300,.0700,.3200,.1600,2*0\$
 \$NAMDUM DUMMY=297.00,2,1,-150,1,23148,.2800,.1520,.1930,.0600,.2490,.0800,2*0\$
 \$NAMDUM DUMMY=297.01,2,1,-150,1,26619,.2700,.1510,.1900,.0300,.2570,.0950,2*0\$
 \$NAMDUM DUMMY=298.00,2,1,-150,1,23020,.2900,.1710,.1980,.0600,.2410,.0800,2*0\$
 \$NAMDUM DUMMY=298.01,2,1,-150,1,24280,.2500,.1400,.1920,.0300,.2780,.0870,2*0\$
 \$NAMDUM DUMMY=299.00,2,1,-254,1,24110,.4700,.1650,.2170,.0500,.3110,.2620,2*0\$
 \$NAMDUM DUMMY=299.03,2,1,-250,1,23651,.4800,.1550,.2040,.0500,.2700,.1720,2*0\$
 \$NAMDUM DUMMY=300.00,2,1,-253,1,24400,.7700,.1480,.2020,.0600,.2750,.2990,2*0\$
 \$NAMDUM DUMMY=300.01,2,1,-250,1,25396,.4700,.1580,.2160,.0600,.2540,.1940,2*0\$
 \$NAMDUM DUMMY=999.99,13*0\$

A LISTING OF THE CONTROL CARDS FOR ONE REGRESSION IS GIVEN BELOW. THESE CARDS WERE USED WITH THE FORM OF DEFINE THAT WAS GIVEN ON THE PREVIOUS PAGE. THE DEPENDENT VARIABLE IS VOLUME. THIS IS SPECIFIED BY THE 6 ON THE NAMUSE CARD. SKIPPING IS PERFORMED ON THE THIRD AND THE FIFTH INDEPENDENT VARIABLES, WHICH ARE THE STRUCTURE AND THE PROJECTILE RESPECTIVELY. IN BOTH CASES THE VALUE 1.0 WAS SKIPPED, WHICH MEANS THAT ONLY DELRIN PROJECTILE AND HONEYCOMB DATA WOULD BE INCLUDED IN THE REGRESSION. THIS CASE WAS RUN WITH ONLY THE SYLGARD DATA, SO THE MATERIAL VARIABLE DID NOT HAVE TO BE USED FOR SKIPPING.

```
$NAMCON NR0W=6,ISKIP=-1,-1,1,-1,1,-1$
      SYLGARD H.C. WITH DELRIN PROJECTILE
              VELOCITY IN CM/SEC
              TOTAL VOLUME IN CC
1.0
1.0
$NAMUSE NUSE=6,7*0$
```

THE LAST CONTROL CARD SHOULD BE

```
$NAMCON NR0W=100,ISKIP=-1,-1,-1,-1,-1,-1$
```

HOWEVER. AS MANY CASES AS DESIRED CAN BE RUN AT ONE TIME.

```

      SUBROUTINE DEFINE
      DIMENSION X(6,250),AID(250),FMAT(250),STRUC(250),TEMP(250),PROJ(25
10),VEL(250),D(8,250),T(9),NUSE(8),Y(250),U(10,10),AMAT(10,250),
2A(10),Z(250),G(10),XX(6,250),F(250),DD(8,250),DUMMY(14),ISKIP(6),
3ISKIP1(6),SKIP(6,250),PLX(250)
      COMMON X,AID,FMAT,STRUC,TEMP,PROJ,VEL,D, NUSE,Y,U,AMAT,A,Z,G,XX,
1DD,F,AROW,NCCL,SKIP,DUMMY,ISKIP,ISKIP1,PLX
C      DEFINE AMAT AND F IN THIS ROUTINE
      DO 2 K=1,NCCL
C      DEFINE AMAT(L,K)
      AMAT(1,K)=1.0
      AMAT(2,K)=30.48*VEL(K)*1.0E-6
      IF (TEMP(K)) 101,101,102
101 IF (TEMP(K)+200.0) 103,103,104
103 ST=-0.5
      CV=-0.5
      GO TO 105
104 ST=0.0
      CV=1.0
      GO TO 105
102 ST=0.5
      CV=-0.5
105 AMAT(3,K)=ST
      AMAT(4,K)=CV
      AMAT(5,K)=ST*AMAT(2,K)
      AMAT(6,K)=CV*AMAT(2,K)
      IF (VEL(K)-13000.0) 106,106,107
106 AMAT(7,K)=30.48*(13000.0-VEL(K))
      GO TO 108
107 AMAT(7,K)=0.0
108 AMAT(8,K)=AMAT(7,K)*ST
      AMAT(9,K)=AMAT(7,K)*CV
      2 CONTINUE
      DO 3 K=1,NCCL
C      DEFINE F(K)
      IF (NUSE(1)-6) 201,202,201
201 F(K)=2.54*Y(K)
      GO TO 203
202 F(K)=Y(K)
203 PLX(K)=AMAT(2,K)
      3 CONTINUE
      RETURN
      END

```

Above is a listing of the subroutine DEFINE as it was used to obtain the regressions given in Appendix D. The first six AMAT's define the form given for those regressions. The last three define a function which is zero above the transition region and which is used to decouple the transition region data from the regression. By specifying that NROW = 6, these terms will not be included in the regressions.

APPENDIX B

ANALYSIS OF EXPLODING FOIL PROCESS

by
Edwin Langberg

I. INTRODUCTION

Acceleration of small projectiles to velocity approximating meteoroid impacts has been currently accomplished^{1, 2} by means of exploding foil guns. In this connection, it is important to develop an analysis of pertinent factors leading to the optimization of experimental conditions. Such an analysis is the main goal of this report.

The basic novelty of the present analysis in comparison with a number of similar studies relating to exploding wires and exploding foils is the choice of thermodynamic variables used to analyze the resistance of the exploding foil. It has been recognized for some time,³ that energy dissipation alone cannot account for the behavior of resistance of exploding conductors. There is ample physical reason for the assumption that one of the fundamental variables which determines the foil resistivity is the atomic separation. The dynamic behavior of atomic separation in the exploding foil is considered in detail in this report and the results of an analog computer simulation of the explosion are compared with experimental results. The agreement between the two is very satisfactory.

II. THERMODYNAMICS OF FOIL EXPLOSION

The electrical power dissipation in the foil during the first microsecond is typically of the order of 500 megawatts. This power dissipation is so high that by comparison thermal losses by conduction or radiation are negligible.^{4, 5} There is, therefore, little error in the assumption that during the explosion the electrical energy Q is converted only into the internal energy of the foil and the kinetic energy of the projectile:

$$Q = M_f u + 1/2 M_s \dot{x}^2 \quad (2.1)$$

In equation (2.1) M_f is the mass of the foil, M_s is the mass of the projectile, u is the internal energy per unit mass of the foil (which will be referred to as energy density) and \dot{x} is the velocity of the projectile.

Equation (2.1) is the result of the first law of thermodynamics where the exploding foil is considered the working fluid expanding against the projectile which is equivalent to a piston.

The energy density is dissipated in energy associated with the frozen flow u^* (which includes heat of vaporization, excitation, and ionization) and is converted into translational velocity of the foil atoms:

$$u = u^* + c^2/2 \quad (2.2)$$

where c is the rms speed of foil atoms.

In order to use equation (2.1) one must establish a relationship between u^* , c and \dot{x} . This relationship is obtained from the assumption that the projectile velocity is equal to the average x -directed velocity of the foil. Then the kinetic theory of gases specifies that:

$$c^2 = 3 \dot{x}^2 \quad (2.3)$$

The justification for the above-mentioned assumption is as follows: The projectile velocity clearly cannot be faster than the average forward velocity of the atoms of the exploding foil since it is the interaction of the two which causes projectile acceleration. On the other hand, if the projectile velocity \dot{x} were substantially slower than c , there would be a strong buildup of pressure which would cause projectile acceleration until the condition in equation (2.3) is satisfied.

Assuming further that the internal energy u is divided equally between translational energy density of the foil atoms $c^2/2$ and the energy dissipated in u^* , one can obtain the relationship between projectile velocity \dot{x} and the internal energy of the foil:

$$u = u^* + c^2/2 = u^* + 3\dot{x}^2/2 = 3\dot{x}^2 \quad (2.4)$$

Substituting into equation (2.1) the relationship between the heat dissipation Q and the velocity \dot{x} is:

$$Q = (3M_f + M_s/2)\dot{x}^2 = M\dot{x}^2/2 \quad (2.5)$$

where M is the effective mass defined as:

$$M = 6M_f + M_s \quad (2.6)$$

Consequently the relationship between the thermodynamic variables of the exploding foil system and the dissipated heat is

$$u^* = 3/2\dot{x}^2 = 3Q/M \quad (2.7)$$

III. BEHAVIOR OF RESISTANCE DURING THE EXPLOSION

The resistivity is a function of thermodynamic variables of the exploding foil. Since the equation of state for the range of conditions corresponding to foil explosion is not known, transformation of variables is not possible, and it is important to choose the thermodynamic variables which most directly effect the resistance change.

A number of calculations^{6, 7, 8} of resistivity in exploding metallic conductors have been carried out in the past using only temperature and/or energy density dependence. From physical considerations, it is, however, clear that one of the most critical variables is inter-atomic distance which relates to specific density of the exploding foil. The inter-atomic distance is related to specific volume. It is therefore convenient to use the energy density u , and the specific volume v for thermodynamic variables:

$$\rho = \rho(u, v) \quad (3.1)$$

The resistivity of the foil in the solid state and at room temperature is of little significance since the heat of melting is only a minute fraction of the energy dissipated in the foil. A more significant approximation to the initial conduction through the foil can be obtained by considering the foil to be liquid and yet substantially of the same geometrical configuration as the original solid shape. Even when energy density exceeds the heat of formation u_f , the foil remains liquid because it cannot expand freely due to the restraint of the projectile. Actually, the distinction between the liquid and the gas phases vanishes because the pressure is most likely much higher than the critical pressure.

The temperatures and pressures in the exploding foil are for the most part outside of the range of the available laboratory data. One must therefore rely on the basic physics of the electron conduction in order to predict the behavior of resistivity throughout the range of parameters which one can encounter during the explosion.

The electrical resistivity is in general given by the equation

$$\rho = mcNQ^*/ne^2 \quad (3.2)$$

where m is the electron mass, c is the electron velocity, n is the number of electrons, e is the electron charge, Q^* is the electron scattering cross-section, and N is the number of scattering centers.

In spite of the apparent simplicity of equations (3.2), the proper evaluation of its parameters depends on the physical conditions of the metal and can be quite

complex. In a solid metal*, NQ^* is determined by quantum mechanics of scattering of electrons by thermal lattice vibrations. In a perfectly regular lattice (i. e., perfect crystal at the absolute zero temperature) there is no scattering and NQ^* is zero. As temperature increases, the displacement ξ of the lattice atoms from the equilibrium position is given by:

$$s\xi^2 = 2kT \quad (3.3)$$

where s is the atomic bond spring constant, and k is the Boltzmann's constant. The cross-section area for scattering of electrons is proportional to ξ^2 . Consequently,

$$Q^* \propto \xi^2 \propto T/s \quad (3.4)$$

Equation (3.4) when substituted in equation (3.2) gives the linear dependence of resistivity on temperature. However, since the atomic bond spring constant s varies in turn with temperature, this linear dependence is valid only over a restricted range.

In liquid metals** the scattering cross section for free electrons is no longer directly dependent on temperature. In the liquid state one can picture the metallic ions as hard spheres bouncing around without directional atomic bond constraints. The free volume of the ionic motion is given by $(v - v_0)A$ where v_0 is the specific volume occupied by the "hard" ions and A is the atomic mass. Consequently, the average distance between ions is $[(v - v_0)A]^{1/3}$. The scattering cross-section is therefore proportional to:

$$Q_e = [(v - v_0)A]^{2/3} \quad (3.5)$$

The electron velocity corresponding to the top of the Fermi level is proportional to the interatomic distance:

$$c \propto [(v - v_0)A]^{1/3} \quad (3.6)$$

The density of conduction electrons is proportional to the density of atoms:

$$n \propto N \quad (3.7)$$

Substituting into equation (3.2) the resistivity of liquid metal is proportional to:

* The description of conduction presented here is of necessity very simplified. A more detailed description of conduction in solids is given in reference 9.

** Discussion of conduction in liquid metals near the melting point is given in reference 10. However, the postulated resistivity formulation is new and not related to the above reference.

$$\rho \propto (v - v_0)A/N \quad (3.8)$$

Noting that $N \propto 1/v$

$$\rho = B v(v - v_0) \quad (3.9)$$

The constants B and v_0 in equation (3.9) which represent the conduction through liquid metal can be obtained from resistivity and density data for liquid metals.¹¹ The handbook information is available for the temperature range between melting point and several hundred degrees above it. If values at two temperatures indicated by subscript a (lower) and b (higher) are known, then substitution in equation (3.9) gives the solution for the two constants B and v_0 :

$$B = (v_b \rho_a - v_a \rho_b) / (v_a^2 v_b - v_a v_b^2) \quad (3.10)$$

$$v_0 = v_a - (\rho_a / B v_a) \quad (3.11)$$

The metallic resistivity in equation (3.9) is an explicit function of specific volume only. At atmospheric pressure the temperature dependence can, of course, be obtained from the equation of state. Equation (3.9) fits the available experimental results for solid and liquid metals, including the change of phase, much better than the linear temperature dependence approximation.

As the internal energy and the interatomic distance increases the point is reached when metallic conduction ends and the resistivity is obtained from equation (3.2) by classical calculation for a gaseous plasma:

$$\rho = mcQ/e^2 g \quad (3.12)$$

where g is the degree of ionization defined as

$$g = n/N \quad (3.13)$$

In order to calculate the degree of ionization it will be assumed that the energy of frozen flow u^* is dissipated into evaporation and ionization only:

$$g = (u^* - u_f)/u_i \quad (3.14)$$

where u_f is the heat of formation and u_i is the heat of ionization. Substituting for u^* the expression derived in equation (2.7):

$$g = (3Q/M - u_f)/u_i \quad (3.15)$$

In the range of electron energies encountered in the explosion the collision cross-section Q^* tends to decrease with electron speed c so that the product

cQ^* can be considered approximately constant. The collision cross-section Q^* is determined approximately by the atomic radius, and the electron speed c corresponds approximately to the first ionization potential. The plasma resistivity under these conditions and for $g = 1/2$ is defined as K

$$K = \frac{2m}{e^2} \sqrt{\frac{2e v_i}{m}} \pi r_o^2 \quad (3.16)$$

where v_i is the ionization potential in electron-volts. If r_o is the atomic radius in Angstrom units then numerically equation (3.12) is

$$\rho = 1.32 \times 10^{-4} \quad r_o^2 \sqrt{v_i} u_i (3Q/M - u_f) = K/2g \quad (3.17)$$

The plasma resistivity in equation (3.17) represents only an approximate value. There is a possibility of an error in the estimate of collision cross-section and the average electron velocity. The energy absorbed in excited states is not included in the derivation; neither is the possibility of occurrence of multiple ionization.

However, these shortcomings are more likely to effect the numerical value of the proportionality constant in equation (3.17) than the basic dependence on the heat dissipation. The proportionality constant can be adjusted to fit experimental results. The known functional dependence of the pertinent variables makes it possible to use the resistivity equation in an analog computer study.

IV. SYSTEM OF EQUATIONS DESCRIBING THE EXPLODING FOIL

The basic electric circuit of the exploding foil consists of a series connection of the following elements:

- a. Storage capacity C.
- b. Inductance L which is partially distributed and partially confined to the leads and to the foil. The inductance is assumed constant
- c. Constants resistance R_1 of the circuit outside of the foil
- d. Variable resistance R of the foil itself.

The basic differential equation describing the above mentioned circuit is

$$L \frac{di}{dt} + [R_1 + R(x, u)] + \frac{1}{C} \int i dt = E_0 \quad (4.1)$$

where i is the current and t is the time. The initial capacitor voltage is E_0 . The electrical energy dissipated in the foil is derived from joule heating and is

$$Q = \int_0^t i^2 R dt \quad (4.2)$$

The initial energy stored in the capacitor is:

$$Q_0 = CE_0^2/2 \quad (4.3)$$

The velocity of the projectile is derived in equation (2.7):

$$\dot{x} = \sqrt{2Q/M} \quad (4.4)$$

Consequently the thickness of the exploding foil is

$$x = \int_0^t \sqrt{2Q/M} dt + a \quad (4.5)$$

where a is the initial foil thickness

Assuming a uniform expanding thickness of the foil, and a square foil area, the foil resistance is related to the resistivity and the thickness

$$R = \rho/x = \rho v_1/av \quad (4.6)$$

where v_1 is the initial specific volume.

The foil resistance R_a during metallic conduction can be obtained from equation (3.9)

$$R_a = Bv_1(v - v_0)/a = B(v_1/a)^2(x - av_0/v_1) \quad (4.7)$$

Similarly, the resistance R_b of the plasma created by the exploding foil can be obtained from equation (3.17)

$$1/R_b = 2x(3Q/M - u_f)/Ku_1; \quad (4.8)$$

The solution of the system of equations described here in closed form is impractical. However, the solution can be obtained readily on an analog computer.

V. ANALOG COMPUTER SOLUTION

The thermodynamic conditions, the electrical conductivity, and the circuit properties derived in previous sections lead to the following set of equations for the exploding foil gun;

$$dI/dr + [r_1 + r(q, z)] I + \int I dr = 1 \quad (5.1)$$

The initial conditions are that $I(0) = 0$, $dI/dr = 1$

$$q = 2 \int I^2 r dr \quad (5.2)$$

$$z = \int \sqrt{q} dr \quad (5.3)$$

$$r_a = az + r_0 \quad (5.4a)$$

$$1/r_b = \beta(z + a\omega/p)(qp^2/u_f - 2/3) \quad (5.4b)$$

These are four equations in four normalized unknowns:

I is the ratio of current i to peak current:

$$I = i/E_0 \omega C \quad (5.5)$$

q is the ratio of heat dissipation Q in the foil to energy stored:

$$q = 2Q/E_0^2 C \quad (5.6)$$

z is the normalized distance defined in terms of the instantaneous foil thickness x as:

$$z = \int \sqrt{q} dr = \frac{\omega}{p} (x - a)$$

where p is the normalized peak velocity:

$$p = \sqrt{2Q_0/M} \quad (5.8)$$

r is the ratio of foil resistance to capacitive impedance:

$$r = R\omega C \quad (5.9)$$

The independent variable is the normalized time:

$$\tau = \omega t \quad (5.10)$$

The analog computer output consists of the plot of the four variables mentioned. In addition the plot of dl/dr is recorded since it corresponds to the experimentally measured potential across an inductance. There are six normalized parameters which determine the solution. The definition of these parameters is given below.

Circuit dumping coefficient:

$$r_1 = \omega CR_1 \quad (5.11)$$

Initial resistance coefficient

$$r_0 = \omega C\rho_0/a \quad (5.12)$$

Metallic resistance coefficient of expansion:

$$\alpha = CB p v_1^2/a^2 \quad (5.13)$$

Plasma conductance coefficient of expansion:

$$\beta = 3p u_f/\omega^2 C K u_i \quad (5.14)$$

Displacement coefficient:

$$a\omega/p \quad (5.15)$$

Energy density coefficient:

$$p^2/u_f \quad (5.16)$$

These parameters are determined from the experimental constants corresponding to the currently used conditions listed in table I.

TABLE I
EXPERIMENTAL CONSTANTS

Ring Frequency	$\omega = 4.46 \times 10^6 \text{ rad/sec; } f = 710\text{kc}$
Storage Capacity	$C = 0.84 \text{ } \mu\text{F}$
Initial Voltage	$E_0 = 80 \text{ kv}$
Foil Thickness	$a = 6.35 \times 10^{-4} \text{ cm} = 0.25 \times 10^{-3} \text{ in.}$
Foil Mass	$M_f = 5.66 \times 10^{-4} \text{ g}$
Projectile Mass	$M_s = 10^{-2} \text{ g}$
Circuit Dumping Factor	$\omega CR_1 = 0.1$
<u>For Aluminum</u>	
B	$B = 5.35 \times 10^{-4} (\text{ohm-cm}) (\text{g/cm}^3)^2$
K	$K = 7.05 \times 10^{-3} (\text{ohm-cm})$
Initial Foil Density	$1/v_1 = 2.7 \text{ g/cm}^3$
Heat of Formation	$u_f = 11.58 \text{ k joule/g}$
Heat of Ionization	$u_i = 5.77 \text{ k joule/g}$
Initial Resistivity	$\rho_0 = 2.62 \times 10^{-6} \text{ ohm-cm}$

From the experimental constants in table I one can derive composite constants listed in table II

TABLE II
COMPOSITE CONSTANTS

Capacitive Admittance	$\omega C = 3.74 \text{ mho}$
Initial Charge	$Q_o = E_o C = 2.68 \text{ k coulomb}$
Effective Mass	$M = 6 M_f + M_s = 1.34 \times 10^{-2} \text{ g}$
Ideal Peak Velocity	$p = \sqrt{2Q_o/M} = 2 \times 10^6 \text{ cm/sec}$
	$p^2 = 4 \times 10^2 \text{ k joule/g}$

From the values listed in table I and table II one can derive the six normalized constants defined in equations 5.11 to 5.16.

TABLE III
NORMALIZED CONSTANTS

$r_l = 0.1$	$a = 305$	$a \omega / p = 1.42 \times 10^{-3}$
$r_o = 1.54 \times 10^{-2}$	$\beta = 1030$	$p^2 / u_f = 34.5$

The solution is initiated on the computer by programming equation (5.1) to (5.4a). When

$$q = u_f / p^2 \quad (5.17)$$

the solution for r_b , as given by equation (5.4b), starts getting generated. This solution is compared with r_a , and when they reach equality r_b replaces r_a in the solution of the system of equations.

The procedure outlined above is, strictly speaking, correct only for the case of singly ionized plasma. Multiple ionization requires a modification of equation (5.4b). However, when the plasma temperature is sufficiently high for significant multiple ionization, r_b is typically so low that the heat dissipation in the plasma can be ignored. Equation (5.4b) is therefore adequate for the analysis.

The computer run is continued until q reaches a steady value. Beyond this point the effect of r becomes quite small, q reaches an asymptotic value and the projectile acceleration process ends. If the calculation of current in the circuit is required beyond this point it can be obtained from the linear differential equation:

$$dI/dr + r_1 I + \int I dr = 1 \quad (5.18)$$

The initial conditions for the linear solution are obtained from the final values of the computer run.

VI. COMPARISON OF THEORY AND EXPERIMENT

The schematic of the experimental set-up prepared under the direction of R. R. McMath is shown in figure 1. The deflection plates of the oscilloscope are connected to two points on the current return bar about 1 inch apart. The resistance of this segment of the bar is negligible in comparison with its inductance. Consequently the voltage developed between the points is proportional to di/dt .

The signal is delayed by 80 feet of RG 63 coaxial cable. This delay is necessary for proper triggering of the scope sweep. The oscilloscope trace is shown in figure 2. The time scale is $0.1 \mu s$ / division so that the photograph represents approximately $0.7 \mu s$.

Since the resonant frequency of the exploding foil circuit is 4.46×10^6 rad/sec the normalized time represented in the photograph is 3.12. This is very close to one-half of the first cycle.

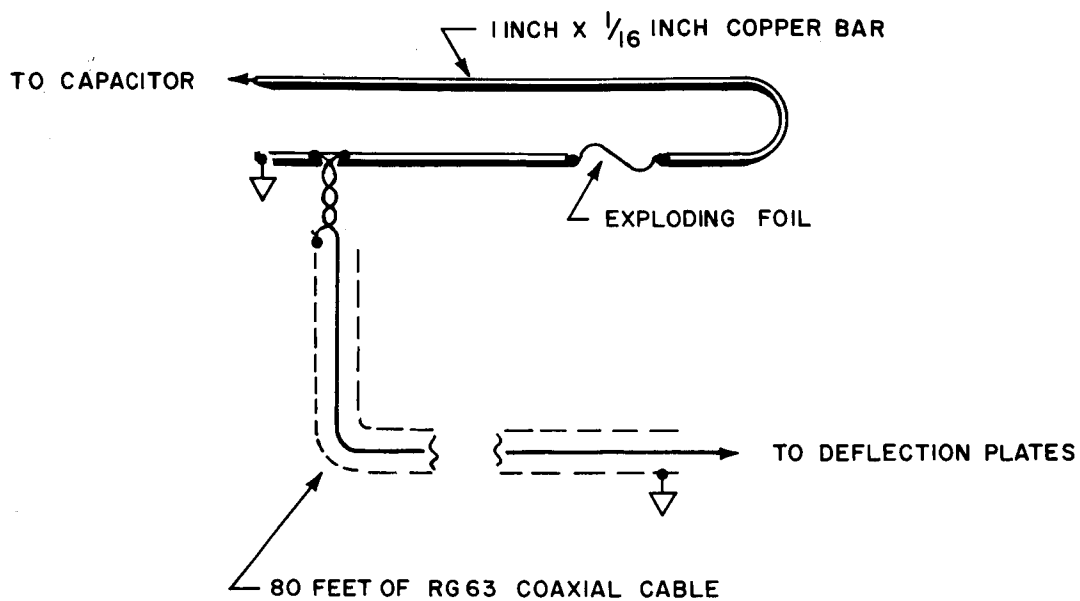
It is clear in the interpretation of figure 2 that spurious ringing at a frequency of about 20Mc is induced by transients in the oscilloscope input circuit. One must therefore deduce the actual form of di/dt within the envelope determined by the peak positive and negative values of the ringing amplitude. These peak experimental points are numbered in figure 3 and the envelope of the ringing signal is also shown there.

The ringing represented by points 1, 2 and 3 is caused by the initial rise in di/dt , from 0 to +1. Between the points 3 and 4 a steep drop in di/dt must be postulated to account for the downward bend in the envelope and the increase in the ringing amplitude (2-3) as compared with (3-4). Beyond this point there are apparently no transients since the ringing amplitude decreases steadily and becomes negligible beyond the point 17.

The interpretation of the experimental trace in figure 2 is complicated by the fact that the $y = 0$ line on the scope does not correspond to y axis for oscillations. On photographs showing the full trace of decaying oscillations it can be seen that the oscillations are centered around the line higher than the initial $y = 0$. This phenomenon is very likely caused by a bias voltage which is spuriously induced and has a long decay time constant compared with $10 \mu s$.

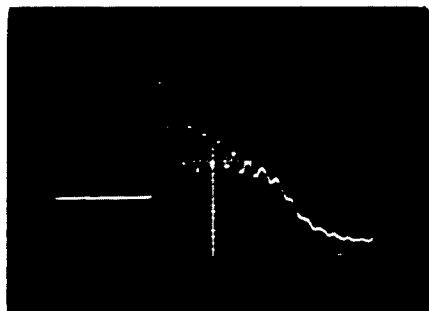
Figure 3 represents an interpretation of experimental results on a normalized scale which includes estimated correction for the above mentioned zero axis shift. The di/dt scale was obtained from the assumption that for the point halfway between the experimental points No. 1 and 2, corresponding to $r \approx 0.2$, di/dt is equal to 0.9.

The general trend of the di/dt curve can now be reconstructed: The curve starts at +1, decreases smoothly up to $r \approx 0.3$ and then drops sharply at about $r = 0.45$.



85-0024

Figure 1 SCHEMATIC OF THE EXPERIMENT



TIME SCALE $0.1 \mu\text{sec} / \text{division}$

85-0025

Figure 2 OSCILLOSCOPE TRACE

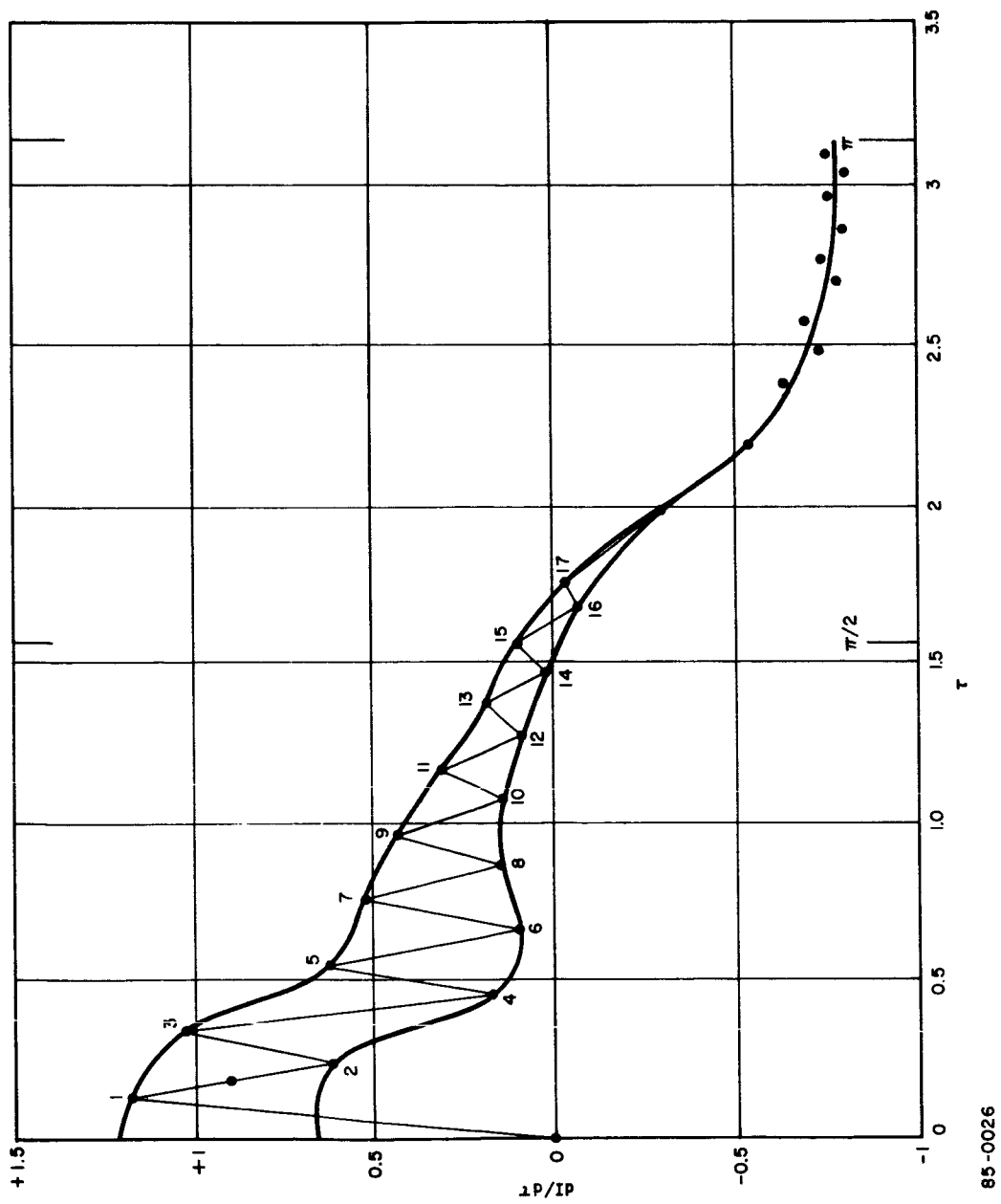


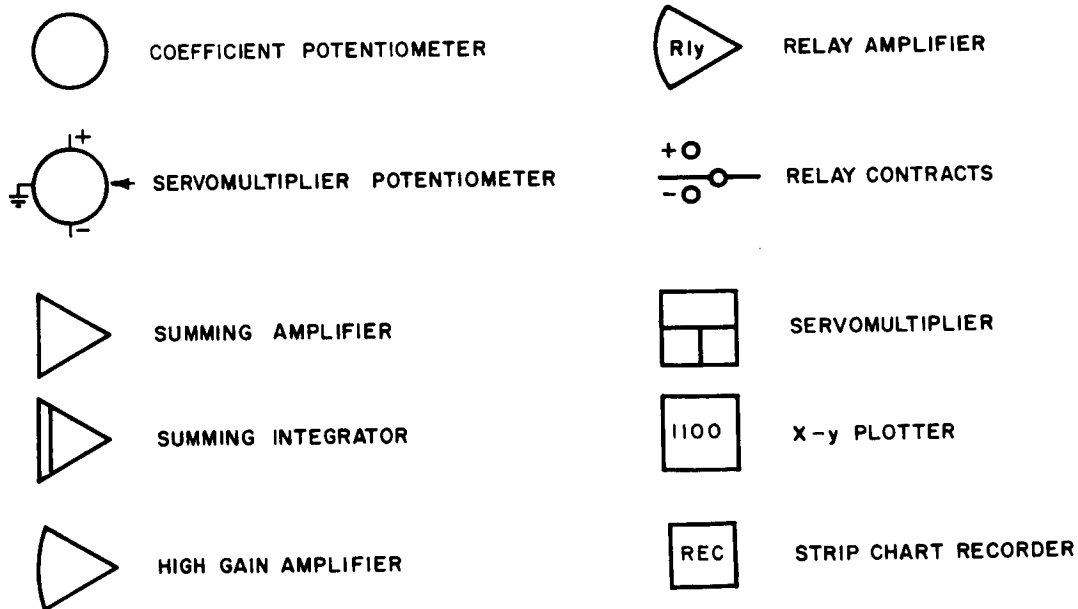
Figure 3 NORMALIZED EXPERIMENTAL RESULTS

Subsequently, it increases up to $r \approx 0.55$ and from that time on follows essentially a sinusoidal oscillation which crosses the γ axis at about $r \approx 1.6$ and has a negative peak at $r \approx \pi$.

In addition to the dI/dr curve the experimentally determined kinetic energy of the projectile is important for comparison with the theory. The measured velocity of the 10mg projectile is 17×10^3 ft/sec or 5.18×10^3 m/sec. Consequently, the energy of the projectile is 134 joules. In comparison with the stored energy of 2830 joules, this represents 4.73 percent conversion efficiency.

The analog computer program prepared by Mr. L. Somers from the Analog Group, Avco RAD is shown in figure 4.

The symbols used in the preparation of the analog diagram have the following meaning:



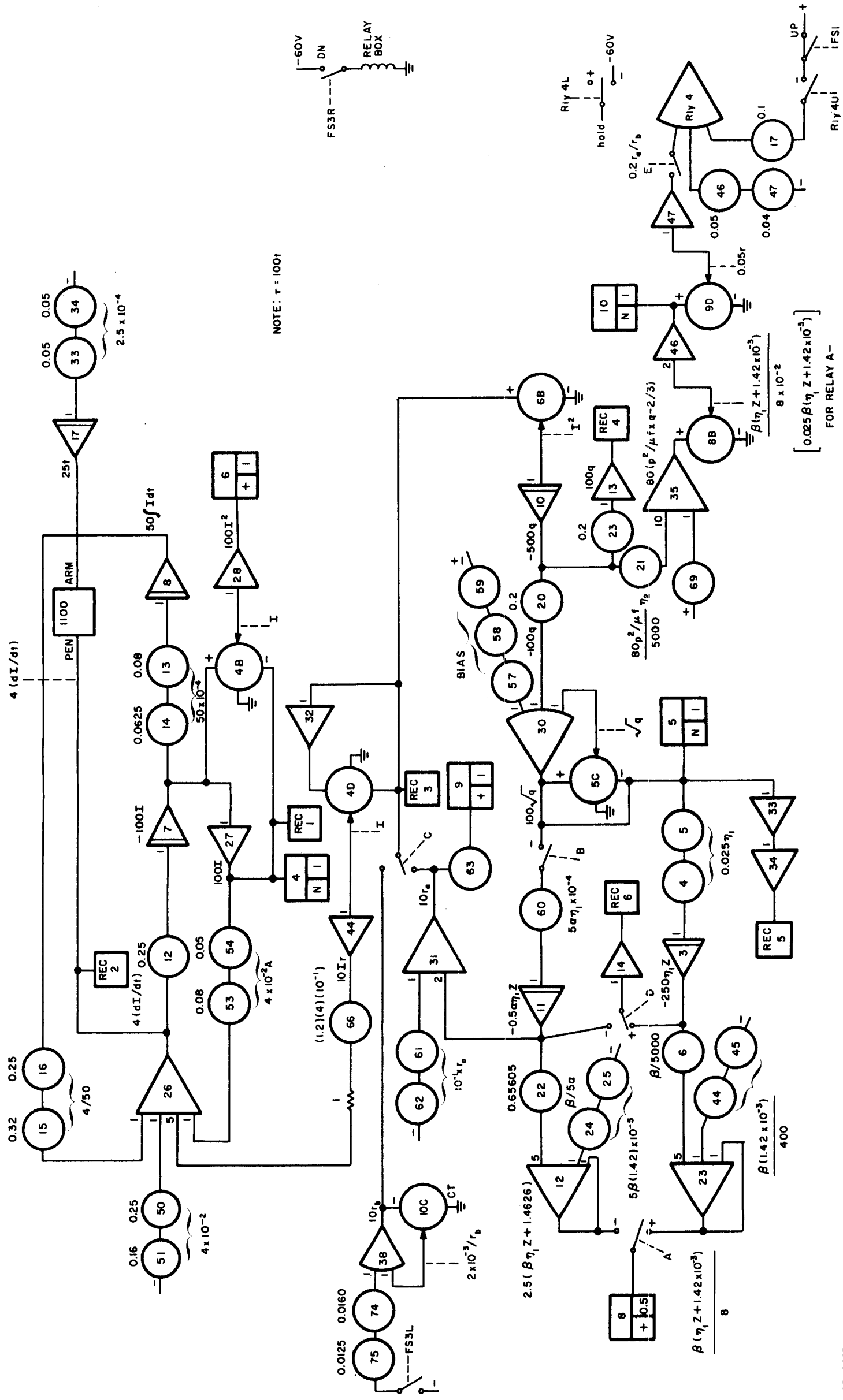


Figure 4 ANALOG COMPUTER PROGRAM

The problem operates as follows. Initially, function switches (FS) 1 and 3 are in the up positions. In this mode r_a is used in the system equations but is being continuously compared with r_b . When $r_a = r_b$, the computer is automatically placed in "hold". Function switch 3 is manually put into its down position. In this position r_b is switched into the problem, replacing r_a , and in addition scale changing of the program takes place. After a brief settling time, function switch 1 is put into its down position returning the computer to the "operate" mode for completion of the problem. At the end of the run the computer is manually placed in the "reset" mode, function switches 1 and 3 are returned to their up positions, and the problem is readied for the next run.

The dl/dr curve obtained from a computer run based on values listed in section 4 is shown in figure 5. Comparison of theoretical (figure 3) and experimental (figure 5) results shows qualitative agreement but quantitative discrepancies. Specifically the drop due to conduction cross-over occurs too early ($\tau = 0.25$ versus $\tau = 0.45$ for experiment), and the maximum amplitude after cross-over is too high (0.85 versus 0.60).

The same computer run gives the asymptotic value of the normalized explosion energy dissipation as $q = 0.04$. Based on the assumption in equation (2.7) $q = 0.04$ corresponds to kinetic energy conversion efficiency of the projectile equal to $q M_s / M$ which is 3 percent. The theoretical efficiency is therefore somewhat low; 3 percent as compared with experimentally measured 4.73 percent. In view of the approximate nature of the assumption and the uncertainty both in evaluation of the problem parameters and experimental resolution the agreement is however quite satisfactory.

The assumption regarding the energy distribution underlying the analysis cannot be expected to be exactly valid. It is therefore interesting to assume departures from this nominal distribution and to examine the effect of such adjustments on the solution.

The first adjustment assumes that the velocity of the projectile is less than the forward velocity component of the exploding gas by a fraction η_1 . There is experimental justification for this adjustment; the measured forward plasma velocity is several times greater than the projectile velocity. The only change in the system of equations (5.1) to (5.4) required to accommodate this adjustment is the modification of equation (5.3):

$$z = \eta_1 \int \sqrt{q} \, dr$$

The second assumption which warrants re-examination is the complete conversion of the frozen flow energy u^* into vaporization and ionization which is postulated in equation (3.14). If the energy of excited atomic and molecular states

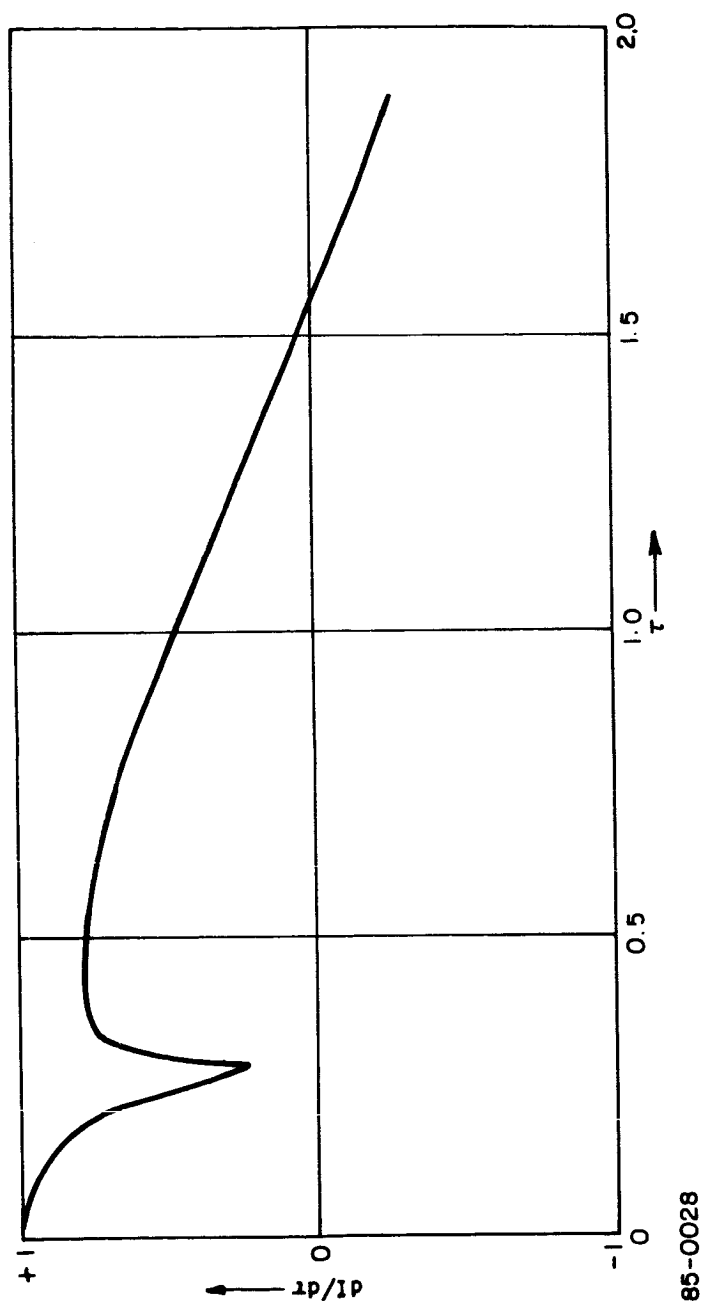


Figure 5 COMPUTED di/dr CURVE FOR NOMINAL CONDITIONS

is not negligible, it is more appropriate to define an ionization efficiency factor η_2 which modifies equation (3. 16):

$$g = (\eta_2 u^* - u_f)/u_i \quad (6. 2)$$

The result of this change appears in modification of equation (5. 4b)

$$1/\tau_b = \beta(z + a \omega/p) (\eta_2 q p^2/u_f - 2/3) \quad (6. 3)$$

A typical result of the energy distribution adjustment on the $dI/d\tau$ curve is shown in figure 6. The value of the adjustment parameters are $\eta_1 = 1/\sqrt{2}$ and $\eta_2 = 0.25$. Also r_1 , was changed to $r_1 = 0.2$ since this is closer to the experimentally observed value. The adjusted solution fits the experimental cross-over time and the maximum amplitude after cross-over within the experimental error. The asymptotic value of q obtained for the adjusted solution is $q = 0.12$. The efficiency of conversion to projectile kinetic energy is $q \eta^2 \cdot M_s/M = 0.043$ or 4.3 percent. The results of the adjusted solution show very good agreement between theory and experiment and substantiate the validity of the analog computer program developed here for the analysis of the exploding conductor phenomena.

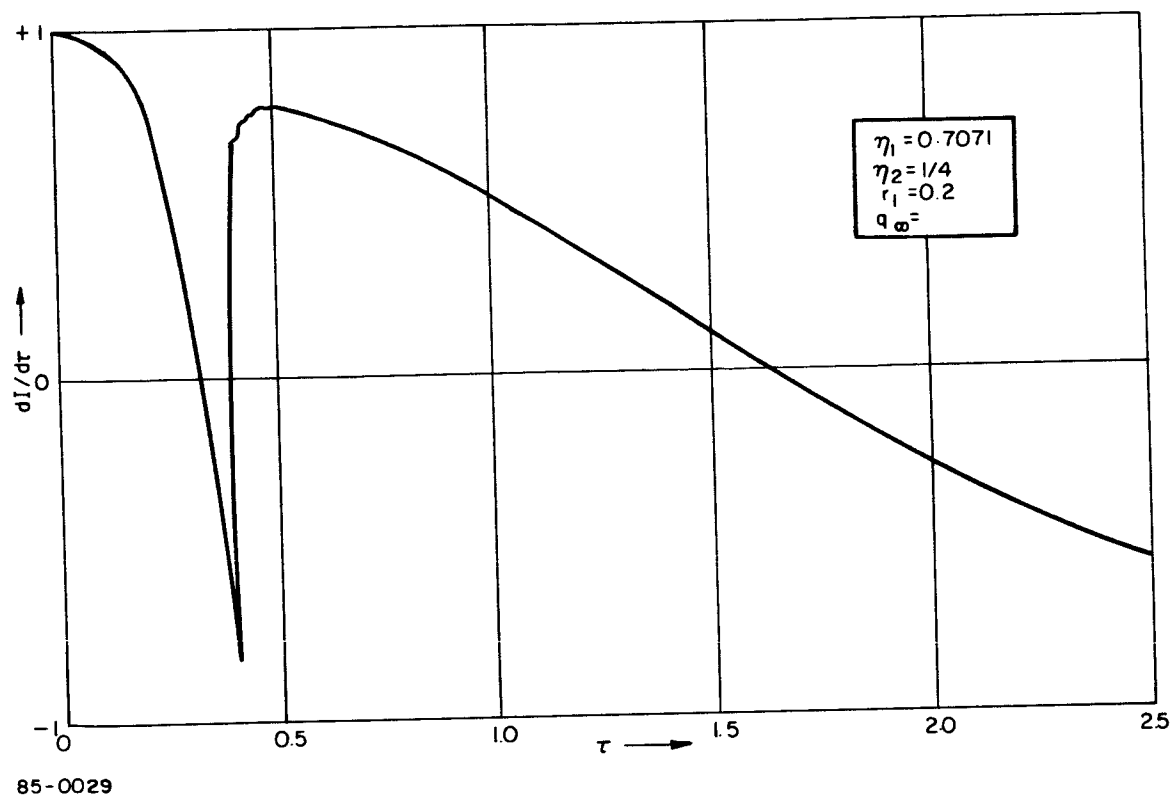


Figure 6 COMPUTER dI/dr CURVE FOR ADJUSTED CONDITIONS

VII. RESULTS AND CONCLUSIONS

The comparison of the analog computer simulation and the experimental observations, discussed in Section VI, indicates a sufficient agreement to make this analysis a valid optimization tool in the design of an improved hypervelocity gun. However, the overall improvement, which could be expected under ideal experimental conditions, was evaluated before this optimization was undertaken.

The exploding foil process derives its energy from the joule heat dissipation in the foil due to the passage of the current through it. The resistance of the plasma formed by the foil explosion is very low resulting in a corresponding reduction of the heat dissipation. As the previous analysis indicates, the relationship between the variables of the explosion process is quite complex. However, an approximate insight into the problem can be gained by assuming that the transition from the metallic conductivity to the plasma conductivity occurs approximately at the point when the heat dissipated into the internal energy u^* is equal to the sum of the heat of formation u_f and the heat of ionization u_i :

$$u^* = u_i + u_f \quad (7.1)$$

For aluminum foil $u_f = 11.58 \times 10^6$ joule/kg, $u_i = 5.77 \times 10^6$ joule/kg giving the critical internal energy:

$$u^* = 17.35 \times 10^6 \text{ joule/kg} \quad (7.2)$$

A relationship between the projectile velocity \dot{x} and the internal energy is derived in Eq. (2.7):

$$\dot{x} = 2u^*/3 = 3.4 \text{ km/sec} \quad (7.3)$$

It should be emphasized very strongly that Eq. (7.3) is meant to serve only as an order of magnitude estimate. However, qualitatively one can see from the above considerations that there is an upper limit to the thermal energy which can be dissipated in the foil, while maintaining its metallic conductivity. The only way to exceed this energy density limitation is by dumping the energy into the foil so fast that the inertia of the foil mass prevents the atoms from flying apart. If the atoms are closely packed even after the critical internal energy is supplied, the foil resistance is reasonably high and additional energy can be imparted to the projectile. Under the experimental conditions an improvement of approximately a factor of 2 over Eq. (7.3) is obtained.

There are, however, practical limitations on the shortest practical time for dumping of energy into the foil:

- (1) Even with a most careful design, the capacitor plates and the leads to the foil have finite inductance which limits the current raise.

(2) Fast energy dumping corresponds to a greater acceleration of the projectile and may lead to projectile disintegration.

Under the current experimental conditions, the inductance of the leads have been minimized and the voltage on the capacitor has been increased to the point where tearing of the projectile occurs. It is, therefore, not very likely that, regardless of the results of the optimization analysis, the experimental conditions can be significantly improved as far as the shortening of the energy dumping time is concerned.

There is possibly more hope to improve the performance by optimization of the foil geometry, of the projectile-to-foil mass ratio, and in the selection of the projectile and foil materials. However, in view of the basic energy limitations expressed in Eq. (7.1) it is not immediately clear that a very significant improvement of the present performance could be achieved.

In view of the limitations on the time and on the funds under this contract, a decision had to be made whether the potential payoff of a complete optimization analysis represents a more promising approach than the modification on the projectile acceleration mechanism, as described in Section VII. After careful consideration of the two alternatives it was to concentrate on the modification of the acceleration mechanism using $j \times B$ post-acceleration.

VIII. DESIGN OF THE $j \times B$ POST-ACCELERATION STAGE

The joule energy dissipation in the exploding foil ends when the foil conductivity changes from the metallic to the plasma conductivity; the plasma conductivity is so low that the heat dissipation in the foil products is not significant. If the capacitor voltage is applied to the two rails protruding beyond the foil, an additional acceleration process is introduced (See figure 7). The current through the plasma between the rails induces a magnetic field resulting in a force:

$$F = j \times B \quad (8.1)$$

which is directed along the rails, and which causes plasma post-acceleration of the foil explosion products.

The commonly used plasma accelerator geometry is coaxial. However, for the post-acceleration stage of a projectile, a rectangular geometry is preferable for the following reasons:

- a. The current and the magnetic field are inversely proportional to the radius and therefore the forces in coaxial accelerator vary as $(1/r)^2$. This leads in turn to non-uniform projectile velocity and the possibility of tearing.
- b. The inductance of a coaxial accelerator with $r_o / r_i = 3$ is $0.22 \mu H / m$. The inductance of a rectangular configuration with equal rail width and distance is $1.26 \mu H / m$. The larger inductance leads to a more efficient coupling to a capacitor, as will be seen in the calculations which follow. The emf associated with the motion of the plasma "short" along the rails is

$$E = I (dL/dt) = I (dL/dx) v \quad (8.2)$$

The following are typical values for the experiment:

$$I = 2 \times 10^5 \text{ amp}$$

$$dL/dx = 10^{-6}$$

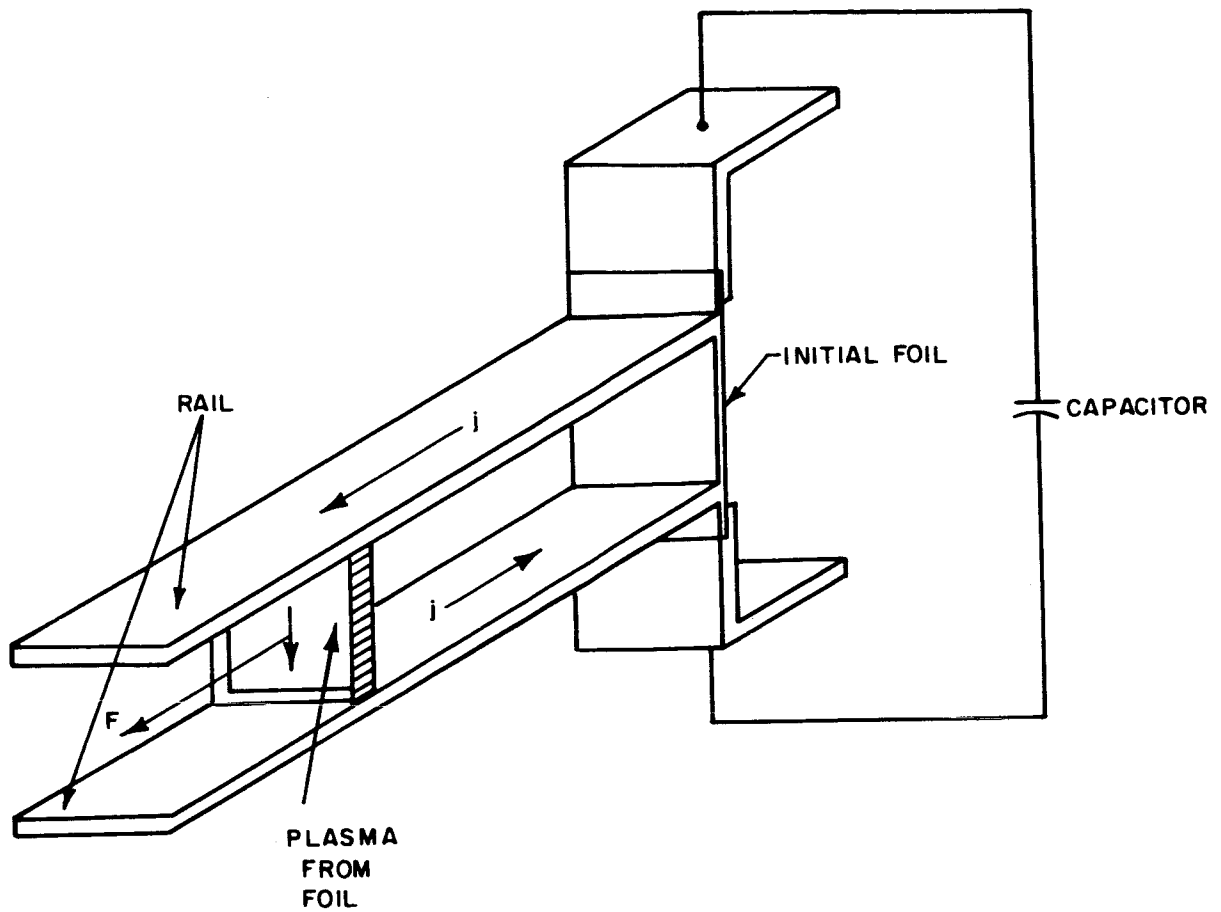
$$v = 10^4 \text{ m/sec}$$

So that

$$E = 2 \text{ kv}$$

The power delivered to the moving system is

$$P = IE = 4. \times 10^8 \text{ watts} \quad (8.3)$$



86-1467

Figure 7 $\mathbf{j} \times \mathbf{B}$ POST-ACCELERATION

The duration of acceleration is given by the ratio of the rail length ($D = 0.1\text{m}$) and the velocity v :

$$t = 0.1/10^4 = 10^{-5} \text{ sec} = 10 \mu\text{s} \quad (8.4)$$

The total energy delivered under these circumstances to the projectile and to the plasma is

$$u = pt = 4 \text{ k joules}$$

This indicates very adequate coupling with the present capacitor system.

The conduction of a current in the plasma created by the explosion of the foil material is carried out primarily by electrons. There is consequently an initial current deficiency at the negative electrode since the current of the positive ions is insufficient to match the plasma electron current. The result is a build-up of an ion acceleration region in the vicinity of the cathode and an intense cathode heating by ion bombardment, creating eventually electron emission from the cathode. The emitted electron current adds to the impinging ion current in carrying the plasma current.

It is desirable to achieve the maximum electron emission current combined with a minimum of cathode evaporation. The most desirable cathode material is a metal which has the lowest ratio of emission work function to temperature corresponding to 10^{-5} Torr⁽¹²⁾. This ratio for six most interesting materials is listed below:

Ta	W	Hf	Th	C	Mo
1.5	1.6	1.65	1.8	1.8	1.9

It is not necessary to make the entire cathode of the chosen material. The cathode rail can be lined with a foil of tantalum or covered with a sheath of tungsten.

Originally it was anticipated that instabilities may create a practical limitation on the jxB post-acceleration process. Magnetic forces tend to constrict the current flow into filaments. If this should turn out to be the case it was anticipated that the foil would be non-uniformly accelerated and that tears may result. The possibility was also considered that electron emission may have a tendency to emanate from "hot spots" and not uniformly from the entire cathode surface. However, related work reported in the literature⁽¹³⁾ did not mention such instabilities and consequently it was considered that the acceleration by means of jxB process is sufficiently promising to warrant its choice in comparison with the continuation of the optimization analysis.

The experimental results proved disappointing because of an entirely unexpected cause. In view of the size of the projectile chamber and the limitations of the

existing vacuum pumping equipment, the best vacuum which could be obtained was of the order of 50 microns. This residual air pressure was sufficient to cause breakdown between the rails which shorted the capacitor and prevented any useful energy transfer into the foil explosion or post-acceleration process. The breakdown between the rail points caused the formation of small craters on the rails probably due to ion impact.

There is presently no reason to doubt the basic feasibility of the jxB post-acceleration mechanism. It is, however, clear that the design of a superior vacuum-tight chamber and the application of higher capacity pump is necessary, so that the residual gas pressure can be reduced by several orders of magnitude.

IX. REFERENCES

1. McMath. R. R. , Study of Meteoroid Impact, Rpt. 1, Avco/RAD Contract NAS-3404 (October 1964).
2. Sherrer. V. E. , An Exploding Wire Hypervelocity Projector, Exploding Wires, Vol. 2, edited by W. G. Chace and H. K. Moore, Plenum Press (1962).
3. Maninger, R. C. , Preburst Resistance and Temperature of Exploding Wires, Exploding Wires, Vol. 3, edited by W. G. Chace and H. K. Moore, Plenum Press (1964).
4. Baxter, H. W. , Electric Fuses Edward Arnold, Ltd. , London (1950).
5. Meeker, M. E. , Solid and Liquid Phases in Wires at High Current Densities, Sandia Corporation Report SCTM 314-58(51) (1959).
6. Anderson, G. W. , E. W. Neilson, Use of the Action Integral in Exploding Wire Studies, Exploding Wires, Vol 1, edited by W. G. Chace and H. K. Moore, Plenum Press, New York (1959).
7. Borodovskaia, L. N. , and S. V. Lebedev, Dependence of the Electrical Conductivity and Electron Emission on the Energy of a Metal in the Process of its Heating by a Current of High Density, Soviet Physics JETP 1, 71 (1955).
8. Bennett, F. D. , G. D. Kahl, and E. H. Wedemeyer, Resistance Changes Caused by Vaporization Waves in Exploding Wires, Exploding Wires, Vol. 3 edited by W. G. Chace and H. K. Moore, Plenum Press, New York, (1964).
9. Dekker, A. J. , Solid State Physics, Prentice Hall (1957).
10. Mott, F. , H. Jones, The Theory of the Properties of Metals and Alloys, Dover Publications (1958).
11. Handbook of Liquid Metals, Department of the Navy, Washington, D. C. , Atomic Energy Commission, NAVEXOS p. 733 (Rev.) (June 1952).
12. Kohl, Walter H. , "Materials and Techniques for Electron Tubes", Reinhold Publishing Corp. , 1960, p. 524.
13. Rosebrock, T. L. , D. L. Clingman, D. G. Gubbins, "Repetitive Pulses Acceleration of Plasmas Derived from Exploding Metal Films," Exploding Wires, Vol. 3, Plenum Press, New York, 1964.

APPENDIX C

HEAT SHIELD IMPACT DATA

The data for this program are printed on the following pages. The printout was done from the data cards used in the regression program. These cards have been verified with the original data sheets.

There are some points that should be made regarding these data.

1. The temperature listed is the nominal temperature. Only in one case was the actual temperature significantly different from the nominal; this was for shot No. 95 into Avcoat, which showed no significant variation of crater parameters with temperature.
2. The program interprets a value identically equal to zero as missing data, and that shot is not included in regressions on that variable. Hence missing data are printed out as -0.0000. The minus sign is meaningless, but serves to signify this data. Data recorded as "small" or "slight" are given a small value (0.0001 or 0.0010) different from zero.
3. Very irregular spall and crater shapes were common, and often two values (at right angles) of diameter would be reported. An average value was used in the program. Also an average value was used for damage reported in units of honeycomb cells.

IMPACT TEST RESULTS
PROJECTILE DELRIN SPHERE 1/16 IN DIA, .0030 GM
JET MATERIAL AVCOAT 5026 HC

NUMBER	TEMP (DEG. F)	VELOCITY (FT/SEC)	SPALL DIAMETER (IN)	CRATER DIAMETER (IN)	PENETRATION (IN)	SPALL DEPTH (IN)	TOTAL DAMAGE DEPTH (IN)	TOTAL CRATER VOLUME (CC)
1 R C	68	9568	0.0001	0.0000	0.2340	0.0001	0.2110	0.04880
2 R C	68	10225	0.0001	0.1030	0.2150	0.0001	0.2400	0.03740
3 R C	-150	11098	0.0001	0.1390	0.2340	0.0001	0.2370	0.06820
4 R C	-150	9960	0.0001	0.1390	0.2240	0.0001	0.2240	0.05330
5 R C	-250	9133	0.0001	0.1390	0.2380	0.0001	0.2430	0.04270
6 R C	-250	9726	0.1301	0.1040	0.2560	0.0201	0.2240	0.06780
13 R C	68	17495	0.2800	0.1830	0.3860	0.0300	-0.0000	0.29700
13 R C	68	14881	0.2100	0.1440	0.3010	0.0600	-0.0000	0.09700
14 R C	68	17773	0.3100	0.2230	0.3220	0.0500	-0.0000	0.35300
15 R C	-150	15346	0.2200	0.1720	0.2920	0.0200	-0.0000	0.15600
16 R C	-150	15276	0.2600	0.2350	0.2500	0.0200	-0.0000	0.12200
17 R C	-250	15491	0.2500	0.1610	0.3040	0.0200	-0.0000	0.12900
18 R C	-250	14893	0.2600	0.1940	0.2640	0.0500	-0.0000	0.14300
25 R C	68	18552	0.2600	0.2030	0.2880	0.0200	-0.0000	0.29400
26 R C	68	18590	0.2700	0.2230	0.2840	0.0300	-0.0000	0.29400
27 R C	-150	21604	0.3700	0.2470	0.3050	0.1000	-0.0000	0.42400
28 R C	-150	21176	0.3000	0.2350	0.3190	0.0600	-0.0000	0.25100
29 R C	-250	22311	0.4300	0.2120	0.3010	0.1000	-0.0000	0.41000
30 R C	-250	21705	0.3300	0.1920	0.3150	0.0300	-0.0000	0.30200
37 R C	68	22885	0.4100	0.2820	0.3310	0.0800	-0.0000	0.49500
37 R C	68	23698	0.3750	0.2600	0.3120	0.0300	-0.0000	0.31800
37 R C	68	22957	0.3600	0.2740	0.3190	0.0400	-0.0000	0.41600
37 R C	68	22764	0.3700	0.2000	0.4040	0.0900	-0.0000	0.34200
38 R C	68	23396	0.3700	0.2430	0.3450	0.1200	-0.0000	0.40600
38 R C	68	22691	0.3900	0.2890	0.3220	0.0300	-0.0000	0.39500
38 R C	68	23310	0.4600	0.3000	0.3930	0.0800	-0.0000	0.46300
38 R C	68	25082	0.3800	0.2540	0.3460	0.0300	-0.0000	0.38100
39 R C	-150	23466	0.4200	0.2950	0.3600	0.0800	-0.0000	0.46100
40 R C	-250	23584	0.3901	0.2830	0.3210	0.0800	-0.0000	0.39500
41 R C	-250	23912	0.4000	0.2820	0.3490	0.0700	-0.0000	0.39200
42 R C	-250	23607	0.4100	0.2930	0.3400	0.0600	-0.0000	0.38700
42 R C	-250	24618	0.4300	0.2700	0.3610	0.0600	-0.0000	0.51400
42 R C	-250	23540	0.4350	0.2840	0.3560	0.0800	-0.0000	0.41600

IMPACT TEST RESULTS
PROJECTILE DELRIN SPHERE 1/16 IN DIA, .0030 GM
TARGET MATERIAL AVCOAT 5026 TILE

NUMBER	TEMP (DEG. F)	VELOCITY (FT/SEC)	SPALL DIAMETER (IN)	CRATER DIAMETER (IN)	PENETRATION (IN)	SPALL DEPTH (IN)	TOTAL DAMAGE DEPTH (IN)	TOTAL CRATER VOLUME (CC)
7 R C	68	9029	0.0001	0.0960	0.1460	0.0001	0.1620	0.01140
7 R C	68	7143	0.0001	0.0800	0.0980	0.0001	-0.0000	0.00870
8 R C	68	10624	0.0001	0.1270	0.1950	0.0001	0.1970	0.03880
9 R C	-150	8127	0.0001	0.1090	0.1670	0.0001	0.1740	0.01470
10 R C	-150	8564	0.0001	0.1110	0.1290	0.0001	0.1870	0.02000
11 R C	-250	10283	0.1600	0.1500	0.1950	0.0200	0.1950	0.05940
12 R C	-250	9653	0.0001	0.1220	0.1590	0.0001	0.1590	0.03660
15 R C	68	14558	0.2400	0.1510	0.2100	0.0200	-0.0000	0.07700
19 R C	68	12626	0.1700	0.1370	0.1880	0.0200	-0.0000	0.05500
20 R C	68	15123	0.2200	0.1650	0.2060	0.0200	-0.0000	0.07300
21 R C	-150	16019	0.2300	0.1760	0.2080	0.0200	-0.0000	0.08000
22 R C	-150	14674	0.1900	0.1540	0.2140	0.0200	-0.0000	0.06900
23 R C	-250	13528	0.1600	0.1550	0.2060	0.0001	-0.0000	0.07200
24 R C	-250	13624	0.2600	0.1790	0.2200	0.0200	-0.0000	0.30300
31 R C	68	19171	0.2000	0.1800	0.2100	0.0100	-0.0000	0.09200
31 R C	68	21219	0.3300	0.2120	0.2530	0.0400	-0.0000	0.28300
32 R C	68	22296	0.4100	0.2420	0.2530	0.0500	-0.0000	0.23100
32 R C	68	21818	0.2900	0.2120	0.2140	0.0500	-0.0000	0.21000
32 R C	68	19081	0.2400	0.2000	0.2420	0.0100	-0.0000	0.10500
33 R C	-150	21898	0.3900	0.2330	0.2960	0.0500	-0.0000	0.37000
33 R C	-150	22184	0.3800	0.2270	0.2530	0.0400	-0.0000	0.18300
34 R C	-150	21345	0.4200	0.2500	0.2500	0.0500	-0.0000	0.21800
35 R C	-250	20621	0.2800	0.1940	0.2200	0.0300	-0.0000	0.11500
36 R C	-250	21012	0.3100	0.2250	0.2650	0.0300	-0.0000	0.29600
43 R C	68	23641	0.3400	0.2200	0.2370	0.0300	-0.0000	0.17300
43 R C	68	23148	0.4300	0.2650	0.2840	0.0500	-0.0000	0.27100
44 R C	68	22763	0.4300	0.2430	0.2600	0.0700	-0.0000	0.22600
44 R C	68	24154	0.3450	0.2400	0.2670	0.0500	-0.0000	0.14300
44 R C	68	23431	0.3650	0.2650	0.2750	0.0500	-0.0000	-0.00000
44 R C	68	23757	0.4400	0.2420	0.2640	0.0400	-0.0000	0.20300
45 R C	-150	24170	0.3600	0.2240	0.2470	0.0400	-0.0000	0.31600
46 R C	-150	23085	0.3300	0.2110	0.2310	0.0500	-0.0000	0.14600
47 R C	-250	23231	0.3200	0.2390	0.2440	0.0400	-0.0000	0.20300
47 R C	-250	23981	0.4000	0.2690	0.2790	0.0400	-0.0000	0.26200
48 R C	-250	24582	0.4300	0.2490	0.2870	0.0600	-0.0000	0.27100

IMPACT TEST RESULTS

PROJECTILE ALUMINUM SPHERE 1/16 IN DIA, .0058 GM

TARGET MATERIAL AVCOAT 5026 HC

NUMBER	TEMP (DEG. F)	VELOCITY (FT/SEC)	SPALL DIAMETER (IN)	CRATER DIAMETER (IN)	PENETRATION (IN)	SPALL DEPTH (IN)	TOTAL DAMAGE DEPTH (IN)	TOTAL CRATER VOLUME (CC)
85 R C	68	8859	0.0001	0.1270	0.3630	0.0001	0.4290	0.07000
86 R C	68	9375	0.0001	0.1160	0.4760	0.0001	0.5550	0.09500
87 R C	-150	8321	0.0001	0.1360	0.4930	0.0001	0.4830	0.06500
88 R C	-150	11775	0.0001	0.1420	0.4420	0.0001	0.4890	0.13000
89 R C	-250	9910	0.0001	0.1130	0.5570	0.0001	0.6140	0.12000
90 R C	-250	9939	0.0001	0.1490	0.4300	0.0001	0.4750	0.15500
91 R C	68	14847	0.0001	0.1920	0.4560	0.0001	-0.0000	0.21000
92 R C	68	14232	0.0001	0.1750	0.4060	0.0001	-0.0000	0.17000
93 R C	-150	15051	0.0001	0.2170	0.3790	0.0001	-0.0000	0.22000
100 R C	-150	15278	0.0001	0.1970	0.4040	0.0001	-0.0000	0.26000
101 R C	-250	15385	0.3100	0.2020	0.4640	0.0400	-0.0000	0.27000
102 R C	-250	14829	0.3170	0.2320	0.4030	0.0700	-0.0000	0.31000
103 R C	68	19450	0.0001	0.2630	0.4020	0.0001	-0.0000	0.37000
110 R C	68	21182	0.3750	0.2830	0.4250	0.0700	-0.0000	0.46000
110 R 1	68	18400	0.4200	0.2960	0.4810	0.0400	-0.0000	0.44000
110 R 2	68	19802	0.3900	0.2890	0.4820	0.0700	-0.0000	0.45000
110 R 2	68	20325	0.3700	0.2740	0.5020	0.0500	-0.0000	0.34000
110 R 3	68	19639	0.4780	-0.0000	0.4380	0.0670	-0.0000	0.46000
110 R 5	68	19438	0.3900	0.2810	0.4260	0.0200	-0.0000	0.33000
110 R 6	68	19760	0.3800	0.2760	0.3980	0.0750	-0.0000	0.35000
110 R 6	68	19546	0.3700	0.2510	0.4940	0.0520	-0.0000	0.36000
110 R 7	68	20379	0.3900	0.3020	0.5540	0.0750	-0.0000	0.61000
110 R 9	68	19755	0.4000	0.3100	0.5780	0.0400	-0.0000	0.61000
110 R 10	68	19146	0.3100	0.2410	0.4220	0.0500	-0.0000	0.42300
111 R C	68	18462	0.2900	0.2370	0.3750	0.0500	-0.0000	0.37200
111 R C	-150	21909	0.4200	0.2770	0.4900	0.0480	-0.0000	0.50000
112 R C	-150	21713	0.3901	0.3060	0.5040	0.0830	-0.0000	0.51000
113 R C	-250	19801	0.0001	0.2690	0.3800	0.0001	-0.0000	0.50000
114 R C	-250	19845	0.3901	0.3160	0.4700	0.0560	-0.0000	0.54000
121 R C	68	23483	0.3600	0.2900	0.4700	0.0001	-0.0000	0.61000
121 R 1	68	26448	0.4700	0.3440	0.4880	0.0900	-0.0000	0.88400
121 R 2	68	22599	0.3850	0.2970	0.4880	0.1000	-0.0000	0.62400
122 R C	68	23828	0.5000	0.3200	0.6050	0.1200	-0.0000	0.70000
122 R 1	68	23652	0.0001	0.3670	0.5930	0.0001	-0.0000	0.94700
122 R 2	68	24510	0.0001	0.3450	0.5460	0.0001	-0.0000	0.84100
123 R C	-150	23835	0.5100	0.2700	0.4660	0.1400	-0.0000	0.55000
124 R C	-150	22762	0.4600	0.3240	0.5260	0.1000	-0.0000	0.69000
124 R 1	-150	23464	0.4400	0.2960	0.5300	0.1000	-0.0000	0.77800
124 R 2	-150	24618	0.4750	0.3290	0.4520	0.0700	-0.0000	0.70100
125 R C	-250	23297	0.3400	0.3090	0.4920	0.0001	-0.0000	0.65900
125 R 1	-250	24492	0.4900	0.2910	0.5410	0.1000	-0.0000	0.77800
126 R C	-250	25249	0.3400	0.3200	0.4430	0.0600	-0.0000	0.64700
126 R 1	-250	23667	0.2950	0.2910	0.4300	0.0800	-0.0000	0.55700

IMPACT TEST RESULTS
PROJECTILE ALUMINUM SPHERE 1/16 IN DIA, .0058 GM
TARGET MATERIAL AVCOAT 5026 TILE

NUMBER	TEMP (DEG. F)	VELOCITY (FT/SEC)	SPALL DIAMETER (IN)	CRATER DIAMETER (IN)	PENETRATION (IN)	SPALL DEPTH (IN)	TOTAL DAMAGE DEPTH (IN)	TOTAL CRATER VOLUME (CC)
91 R C	68	9203	0.0001	0.1100	0.3480	0.0001	0.3870	0.05500
92 R C	68	8441	0.0001	0.1050	0.3790	0.0001	0.4170	0.05000
93 R C	-150	8616	0.0001	0.1160	0.2930	0.0001	0.3450	0.05000
94 R C	-150	8653	0.0001	0.0990	0.3140	0.0001	0.3150	0.04000
95 R C	-250	8630	0.0001	0.1110	0.3410	0.0001	0.4100	0.06000
96 R C	-250	8653	0.0001	0.1260	0.2800	0.0001	0.3690	0.06000
103 R C	68	15924	0.0001	0.2270	0.3750	0.0001	-0.0000	0.24000
104 R C	68	14107	0.0001	0.1640	0.3180	0.0001	-0.0000	0.10000
105 R C	-150	15189	0.0001	0.1880	0.3610	0.0001	-0.0000	0.17000
106 R C	-150	14350	0.0001	0.1740	0.2830	0.0001	-0.0000	0.10500
107 R C	-250	15178	0.0001	0.2140	0.3890	0.0001	-0.0000	0.25000
108 R C	-250	13345	0.0001	0.1450	0.2970	0.0001	-0.0000	0.08000
115 R C	68	17862	0.0001	0.2350	0.3380	0.0001	-0.0000	0.23000
116 R 1	68	19410	0.4340	0.2570	0.3790	0.0800	-0.0000	0.37000
116 R 0	68	19254	0.0001	0.3330	0.4440	0.0001	-0.0000	0.54000
116 R 1	68	19410	0.3700	0.2530	0.3670	0.0550	-0.0000	0.23000
116 R 2	68	19247	0.3370	0.2250	0.2630	0.0440	-0.0000	0.16000
116 R 2	68	19773	0.3590	0.2250	0.2770	0.0500	-0.0000	0.17000
116 R 3	68	20000	0.4200	0.2630	0.3270	0.0680	-0.0000	0.23000
116 R 5	68	20497	0.3600	0.2400	0.3870	0.0640	-0.0000	0.24000
116 R 6	68	19218	0.3460	0.2250	0.3910	0.1450	-0.0000	0.31000
116 R 6	68	19187	0.4100	0.2400	0.3510	0.0520	-0.0000	0.21000
116 R 7	68	19440	0.4400	0.2490	0.3050	0.0400	-0.0000	0.25000
116 R 5	68	18400	0.3600	0.2260	0.3240	0.0350	-0.0000	0.21000
117 R C	-150	20040	0.5380	0.2580	0.2950	0.0680	-0.0000	0.28000
118 R C	-150	20826	0.4300	0.2750	0.3310	0.0600	-0.0000	0.31000
119 R C	-250	19320	0.4150	0.2610	0.3530	0.0490	-0.0000	0.32000
120 R C	-250	20163	0.3200	0.2420	0.3090	0.0001	-0.0000	0.21000
127 R C	68	22928	0.4100	0.2900	0.3910	0.0650	-0.0000	0.39000
127 R 1	68	24950	0.4300	0.2940	0.3680	0.0300	-0.0000	0.46900
127 R 2	68	24759	0.4400	0.2750	0.4060	0.0600	-0.0000	0.37800
127 R 2	68	23732	-0.0000	0.2880	0.3720	0.0300	-0.0000	-0.00000
128 R C	68	23232	0.4050	0.2730	0.3680	0.0600	-0.0000	0.38000
128 R 1	68	22532	0.5100	0.2980	0.3660	0.0400	-0.0000	0.43300
128 R 2	68	25815	0.5100	0.2850	0.3720	0.0500	-0.0000	0.43600
129 R C	-150	24169	0.4500	0.2820	0.4300	0.0600	-0.0000	0.44000
130 R C	-150	22522	0.3600	0.2710	0.3420	0.0500	-0.0000	0.31000
130 R 1	-150	23474	0.3600	0.3040	0.4160	0.0600	-0.0000	0.47600
130 R 2	-150	23721	0.5000	0.3050	0.3630	0.0500	-0.0000	0.49200
130 R 3	-150	25225	0.4700	0.2870	0.3890	0.0600	-0.0000	0.41700
131 R C	-250	22980	0.2800	0.2780	0.4240	0.0400	-0.0000	0.43100
131 R 1	-250	24938	0.4700	0.3450	0.3880	0.0800	-0.0000	0.58600
131 R 2	-250	26408	0.4550	0.3040	0.4610	0.0600	-0.0000	0.54900
132 R C	-250	23784	0.5300	0.3140	0.4670	0.0800	-0.0000	0.78200

IMPACT TEST RESULTS

PROJECTILE DELRIN SPHERE 1/16 IN DIA, .0030 GM

TARGET MATERIAL SYLGARD 325 HC

NUMBER	TEMP (DEG. F)	VELOCITY (FT/SEC)	SPALL DIAMETER (IN)	CRATER DIAMETER (IN)	PENETRATION (IN)	SPALL DEPTH (IN)	TOTAL DAMAGE DEPTH (IN)	TOTAL CRATER VOLUME (CC)
165 R C	68	11369	0.2001	0.0810	0.0950	0.0400	0.2040	0.01740
170 R C	68	10460	0.1300	0.0660	0.0860	0.0200	0.1110	0.01000
171 R C	-150	10436	0.1300	0.0650	0.0530	0.0200	0.0940	0.00600
171 R 1	-150	7520	0.1100	0.0390	0.0510	0.0001	0.1180	0.00500
171 R 2	-150	11478	0.1500	0.0520	0.0380	0.0001	0.0900	0.00740
172 R C	-150	9494	0.1200	0.0500	0.0610	0.0100	0.0970	0.00600
173 R C	-250	10333	0.1800	0.0700	0.0720	0.0400	0.1520	0.01000
174 R C	-250	9739	0.1700	0.0570	0.0200	0.0200	0.0740	0.01100
181 R C	68	14105	0.2001	0.0780	0.0540	0.0300	0.1390	0.01400
182 R C	68	15430	0.2001	0.1010	0.1240	0.0500	0.1830	0.03400
183 R C	-150	15286	0.1900	0.0810	0.1190	0.0300	0.2050	0.02400
184 R C	-150	15458	0.1900	0.0840	0.1160	0.0500	0.1860	0.02000
185 R C	-250	15613	0.3000	0.0860	0.0950	0.0400	0.1210	0.03200
186 R C	-250	15864	0.2500	0.0900	0.1110	0.0300	0.1970	0.03000
193 R C	68	21392	0.2832	0.1390	0.1350	0.0600	0.3020	0.06900
192 R 1	68	20829	0.2500	0.1390	0.1420	0.0300	0.2400	0.04500
194 R C	-68	21183	0.2001	0.1550	0.1630	0.0700	0.5340	0.06200
195 R C	-150	20587	0.2300	0.1150	0.1380	0.0800	0.1900	0.04400
196 R C	-150	20516	0.2800	0.1070	0.1540	0.0900	0.2150	0.06300
197 R C	-250	22184	0.2900	0.1100	0.0820	0.0300	0.0620	0.05700
197 R 1	-250	18942	0.3150	0.1120	0.1070	0.0300	0.1370	0.04200
198 R C	-250	19927	0.2800	0.0900	0.1080	0.0600	0.2550	0.04200
198 R 1	-250	22211	0.4200	0.1290	0.1300	0.0300	0.1740	0.08200
198 R 2	-250	20858	0.2100	0.0810	0.0900	0.0500	0.2470	0.03600
205 R C	-68	24080	0.2600	0.1510	0.1670	0.0700	0.3200	0.07300
206 R C	68	23793	0.2832	0.1570	0.1480	0.0700	0.3010	0.08500
207 R C	-150	24025	0.2300	0.1180	0.1680	0.0600	0.2900	0.05900
207 R 1	-150	23142	0.2300	0.1250	0.1180	0.0300	0.2410	0.06300
208 R C	-150	23979	0.2001	0.1020	0.1580	0.0300	0.1820	0.05900
209 R C	-250	23609	0.3600	0.1250	0.0960	0.0500	0.2530	0.07800
209 R 1	-250	24762	0.3470	0.0000	0.2910	0.1100	0.4480	0.30700
209 R 2	-250	23307	0.3600	0.1660	0.1280	0.0300	0.1470	0.07100
210 R C	-250	23970	0.2900	0.1130	0.0740	0.0100	0.1950	0.05000

IMPACT TEST RESULTS

PROJECTILE DELRIN SPHERE 1/16 IN DIA, .0030 GM

TARGET MATERIAL SYLGARD 325 TILE

NUMBER	TEMP (DEG. F)	VELOCITY (FT/SEC)	SPALL DIAMETER (IN)	CRATER DIAMETER (IN)	PENETRATION (IN)	SPALL DEPTH (IN)	TOTAL DAMAGE DEPTH (IN)	TOTAL CRATER VOLUME (CC)
175 R C	68	10209	0.1500	0.0450	0.0750	-0.0000	0.1320	0.00900
176 R C	68	10606	0.1200	0.0590	0.0840	0.0200	0.1080	0.01100
177 R C	-150	10269	0.1900	0.0840	0.0660	0.0200	0.0950	0.00600
178 R C	-150	11667	0.1200	0.0640	0.0580	0.0200	0.1010	0.00500
179 R C	-250	9892	0.2500	0.0590	0.0510	0.0200	0.0720	0.01500
180 R C	-250	9924	0.1800	0.0660	0.0510	0.0200	0.0800	0.00900
187 R C	68	13505	0.1500	0.0910	0.0650	-0.0000	0.1660	0.00900
188 R C	68	15477	0.1800	0.1000	0.1130	0.0200	0.2020	0.01300
189 R C	-150	15170	0.1500	0.0910	0.0940	0.0200	0.1410	0.01100
190 R C	-150	15576	0.1700	0.0920	0.0880	0.0200	0.1310	0.01300
191 R C	-250	15695	0.2500	0.0950	0.0970	0.0300	0.1080	0.02400
192 R C	-250	14697	0.2800	0.0790	0.0900	0.0300	0.1080	0.04300
199 R C	68	19552	0.2200	0.1370	0.1380	0.0300	0.1900	0.04000
200 R C	68	19873	0.2500	0.1470	0.1440	0.0500	0.2050	0.04800
201 R C	-150	21615	0.2700	0.1210	0.1170	0.0500	0.1400	0.03900
202 R C	-150	20652	0.2200	0.1240	0.1090	0.0400	0.1550	0.02900
203 R C	-250	20411	0.3700	0.1150	0.1100	0.0300	0.1140	0.05100
204 R C	-250	19483	0.3600	0.1190	0.1110	0.0400	0.1300	0.05500
211 R C	68	22520	0.2700	0.1500	0.1540	0.0400	0.2650	0.06200
211 R 1	68	23485	0.2700	0.1380	0.1610	0.0300	0.2480	0.06600
211 R 2	68	23310	0.2700	0.1510	0.1270	0.0300	0.2320	0.06500
211 R 3	68	24133	0.2800	0.1410	0.1540	0.0300	0.3160	0.05500
211 R 4	68	23696	0.2900	0.1550	0.1490	0.0400	0.2390	0.06200
212 R C	68	24011	0.2600	0.1490	0.1580	0.0400	0.2150	0.05200
212 R 1	68	23298	0.3000	0.1480	0.1530	0.0400	0.2310	0.06600
213 R C	-150	23981	0.2200	0.1220	0.1350	0.0300	0.1880	0.03500
213 R 1	-150	22534	0.2200	0.1240	0.1280	0.0400	0.1590	0.05100
214 R C	-150	23496	0.2400	0.1250	0.1360	0.0500	0.1520	0.04200
214 R 1	-150	25769	0.2900	0.1500	0.1450	0.0300	0.1790	0.06400
215 R C	-250	25640	0.4600	0.1240	0.1330	0.0500	0.1600	0.11000
216 R C	-250	23023	0.3300	0.1220	0.1270	0.0400	0.1730	0.08200
216 R 1	-250	23928	0.3750	0.1310	0.1400	0.0400	0.1670	0.11200
216 R 2	-250	24655	0.4100	0.1500	0.1520	0.0400	0.1870	0.09500

IMPACT TEST RESULTS

PROJECTILE ALUMINUM SPHERE 1/16 IN DIA, .0058 GM

TARGET MATERIAL SYLGARD 325 HC

NUMBER	TEMP (DEG. F)	VELOCITY (FT/SEC)	SPALL DIAMETER (IN)	CRATER DIAMETER (IN)	PENETRATION (IN)	SPALL DEPTH (IN)	TOTAL DAMAGE DEPTH (IN)	TOTAL CRATER VOLUME (CC)
253 R C	68	9784	0.1200	0.0800	0.3040	0.0500	0.3040	0.00100
254 R C	68	9649	0.1200	0.0770	0.3090	0.0500	0.4550	0.00100
255 R C	-150	9868	0.0930	0.0750	0.2730	-0.0000	0.2730	0.00100
256 R C	-150	10351	0.1700	0.0700	0.2300	0.0200	0.2300	0.00100
257 R C	-250	9718	0.1800	0.0500	0.2120	0.0550	0.2120	0.00100
258 R C	-250	10980	0.1420	0.0790	0.2610	0.0300	0.2610	0.00100
259 R C	68	13287	0.2001	0.1180	0.1600	0.0800	0.3480	0.04500
260 R C	68	16694	0.3350	0.1220	0.1590	0.0600	0.1590	0.06800
261 R C	68	13968	0.2300	0.1400	0.1670	0.0680	0.3520	0.05000
262 R C	-150	13470	0.2001	0.1020	0.1710	0.0620	0.2420	0.03000
263 R C	-150	13269	0.2001	0.1180	0.1520	0.0800	0.2140	0.03000
264 R C	-250	13932	0.2001	0.0810	0.1350	0.0550	0.2330	0.00100
265 R C	-250	13725	0.2450	0.0900	0.1290	0.0570	0.2590	0.00100
266 R C	68	20080	0.3473	0.1540	0.2040	0.0850	0.3200	0.12000
267 R C	68	19246	0.3473	0.1510	0.2250	0.0800	0.4300	0.12000
268 R C	-150	20112	0.2001	0.1570	0.2240	0.0600	0.7200	0.10000
269 R C	-150	20112	0.2832	0.1500	0.2300	0.1100	0.3550	0.06000
270 R C	-150	21320	0.4004	0.2060	0.2800	0.1100	0.4780	0.24000
271 R C	-250	20439	0.4100	0.1180	0.2270	0.0940	0.3200	0.11000
272 R C	-250	19465	0.3830	0.1230	0.2020	0.0730	0.3350	0.12000
273 R C	68	22302	0.3473	0.1970	0.2520	0.0600	0.6700	0.13000
274 R C	68	25493	0.5500	0.2250	0.2360	0.0900	0.4190	0.33400
275 R C	68	23912	0.4000	0.2000	0.2240	0.0800	0.4560	0.28300
276 R C	68	24510	0.4485	0.1900	0.2340	0.0800	0.4200	0.16000
277 R C	68	23100	0.5450	0.2250	0.2090	0.0802	0.3350	0.27700
278 R C	-150	23759	0.3473	0.1700	0.2460	0.2000	0.4100	0.13600
279 R C	-150	22670	0.3500	0.1650	0.2100	0.1000	0.2250	0.10300
280 R C	-150	24919	0.3000	0.1410	0.2020	0.0600	0.4000	0.14900
281 R C	-250	23896	0.3473	0.1470	0.2620	0.1100	0.3070	0.15800
282 R C	-250	25030	0.4050	0.1200	0.1530	0.0500	0.2370	0.10200
283 R C	-250	23481	0.4485	0.1240	0.1020	0.2700	0.2410	0.32300

IMPACT TEST RESULTS

PROJECTILE ALUMINUM SPHERE 1/16 IN DIA, .0058 CM

TARGET MATERIAL SYLGARD 325 TILE

NUMBER	TEMP (DEG. F)	VELOCITY (FT/SEC)	SPALL DIAMETER (IN)	CRATER DIAMETER (IN)	PENETRATION (IN)	SPALL DEPTH (IN)	TOTAL DAMAGE DEPTH (IN)	TOTAL CRATER VOLUME (CC)
255 R C	68	10123	0.1570	0.0920	0.3320	0.0400	0.3320	0.00100
260 R C	68	9930	0.1440	0.1020	0.3380	0.0500	0.3380	0.00100
261 R C	-150	9720	0.0900	0.0700	0.2330	0.0300	0.2330	0.00100
262 R C	-150	10801	0.1020	0.0750	0.2240	0.0300	0.2440	0.00100
263 R C	-250	10769	0.2400	0.0990	0.1700	0.0350	0.1700	0.00100
264 R C	-250	10166	0.2200	0.0750	0.1980	0.0300	0.1980	0.00100
271 R C	68	14286	0.2130	0.1150	0.1600	0.0300	0.3160	0.03000
272 R C	68	14344	0.2130	0.1210	0.1570	0.0300	0.3110	0.03000
273 R C	-150	13935	0.1500	0.0980	0.1520	0.0200	0.1970	0.02000
274 R C	-150	14181	0.1540	0.0960	0.1550	0.0200	0.2020	0.02000
275 R C	-250	14067	0.3800	0.0990	0.1560	0.0550	0.2000	0.07000
276 R C	-250	14308	0.3700	0.0980	0.1520	0.0600	0.1740	0.06000
283 R C	68	21645	0.2850	0.1600	0.2200	0.0300	0.3550	0.08000
283 R 2	68	21244	0.3100	0.1850	0.1980	0.0400	0.3320	0.09000
283 R 2	-68	21276	0.2800	0.1750	0.2210	0.0400	0.3820	0.19900
284 R C	68	19259	0.3200	0.1790	0.2170	0.0600	0.3080	0.11000
284 R C	68	18933	0.2200	0.1730	0.2100	0.0300	0.3870	0.06000
284 R 2	68	19410	0.2300	0.1740	0.1920	0.0300	0.3100	0.06000
284 R 2	68	19547	0.2600	0.1700	0.2160	0.0300	0.4160	0.07000
284 R 4	68	20490	0.2600	0.1800	0.2120	0.0300	0.3370	0.06000
284 R 4	68	21050	0.3250	0.2070	0.2340	0.0300	0.3180	0.12000
285 R C	-150	19184	0.2340	0.1350	0.1880	0.0600	0.2570	0.05500
286 R C	-150	18809	0.1940	0.1370	0.1820	0.0600	0.2500	0.05000
287 R C	-250	18755	0.4500	0.1490	0.1910	0.0580	0.2180	0.12000
288 R C	-250	19887	0.5660	0.1570	0.2130	0.0770	0.2710	0.17000
295 R C	68	22917	0.3500	0.2050	0.2090	0.0450	0.2850	0.16000
295 R C	68	23254	0.3600	0.1780	0.2380	0.0600	0.3810	0.11900
295 R 2	68	24753	0.3300	0.1700	0.2000	0.0400	0.3500	0.10100
296 R C	68	25252	0.3650	0.2060	0.2300	0.0700	0.3200	0.16000
297 R C	-150	23148	0.2800	0.1520	0.1930	0.0600	0.2490	0.08000
297 R C	-150	26619	0.2700	0.1510	0.1900	0.0300	0.2570	0.09500
298 R C	-150	23020	0.2900	0.1710	0.1980	0.0600	0.2410	0.08000
298 R C	-150	24280	0.2500	0.1400	0.1920	0.0300	0.2780	0.08700
299 R C	-250	24110	0.4700	0.1650	0.2170	0.0500	0.3110	0.26200
299 R 2	-250	23651	0.4800	0.1550	0.2040	0.0500	0.2700	0.17200
300 R C	-250	24400	0.7700	0.1480	0.2020	0.0600	0.2750	0.29900
300 R C	-250	25396	0.4700	0.1580	0.2160	0.0600	0.2540	0.19400

APPENDIX D

CRATER PARAMETERS VERSUS VELOCITY

CRATER PARAMETERS VERSUS VELOCITY

<u>Figure</u>	<u>Target</u>	<u>Projectile</u>	<u>Crater Parameter</u>
D1	Sylgard 325 tile	Al	Spall Diameter
D2	Sylgard 325 HC	Al	Spall Diameter
D3	Sylgard 325 tile	Delrin	Spall Diameter
D4	Sylgard 325 HC	Delrin	Spall Diameter
D5	Avcoat 5026 tile	Al	Spall Diameter
D6	Avcoat 5026 HC	Al	Spall Diameter
D7	Avcoat 5026 tile	Delrin	Spall Diameter
D8	Avcoat 5026 HC	Delrin	Spall Diameter
D9	Sylgard 325 tile	Al	Crater Diameter
D10	Sylgard 325 HC	Al	Crater Diameter
D11	Sylgard 325 tile	Delrin	Crater Diameter
D12	Sylgard 325 HC	Delrin	Crater Diameter
D13	Avcoat 5026 tile	Al	Crater Diameter
D14	Avcoat 5026 HC	Al	Crater Diameter
D15	Avcoat 5026 tile	Delrin	Crater Diameter
D16	Avcoat 5026 HC	Delrin	Crater Diameter
D17	Sylgard 325 tile	Al	Penetration
D18	Sylgard 325 HC	Al	Penetration
D19	Sylgard 325 tile	Delrin	Penetration
D20	Sylgard 325 HC	Delrin	Penetration
D21	Avcoat 5026 tile	Al	Penetration
D22	Avcoat 5026 HC	Al	Penetration
D23	Avcoat 5026 tile	Delrin	Penetration
D24	Avcoat 5026 HC	Delrin	Penetration
D25	Sylgard 325 tile	Al	Spall Depth
D26	Sylgard 325 HC	Al	Spall Depth
D27	Sylgard 325 tile	Delrin	Spall Depth
D28	Sylgard 325 HC	Delrin	Spall Depth
D29	Avcoat 5026 tile	Al	Spall Depth
D30	Avcoat 5026 HC	Al	Spall Depth
D31	Avcoat 5026 tile	Delrin	Spall Depth
D32	Avcoat 5026 HC	Delrin	Spall Depth
D33	Sylgard 325 tile	Al	Volume
D34	Sylgard 325 HC	Al	Volume
D35	Sylgard 325 tile	Delrin	Volume
D36	Sylgard 325 HC	Delrin	Volume
D37	Avcoat 5026 tile	Al	Volume
D38	Avcoat 5026 HC	Al	Volume
D39	Avcoat 5026 tile	Delrin	Volume
D40	Avcoat 5026 HC	Delrin	Volume
D41	Sylgard 325 tile	Al	Total Damage Depth
D42	Sylgard 325 HC	Al	Total Damage Depth
D43	Sylgard 325 tile	Delrin	Total Damage Depth
D44	Sylgard 325 HC	Delrin	Total Damage Depth

HONEYCOMB SYMBOLS

TEMPERATURE	SYMBOL
RT	+
-150°F	X
-250°F	*

TILE SYMBOLS

TEMPERATURE	SYMBOL
RT	C
-150°F	O
-250°F	□

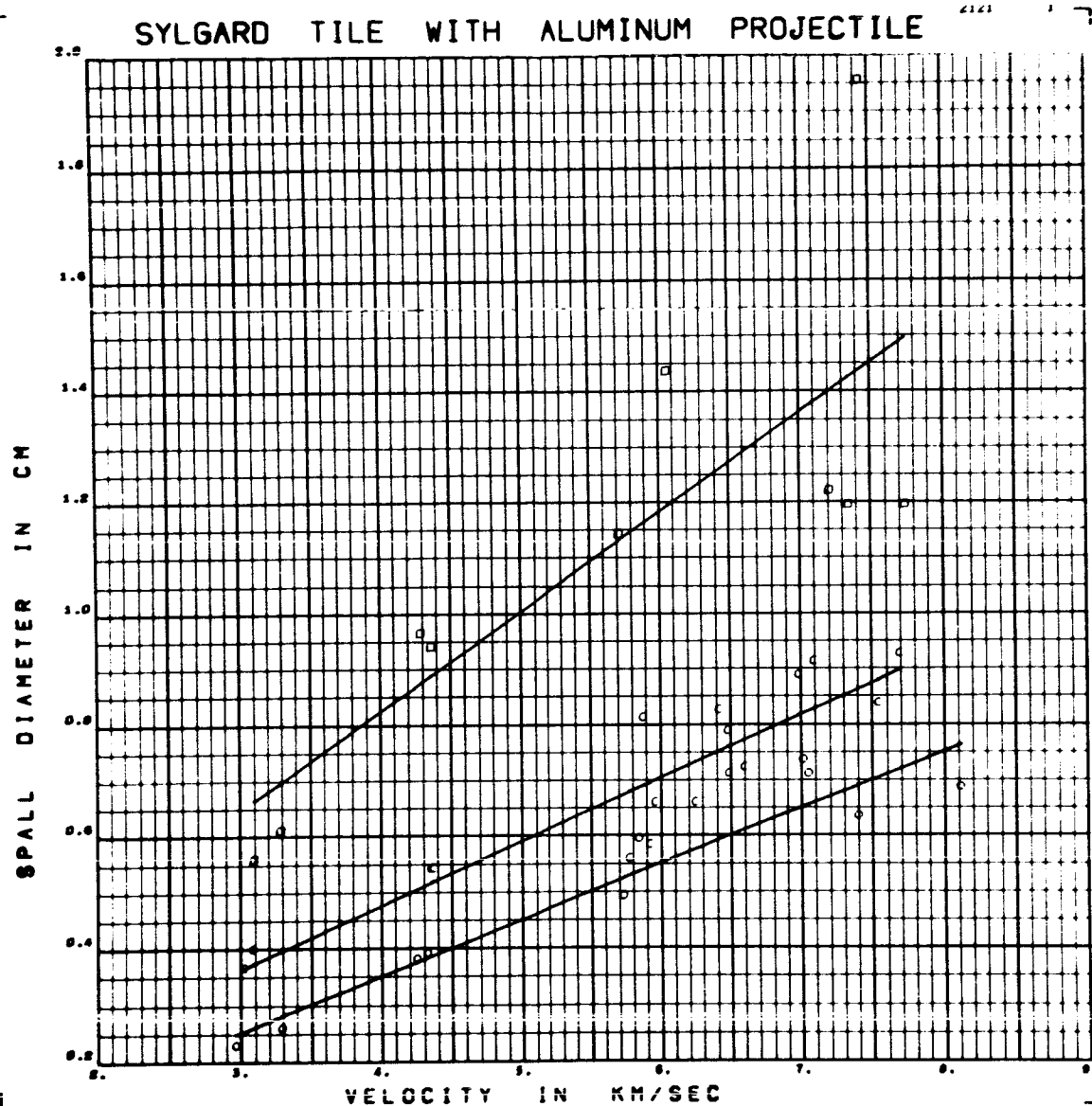


Figure D1 Spall Diameter versus Velocity for Aluminum Projectiles on Sylgard 325 Tile

Form of Regression: $d_s = (.1310 - .0656 ST - .0311 CV) V$

RMS Deviation: .133 cm

$+ .0275 - .0855 ST - .0751 CV$

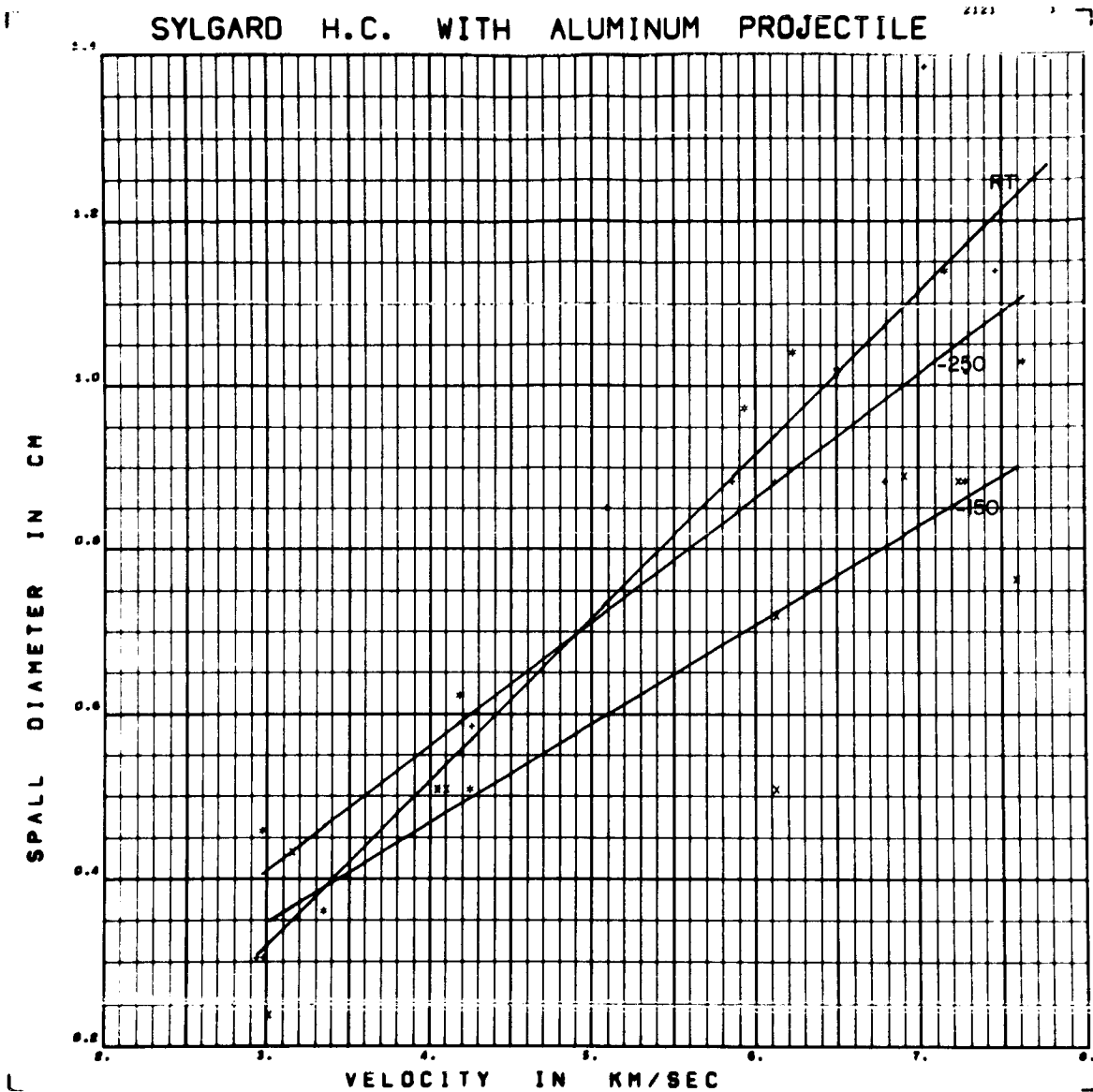


Figure D2 Spall Diameter versus Velocity for Aluminum Projectiles on
Sylgard 325 HC

Form of Regression: $d_s = (.1565 + .0477 ST - .0363 CV) V$

RMS Deviation: .119 cm -.1098 -.2333 ST + .0969 CV

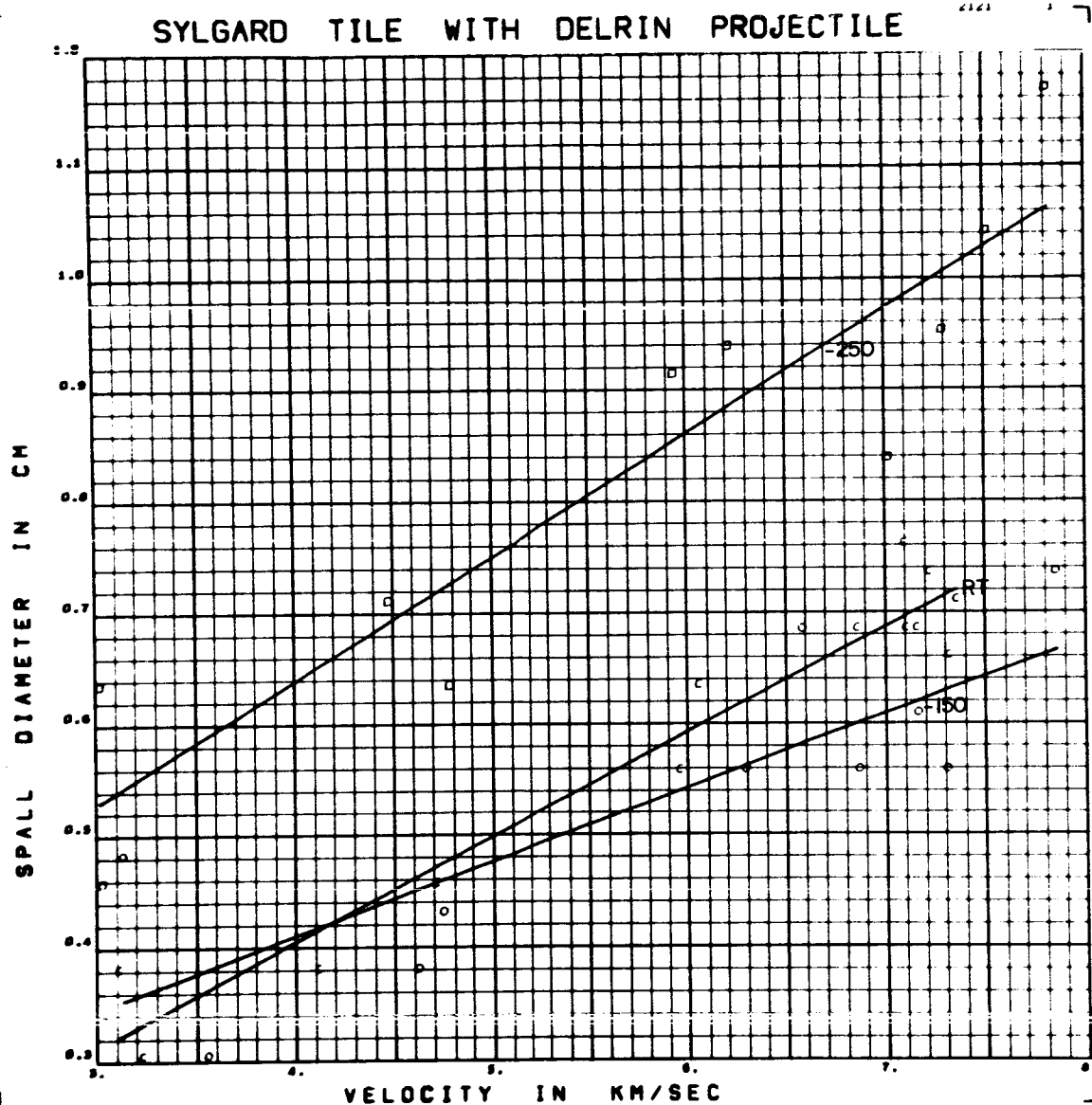


Figure D3 Spall Diameter versus Velocity for Delrin Projectiles on
Sylgard 325 Tile

Form of Regression: $d_s = (.0903 - .0172 ST - .0242 CV) V$

RMS Deviation: .064 cm $+ .1239 - .1650 ST + .0224 CV$

SYLGARD H.C. WITH DELRIN PROJECTILE

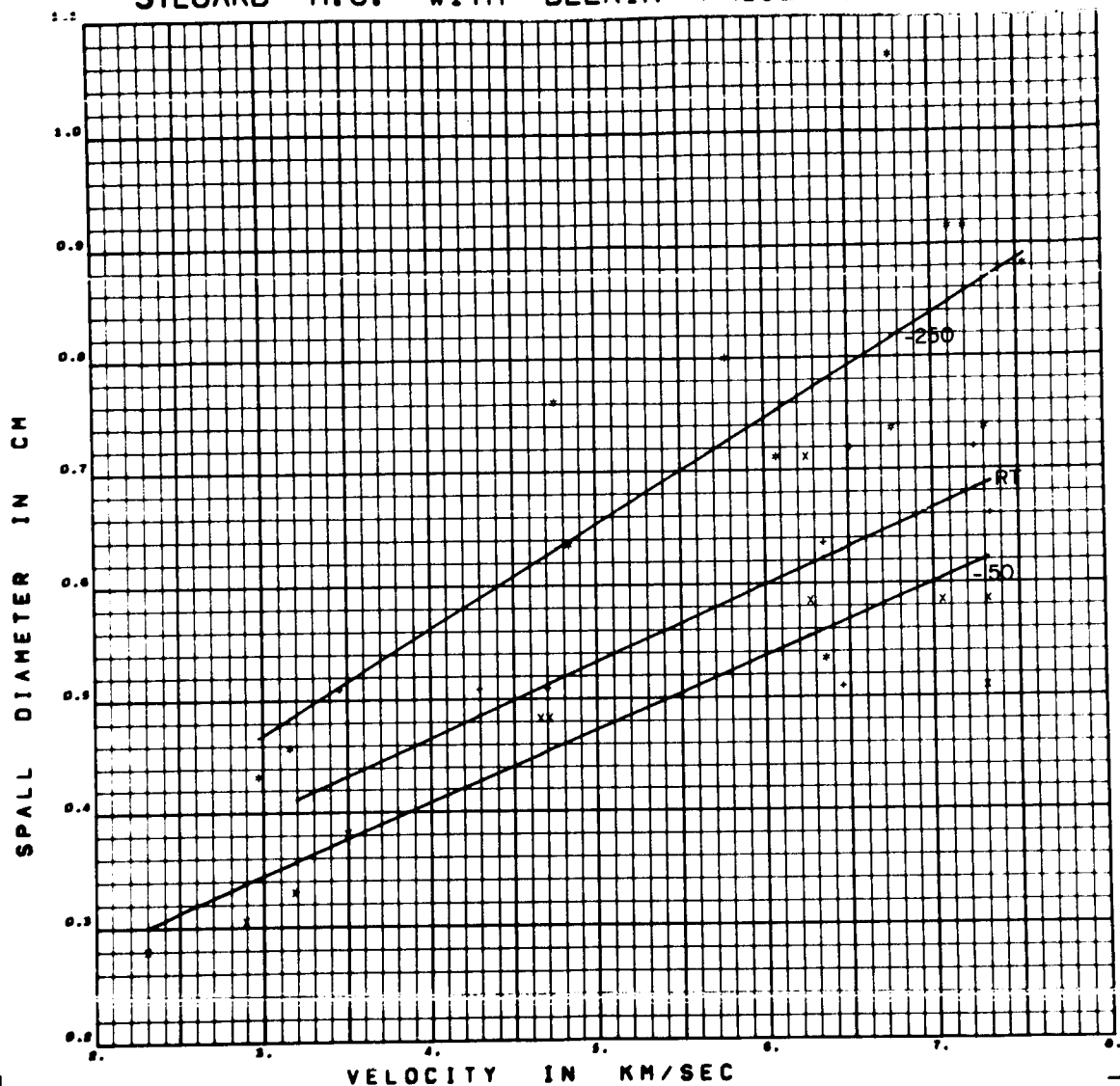


Figure D4 Spall Diameter versus Velocity for Delrin Projectiles on
Sylgard 325 HC

Form of Regression: $d_s = (.0744 - .0258 ST - .0105 CV) V$

RMS Deviation: .090 cm

$+ .1815 + .0071 ST - .0278 CV$

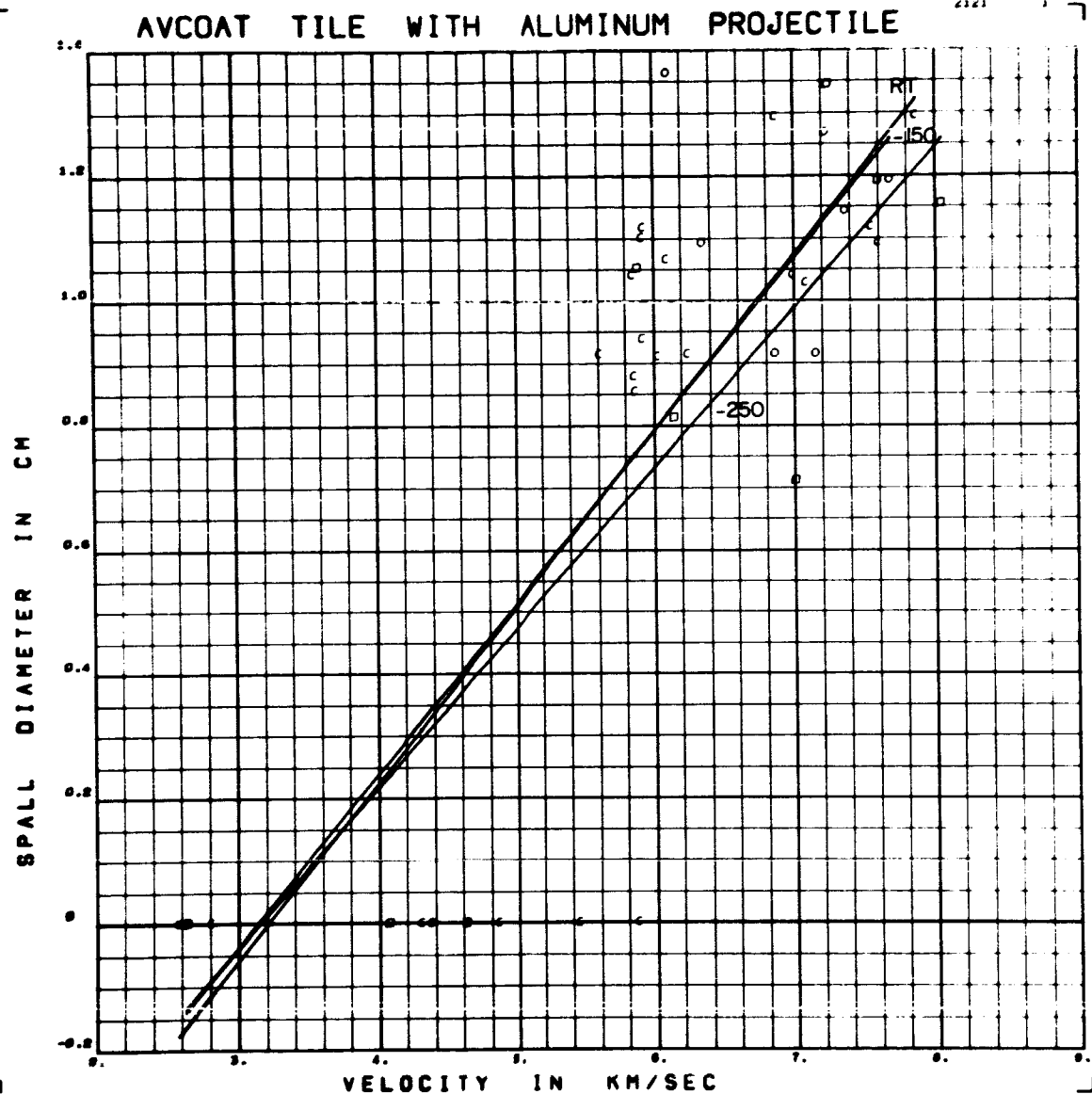


Figure D5 Spall Diameter versus Velocity for Aluminum Projectiles on
Avcoat 5026 Tile

Form of Regression: $d_s = (.2723 + .0260ST + .0044CV)V$

RMS Deviation: .277cm

$-.8611 - .0962ST - .0067CV$

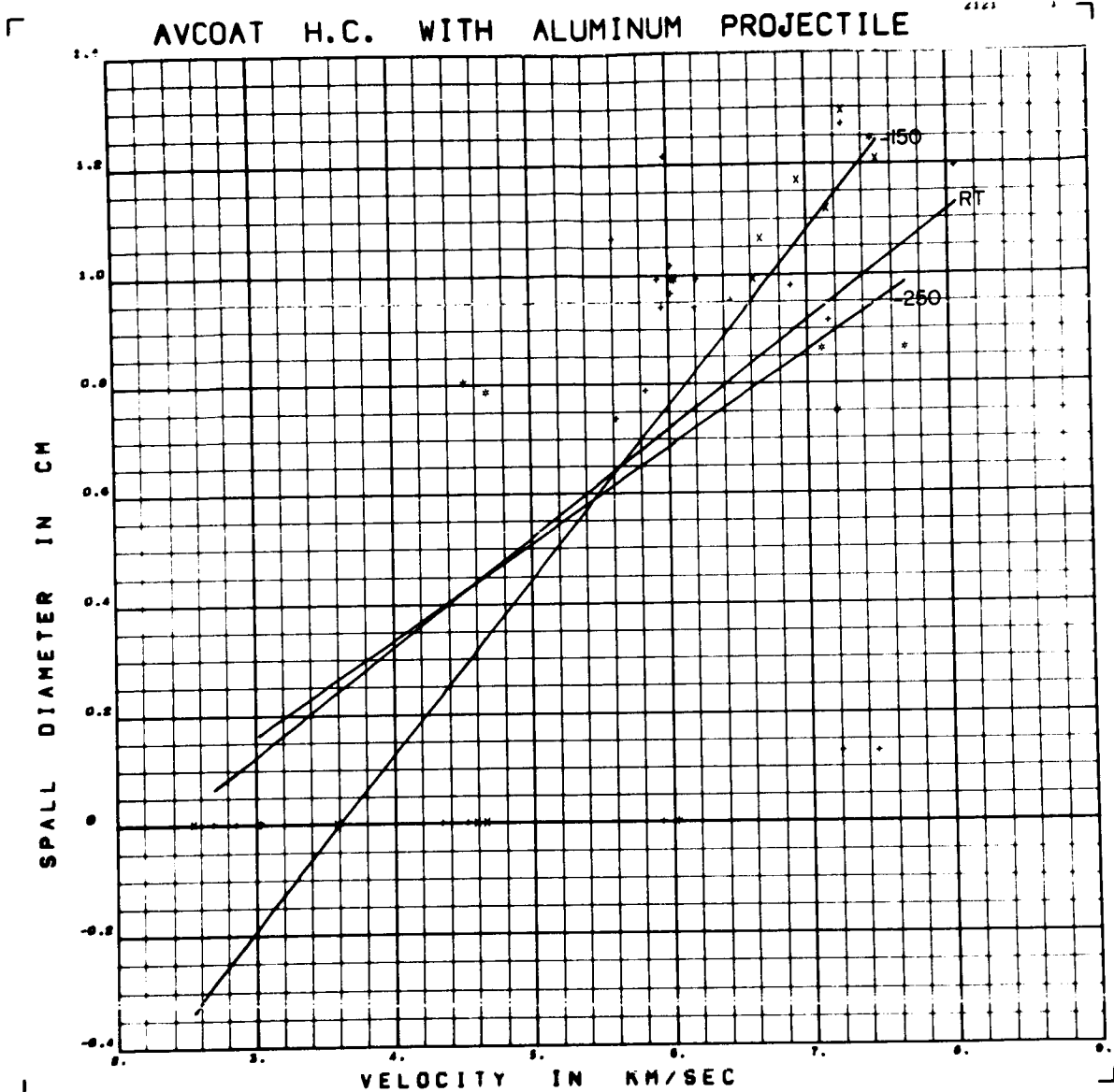


Figure D6 Spall Diameter versus Velocity for Aluminum Projectiles on
Avcoat 5026 HC

Form of Regression: $d_s = (.2306 + .0225ST + .0871CV) V$

RMS Deviation: .334 cm

$-.6605 - .1020ST - .4822CV$

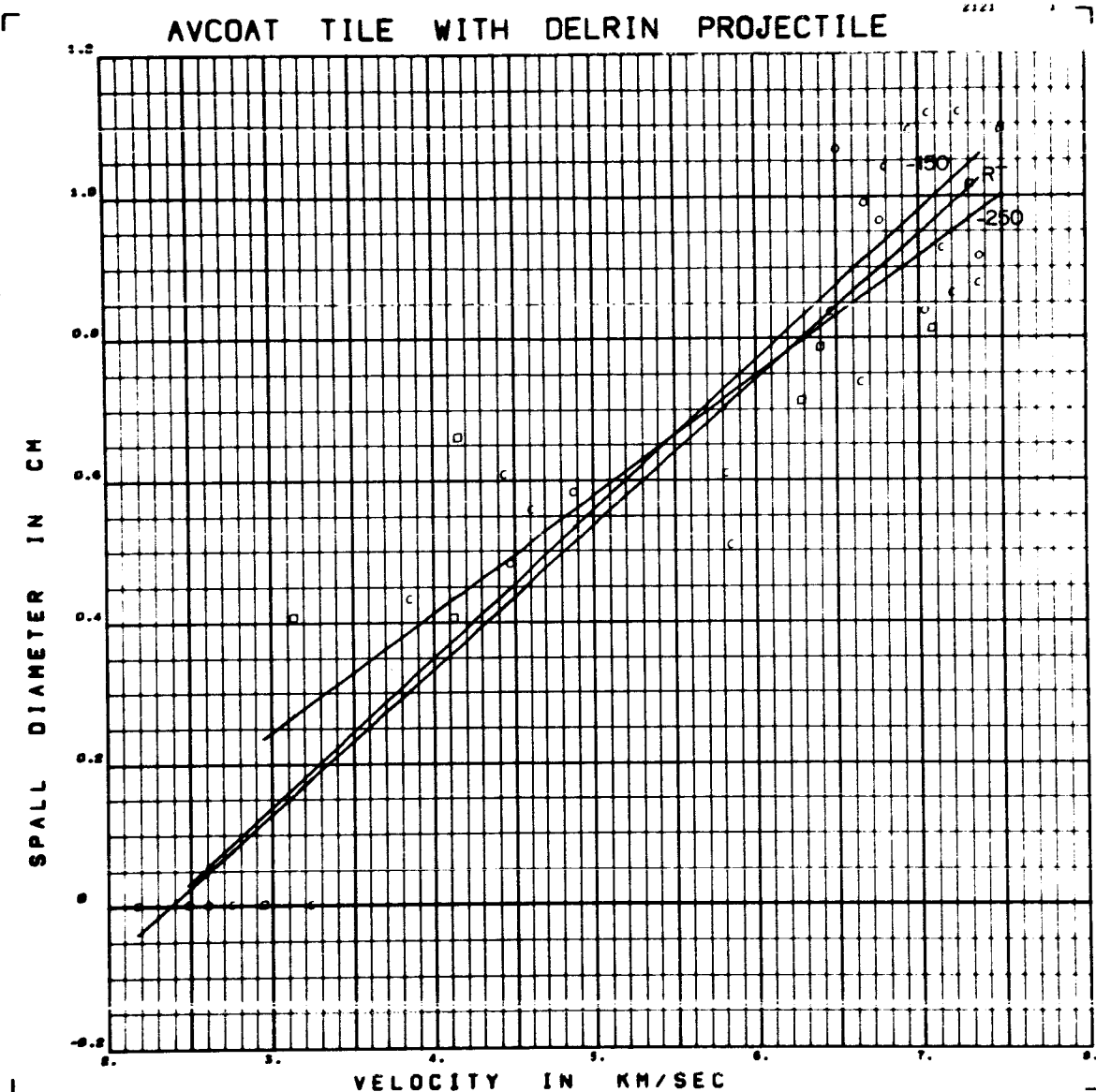


Figure D7 Spall Diameter versus Velocity for Delrin Projectiles on
Avcoat 5026 Tile

Form of Regression: $d_s = (.1946 + .03685T + .0163CV) V$

RMS Deviation: .126

$-.4128 - .22675T - .0815CV$

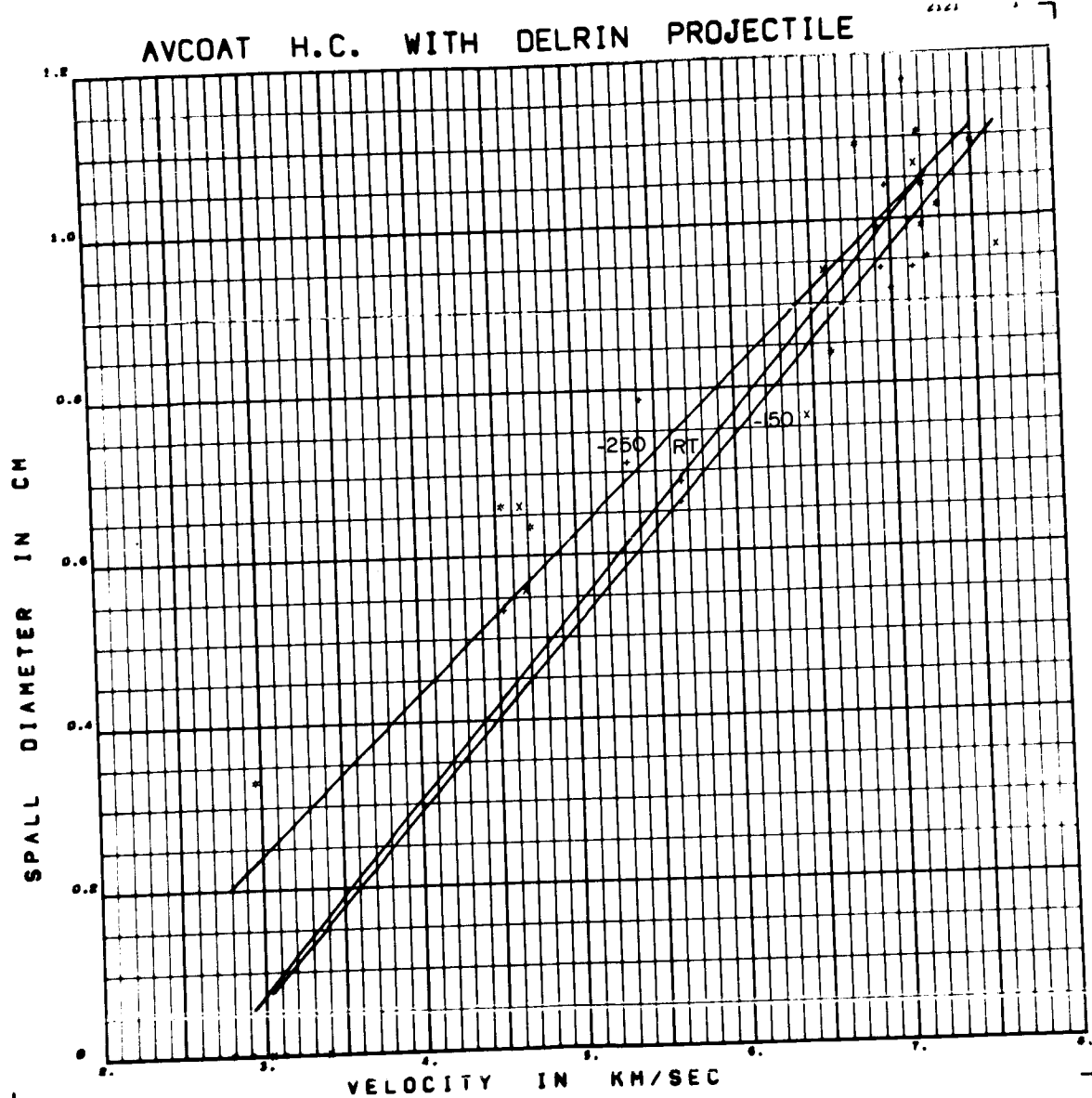


Figure D8 Spall Diameter versus Velocity for Delrin Projectiles on

Avcoat 5026 HC

Form of Regression: $d_s = (.2173 + .0391 + .0084CV) V$

RMS Deviation: .103

$-.5246 \quad -.28445T \quad -.0858CV$

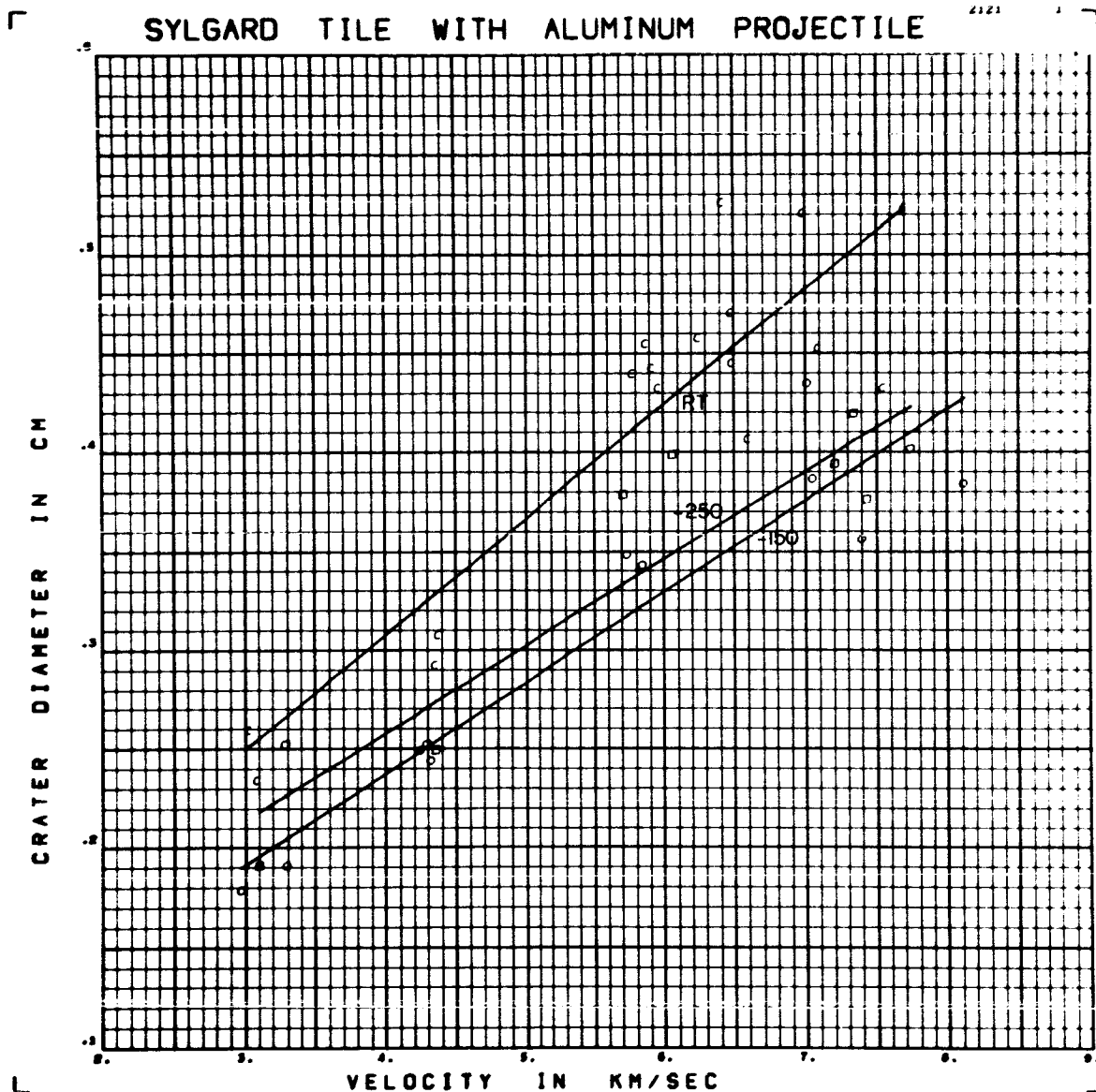


Figure D9 Crater Diameter versus Velocity for Aluminum Projectiles on
Sylgard 325 Tile

Form of Regression: $d = (.0495 + 0.141 ST - 0.0035 CV) V$

RMS Deviation: .034 cm $+ .0697 - .0067 ST - .0164 CV$

SYLGARD H.C. WITH ALUMINUM PROJECTILE

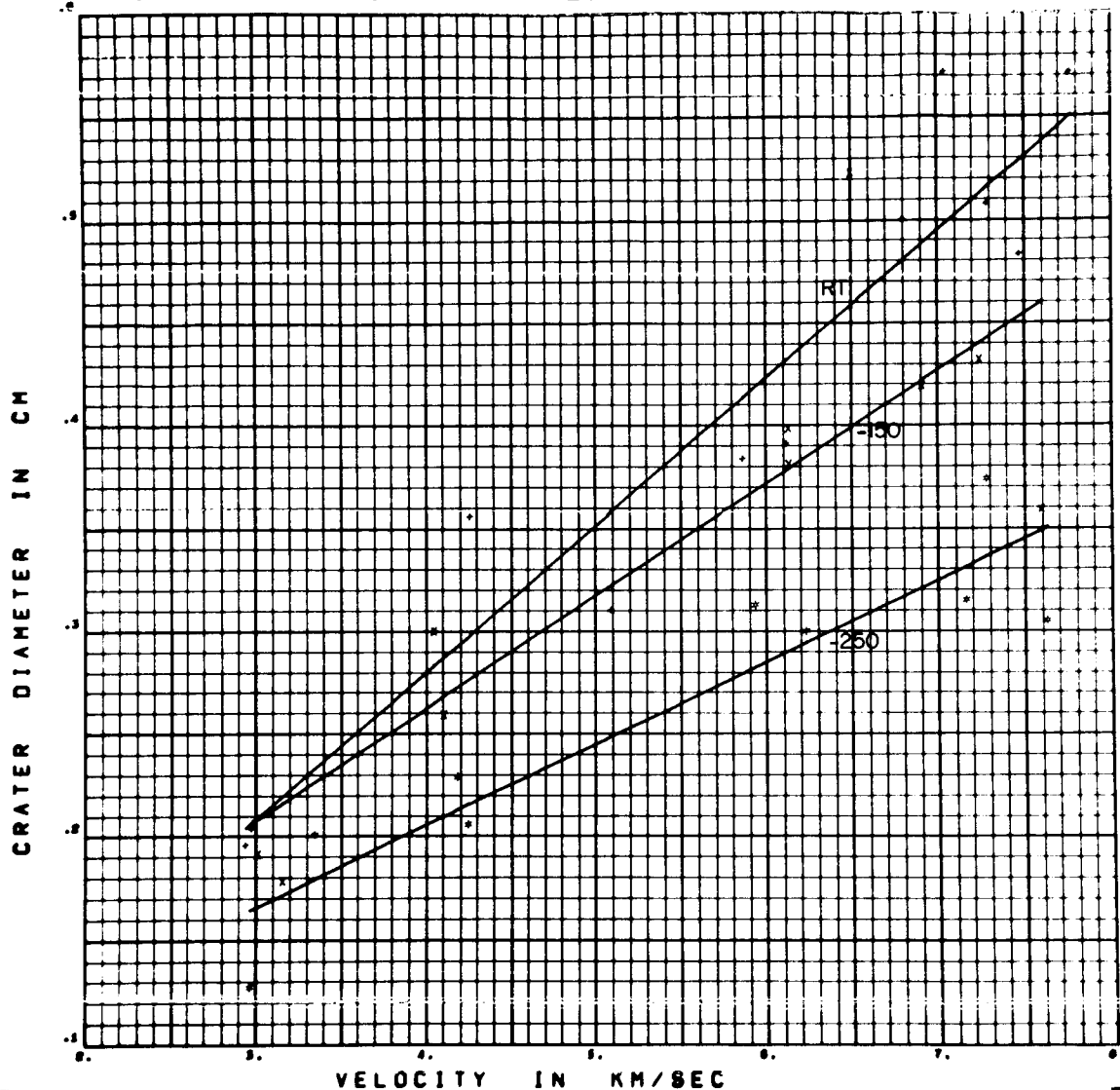


Figure D10 Crater Diameter versus Velocity for Aluminum Projectiles on Sylgard 325 HC

Form of Regression: $d = (.0555 + .03195T - .0006CV)V$

RMS Deviation: .042 cm $+ .0275 - .05335T + .0156CV$

A graph showing the relationship between Crater Diameter (in cm) on the Y-axis and Velocity (in km/sec) on the X-axis. The X-axis ranges from 3.0 to 8.0 km/sec, and the Y-axis ranges from 0.5 to 3.5 cm. Three curves are plotted, representing different materials: -150, -250, and RT. The -150 curve is the uppermost, followed by the -250 curve, and then the RT curve. Data points are plotted as open circles and squares, mostly following the curves. The graph is labeled 'STEELS AND TITANIUM' at the top.

Form of Regression: $d = (.0449 + 1.0166ST - .0078CV) V$

- 189 -

SYLGARD H.C. WITH DELRIN PROJECTILE

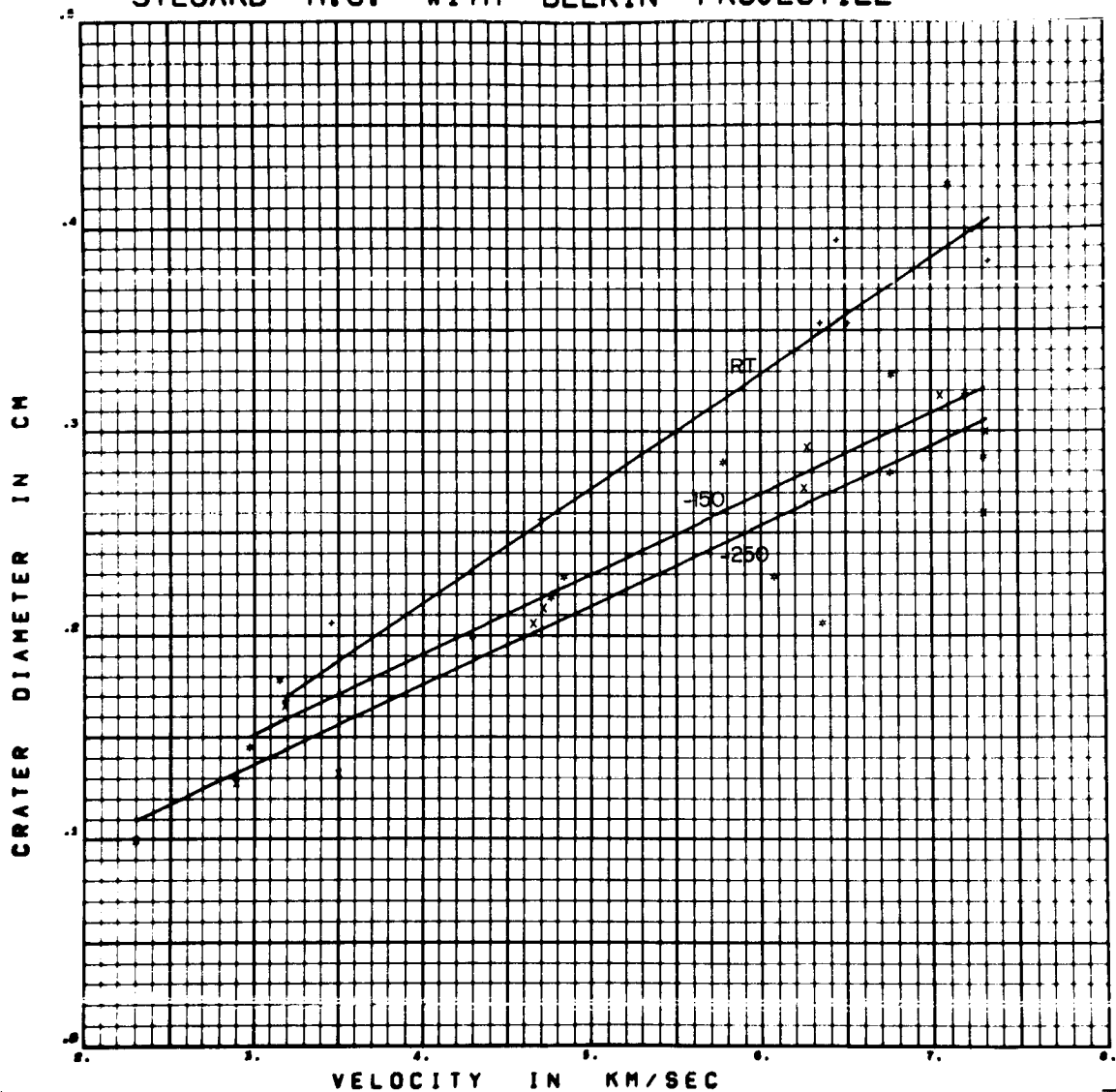


Figure D12 Crater Diameter versus Velocity for Delrin Projectiles on
Sylgard 325 HC

Form of Regression: $d = (.0451 + .0171ST - .0051CV) V$

RMS Deviation: .032 cm $+ .0140 - .0435ST + .0052CV$

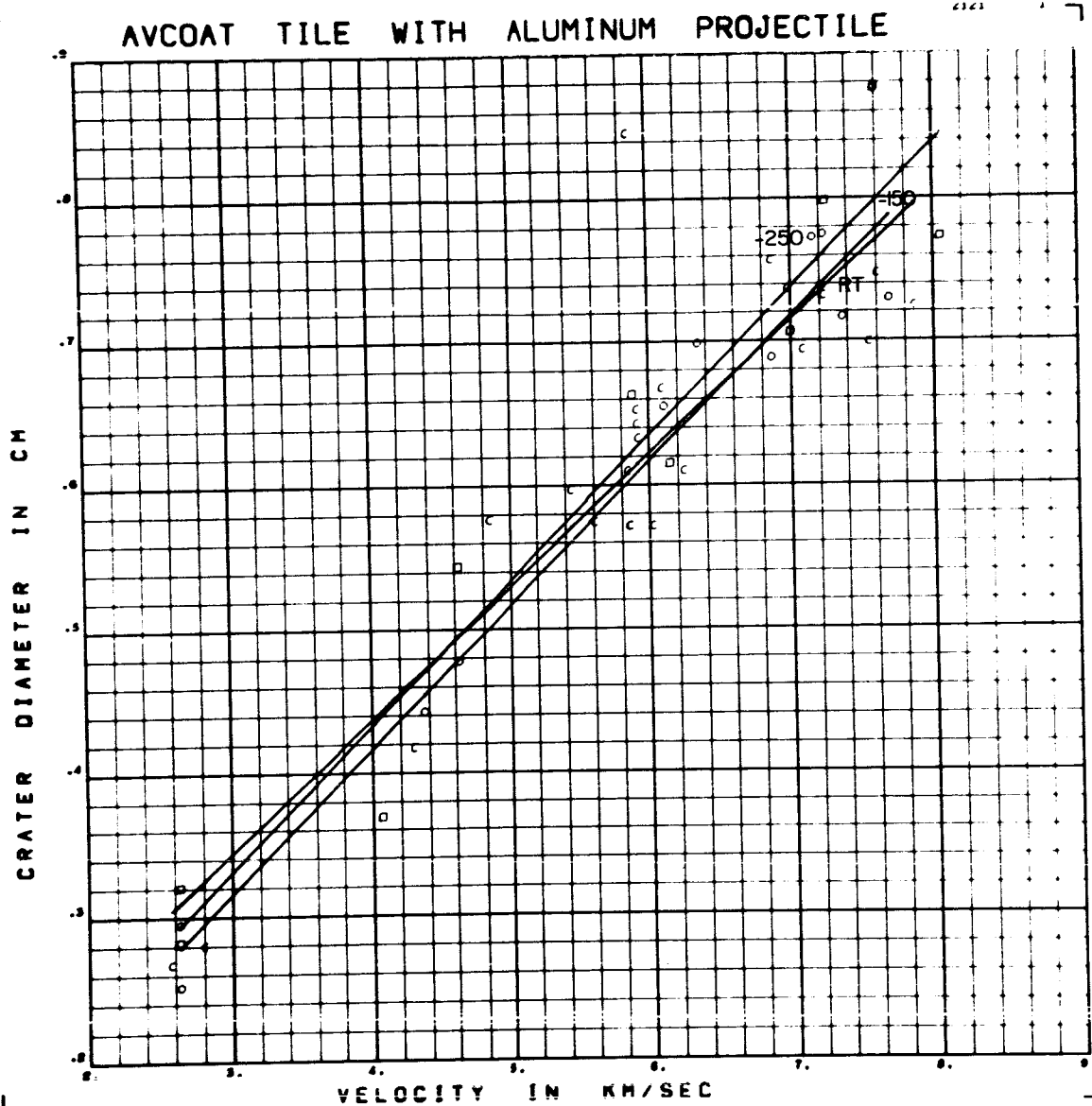


Figure D13 Crater Diameter versus Velocity for Aluminum Projectiles on

Avcoat 5026 Tile

Form of Regression: $d = (.0984 - .0089 ST + .0022 CV) V$

RMS Deviation: $.054 \text{ cm}$ $+ .0354 + .0405 ST - .0210 CV$

AVCOAT H.C. WITH ALUMINUM PROJECTILE

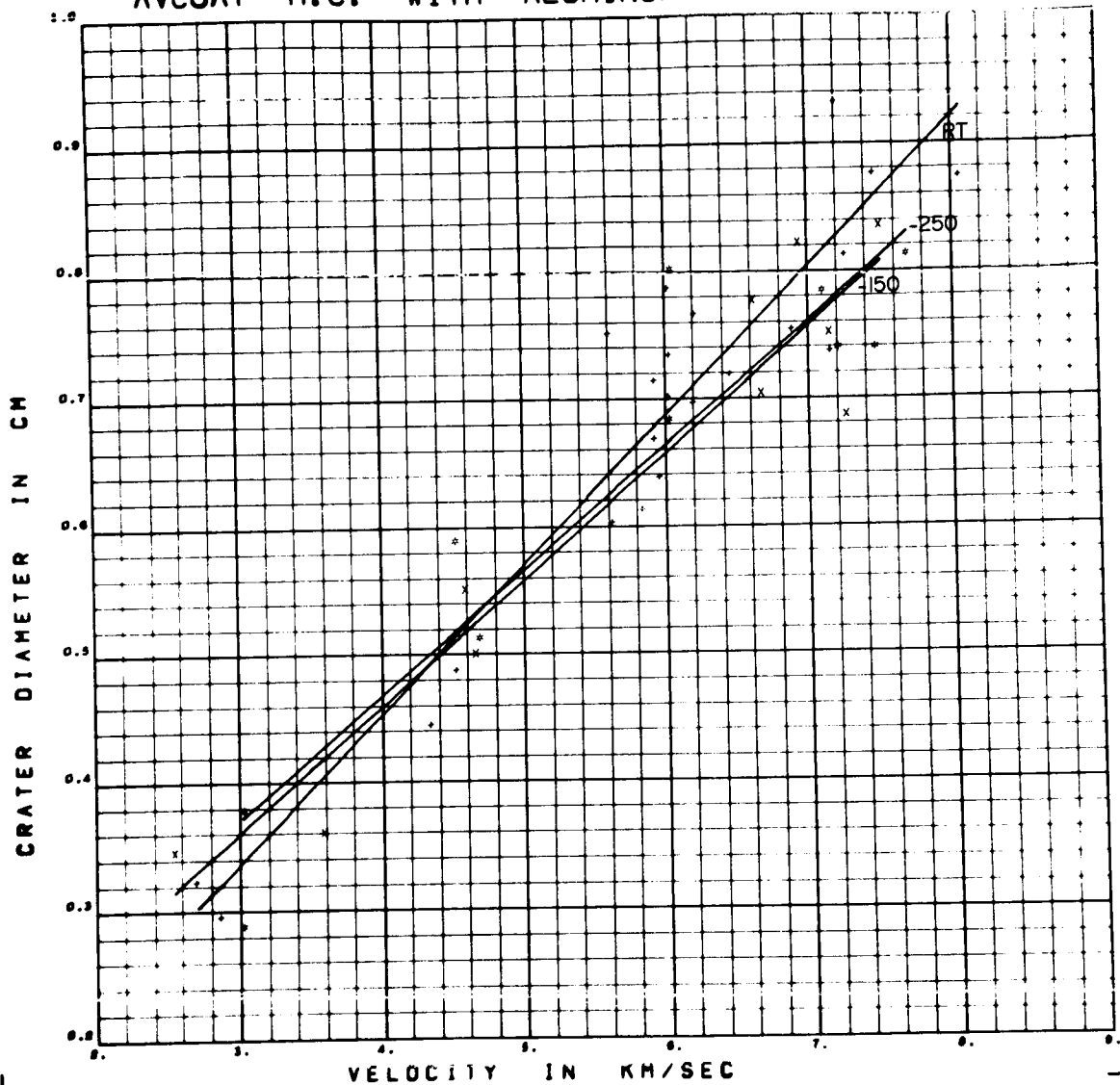


Figure D14 Crater Diameter versus Velocity for Aluminum Projectiles on

Avcoat 5026 HC

Form of Regression: $d = (.1047 + .0187ST - .0054CV) V$

RMS Deviation: .056 cm

+ .0418 - .0889ST + .0205 CV

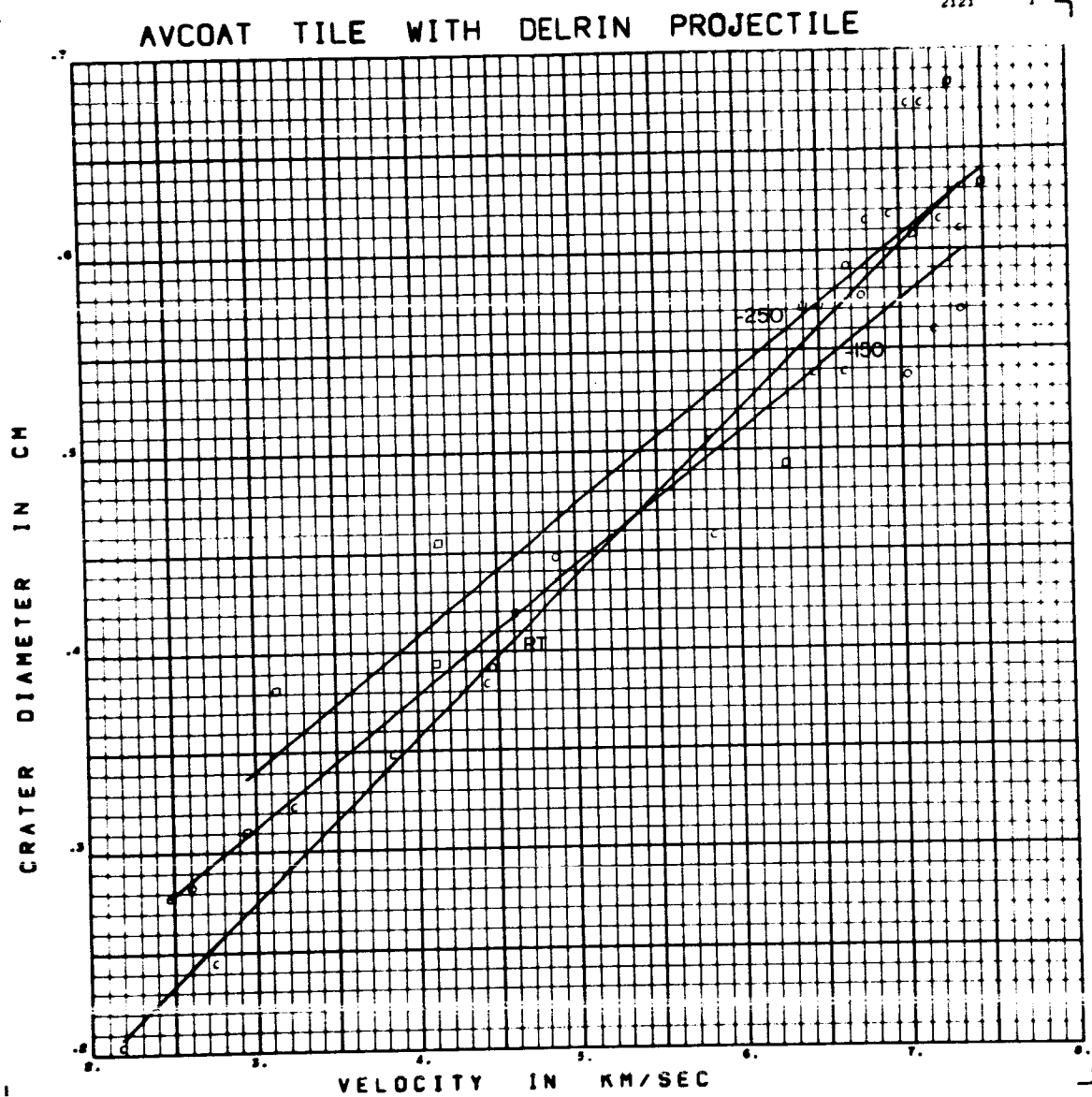


Figure D15 Crater Diameter versus Velocity for Delrin Projectiles on

Avcoat 5026 Tile

Form of Regression: $d = (.0715 + .0152 ST - .0057 CV) V$

RMS Deviation: .032 cm $+ .0945 - .1114 ST + .0200 CV$

AVCOAT H.C. WITH DELRIN PROJECTILE

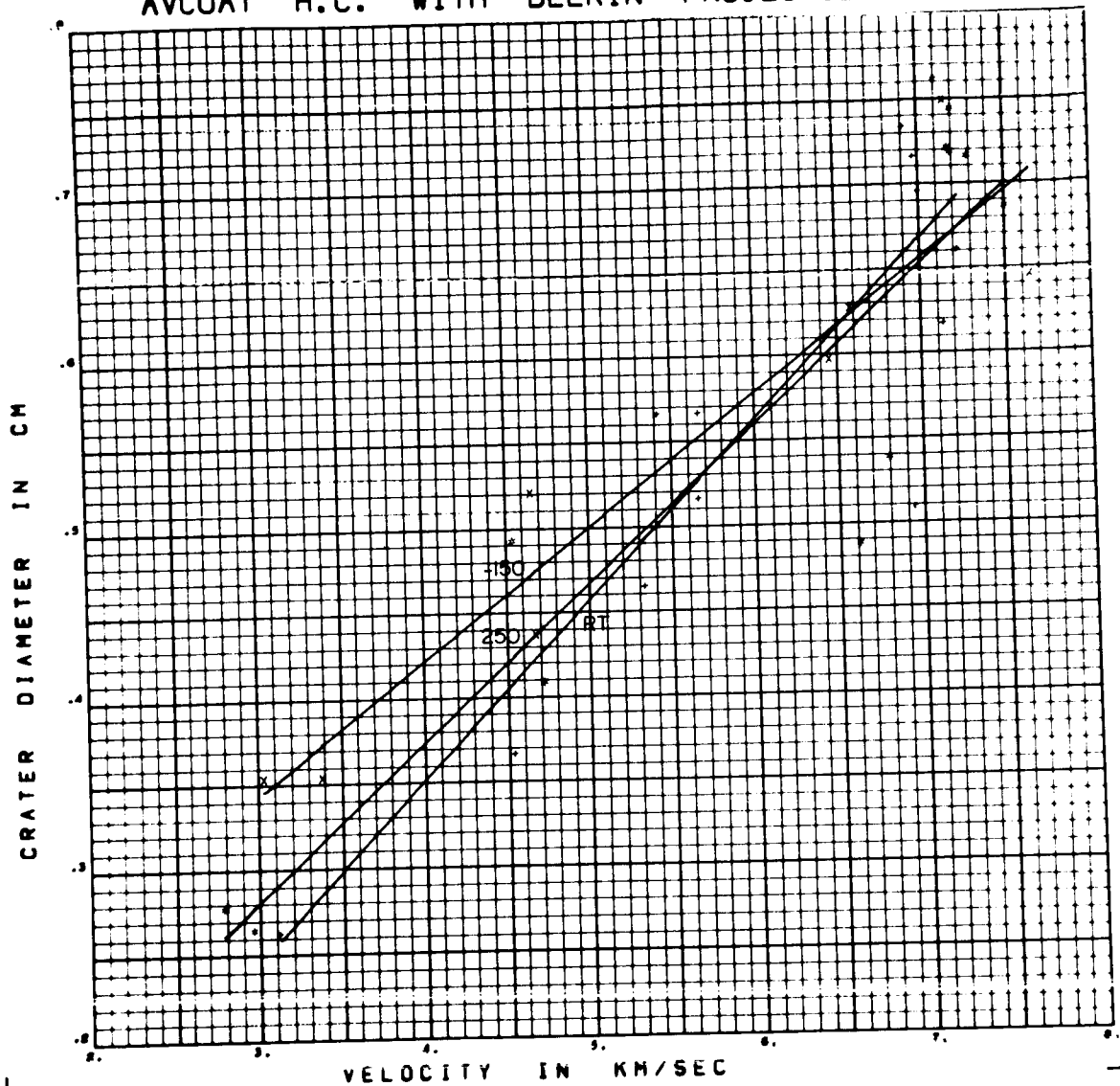


Figure D16 Crater Diameter versus Velocity for Delrin Projectiles on

Avcoat 5026 HC

Form of Regression: $d = (0.925 + 0.125 ST - 0.140 CV) V$

RMS Deviation: .060 cm $+ .0127 - .0723 ST + .0946 CV$

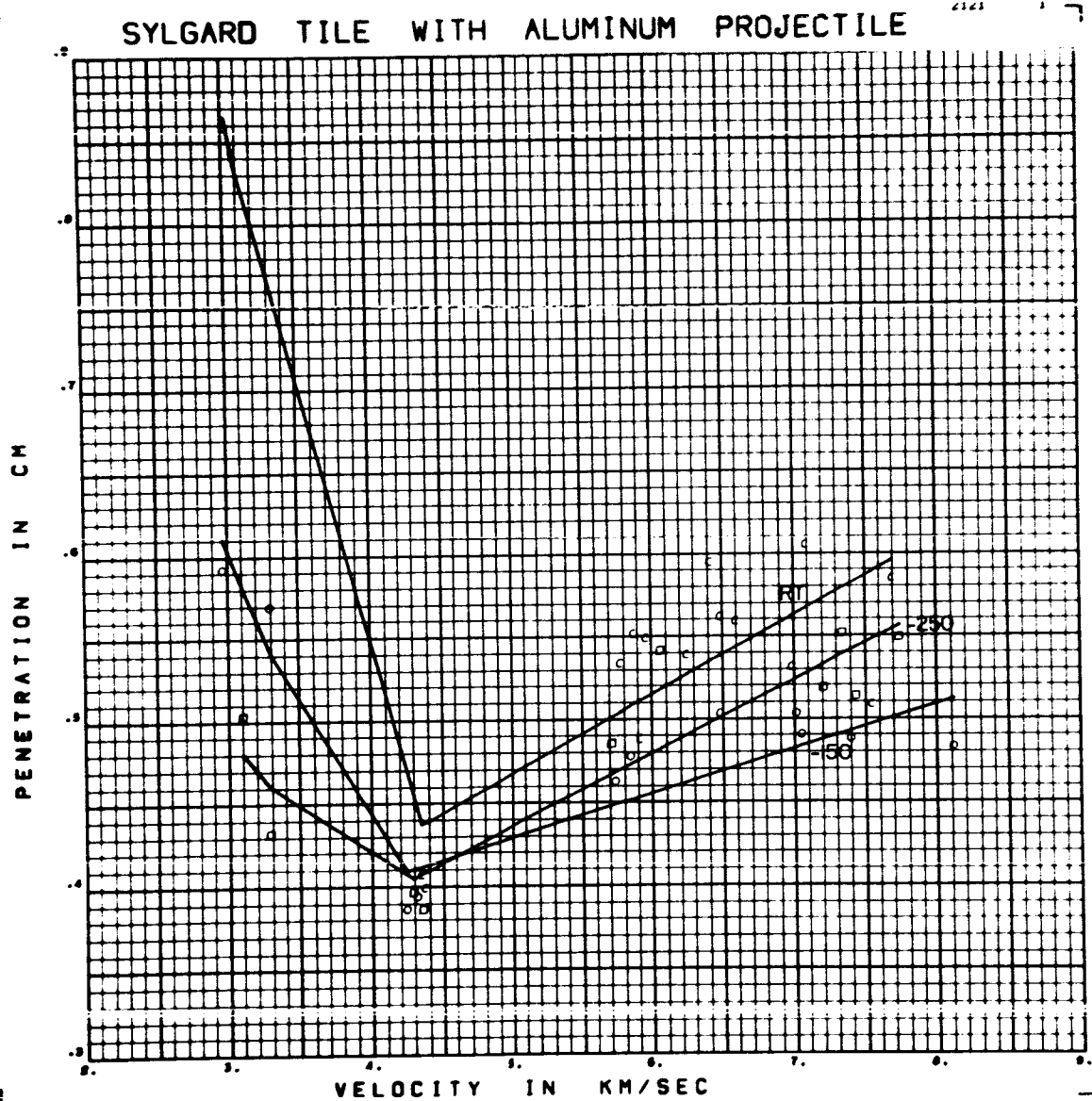


Figure D17 Penetration versus Velocity for Aluminum Projectiles on
Sylgard 325 Tile

Form of Regression: $p = (.0394 + .0032ST - .0127CV) \sqrt{V}$
 RMS Deviation: .030 cm $+ .2471 + .0166 ST + .0485 CV$

SYLGARD H.C. WITH ALUMINUM PROJECTILE

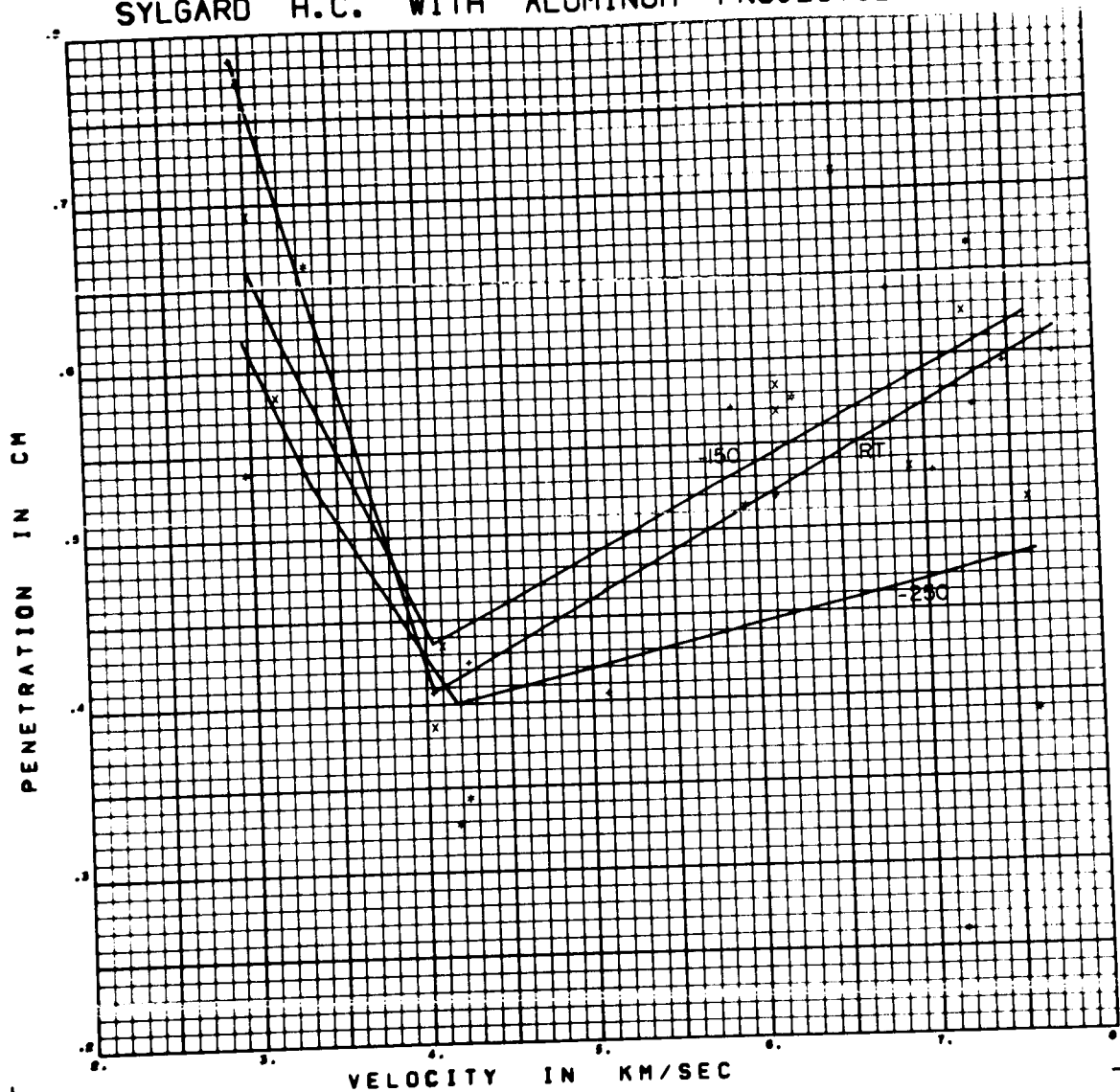


Figure D18 Penetration versus Velocity for Aluminum Projectiles on

Sylgard 325 HC

Form of Regression: $P = (.0443 + .0316 ST + .0085 CV) V$

RMS Deviation: .083 cm + .2342 - .1175 ST - .0113 CV

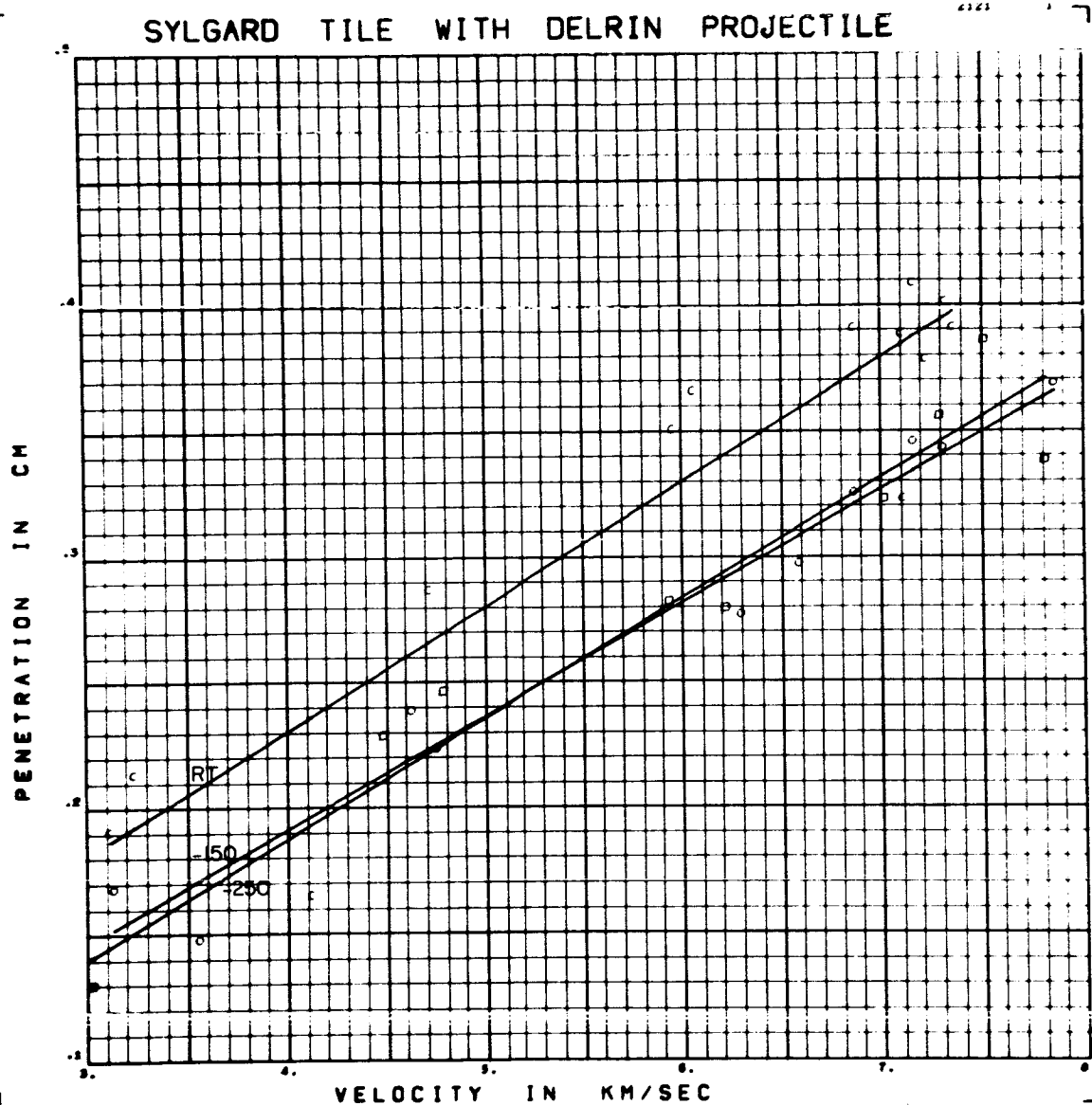
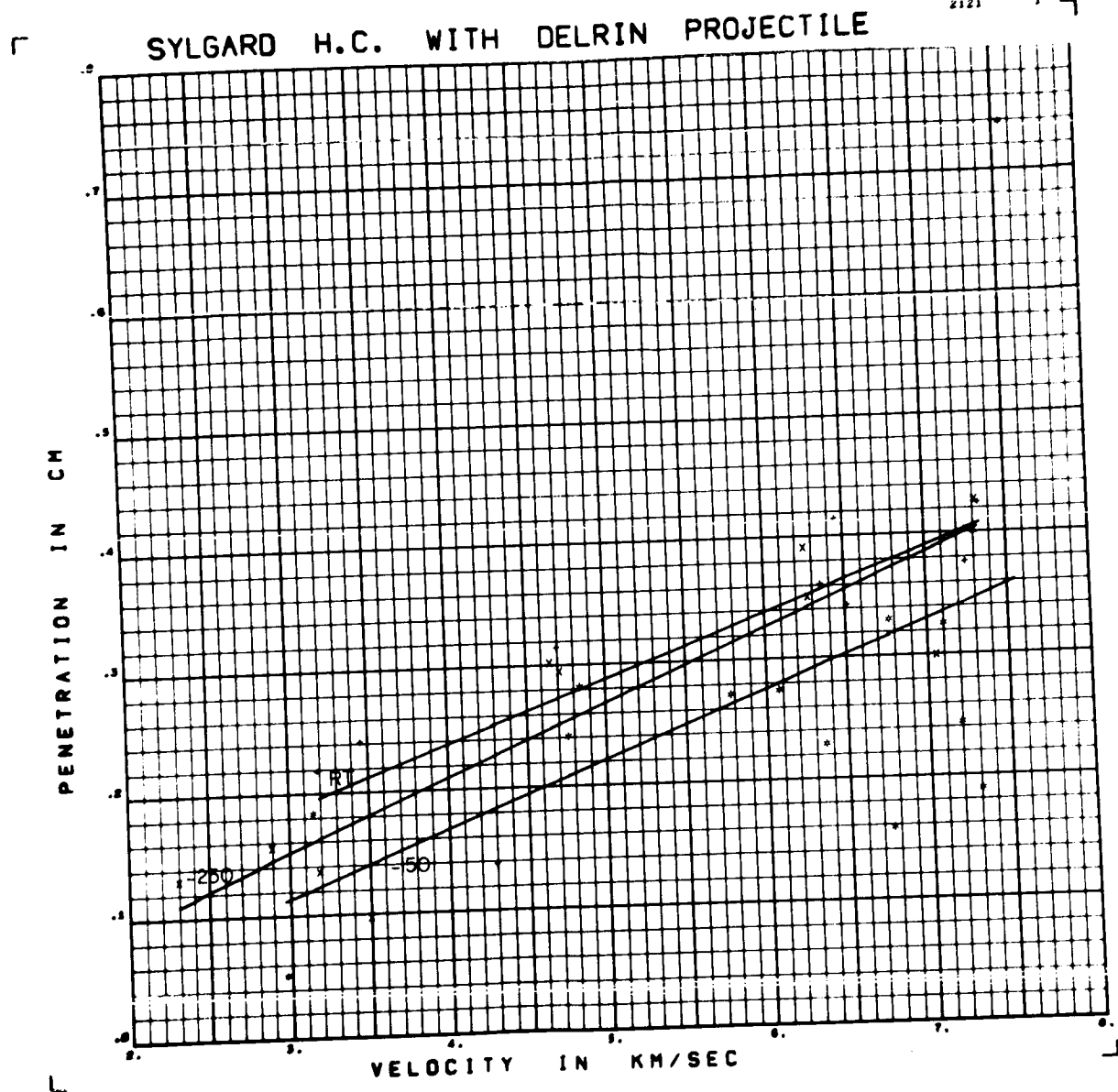


Figure D19 Penetration versus Velocity for Delrin Projectiles on
Sylgard 325 Tile

Form of Regression: $p = (.0476 + .0018 ST - .0024 CV) V$

RMS Deviation: .023 cm $+ .0127 + .0357 ST - .0025 CV$



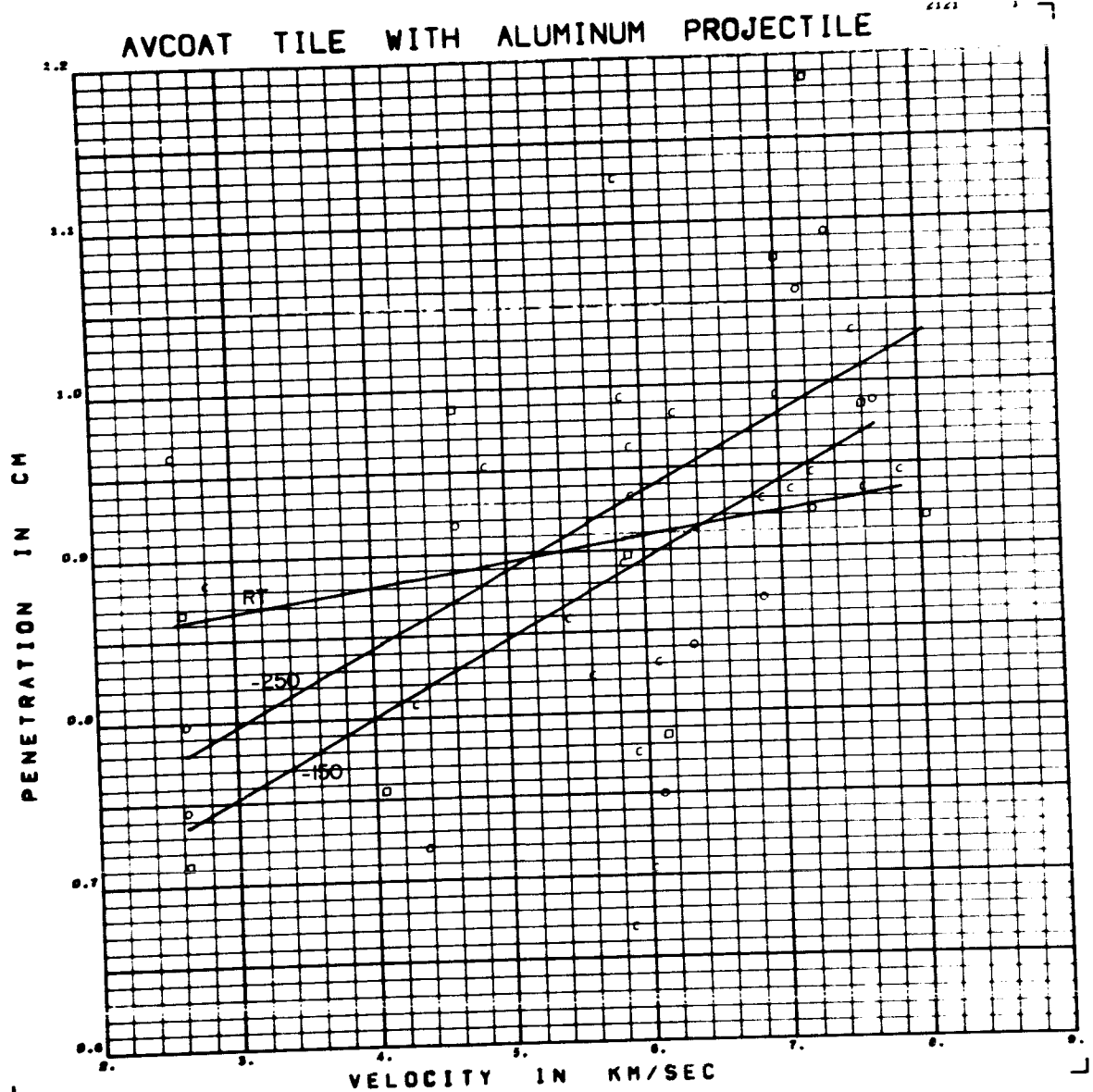


Figure D21 Penetration versus Velocity for Aluminum Projectiles on

Avcoat 5026 Tile

Form of Regression: $p = (.0358 - .0325 ST + .0113 CV) V$
 $+ .6979 + .1673 ST - .0864 CV$

RMS Deviation: .101 cm

AVCOAT H.C. WITH ALUMINUM PROJECTILE

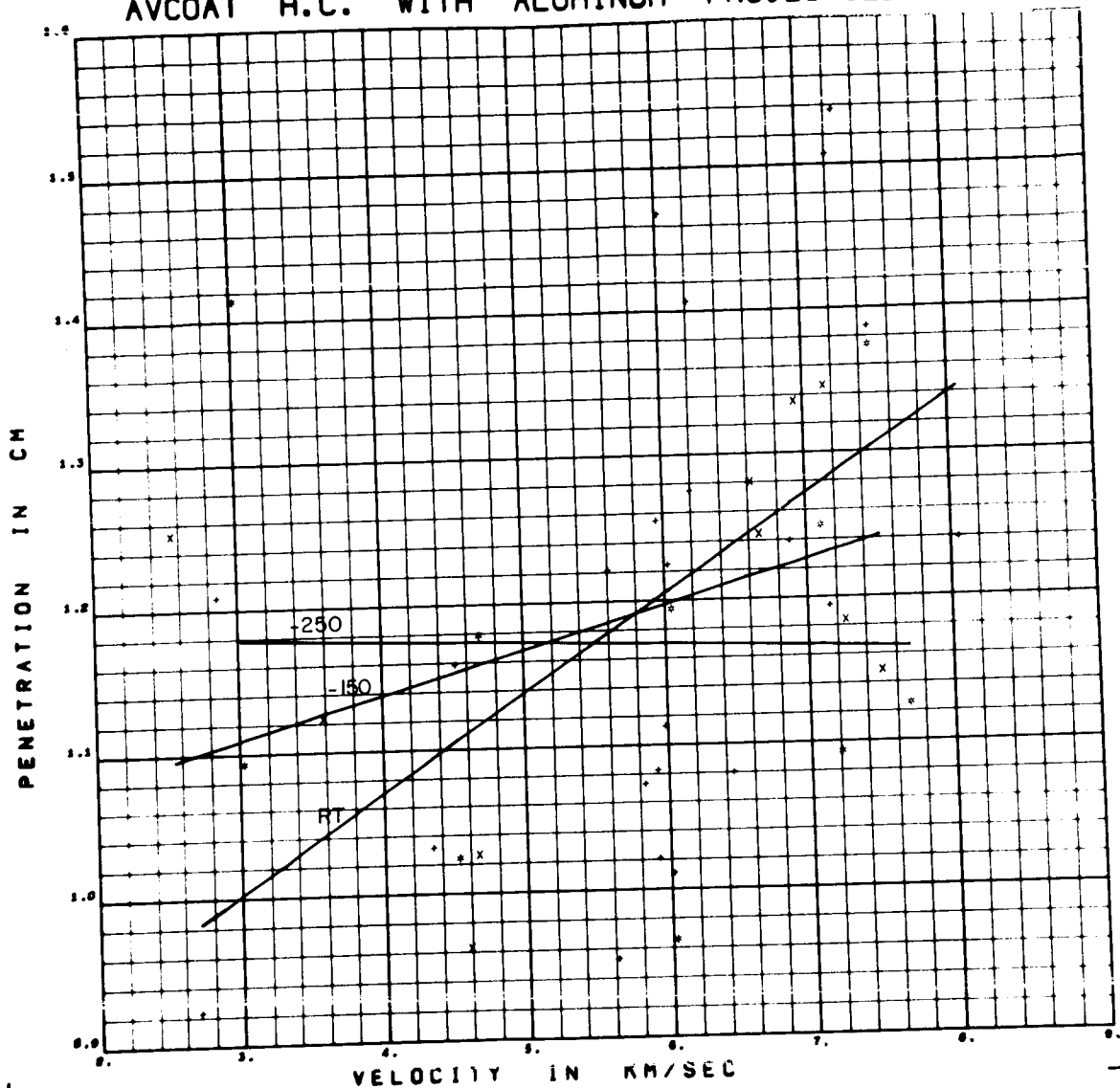


Figure D22 Penetration versus Velocity for Aluminum Projectiles on

Avcoat 5026 HC

Form of Regression: $p = (.0314 + .0701 ST - .0017 CV) V$

RMS Deviation: .138 cm $+ .0100 - .3852 ST + .0170 CV$

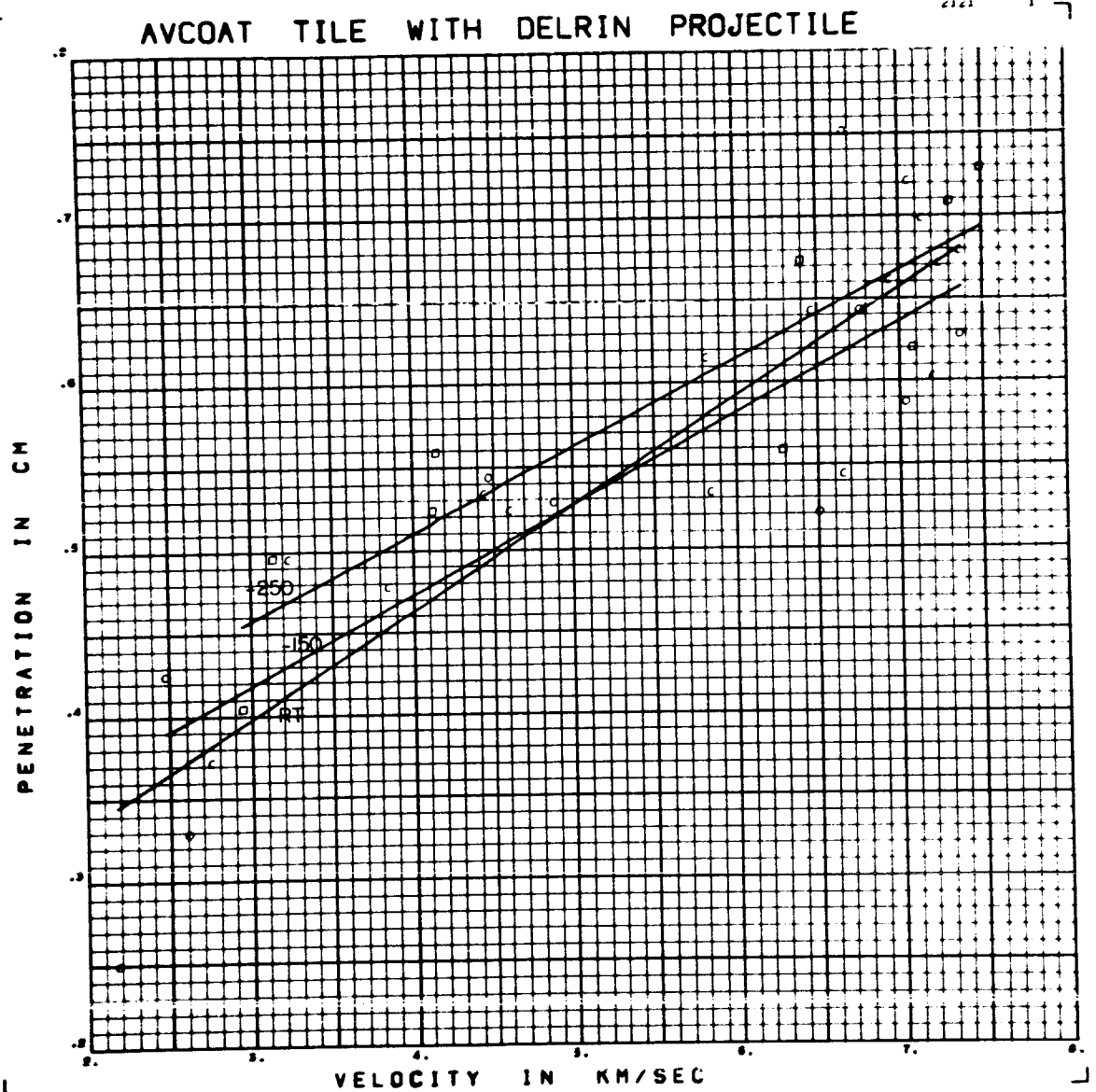


Figure D23 Penetration versus Velocity for Delrin Projectiles on

Avcoat 5026 Tile

Form of Regression: $p = (.0574 + .0121 ST - .0027 CV) V$

RMS Deviation: .053 cm $+ .2525 - .0955 ST + .0016 CV$

AVCOAT H.C. WITH DELRIN PROJECTILE

4163

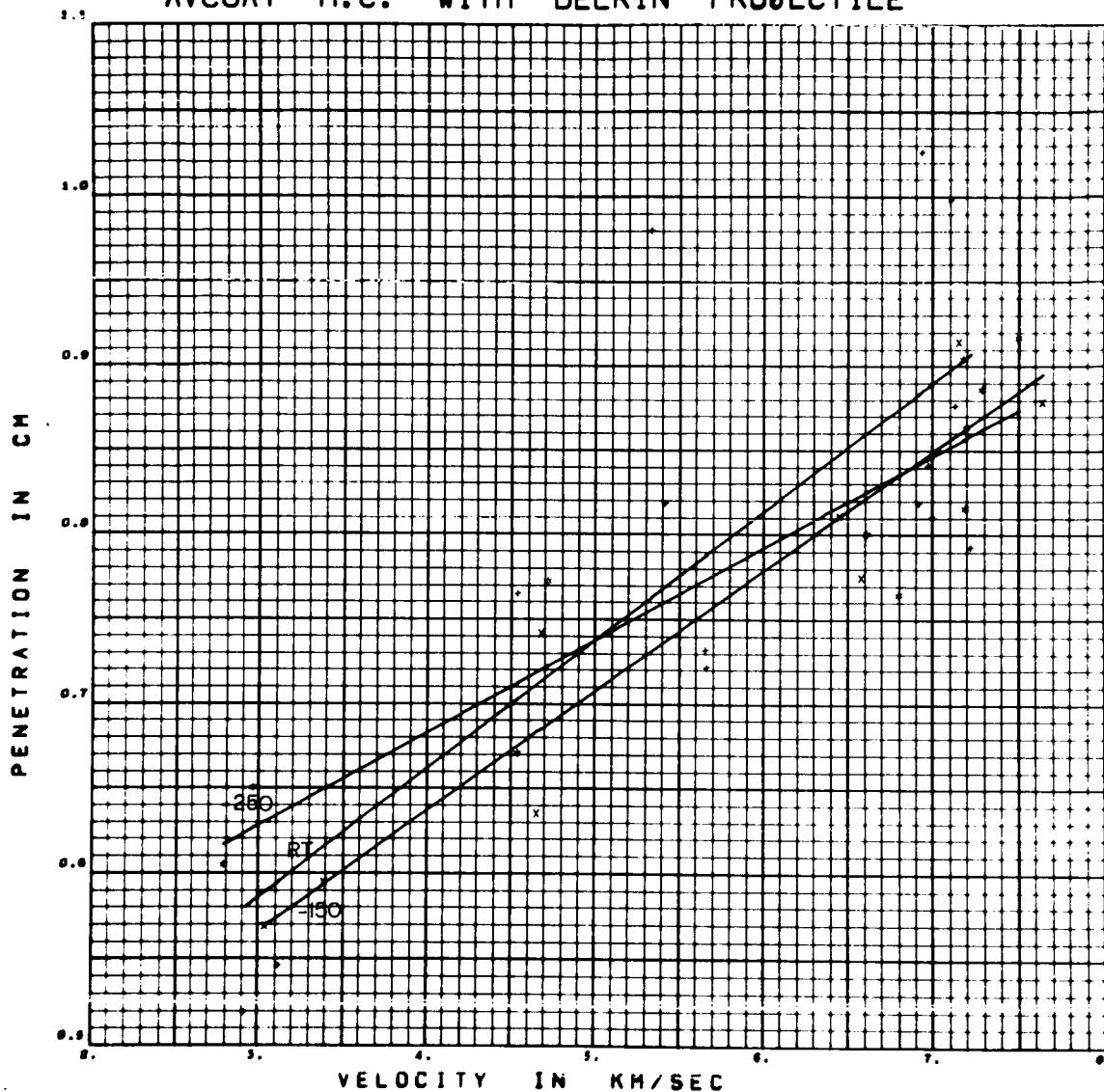


Figure D24 Penetration versus Velocity for Delrin Projectiles on

Avcoat 5026 HC

Form of Regression: $p = (.0671 + .0214 ST + .0036 CV) V$

RMS Deviation: $.069 \text{ cm} + .3926 - .1063 ST - .0378 CV$

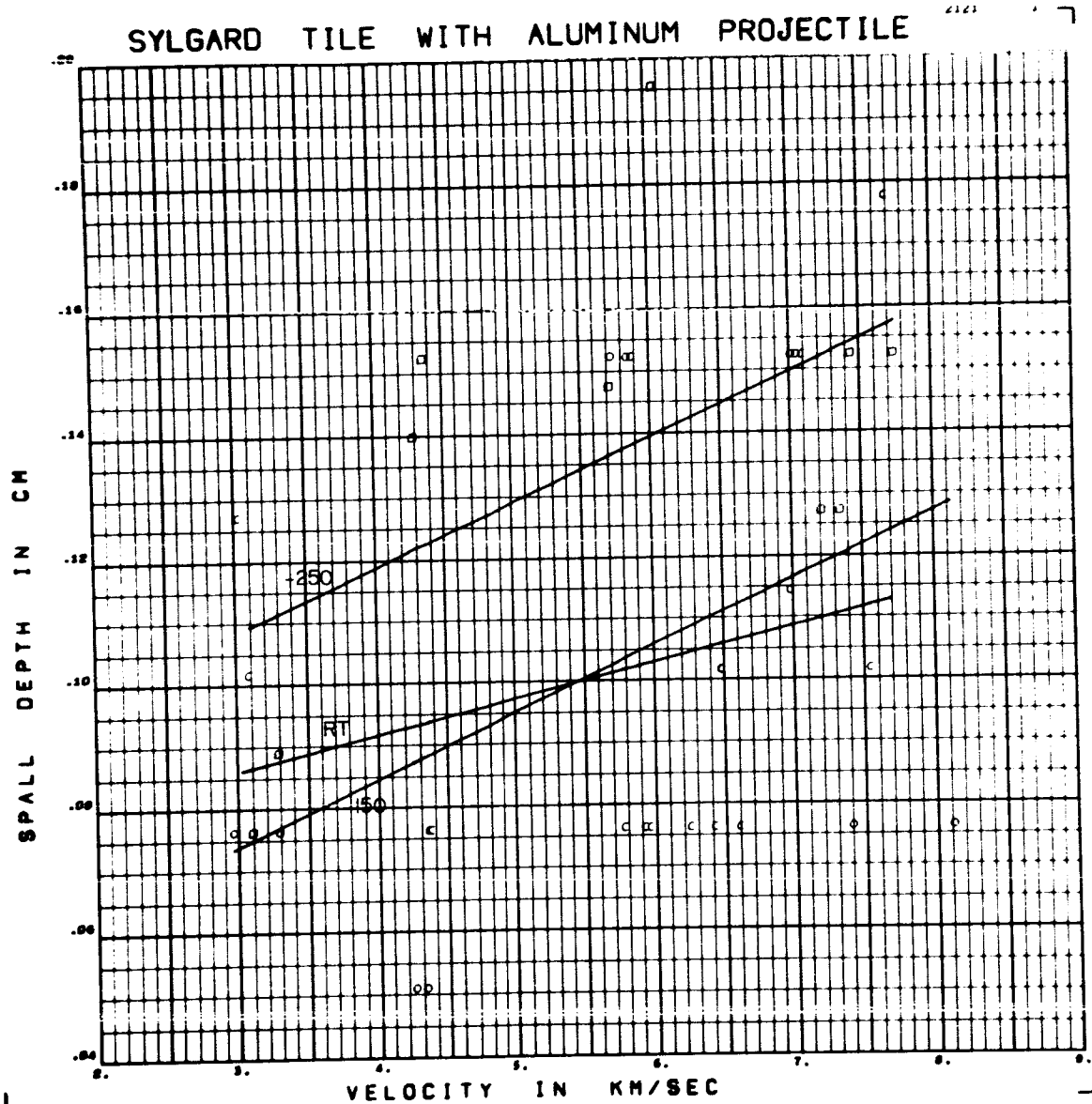


Figure D25 Spall Depth versus Velocity for Aluminum Projectiles on
Sylgard 325 Tile

Form of Regression: $p_s = (.0892 - .0047 ST + .0018 CV) V$
 RMS Deviation: .032 cm $+ .0626 - .0084 ST - .0208 CV$

SYLGARD H.C. WITH ALUMINUM PROJECTILE

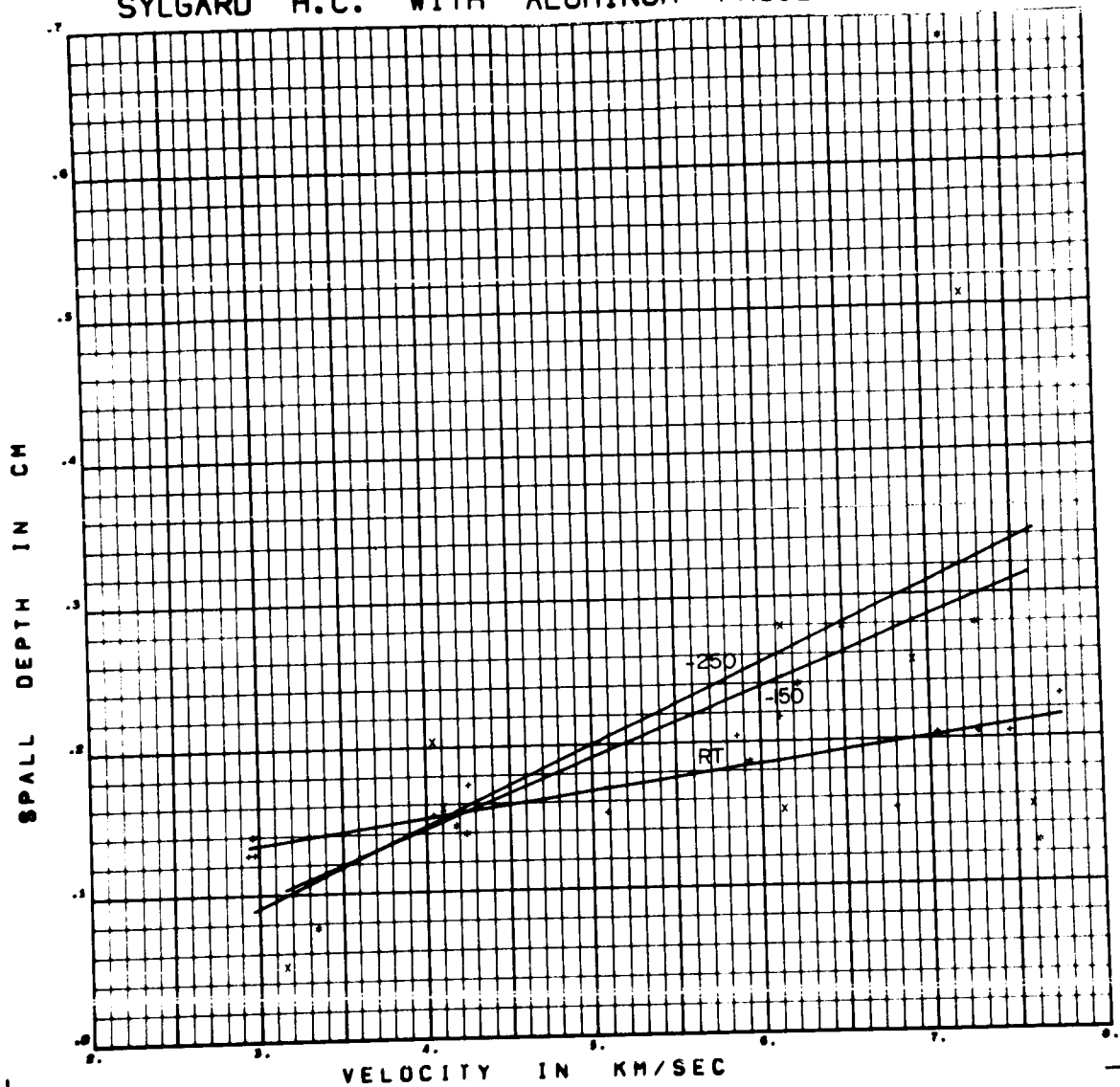


Figure D26 Spall Depth versus Velocity for Aluminum Projectiles on
Sylgard 325 HC

Form of Regression: $P_s = (.0396 - .0378 ST + .0078 CV) V$

RMS Deviation: .099 cm -.0120 +.1565 ST -.0345 CV

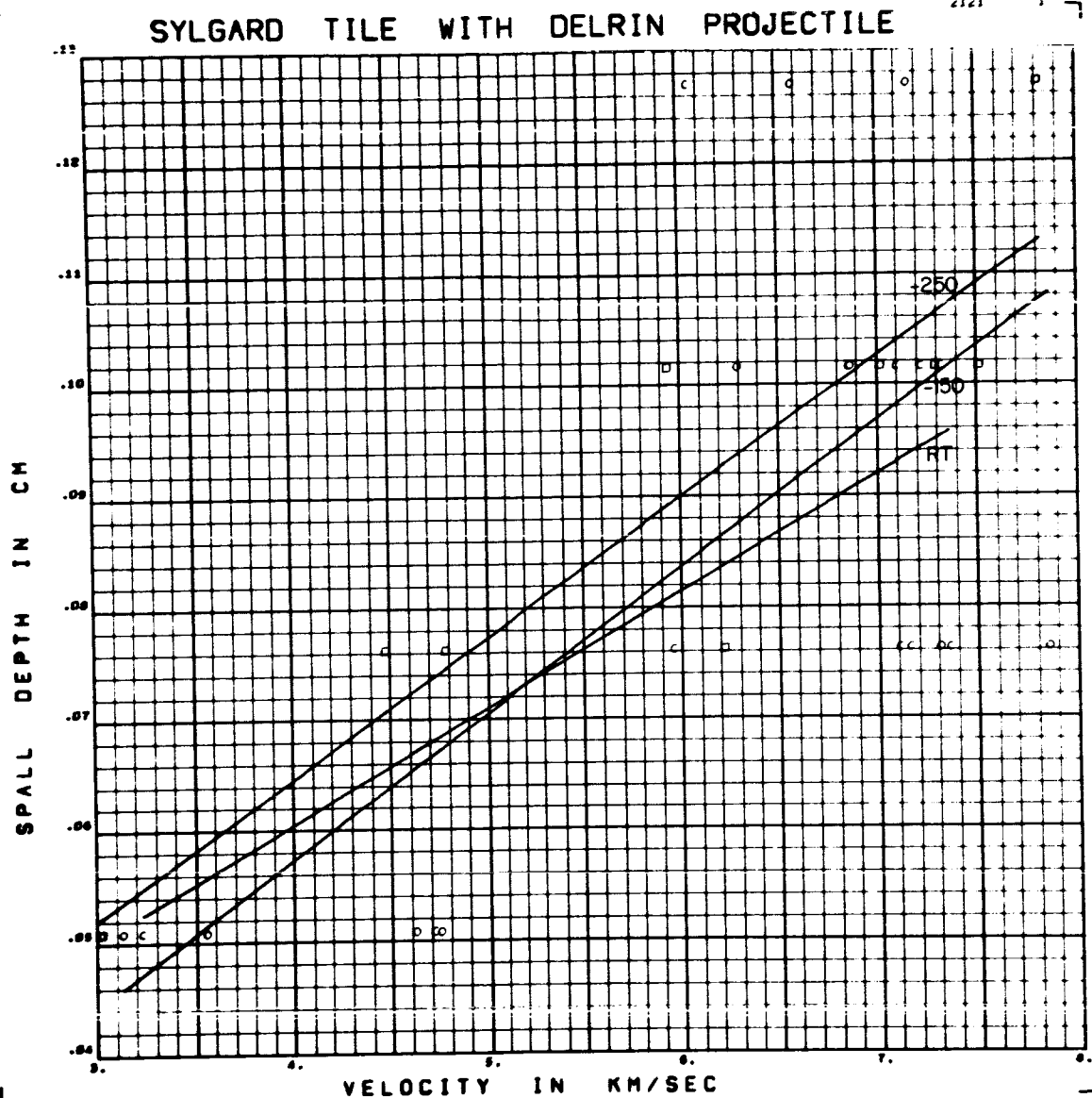


Figure D27 Spall Depth versus Velocity for Delrin Projectiles on
Sylgard 325 Tile

Form of Regression: $p_s = (.0121 - .0022 ST + .0106 CV) V$

RMS Deviation: .017 cm $+ .0124 + .0046 ST - .0077 CV$

SYLGARD H.C. WITH DELRIN PROJECTILE

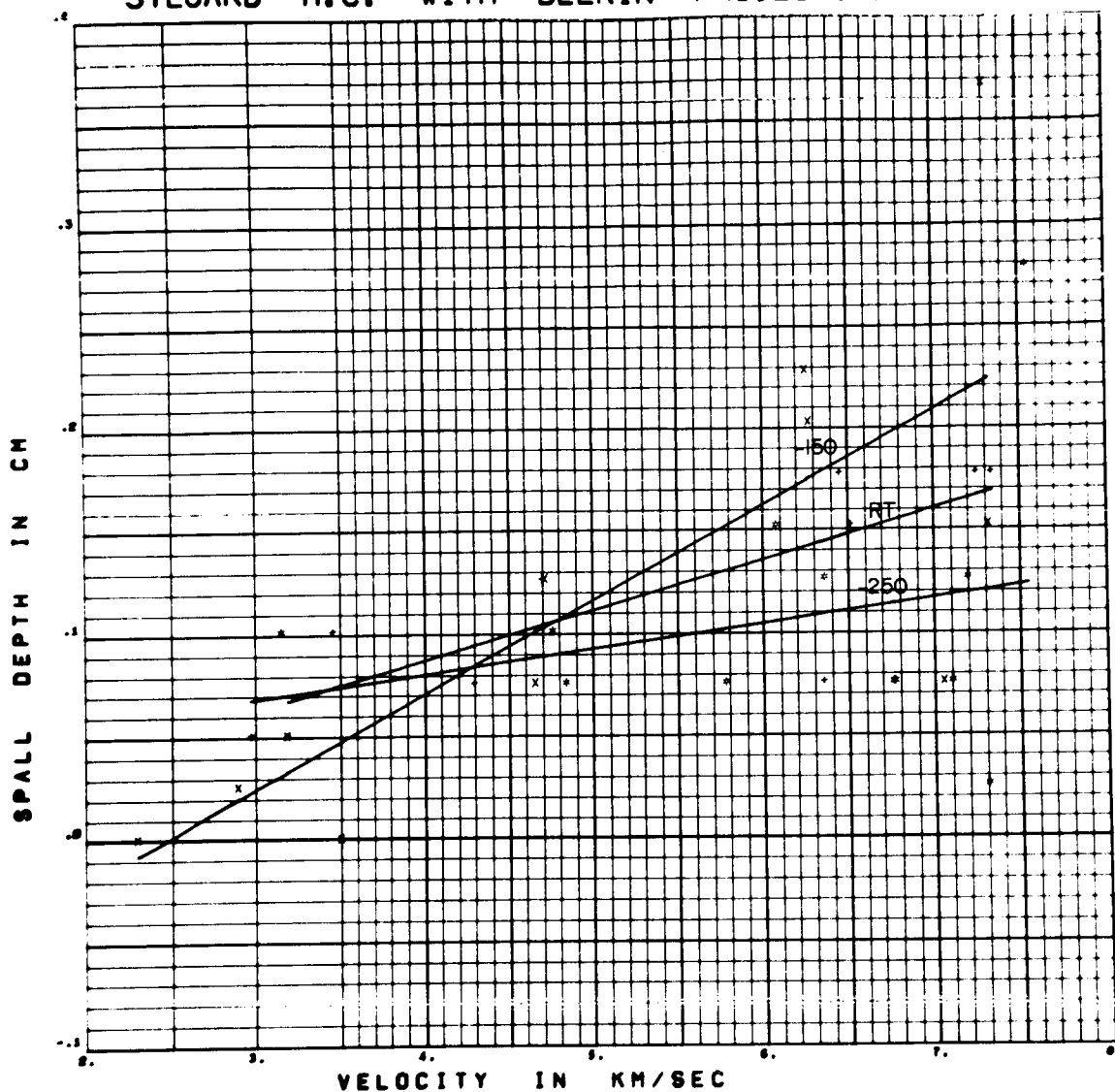


Figure D28 Spall Depth versus Velocity for Delrin Projectiles on

Sylgard 325 HC

Form of Regression: $p_s = (.0275 + .0121 ST + .0186 CV) V$

RMS Deviation: .057 cm $-.0305 - .0413 ST - .0829 CV$

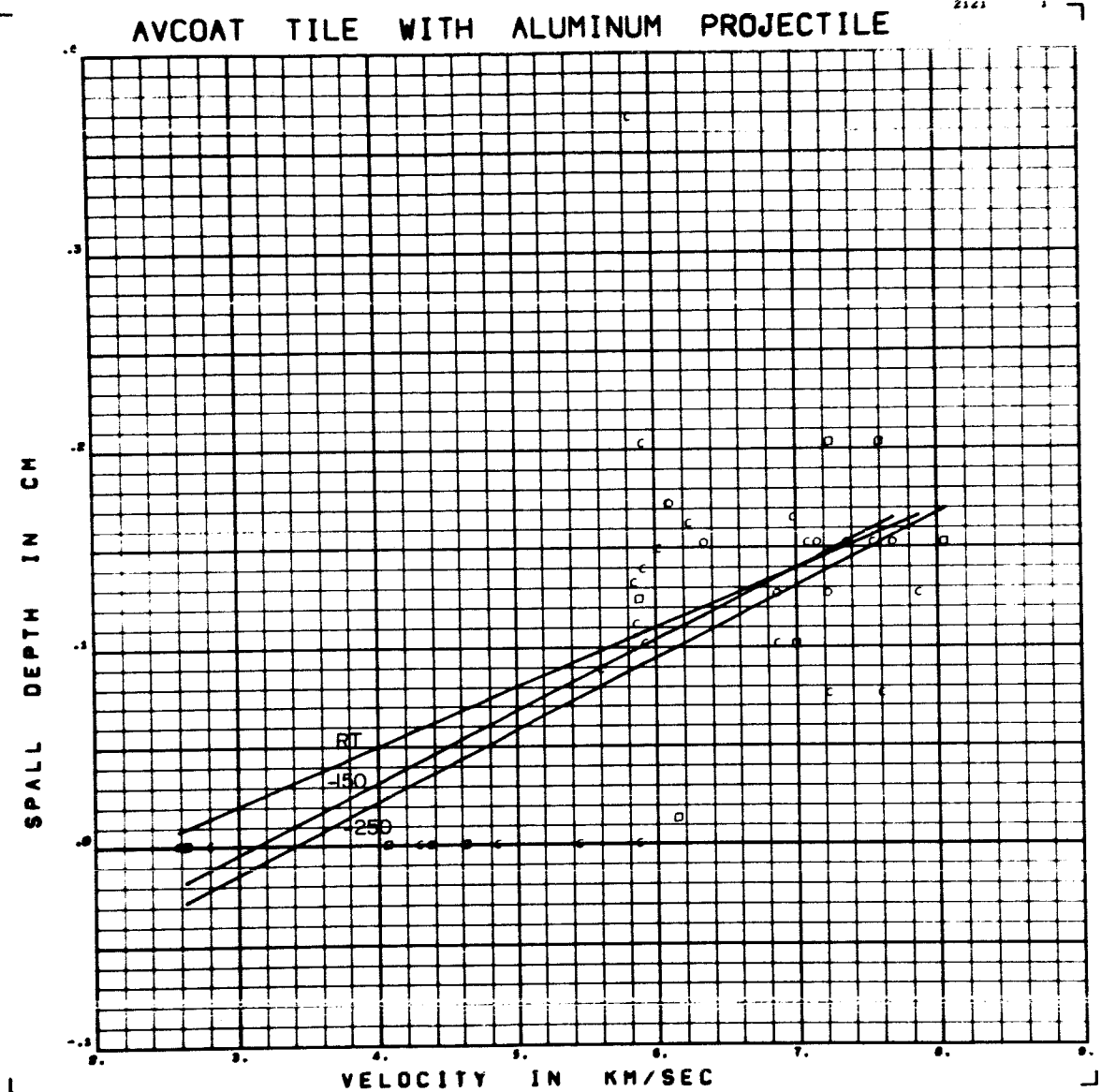


Figure D29 Spall Depth versus Velocity for Aluminum Projectiles on
Avcoat 5026 Tile

Form of Regression: $p_s = (.0341 - .0064 ST + .0020 CV)$

RMS Deviation: .062 cm $-.1017 + .0537 ST - .0107 CV$

AVCOAT H.C. WITH ALUMINUM PROJECTILE

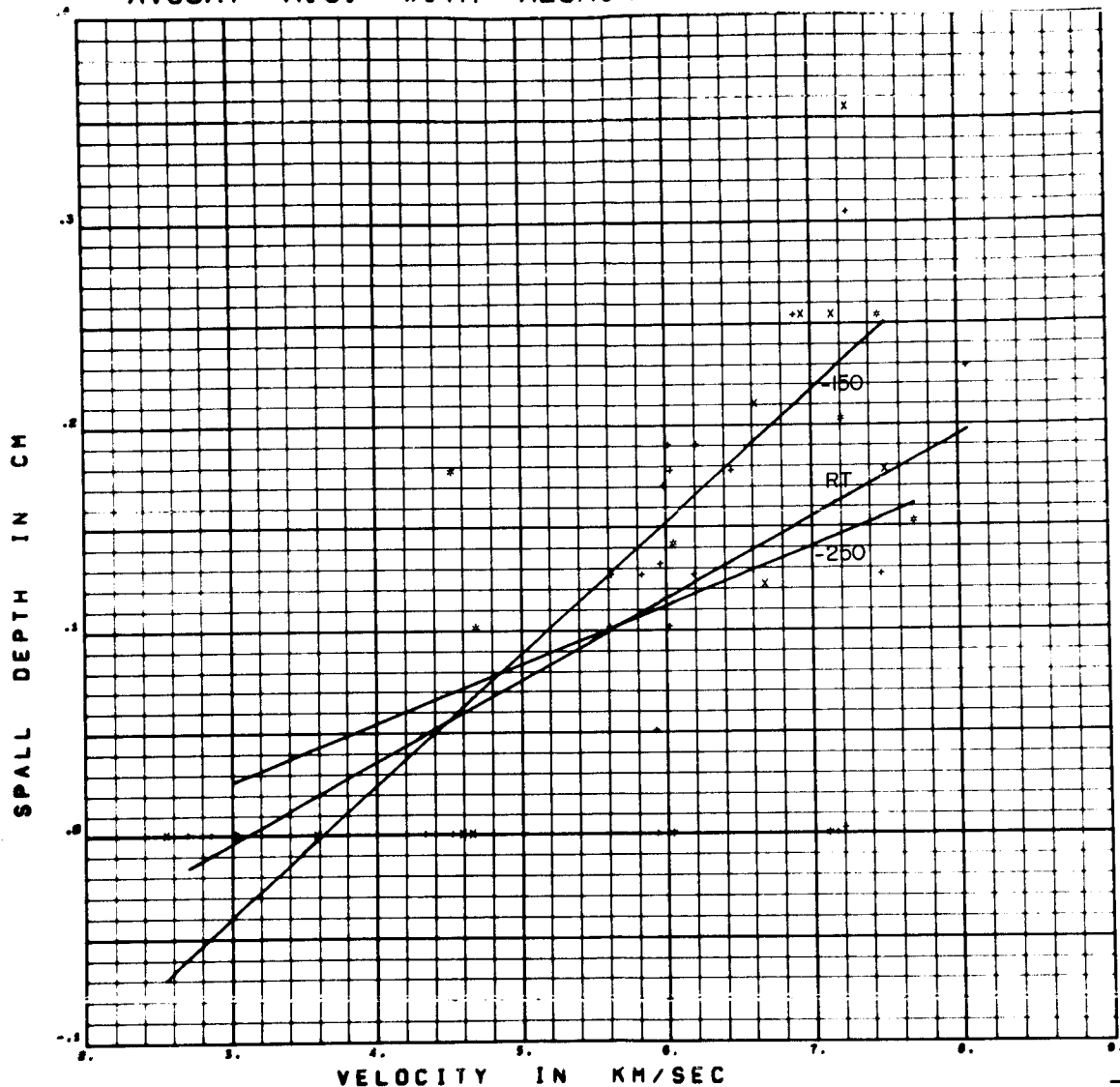


Figure D30 Spall Depth versus Velocity for Aluminum Projectiles on

Avcoat 5026 HC

Form of Regression: $p_s = (.0443 + .0110 ST + .0201 CV) V$

RMS Deviation: .074 cm -.1389 -.0625 ST -.0945 CV

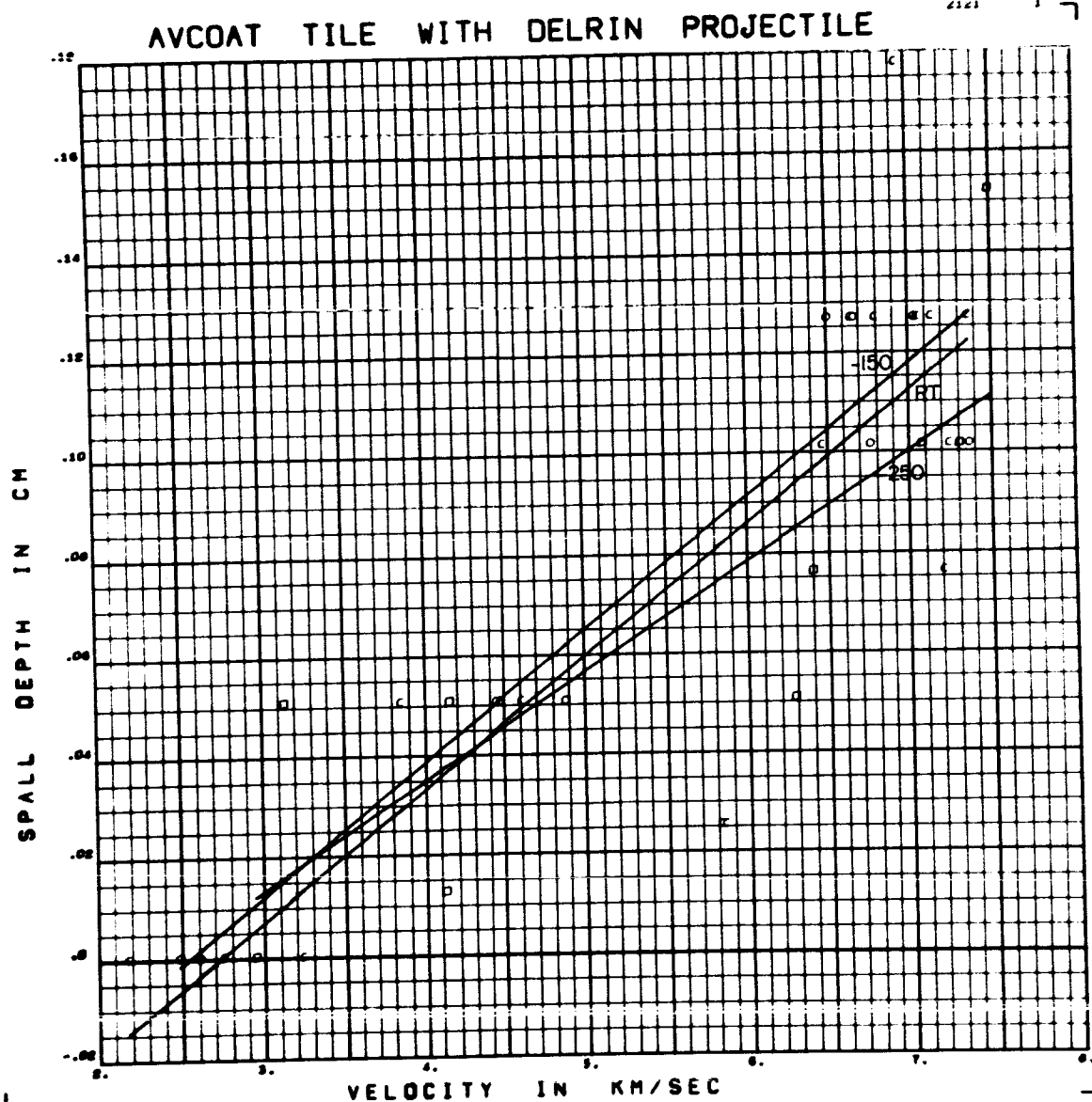


Figure D31 Spall Depth versus Velocity for Delrin Projectiles on

Avcoat 5026 Tile

Form of Regression: $p_s = (.0249 + .0045 ST + .0016 CV) V$
 $-.0637 -.0197 ST -.0034 CV$

RMS Deviation: .025 cm

AVCOAT H.C. WITH DELRIN PROJECTILE

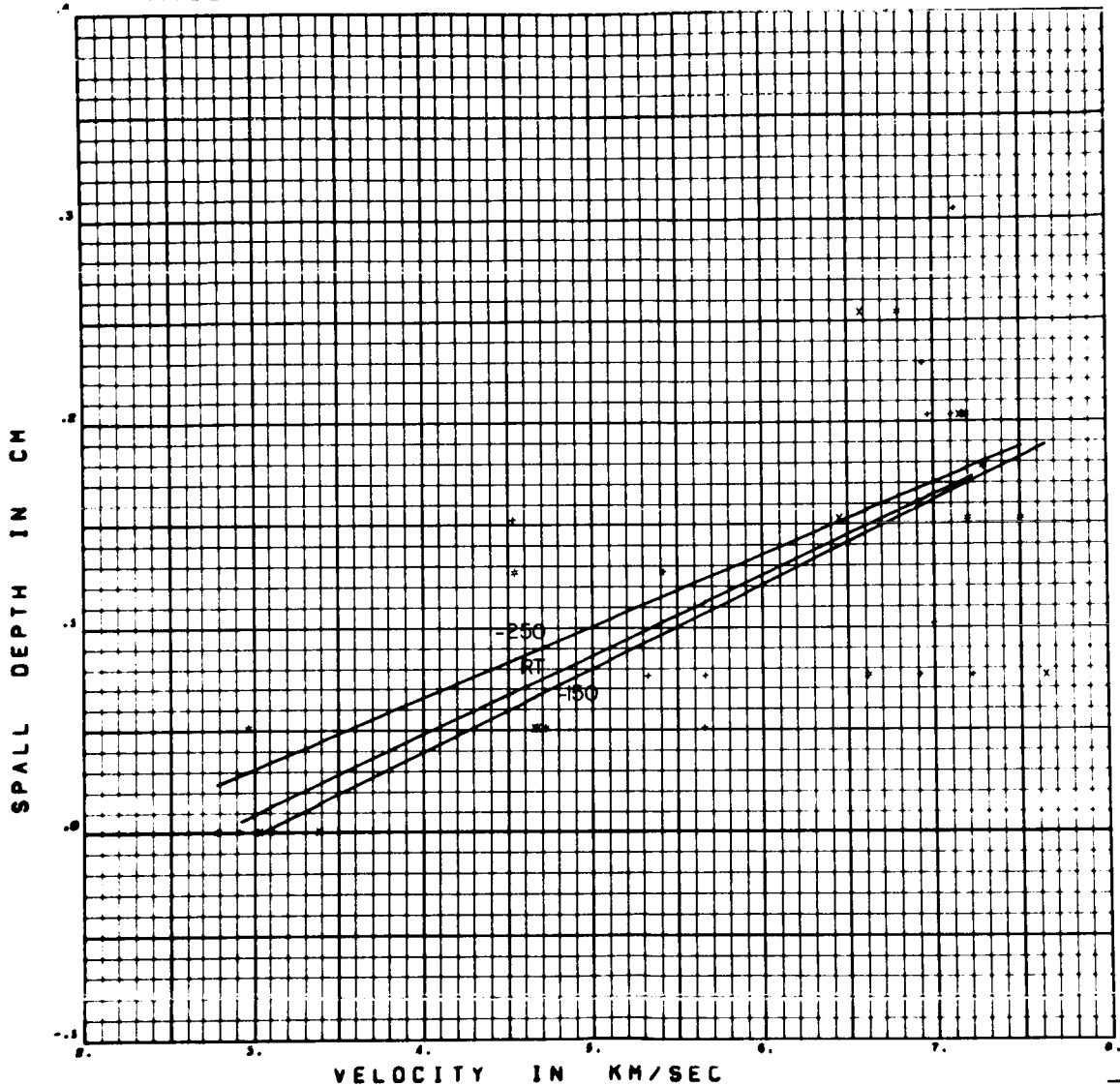


Figure D32 Spall Depth versus Velocity for Delrin Projectiles on

Avcoat 5026 HC

Form of Regression: $p_s = (0.382 + 0.0041 ST + 0.0276 CV) V$

RMS Deviation: .058 cm -.1020 -.0346 ST -.0229 CV

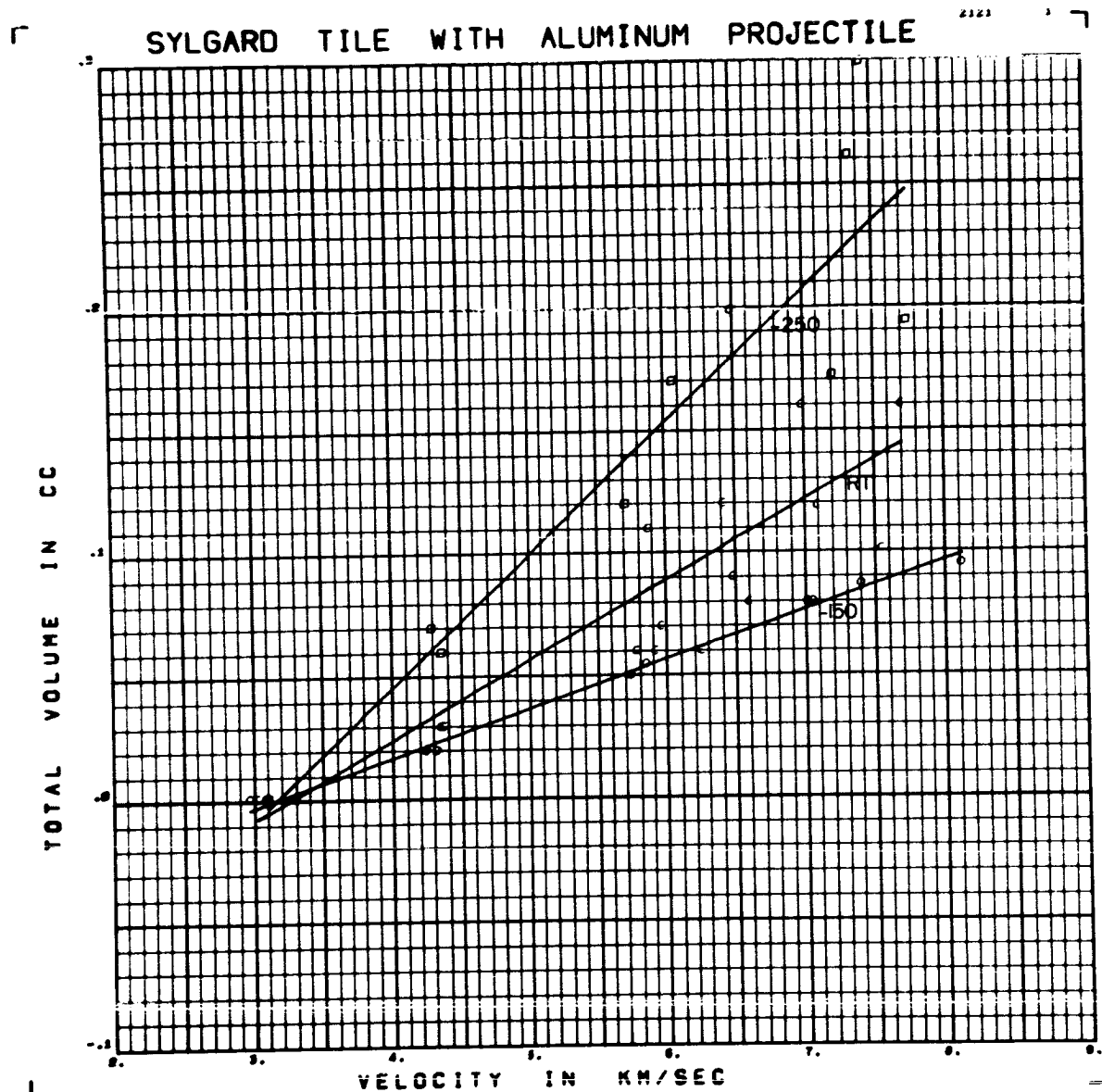


Figure D33 Volume versus Velocity for Aluminum Projectiles on Sylgard 325 Tile

Form of Regression: $V = (.0355 - .0215 ST - .0155 CV) \sqrt{\quad}$

RMS Deviation: .028 CC $-.1128 + .0646 ST + .0501 CV$

SYLGARD H.C. WITH ALUMINUM PROJECTILE

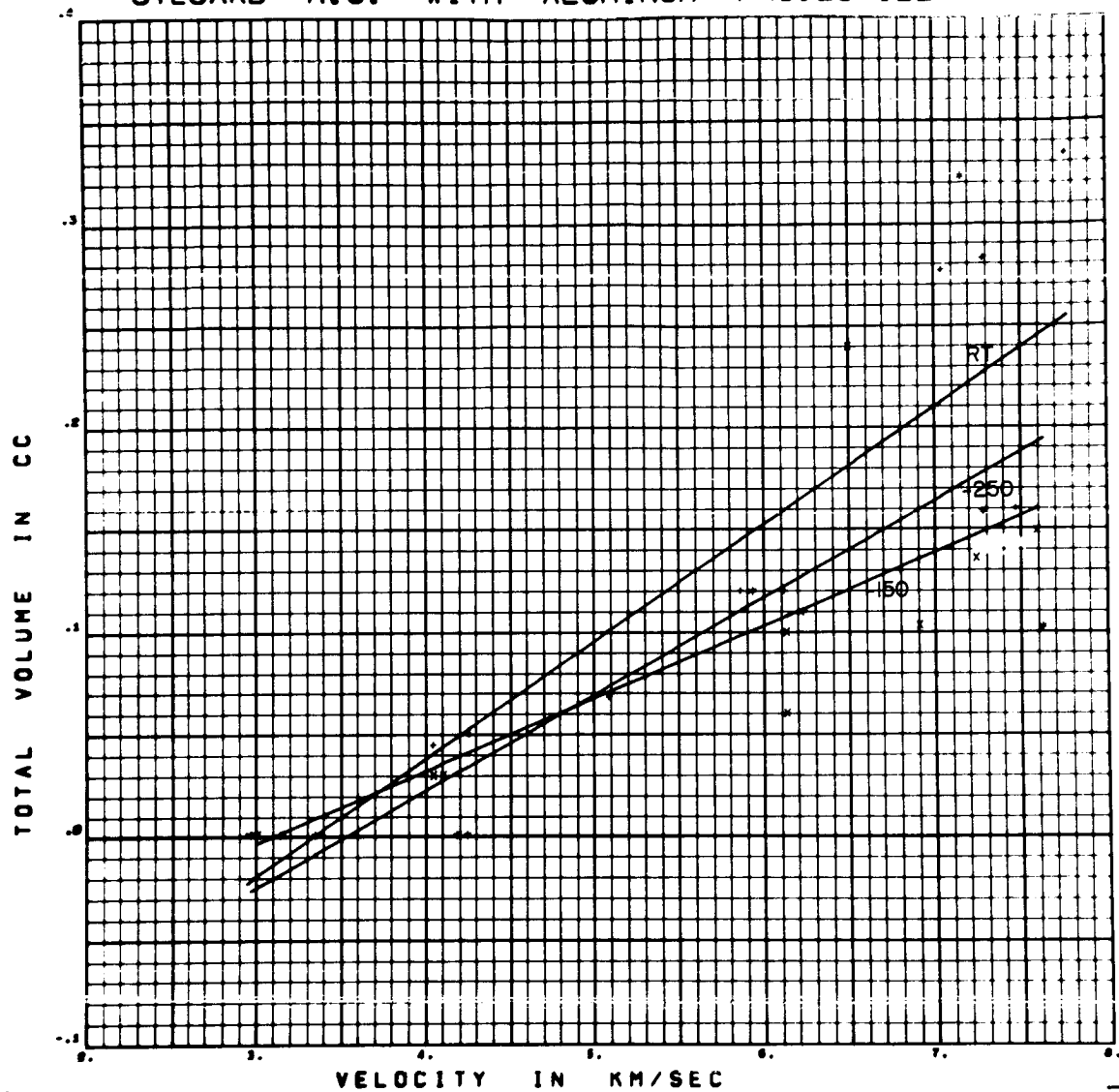


Figure D34 Volume versus Velocity for Aluminum Projectiles on Sylgard 325 HC

Form of Regression: $v = (.0468 + .0102 ST - .0112 CV) V$

RMS Deviation: .052 CC $-.1560 -.0250 ST + .0459 CV$

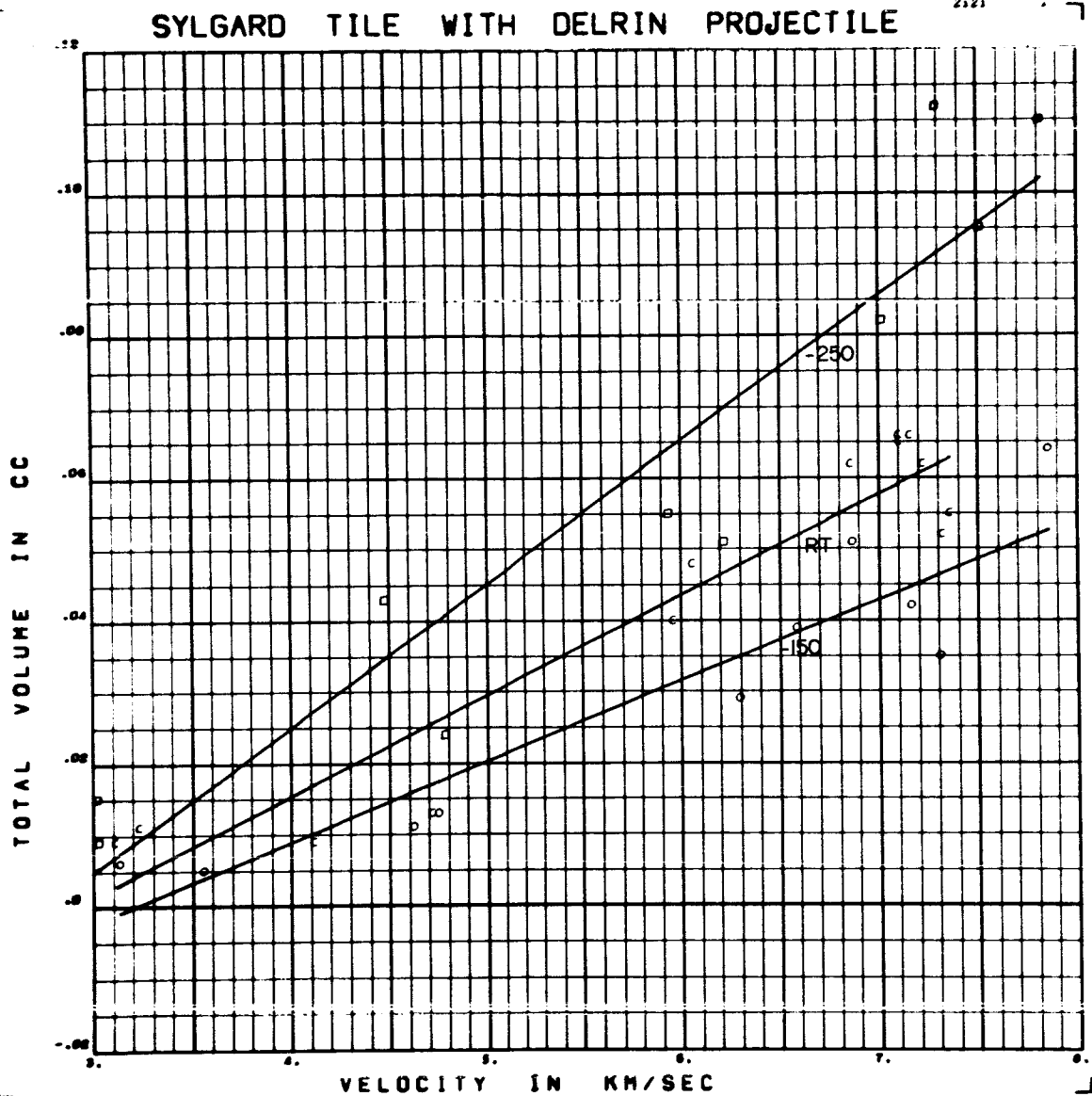


Figure D35 Volume versus Velocity for Delrin Projectiles on Sylgard 325 Tile

Form of Regression: $v = (.0152 - .0061 ST - .0039 CV) V$

RMS Deviation: .009 CC $- .0443 + .0146 ST + .0080 CV$

SYLGARD H.C. WITH DELRIN PROJECTILE

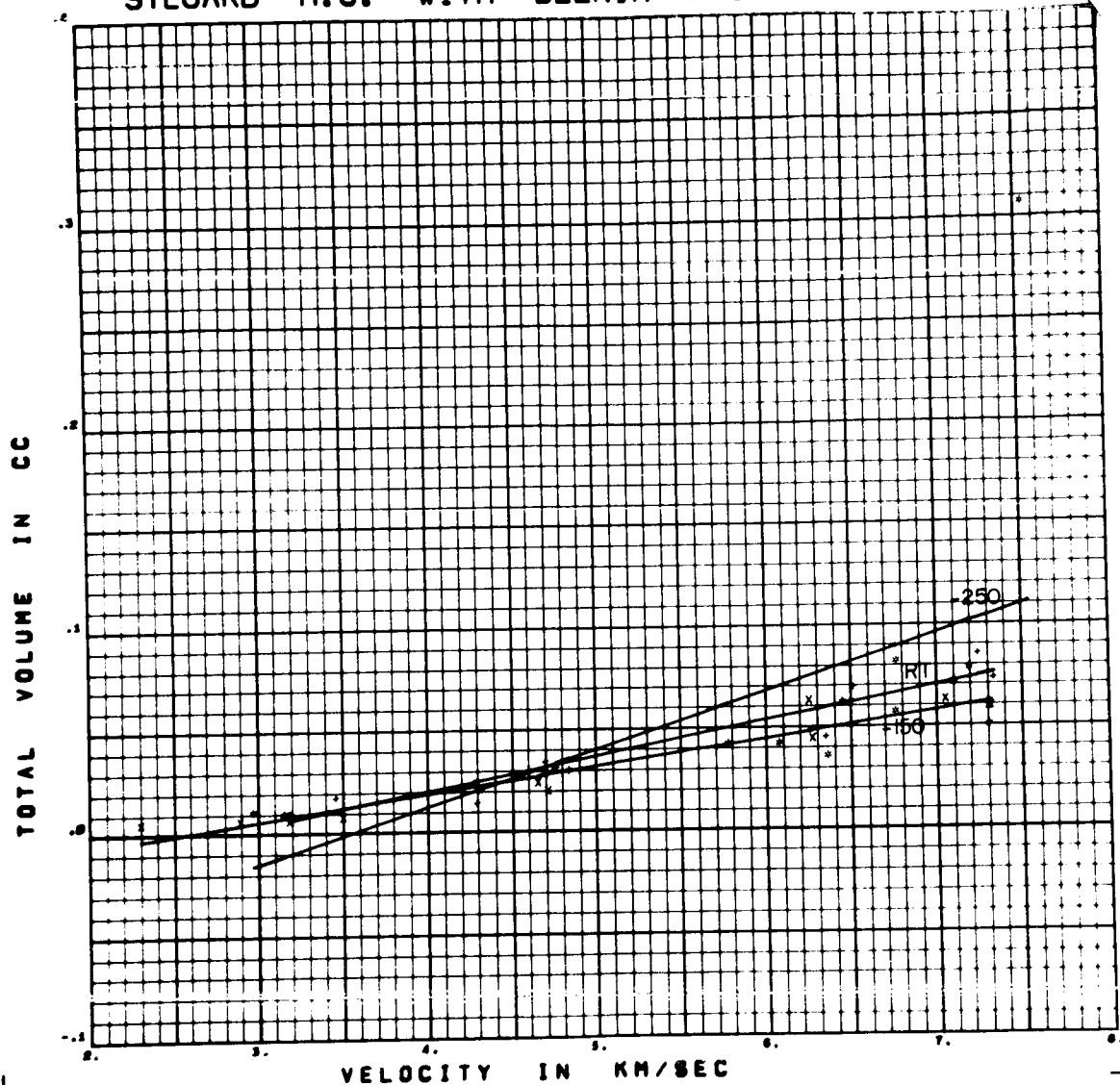


Figure D36 Volume versus Velocity for Delrin Projectiles on Sylgard 325 HC

Form of Regression: $v = (.0191 - .0110 ST - .0062 CV) V$

RMS Deviation: .039 cc $-.0590 + .0514 ST + .0263 CV$

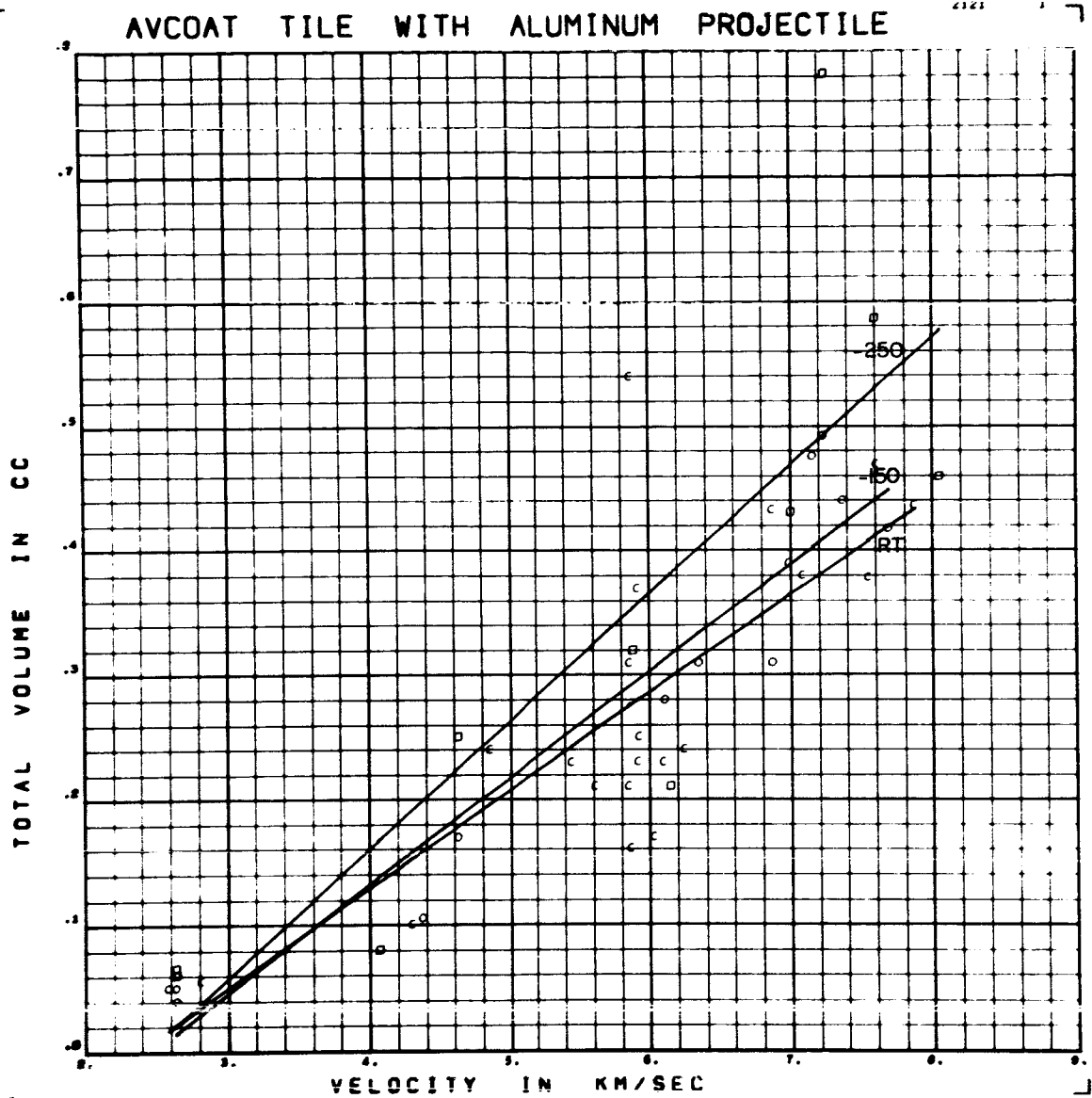


Figure D37 Volume versus Velocity for Aluminum Projectiles on Avcoat 5026 Tile

Form of Regression: $V = (.0891 - .0241 ST - .0032 CV) V$

RMS Deviation: $.086 CC \quad -.2154 + .0649 ST + .0041 CV$

AVCOAT H.C. WITH ALUMINUM PROJECTILE

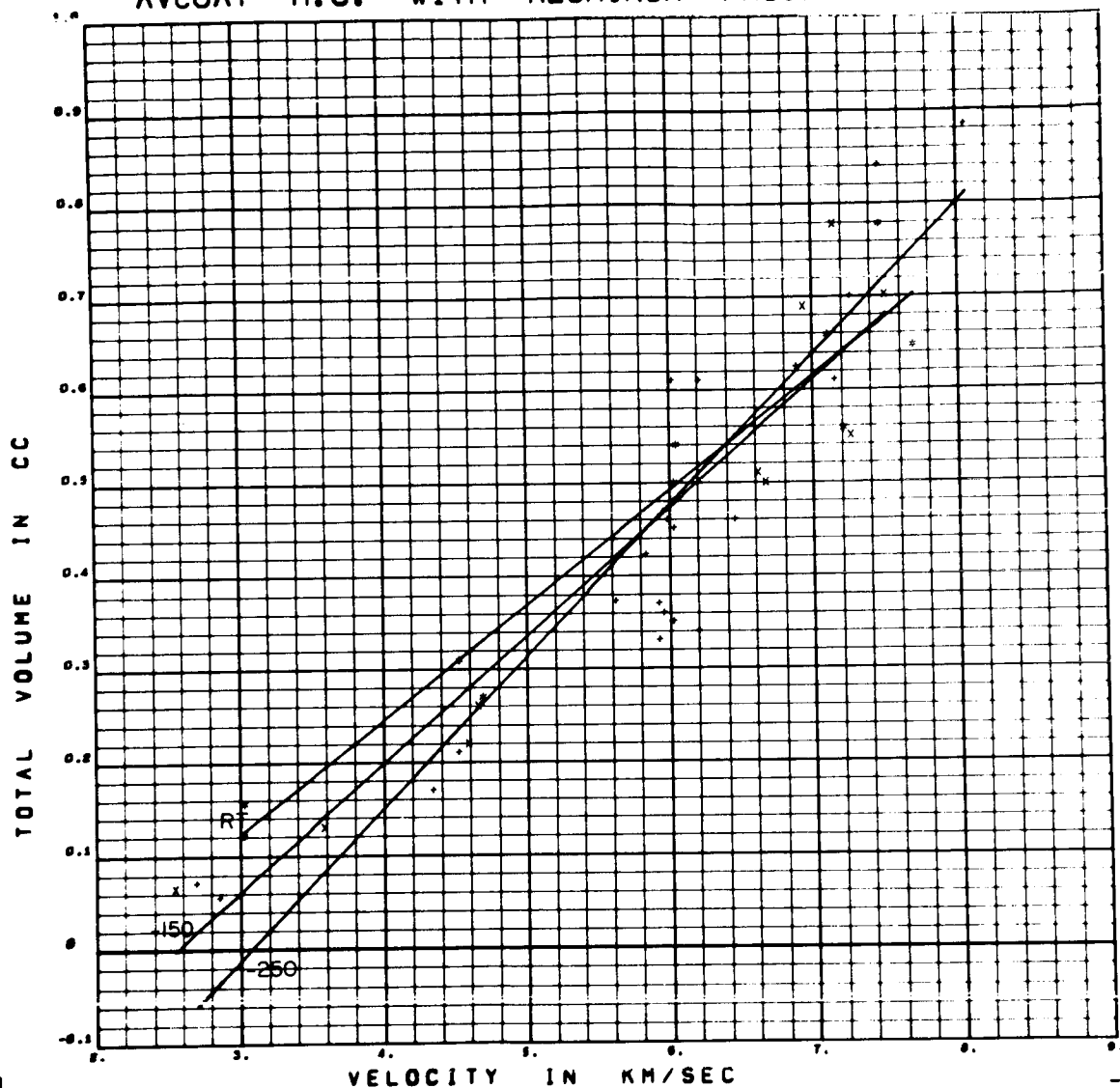


Figure D38 Volume versus Velocity for Aluminum Projectiles on Avcoat 5026 HC

Form of Regression: $V = (.1412 + .0390 ST - .0036 CV) \sqrt{V}$

RMS Deviation: .089 cc $-.3656 - .2501 ST + .0146 CV$

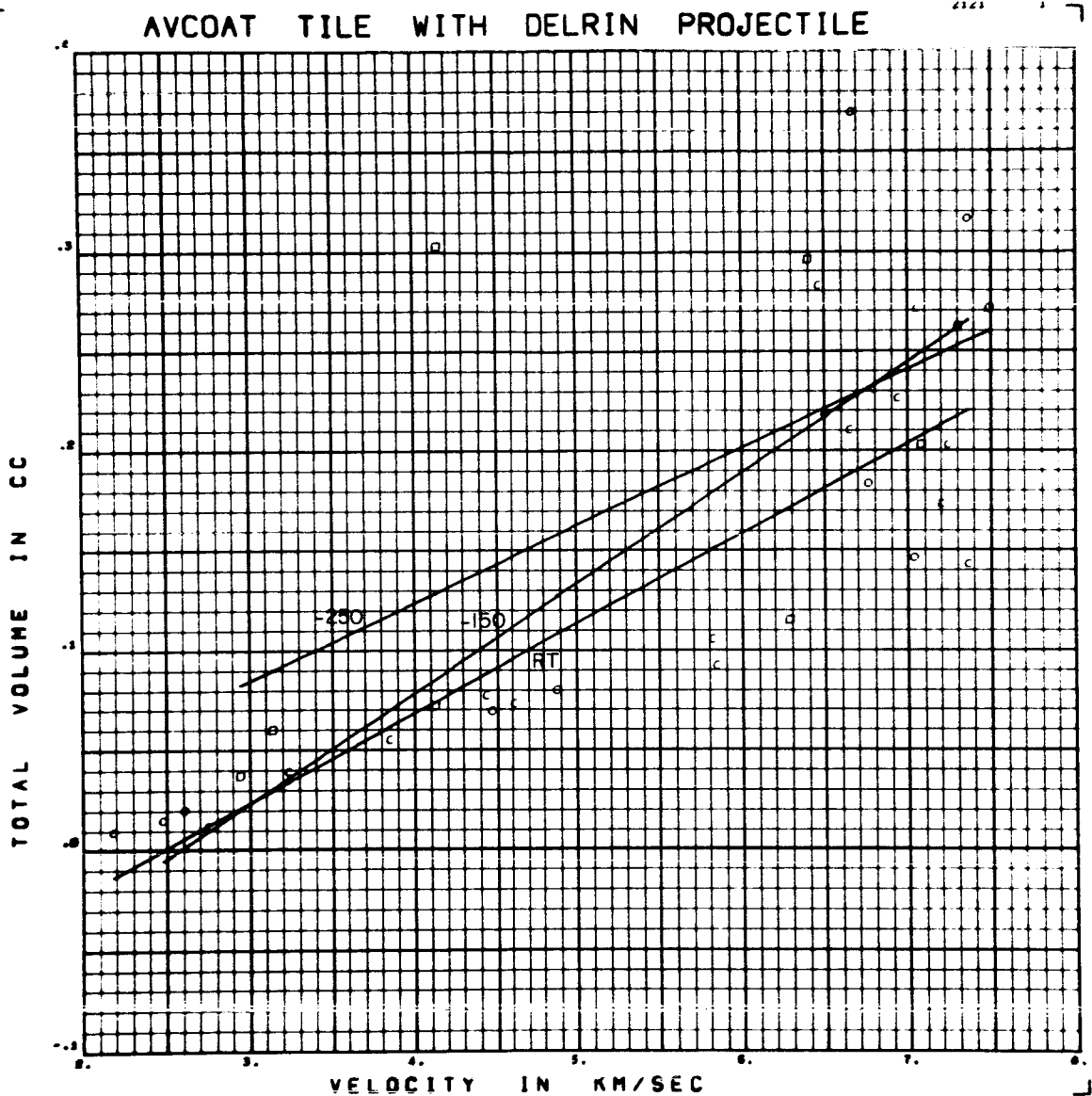


Figure D39 Volume versus Velocity for Delrin Projectiles on Avcoat 5026 Tile

Form of Regression: $v = (.0465 + .0061 ST + .0088 CV) \sqrt{V}$

RMS Deviation: .062 CC $-.0958 \quad -.0793 ST \quad -.0469 CV$

AVCOAT H.C. WITH DELRIN PROJECTILE

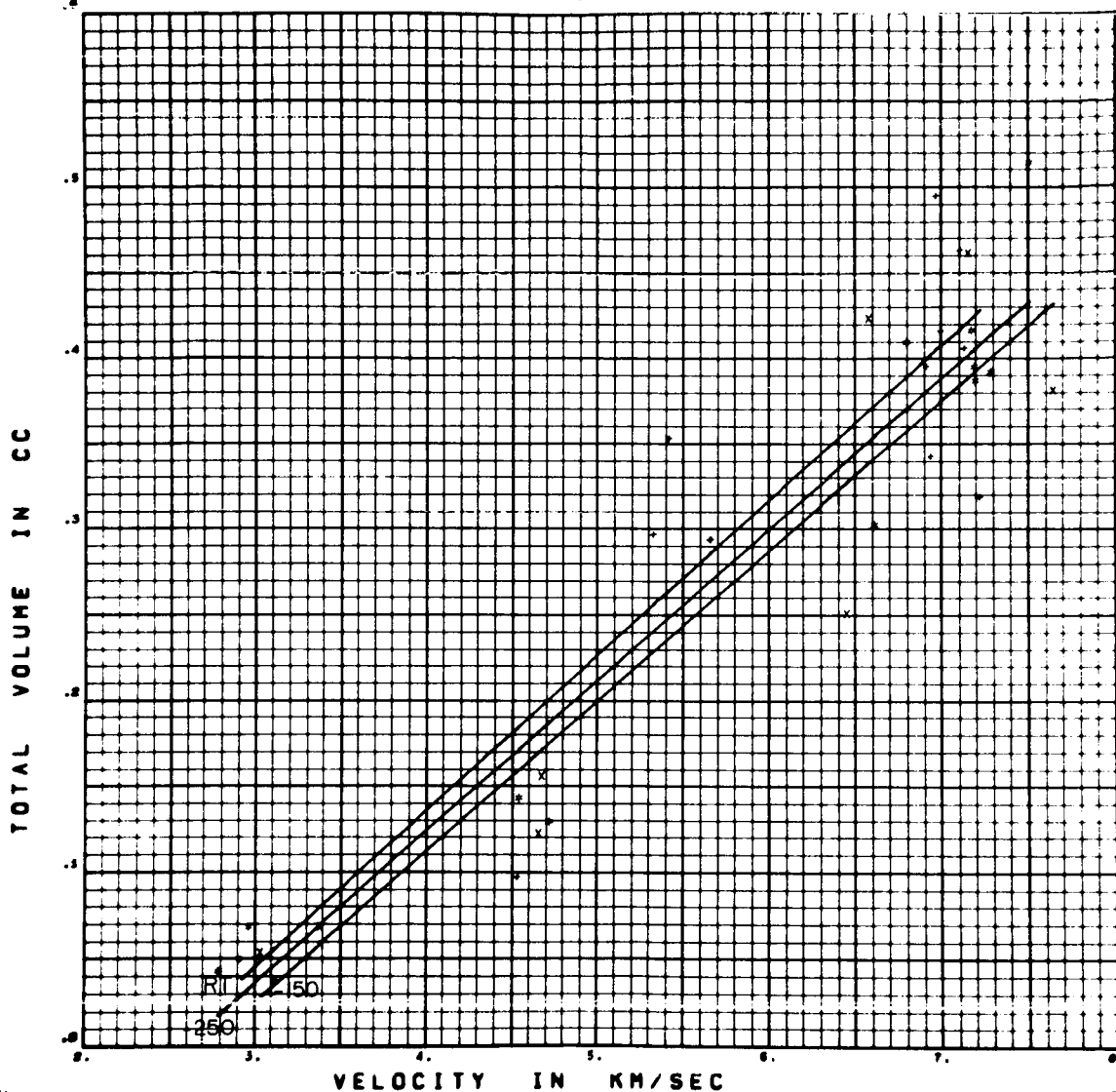


Figure D40 Volume versus Velocity for Delrin Projectiles on Avcoat 5026 HC

Form of Regression: $v = (.0888 + .0024 ST - .0012 CV) V$

RMS Deviation: $.052 cc - .2307 + .0023 ST - .0072 CV$

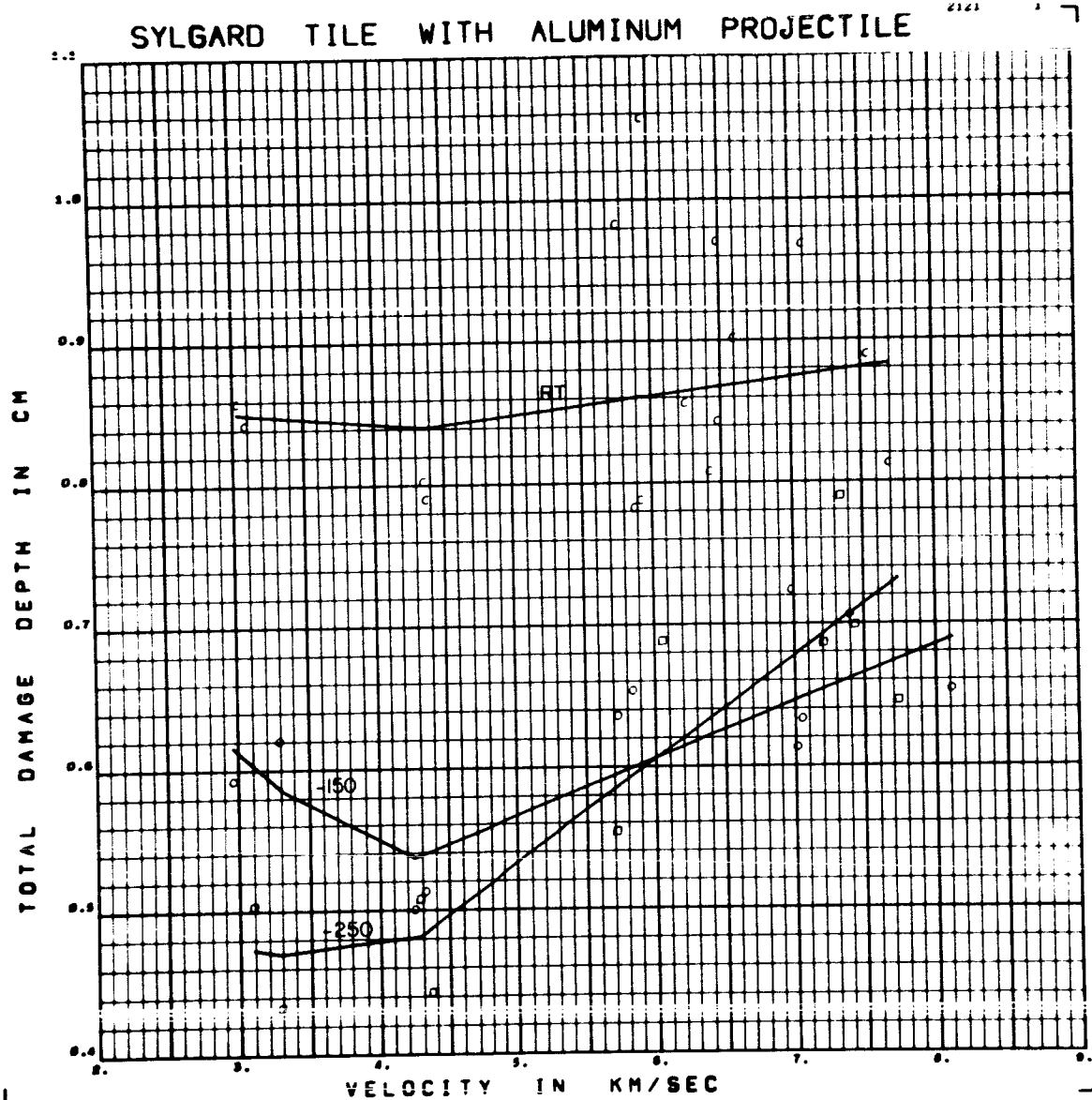


Figure D41 Total Damage Depth versus Velocity for Aluminum Projectiles on
Sylgard 325 Tile

Form of Regression: $p_m = (.0416 - .0596 ST - .0020 CV) V$
 RMS Deviation: .067 cm $+ .4416 + .6133 ST - .0732 CV$

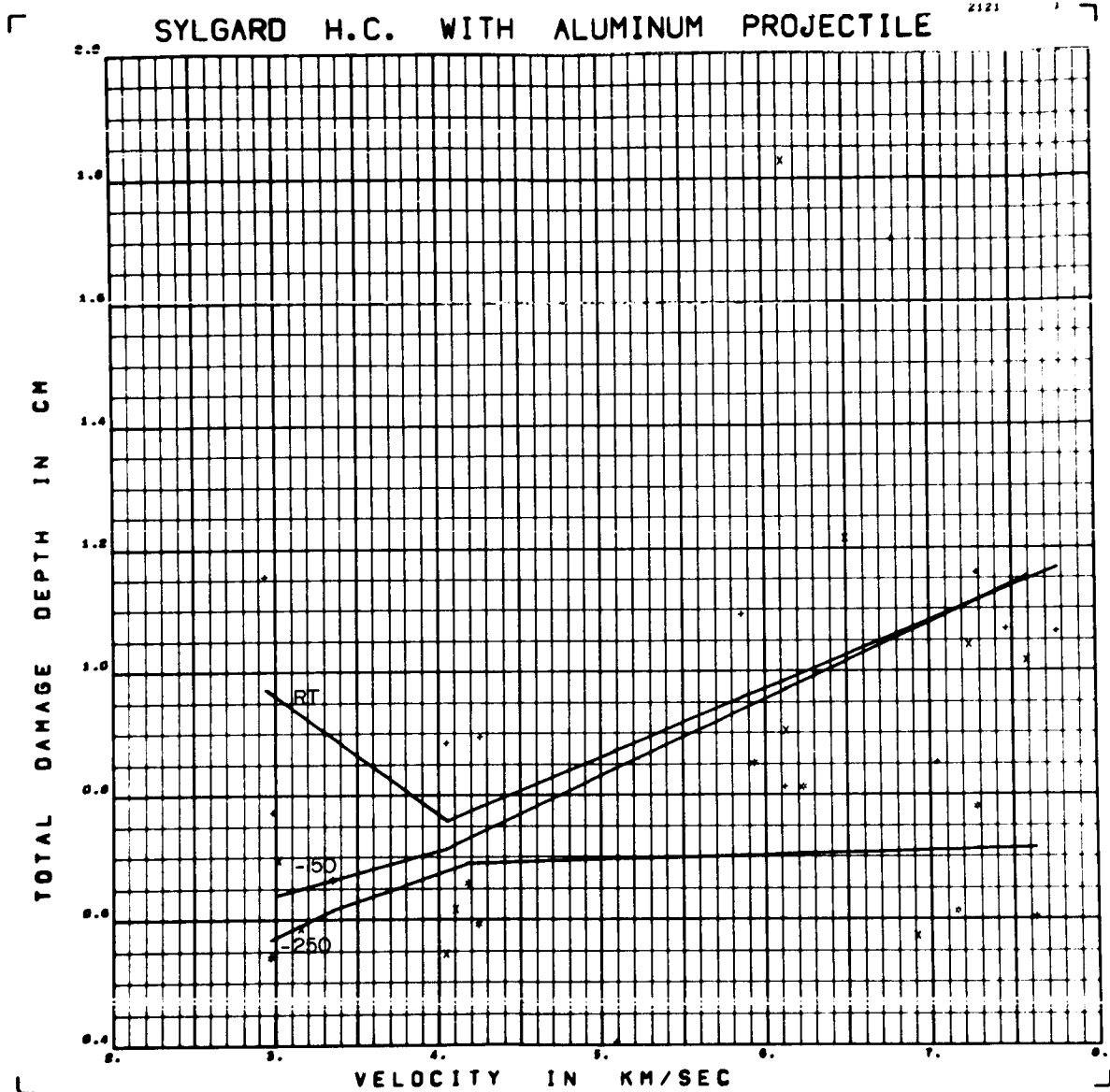


Figure D42 Total Damage Depth versus Velocity for Aluminum Projectiles on
Sylgard 325 HC

Form of Regression: $p_m = (0.0803 + 0.1032 ST + 0.0435 CV) V$

RMS Deviation: .260 cm $+ .395 - .349 ST - .183 CV$

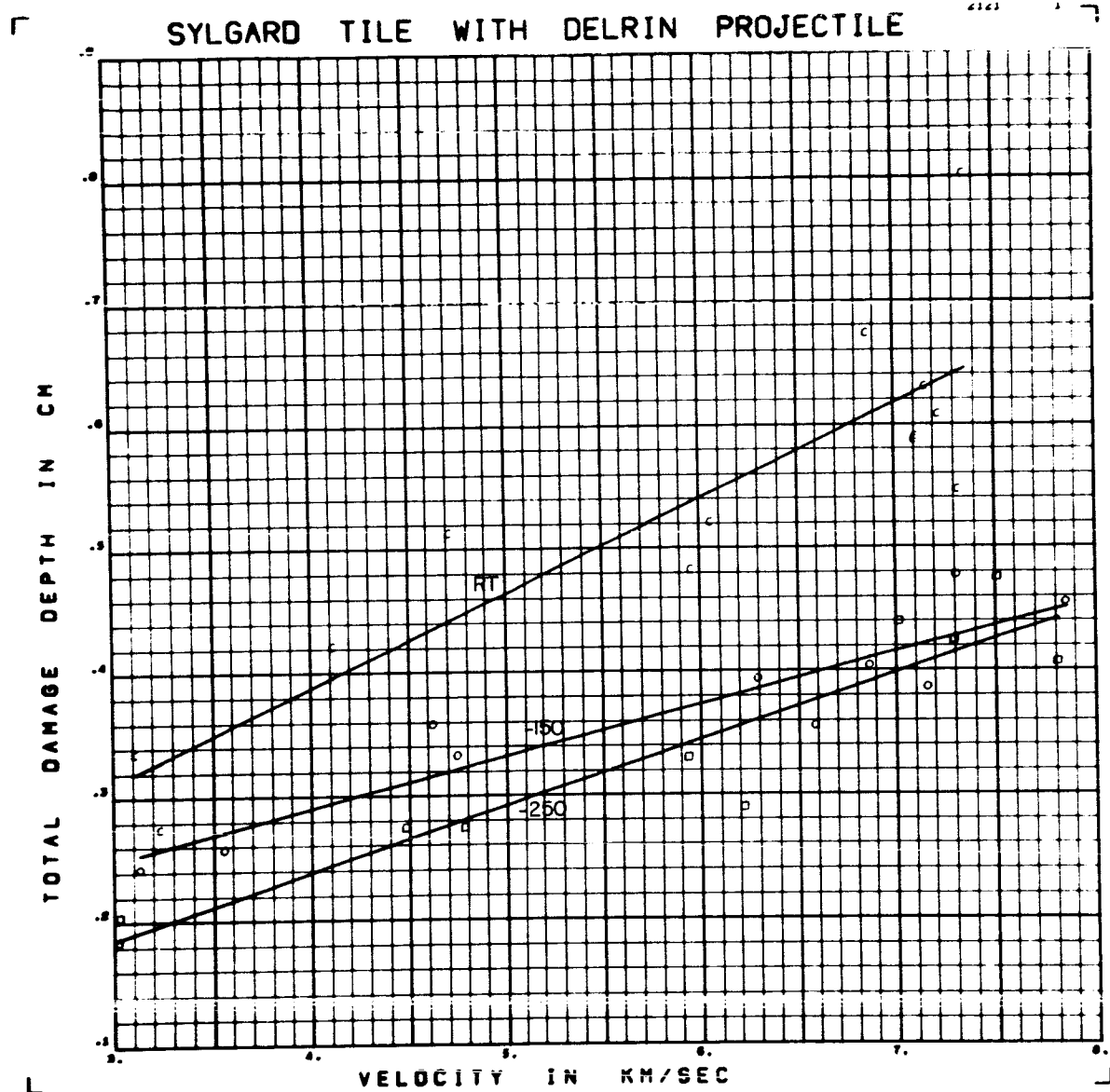


Figure D43 Total Damage Depth versus Velocity for Delrin Projectiles on
Sylgard 325 Tile

Form of Regression: $p_m = (.0573 + .0232 ST - .0154 CV) V$
 $+ .0766 + .0566 ST + 0.462 CV$
 RMS Deviation: .048 cm

SYLGARD H.C. WITH DELRIN PROJECTILE

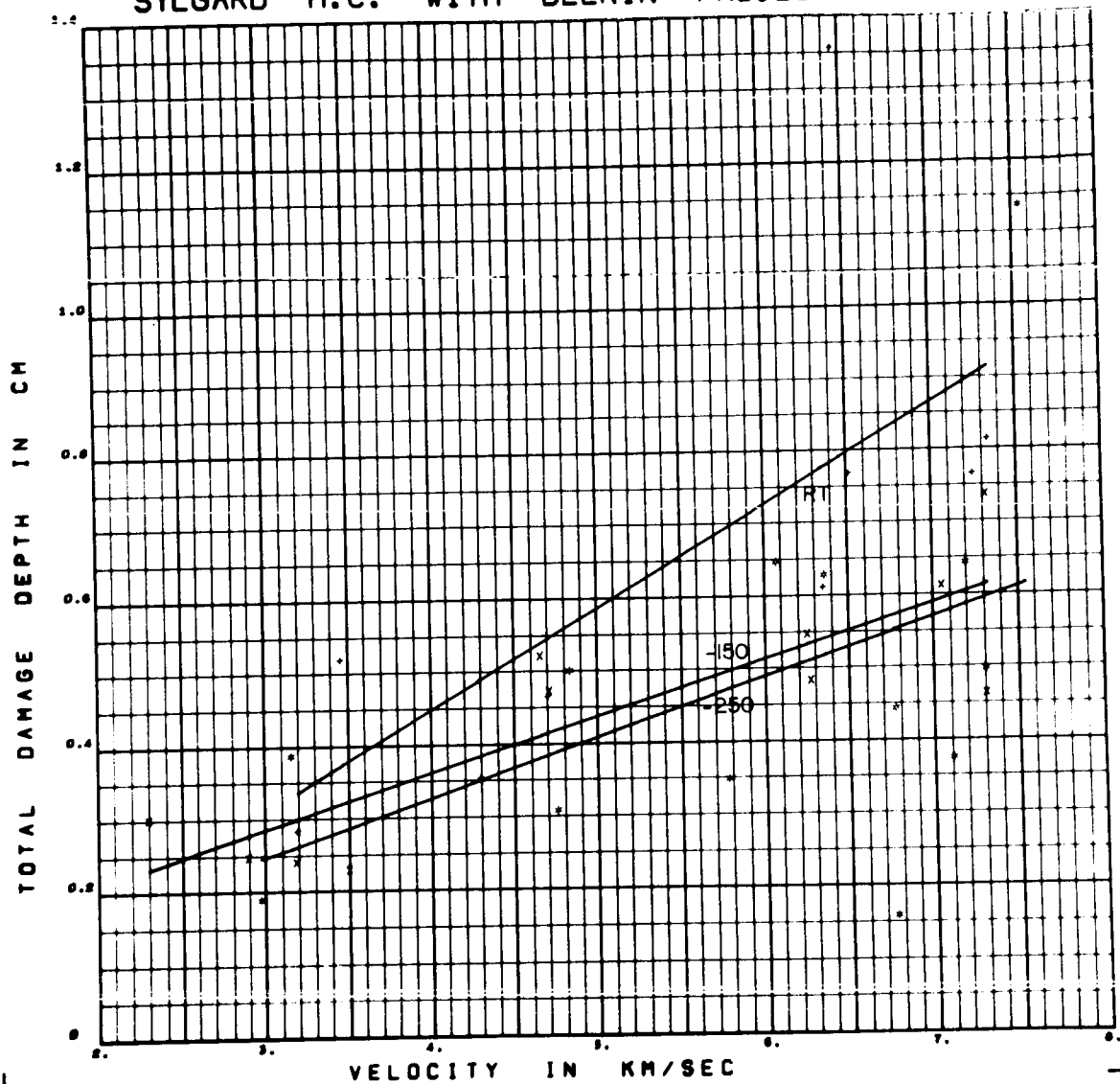


Figure D44 Total Damage Depth versus Velocity for Delrin Projectiles on

Sylgard 325 HC

Form of Regression: $p_m = (.0988 + .0584 ST - .0227 CV) V$

RMS Deviation: .184 cm. $-.0161 - .1131 ST + .0727 CV$

APPENDIX E

CRATER PARAMETERS VERSUS MOMENTUM

CRATER PARAMETERS VERSUS MOMENTUM

<u>Figure</u>	<u>Target</u>	<u>Projectile</u>	<u>Crater Parameter</u>
E1	Sylgard 325 tile	Al	Spall Diameter
E2	Sylgard 325 HC	Al	Spall Diameter
E3	Sylgard 325 tile	Delrin	Spall Diameter
E4	Sylgard 325 HC	Delrin	Spall Diameter
E5	Avcoat 5026	Al	Spall Diameter
E6	Avcoat 5026 HC	Al	Spall Diameter
E7	Avcoat 5026 tile	Delrin	Spall Diameter
E8	Avcoat 5026 HC	Delrin	Spall Diameter
E9	Sylgard 325 tile	Al	Crater Diameter
E10	Sylgard 325 HC	Al	Crater Diameter
E11	Sylgard 325 tile	Delrin	Crater Diameter
E12	Sylgard 325 HC	Delrin	Crater Diameter
E13	Avcoat 5026 tile	Al	Crater Diameter
E14	Avcoat 5026 HC	Al	Crater Diameter
E15	Avcoat 5026 tile	Delrin	Crater Diameter
E16	Avcoat 5026 HC	Delrin	Crater Diameter
E17	Sylgard 325 tile	Al	Penetration
E18	Sylgard 325 HC	Al	Penetration
E19	Sylgard 325 tile	Delrin	Penetration
E20	Sylgard 325 HC	Delrin	Penetration
E21	Avcoat 5026 tile	Al	Penetration
E22	Avcoat 5026 HC	Al	Penetration
E23	Avcoat 5026 tile	Delrin	Penetration
E24	Avcoat 5026 HC	Delrin	Penetration
E25	Sylgard 325 tile	Al	Spall Depth
E26	Sylgard 325 HC	Al	Spall Depth
E27	Sylgard 325 tile	Delrin	Spall Depth
E28	Sylgard 325 HC	Delrin	Spall Depth
E29	Avcoat 5026 tile	Al	Spall Depth
E30	Avcoat 5026 HC	Al	Spall Depth
E31	Avcoat 5026 tile	Delrin	Spall Depth
E32	Avcoat 5026 HC	Delrin	Spall Depth
E33	Sylgard 325 tile	Al	Volume
E34	Sylgard 325 HC	Al	Volume
E35	Sylgard 325 tile	Delrin	Volume
E36	Sylgard 325 HC	Delrin	Volume
E37	Avcoat 5026 tile	Al	Volume
E38	Avcoat 5026 HC	Al	Volume
E39	Avcoat 5026 tile	Delrin	Volume
E40	Avcoat 5026 HC	Delrin	Volume
E41	Sylgard 325 tile	Al	Total Damage Depth
E42	Sylgard 325 HC	Al	Total Damage Depth
E43	Sylgard 325 tile	Delrin	Total Damage Depth
E44	Sylgard 325 HC	Delrin	Total Damage Depth

HONEYCOMB SYMBOLS

TEMPERATURE	SYMBOL
RT	+
-150°F	X
-250°F	*

TILE SYMBOLS

TEMPERATURE	SYMBOL
RT	C
-150°F	O
-250°F	□

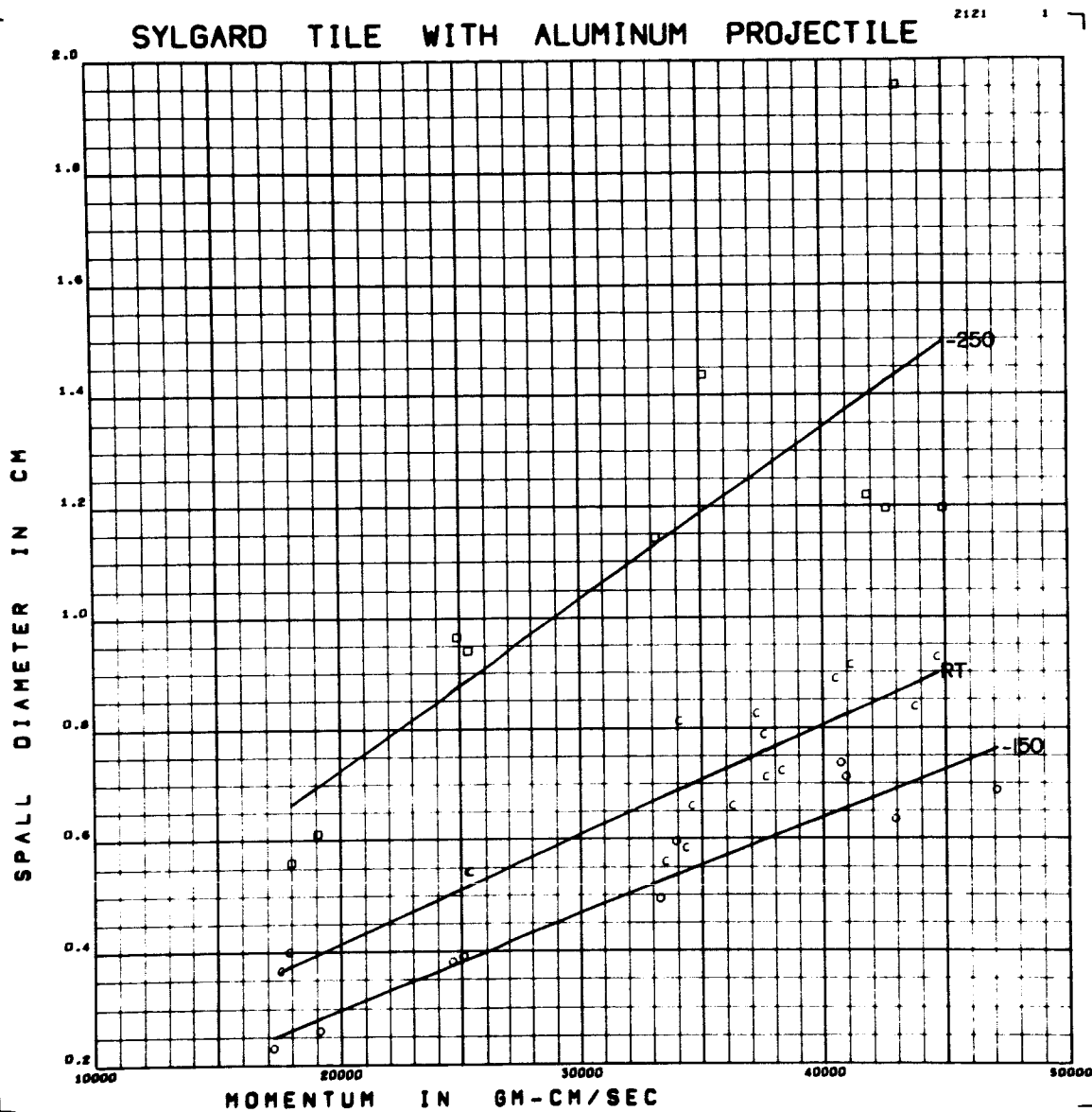


Figure E1 Spall Diameter versus Momentum for Aluminum Projectiles on
Sylgard 325 Tile

Form of Regression: $d_s = (2.255 - 1.1295T - .535CV) \times 10^{-5} M$

RMS Deviation: .132 cm $+ (2.751 - 8.5505T - 7.515CV) \times 10^{-2}$

SYLGARD H.C. WITH ALUMINUM PROJECTILE

2121

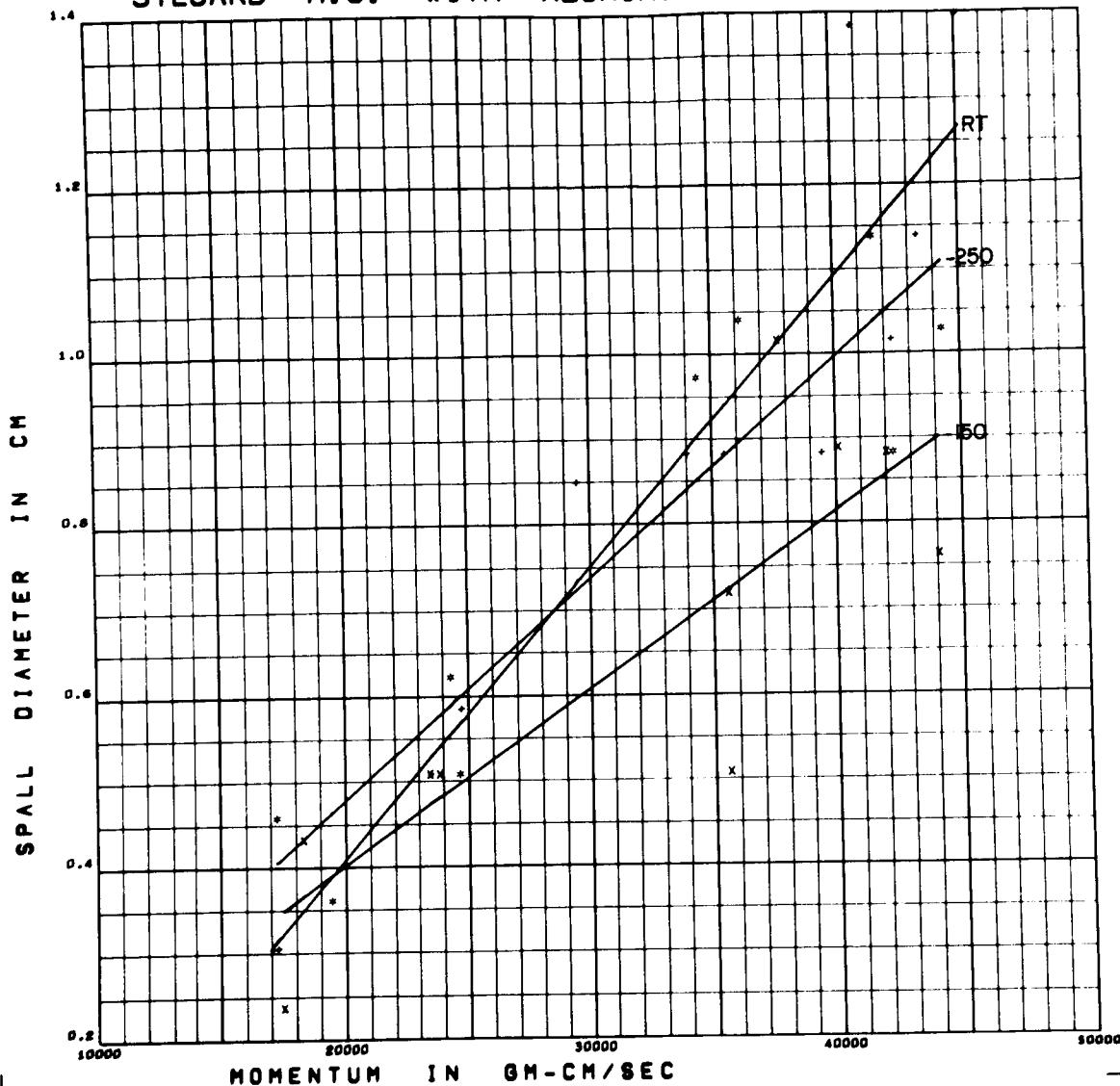


Figure E2 Spall Diameter versus Momentum for Aluminum Projectiles on
Sylgard 325 HC

Form of Regression: $d_s = (2.696 + .8215T - .625CV) \times 10^{-5} M$

RMS Deviation: .119 cm $+ (-10.98 - 23.335T + 9.694CV) \times 10^{-2}$

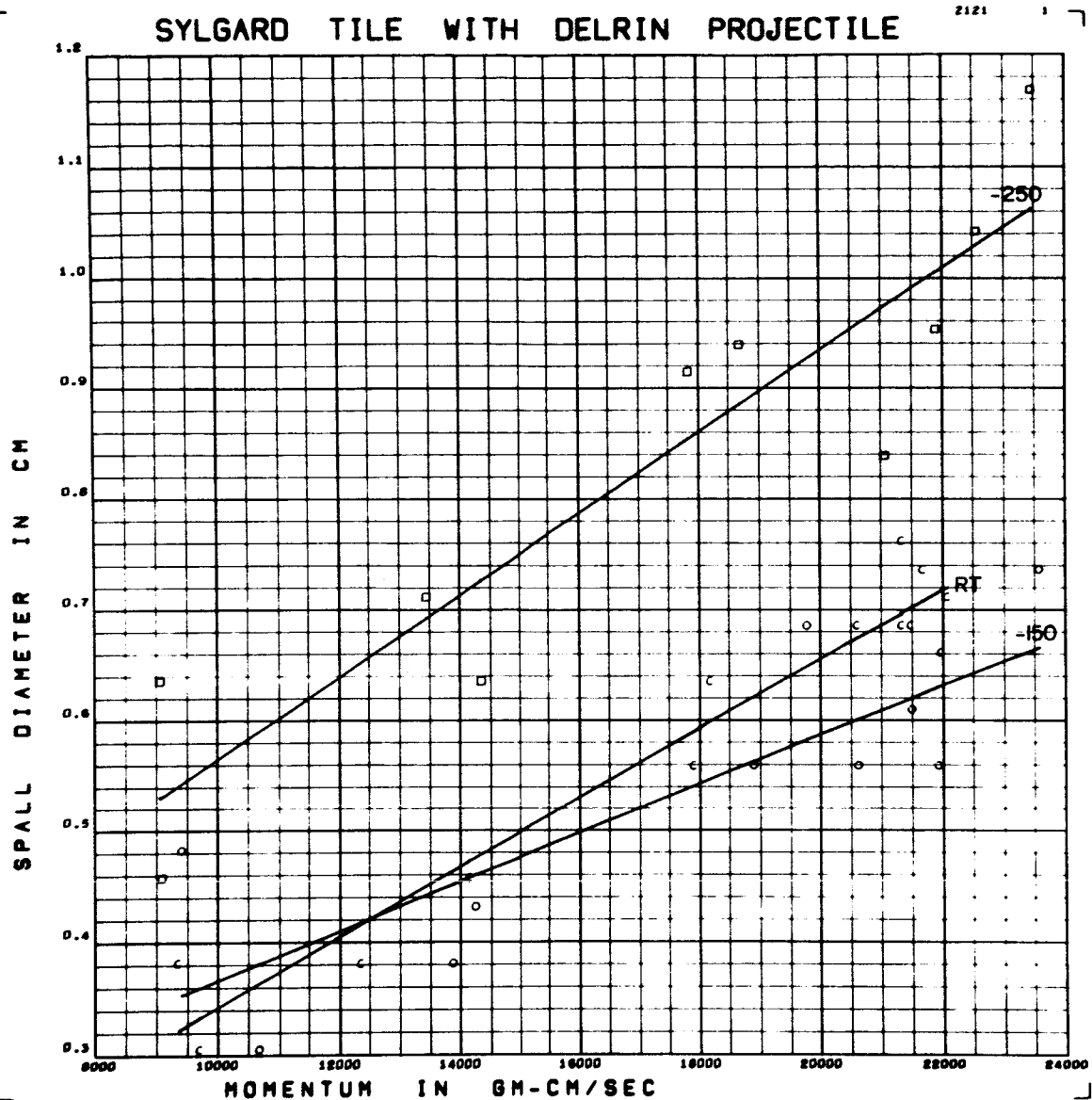


Figure E3 Spall Diameter versus Momentum for Delrin Projectiles on
Sylgard 325 Tile

Form of Regression: $d_s = (3.009 - .575 ST - .805 CV) \times 10^{-5} M$

RMS Deviation: $.064 \text{ cm} + (12.39 - 16.50 ST + 2.24 CV) \times 10^{-2}$

SYLGARD H.C. WITH DELRIN PROJECTILE

2121

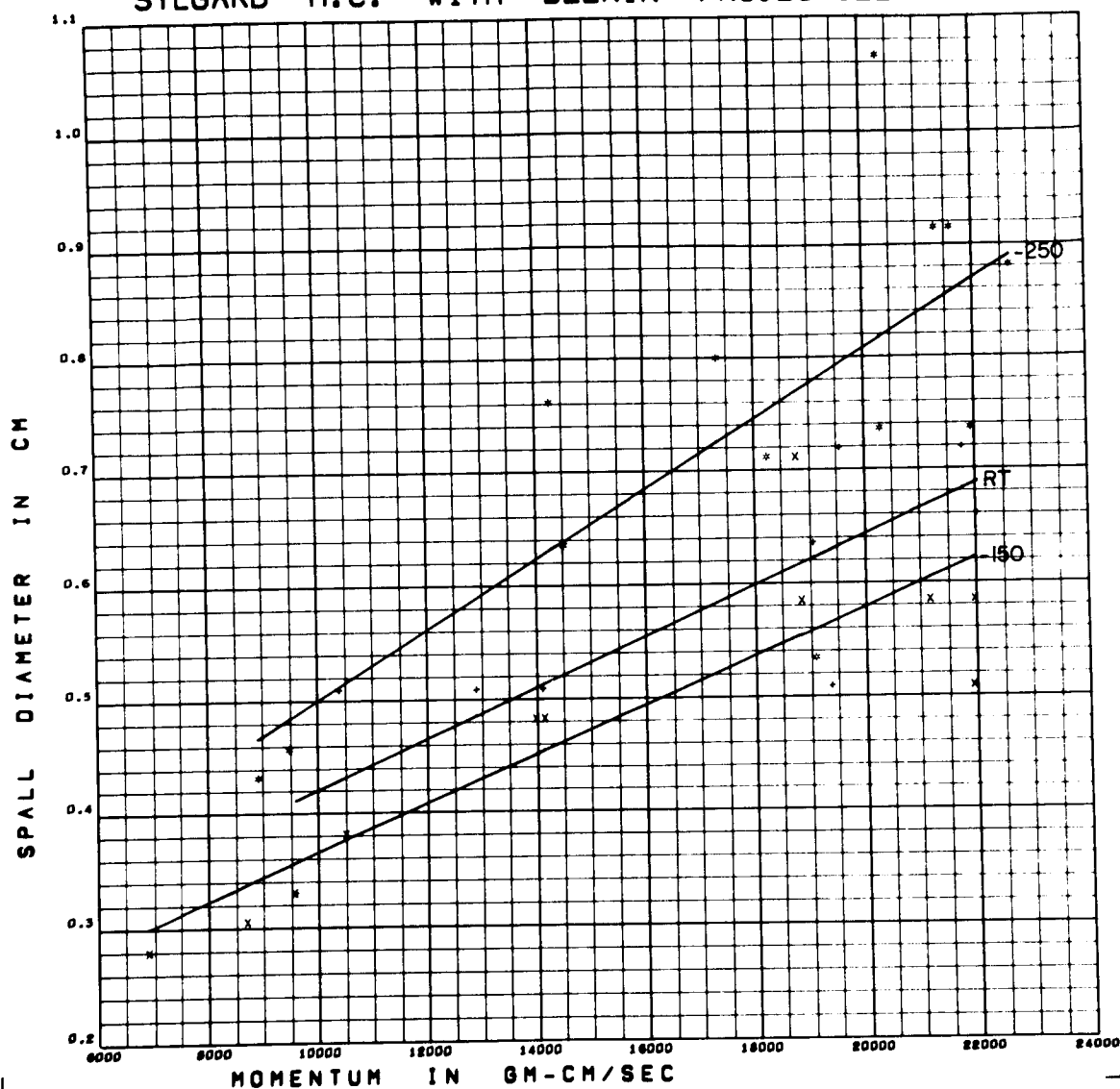


Figure E4 Spall Diameter versus Momentum for Delrin Projectiles on
Sylgard 325 HC

Form of Regression: $d_s = (2.477 - .860 ST - .349 CV) \times 10^{-5} M$

RMS Deviation: $.090 \text{ cm} + (.18.15 + .715 ST - 2.78 CV) \times 10^{-2}$

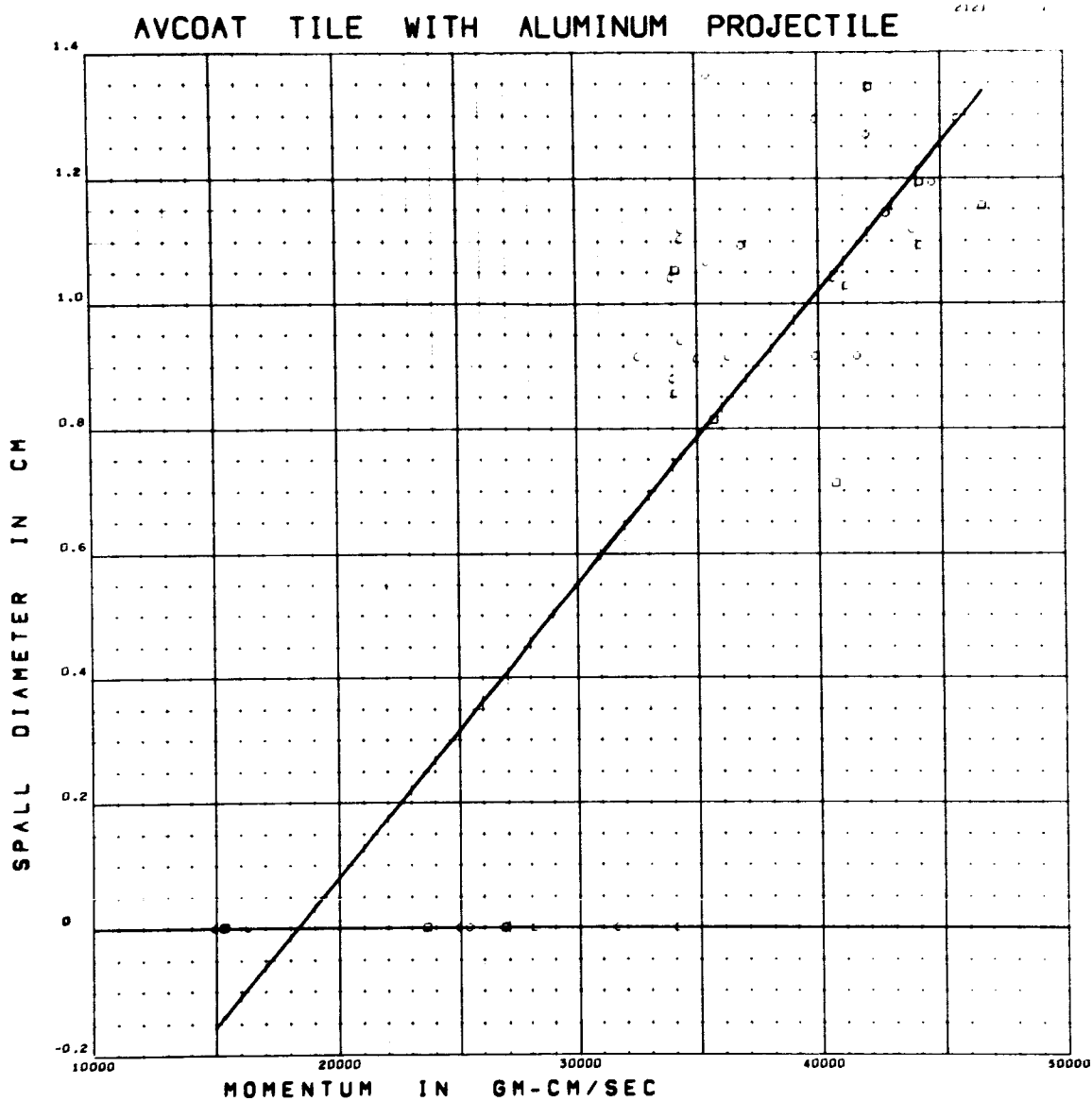


Figure E5 Spall Diameter versus Momentum for Aluminum Projectiles on
Avcoat 5026 Tile

Form of Regression: $d_s = 4.706 \times 10^{-5} M - .8604$

RMS Deviation: .279 cm

AVCOAT H.C. WITH ALUMINUM PROJECTILE

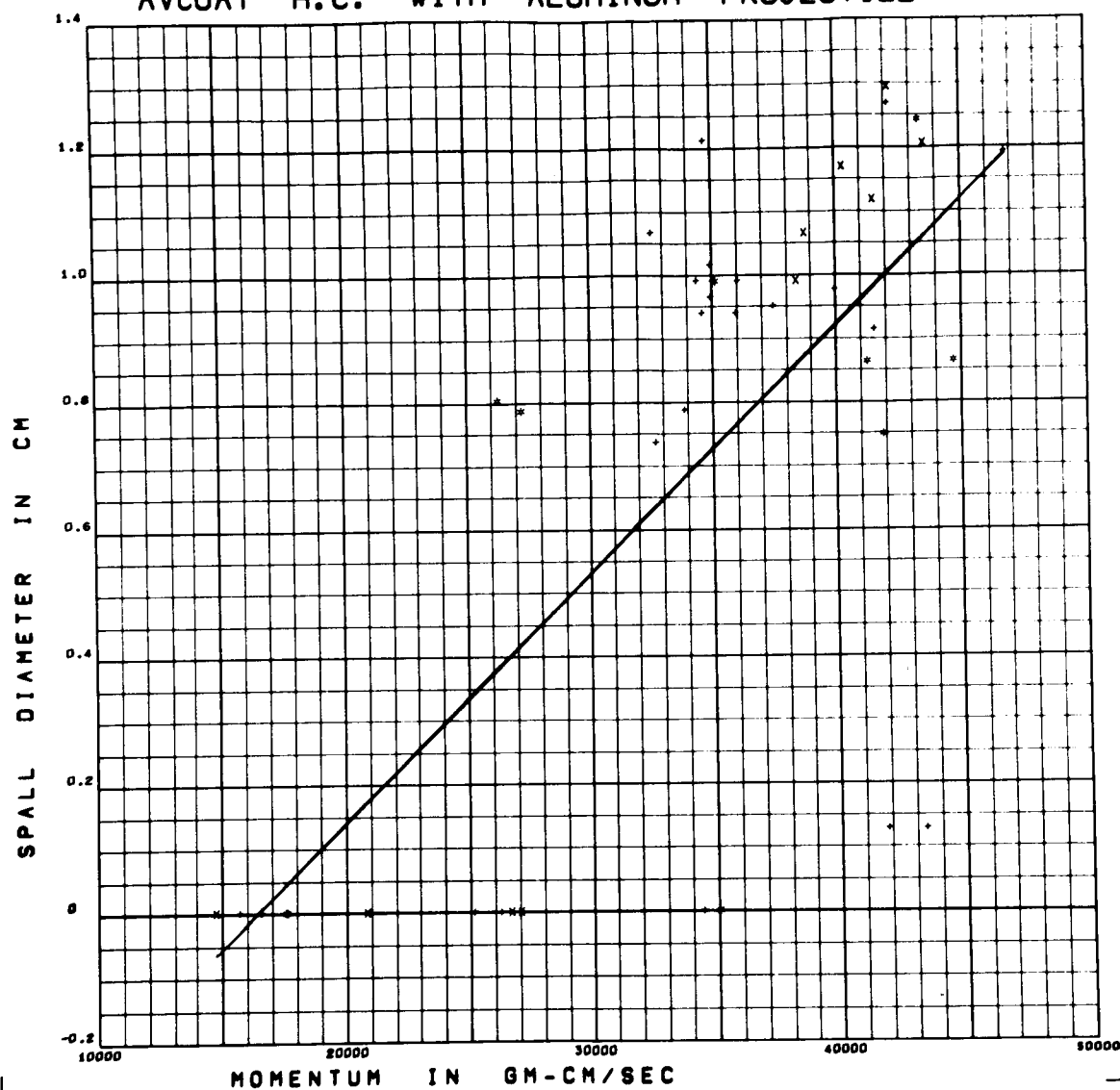


Figure E6 Spall Diameter versus Momentum for Aluminum Projectiles on

Avcoat 5026 HC

Form of Regression: $d_s = 3.910 \times 10^{-5} M^{-.6409}$

RMS Deviation: .346 cm

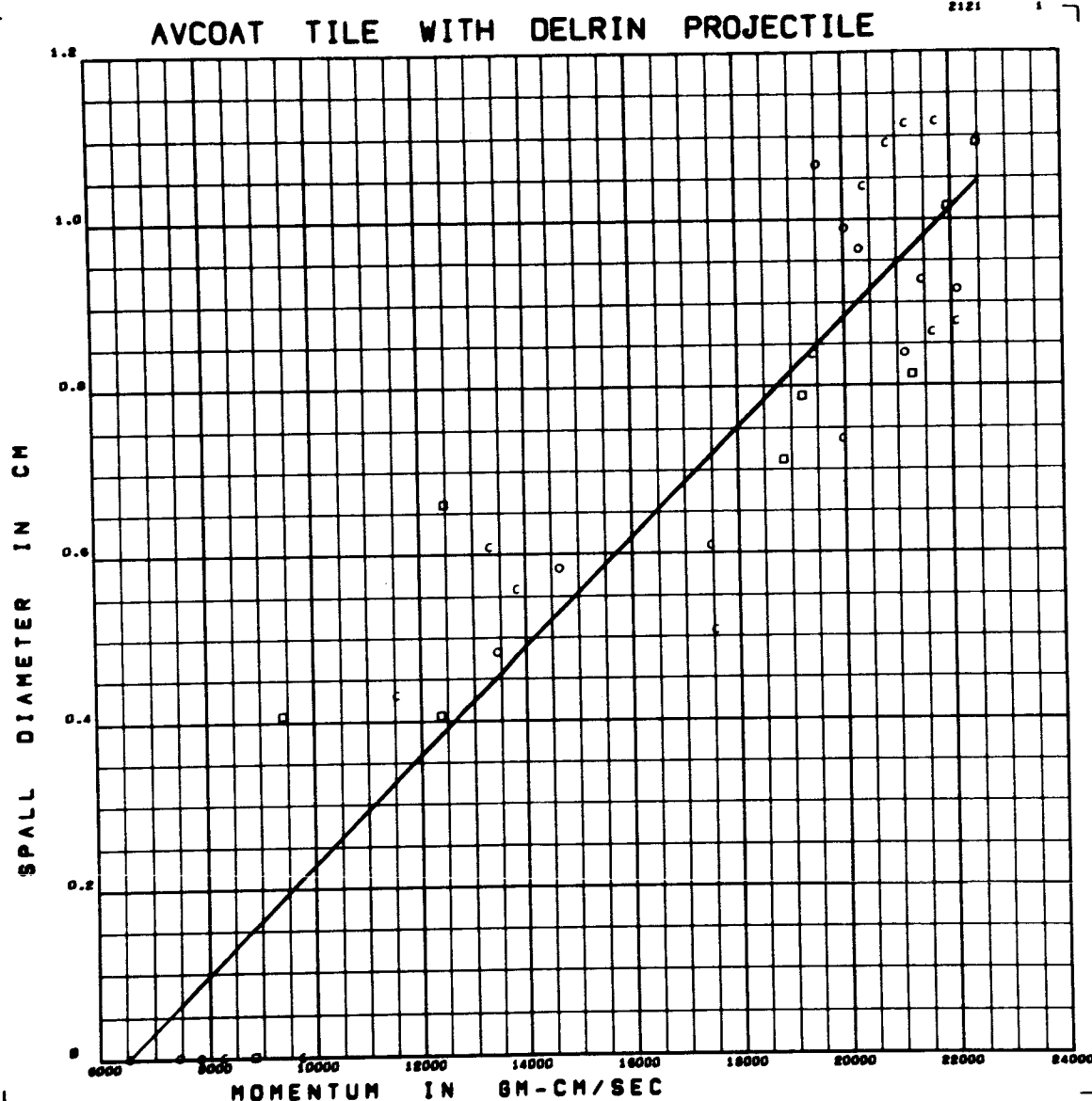


Figure E7 Spall Diameter versus Momentum for Delrin Projectiles on
Avcoat 5026 Tile

Form of Regression: $d_s = 6.550 \times 10^{-5} M - .4270$

RMS Deviation: .13/cm

AVCOAT H.C. WITH DELRIN PROJECTILE

2121

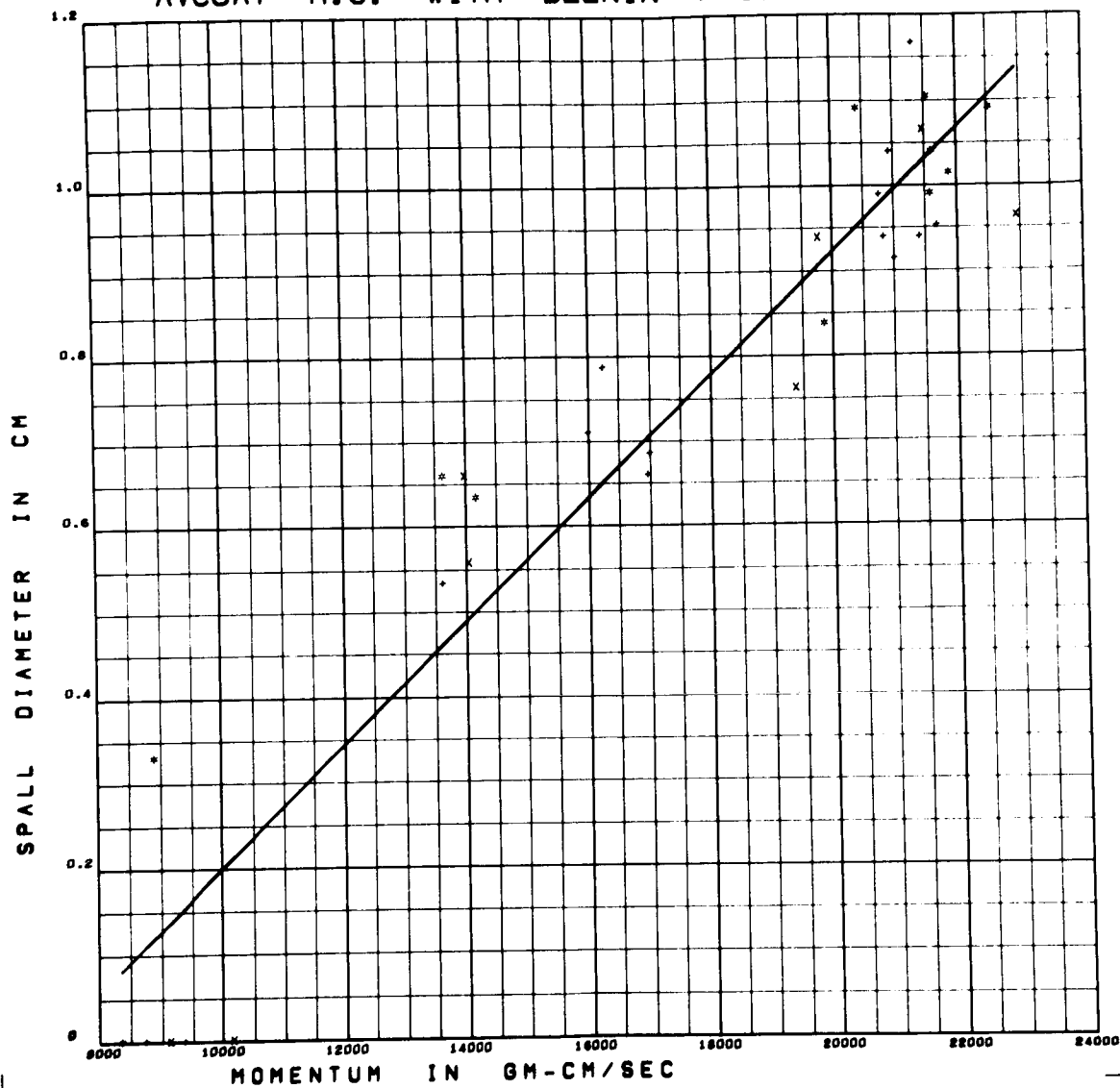


Figure E8 Spall Diameter versus Momentum for Delrin Projectiles on

Avcoat 5026 HC

Form of Regression: $d_s = 7.237 \times 10^{-5} M^{-.5231}$

RMS Deviation: .112 cm

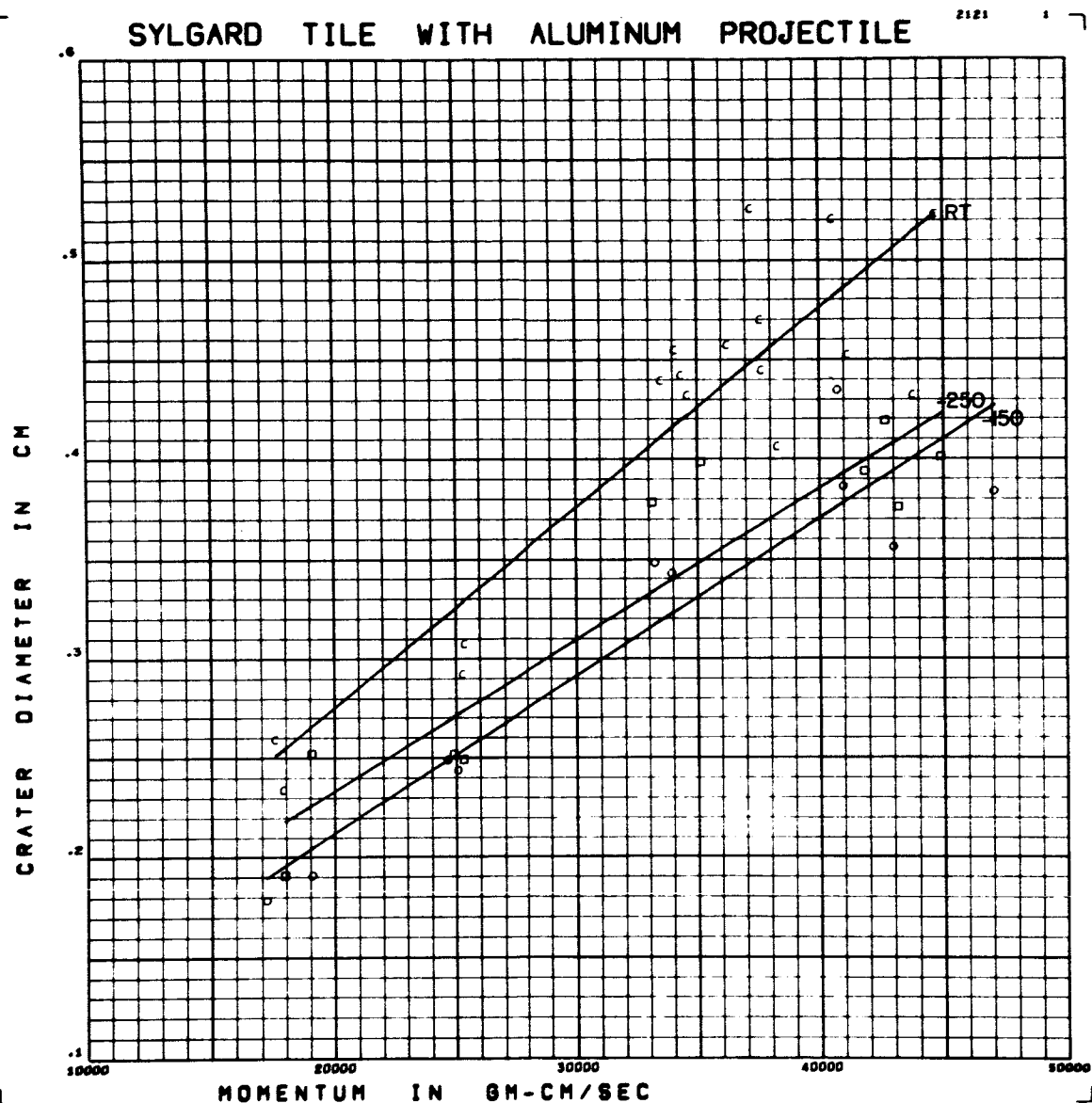


Figure E9 Crater Diameter versus Momentum for Aluminum Projectiles on
Sylgard 325 Tile

Form of Regression: $d = (.825 + .244 ST - .060 CV) \times 10^{-5} M$

RMS Deviation: .034 cm $+ (6.974 - .671 ST - 1.639 CV) \times 10^{-2}$

SYLGARD H.C. WITH ALUMINUM PROJECTILE

2121

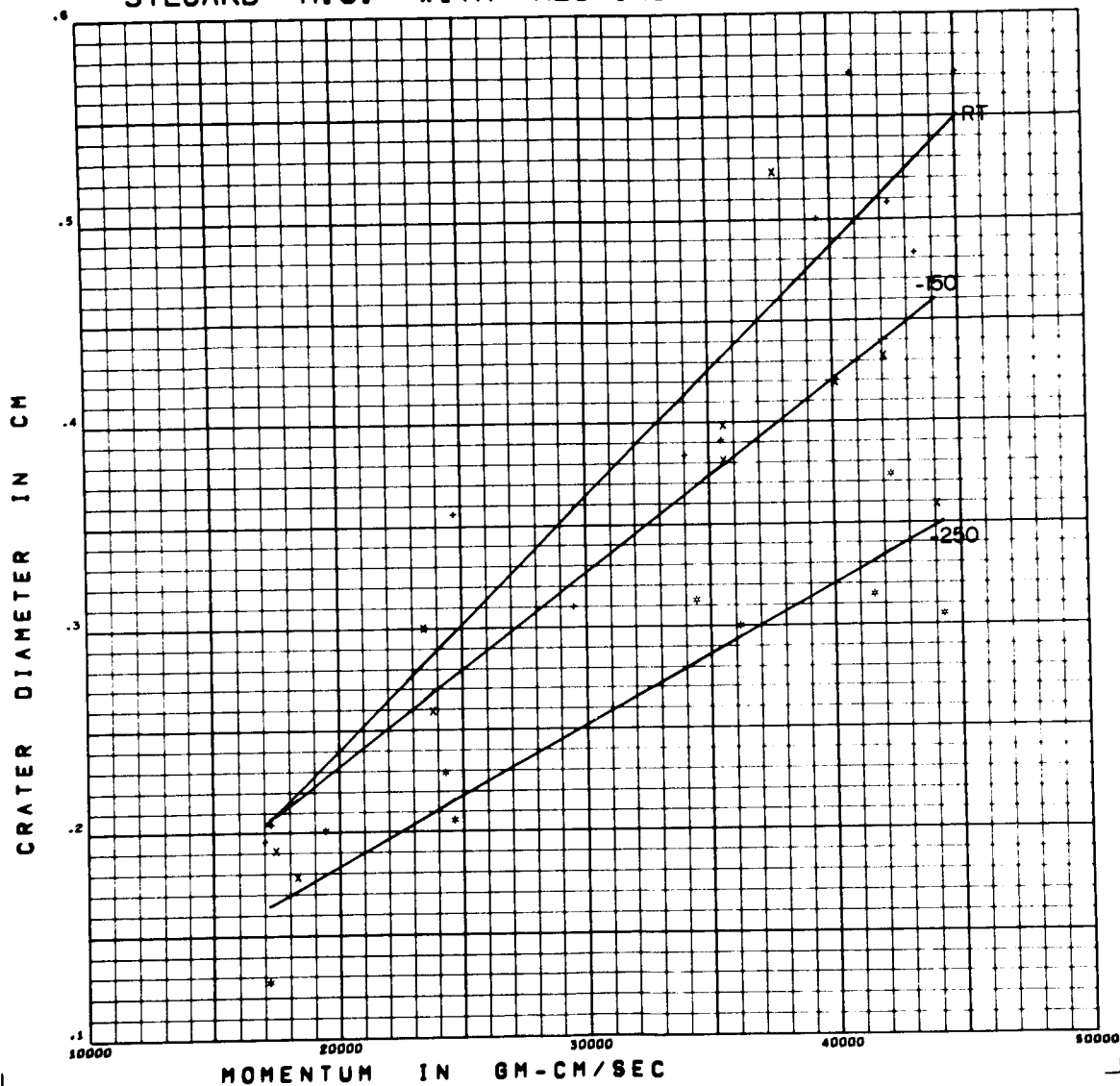


Figure E10 Crater Diameter versus Momentum for Aluminum Projectiles on

Sylgard 325 HC

Form of Regression: $d = (.956 + .550 ST - .010 CV) \times 10^{-5} M$

RMS Deviation: $.042 \text{ cm} + (2.749 - 5.332 ST + 1.558 CV) \times 10^{-2}$

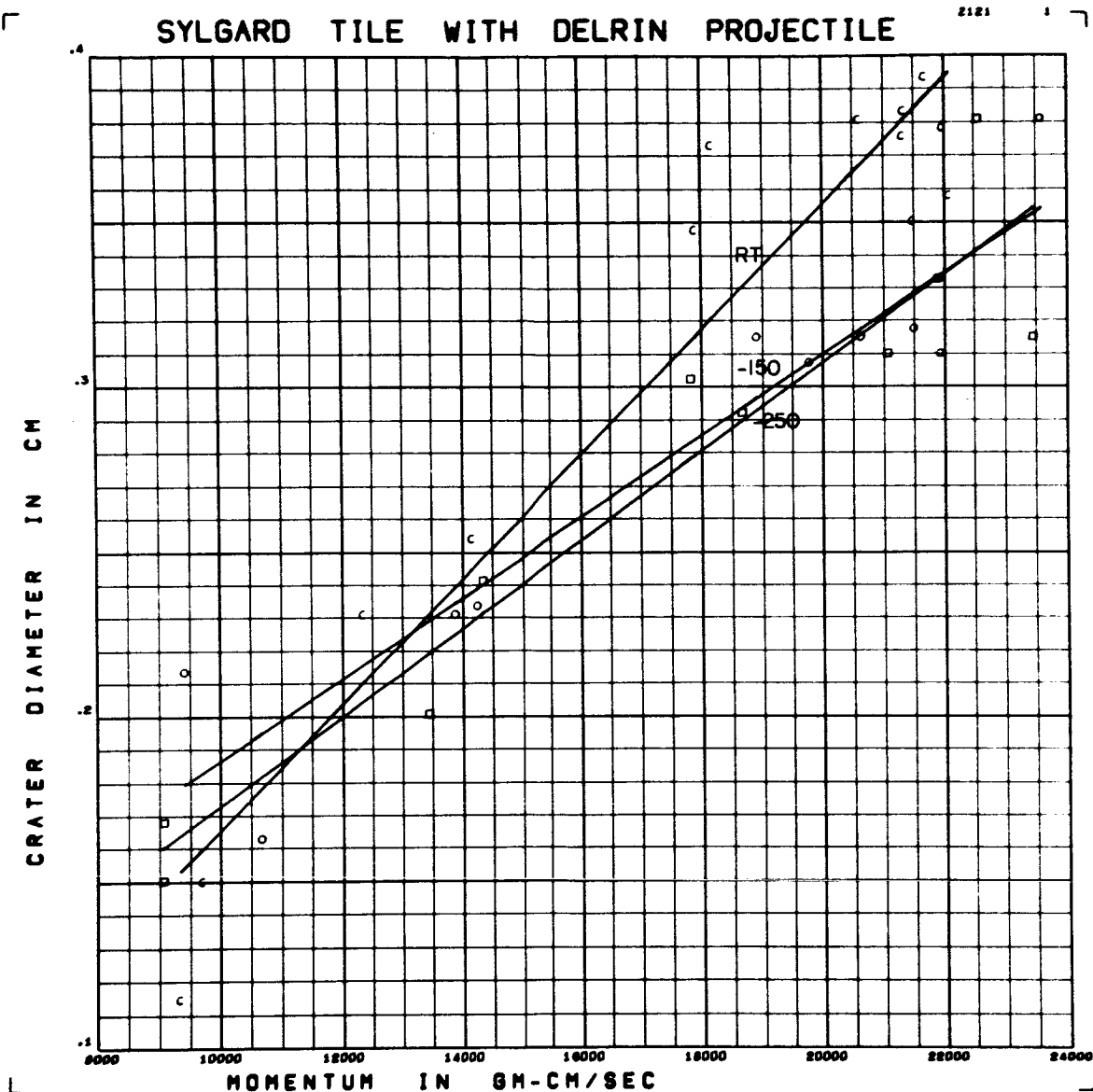


Figure E11 Crater Diameter versus Momentum for Delrin Projectiles on
Sylgard 325 Tile

Form of Regression: $d = (1.494 + .552 ST - .259 CV) \times 10^{-5} M$

RMS Deviation: $.023 \text{ cm} + (2.561 - 6.269 ST + 3.741 CV) \times 10^{-2}$

SYLGARD H.C. WITH DELRIN PROJECTILE

2121

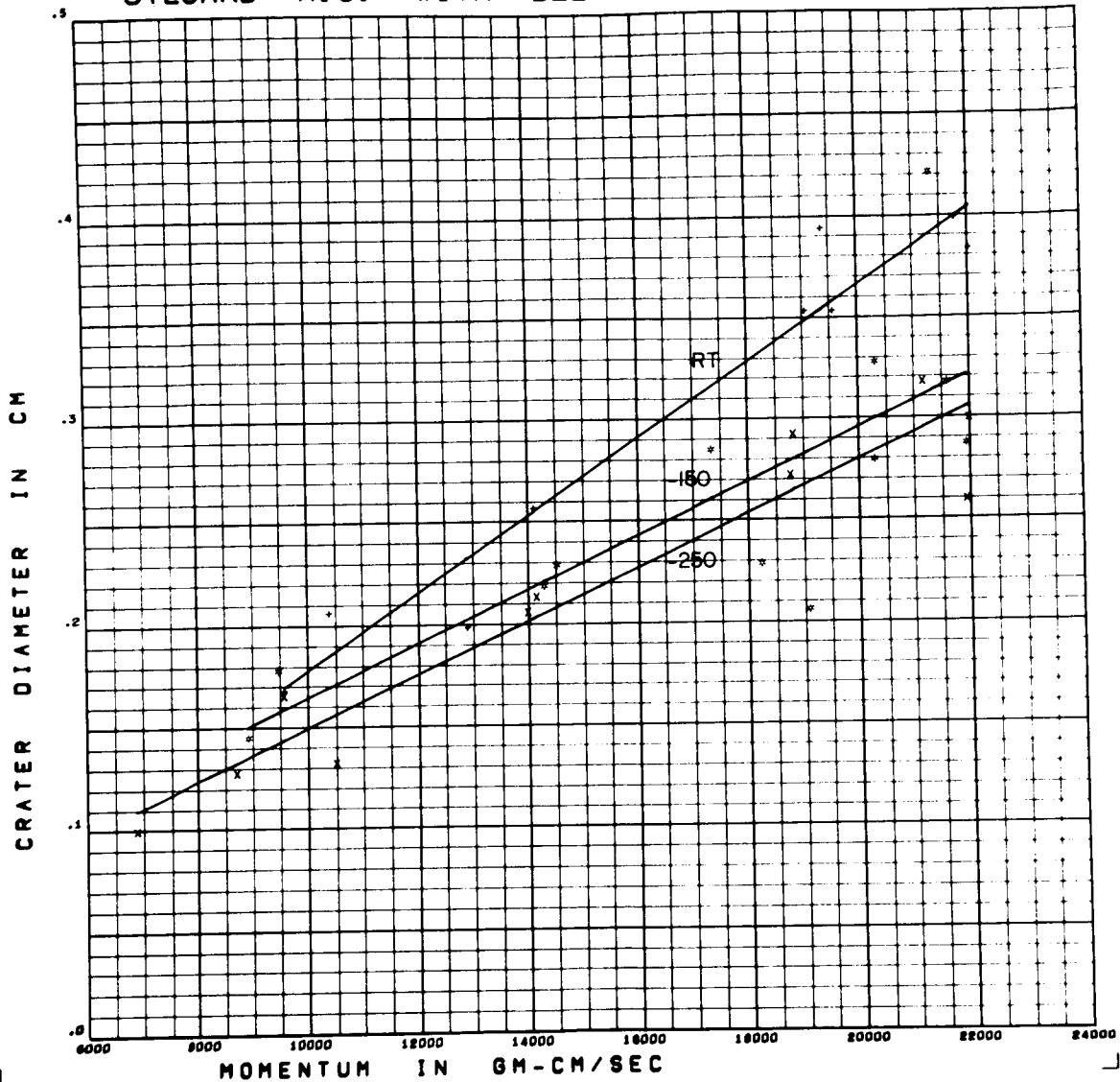


Figure E12 Crater Diameter versus Momentum for Delrin Projectiles on

Sylgard 325 HC

Form of Regression: $d = (1.501 + 5.70 ST - 1.97 CV) \times 10^{-5} M$

RMS Deviation: $.032 cm + (1.399 - 4.350 ST + 5.524 CV) \times 10^{-2}$

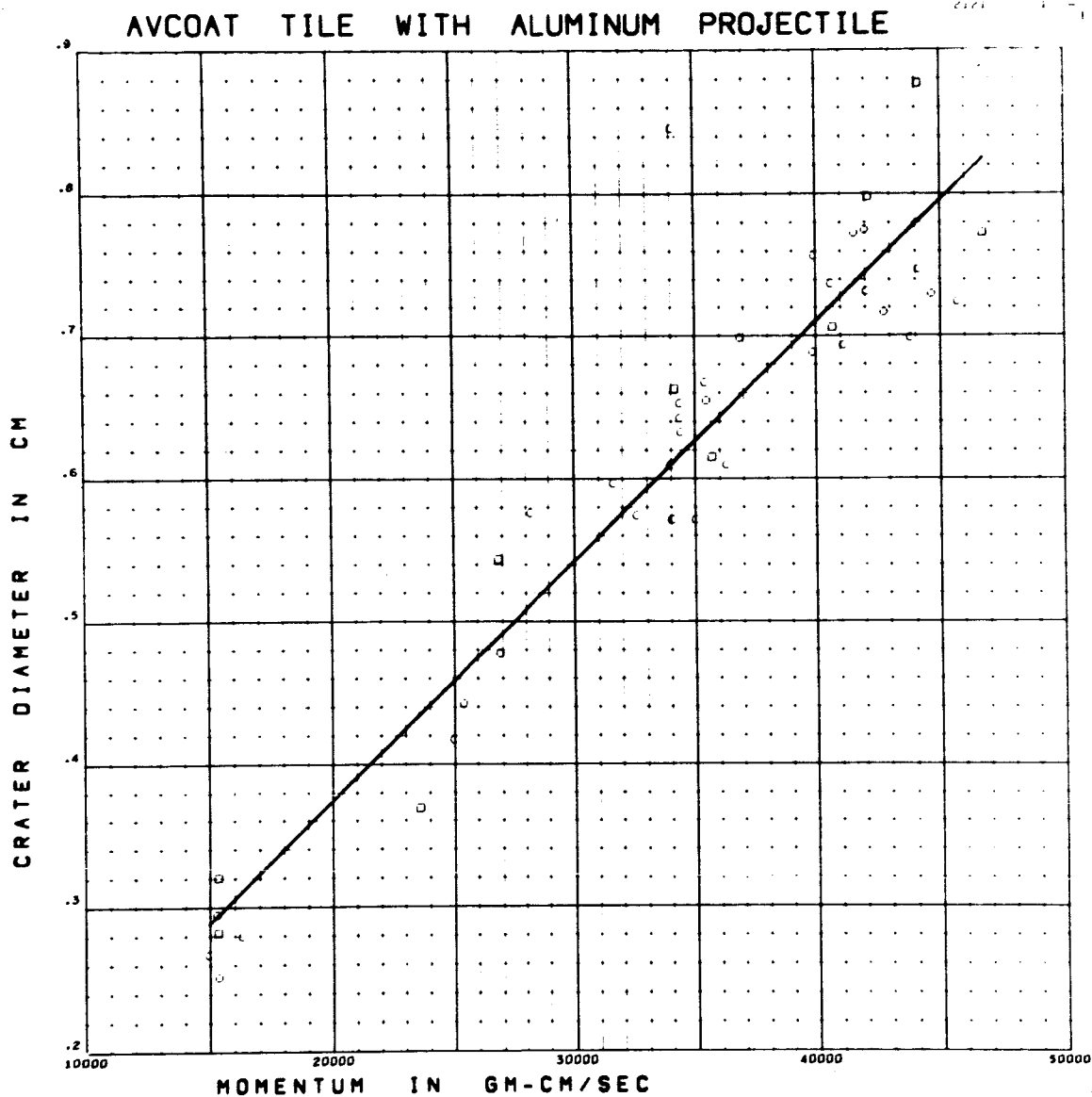


Figure E13 Crater Diameter versus Momentum for Aluminum Projectiles on
Avcoat 5026 Tile

Form of Regression: $d = 1.688 \times 10^{-5} M + 3.635 \times 10^{-2}$

RMS Deviation: .055 cm

AVCOAT H.C. WITH ALUMINUM PROJECTILE

2121

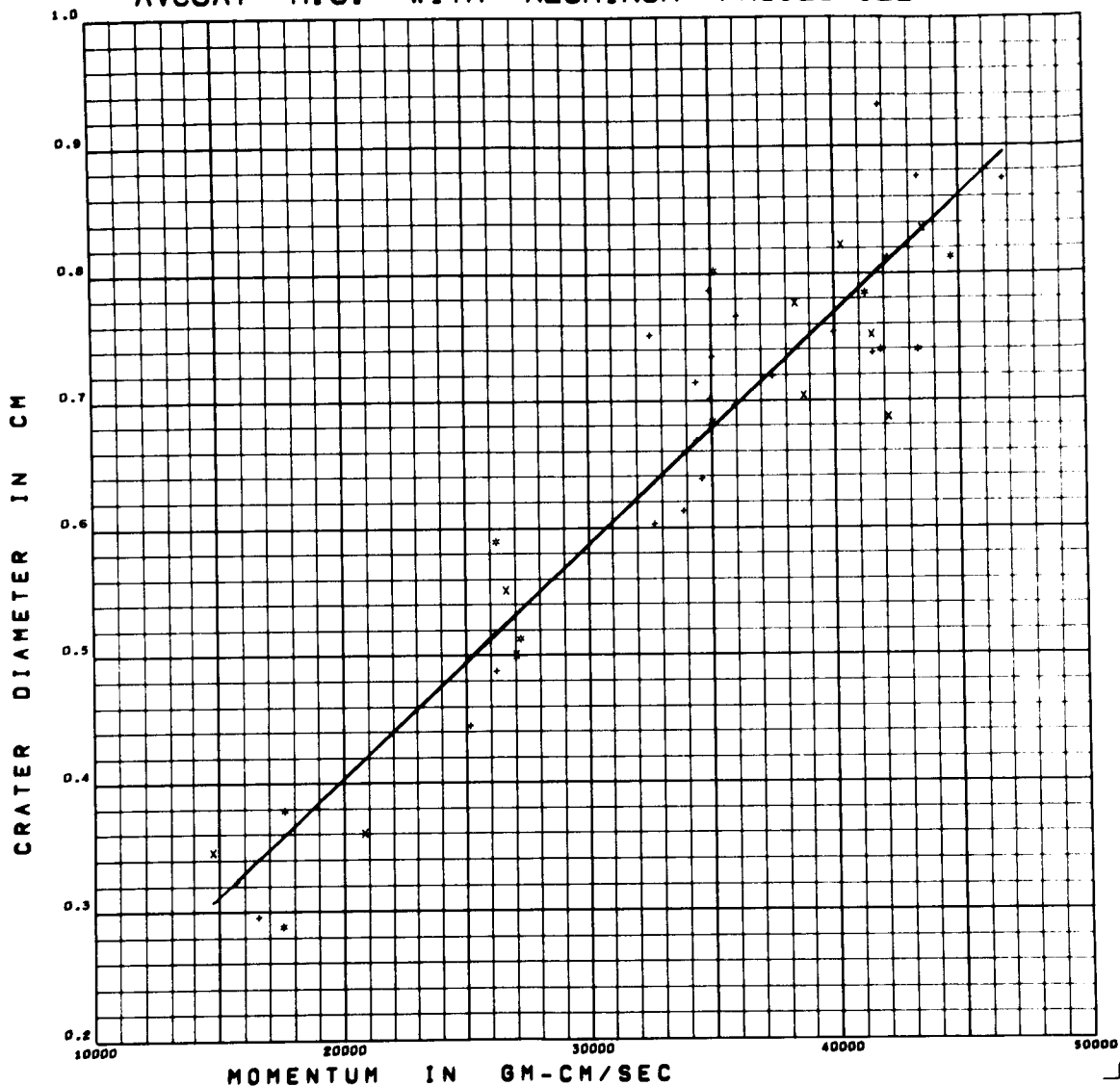


Figure E14 Crater Diameter versus Momentum for Aluminum Projectiles on

Avcoat 5026 HC

Form of Regression: $d = 1.833 \times 10^{-5} M + 3.696 \times 10^{-2}$

RMS Deviation: .058 cm

AVCOAT TILE WITH DELRIN PROJECTILE

2121

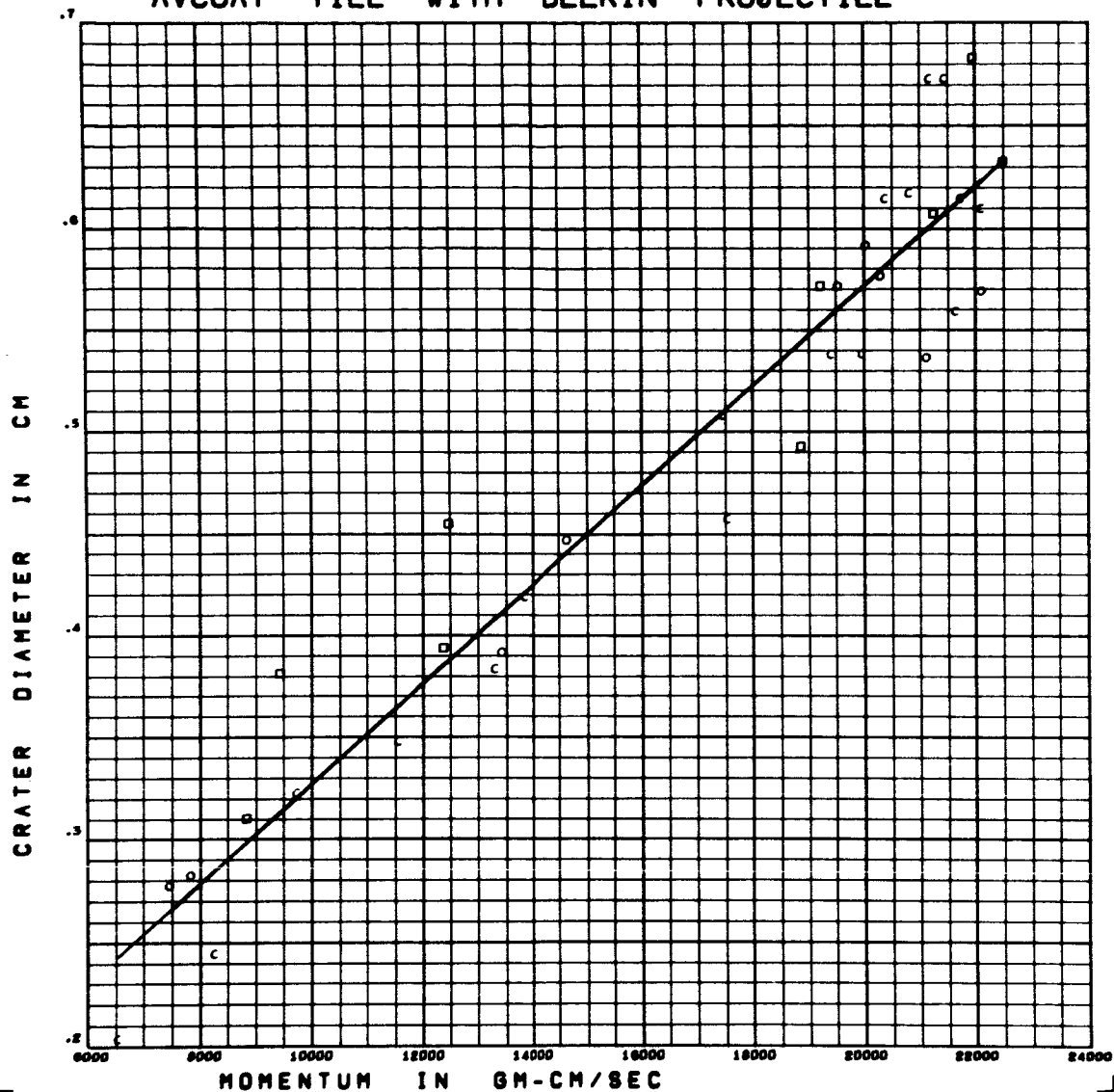


Figure E15 Crater Diameter versus Momentum for Delrin Projectiles on
Avcoat 5026 Tile

Form of Regression: $d = 2.446 \times 10^{-5} M + 8.283 \times 10^{-2}$

RMS Deviation: .037 cm

AVCOAT H.C. WITH DELRIN PROJECTILE

2121

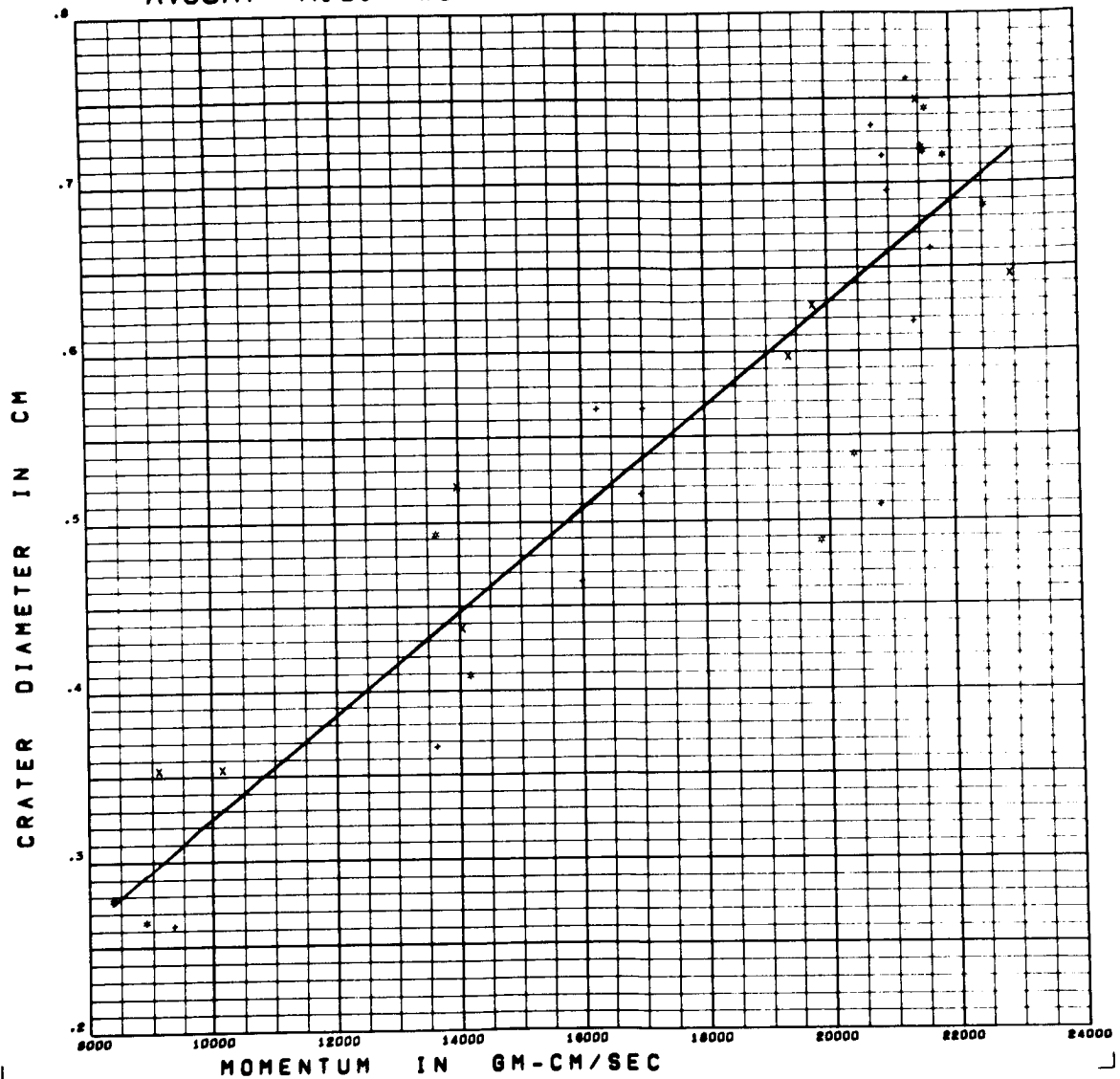


Figure E16 Crater Diameter versus Momentum for Delrin Projectiles on
Avcoat 5026 HC

Form of Regression: $d = 3.039 \times 10^{-5} M + 2.115 \times 10^{-2}$

RMS Deviation: .063 cm

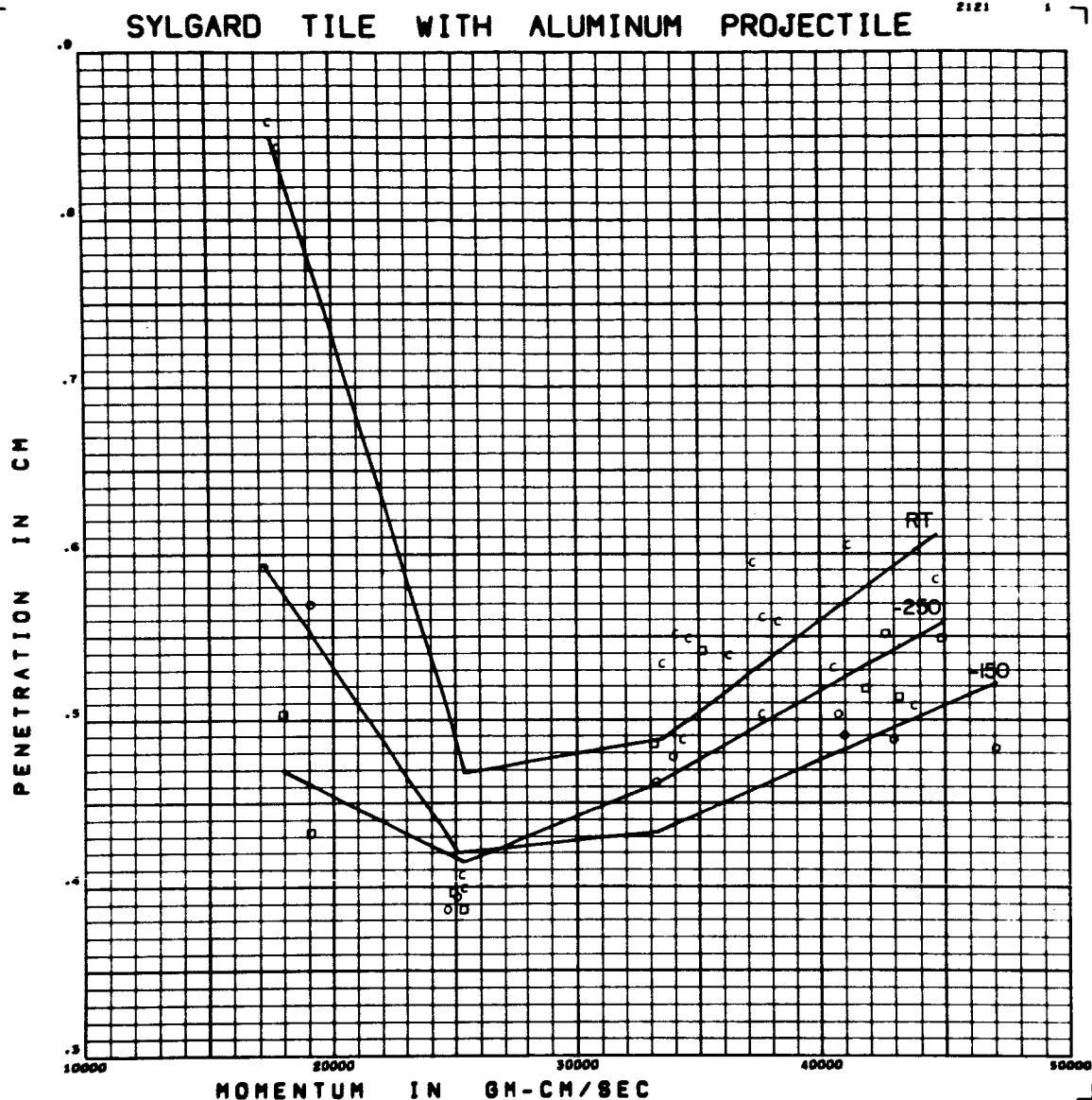


Figure E17 Penetration versus Momentum for Aluminum Projectiles on
Sylgard 325 Tile

Form of Regression: $p = (.860 + .2725T - .212CV) \times 10^{-5} M$

RMS Deviation: $.038 \text{ cm} + (17.34 - 6.6405T + 4.307CV) \times 10^{-2}$

SYLGARD H.C. WITH ALUMINUM PROJECTILE

2121

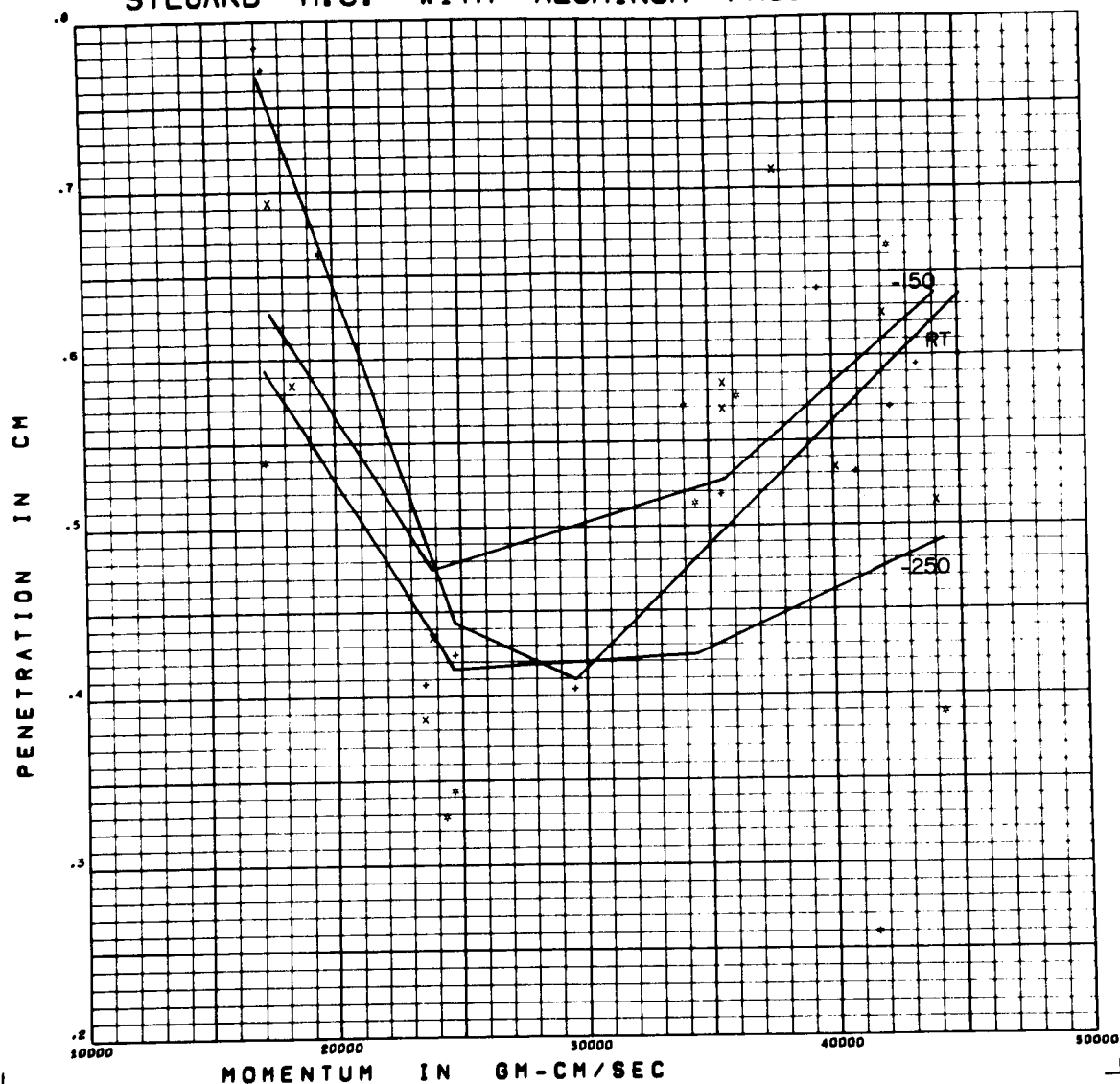


Figure E18 Penetration versus Momentum for Aluminum Projectiles on
Sylgard 325 HC

Form of Regression: $p = (1.144 + 7.805T + 1.150CV) \times 10^{-5} M$

RMS Deviation: .090 cm $+ (7.836 - 21.195T - 1.185CV) \times 10^{-2}$

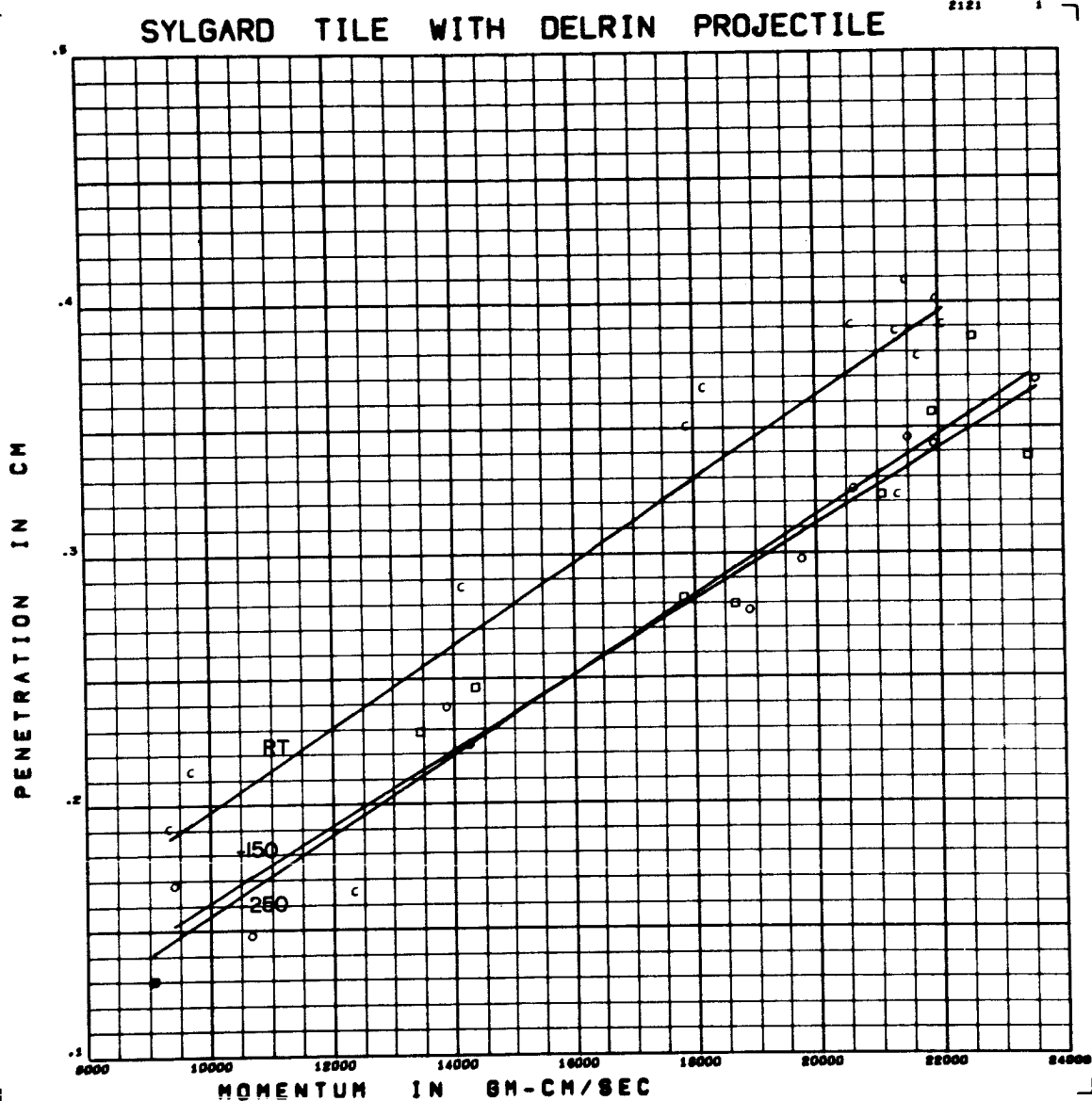


Figure E19 Penetration versus Momentum for Delrin Projectiles on

Sylgard 325 Tile

Form of Regression: $p = (1.586 + .0585T - .078CV) \times 10^{-5} M$

RMS Deviation: .023 cm $+(1.271 + 3.5725T - .256CV) \times 10^{-2}$

SYLGARD H.C. WITH DELRIN PROJECTILE

2121

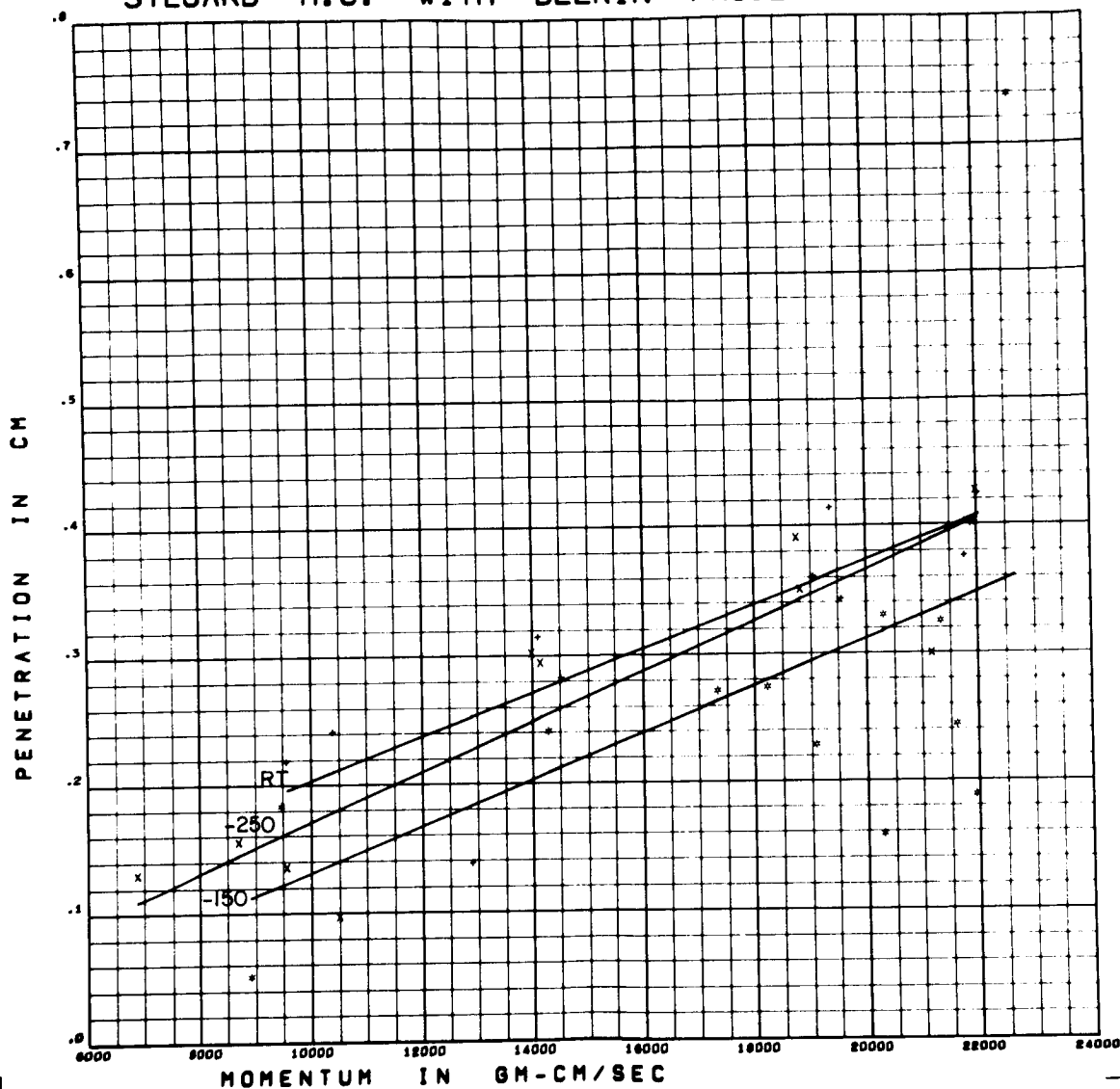
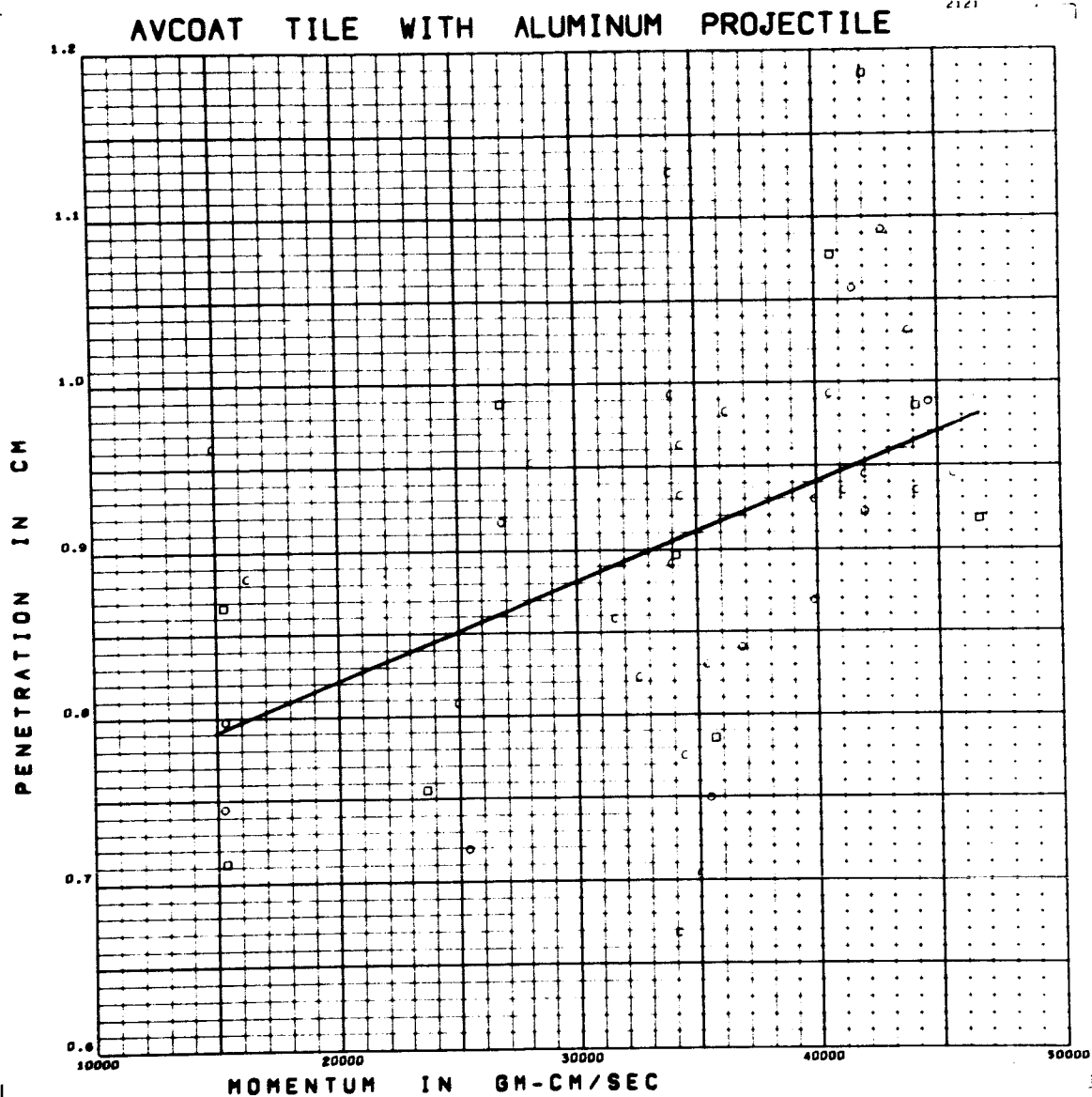


Figure E20 Penetration versus Momentum for Delrin Projectiles on

Sylgard 325 HC

Form of Regression: $p = (1.822 - .108 ST + .134 CV) \times 10^{-5} M$

RMS Deviation: .091 cm $+ (-1.374 + 8.267 ST - 1.118 CV) \times 10^{-2}$



AVCOAT H.C. WITH ALUMINUM PROJECTILE

2121

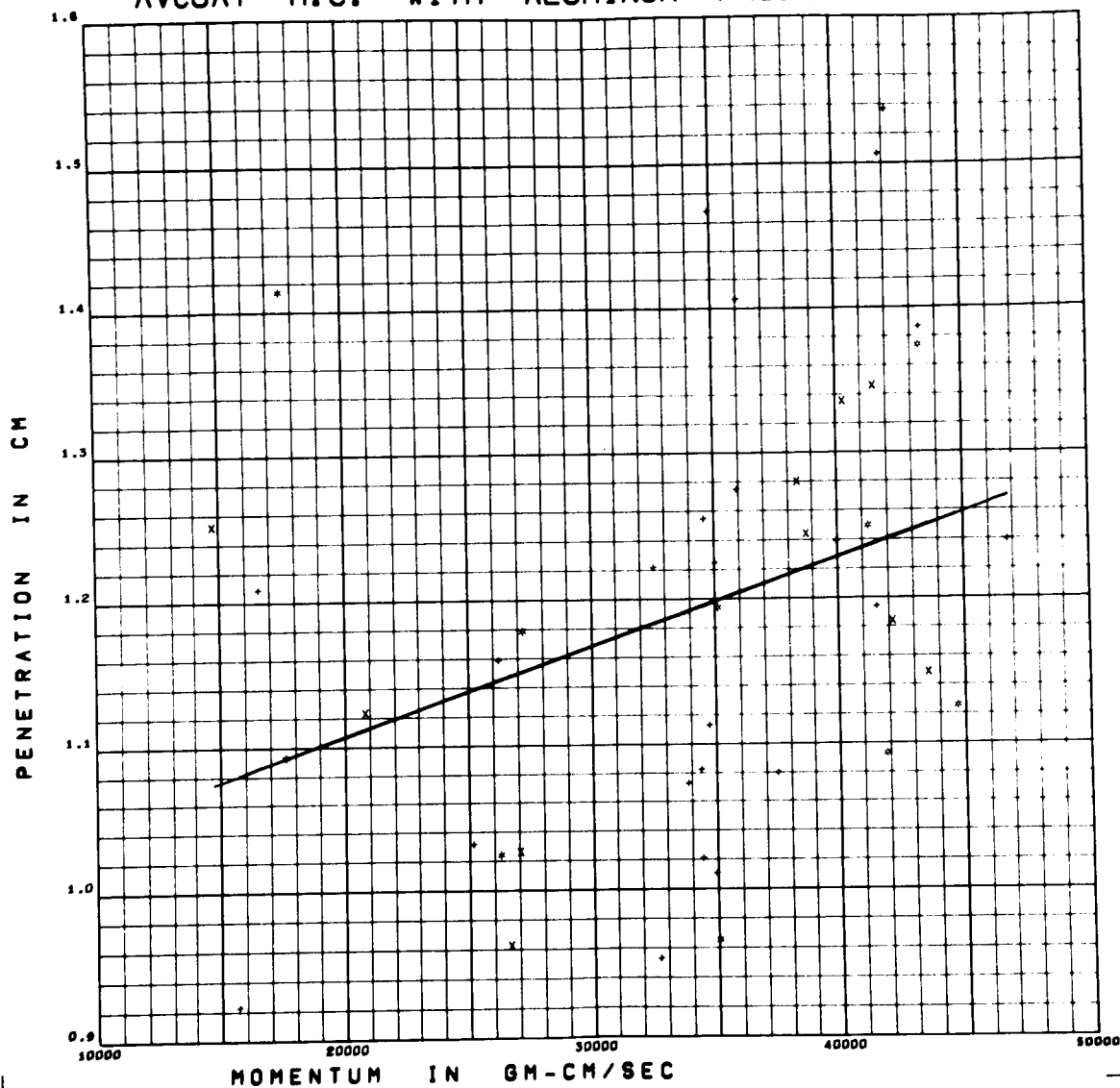


Figure E22 Penetration versus Momentum for Aluminum Projectiles on

Avcoat 5026 HC

Form of Regression: $p = .609 \times 10^{-5} M + .985$

RMS Deviation: .145 cm

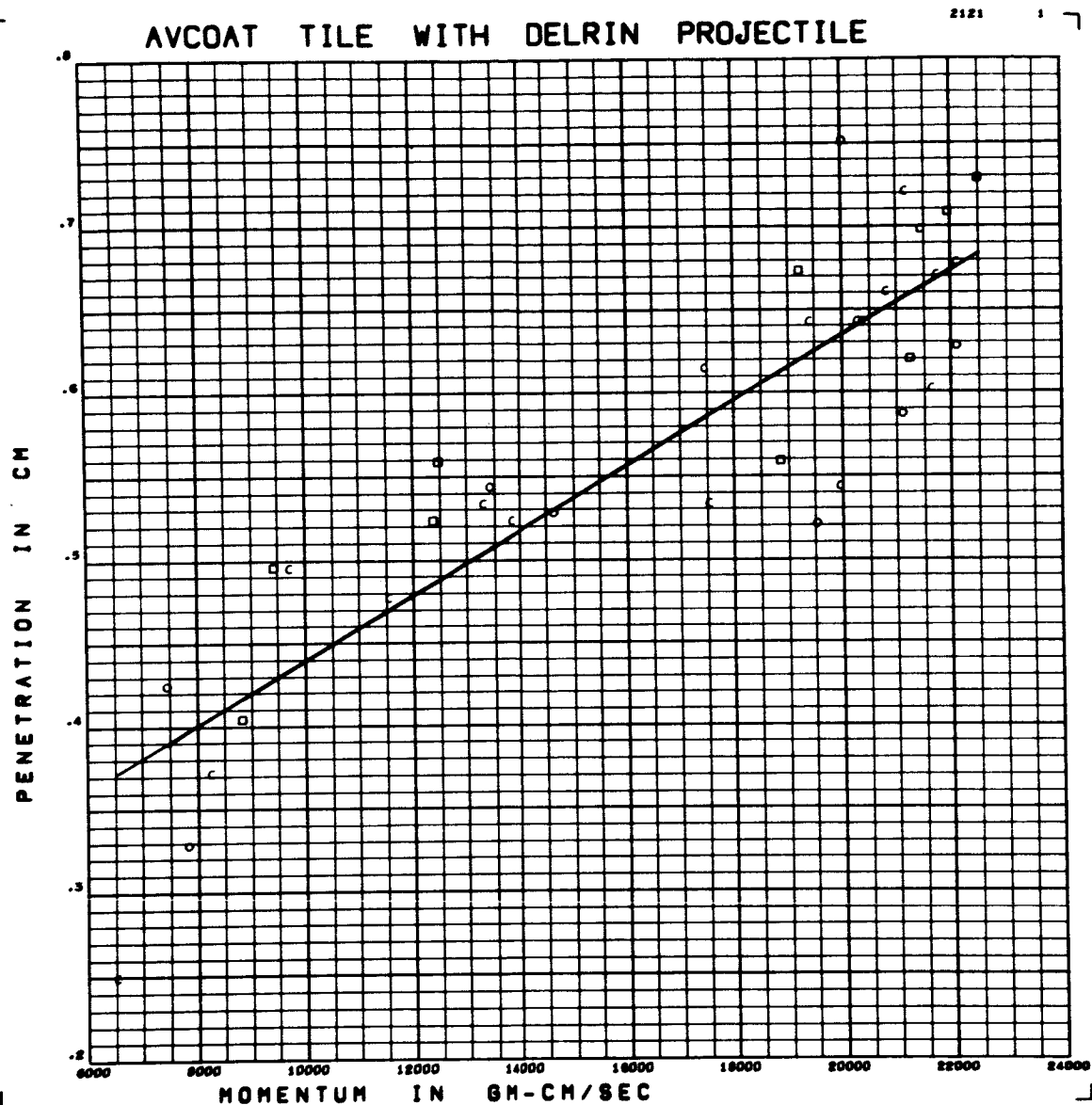


Figure E23 Penetration versus Momentum for Delrin Projectiles on

Avcoat 5026 Tile

Form of Regression: $p = 1.955 \times 10^{-5} M + .244$

RMS Deviation: .055 cm

AVCOAT H.C. WITH DELRIN PROJECTILE

2121

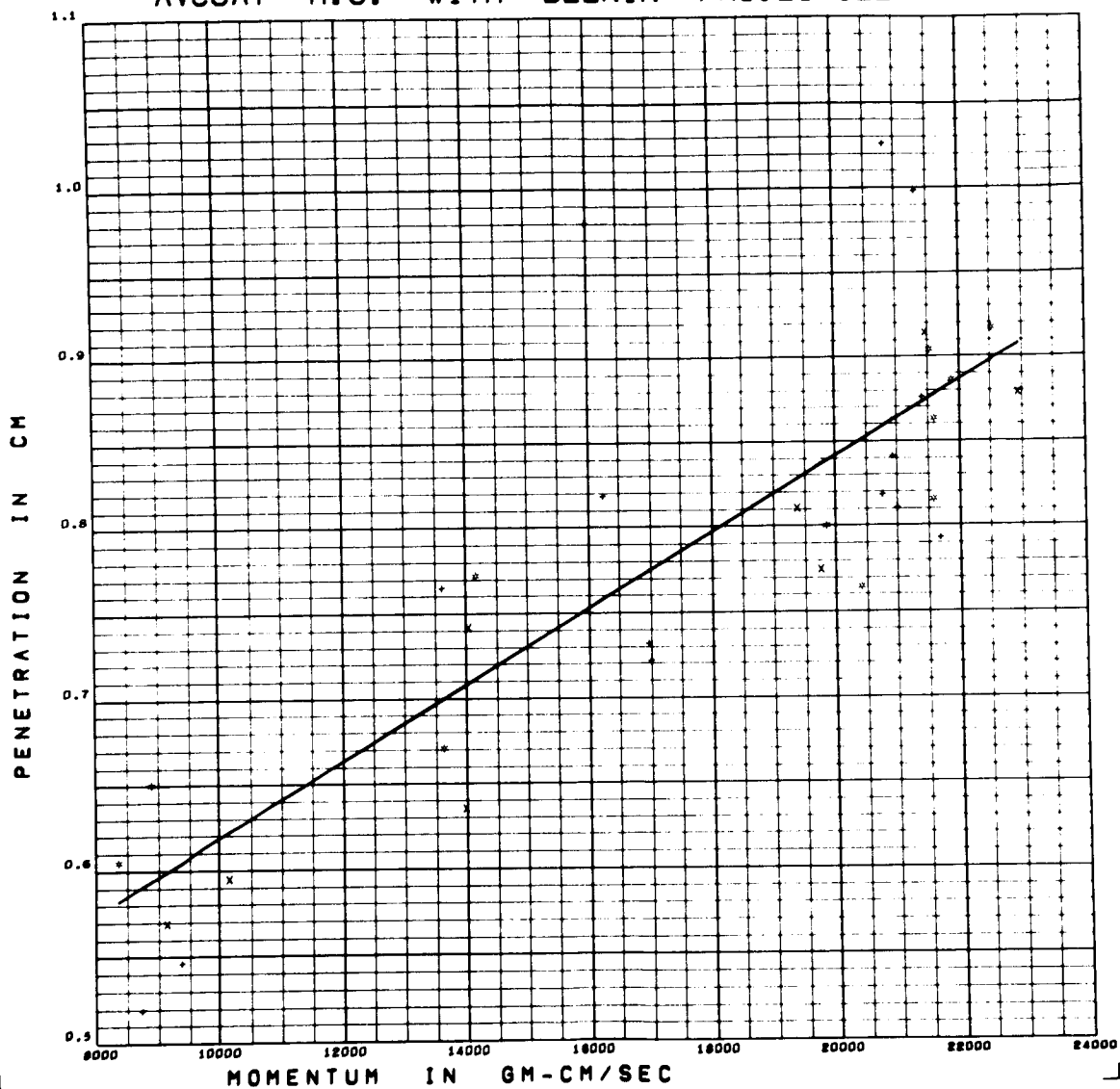


Figure E24 Penetration versus Momentum for Delrin Projectiles on
Avcoat 5026 HC

Form of Regression: $p = 2.231 \times 10^{-5} M + .396$

RMS Deviation: .072 cm

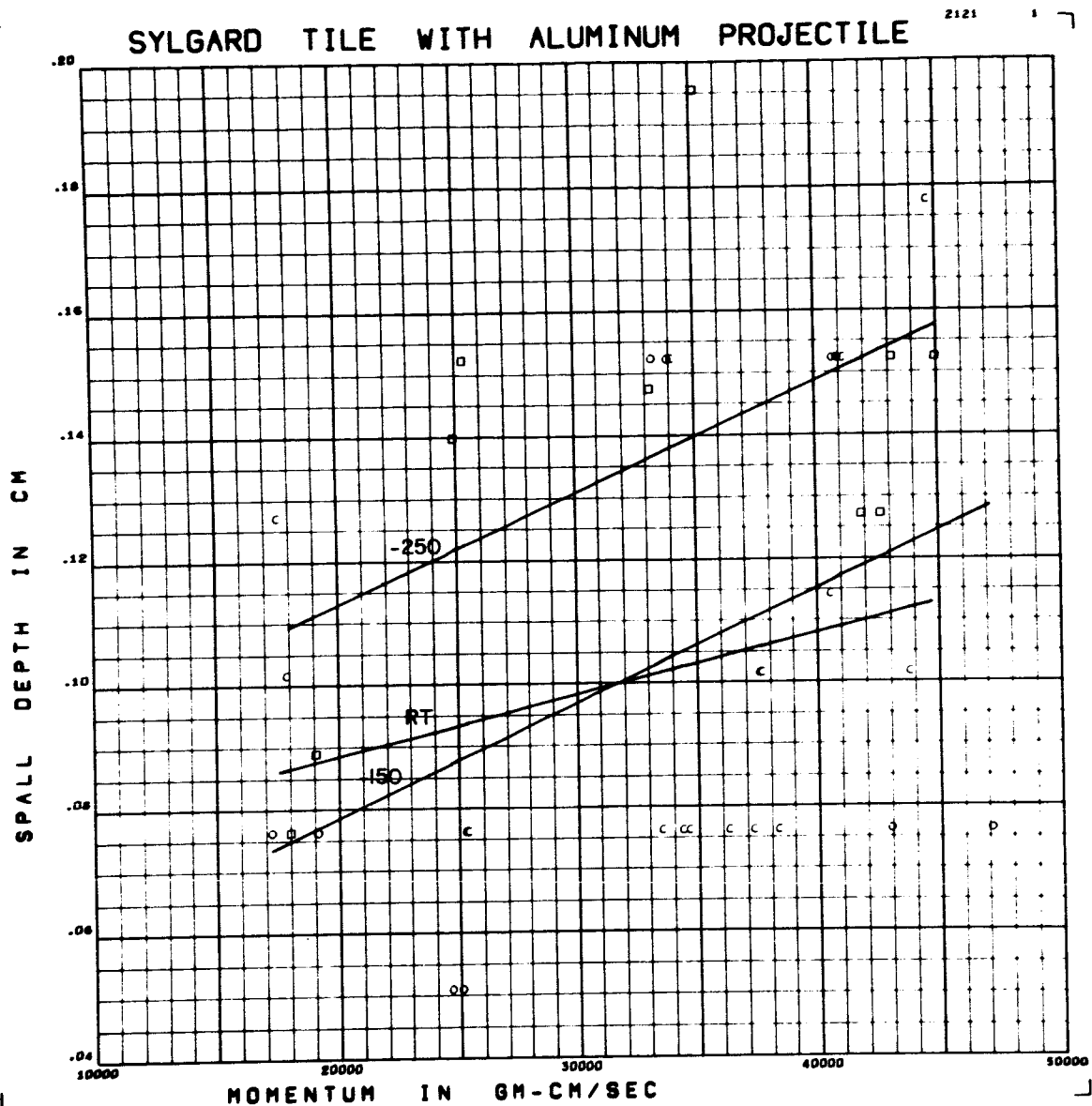


Figure E25 Spall Depth versus Momentum for Aluminum Projectiles on

Sylgard 325 Tile

Form of Regression: $P_s = (.154 - .0805T + .030CV) \times 10^{-5}M$

RMS Deviation: .034 cm. $+(6.26 - .845T - 2.08CV) \times 10^{-2}$

SYLGARD H.C. WITH ALUMINUM PROJECTILE

2121

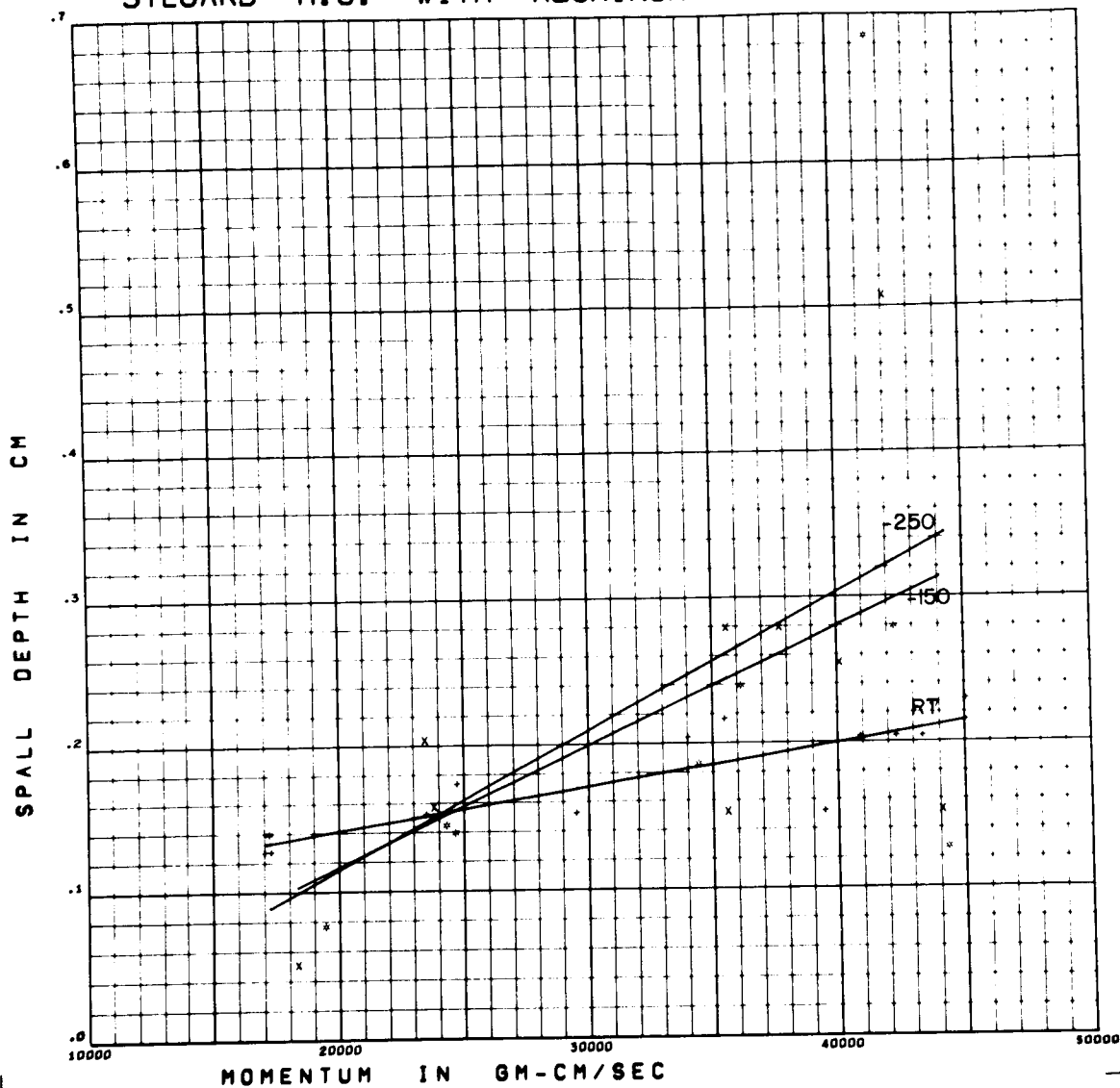


Figure E26 Spall Depth versus Momentum for Aluminum Projectiles on

Sylgard 325 HC

Form of Regression: $P_s = (.682 - .650 ST + .134 CV) \times 10^{-5} M$

RMS Deviation: $.099 \text{ cm} + (-1.20 + 15.67 ST - 3.45 CV) \times 10^{-2}$

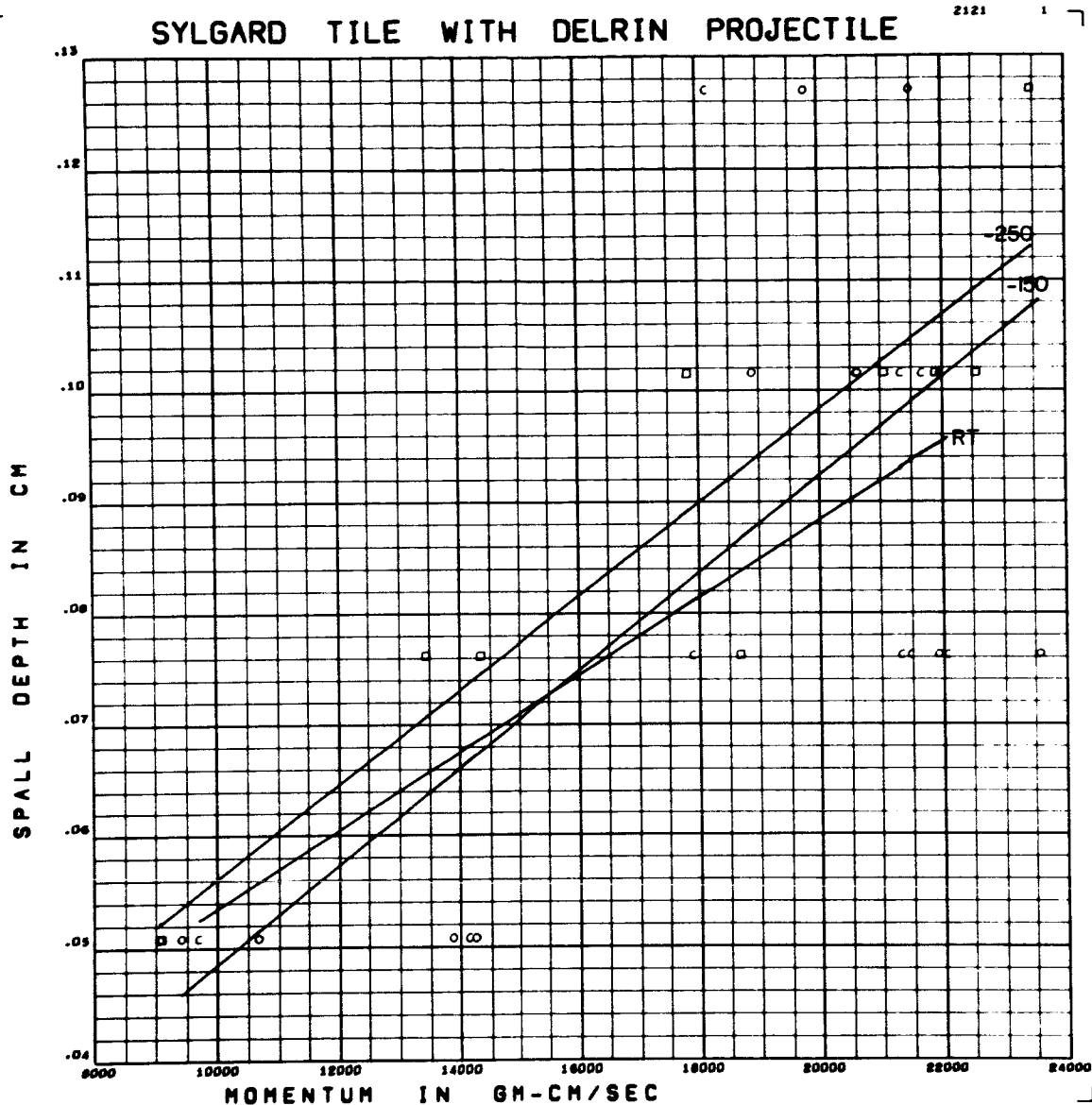


Figure E27 Spall Depth versus Momentum for Delrin Projectiles on
Sylgard 325 Tile

Form of Regression: $p_s = (.404 - .0735T + .035CV) \times 10^{-5} M$

RMS Deviation: $.017 \text{ cm} + (1.24 + .465T - .77CV) \times 10^{-2}$

SYLGARD H.C. WITH DELRIN PROJECTILE

2121

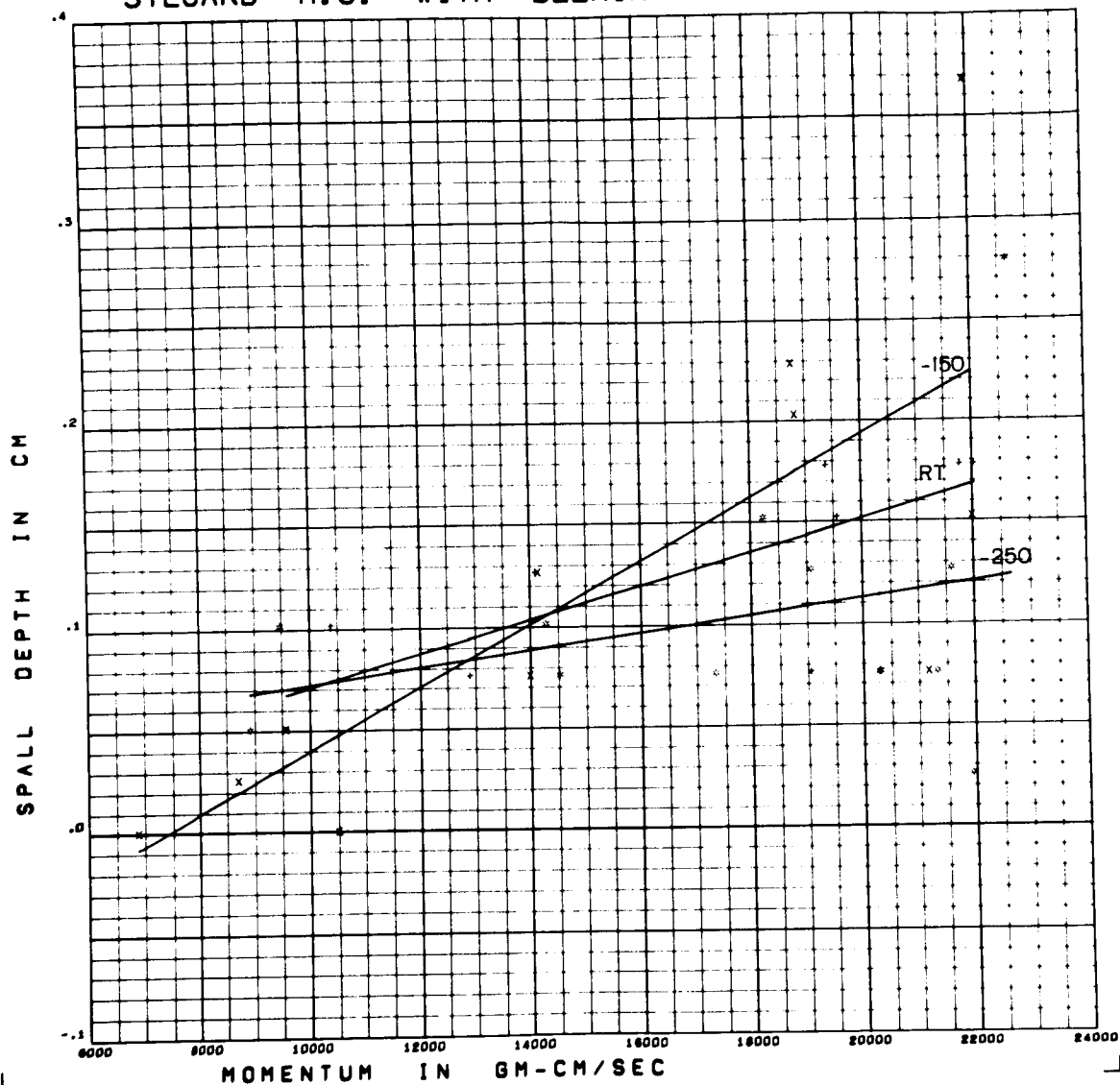


Figure E28 Spall Depth versus Momentum for Delrin Projectiles on

Sylgard 325 HC

Form of Regression: $p_s = (.917 + .403ST + .618CV) \times 10^{-5} M$

RMS Deviation: .057 cm $+ (-3.05 - 4.13ST - 8.29CV) \times 10^{-2}$

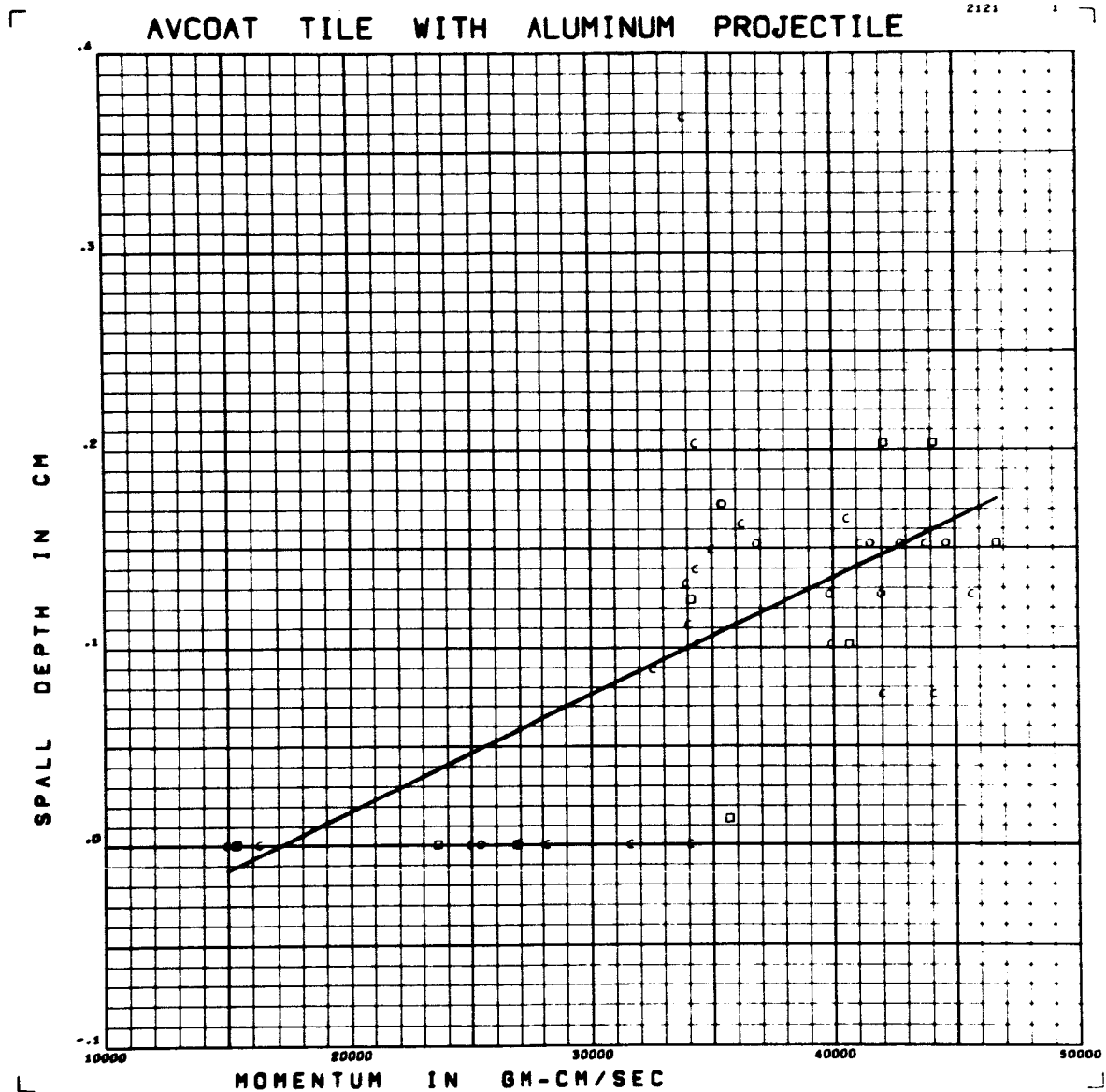


Figure E29 Spall Depth versus Momentum for Aluminum Projectiles on

Avcoat 5026 Tile

Form of Regression: $p_s = .591 \times 10^{-5} M^{-.101}$

RMS Deviation: .062 cm

AVCOAT H.C. WITH ALUMINUM PROJECTILE

2121

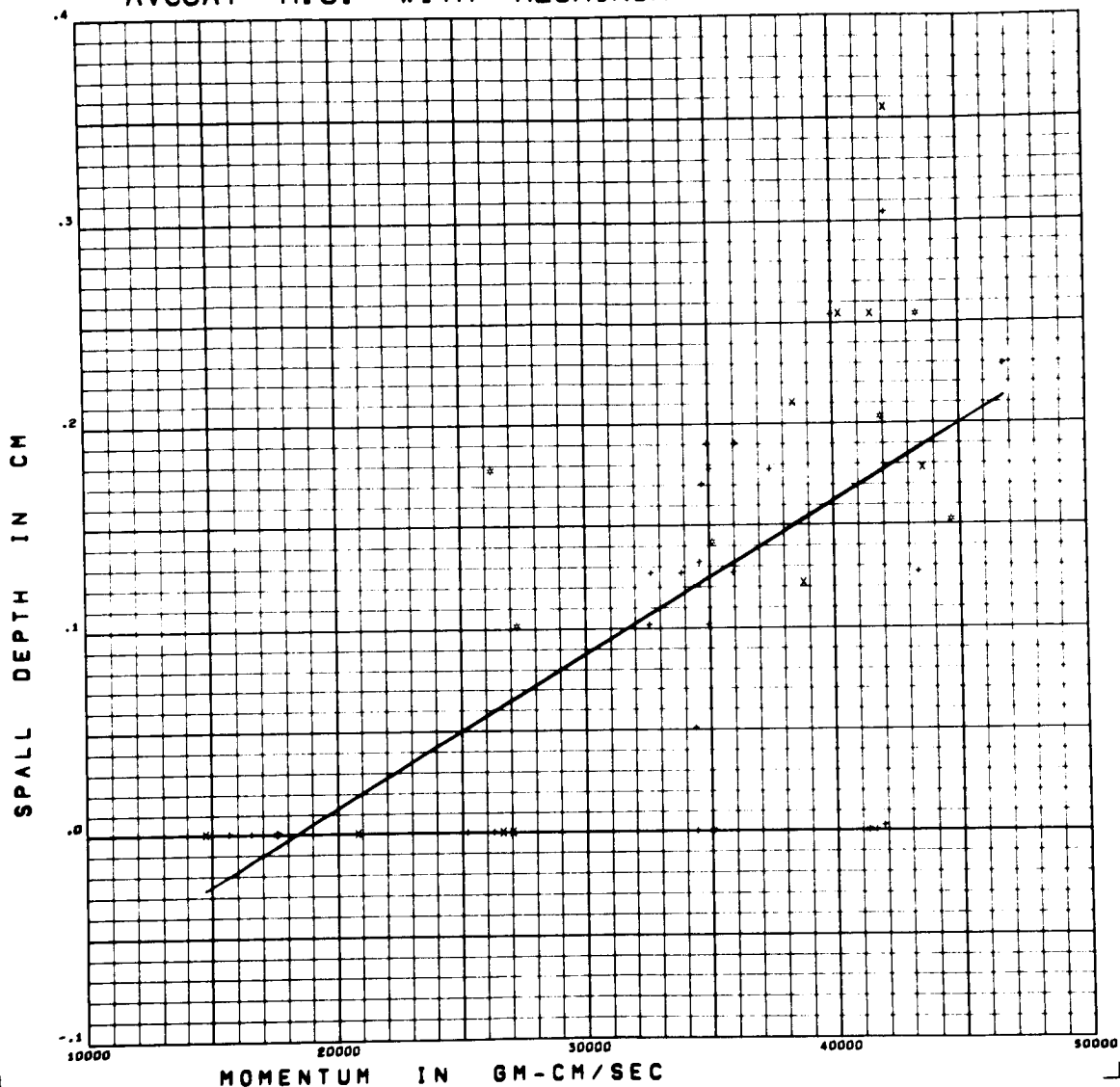


Figure E30 Spall Depth versus Momentum for Aluminum Projectiles on

Avcoat 5026 HC

Form of Regression: $p_s = .749 \times 10^{-5} M^{-.137}$

RMS Deviation: .078 cm

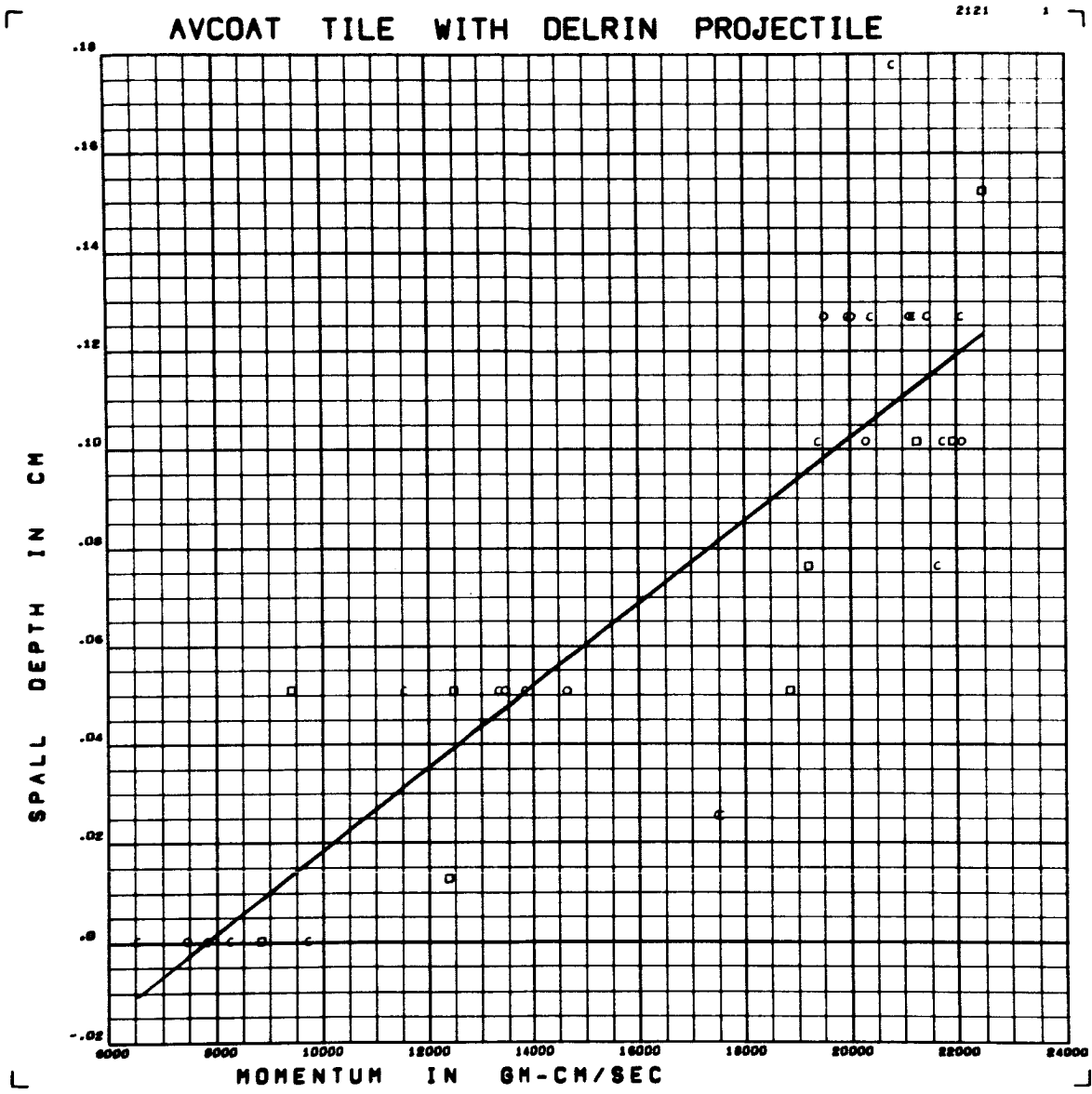


Figure E31 Spall Depth versus Momentum for Delrin Projectiles on

Avcoat 5026 Tile

Form of Regression: $p_s = .839 \times 10^{-5} M^{-.065}$

RMS Deviation: .026 cm

AVCOAT H.C. WITH DELRIN PROJECTILE

2121

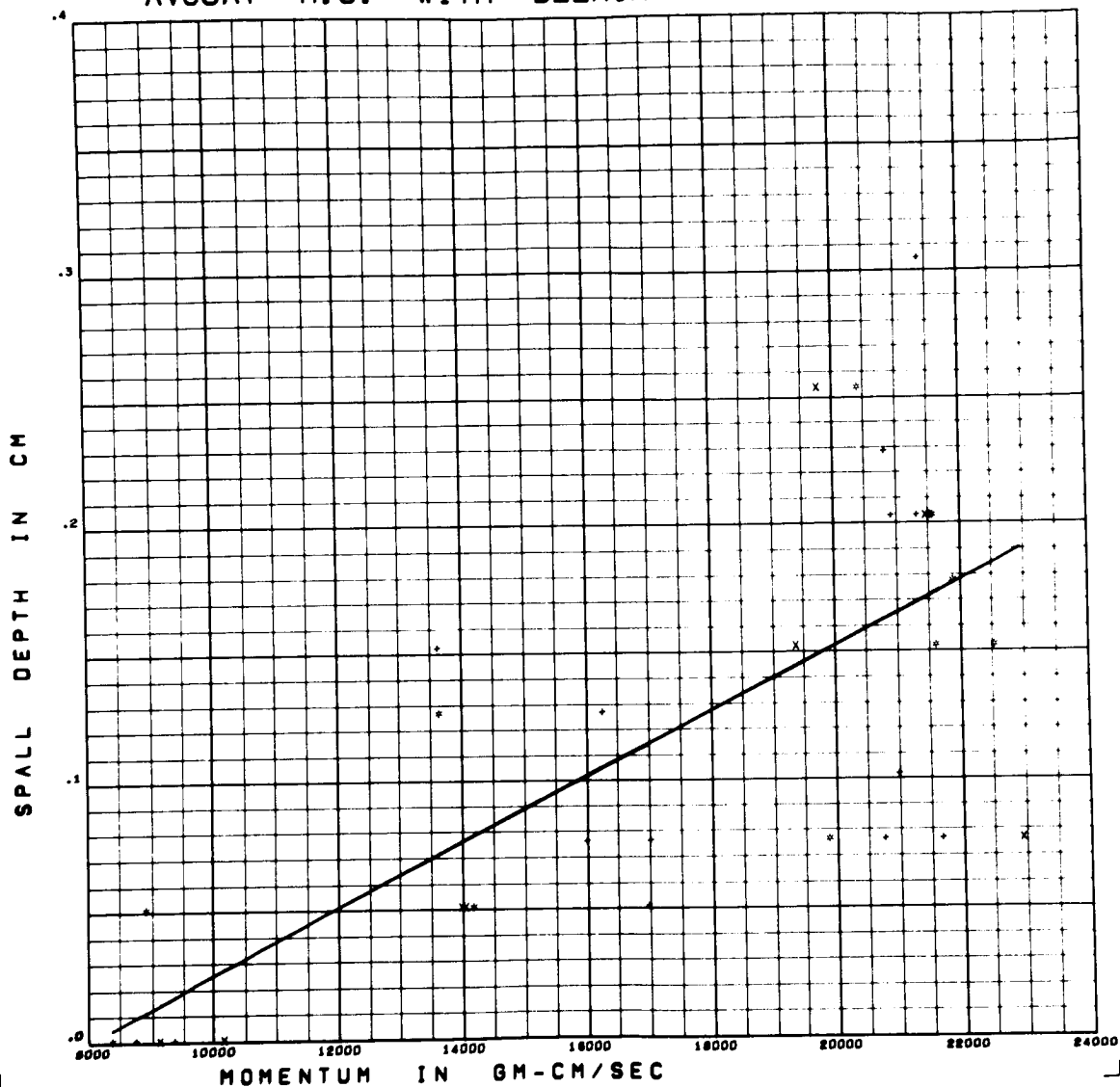


Figure E32 Spall Depth versus Momentum for Delrin Projectiles on
Avcoat 5026 HC

Form of Regression: $p_s = 1.272 \times 10^{-5} M - .102$

RMS Deviation: .059 cm

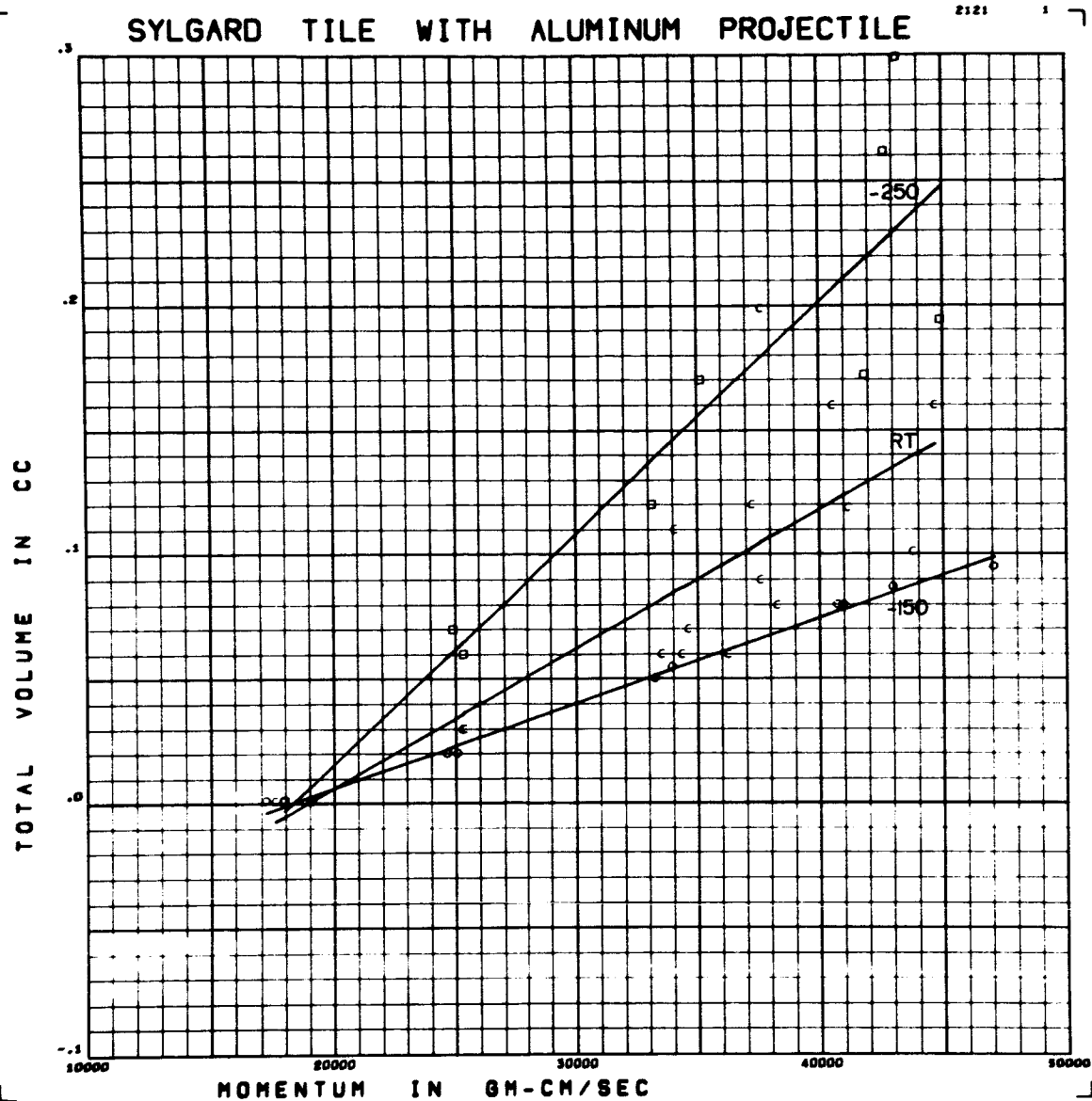


Figure E33 Volume versus Momentum for Aluminum Projectiles on Sylgard 325 Tile

Form of Regression: $v = (.611 - .3705T - .267CV) \times 10^{-5} M$
 $+ (-11.28 + 6.465T + 5.01CV) \times 10^{-2}$

RMS Deviation: .028 cc

SYLGARD H.C. WITH ALUMINUM PROJECTILE

2121

1

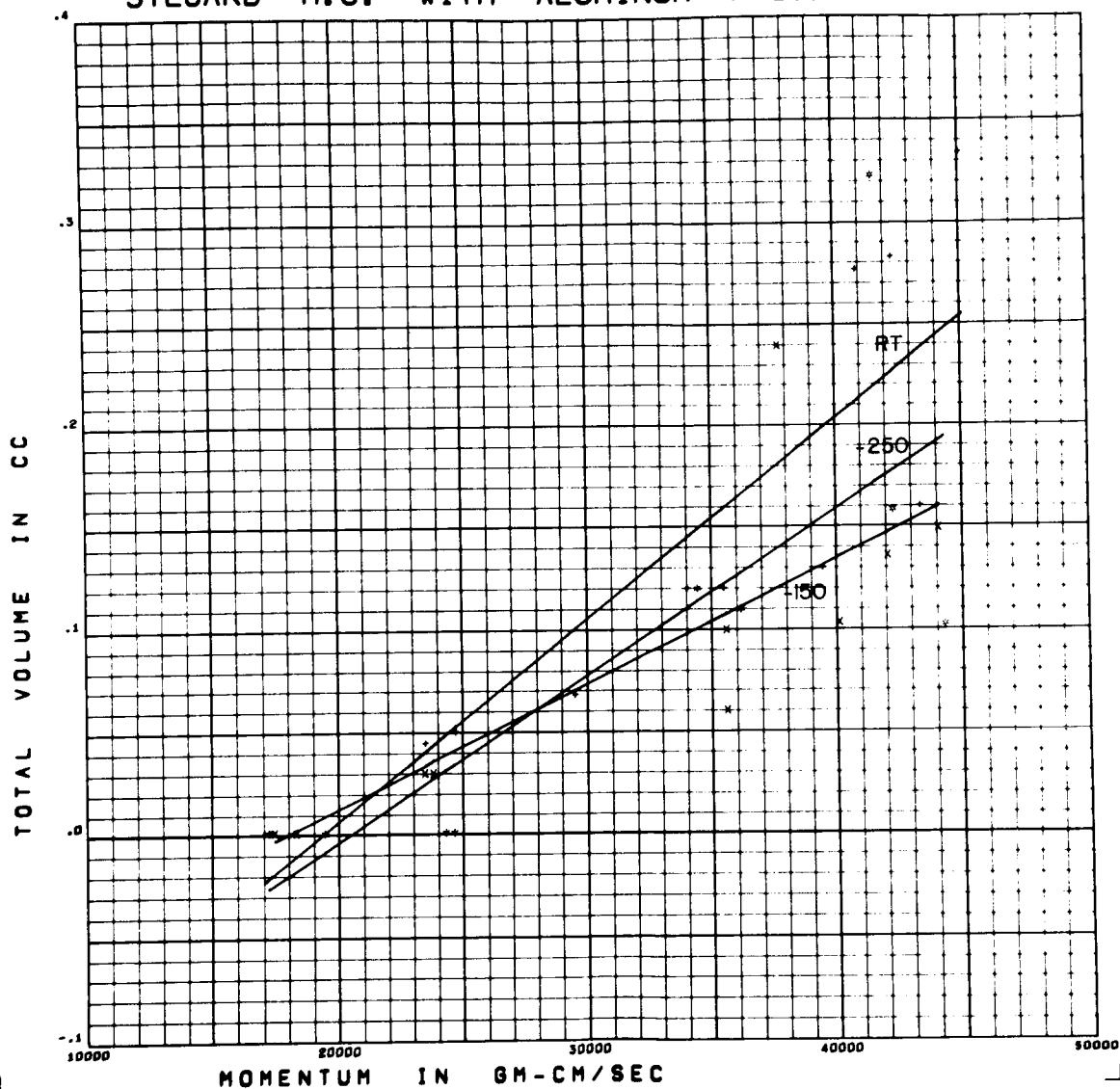


Figure E34 Volume versus Momentum for Aluminum Projectiles on Sylgard 325 HC

Form of Regression: $V = (.805 - .175ST - .193CV) \times 10^{-5} M$

RMS Deviation: $.052CC + (-15.6 - 2.50ST + 4.59CV) \times 10^{-2}$

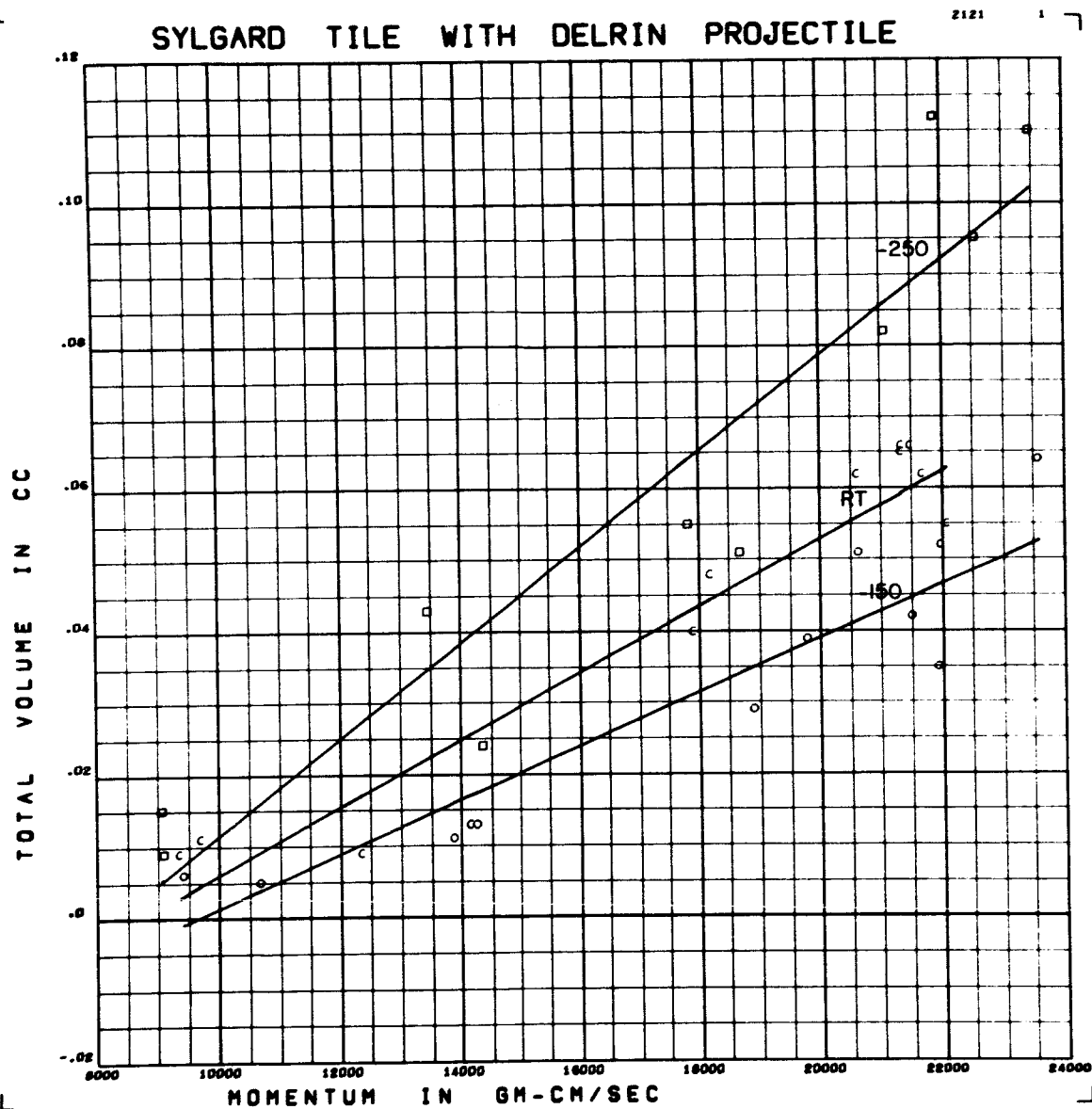


Figure E35 Volume versus Momentum for Delrin Projectiles on Sylgard 325 Tile

Form of Regression: $V = (.506 - .2025T - .129CV) \times 10^{-5} M$

RMS Deviation: $.009cc + (-4.43 + 1.465T + .80CV) \times 10^{-2}$

SYLGARD H.C. WITH DELRIN PROJECTILE

2121

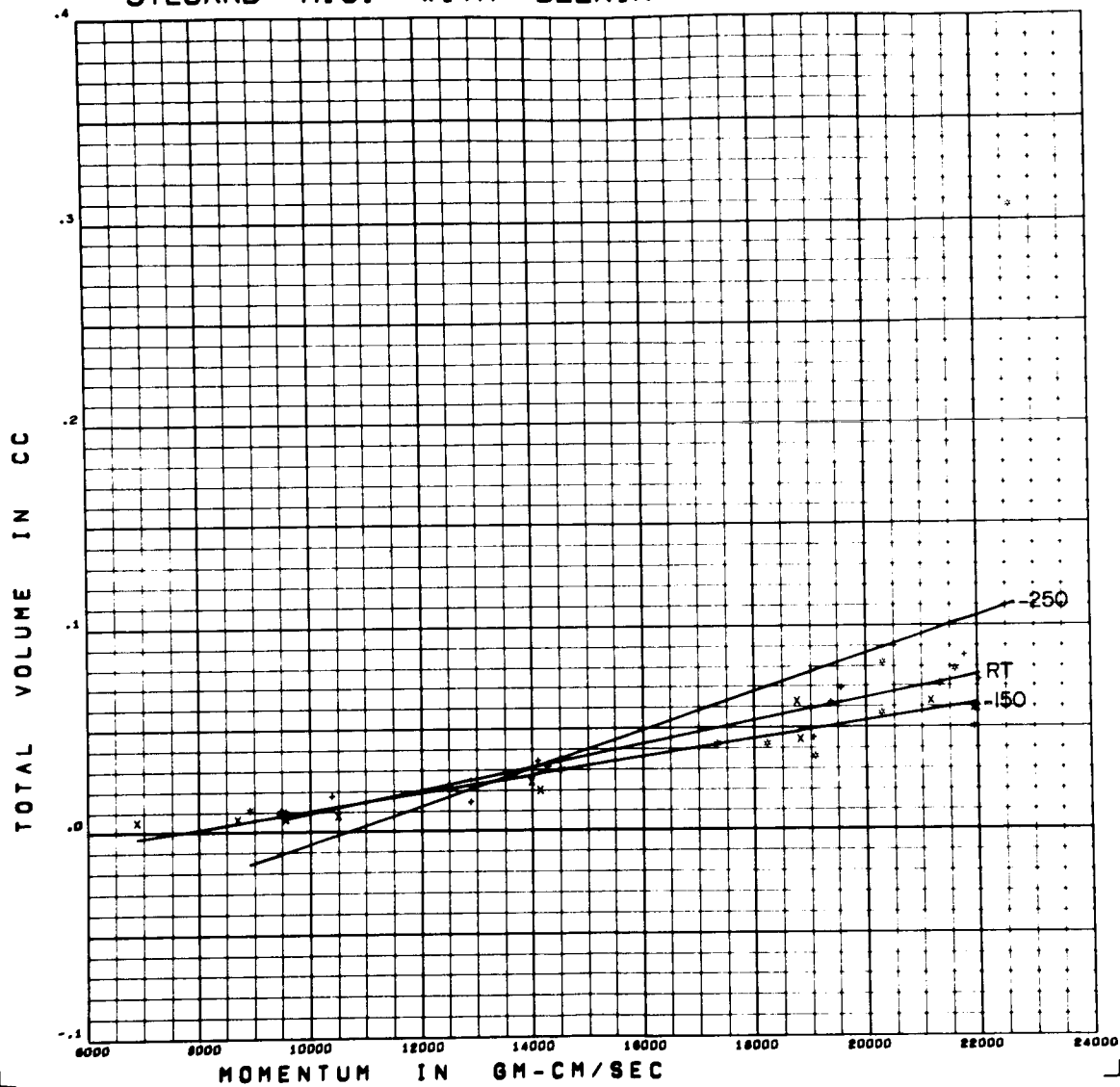


Figure E36 Volume versus Momentum for Delrin Projectiles on Sylgard 325 HC

Form of Regression: $V = (.636 - .366ST - .206CV) \times 10^{-5} M$

RMS Deviation: $.039cc + (-5.90 + 5.14ST + 2.63CV) \times 10^{-2}$

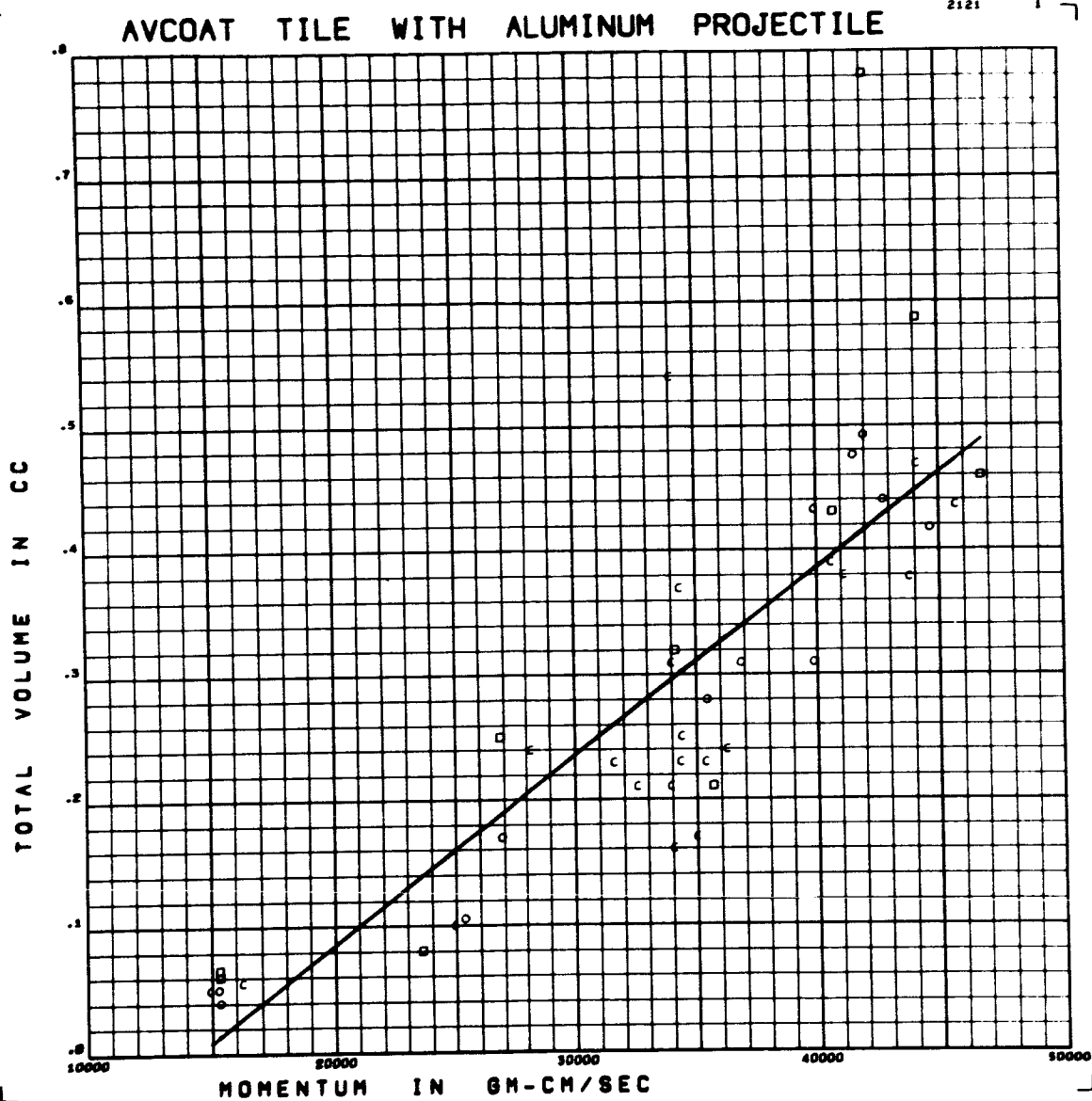


Figure E37 Volume versus Momentum for Aluminum Projectiles on Avcoat 5026 Tile

Form of Regression: $V = 1.510 \times 10^{-5} \cdot M - .217$

RMS Deviation: .092 cc

AVCOAT H.C. WITH ALUMINUM PROJECTILE

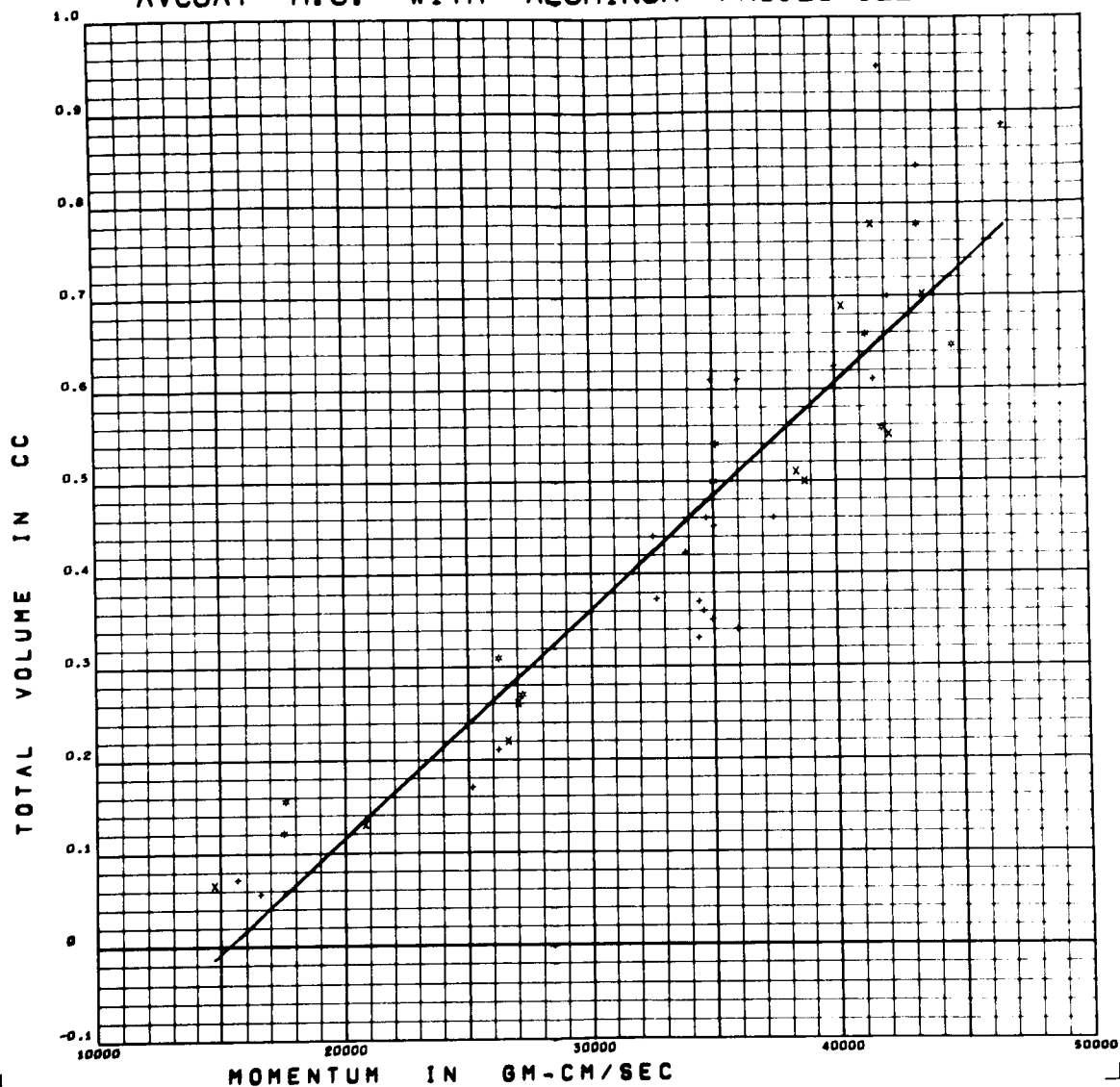


Figure E38 Volume versus Momentum for Aluminum Projectiles on Avcoat 5026 HC

Form of Regression: $V = 2.462 \times 10^{-5} M - .377$

RMS Deviation: .093cc

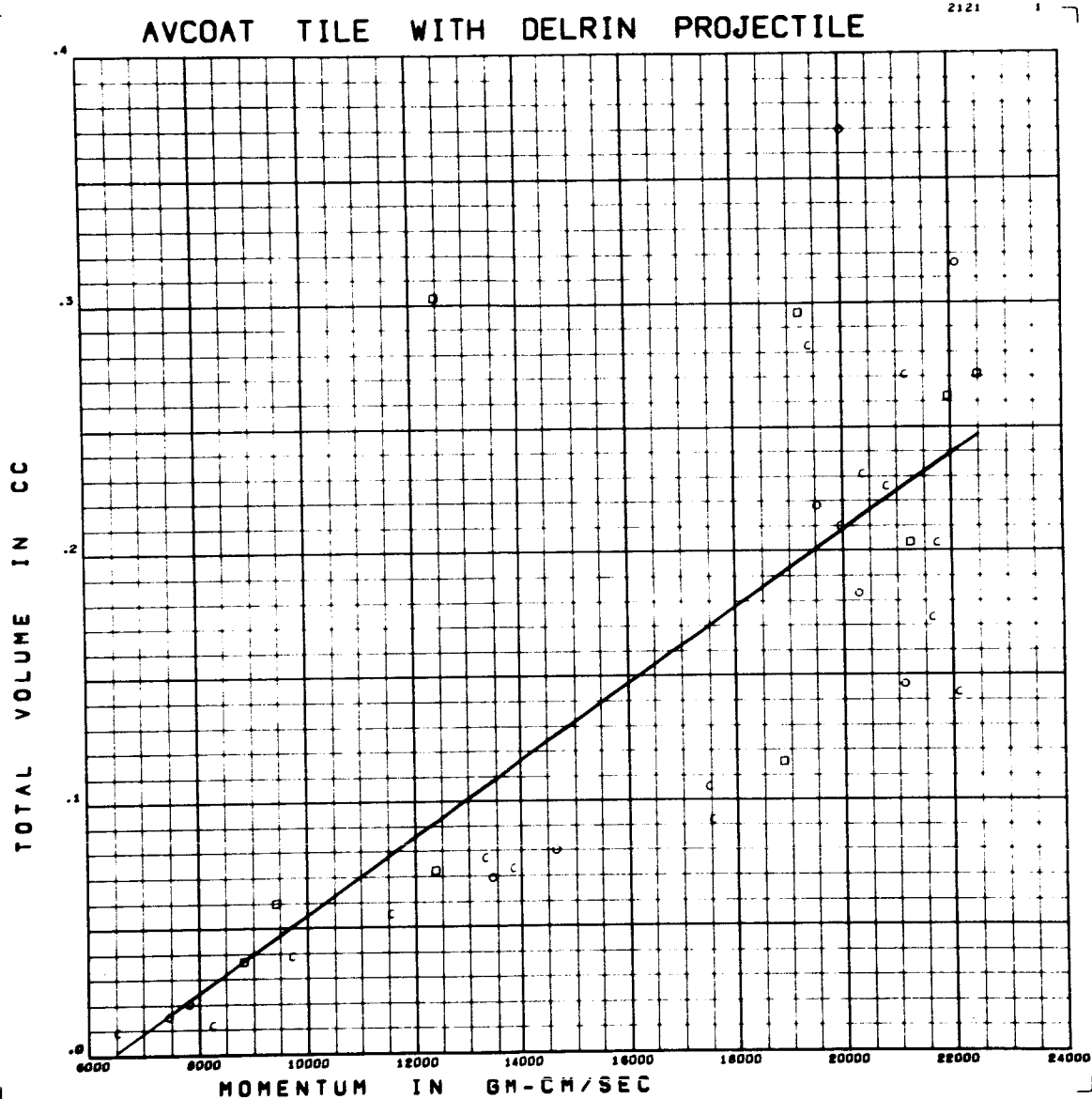


Figure E39 Volume versus Momentum for Delrin Projectiles on Avcoat 5026 Tile

Form of Regression: $V = 1.537 \times 10^{-5} M - .986$

RMS Deviation: .066 cc

AVCOAT H.C. WITH DELRIN PROJECTILE

2121

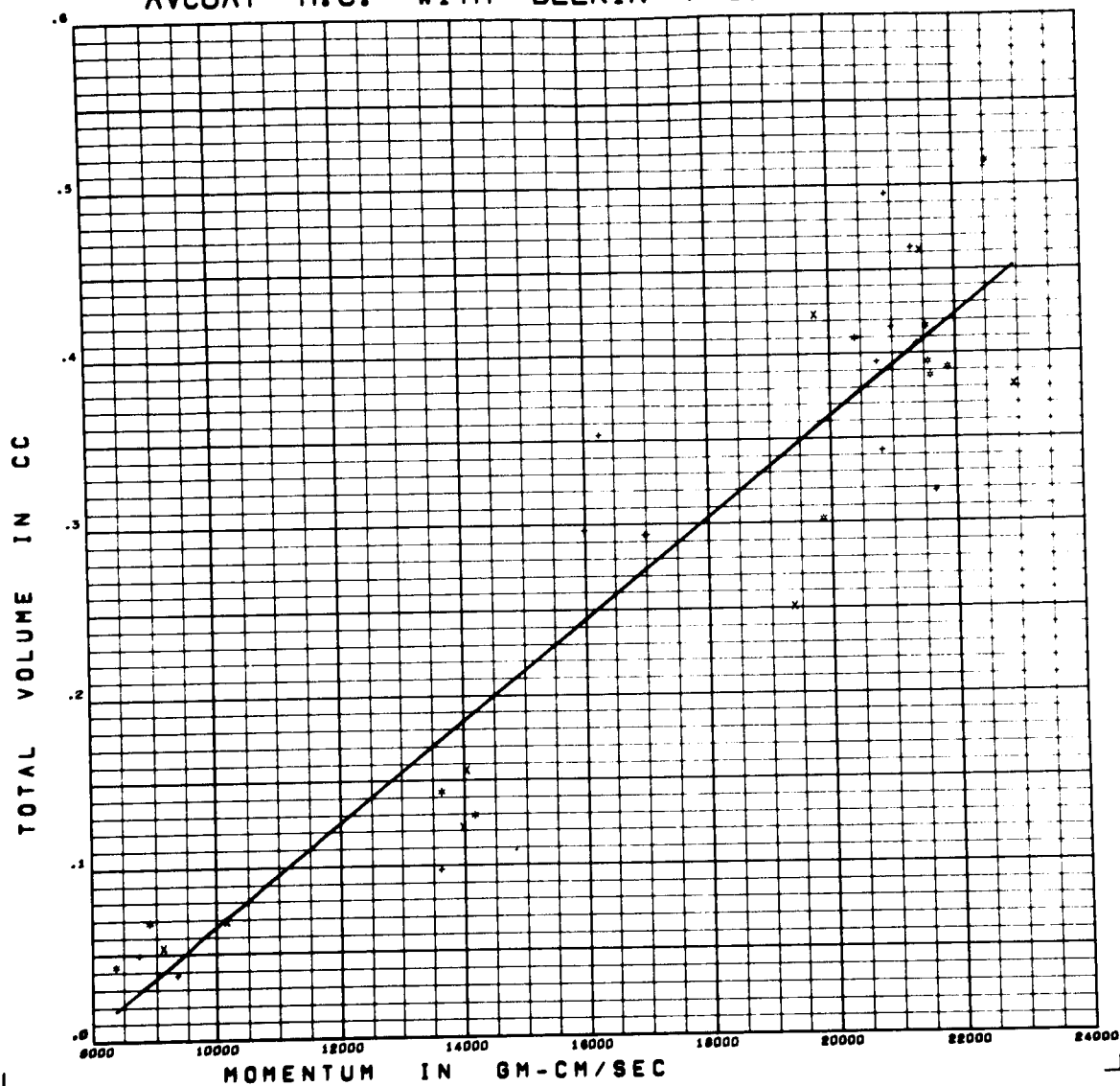


Figure E40 Volume versus Momentum for Delrin Projectiles on Avcoat 5026 HC

Form of Regression: $V = 2.980 \times 10^{-5} M - .232$

RMS Deviation: .053 cc

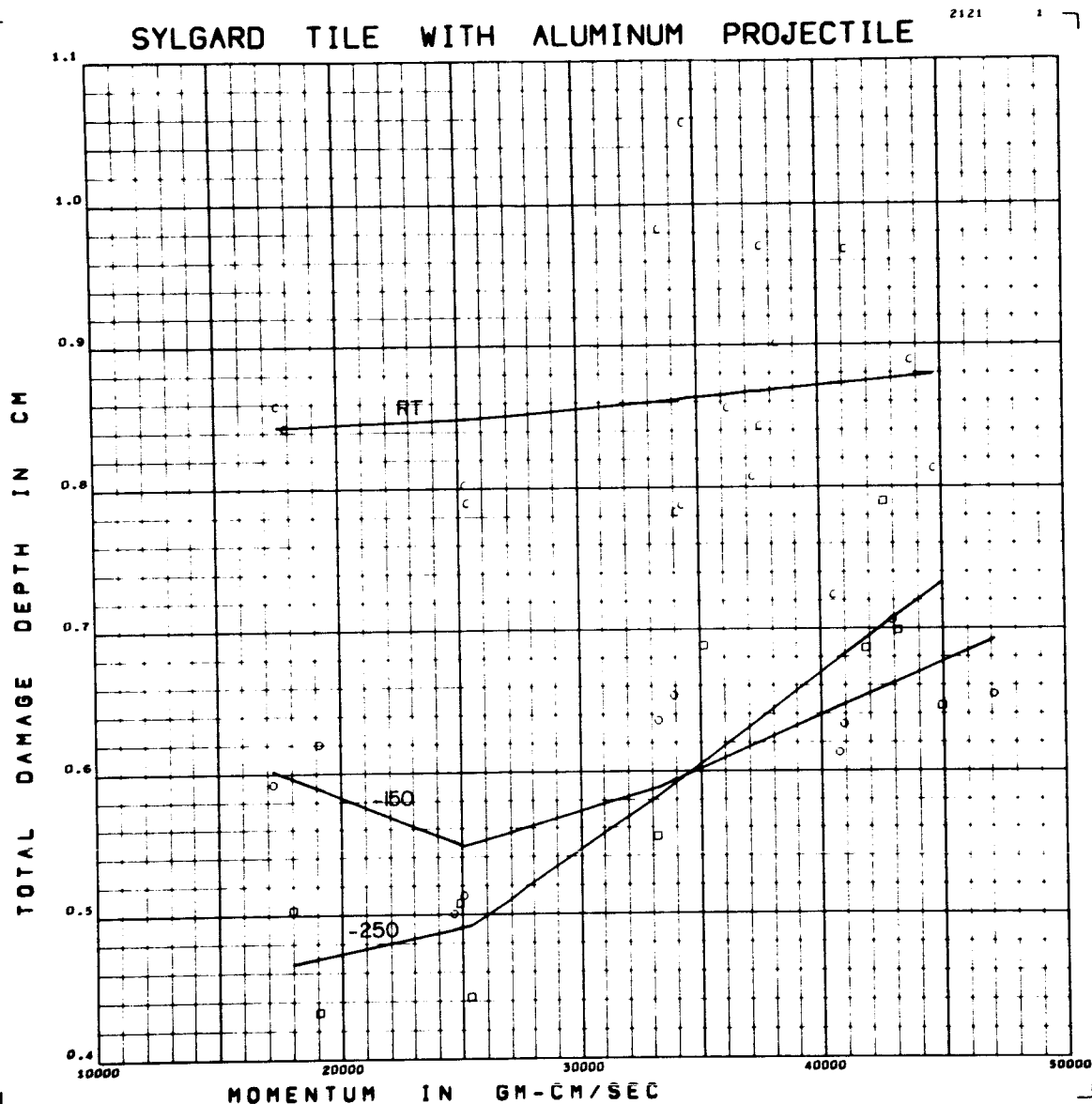


Figure E41 Total Damage Depth versus Momentum for Aluminum Projectiles on Sylgard 325 tile

Form of Regression: $p_m = (.733 - 1.1195T + .017CV) \times 10^{-5} M$

RMS Deviation: $.068 \text{ cm} + (43.35 + 65.055T - 9.43CV) \times 10^{-2}$

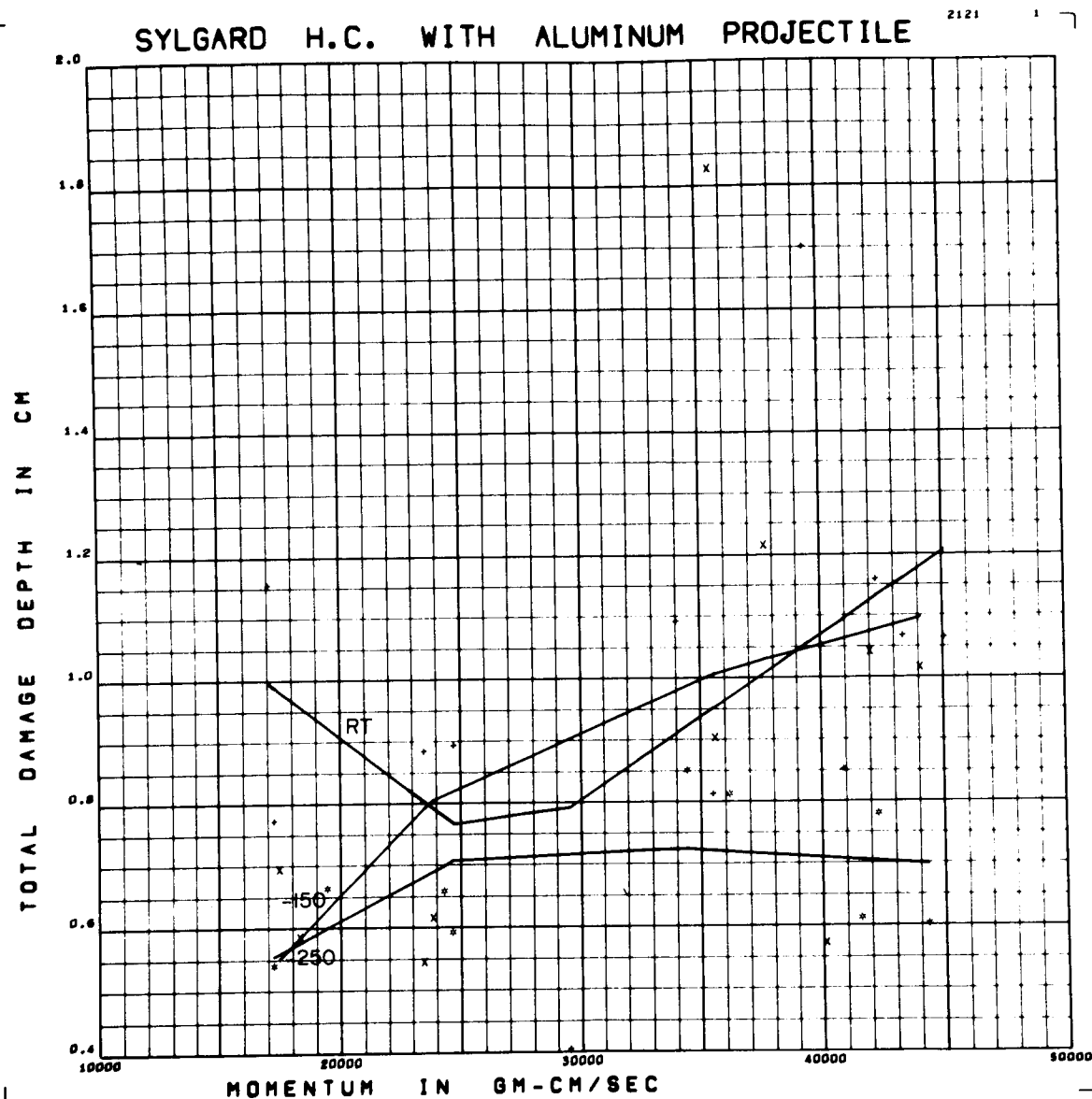


Figure E42 Total Damage Depth versus Momentum for Aluminum Projectiles on
Sylgard 325 HC

Form of Regression: $p_m = (1.147 + 2.931ST - .107CV) \times 10^{-5} M$

RMS Deviation: $.155 \text{ cm} + (48.56 - 81.17ST + 15.24CV) \times 10^{-2}$

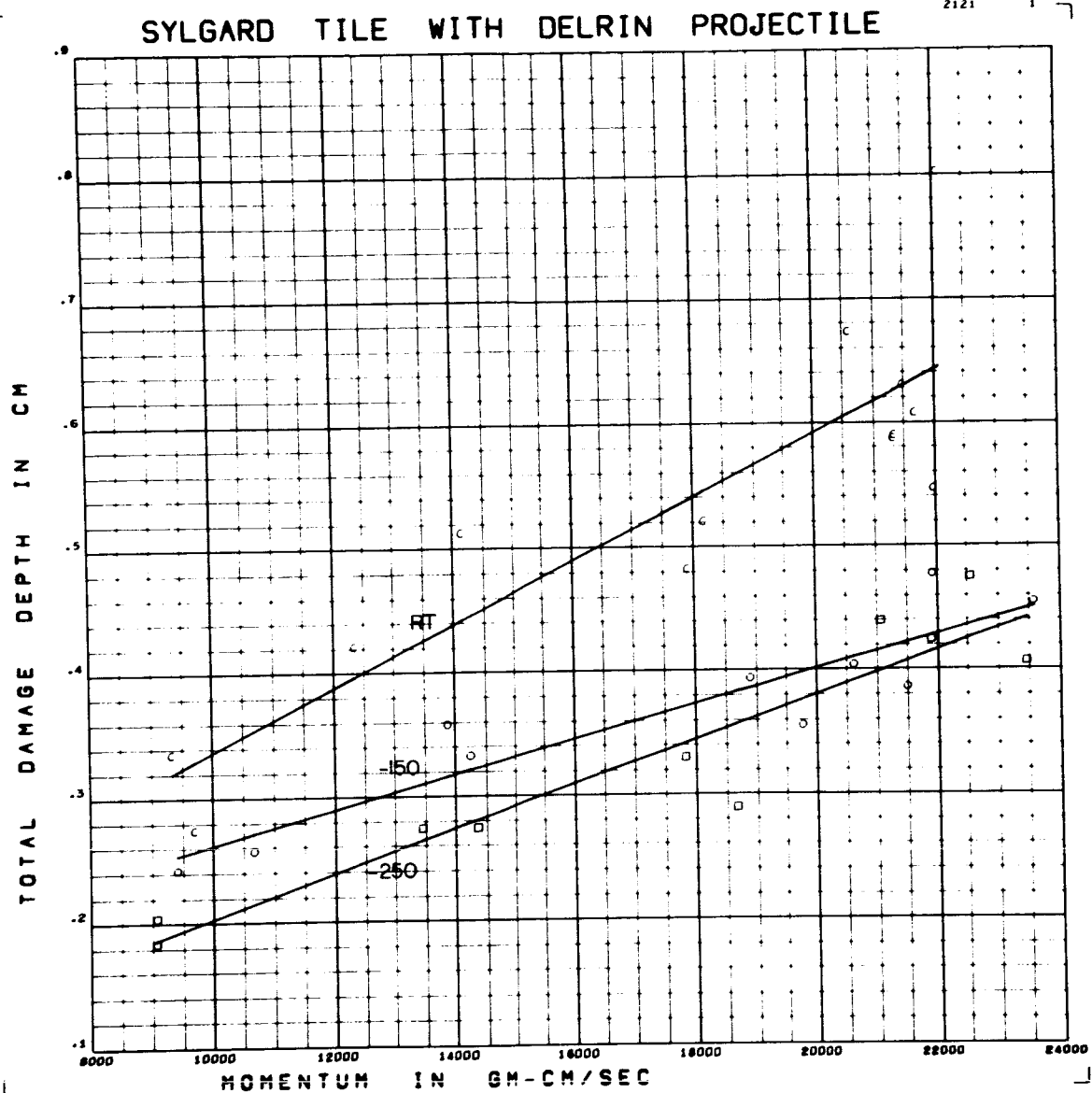


Figure E43 Total Damage Depth versus Momentum for Delrin Projectiles on
Sylgard 325 Tile

Form of Regression: $p_m = (1.907 + .7725T - .513CV) \times 10^{-5} M$

RMS Deviation: $.048 \text{ cm} + (7.66 + 5.665T + 4.62CV) \times 10^{-2}$

SYLGARD H.C. WITH DELRIN PROJECTILE

2121

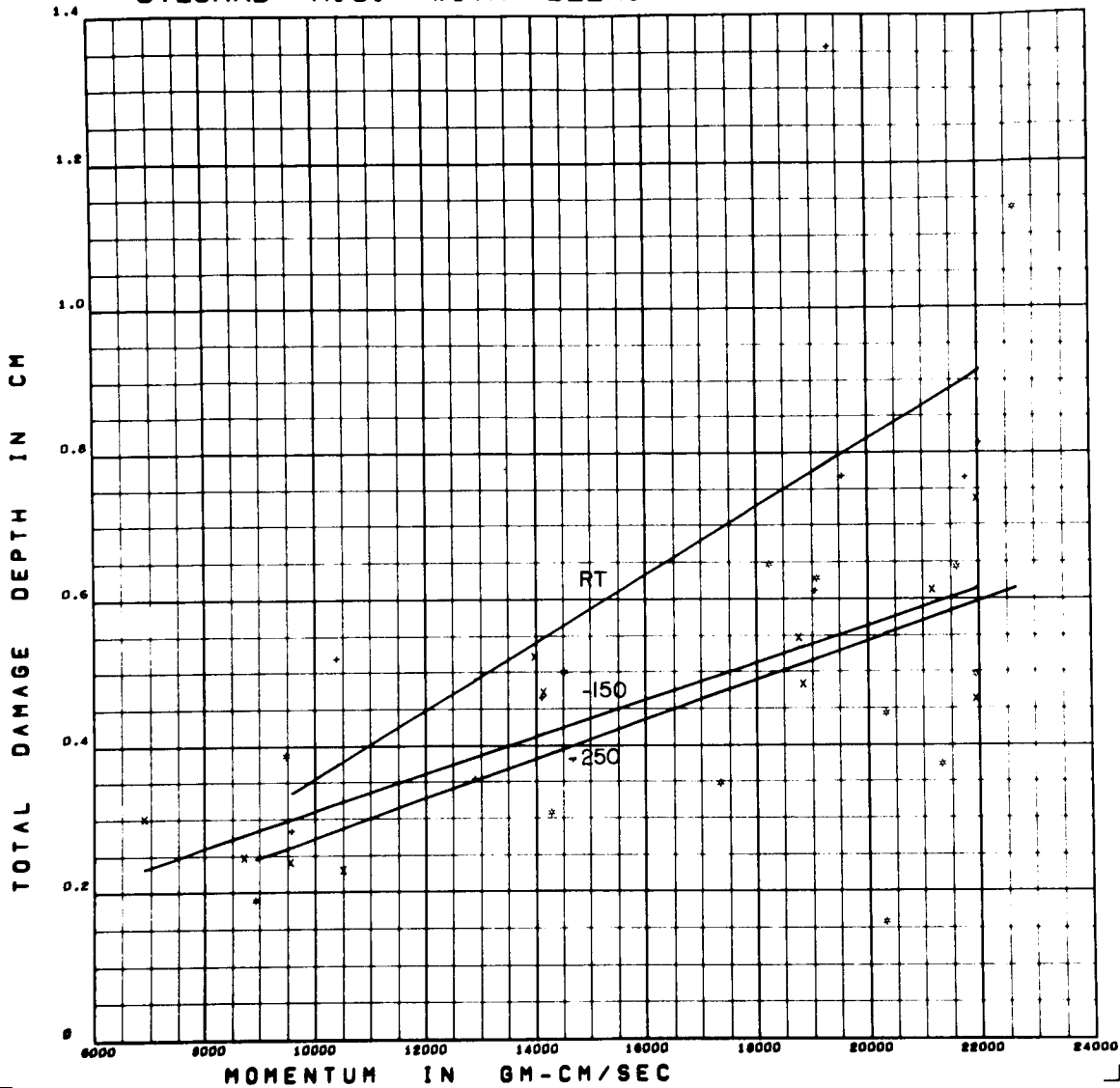


Figure E44 Total Damage Depth versus Momentum for Delrin Projectiles on

Sylgard 325 HC

Form of Regression: $p_m = (3.292 + 1.9465T - .755CV) \times 10^{-2} M$

RMS Deviation: $.184 \text{ cm} + (1.61 - 11.315T + 7.27CV) \times 10^{-2}$

APPENDIX F

CRATER PARAMETERS VERSUS ENERGY

CRATER PARAMETERS VERSUS ENERGY

<u>Figure</u>	<u>Target</u>	<u>Projectile</u>	<u>Crater Parameter</u>
F1	Sylgard 325 tile	A1	Spall Diameter
F2	Sylgard 325 HC	A1	Spall Diameter
F3	Sylgard 325 tile	Delrin	Spall Diameter
F4	Sylgard 325 HC	Delrin	Spall Diameter
F5	Sylgard 5026 tile	A1	Spall Diameter
F6	Avcoat 5026 tile	A1	Spall Diameter
F7	Avcoat 5026 tile	Delrin	Spall Diameter
F8	Avcoat 5026 HC	Delrin	Spall Diameter
F9	Sylgard 325 tile	A1	Crater Diameter
F10	Sylgard 325 HC	A1	Crater Diameter
F11	Sylgard 325 tile	Delrin	Crater Diameter
F12	Sylgard 325 HC	Delrin	Crater Diameter
F13	Avcoat 5026 tile	A1	Crater Diameter
F14	Avcoat 5026 HC	A1	Crater Diameter
F15	Avcoat 5026 tile	Delrin	Crater Diameter
F16	Avcoat 5026 HC	Delrin	Crater Diameter
F17	Sylgard 325 tile	A1	Penetration
F18	Sylgard 325 HC	A1	Penetration
F19	Sylgard 325 tile	Delrin	Penetration
F20	Sylgard 325 HC	Delrin	Penetration
F21	Avcoat 5026 tile	A1	Penetration
F22	Avcoat 5026 HC	A1	Penetration
F23	Avcoat 5026 tile	Delrin	Penetration
F24	Avcoat 5026 HC	Delrin	Penetration
F25	Sylgard 325 tile	A1	Spall Depth
F26	Sylgard 325 HC	A1	Spall Depth
F27	Sylgard 325 tile	Delrin	Spall Depth
F28	Sylgard 325 HC	Delrin	Spall Depth
F29	Avcoat 5026 tile	A1	Spall Depth
F30	Avcoat 5026 HC	A1	Spall Depth
F31	Avcoat 5026 tile	Delrin	Spall Depth
F32	Avcoat 5026 HC	Delrin	Spall Depth
F33	Sylgard 325 tile	A1	Volume
F34	Sylgard 325 HC	A1	Volume
F35	Sylgard 325 tile	Delrin	Volume
F36	Sylgard 325 HC	Delrin	Volume
F37	Avcoat 5026 tile	A1	Volume
F38	Avcoat 5026 HC	A1	Volume
F39	Avcoat 5026 tile	Delrin	Volume
F40	Avcoat 5026 HC	Delrin	Volume
F41	Sylgard 325 tile	A1	Total Damage Depth
F42	Sylgard 325 HC	A1	Total Damage Depth
F43	Sylgard 325 tile	Delrin	Total Damage Depth
F44	Sylgard 325 HC	Delrin	Total Damage Depth

HONEYCOMB SYMBOLS

TEMPERATURE	SYMBOL
RT	+
-150°F	X
-250°F	*

TILE SYMBOLS

TEMPERATURE	SYMBOL
RT	C
-150°F	O
-250°F	□

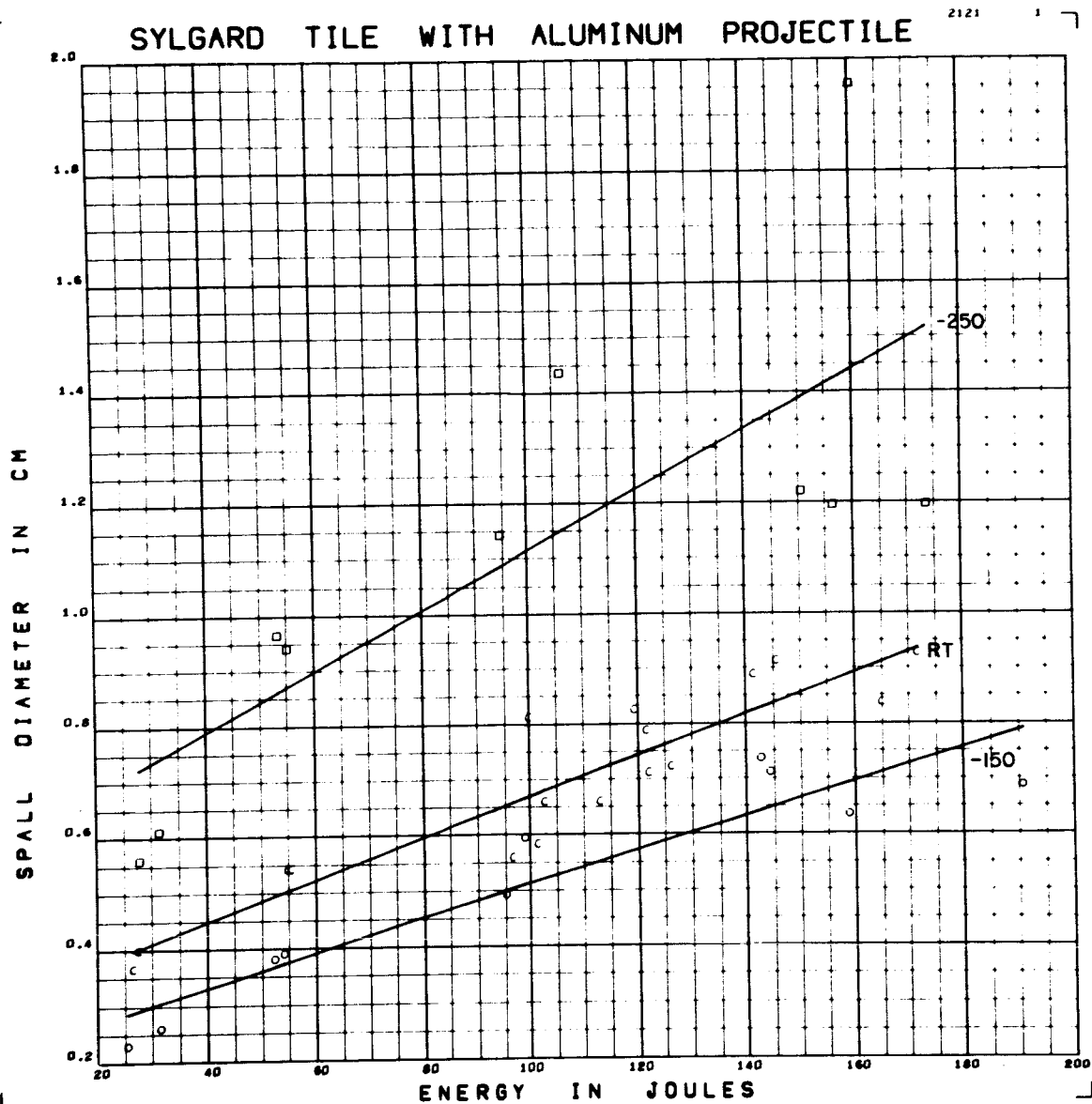


Figure F1 Spall Diameter versus Energy for Aluminum Projectiles on
Sylgard 325 Tile

Form of Regression: $d_s = (4.059 - 1.742 ST - 1.018 CV) \times 10^{-3} E$

RMS Deviation: .140 cm $+ .3608 - .2713 ST - .1517 CV$

SYLGARD H.C. WITH ALUMINUM PROJECTILE

2121

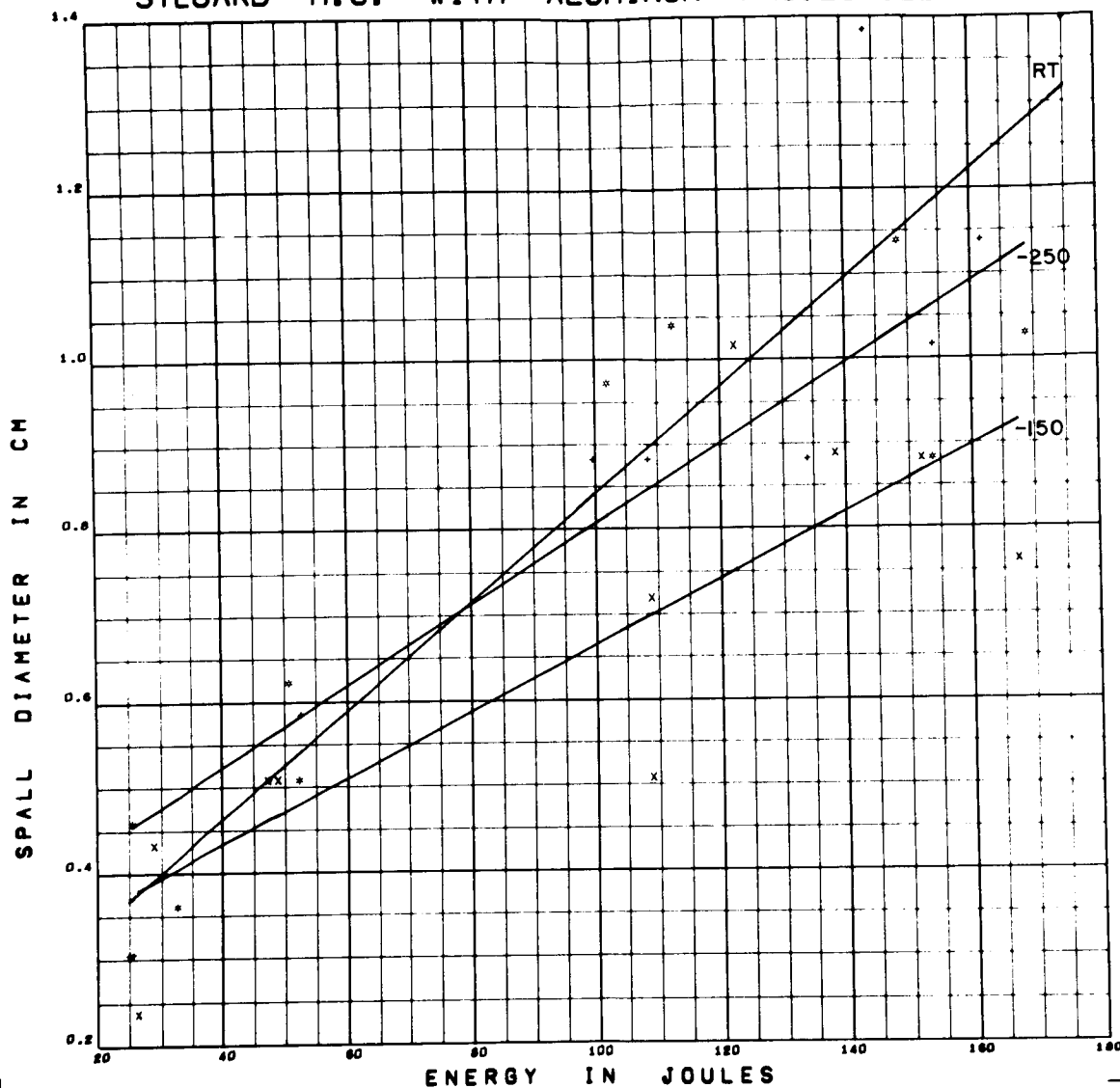


Figure F2 Spall Diameter versus Energy for Aluminum Projectiles on

Sylgard 325 HC

Form of Regression: $d_s = (4.984 + 1.600 ST - 1.107 CV) \times 10^{-3} E$

RMS Deviation: .127 cm $+ .2736 - .1243 ST + .0045 CV$

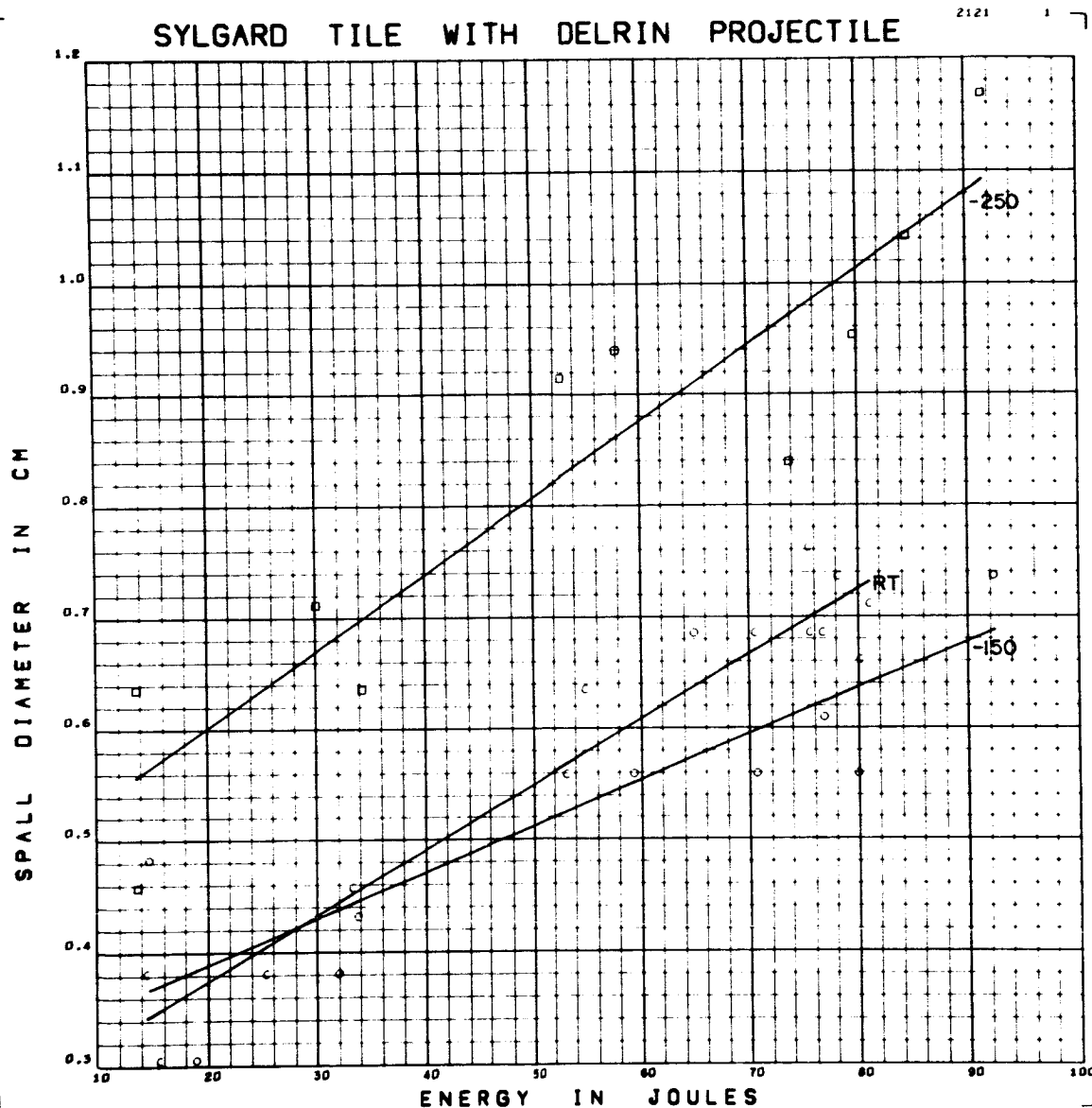


Figure F3 Spall Diameter versus Energy for Delrin Projectiles on
Sylgard 325 Tile

Form of Regression: $d_s = (5.609 - 1.035 ST - 1.493 CV) \times 10^{-3} E$

RMS Deviation: .063 cm $+ .3428 - .2056 ST - .0359 CV$

SYLGARD H.C. WITH DELRIN PROJECTILE

2121

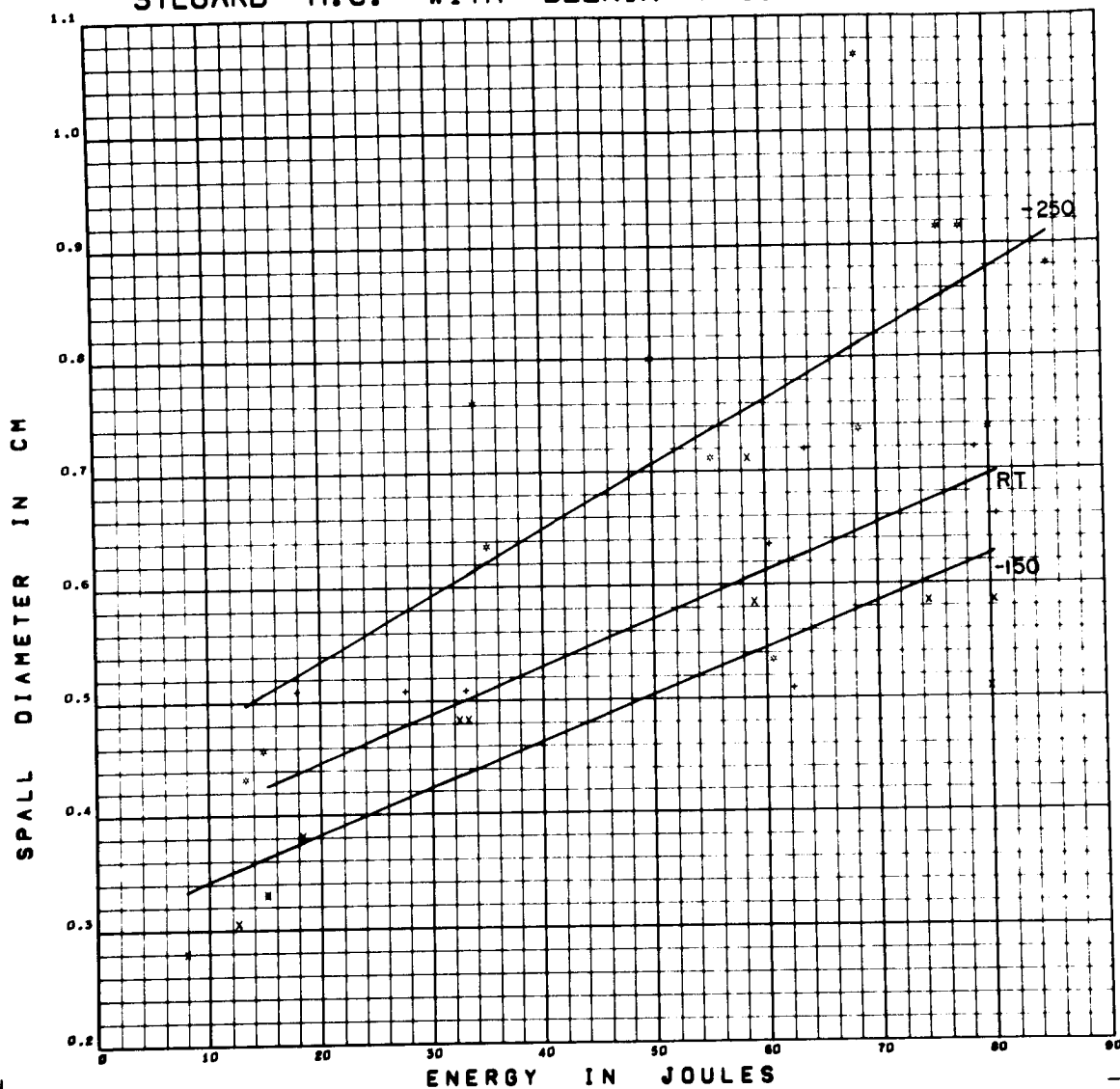


Figure F4 Spall Diameter versus Energy for Delrin Projectiles on

Sylgard 325 HC

Form of Regression: $d_s = (4.639 - 1.555 ST - .589 CV) \times 10^{-3} E$

RMS Deviation: .095 cm $+ .3621 - .0582 ST - .0603 CV$

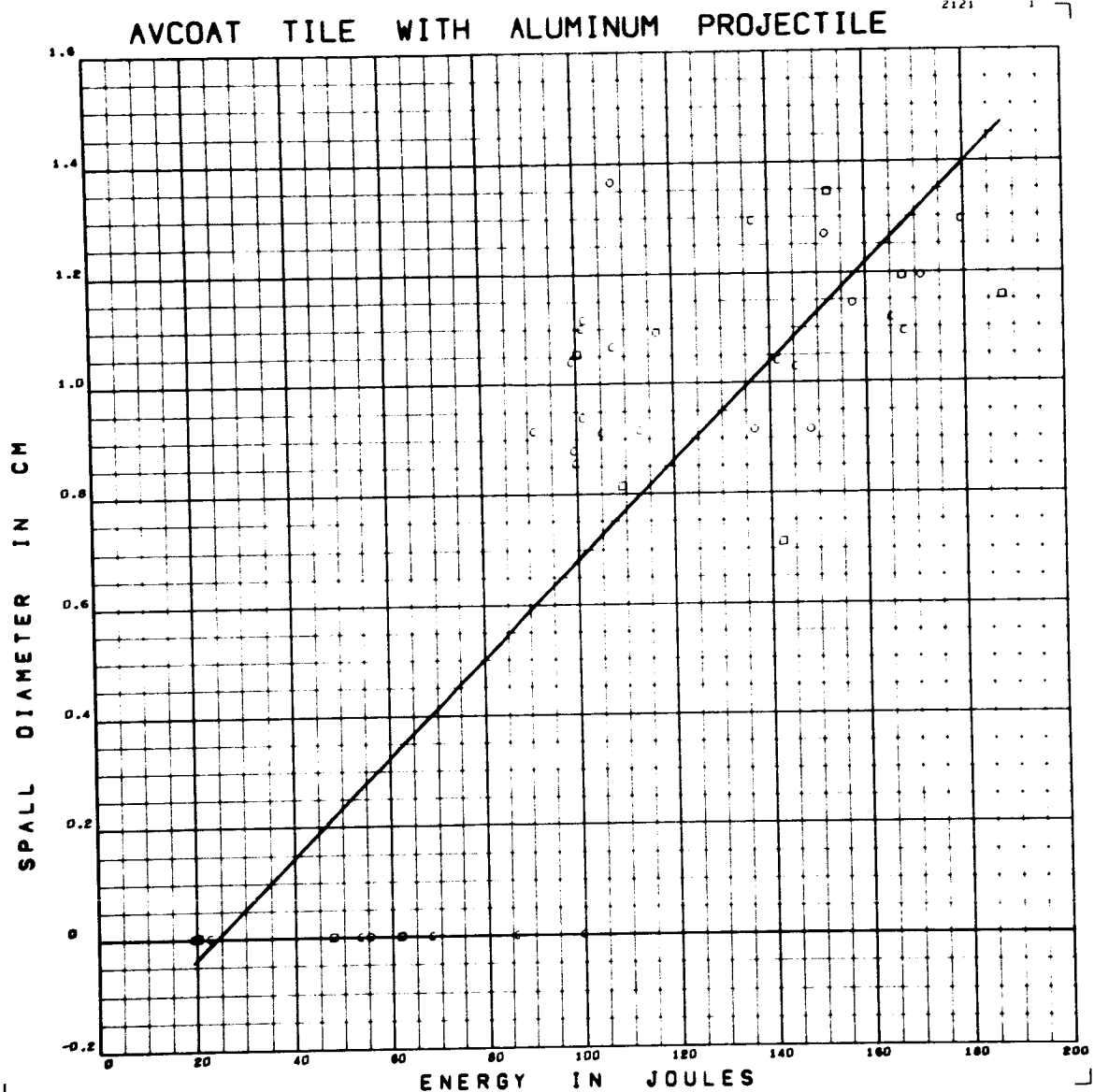


Figure F5 Spall Diameter versus Energy for Aluminum Projectiles on

Avcoat 5026 Tile

Form of Regression: $d_s = 8.960 \times 10^{-3} E^{-.2145}$

RMS Deviation: .281 cm

AVCOAT H.C. WITH ALUMINUM PROJECTILE

2121

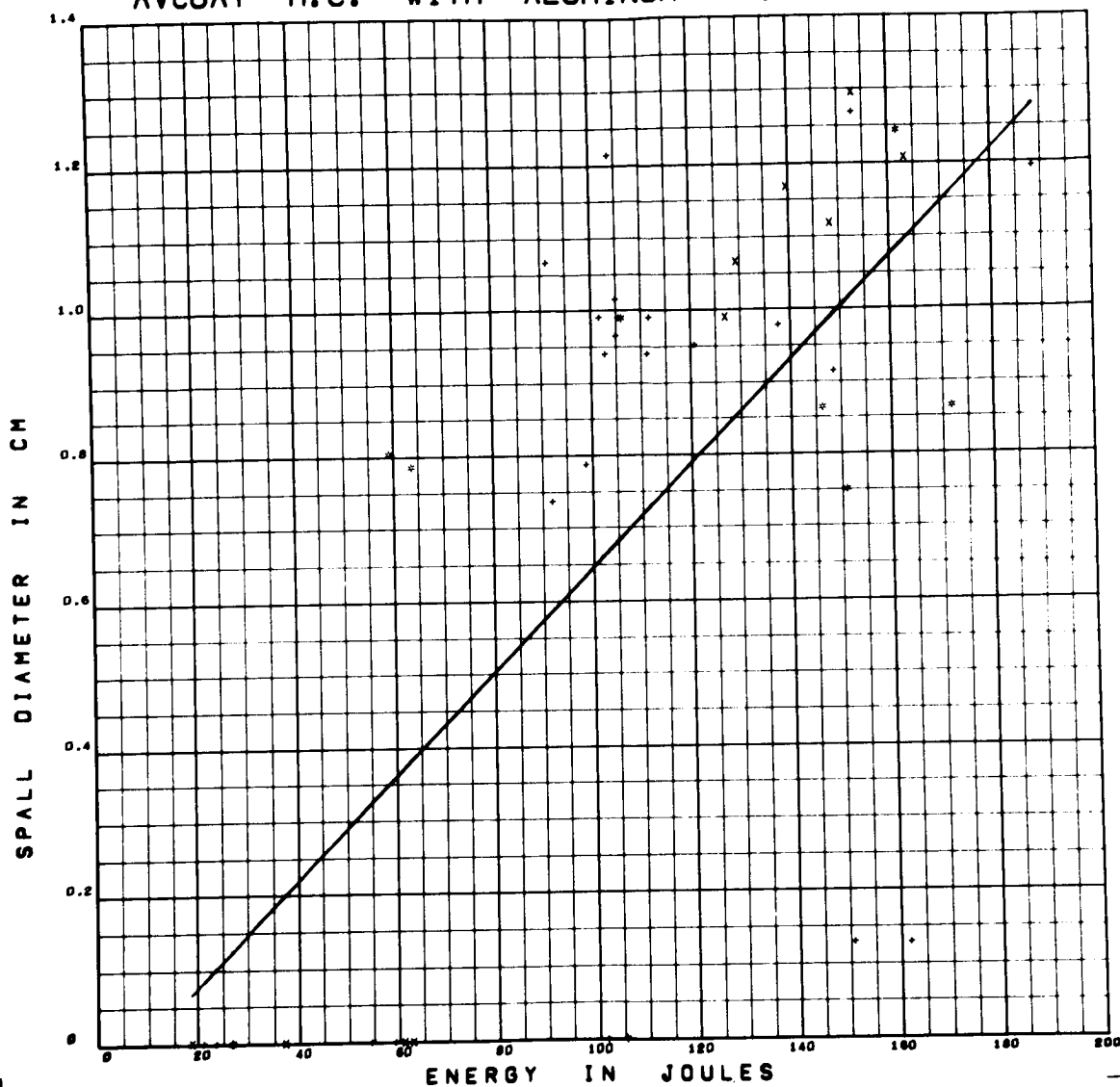


Figure F6 Spall Diameter versus Energy for Aluminum Projectiles on

Avcoat 5026 HC

Form of Regression: $d_s = 7.137 \times 10^{-3} E - .0659$

RMS Deviation: .356 cm

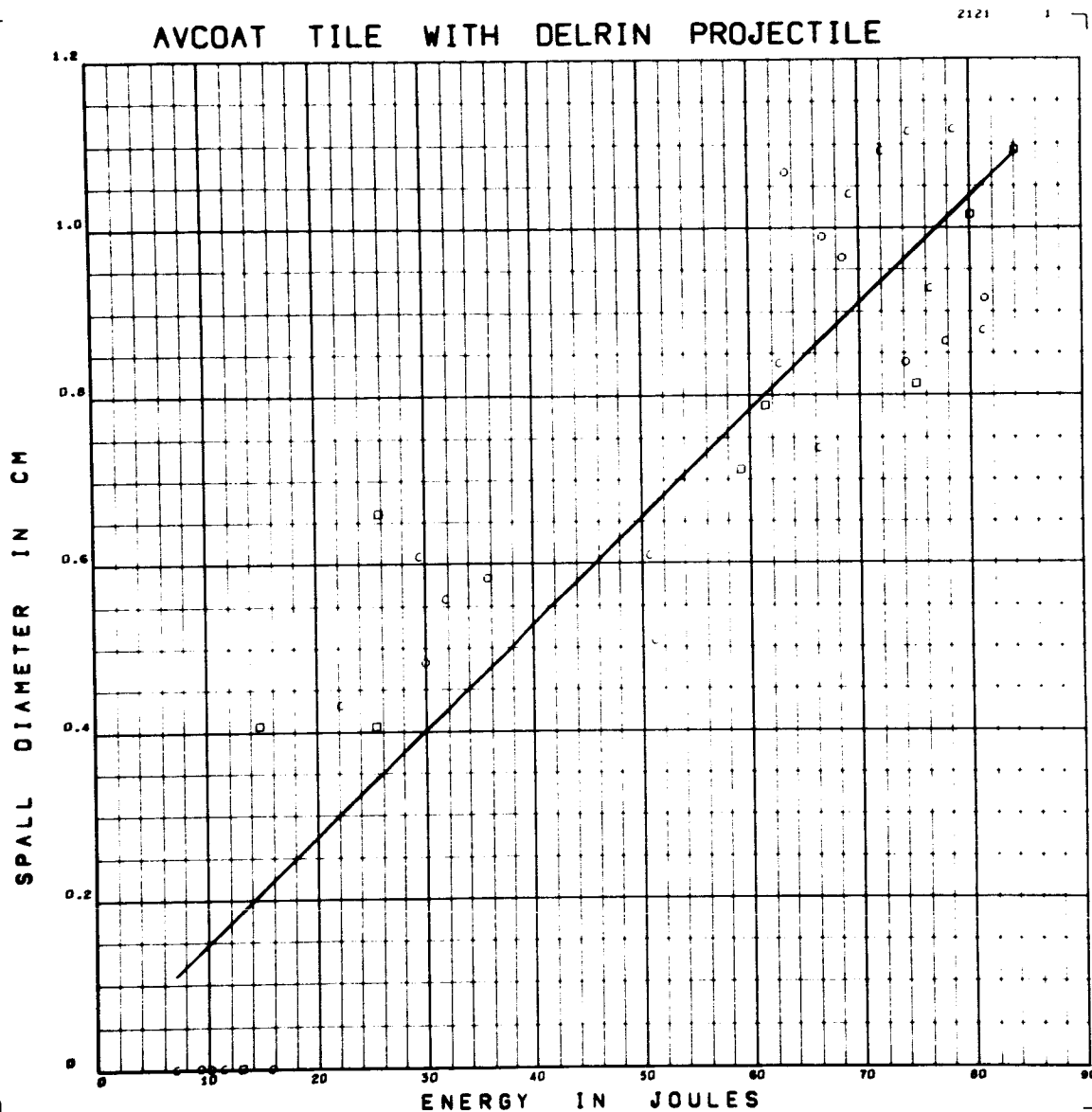


Figure F7 Spall Diameter versus Energy for Delrin Projectiles on

Avcoat 5026 Tile

Form of Regression: $d_s = 12.73 \times 10^{-3} E + .1995$

RMS Deviation: .147 cm

AVCOAT H.C. WITH DELRIN PROJECTILE

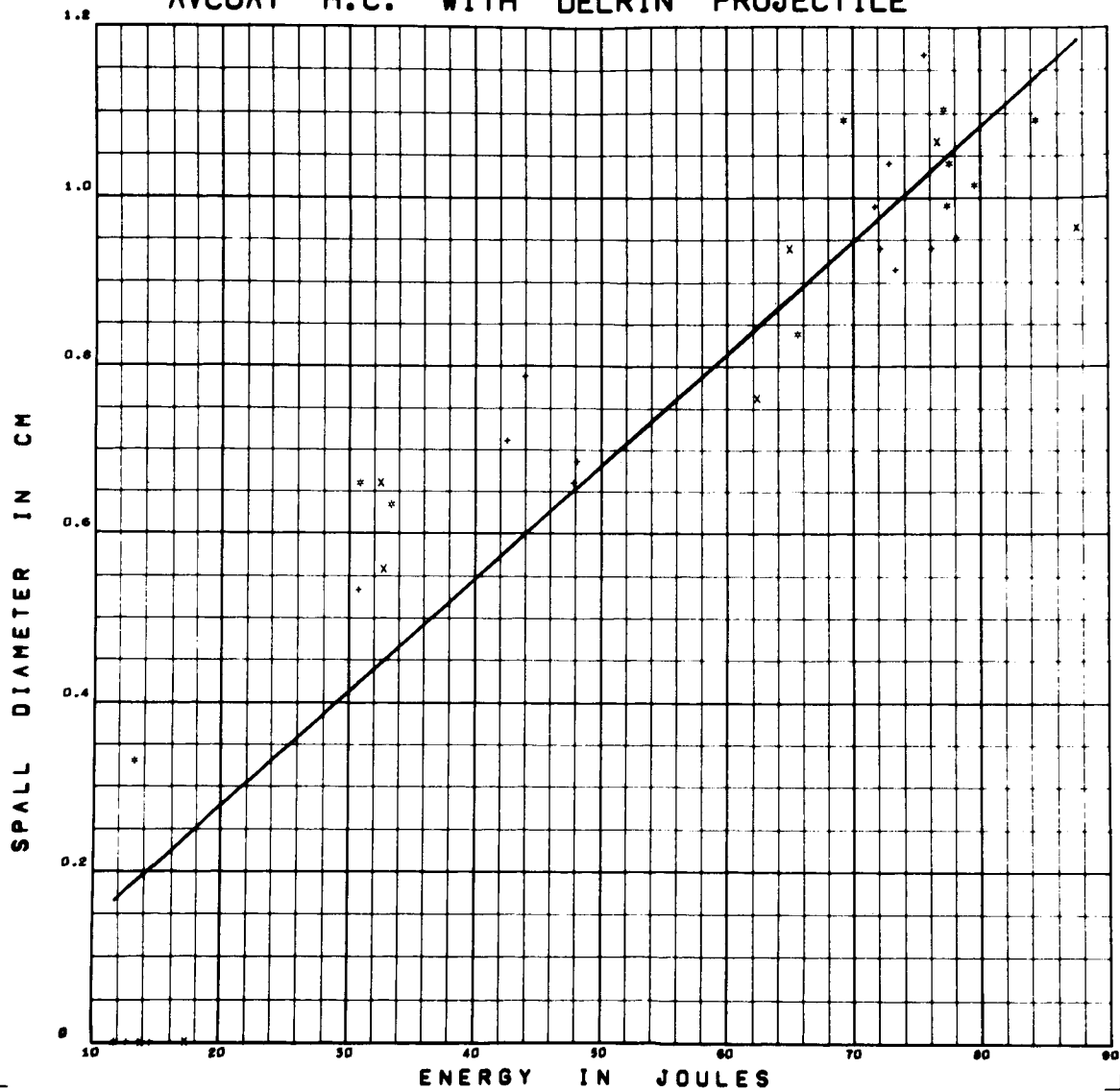


Figure F8 Spall Diameter versus Energy for Delrin Projectiles on
Avcoat 5026 HC

Form of Regression: $d_s = 13.44 \times 10^{-3} E + .0095$

RMS Deviation: .135 cm

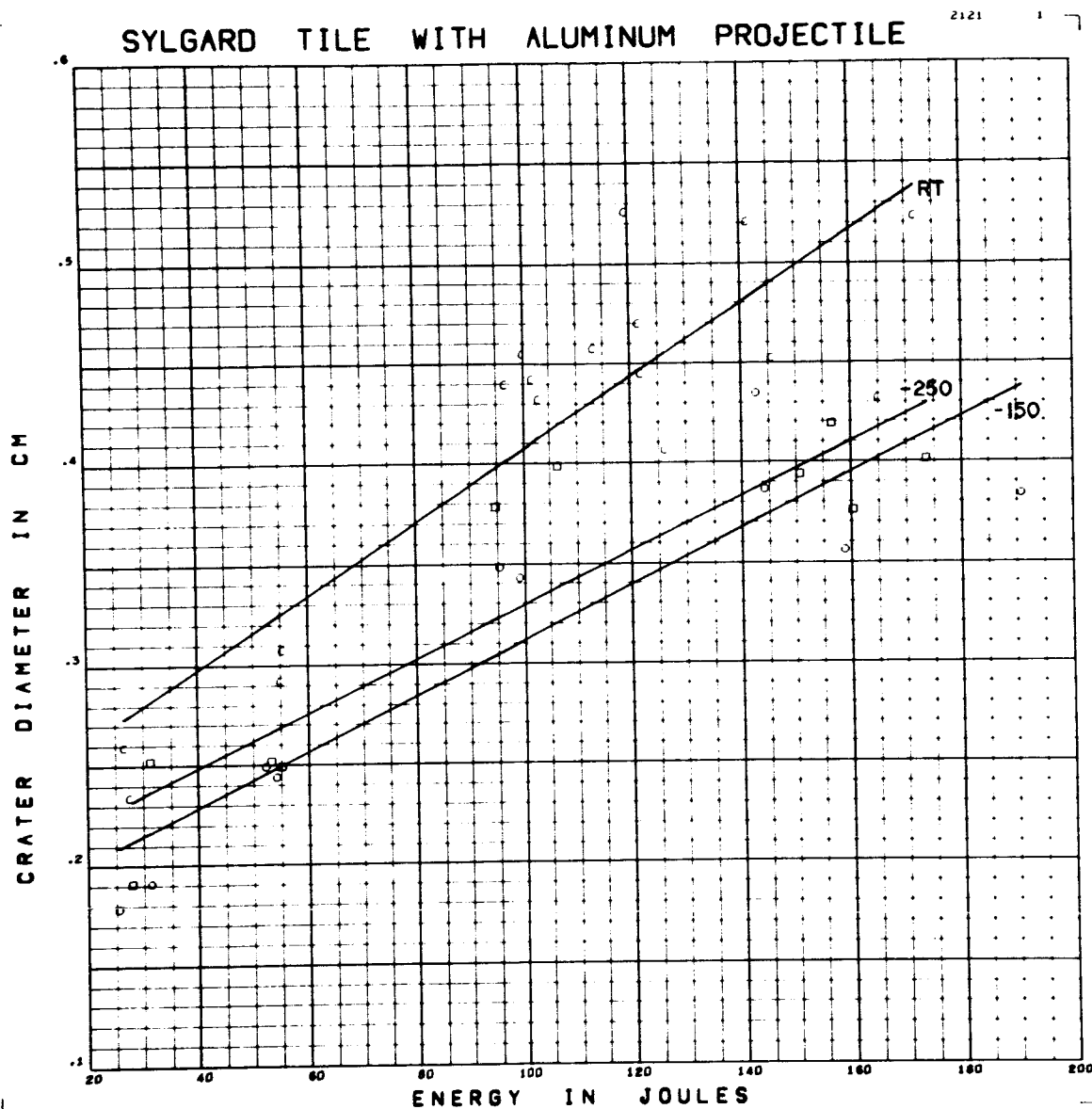


Figure F9 Crater Diameter versus Energy for Aluminum Projectiles on
Sylgard 325 Tile

Form of Regression: $d = (1.522 + .474 ST - .134 CV) \times 10^{-3} E$

RMS Deviation: .039 cm $+ .1974 + .0303 ST - .0243 CV$

SYLGARD H.C. WITH ALUMINUM PROJECTILE

2121

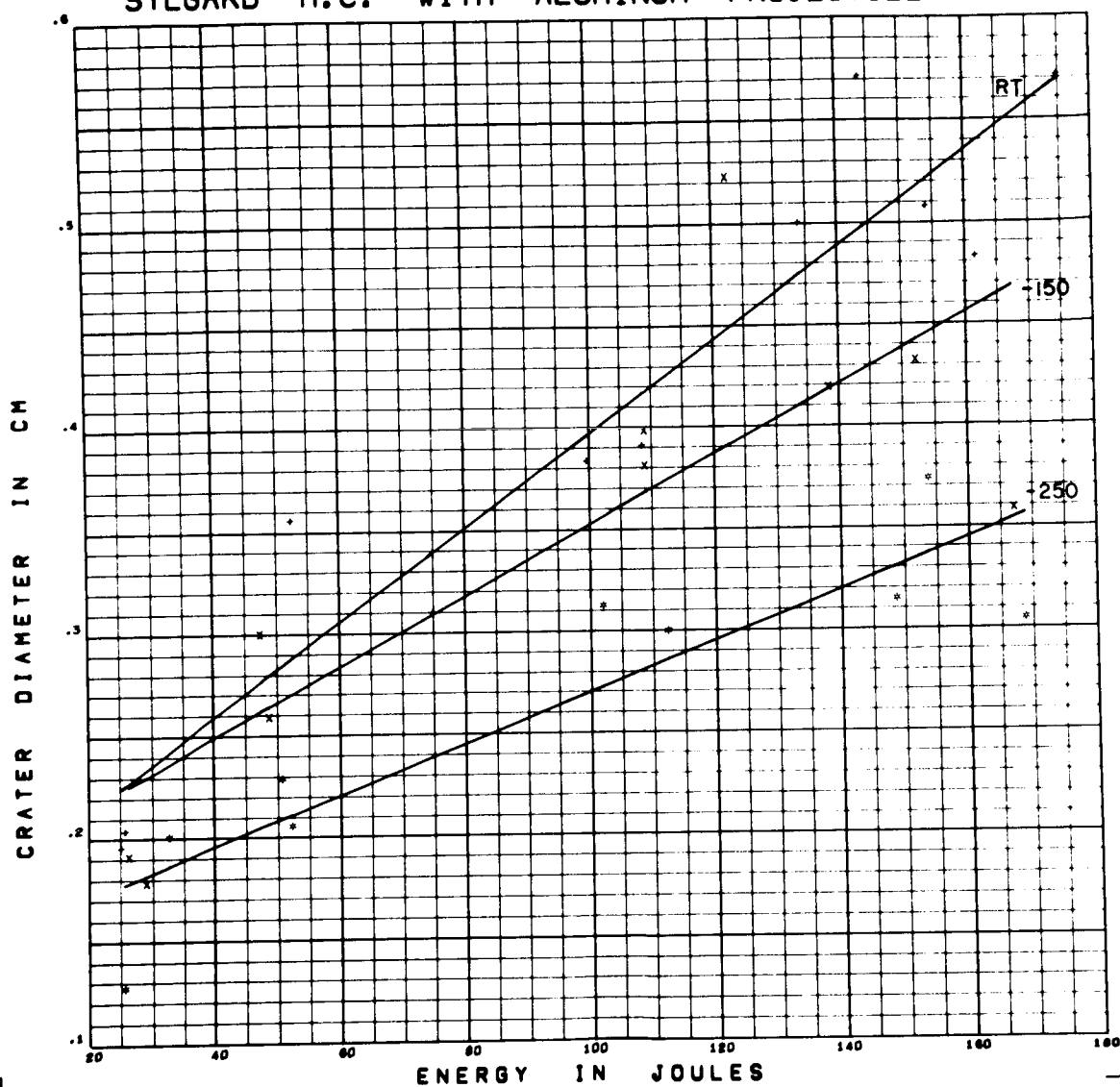


Figure F10 Crater Diameter versus Energy for Aluminum Projectiles on

Sylgard 325 HC

Form of Regression: $d = (1.756 + 1.055 ST - .033 CV) \times 10^{-3} E$

RMS Deviation: .046 cm $+ .1645$ $+ .0212 ST$ $+ .0159 CV$

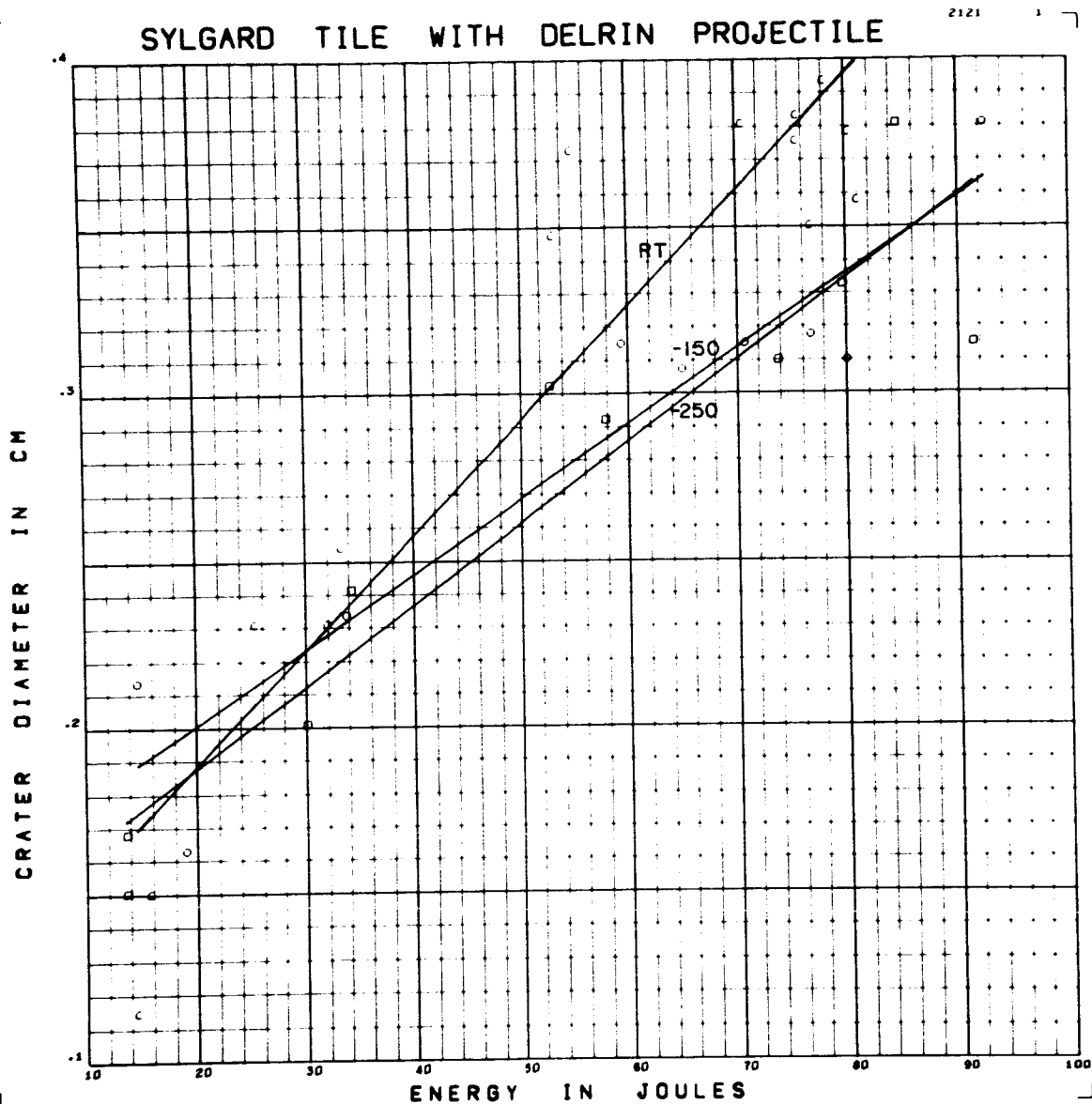


Figure F11 Crater Diameter versus Energy for Delrin Projectiles on
Sylgard 325 Tile

Form of Regression: $d = (2.727 + .999ST - .461CV) \times 10^{-3} E$
 RMS Deviation: .027cm $+ .1377 - .0192ST - .0177CV$

SYLGARD H.C. WITH DELRIN PROJECTILE

2121

1

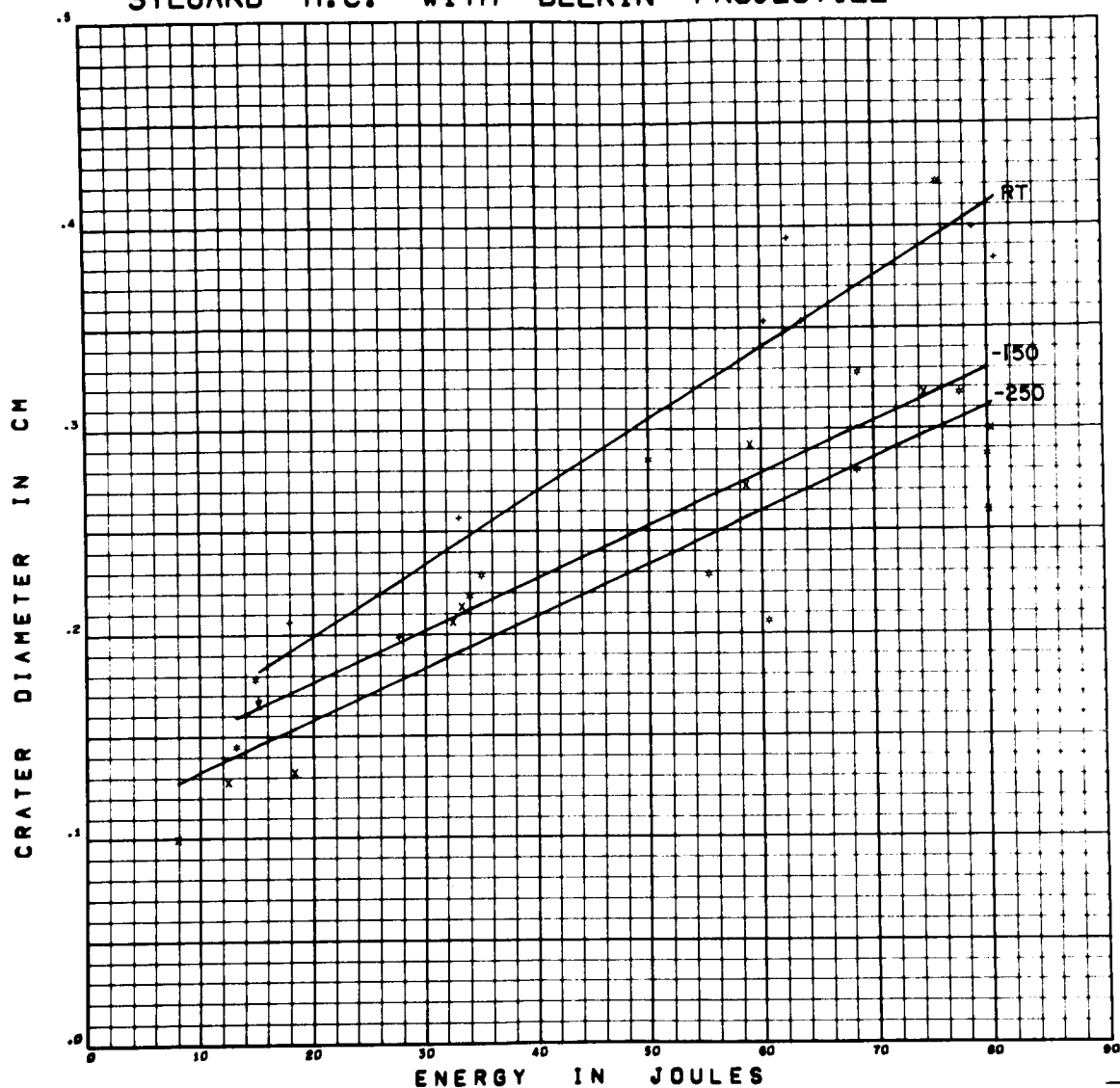


Figure F12 Crater Diameter versus Energy for Delrin Projectiles on

Sylgard 325 HC

Form of Regression: $d = (2.883 + .977 ST - .330 CV) \times 10^{-3} E$

RMS Deviation: .033 cm $+ .1201 + .0031 ST - .0131 CV$

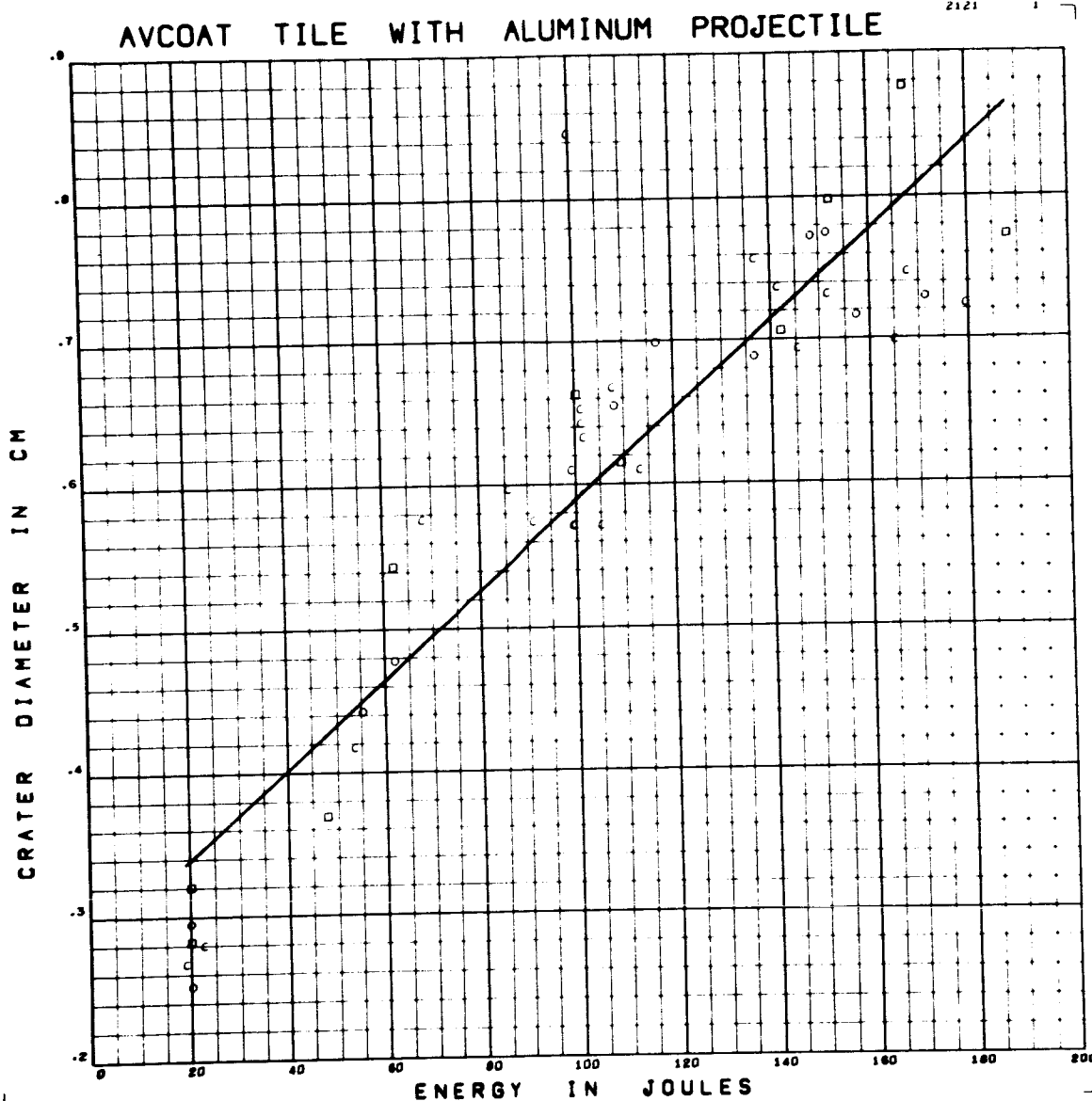


Figure F13 Crater Diameter versus Energy for Aluminum Projectiles on

Avcoat 5026 Tile

Form of Regression: $d = 3.128 \times 10^{-3} E + .2767$

RMS Deviation: .066 cm

AVCOAT H.C. WITH ALUMINUM PROJECTILE

2121

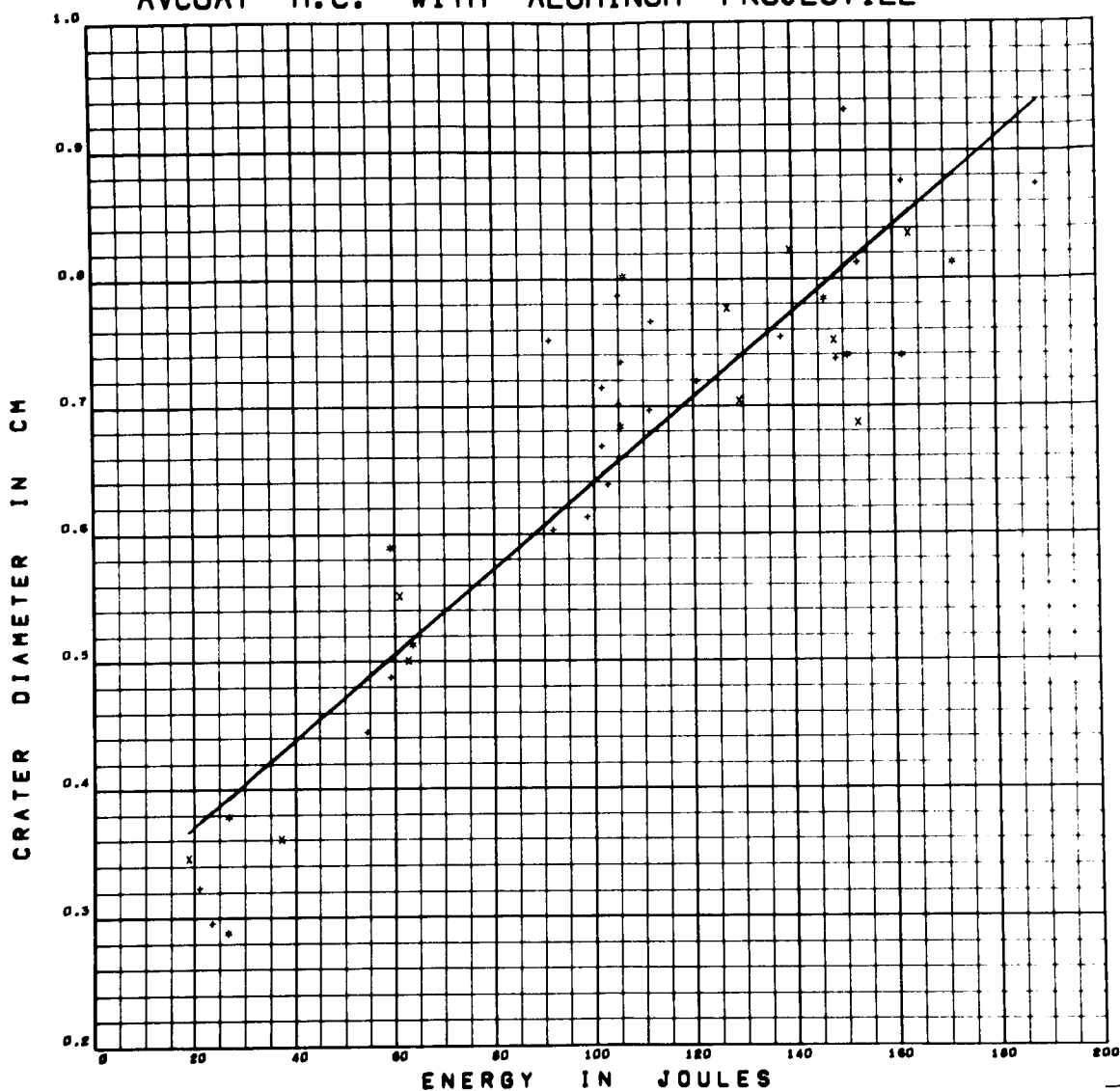


Figure F14 Crater Diameter versus Energy for Aluminum Projectiles on

Avcoat 5026 HC

Form of Regression: $d = 3.372 \times 10^{-3} E + 0.3032$

RMS Deviation: .068 cm

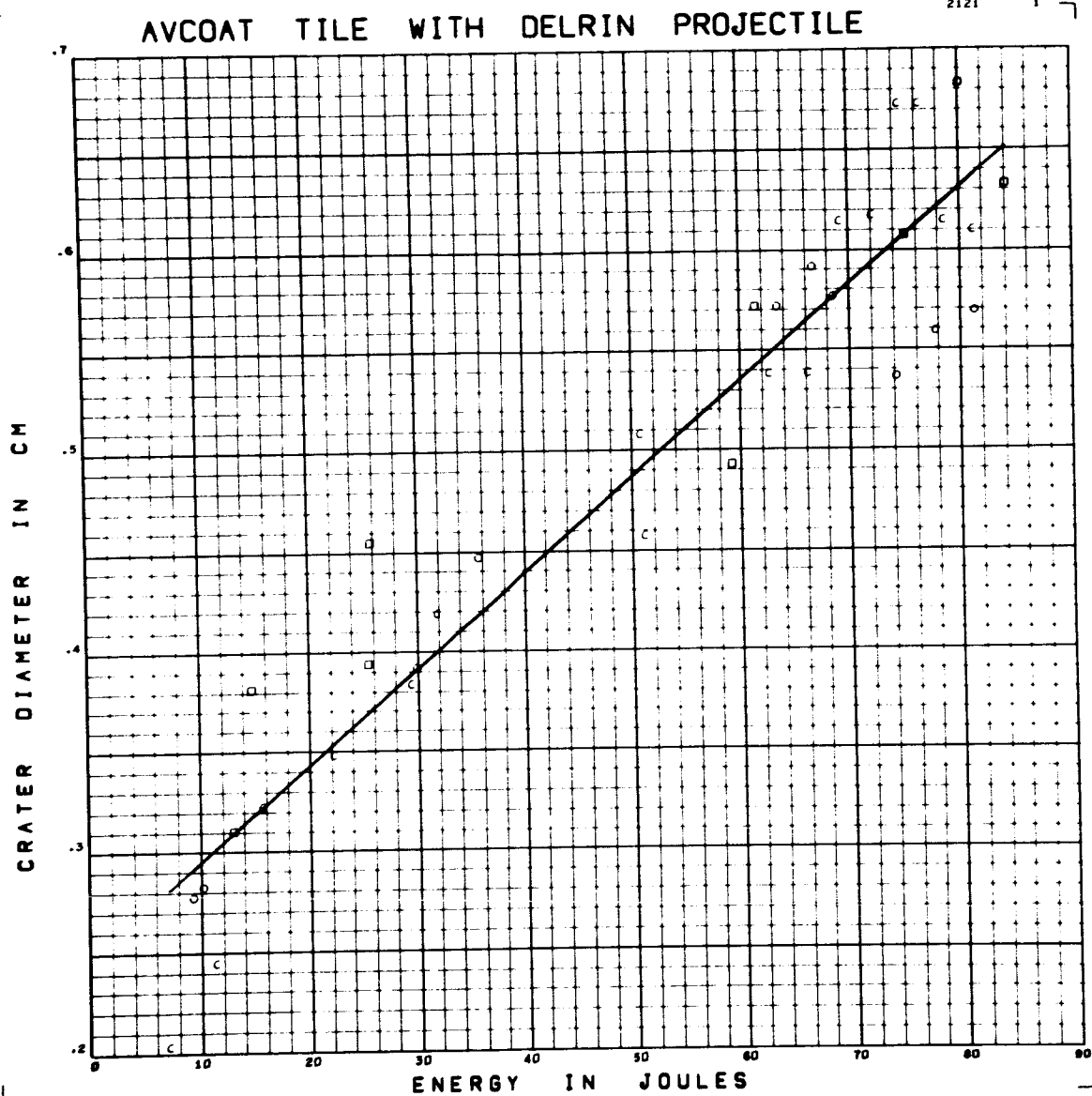


Figure F15 Crater Diameter versus Energy for Delrin Projectiles on

Avcoat 5026 Tile

Form of Regression: $d = 4.808 \times 10^{-3} E + .2470$

RMS Deviation: .040 cm

AVCOAT H.C. WITH DELRIN PROJECTILE

2121

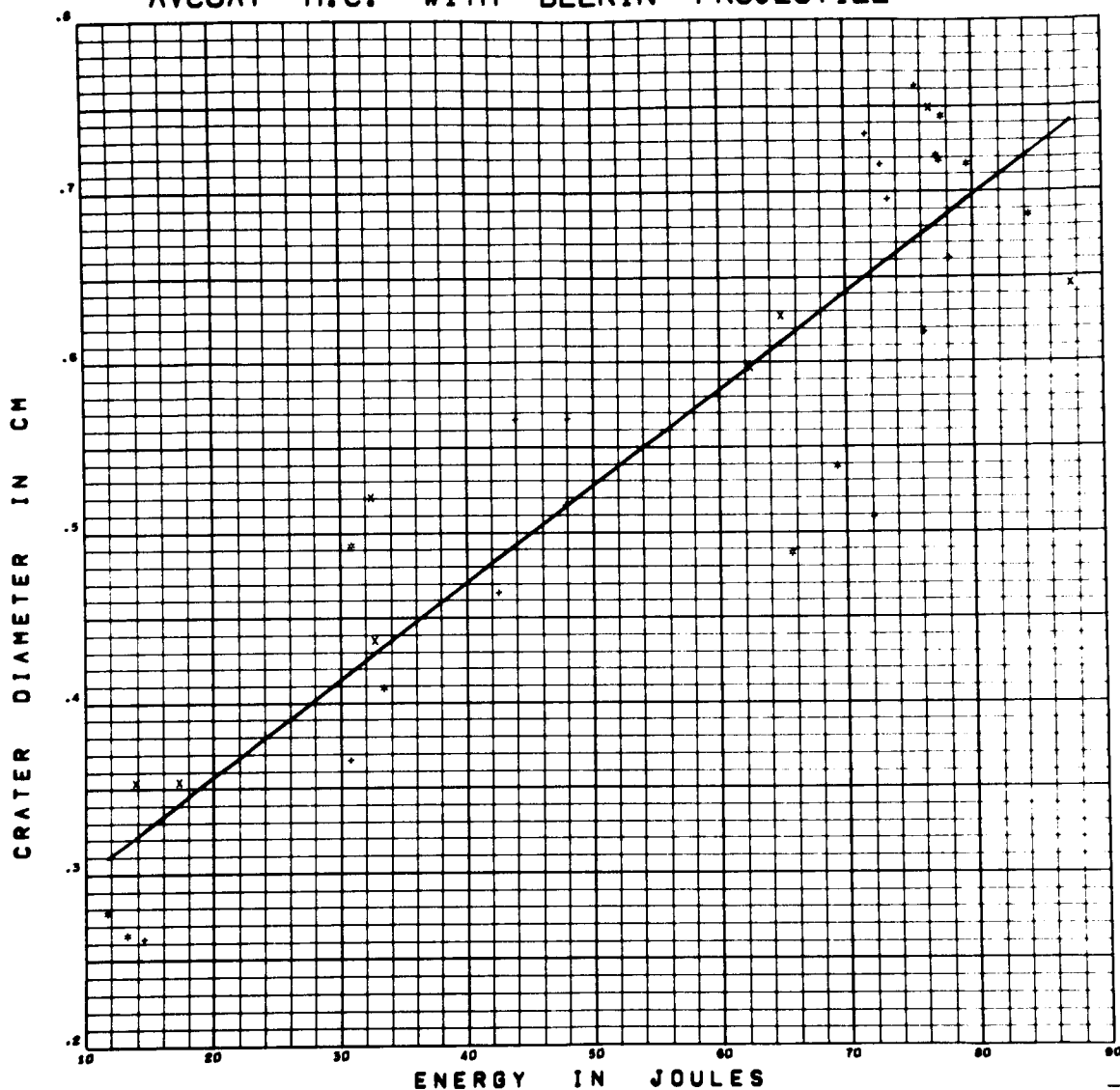


Figure F16 Crater Diameter versus Energy for Delrin Projectiles on

Avcoat 5026 HC

Form of Regression: $d = 5.692 \times 10^{-3} E^{1.2431}$

RMS Deviation: .064 cm

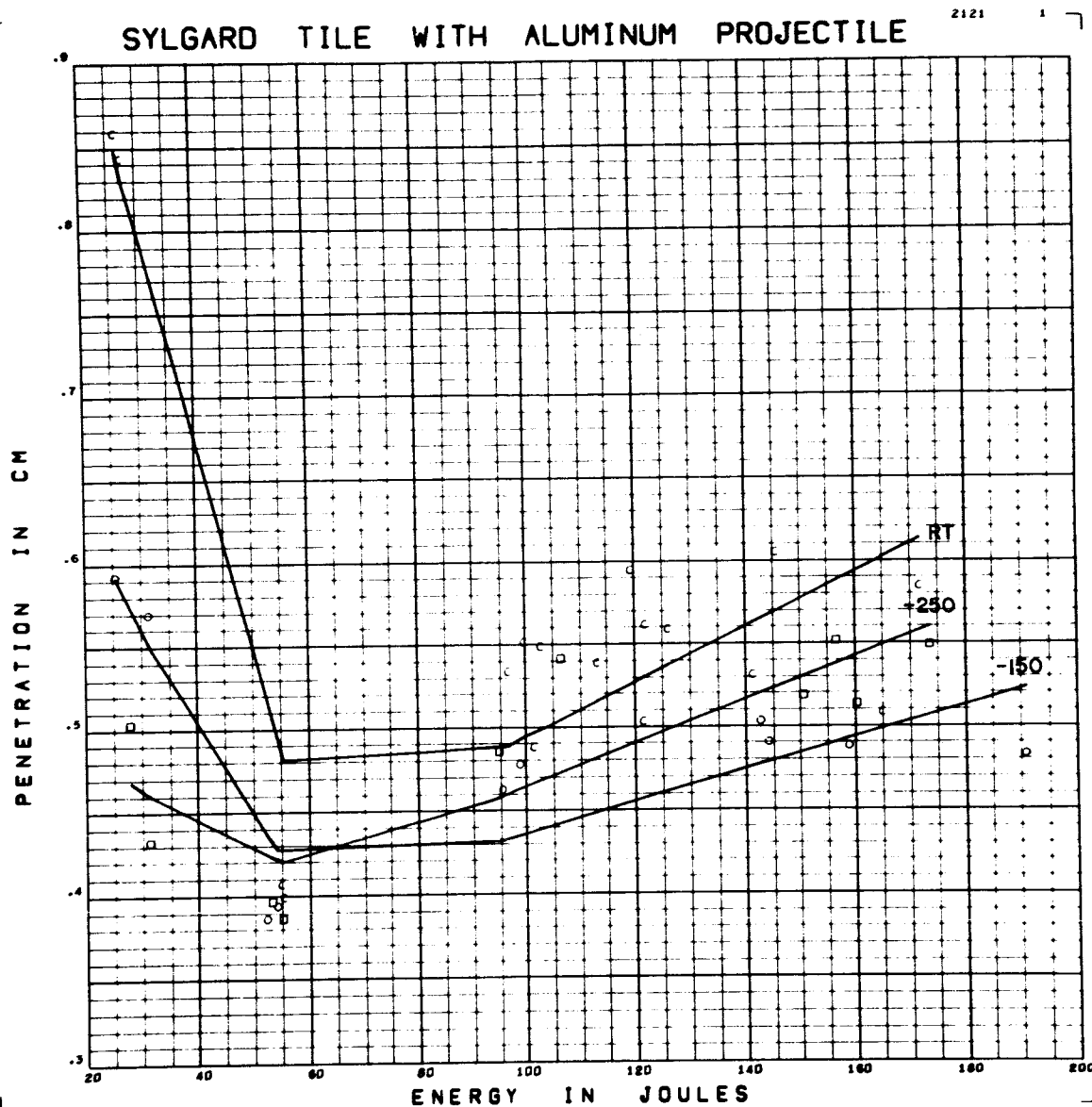


Figure F17 Penetration versus Energy for Aluminum Projectiles on
Sylgard 325 Tile

Form of Regression: $p = (1.306 + .364ST - .342CV) \times 10^{-3} E$
 RMS Deviation: .041 cm $+ .3344 - .0072ST + .0053CV$

SYLGARD H.C. WITH ALUMINUM PROJECTILE

2121

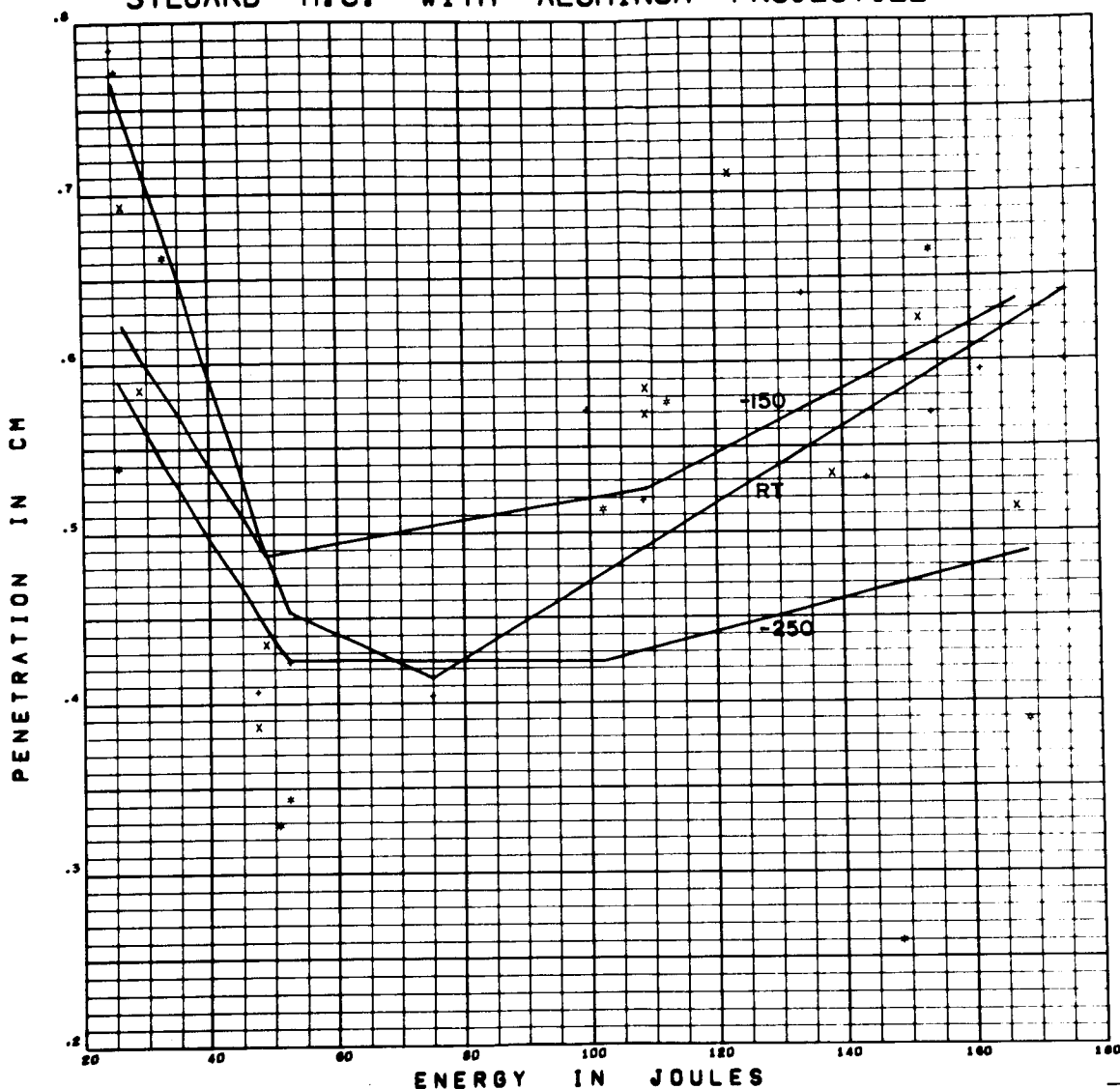


Figure F18 Penetration versus Energy for Aluminum Projectiles on
Sylgard 325 HC

Form of Regression: $p = (1.705 + 1.314 ST + .190 CV) \times 10^{-3} E$
 $+ .2966 - .0823 ST + .0221 CV$
 RMS Deviation: .093 cm

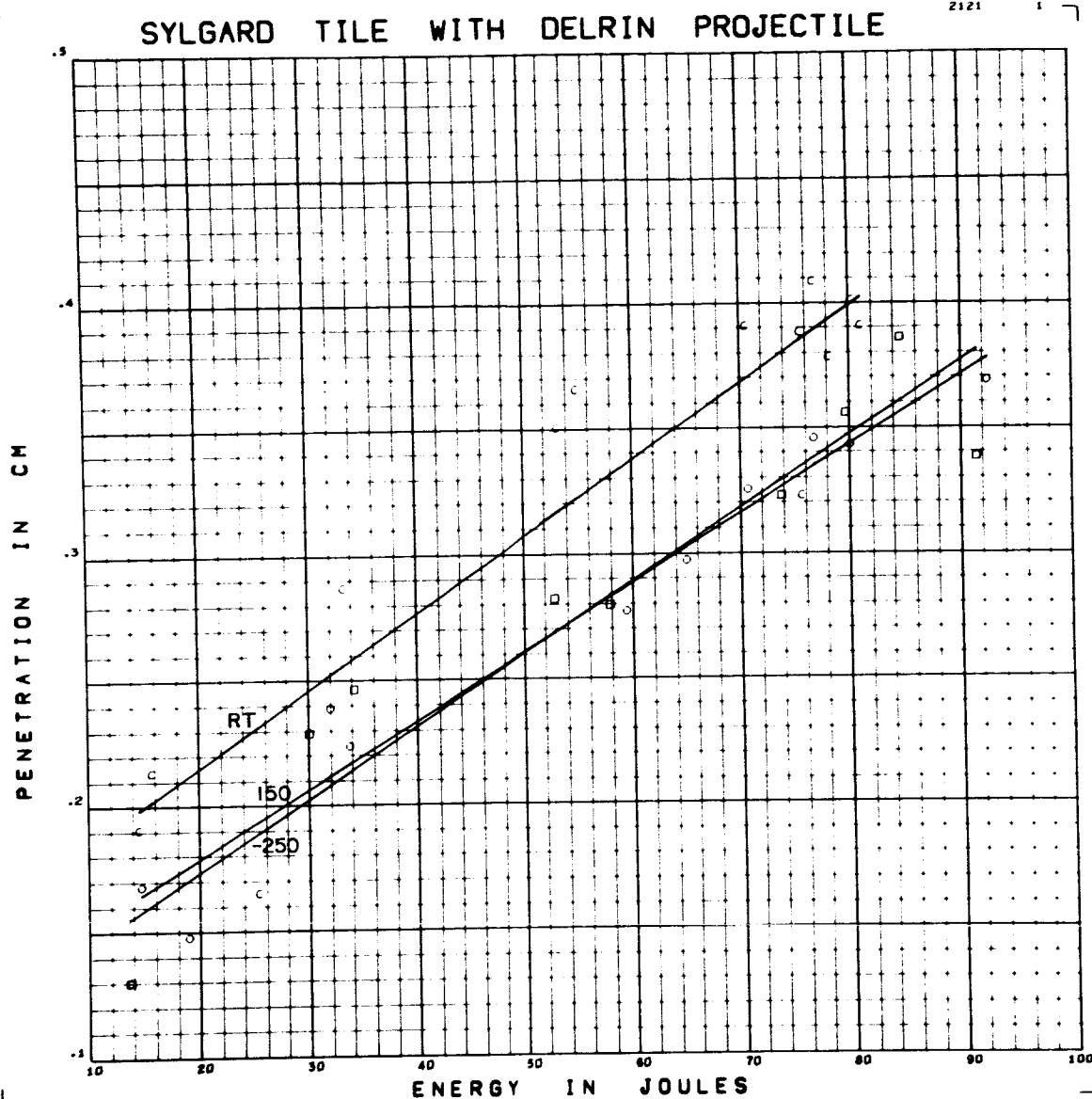


Figure F19 Penetration versus Energy for Delrin Projectiles on

Sylgard 325 Tile

Form of Regression: $p = (2.906 + .1625T - .160CV) \times 10^{-3} E$

RMS Deviation: .026 cm $+ .1310 + .03875T - .0070CV$

SYLGARD H.C. WITH DELRIN PROJECTILE

2121

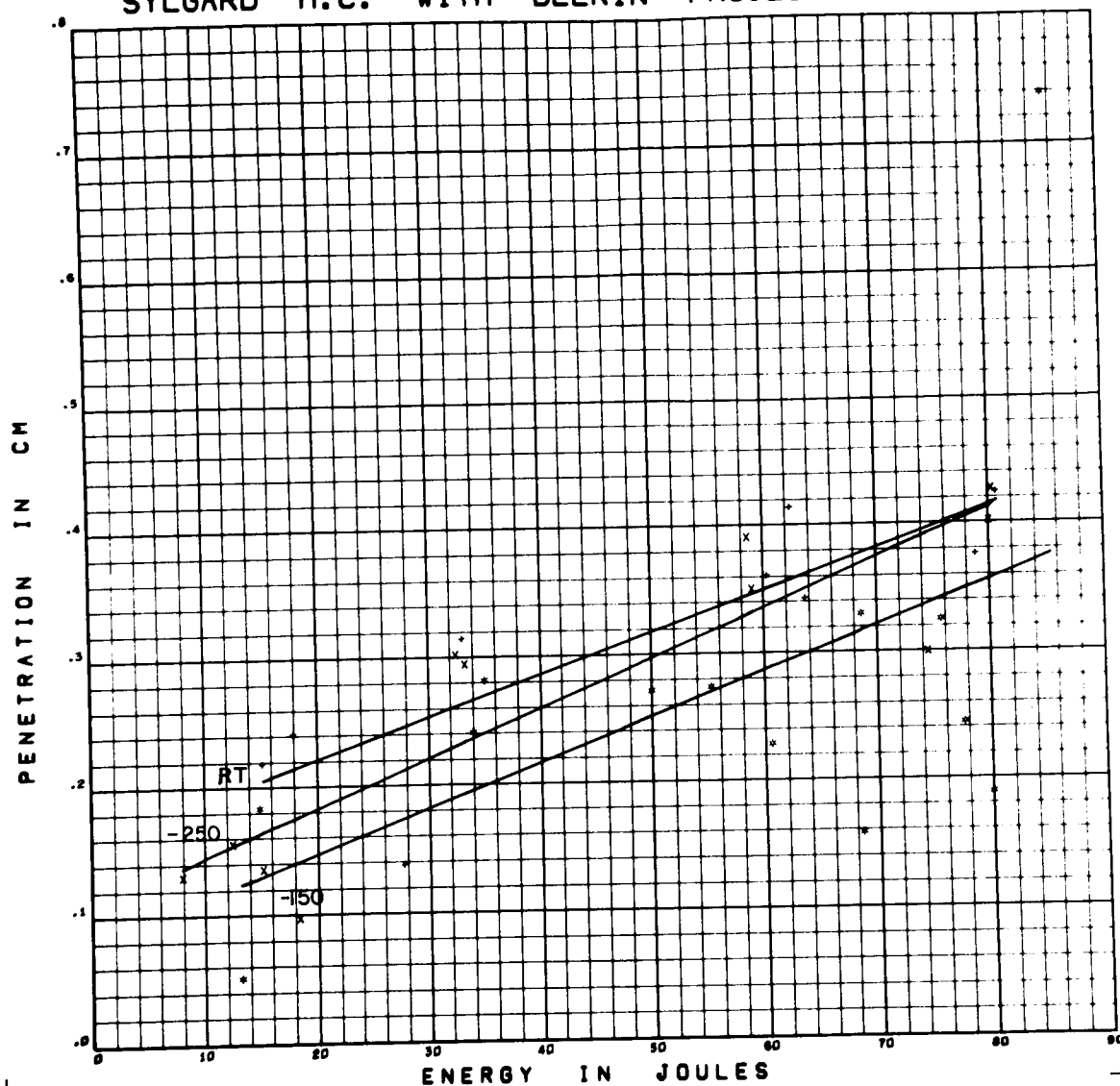


Figure F20 Penetration versus Energy for Delrin Projectiles on

Sylgard 325 HC

Form of Regression: $p = (3.520 - .266 ST + .318 CV) \times 10^{-3} E$

RMS Deviation: .091 cm +.1134 +.0792 ST .0071 CV

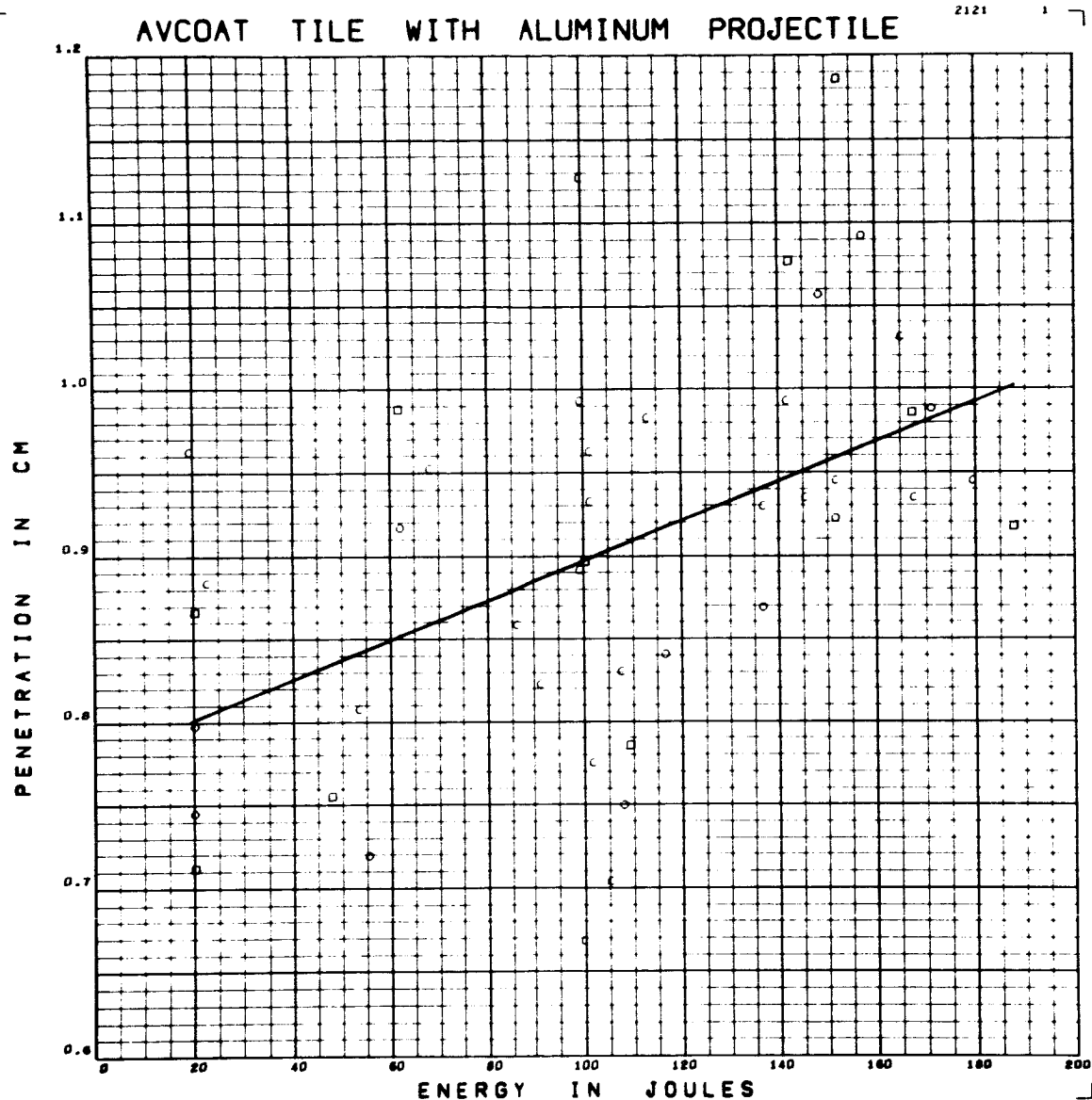


Figure F21 Penetration versus Energy for Aluminum Projectiles on

Avcoat 5026 Tile

Form of Regression: $p = 1.197 \times 10^{-3} E + .7774$

RMS Deviation: .103 cm

AVCOAT H.C. WITH ALUMINUM PROJECTILE

2121

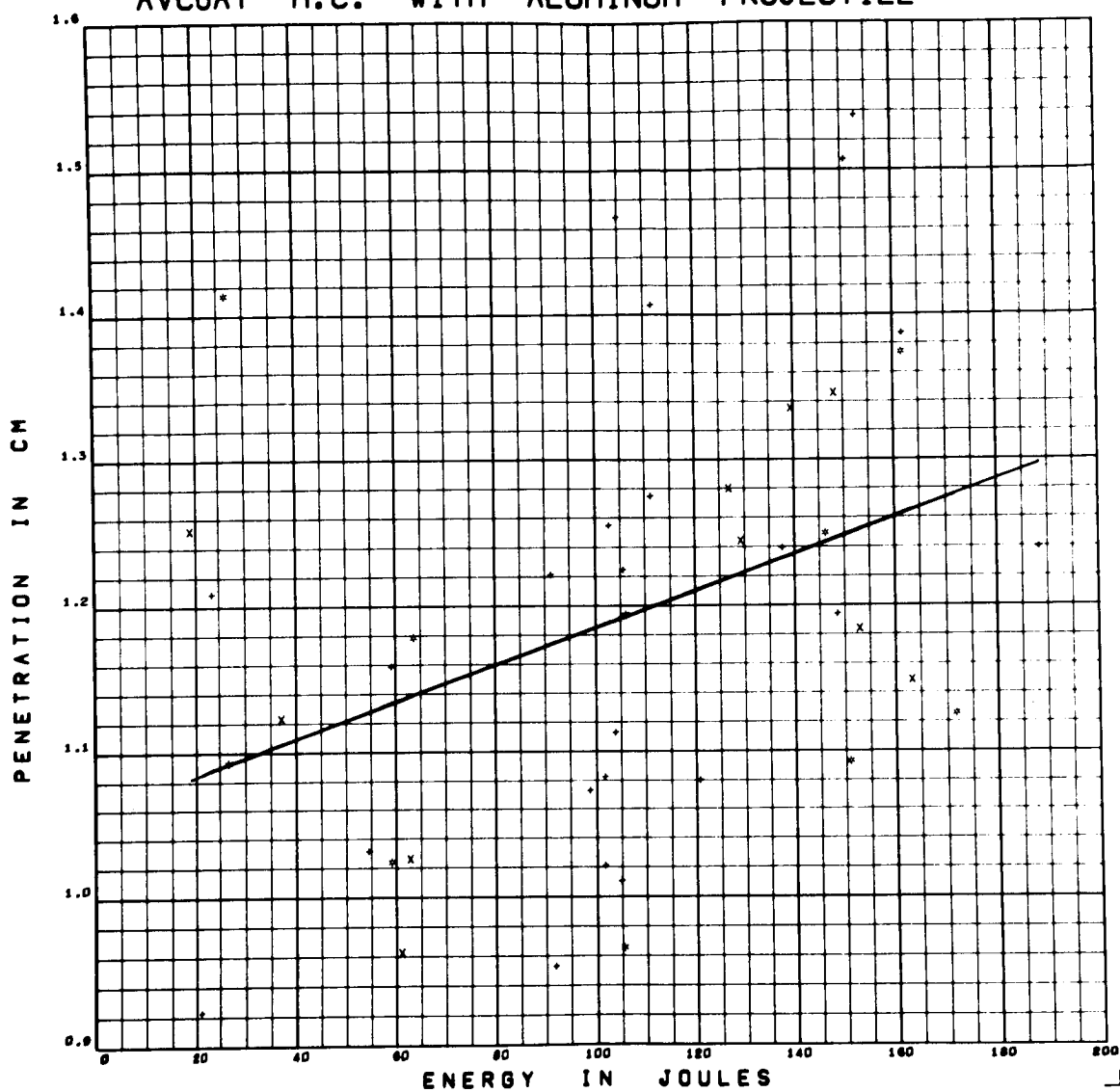


Figure F22 Penetration versus Energy for Aluminum Projectiles on

Avcoat 5026 HC

Form of Regression: $p = 1.266 \times 10^{-3} E + 1.058$

RMS Deviation: .142 cm

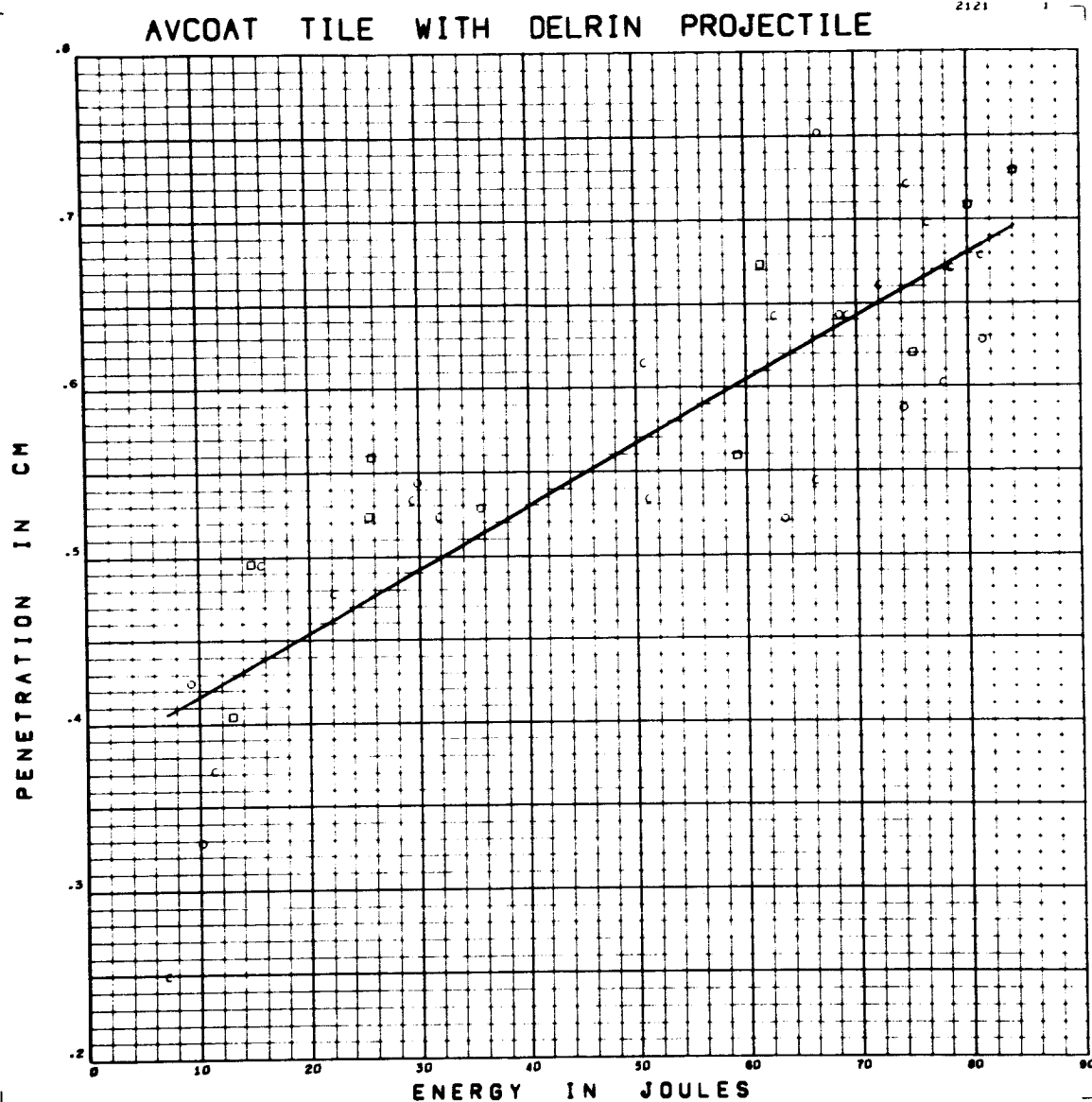


Figure F23 Penetration versus Energy for Delrin Projectiles on

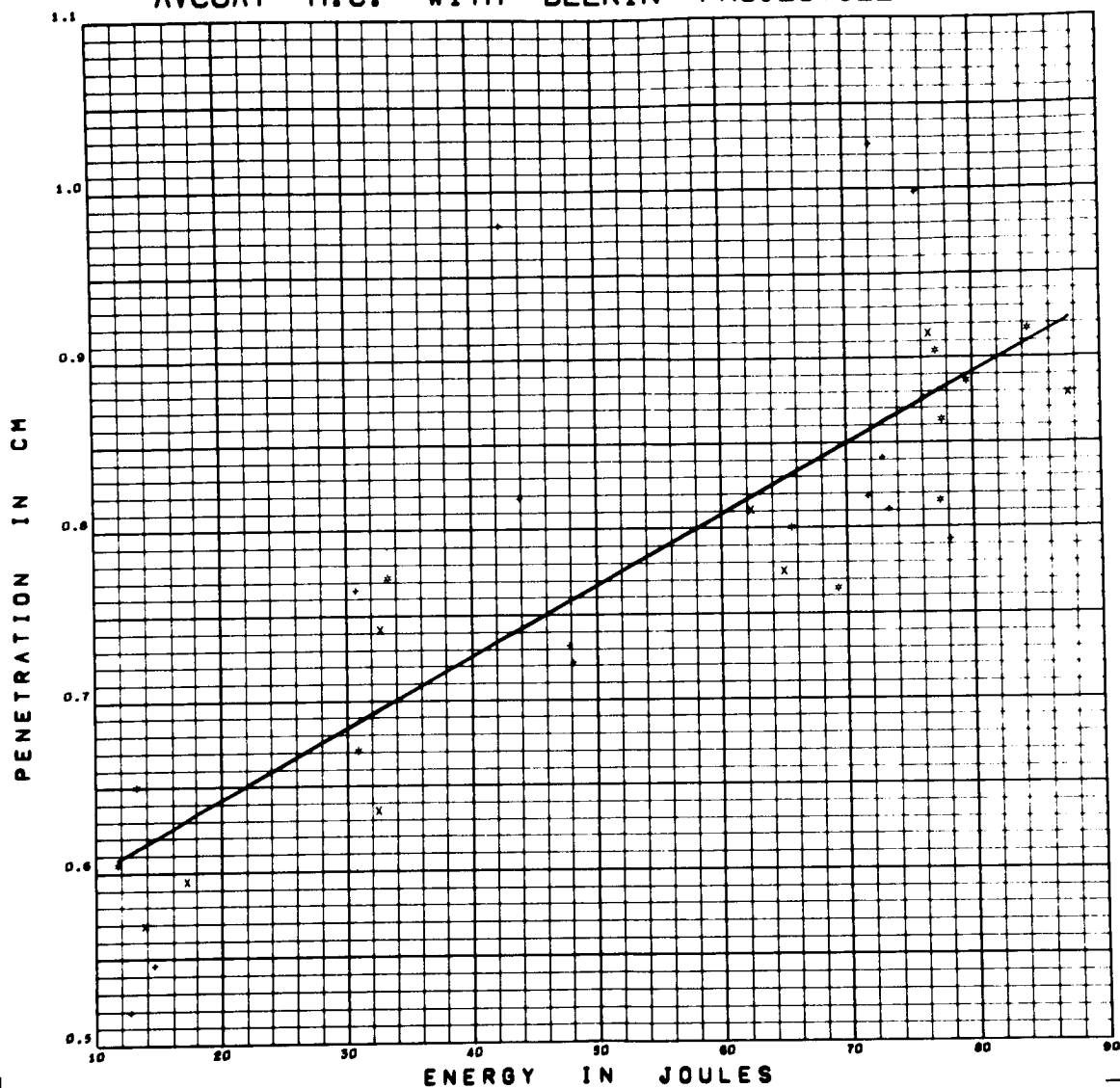
Avcoat 5026 Tile

Form of Regression: $p = 3.778 \times 10^{-3} E + .3784$

RMS Deviation: .060 cm

AVCOAT H.C. WITH DELRIN PROJECTILE

2121



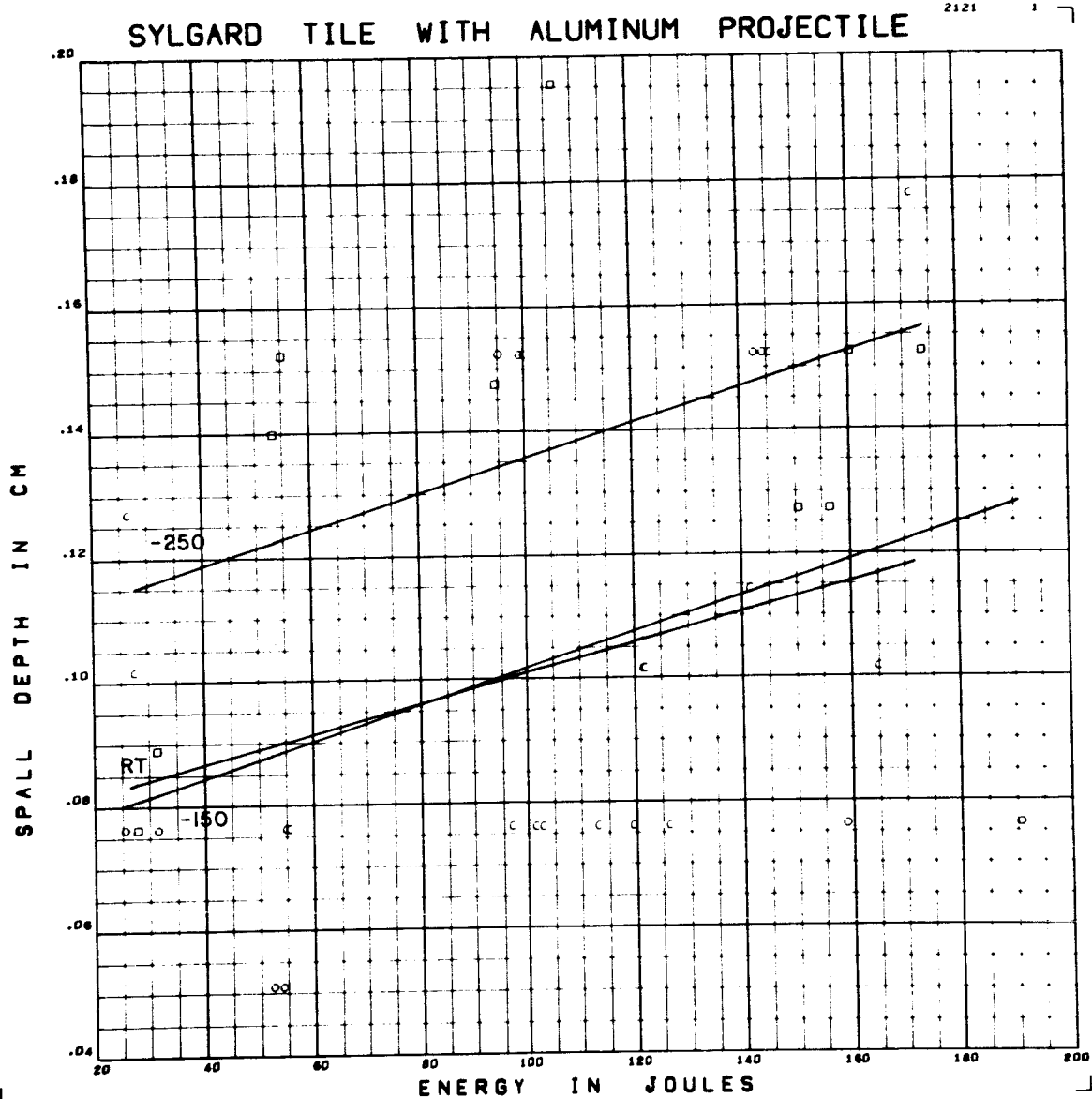


Figure F25 Spall Depth versus Energy for Aluminum Projectiles on
Sylgard 325 Tile

Form of Regression: $p_s = (.271 - .041 ST + .018 CV) \times 10^{-3} E$

RMS Deviation: .033 cm $+ .0857 - .0304 ST - .0129 CV$

SYLGARD H.C. WITH ALUMINUM PROJECTILE

2121

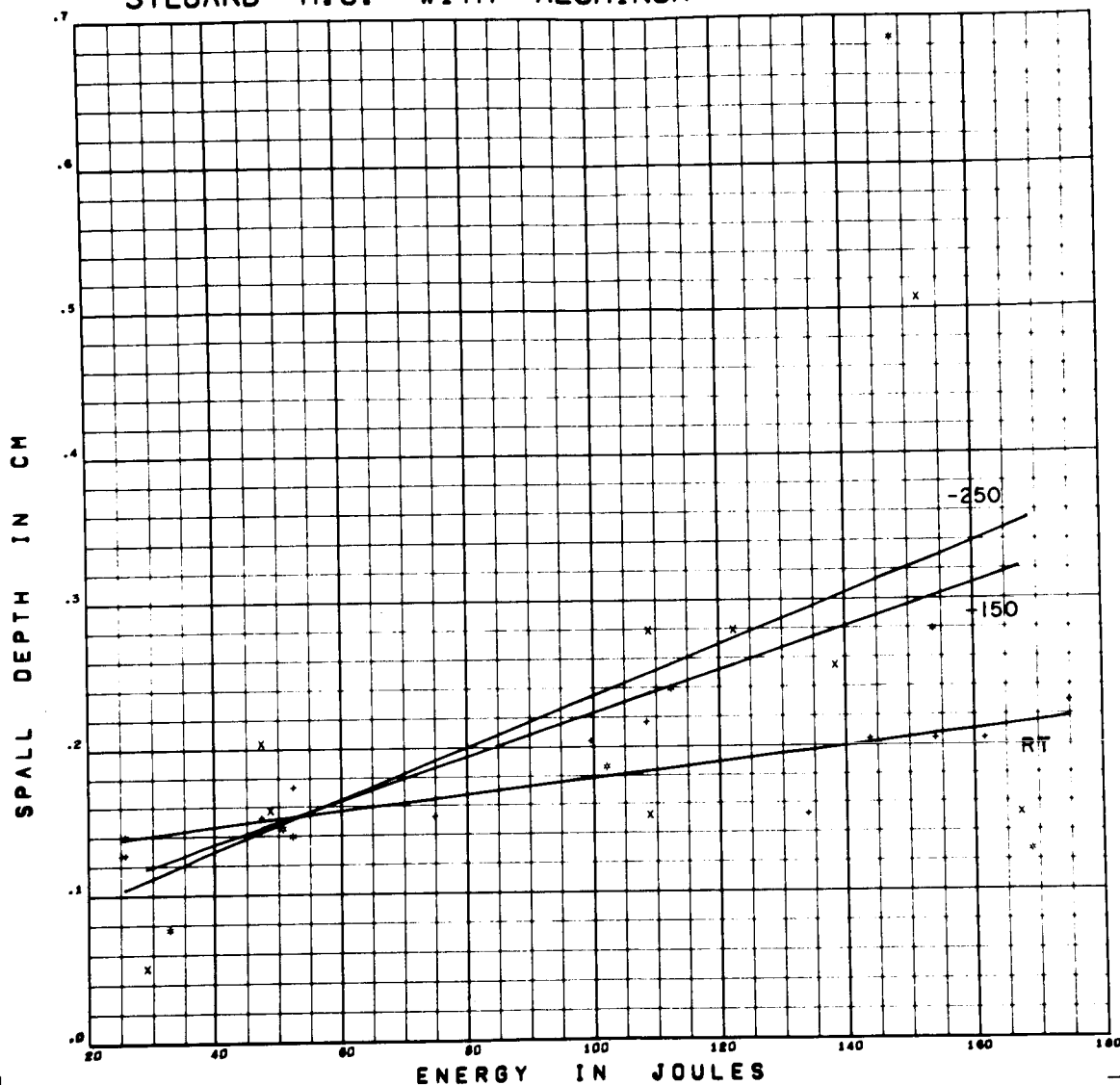


Figure F26 Spall Depth versus Energy for Aluminum Projectiles on

Sylgard 325 HC

Form of Regression: $p_s = (1.248 - 1.215 ST + .219 CV) \times 10^{-3} E$

RMS Deviation: .100 cm. $+ .0870 + .0654 ST - .0112 CV$

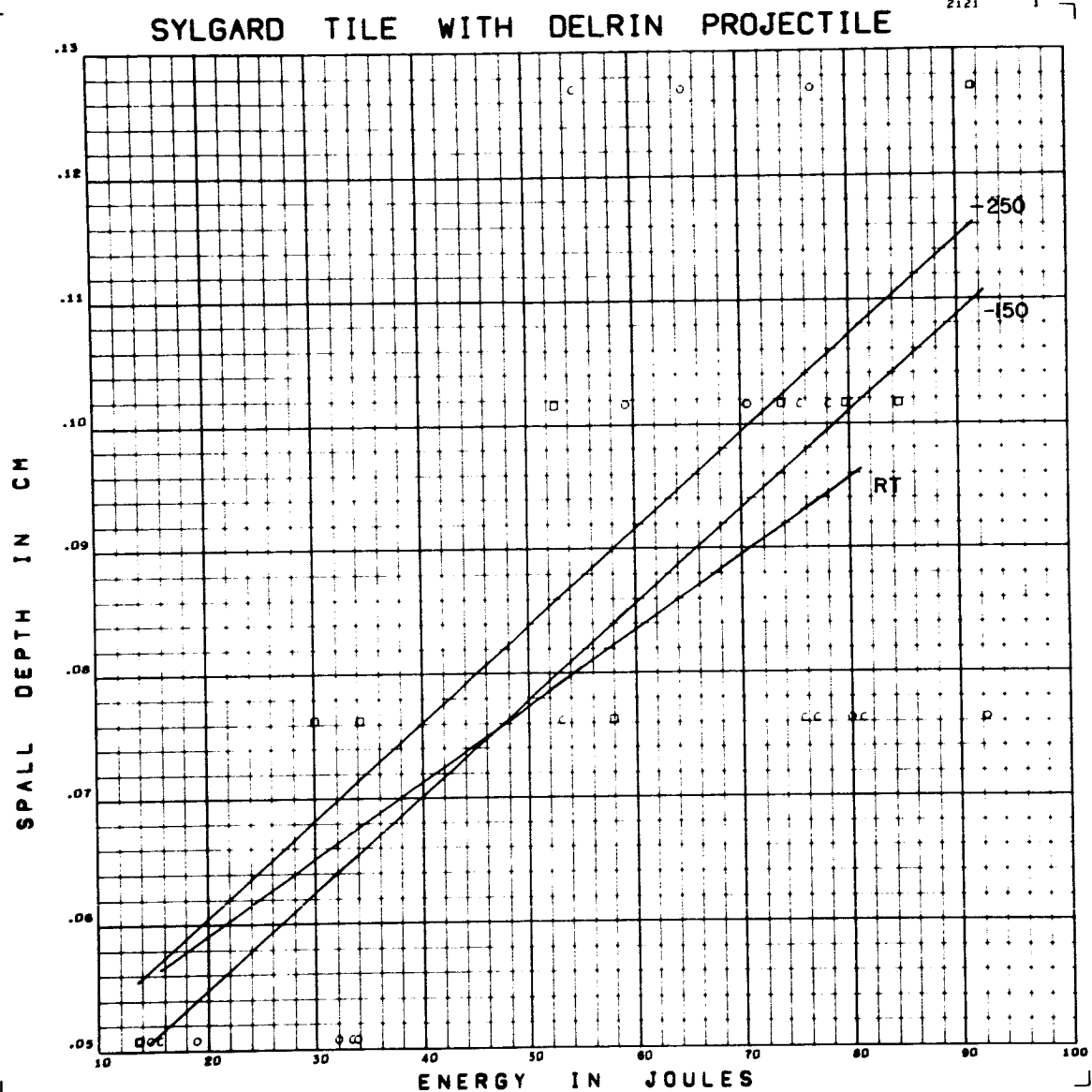


Figure F27 Spall Depth versus Energy for Delrin Projectiles on
Sylgard 325 Tile

Form of Regression: $p_s = (.720 - .170 ST + .051 CV) \times 10^{-3} E$

RMS Deviation: .017 cm $+ .0437 - .0020 ST + .0044 CV$

SYLGARD H.C. WITH DELRIN PROJECTILE

2121

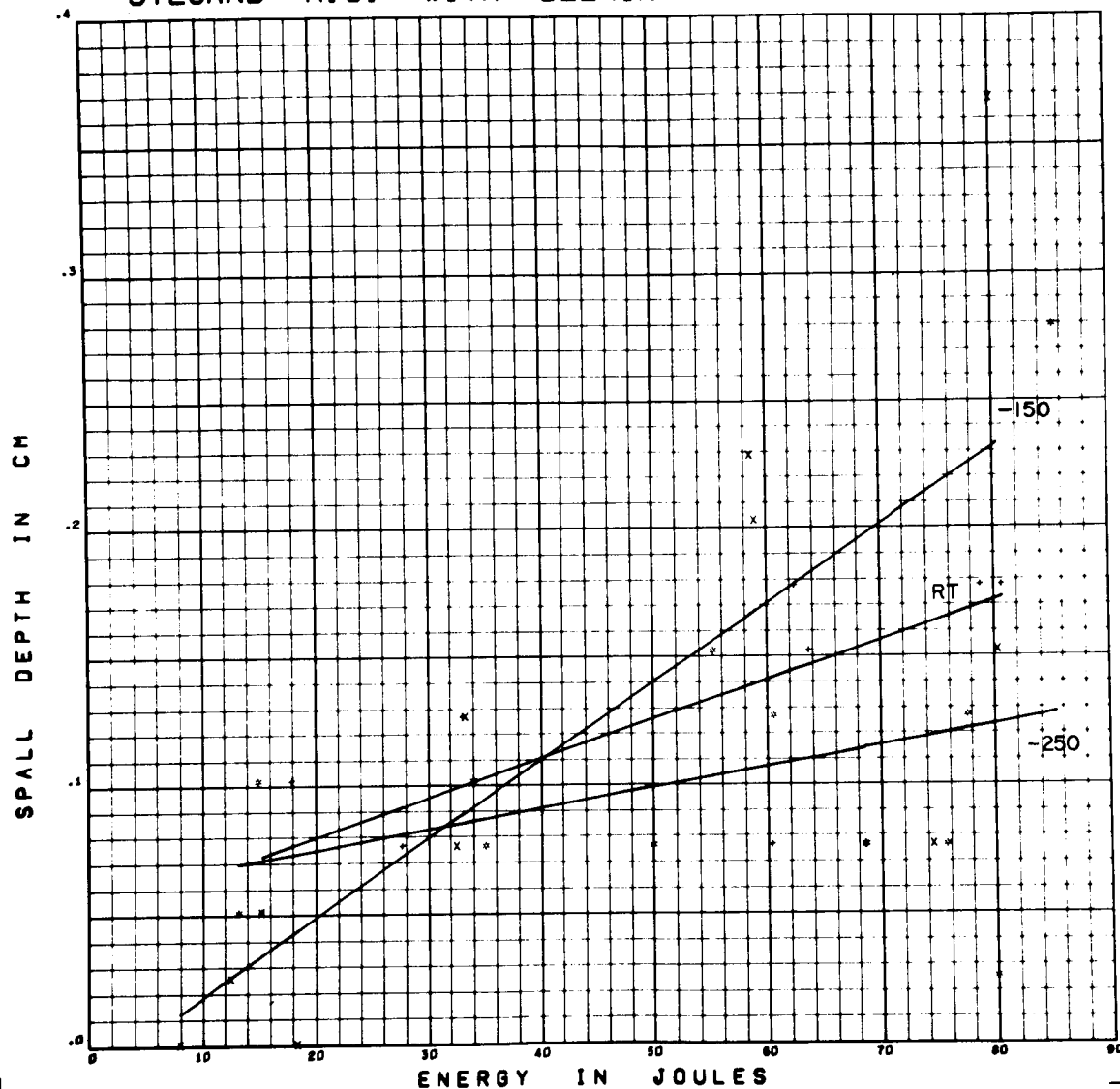


Figure F28 Spall Depth versus Energy for Delrin Projectiles on

Sylgard 325 HC

Form of Regression: $p_s = (1.799 + .728 ST + 1.248 CV) \times 10^{-3} E$

RMS Deviation: .057 cm $+ .0319 - .0098 ST - .0438 CV$

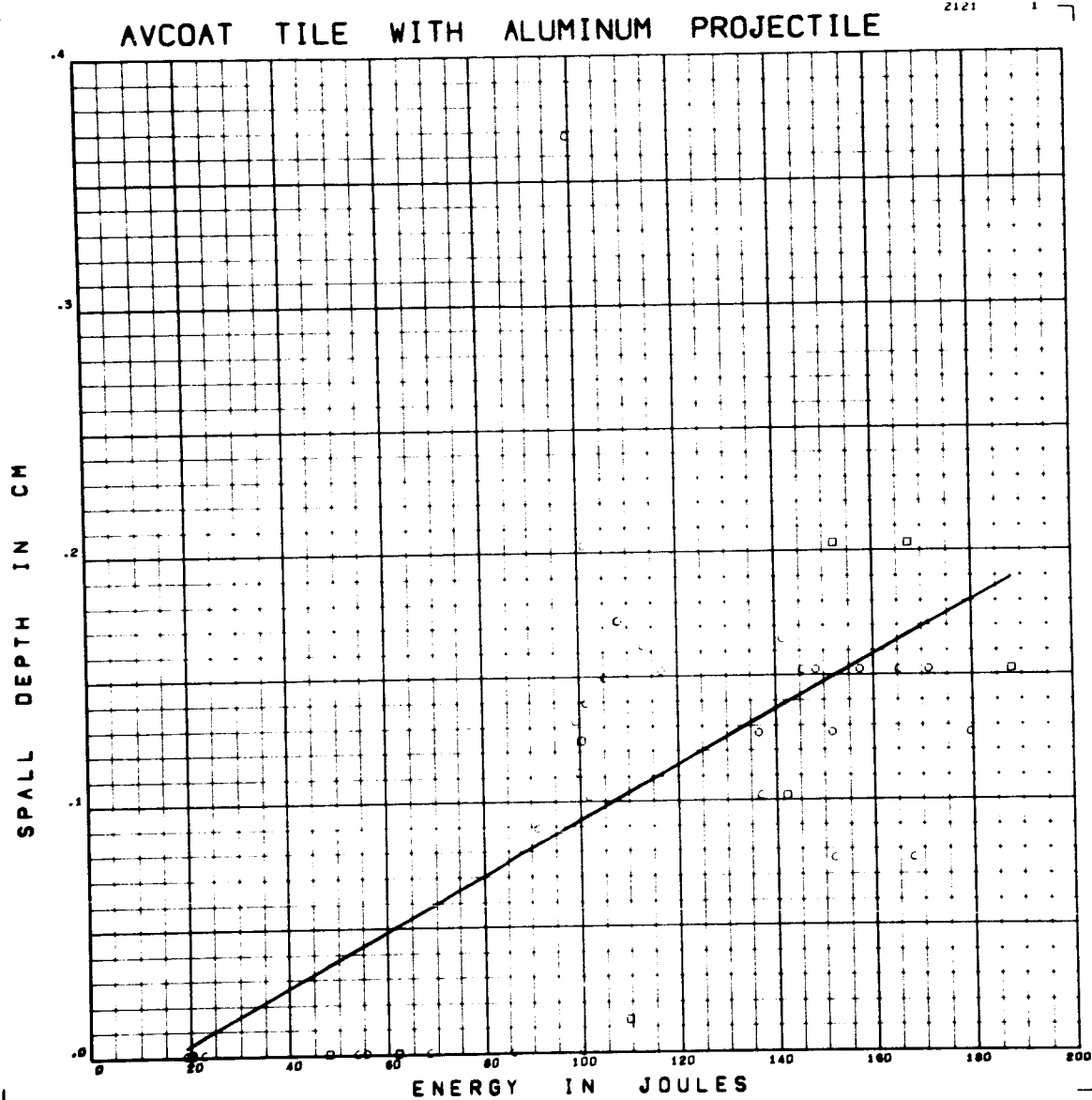


Figure F29 Spall Depth versus Energy for Aluminum Projectiles on

Avcoat 5026 Tile

Form of Regression: $p_s = 1.100 \times 10^{-3} E - .0172$

RMS Deviation: .064 cm

AVCOAT H.C. WITH ALUMINUM PROJECTILE

2121

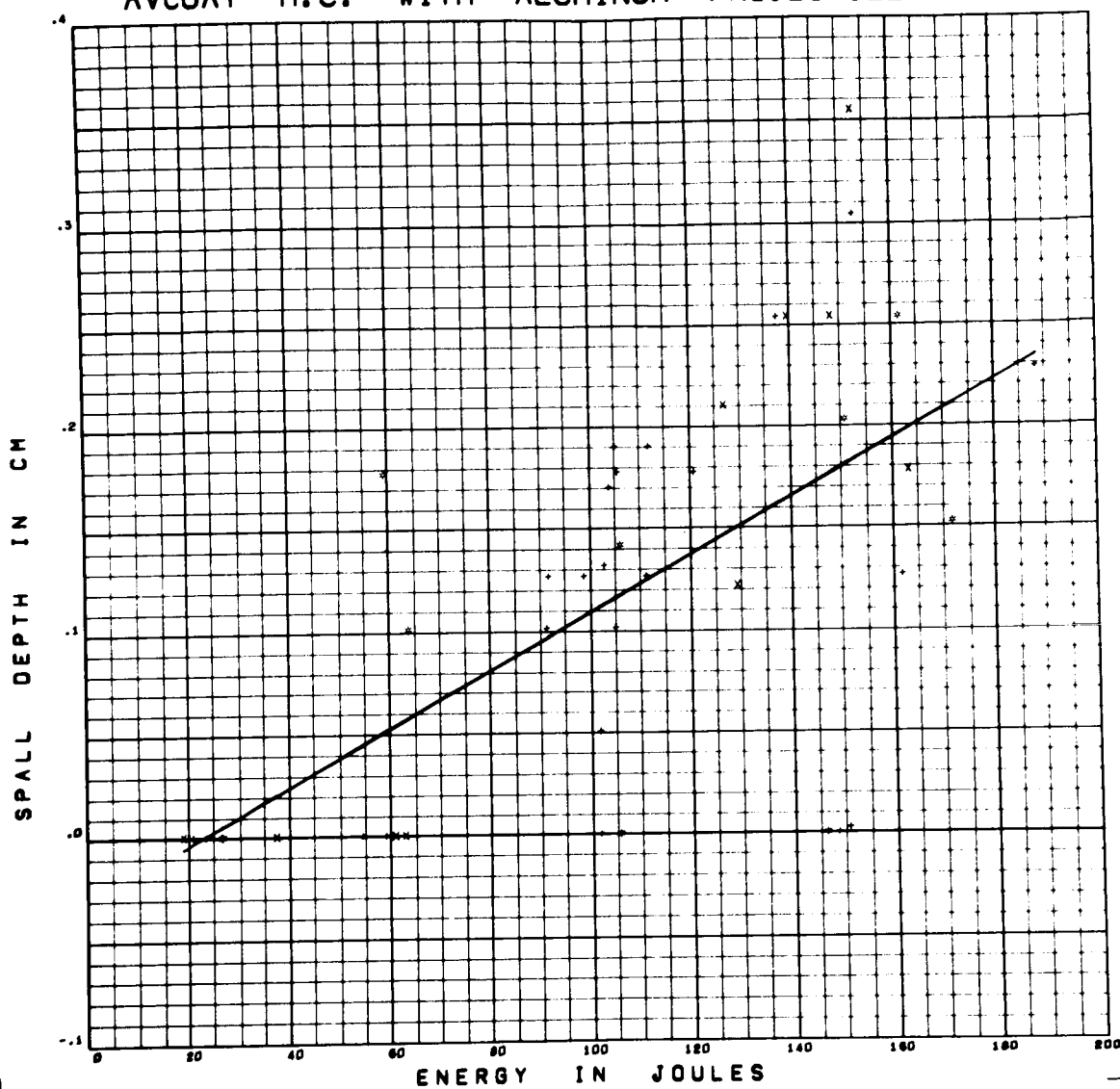


Figure F30 Spall Depth versus Energy for Aluminum Projectiles on
Avcoat 5026 HC

Form of Regression: $p_s = 1.414 \times 10^{-3} E - .0320$

RMS Deviation: .078 cm

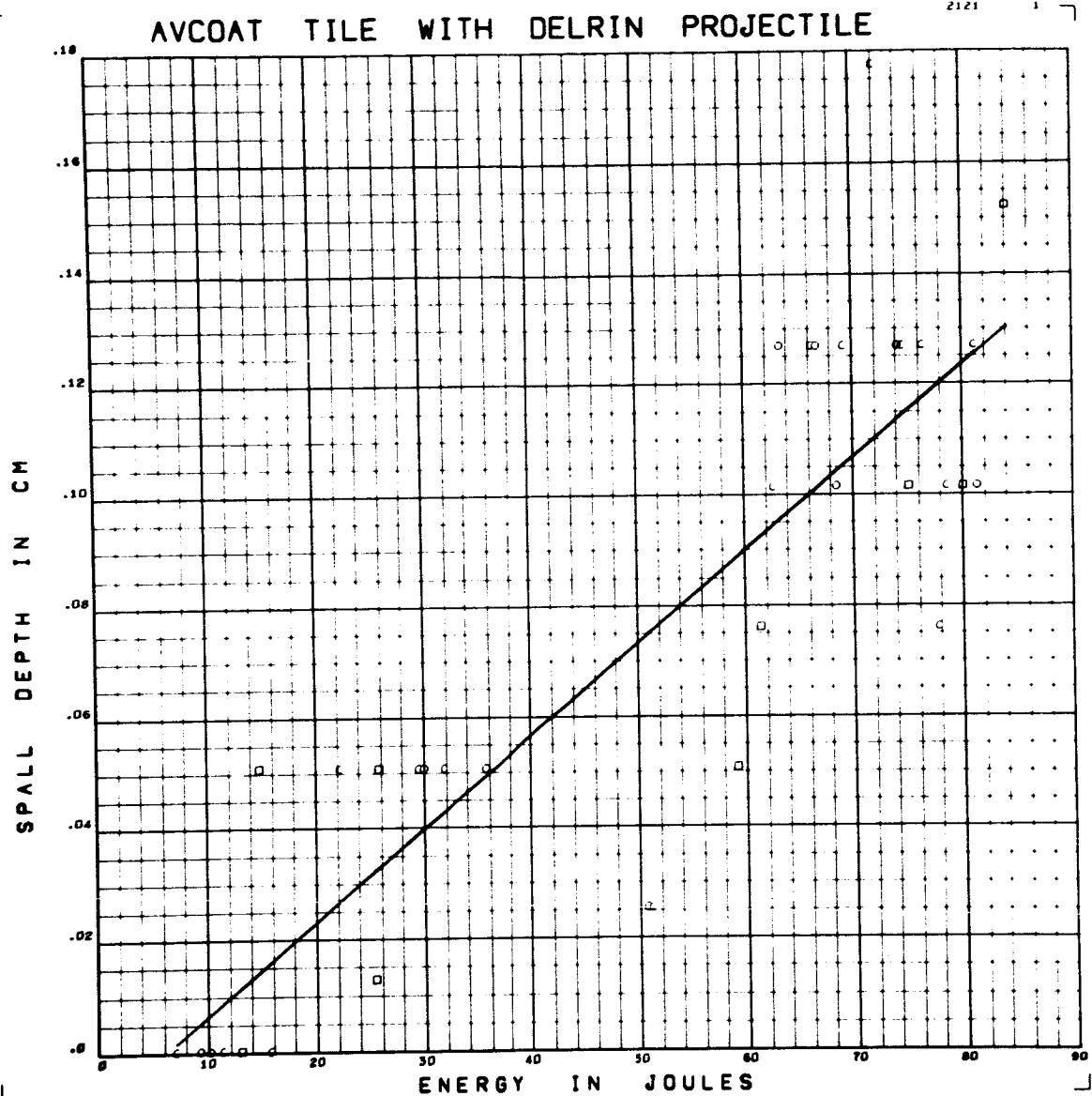


Figure F31 Spall Depth versus Energy for Delrin Projectiles on

Avcoat 5026 Tile

Form of Regression: $p_s = 1.673 \times 10^{-3} E - .0103$

RMS Deviation: .025 cm

AVCOAT H.C. WITH DELRIN PROJECTILE

2121

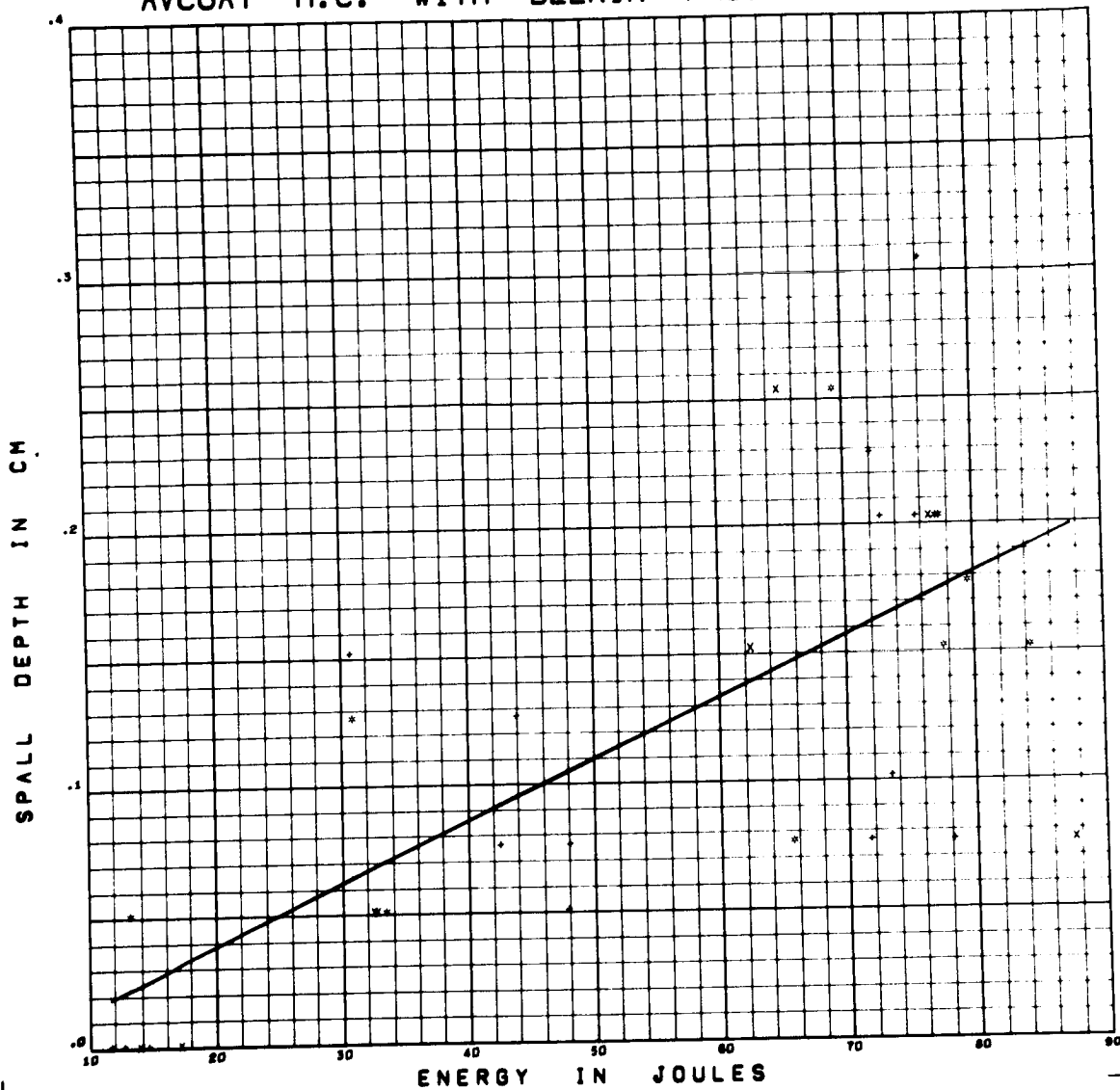


Figure F32 Spall Depth versus Energy for Delrin Projectiles on

Avcoat 5026 HC

Form of Regression: $p_s = 2.382 \times 10^{-3} E - .0091$

RMS Deviation: .060 cm

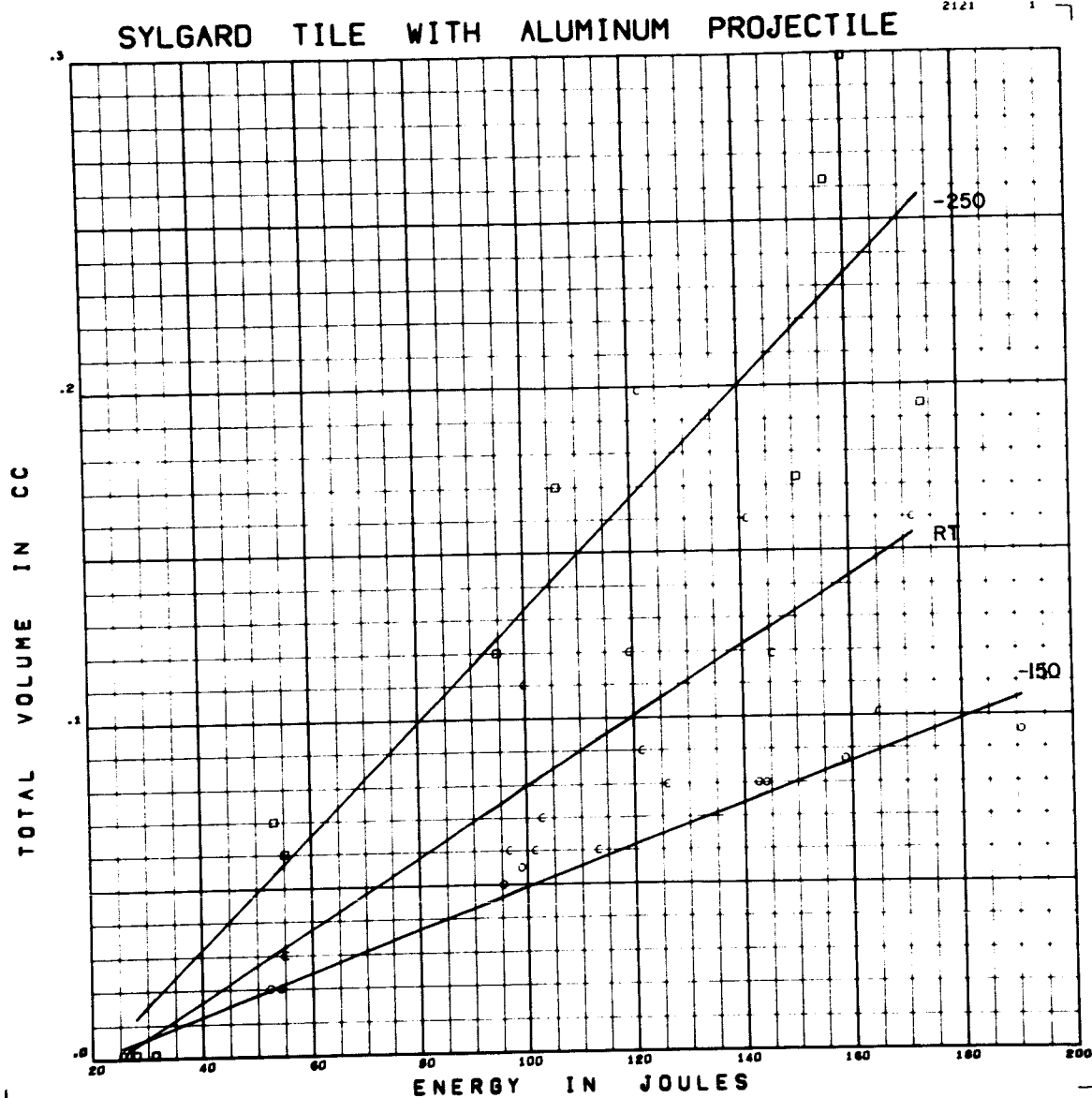


Figure F33 Volume versus Energy for Aluminum Projectiles on Sylgard 325 Tile

Form of Regression: $v = (1.118 - .633 ST - .499 CV) \times 10^{-3} E$
 $- .0245 + .0098 ST + .0117 CV$

RMS Deviation: .029 cc

SYLGARD H.C. WITH ALUMINUM PROJECTILE

2121

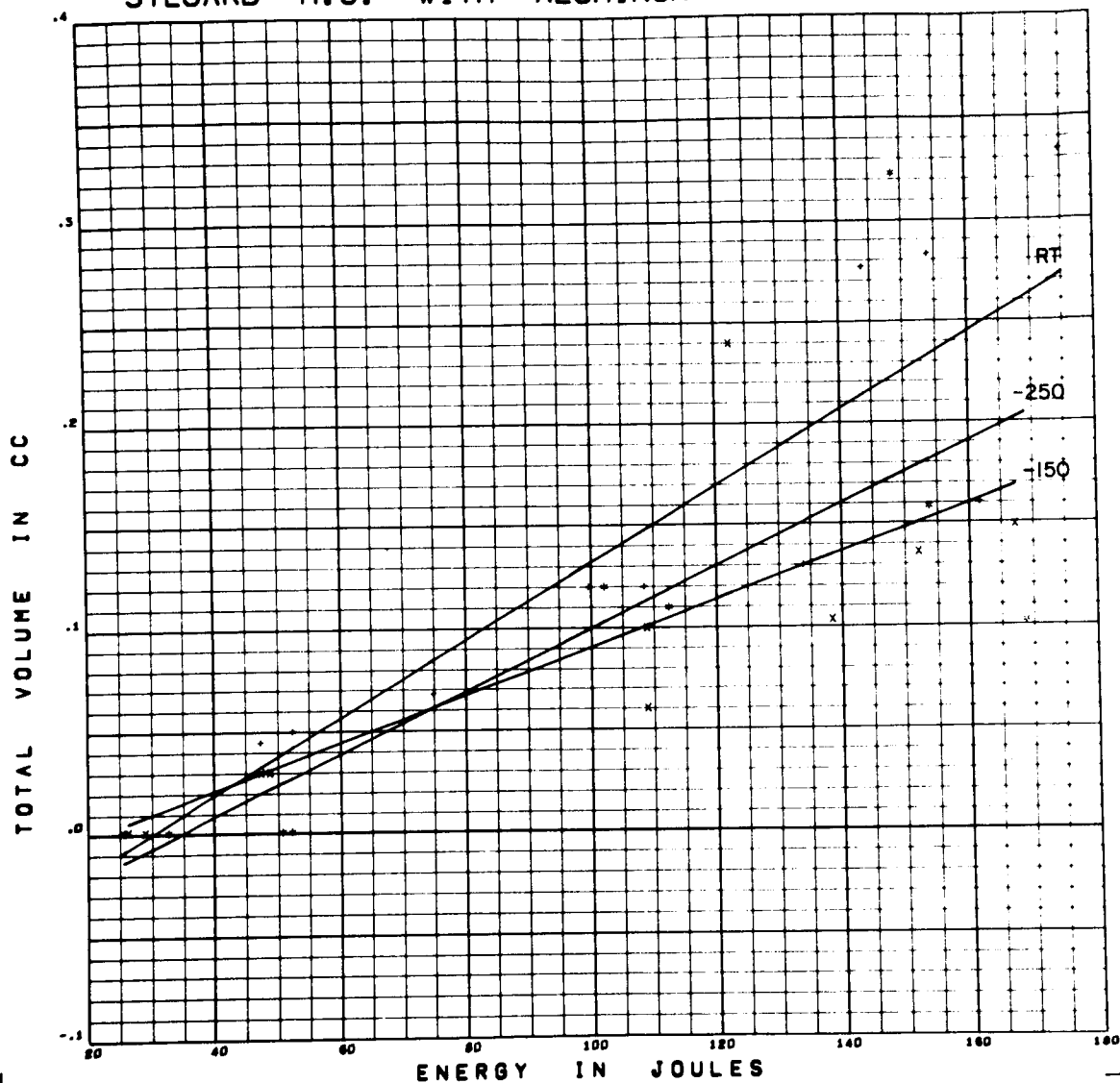


Figure F34 Volume versus Energy for Aluminum Projectiles on Sylgard 325 HC

Form of Regression: $v = (1.520 + .367 ST - .363 CV) \times 10^{-3} E$

RMS Deviation: .051 CC -.0445 -.0045 ST +.0197 CV

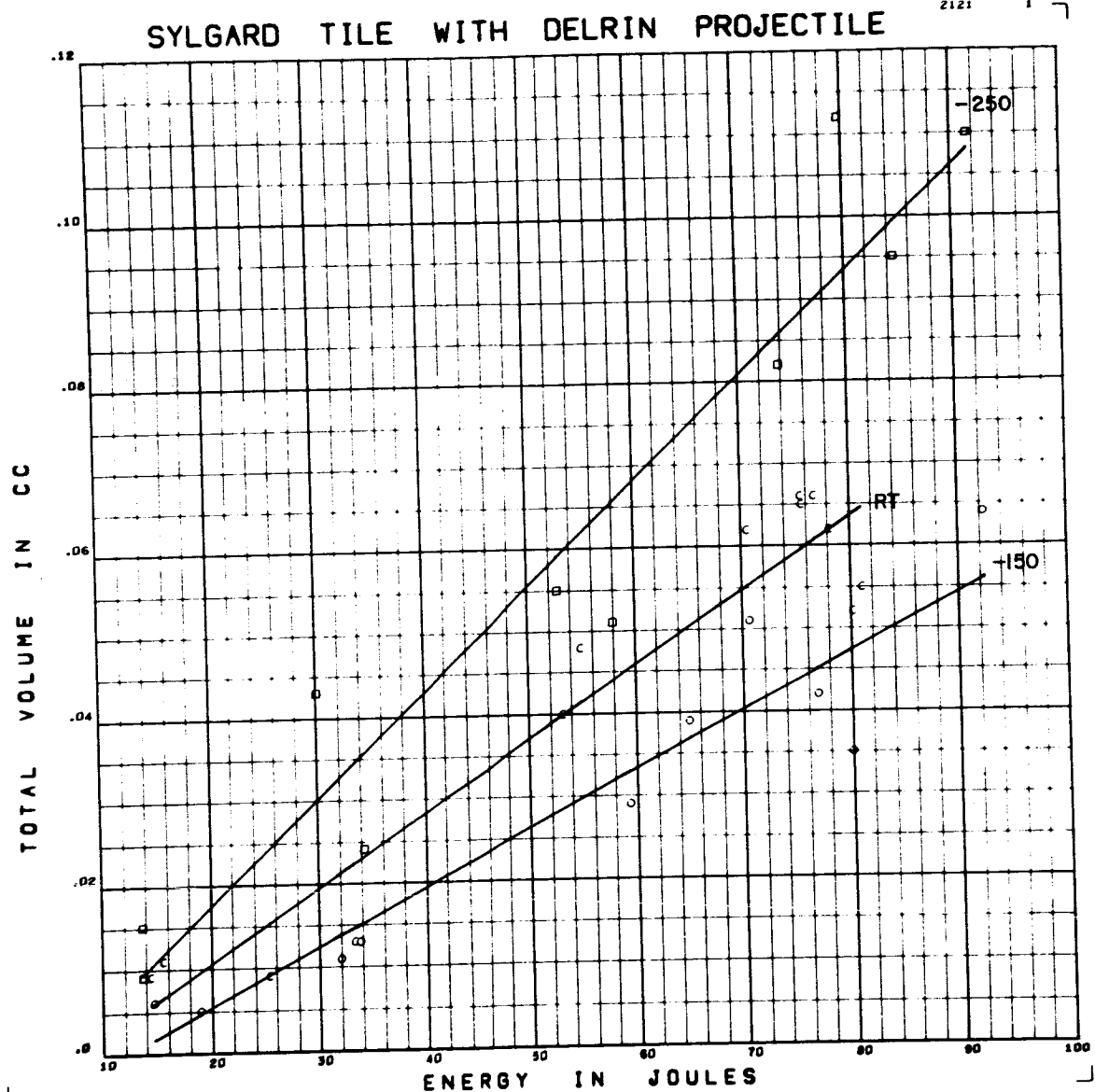


Figure F35 Volume versus Energy for Delrin Projectiles on Sylgard 325 Tile

Form of Regression: $V = (.951 - .385 ST - .251 CV) \times 10^{-3} E$

RMS Deviation: .007 cc -.0078 +.0009 ST -.0007 CV

SYLGARD H.C. WITH DELRIN PROJECTILE

2121

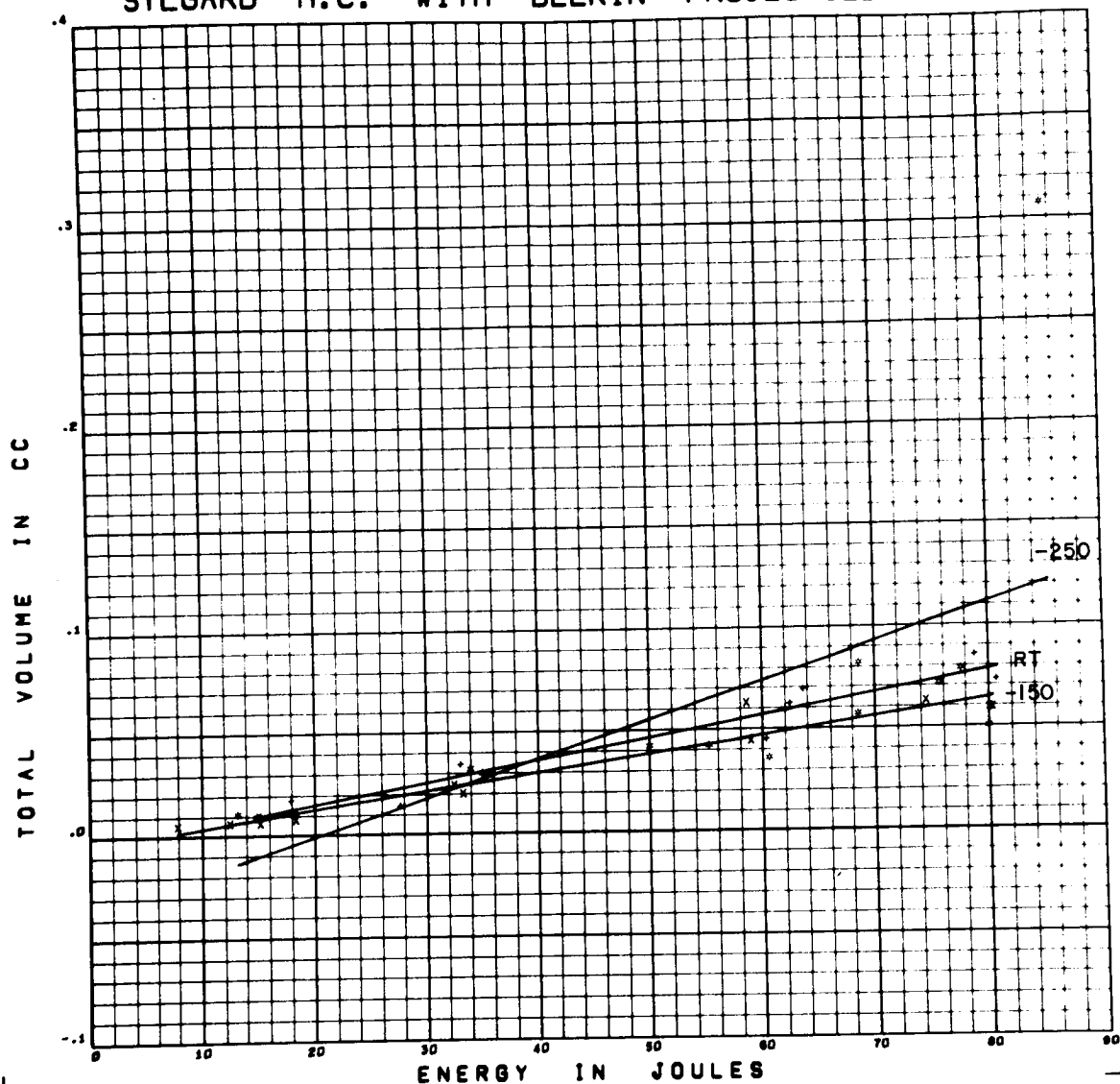


Figure F36 Volume versus Energy for Delrin Projectiles on Sylgard 325 HC

Form of Regression: $V = (1.266 - .816 ST - .401 CV) \times 10^{-3} E$

RMS Deviation: $.038cc - .0147 + .0321 ST + .0117 CV$

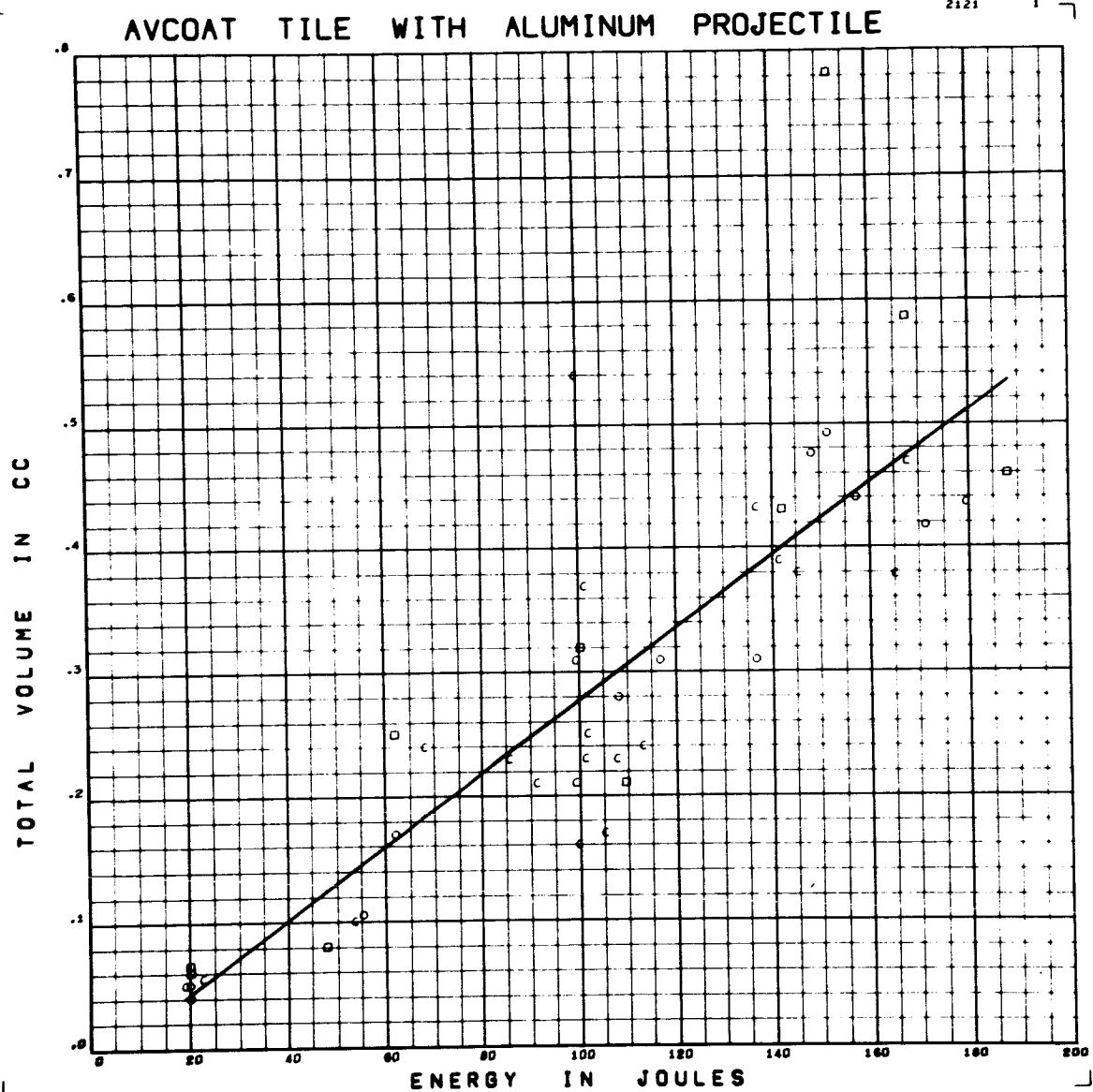


Figure F37 Volume versus Energy for Aluminum Projectiles on Avcoat 5026 Tile

Form of Regression: $V = 2.928 \times 10^{-3} E - .0154$

RMS Deviation: .089 cc

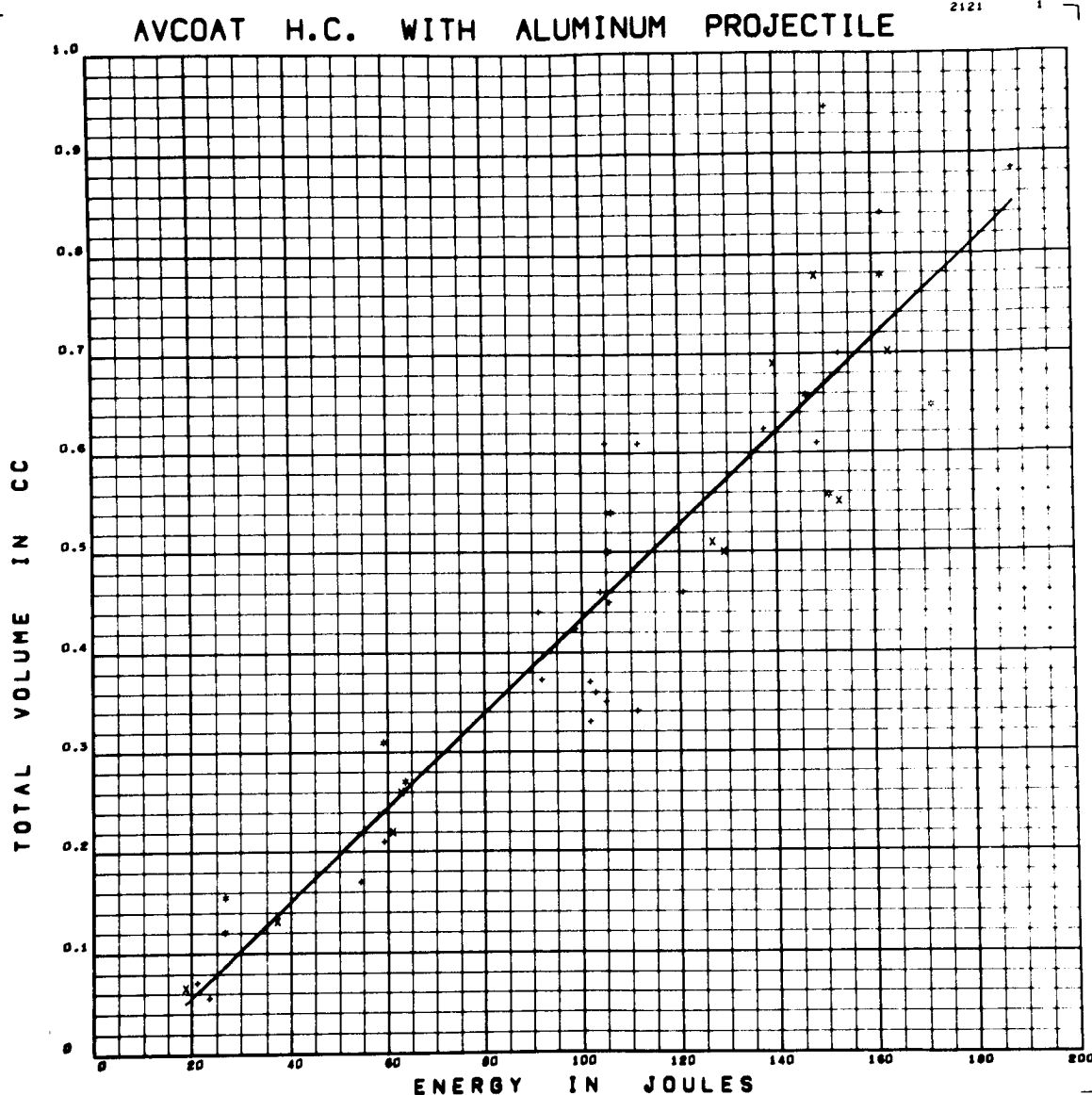


Figure F38 Volume versus Energy for Aluminum Projectiles on Avcoat 5026 HC

Form of Regression: $V = 4.717 \times 10^{-3} E - .0383$

RMS Deviation: .084 cc

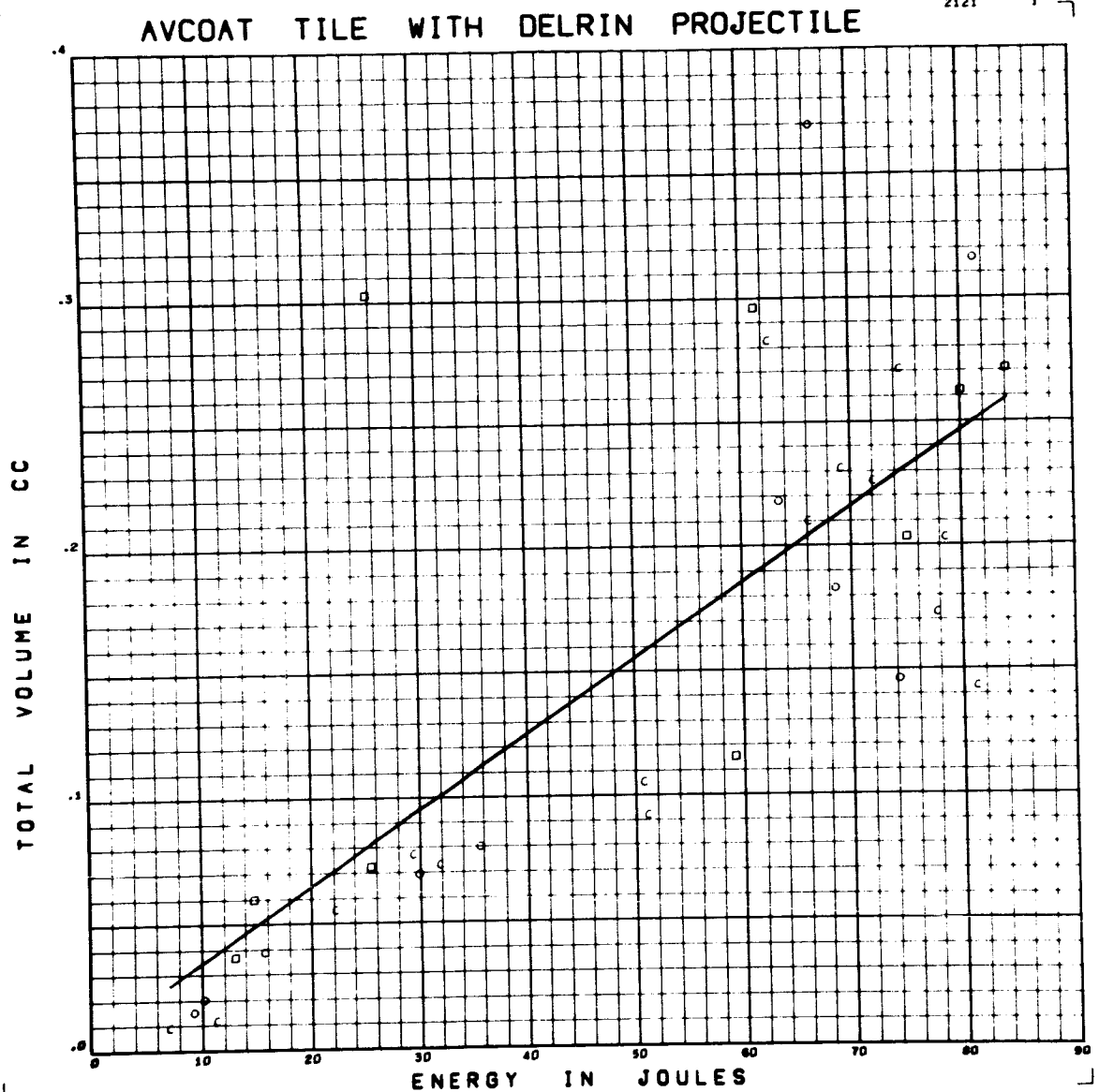


Figure F39 Volume versus Energy for Delrin Projectiles on Avcoat 5026 Tile

Form of Regression: $v = 3.032 \times 10^{-3} E + .0042$

RMS Deviation: .066 cc

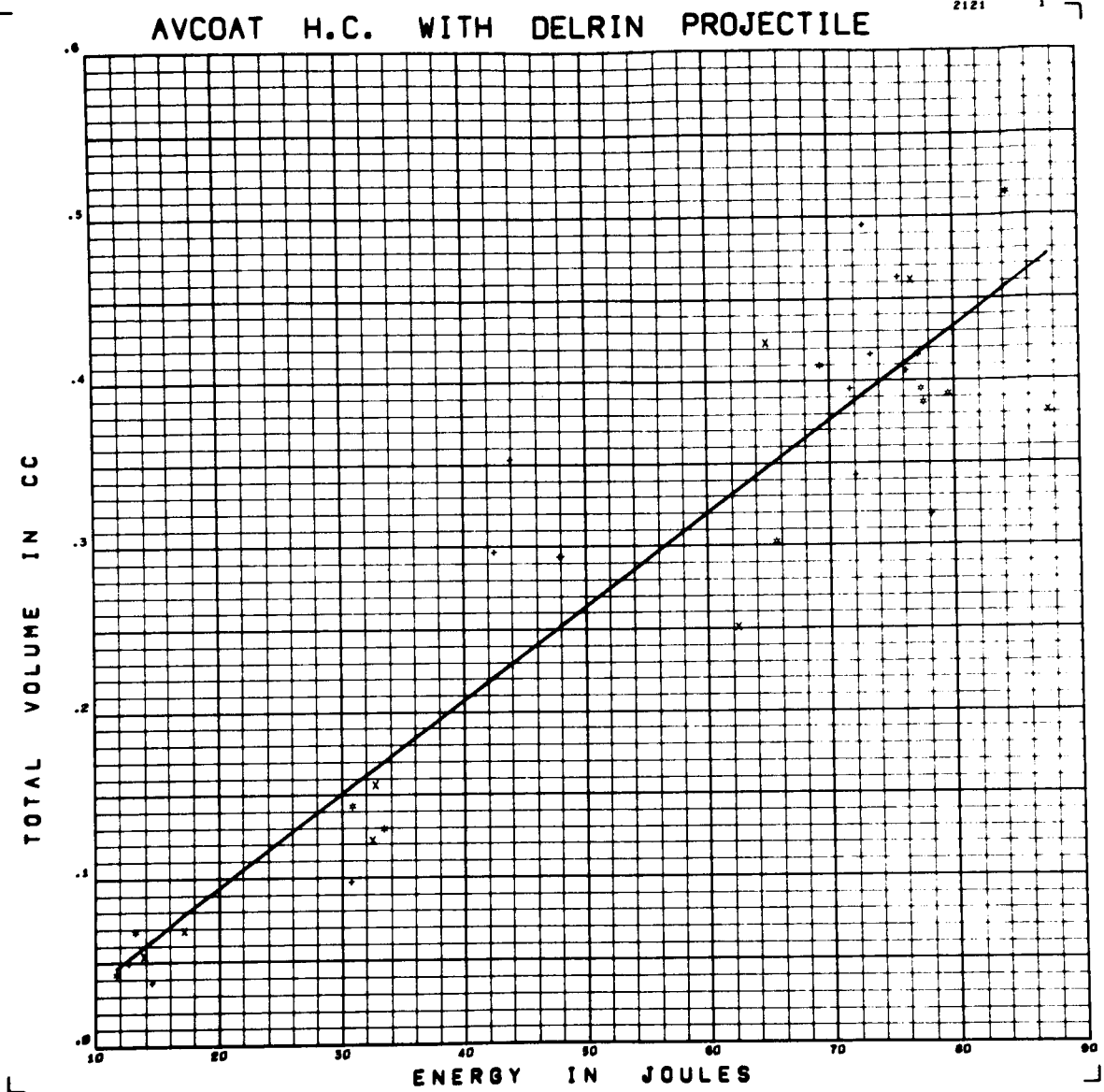


Figure F40 Volume versus Energy for Delrin Projectiles on Avcoat 5026 HC

Form of Regression: $V = 5.652 \times 10^{-3} E - .0189$

RMS Deviation: .054 cc

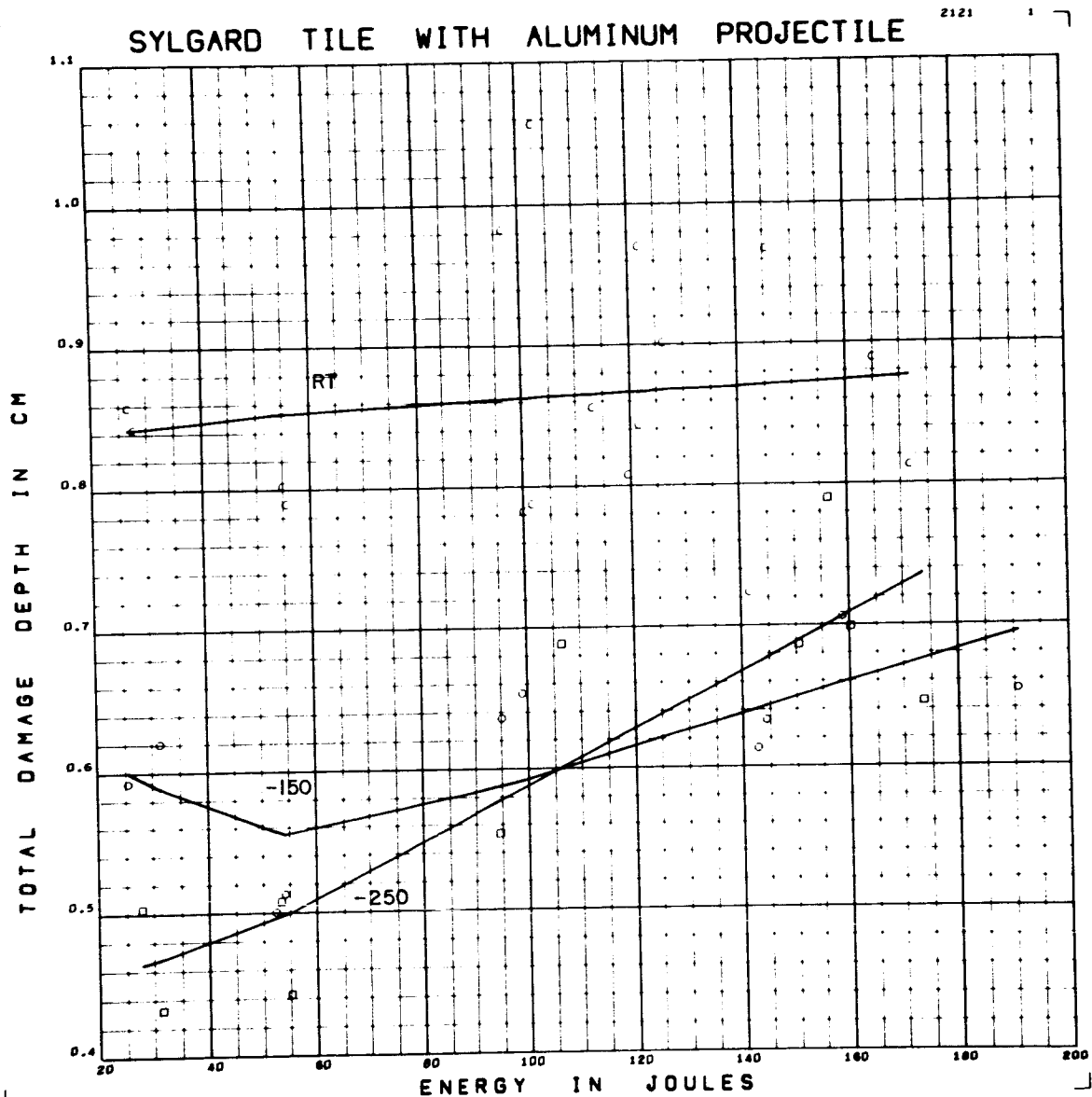


Figure F41 Total Damage Depth versus Energy for Aluminum Projectiles on Sylgard 325 Tile

Form of Regression: $p_m = (1.110 - 1.827 ST + 0.015 CV) \times 10^{-3} E$
 $+ .5702 + .4581 ST - .0898 CV$
 RMS Deviation: .069 cm

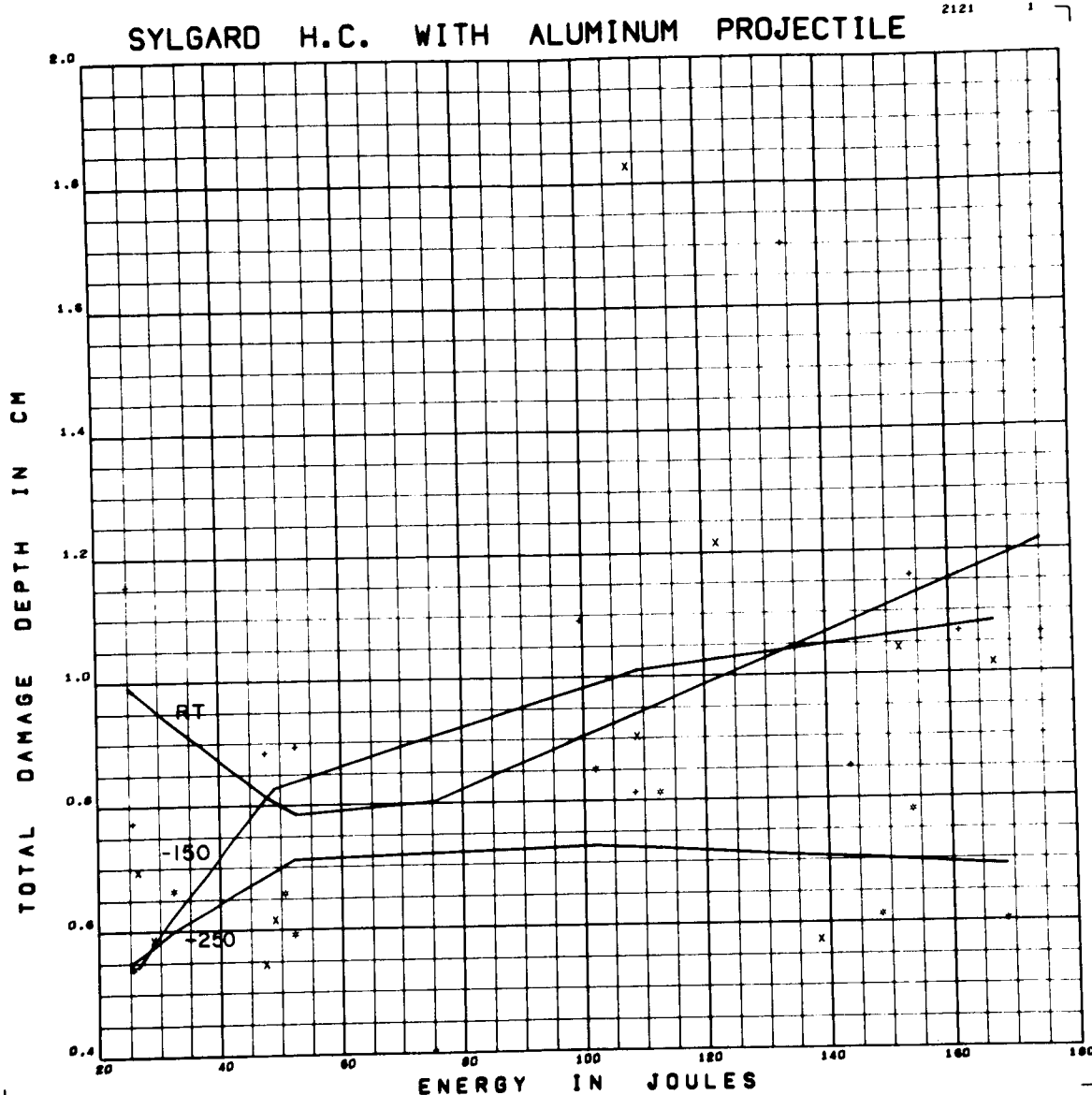
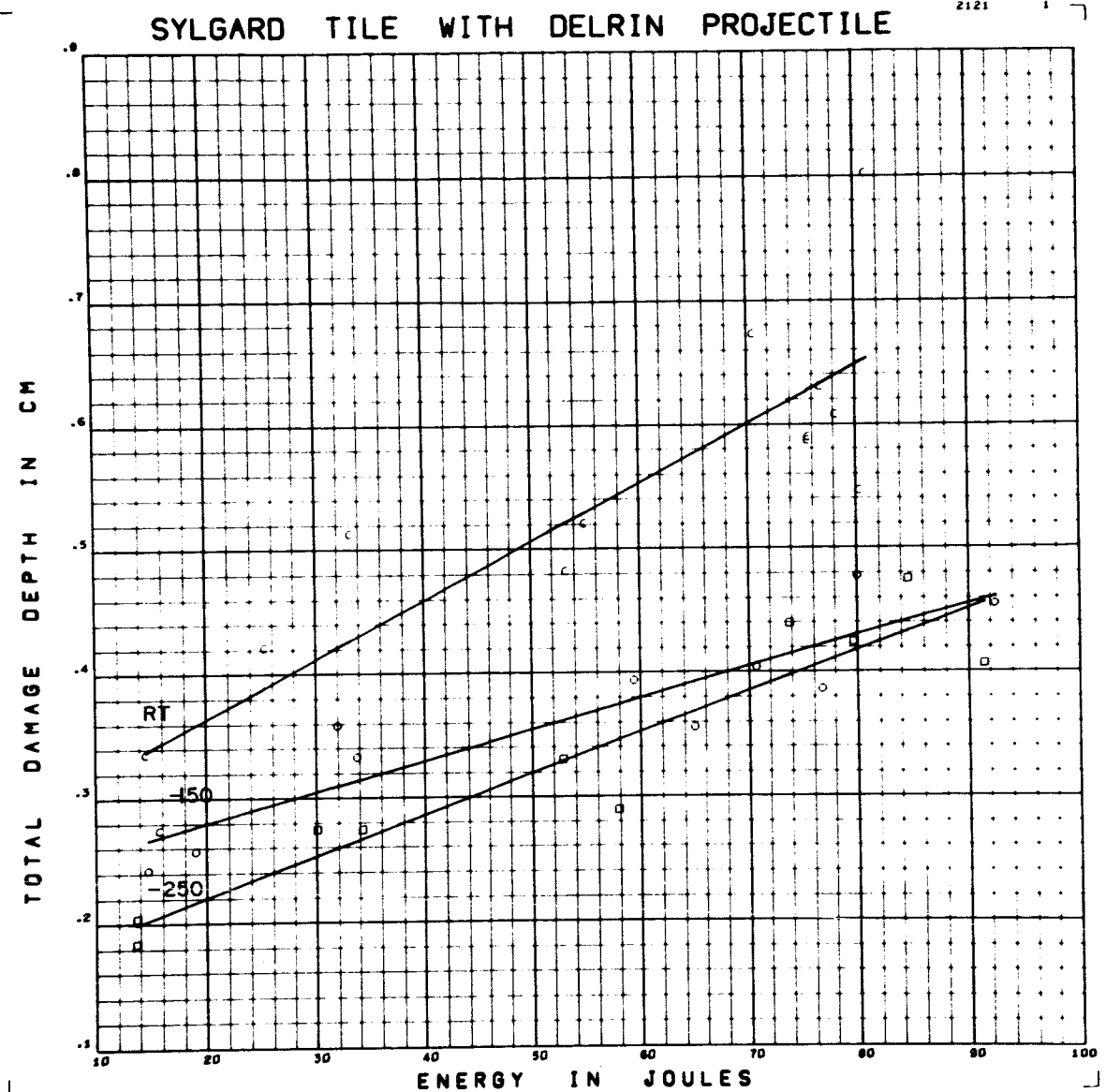


Figure F42 Total Damage Depth versus Energy for Aluminum Projectiles on
Sylgard 325 HC

Form of Regression: $p_m = (1.605 + 4.705ST - .357CV$
 RMS Deviation: $.256 \text{ cm} \quad +.7175 \quad -.2953ST +.1577CV$



• Figure F43 Total Damage Depth versus Energy for Delrin Projectiles on Sylgard 325 Tile

Form of Regression: $p_m = (3.520 + 1.432 ST - 1.006 CV) \times 10^{-3} E$

RMS Deviation: .049 cm $+ .2174 + .1152 ST + .0118 CV$

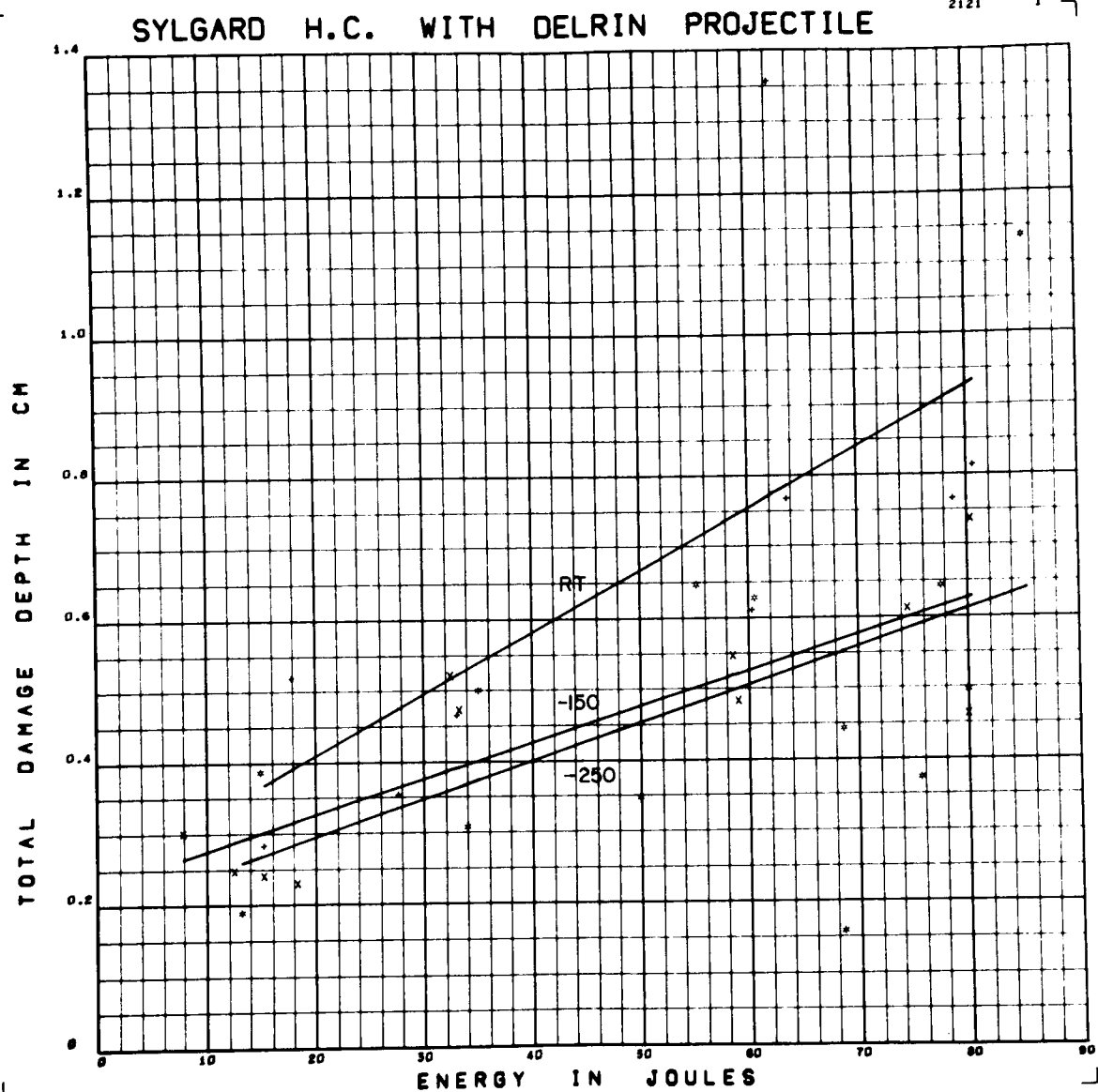


Figure F44 Total Damage Depth versus Energy for Delrin Projectiles on
Sylgard 325 HC

Form of Regression: $p_m = (6.316 + 3.329 ST - 1.304 CV) \times 10^{-3} E$

RMS Deviation: .184 cm $+ .2156 + .0486 ST + .0088 CV$

APPENDIX G

SELECTED DATA PLOTS

SELECTED PLOTS OF DATA WITH QUESTIONABLE POINTS REMOVED

<u>Figure</u>	<u>Material</u>	<u>Projectile</u>	<u>Parameter</u>
G1	Sylgard 325 tile	Al	Damage Diameter
G2	Sylgard 325 tile	Al	Damage Diameter
G3	Sylgard 325 HC	Al	Damage Diameter
G4	Sylgard 325 tile	Delrin	Damage Diameter
G5	Sylgard 325 tile	Delrin	Damage Diameter
G6	Sylgard 325 HC	Delrin	Damage Diameter
G7	Avcoat 5026 tile	Al	Damage Diameter
G8	Avcoat 5026 HC	Al	Damage Diameter
G9	Avcoat 5026 tile	Delrin	Damage Diameter
G10	Avcoat 5026 HC	Delrin	Damage Diameter
G11	Avcoat 5026	Al	Damage Diameter
G12	Avcoat 5026	Delrin	Damage Diameter
G13	Sylgard 325 tile	Al	Crater Diameter
G14	Sylgard 325 tile	Al	Crater Diameter
G15	Sylgard 325 HC	Al	Crater Diameter
G16	Sylgard 325 tile	Delrin	Crater Diameter
G17	Sylgard 325 tile	Delrin	Crater Diameter
G18	Sylgard 325 HC	Delrin	Crater Diameter
G19	Sylgard 325	Al	Crater Diameter
G20	Sylgard 325	Delrin	Crater Diameter
G21	Avcoat 5026 tile	Al	Crater Diameter
G22	Avcoat 5026 HC	Al	Crater Diameter
G23	Avcoat 5026 tile	Delrin	Crater Diameter
G24	Avcoat 5026 HC	Delrin	Crater Diameter
G25	Avcoat 5026	Al	Crater Diameter
G26	Avcoat 5026	Delrin	Crater Diameter
G27	Sylgard 325 tile	Al	Penetration
G28	Sylgard 325 HC	Al	Penetration
G29	Sylgard 325 tile	Delrin	Penetration
G30	Sylgard 325 tile	Delrin	Penetration
G31	Sylgard 325 HC	Delrin	Penetration
G32	Sylgard 325 HC	Delrin	Penetration
G33	Sylgard 325	Delrin	Penetration
G34	Sylgard 325	Delrin	Penetration
G35	Avcoat 5026 tile	Delrin	Penetration
G36	Avcoat 5026 HC	Delrin	Penetration
G37	Avcoat 5026	Delrin	Penetration
G38	Sylgard 325 tile	Al	Volume
G39	Sylgard 325 tile	Al	Volume
G40	Sylgard 325 tile	Al	Volume
G41	Sylgard 325 HC	Al	Volume
G42	Sylgard 325 HC	Al	Volume
G43	Sylgard 325 tile	Delrin	Volume
G44	Sylgard 325 tile	Delrin	Volume
G45	Sylgard 325 HC	Delrin	Volume
G46	Sylgard 325 HC	Delrin	Volume
G47	Avcoat 5026 tile	Al	Volume
G48	Avcoat 5026 tile	Al	Volume
G49	Avcoat 5026 HC	Al	Volume
G50	Avcoat 5026 tile	Delrin	Volume
G51	Avcoat 5026 tile	Delrin	Volume
G52	Avcoat 5026 HC	Delrin	Volume

HONEYCOMB SYMBOLS

TEMPERATURE	SYMBOL
RT	+
-150°F	X
-250°F	*

TILE SYMBOLS

TEMPERATURE	SYMBOL
RT	C
-150°F	O
-250°F	□

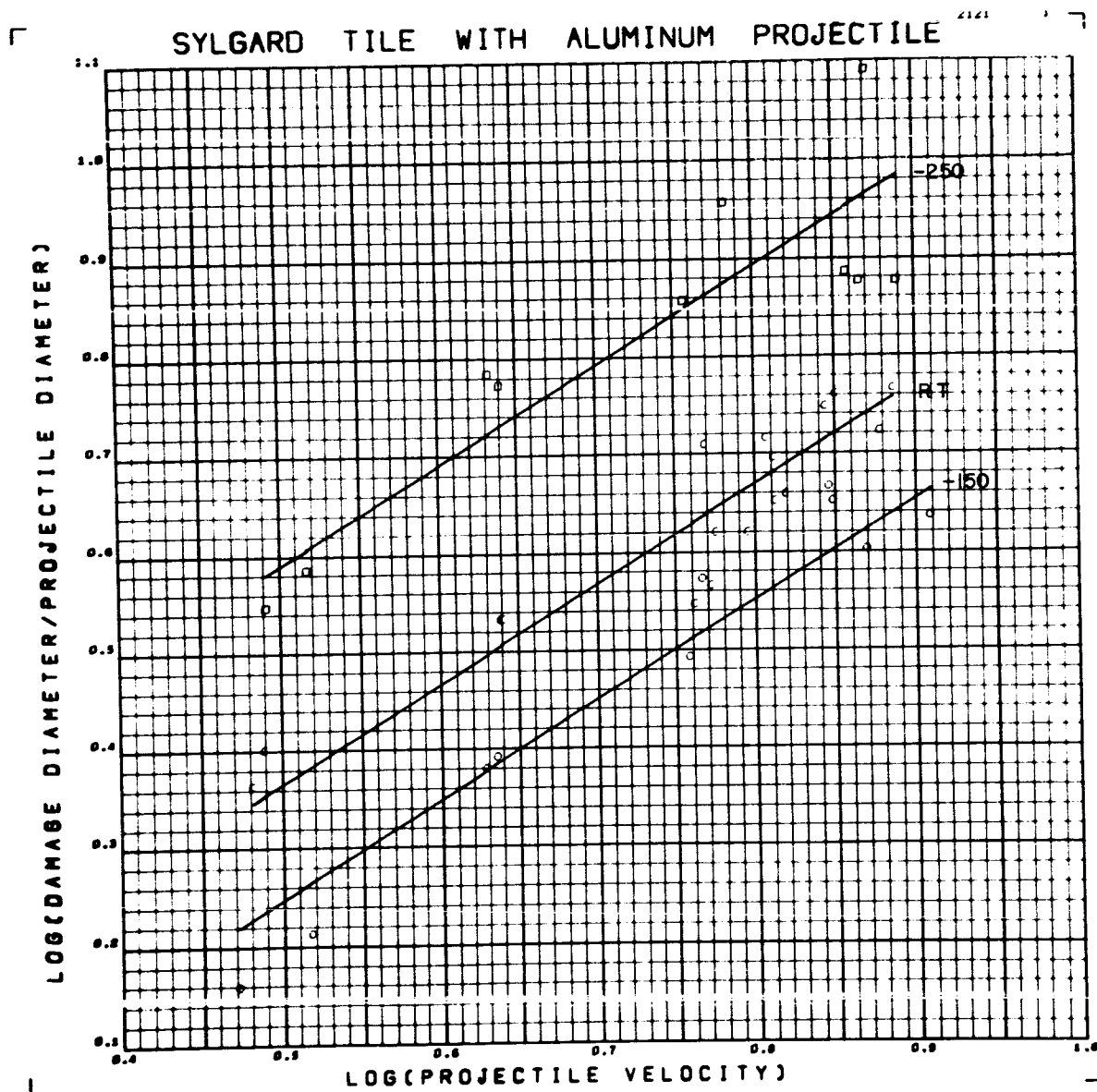


Figure G1 Log Reduced Damage Diameter versus Log Velocity for Aluminum

Projectiles on Sylgard 325 Tile

Data Points Skipped: none

Form of Regression: $\log_{10}\left(\frac{d_s}{D}\right) = -.1059 + 1.014 \log_{10} V - .2238 ST - .1530 CV$

RMS Deviation: 13%

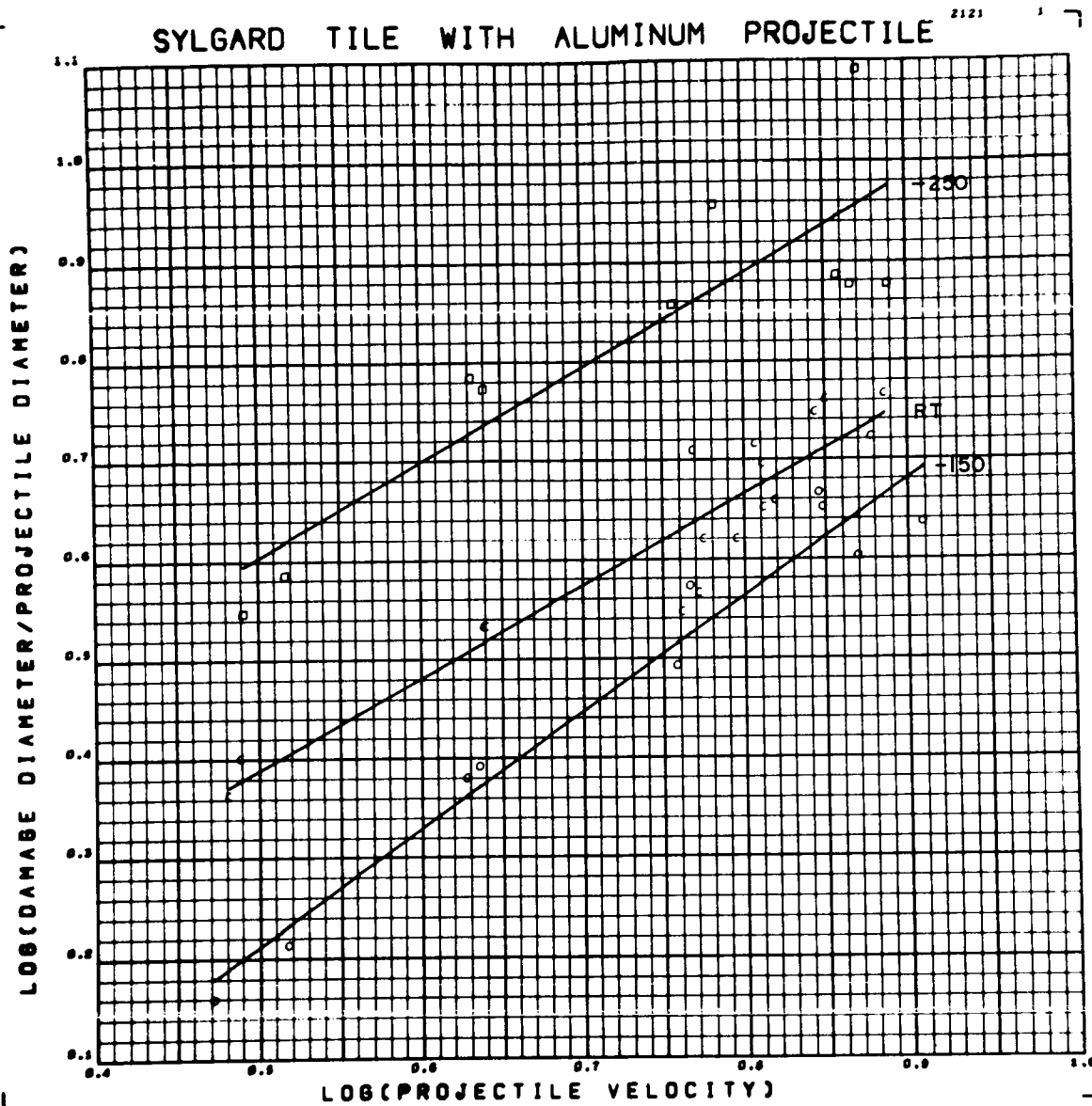


Figure G2 Log Reduced Damage Diameter versus Log Velocity for Aluminum

Projectiles on Sylgard 325 Tile

Data Points Skipped: none

Form of Regression: $\log_{10} \left(\frac{d_s}{D} \right) = -.1071 + 1.017 \log_{10} V - .1983 ST - .2669 CV$

RMS Deviation: 12% $-.0320 ST \cdot \log_{10} V + .1558 CV \cdot \log_{10} V$

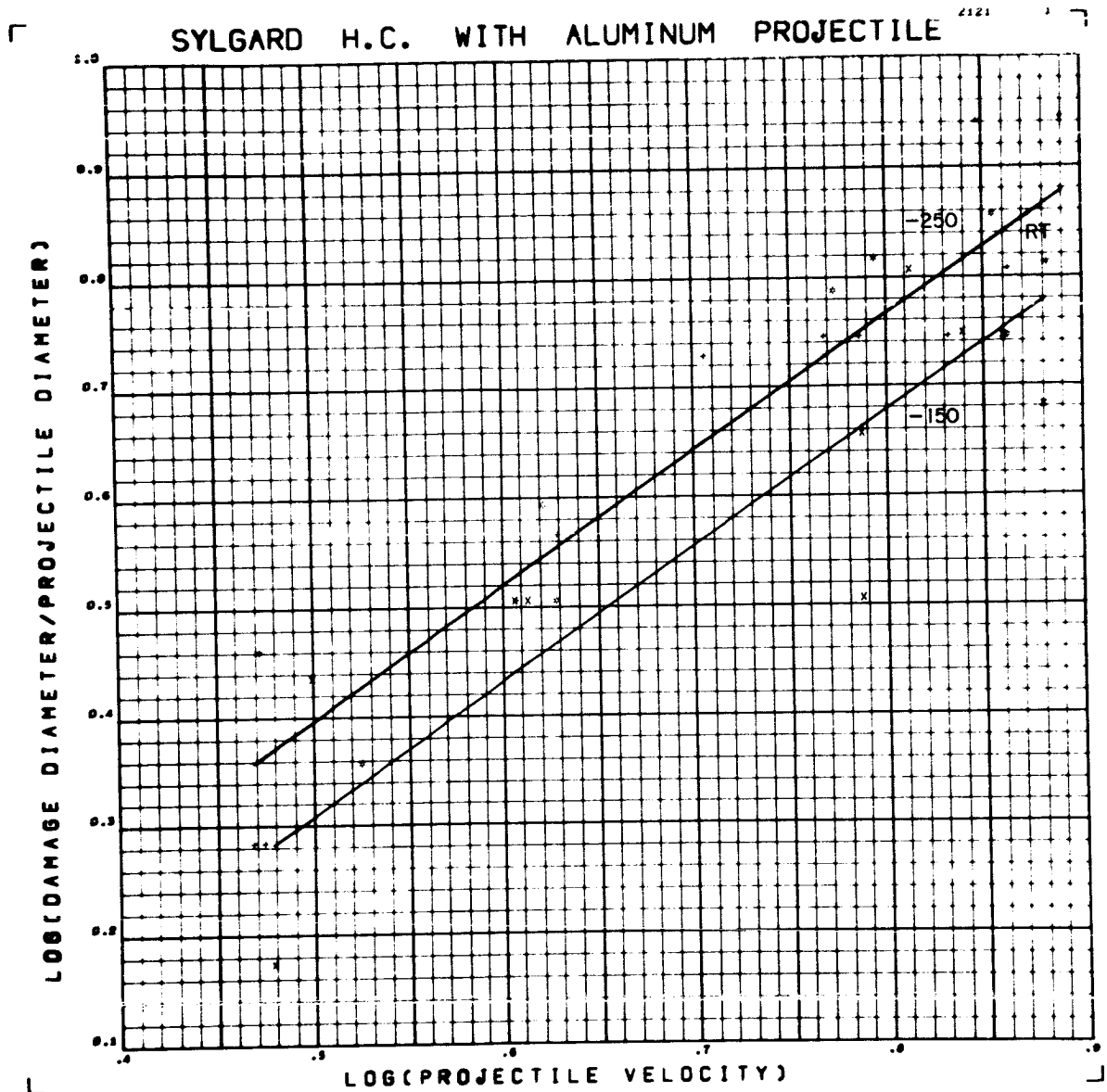


Figure G3 Log Reduced Damage Diameter versus Log Velocity for Aluminum

Projectiles on Sylgard 325 HC

Data Points Skipped: none

Form of Regression: $\log_{10}\left(\frac{d_s}{D}\right) = -.2489 + 1.233 \log_{10} V - .00025T - .0585 CV$

RMS Deviation: 19%

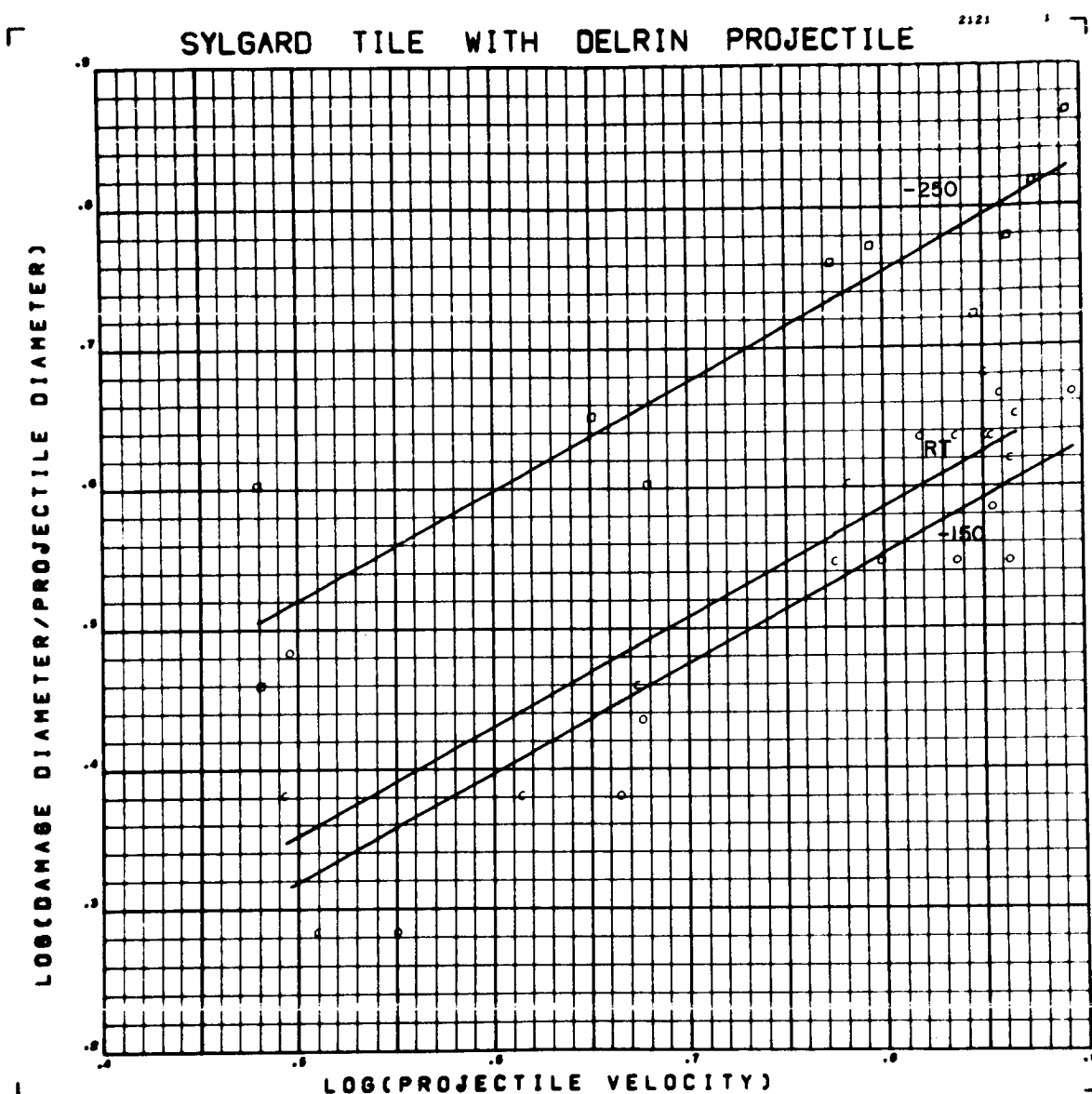


Figure G4 Log Reduced Damage Diameter versus Log Velocity for Delrin

Projectiles on Sylgard 325 Tile

Data Points Skipped: none

Form of Regression: $\log_{10}\left(\frac{d_s}{D}\right) = .0081 + .7790 \log_{10} V - .1689 ST - .0783 CV$

RMS Deviation: 13 %

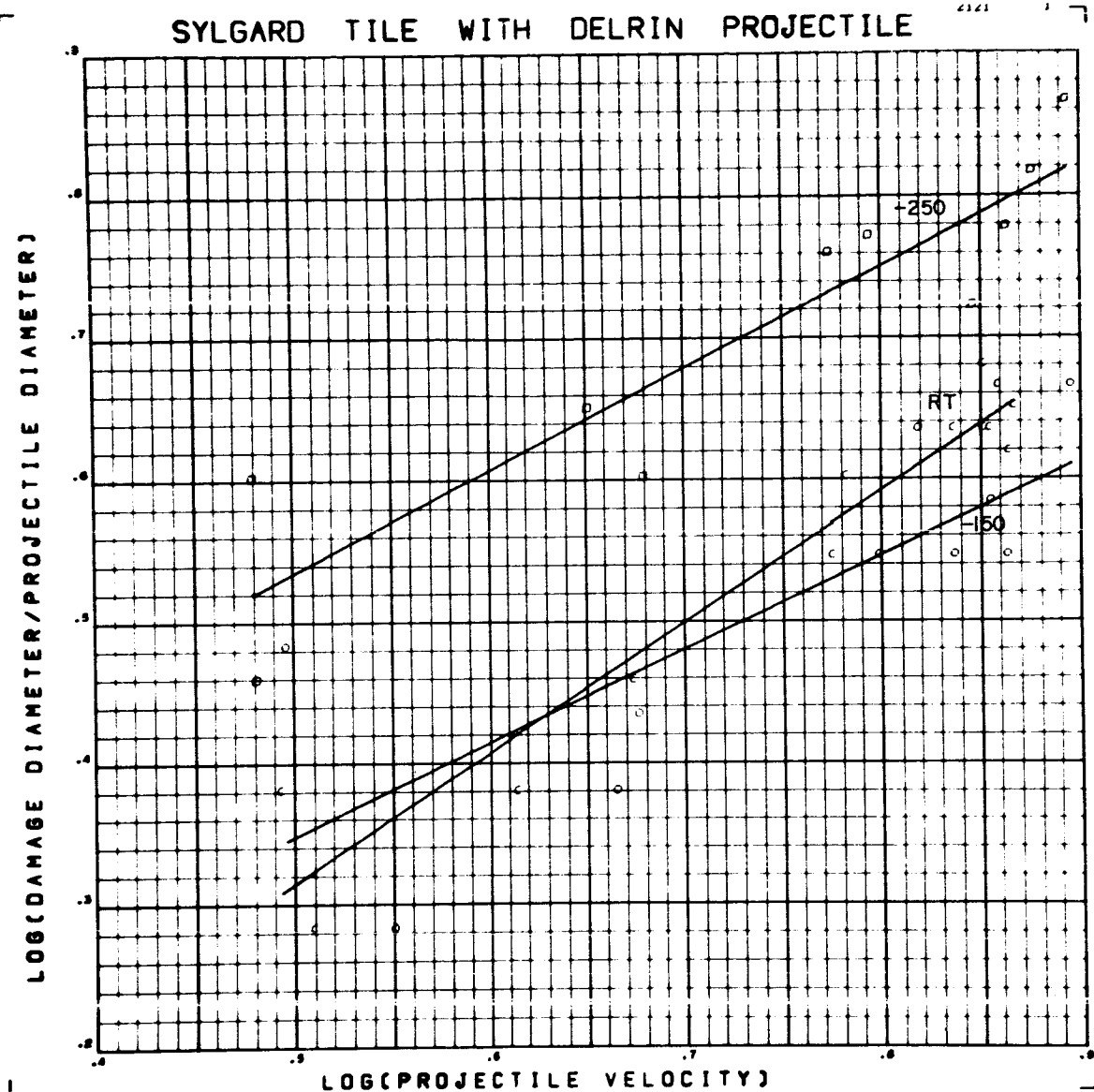


Figure G5 Log Reduced Damage Diameter versus Log Velocity for Delrin

Projectiles on Sylgard 325 Tile

Data Points Skipped: none

Form of Regression: $\log_{10}\left(\frac{d_s}{D}\right) = .0143 + .7697 \log_{10} V - .3218 ST + .0025 CV$

RMS Deviation: 13%

SYLGARD H.C. WITH DELRIN PROJECTILE

2121

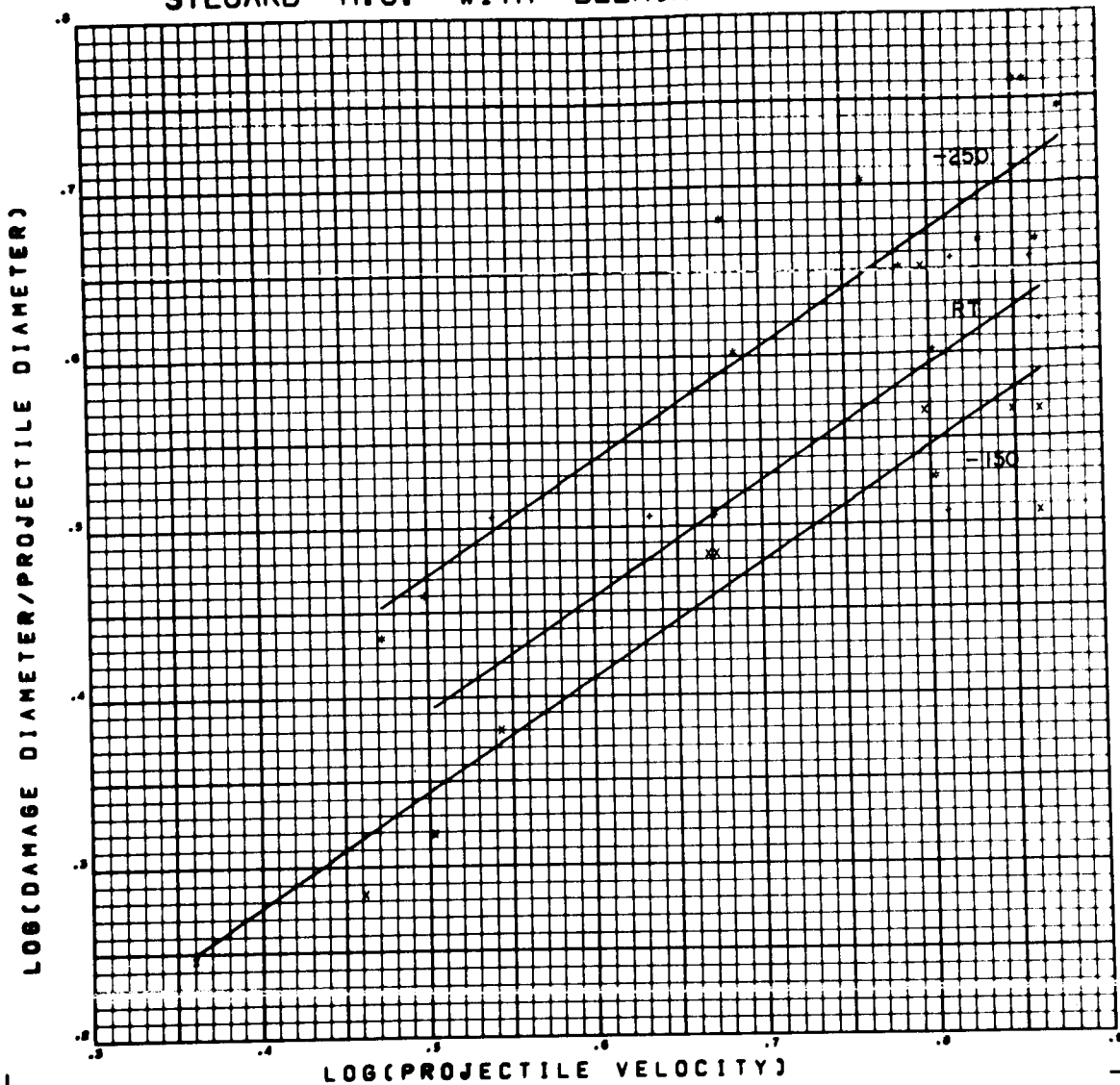


Figure G6 Log Reduced Damage Diameter versus Log Velocity for Delrin

Projectiles on Sylgard 325 HC

Data Points Skipped: 198 R1

Form of Regression: $\log_{10}\left(\frac{d_t}{D}\right) = .0658 + .6733 \log_{10} V - .0802 ST - .0587 CV$

RMS Deviation: 13%

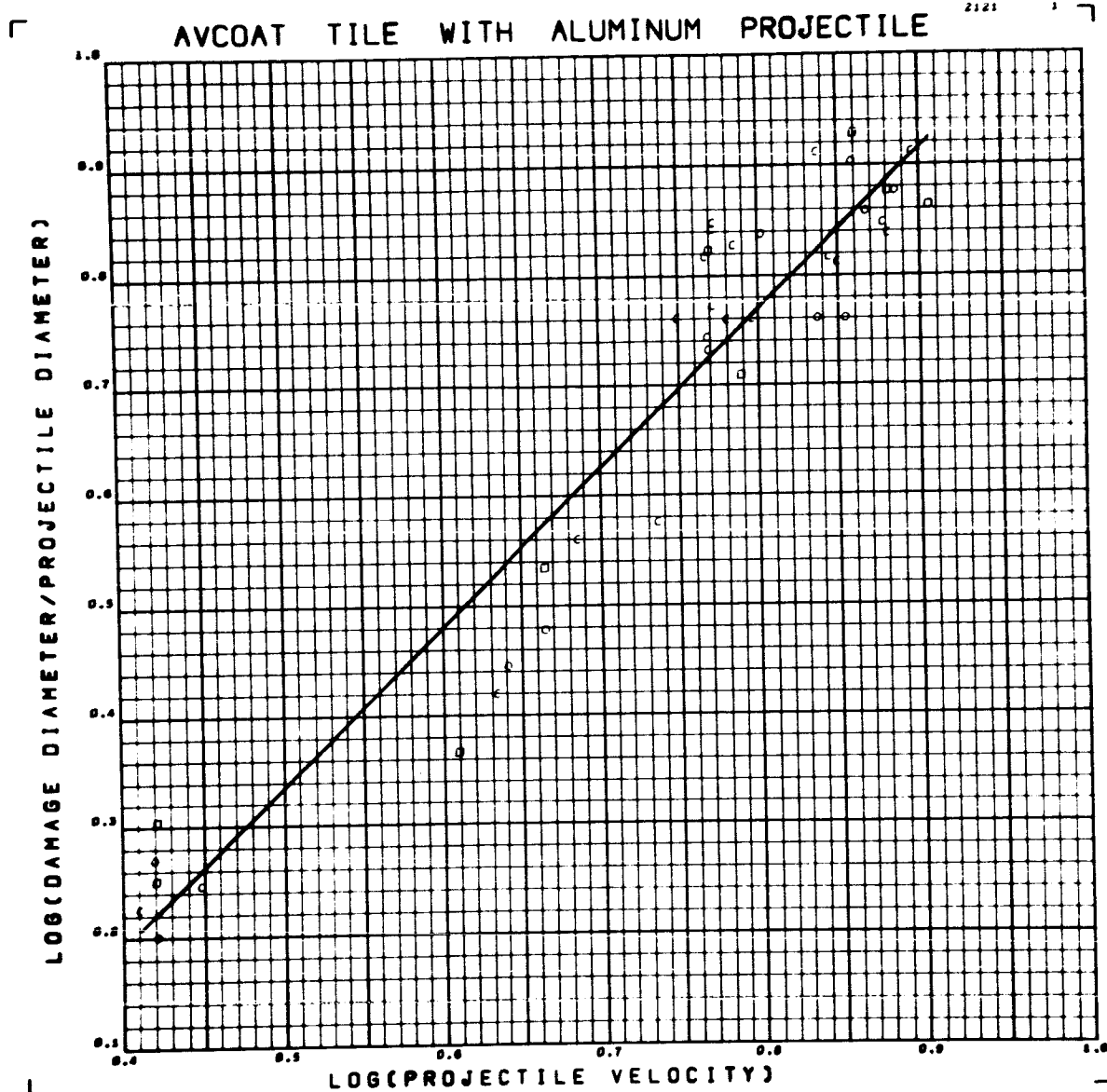


Figure G7 Log Reduced Damage Diameter versus Log Velocity for Aluminum

Projectiles on Avcoat 5026 Tile

Data Points Skipped: 116, 117, 131

Form of Regression: $\log_{10} \left(\frac{d_s}{d} \right) = -0.3380 + 1.448 \log_{10} V$

RMS Deviation: 17%

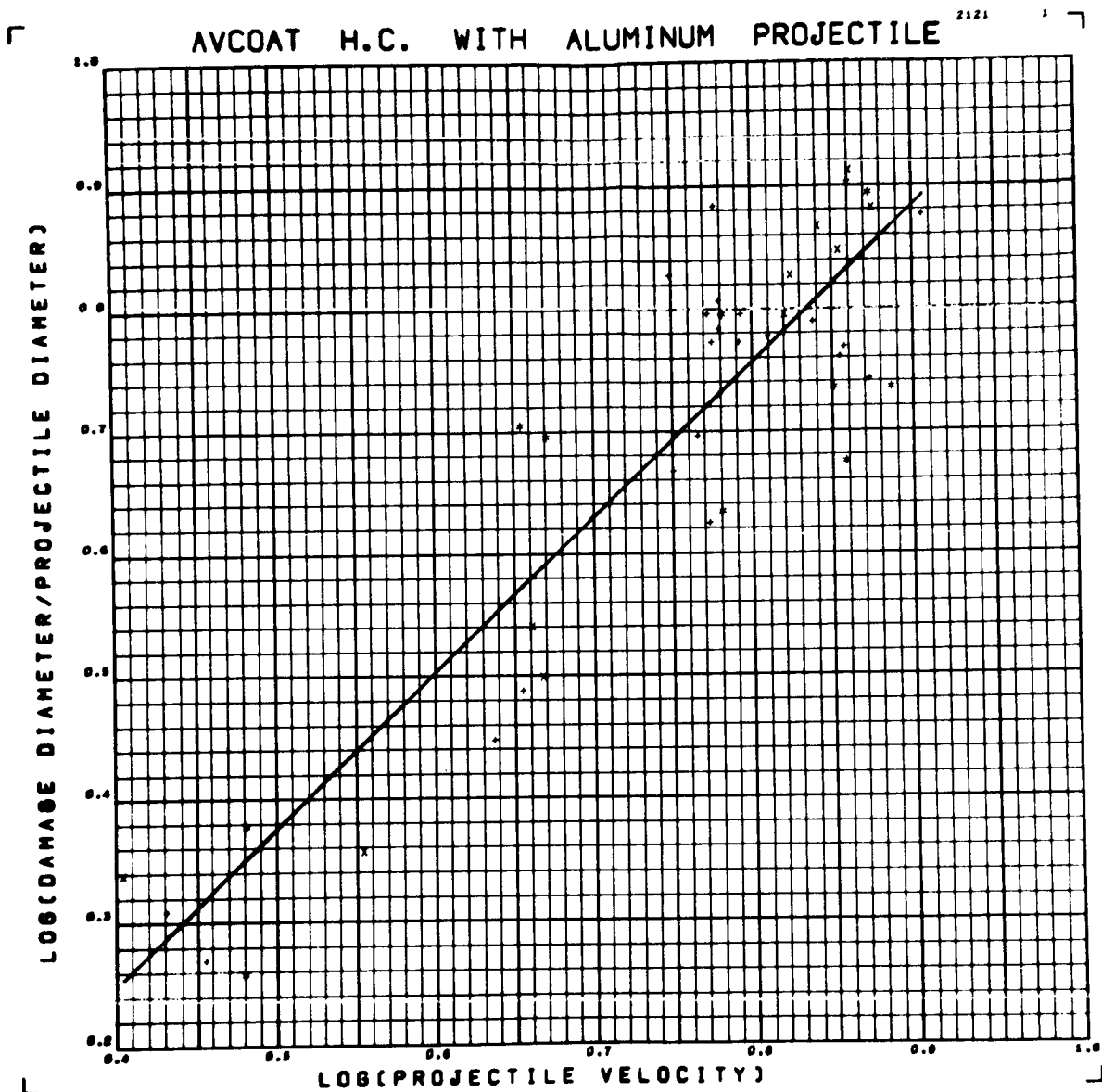


Figure G8 Log Reduced Damage Diameter versus Log Velocity for Aluminum

Projectiles on Avcoat 5026 HC

Data Points Skipped: *none*

Form of Regression: $\log_{10} \left(\frac{ds}{D} \right) = -.2590 + 1.271 \log_{10} V$

RMS Deviation: 20 %

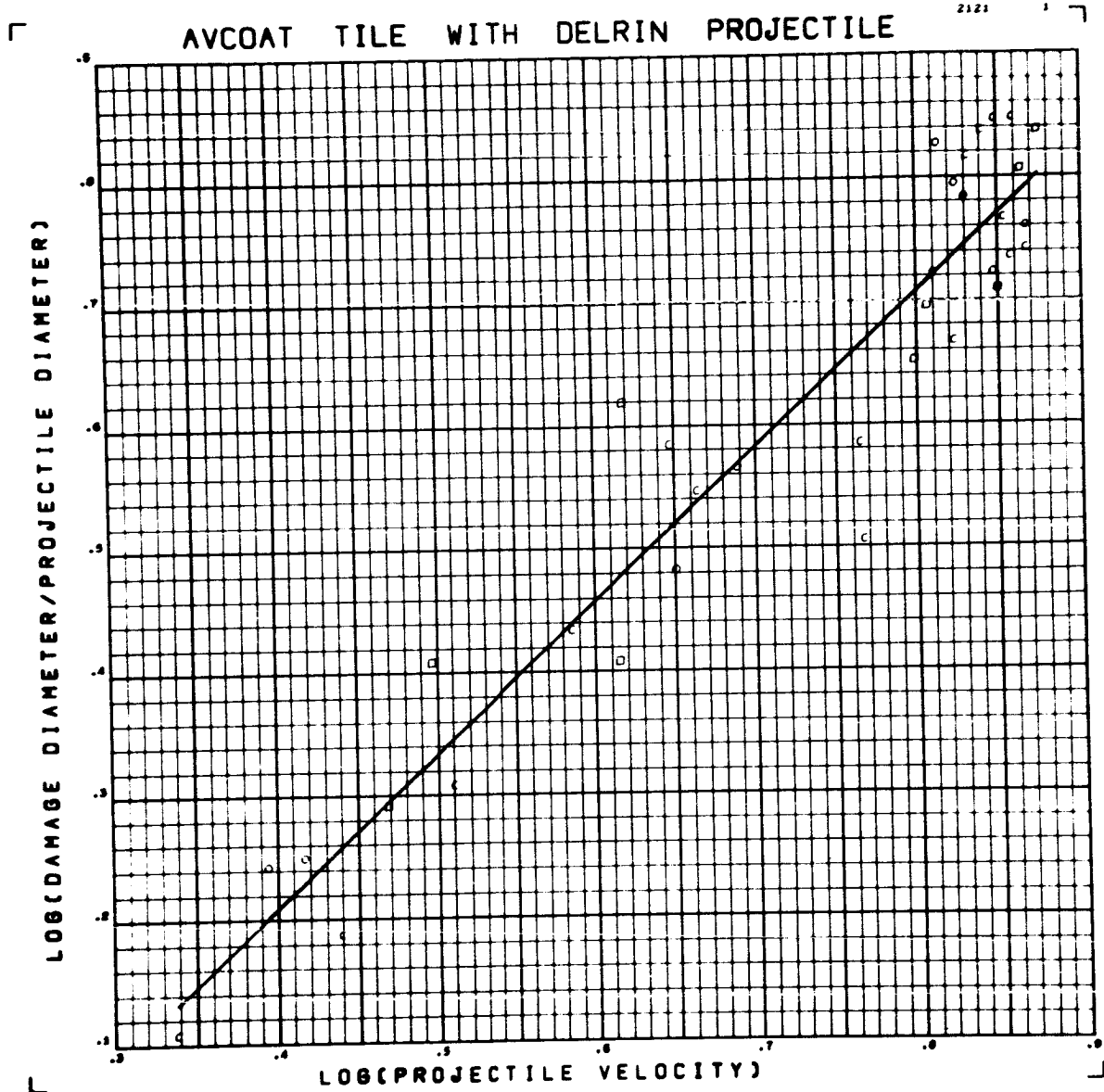


Figure G9 Log Reduced Damage Diameter versus Log Velocity for Delrin

Projectiles on Avcoat 5026 Tile

Data Points Skipped: none

Form of Regression: $\log_{10} \left(\frac{d_s}{d} \right) = -.2899 + 1.248 \log_{10} V$

RMS Deviation: 16 %

AVCOAT H.C. WITH DELRIN PROJECTILE

2121

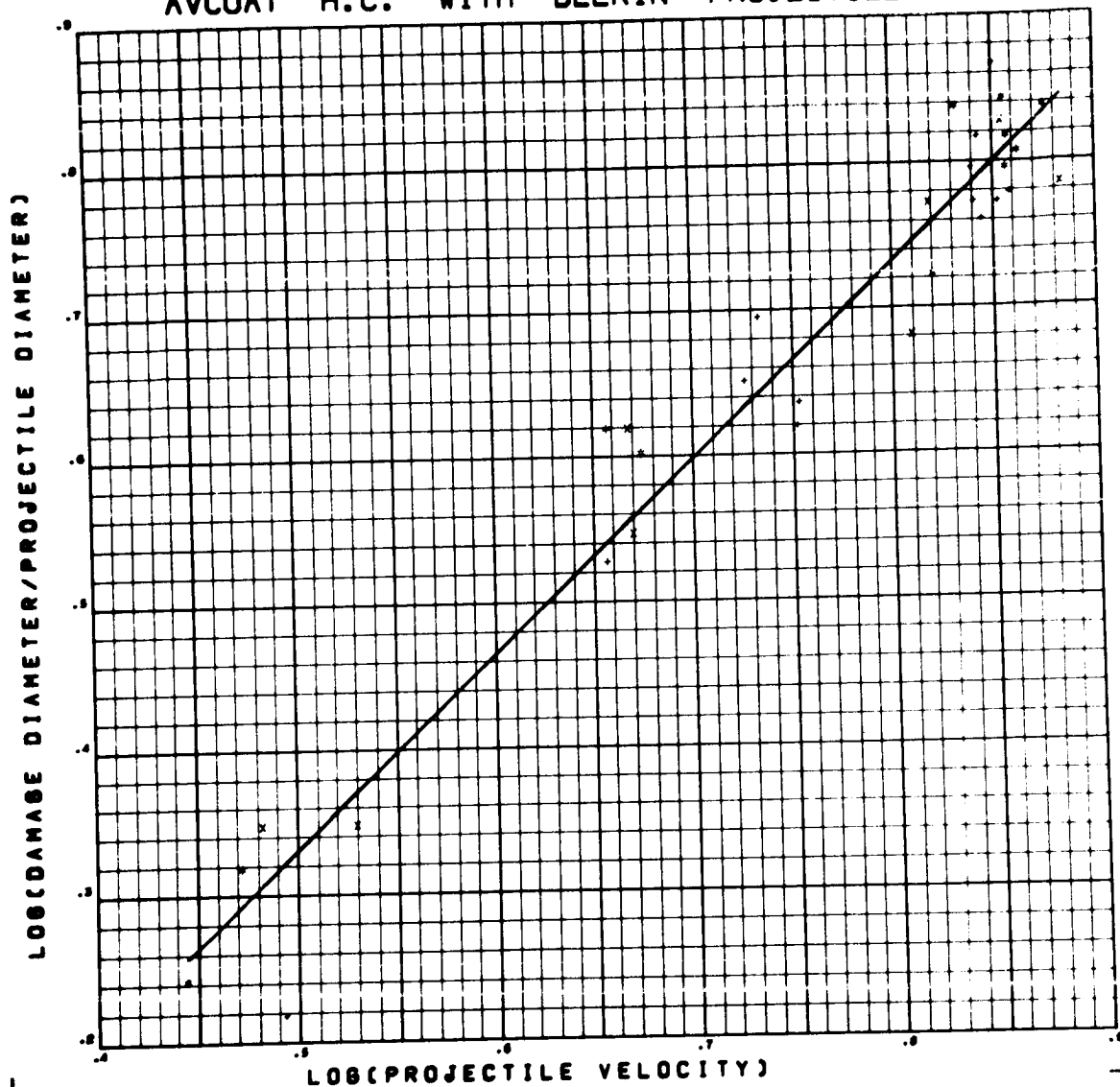


Figure G10 Log Reduced Damage Diameter versus Log Velocity for Delrin

Projectiles on Avcoat 5026 HC

Data Points Skipped: /

Form of Regression: $\log_{10} \left(\frac{d_s}{D} \right) = -.3380 + 1.338 \log_{10} V$

RMS Deviation: 10 %

AVCOAT WITH ALUMINUM PROJECTILE

2121

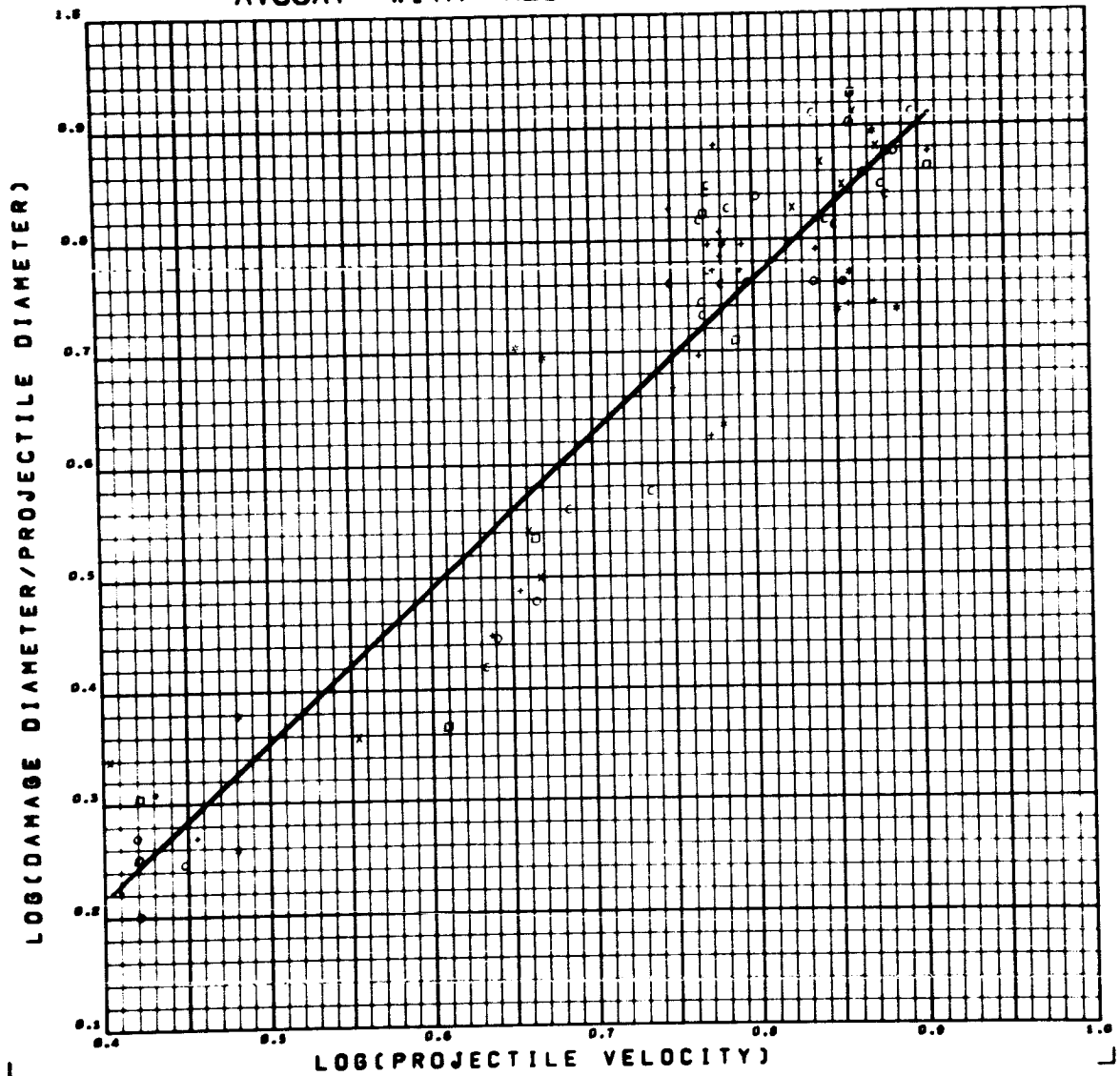


Figure G11 Log Reduced Damage Diameter versus Log Velocity for Aluminum

Projectiles on Avcoat 5026

Data Points Skipped: 116 , 117, 131

Form of Regression: $\log_{10}\left(\frac{d_s}{D}\right) = -.0330 + 1.372 \log_{10} V - .0014 H$

RMS Deviation: 18 %

AVCOAT WITH DELRIN PROJECTILE

2121

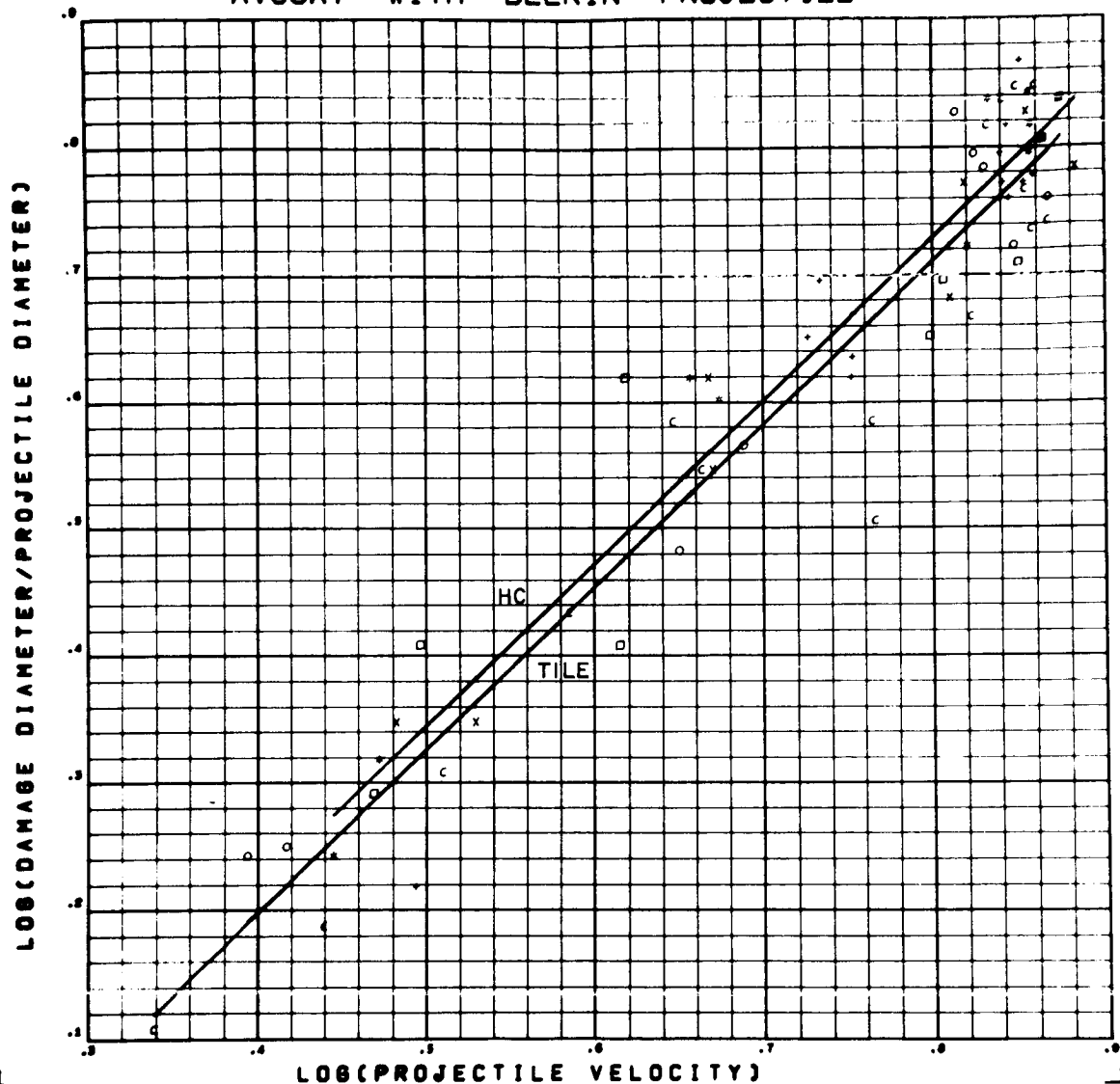


Figure G12 Log Reduced Damage Diameter versus Log Velocity for Delrin

Projectiles on Avcoat 5026

Data Points Skipped: /

Form of Regression: $\log_{10} \left(\frac{d_f}{D} \right) = -.3058 + 1.283 \log_{10} V + .0185 H$

RMS Deviation: 13%

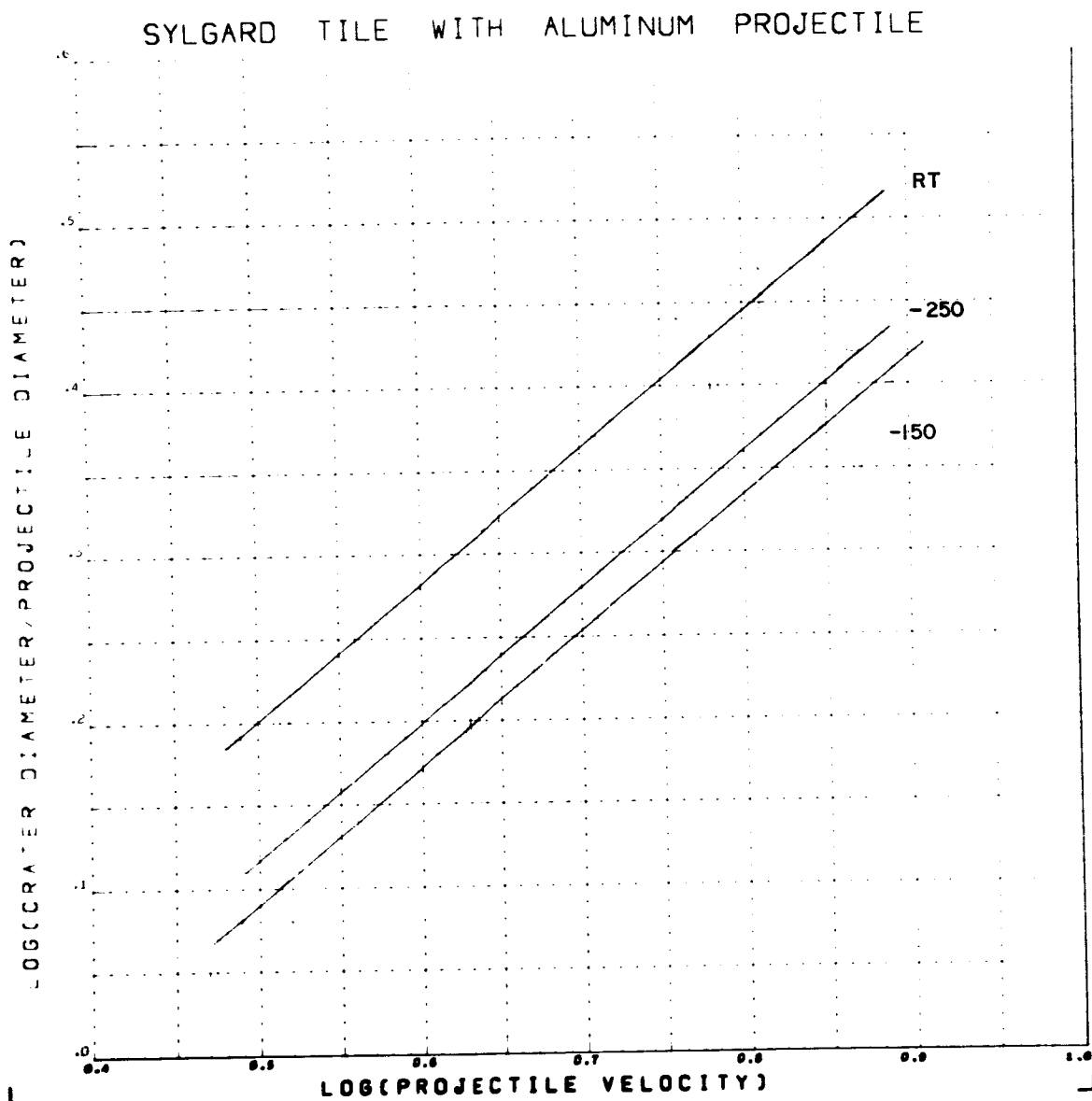


Figure G13 Log Reduced Crater Diameter versus Log Velocity for Aluminum

Projectiles on Sylgard 325 Tile

Data Points Skipped: none

Form of Regression: $\log_{10} \left(\frac{d}{D} \right) = -.2727 + .8167 \log_{10} V + .0838 ST -.0453 CV$

RMS Deviation: 9%

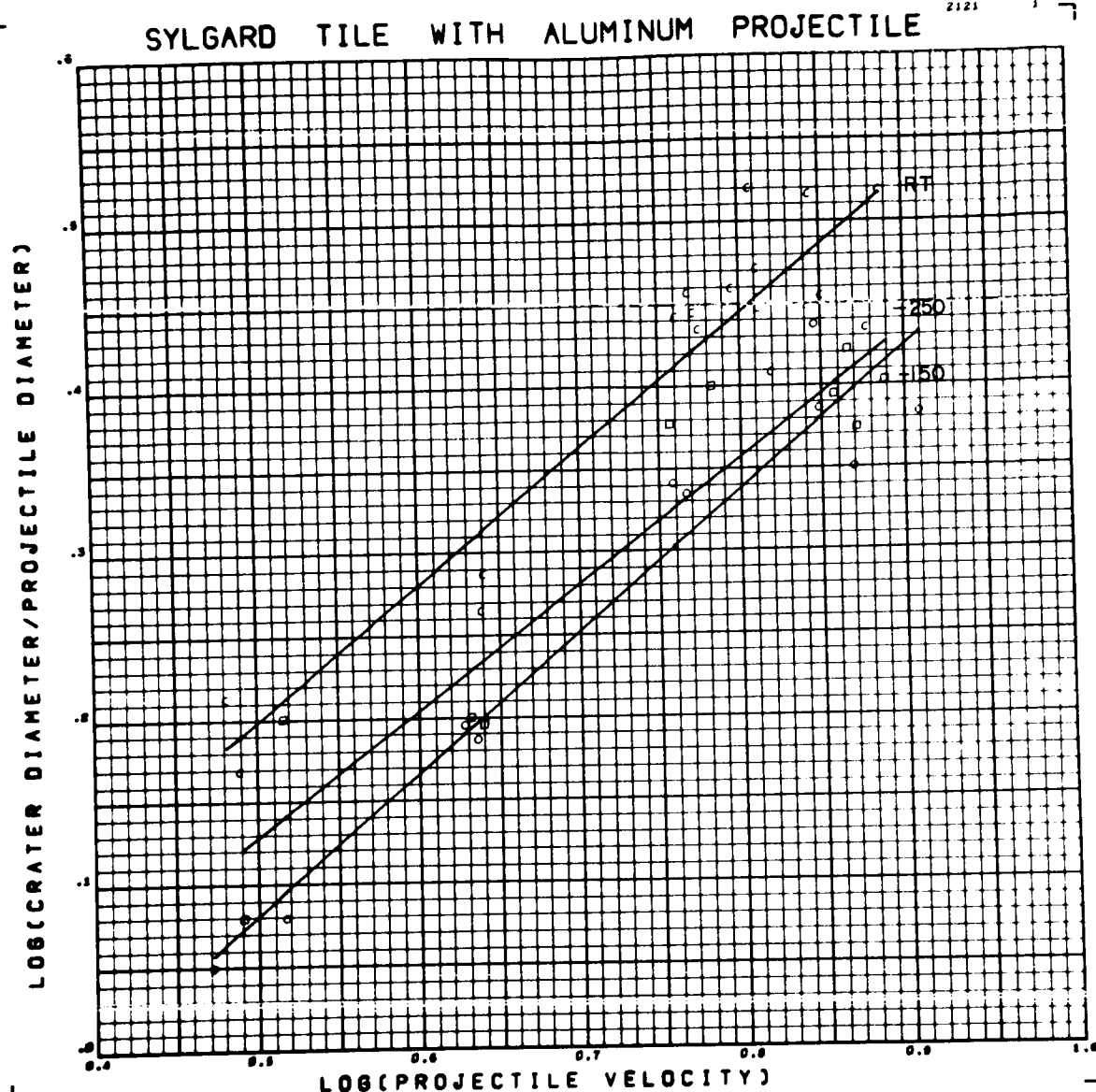


Figure G14 Log Reduced Crater Diameter versus Log Velocity for Aluminum

Projectiles on Sylgard 325 Tile

Data Points Skipped: none

Form of Regression: $\log_{10}\left(\frac{d}{D}\right) = -.2720 + .8158/\log_{10} V + .0420 ST - .0768 CV$

RMS Deviation: 9% $+ .0571 ST \cdot \log_{10} V + .0434 CV \cdot \log_{10} V$

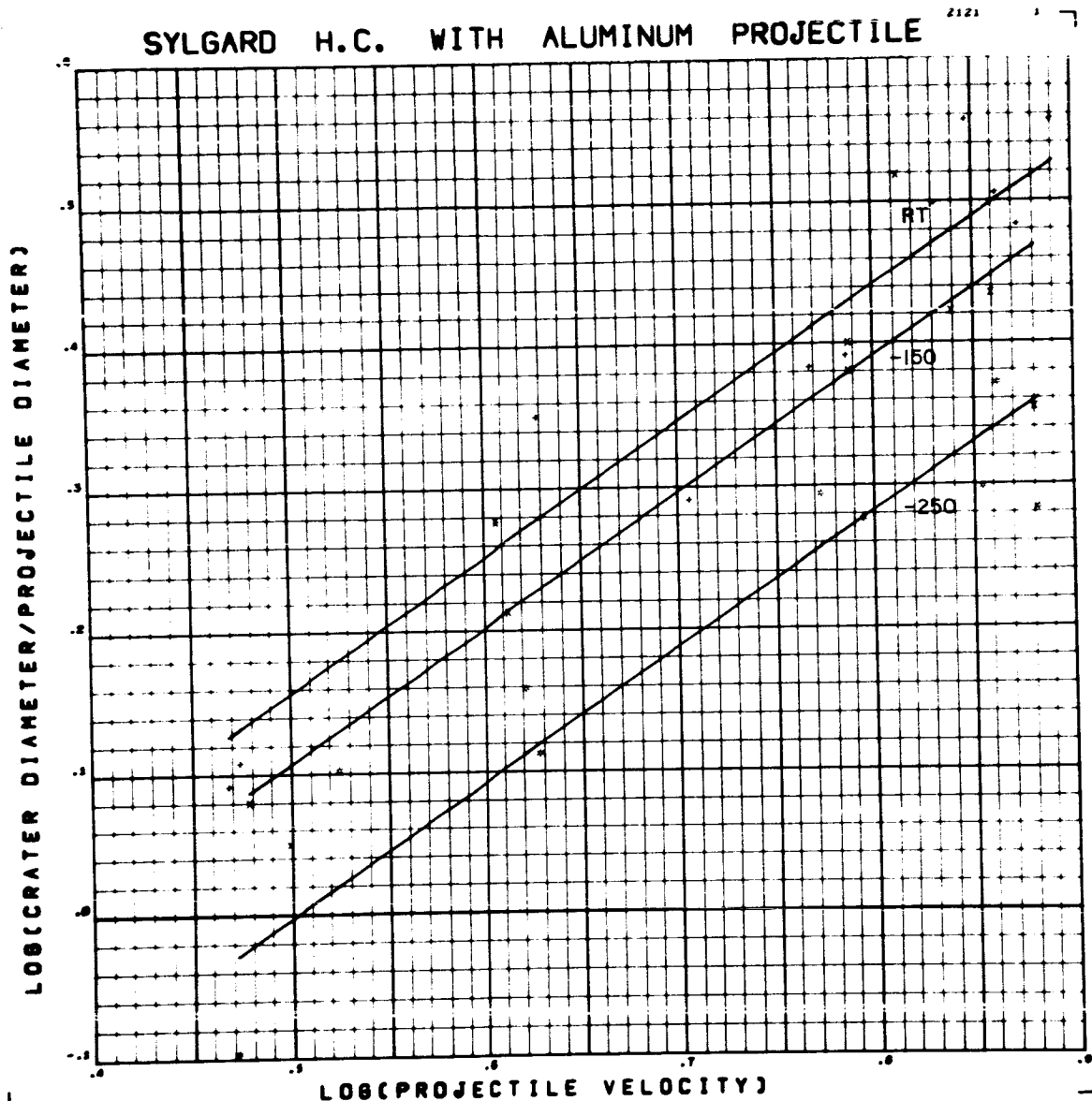


Figure G15 Log Reduced Crater Diameter versus Log Velocity for Aluminum

Projectiles on Sylgard 325 HC

Data Points Skipped: none

Form of Regression: $\log_{10}\left(\frac{d}{D}\right) = -0.3876 + 0.9496 \log_{10} V + 0.1587 ST + 0.0197 CV$

RMS Deviation: 13%

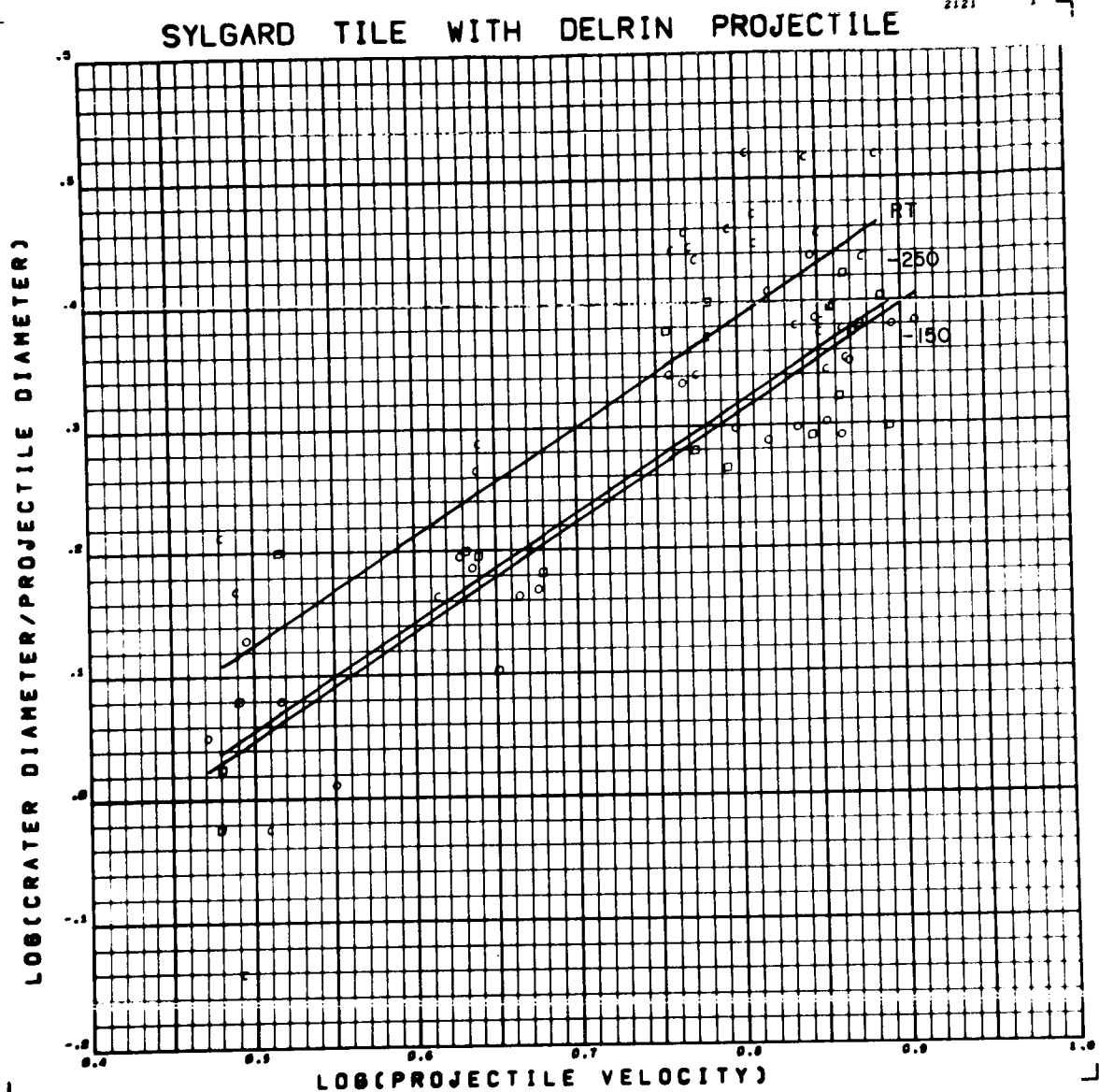


Figure G16 Log Reduced Crater Diameter versus Log Velocity for Delrin
Projectiles on Sylgard 325 Tile

Data Points Skipped: none

Form of Regression: $\log\left(\frac{d}{D}\right) = -0.3611 + 0.8742 \log_{10} V + 0.0701 ST - 0.0285 CV$

RMS Deviation: 18%

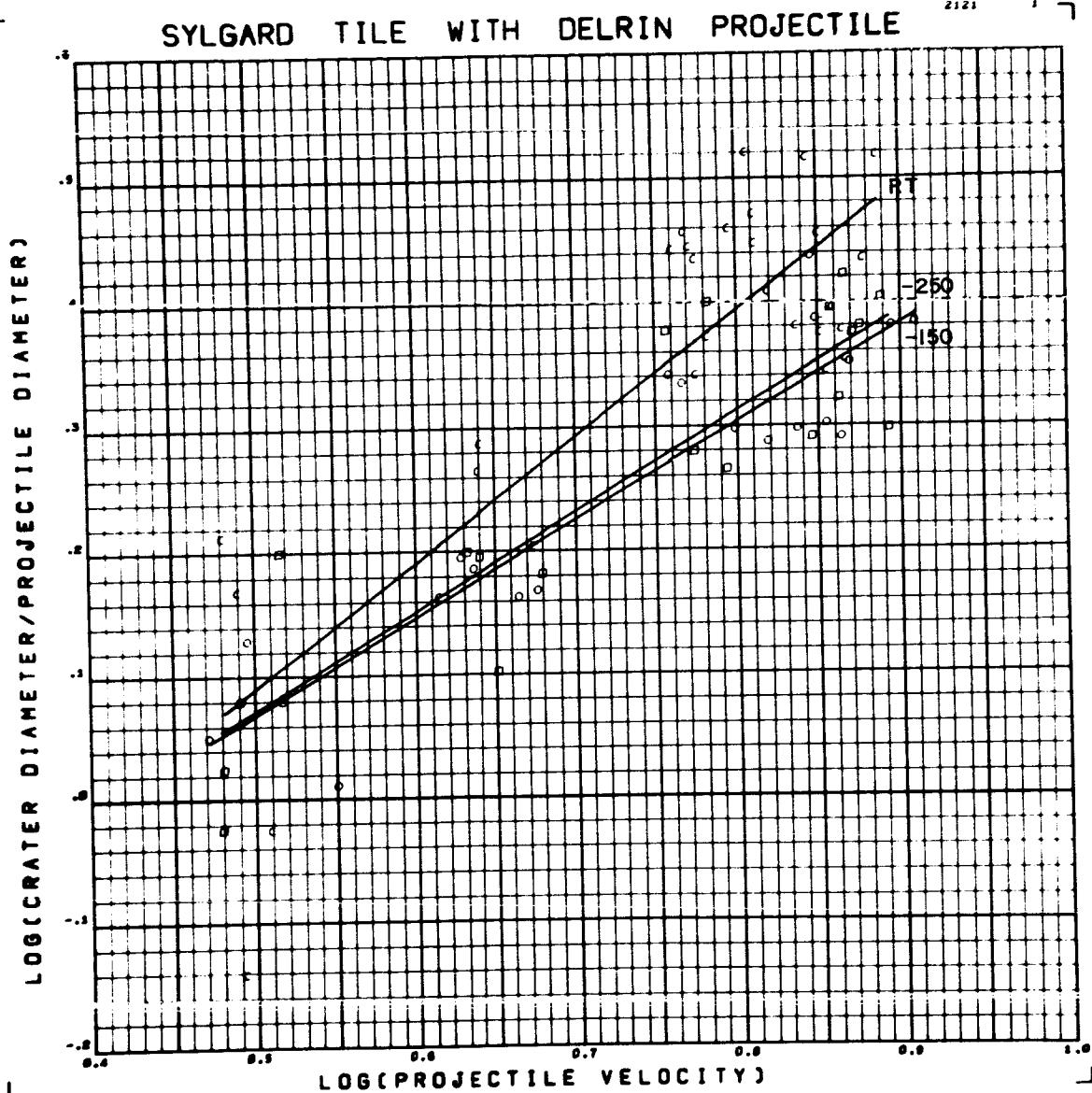


Figure G17 Log Reduced Crater Diameter versus Log Velocity for Delrin
Projectiles on Sylgard 325 Tile

Data Points Skipped: none

Form of Regression: $\log_{10}\left(\frac{d}{D}\right) = -0.3572 + 0.8675 \log_{10} V - 0.0862 ST + 0.0324 CV$
 $+ 0.2090 ST \cdot \log_{10} V - 0.0815 CV \cdot \log_{10} V$

RMS Deviation: 17 %

SYLGARD H.C. WITH DELRIN PROJECTILE

2121

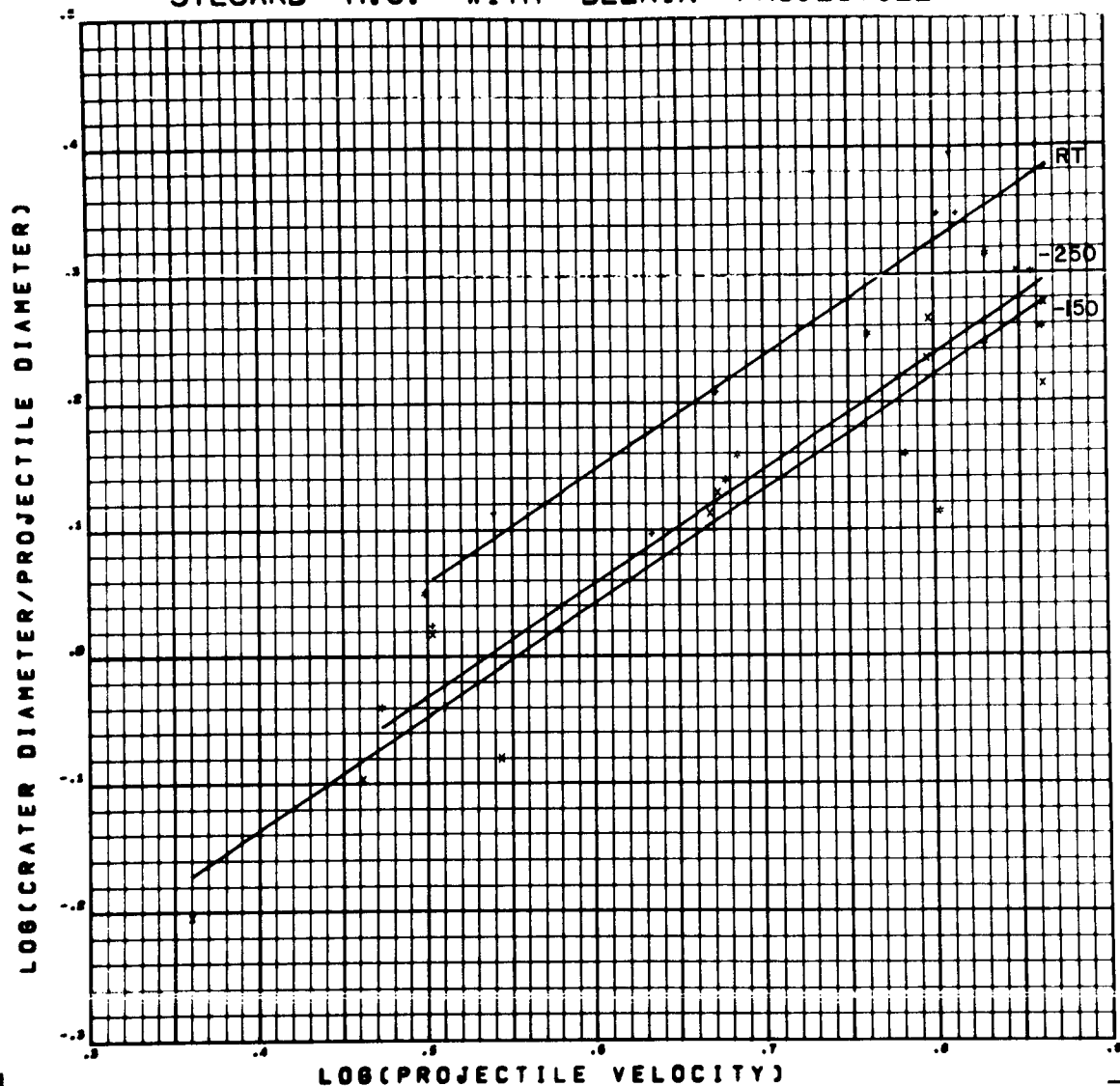


Figure G10 Log Reduced Crater Diameter versus Log Velocity for Delrin

Projectiles on Sylgard 325 HC

Data Points Skipped: 209 R2

Form of Regression: $\log_{10}\left(\frac{d}{D}\right) = -.4529 + .8930 \log_{10} V + .0892 ST - .0403 CV$

RMS Deviation: 12 %

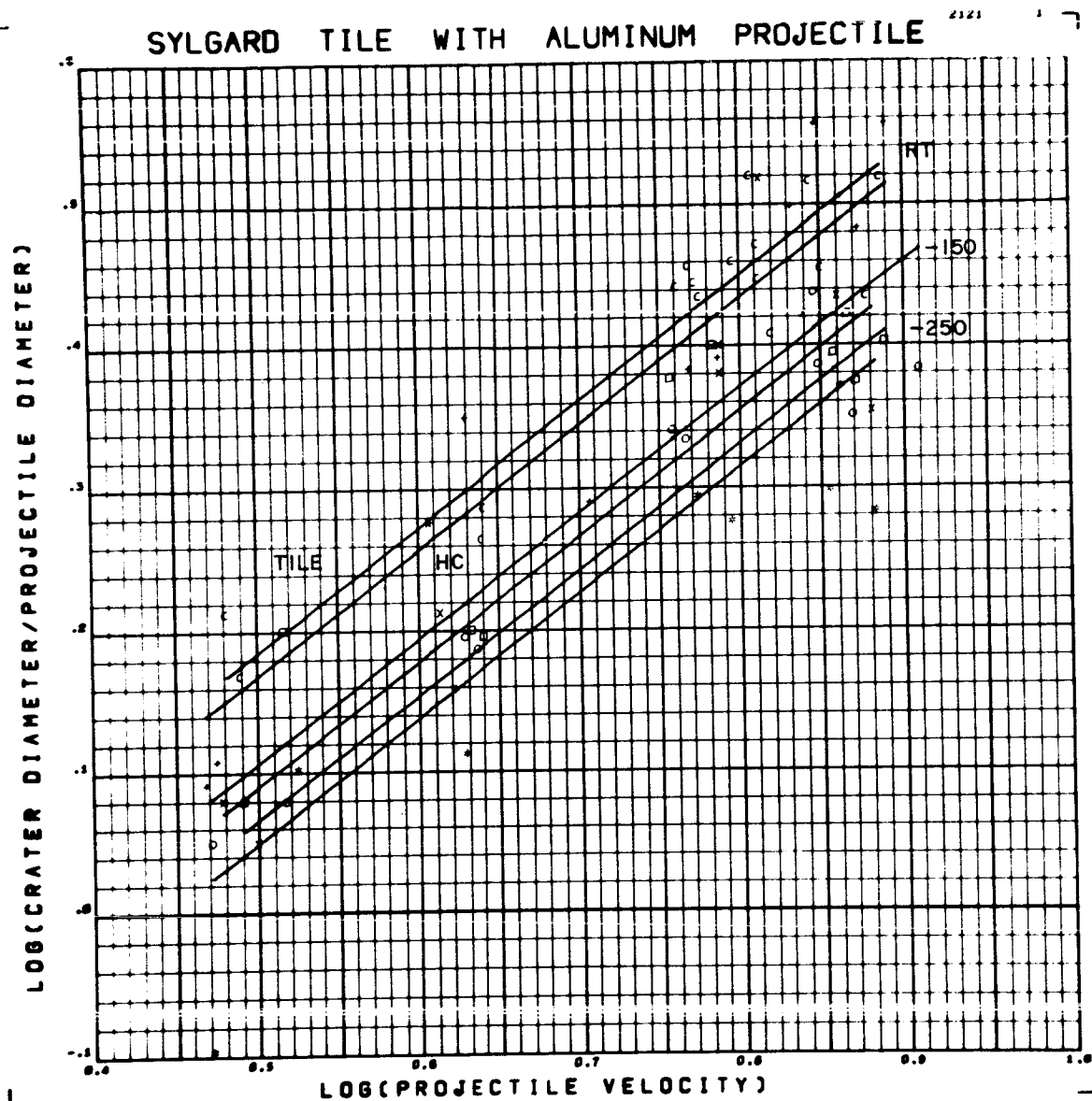


Figure G19 Log Reduced Crater Diameter versus Log Velocity for Aluminum
Projectiles on Sylgard 325

Data Points Skipped: none

Form of Regression: $\log_{10}\left(\frac{d}{D}\right) = -.3316 + .8850 \log_{10} V + .1186 ST -.0130 CV$
 $-.0162 H$

RMS Deviation: 13%

SYLGARD WITH DELRIN PROJECTILE

2121

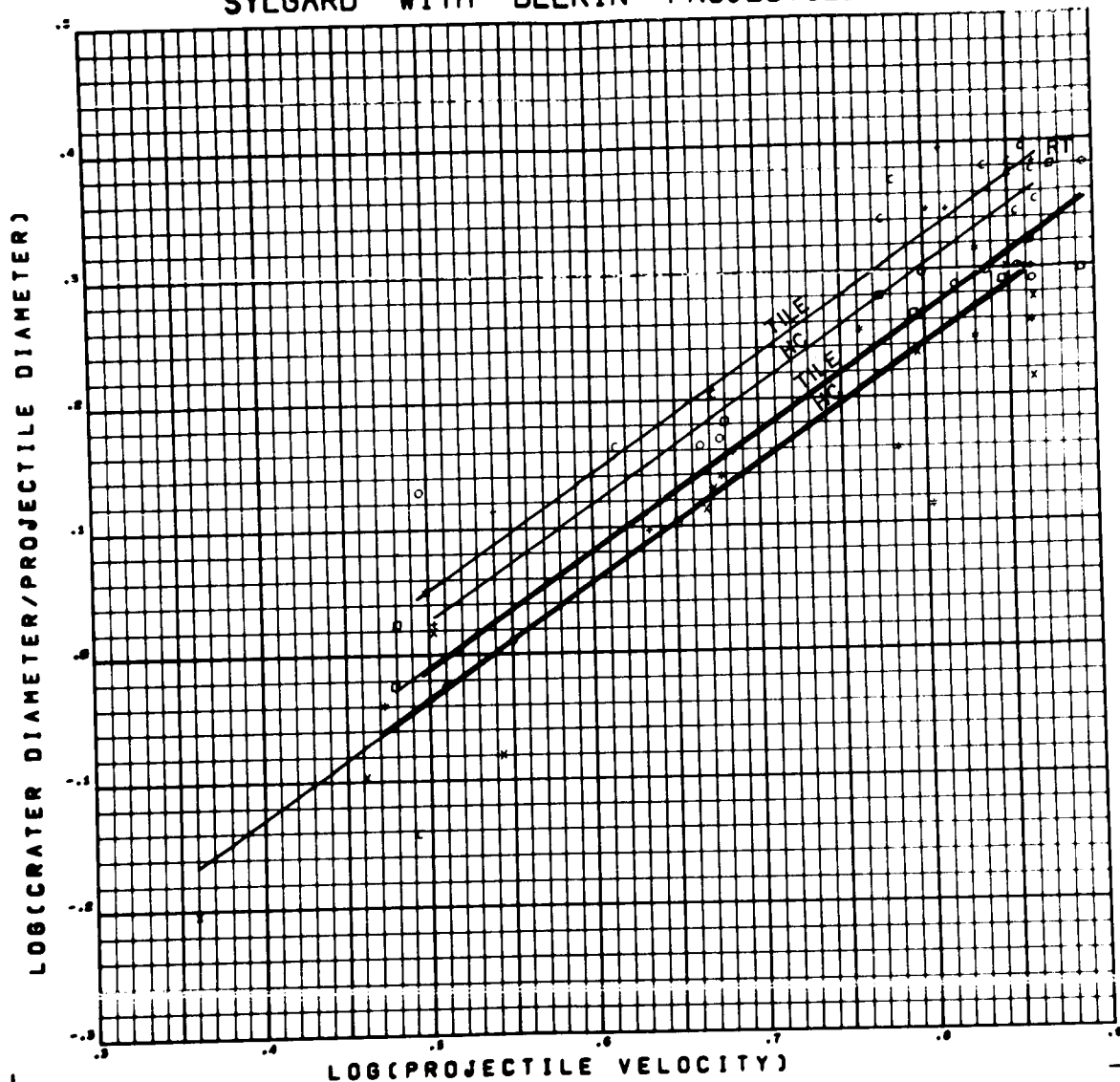


Figure G20 Log Reduced Crater Diameter versus Log Velocity for Delrin

Projectiles on Sylgard 325

Data Points Skipped: 209 R2

Form of Regression: $\log_{10} \left(\frac{d}{D} \right) = -.4647 + .9246 \log_{10} V + .0602 ST - .0219 CV - .0243 H$

RMS Deviation: 13 %

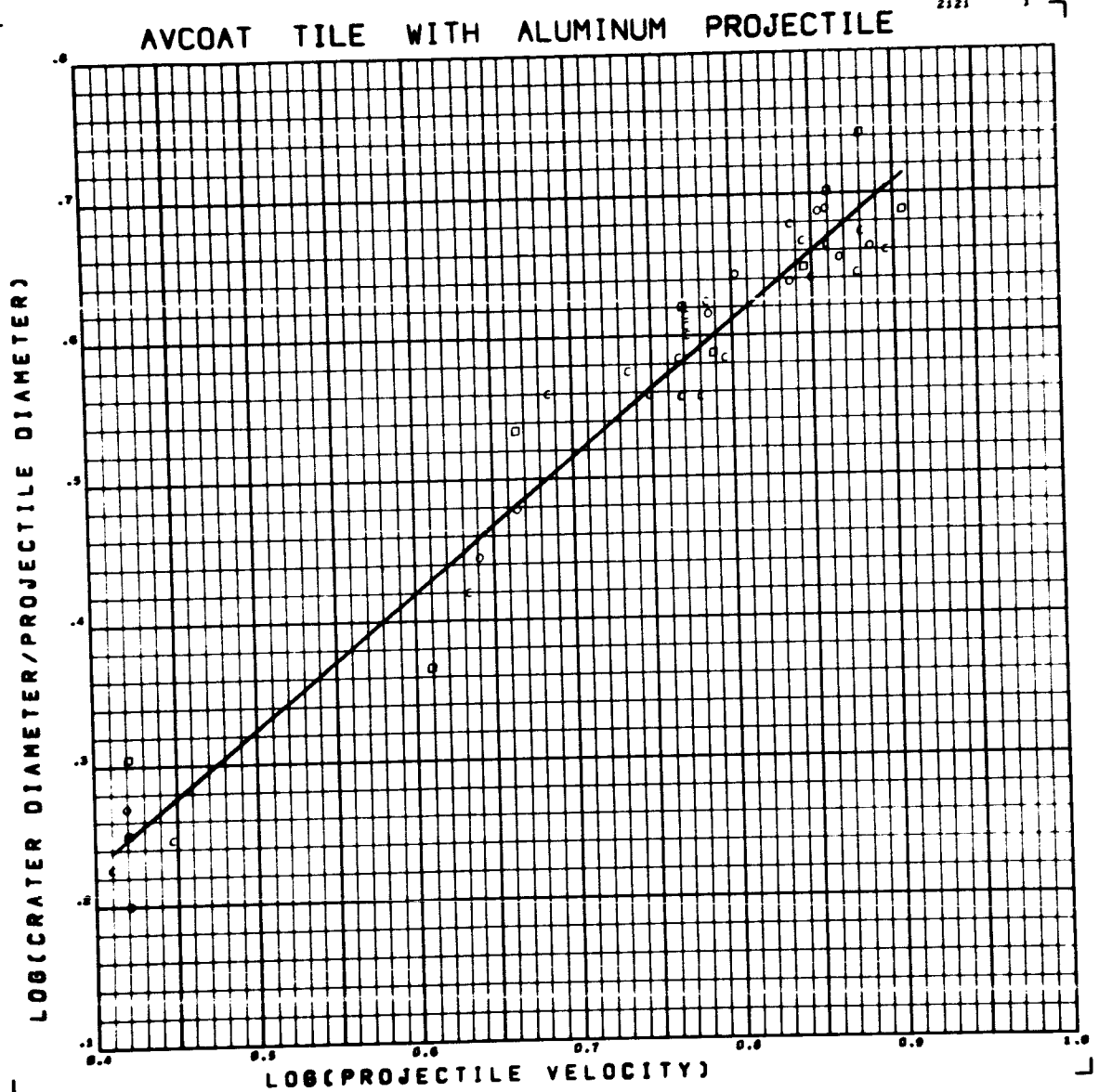


Figure G21 Log Reduced Crater Diameter versus Log Velocity for Aluminum

Projectiles on Avcoat 5026 Tile

Data Points Skipped: 116

Form of Regression: $\log_{10}\left(\frac{d}{D}\right) = -1.555 + .9594 \log_{10} V$

RMS Deviation: 7%

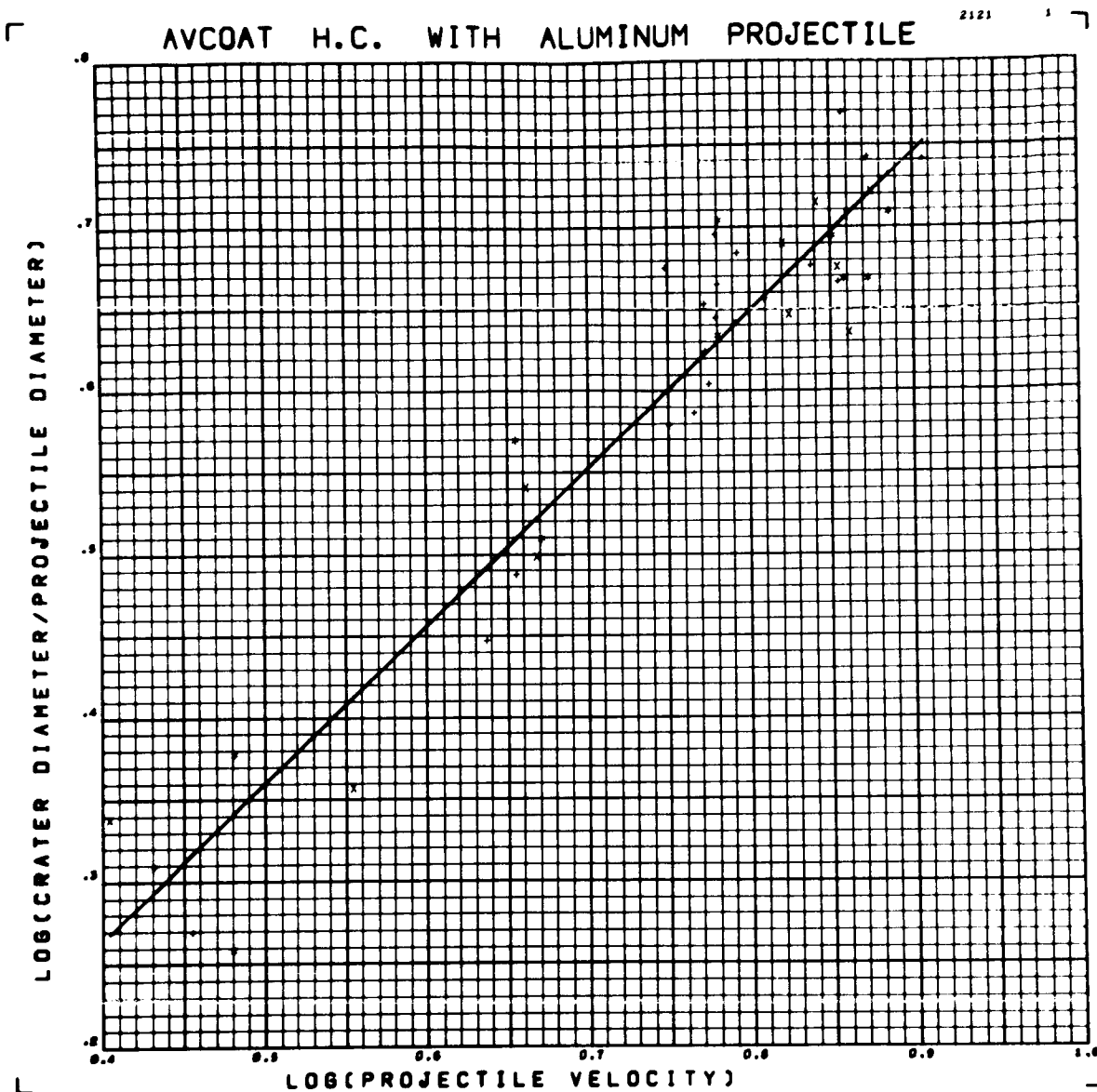


Figure G22 Log Reduced Crater Diameter versus Log Velocity for Aluminum

Projectiles on Avcoat 5026 HC

Data Points Skipped: *none*

Form of Regression: $\log_{10} \left(\frac{d}{D} \right) = -.1217 + .9638 \log_{10} V$

RMS Deviation: 10 %

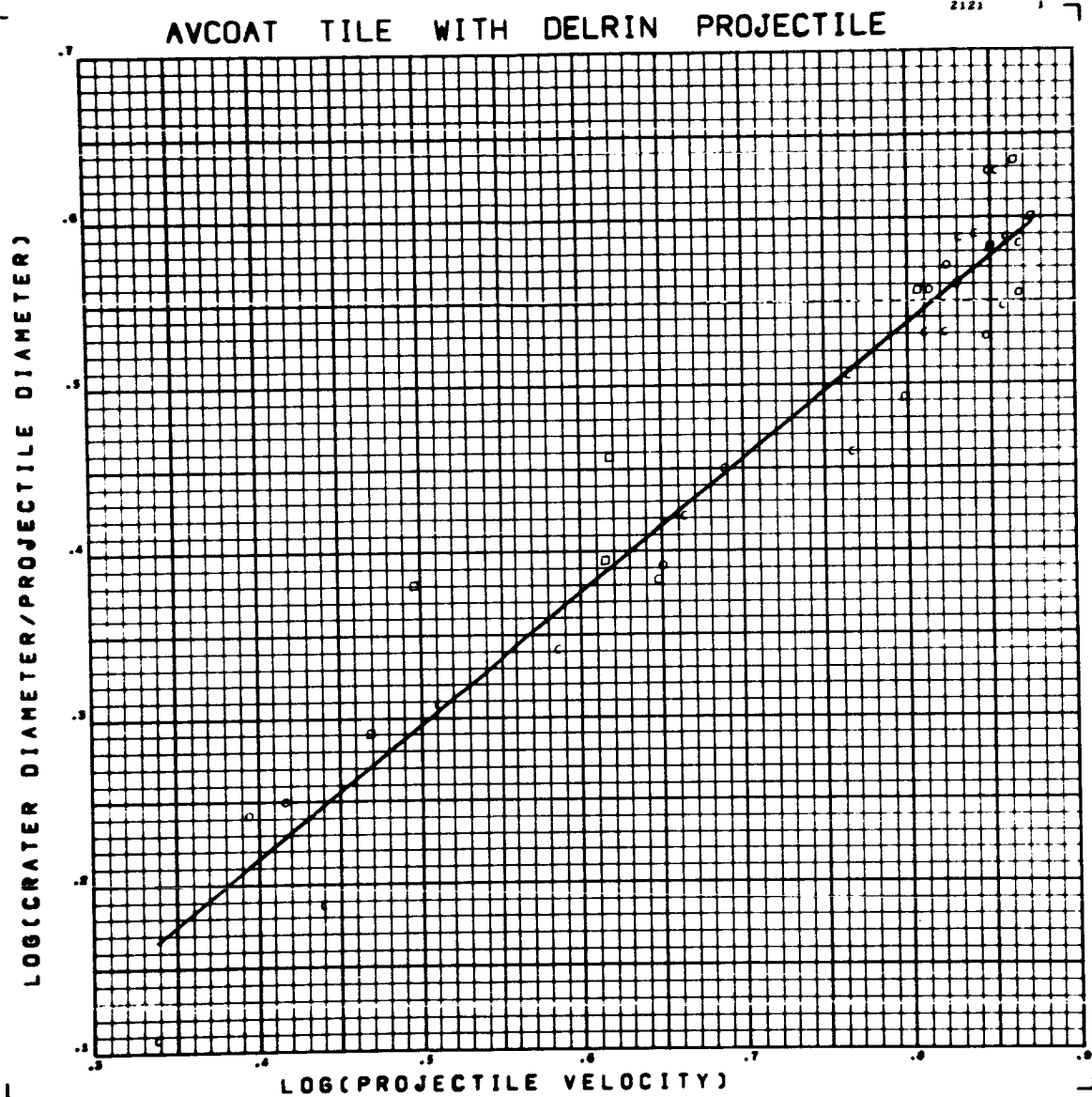


Figure G23 Log Reduced Crater Diameter versus Log Velocity for Delrin

Projectiles on Avcoat 5026 Tile

Data Points Skipped: none

Form of Regression: $\log_{10}\left(\frac{d}{D}\right) = -.1061 + .8041 \log_{10} V$

RMS Deviation: 8 %

AVCOAT H.C. WITH DELRIN PROJECTILE

2121

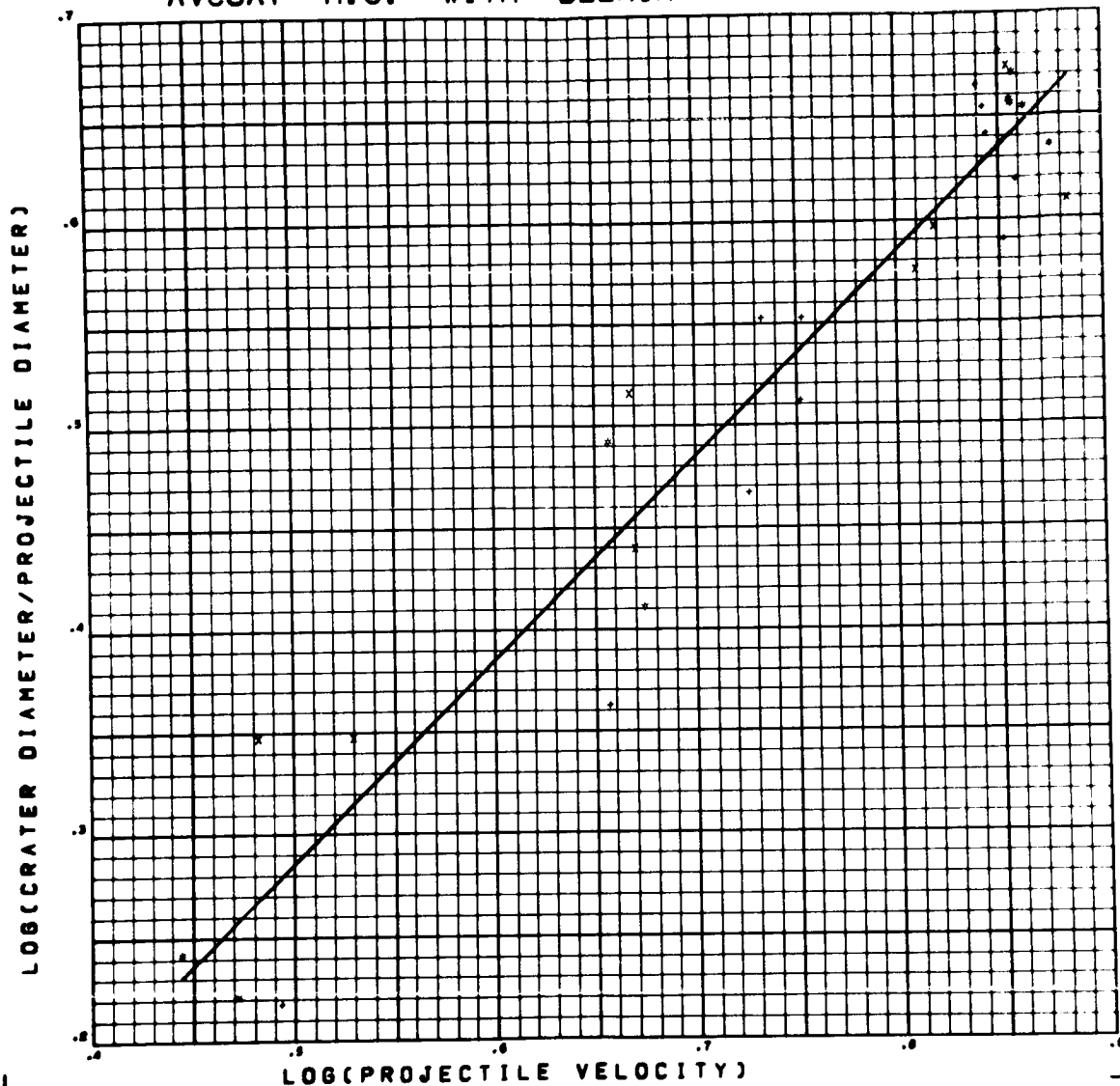


Figure G24 Log Reduced Crater Diameter versus Log Velocity for Delrin

Projectiles on Avcoat 5026 HC

Data Points Skipped: 29, 30, 37 R3

Form of Regression: $\log_{10}\left(\frac{d}{D}\right) = -0.2127 + 0.9976 \log_{10} V$

RMS Deviation: 10 %

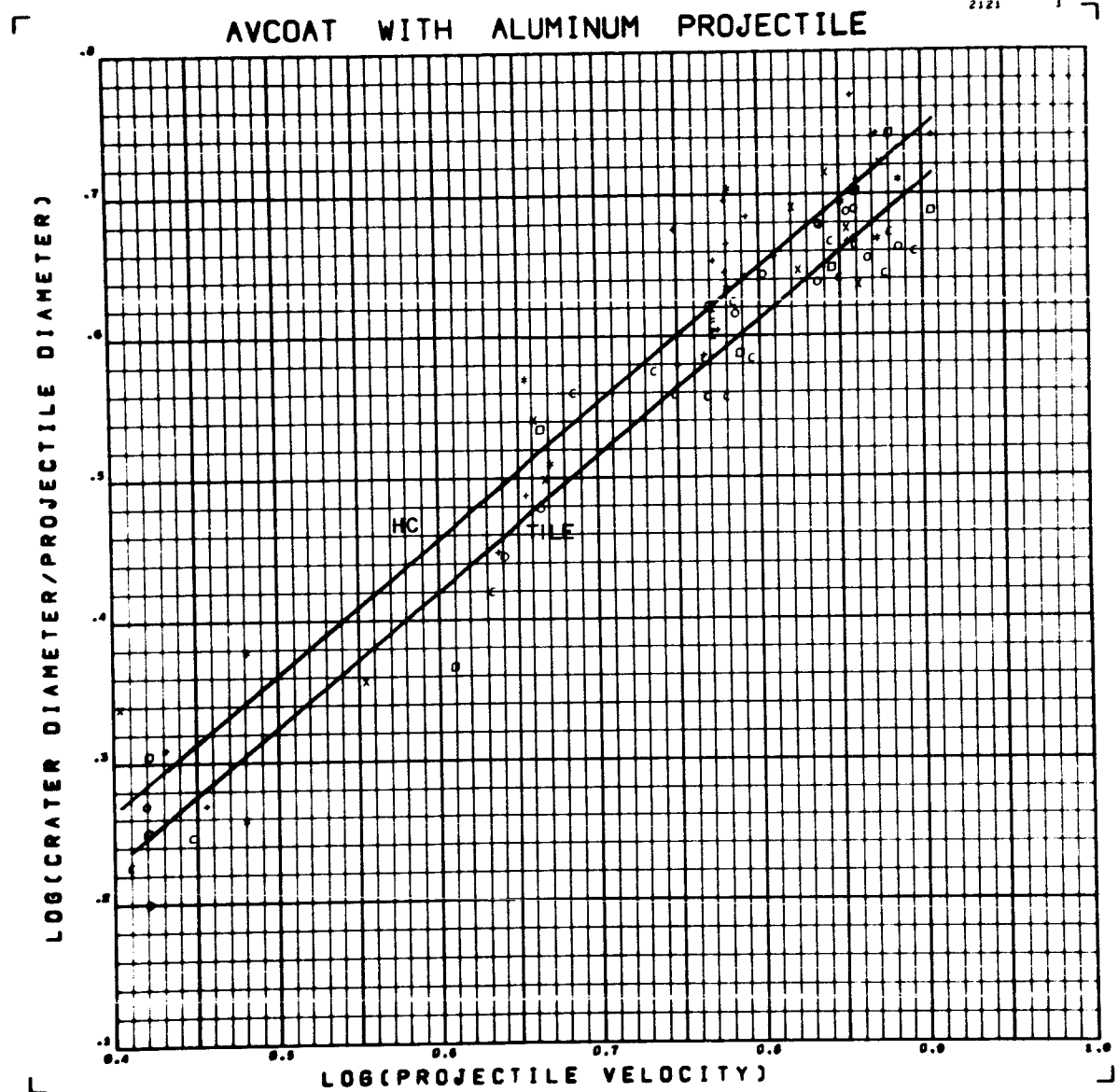


Figure G25 Log Reduced Crater Diameter versus Log Velocity for Aluminum
Projectiles on Avcoat 5026

Data Points Skipped: 116

Form of Regression: $\log_{10} \left(\frac{d}{D} \right) = -.1385 + .9614 \log_{10} V + .0371 H$

RMS Deviation: 9 %

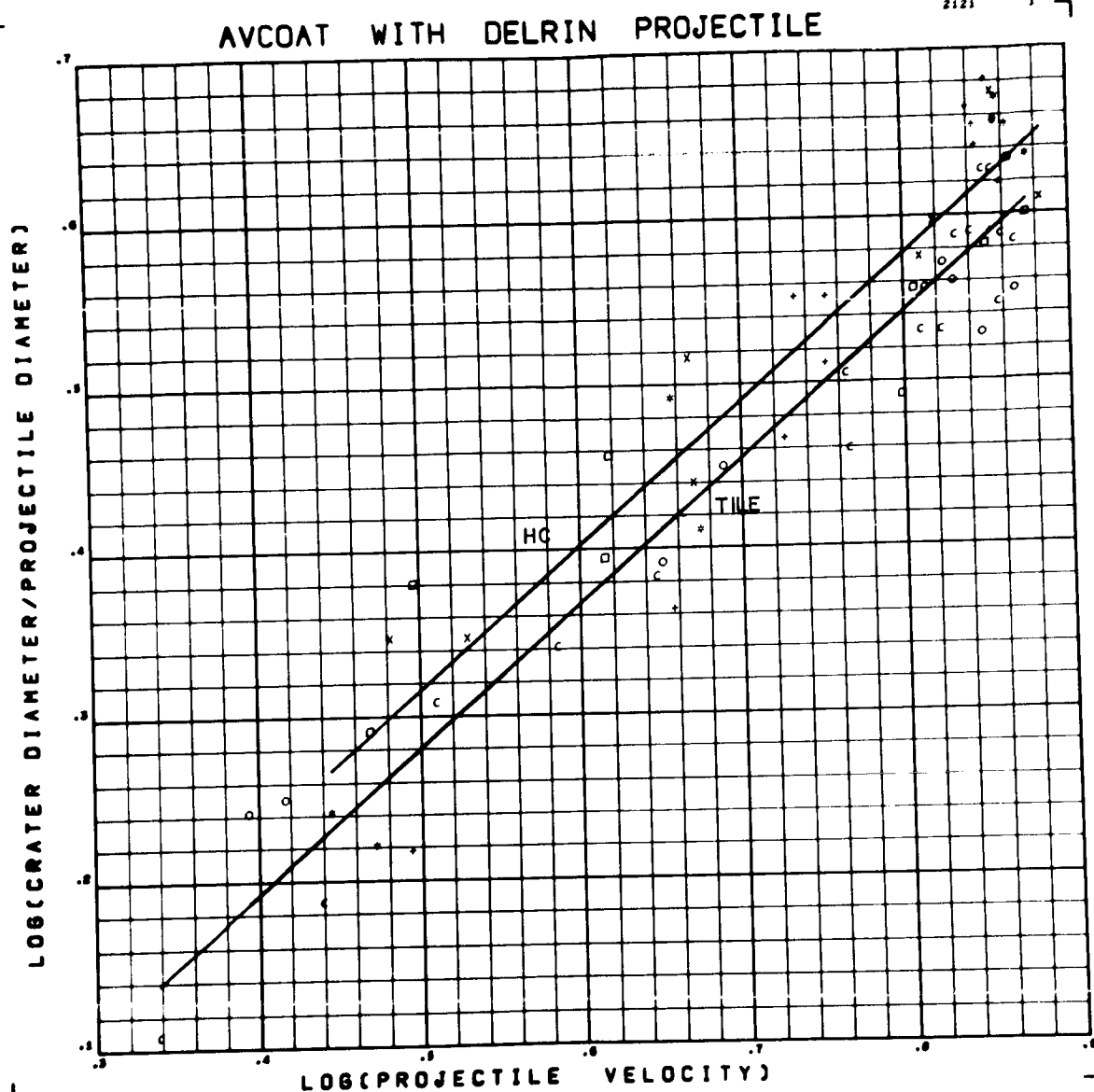


Figure G26 Log Reduced Crater Diameter versus Log Velocity for Delrin

Projectiles on Avcoat 5026

Data Points Skipped: 29, 30, 37 R3

Form of Regression: $\log\left(\frac{d}{D}\right) = -1.403 + .8763 \log_{10} V + .0349 H$

RMS Deviation: 10 %

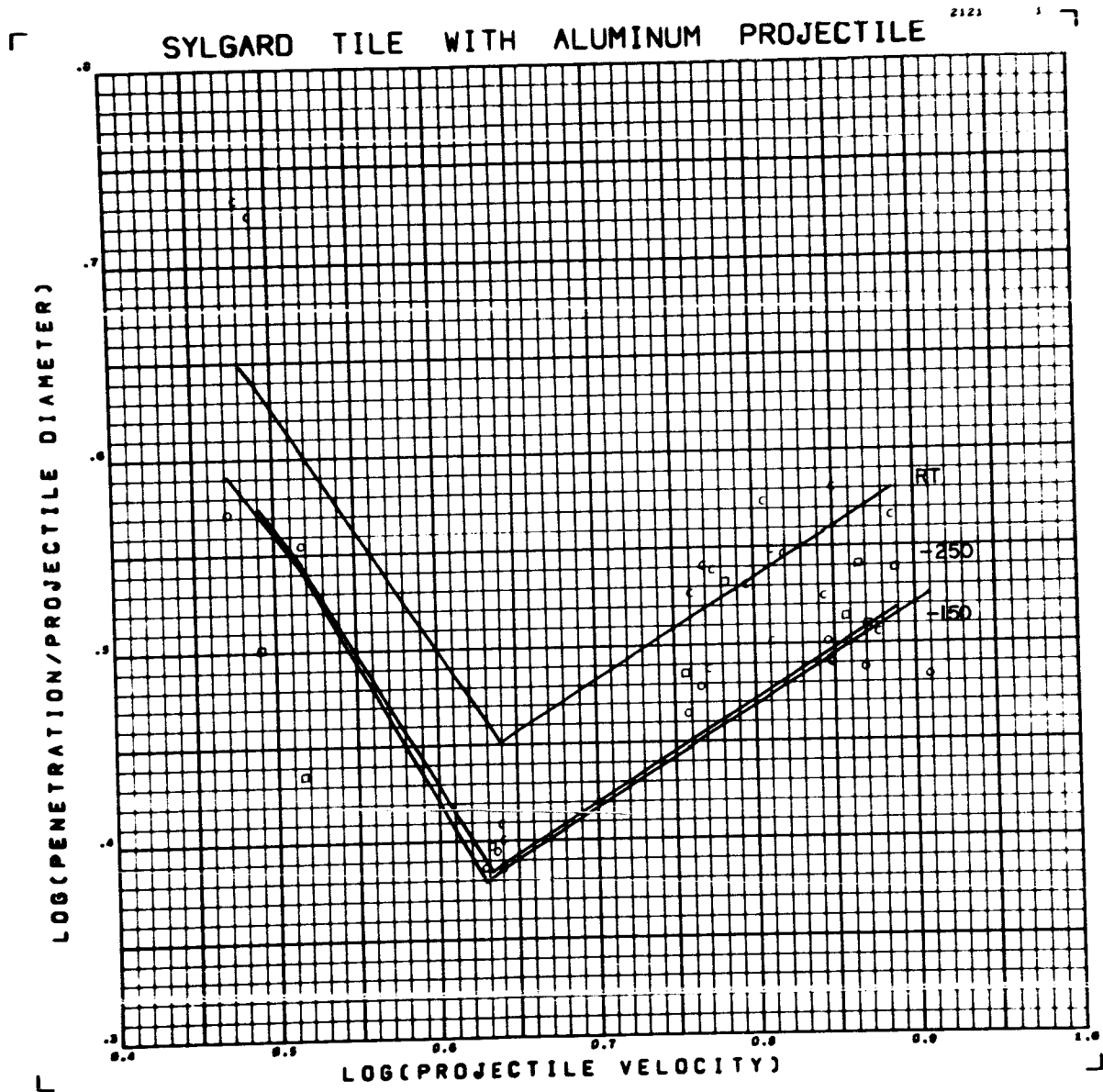


Figure G27 Log Reduced Penetration versus Log Velocity for Aluminum

Projectiles on Sylgard 325 Tile

Data Points Skipped: none

Form of Regression: $\log_{10}\left(\frac{P}{D}\right) = .0749 + .5210 \log_{10} V + .0631 ST - .0231 CV$

RMS Deviation: 10 %

for $V > 4.5 \text{ km/sec}$

SYLGARD H.C. WITH ALUMINUM PROJECTILE

2121

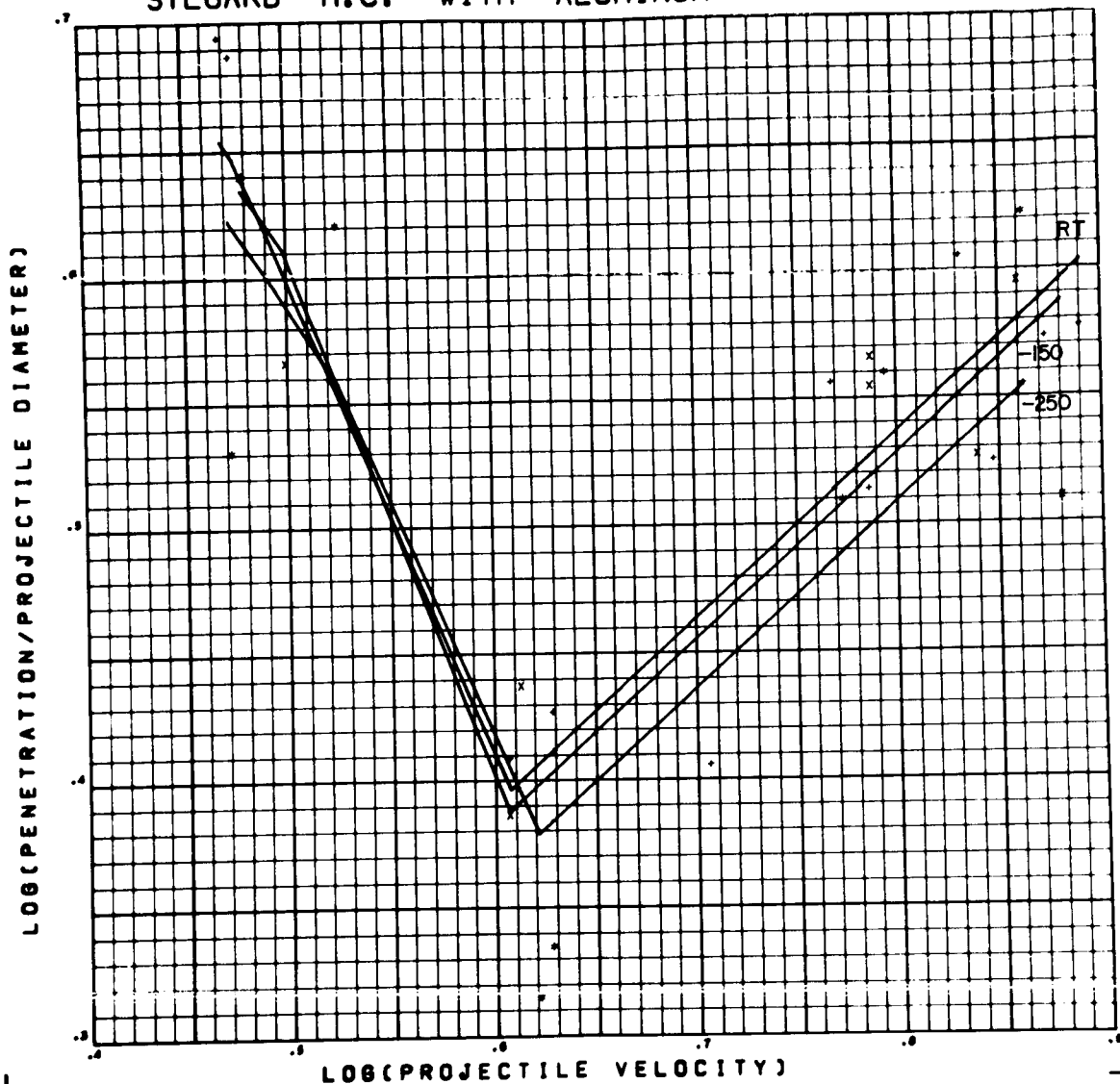


Figure G28 Log Reduced Penetration versus Log Velocity for Aluminum

Projectiles on Sylgard 325 HC

Data Points Skipped: 280 R1, 293 R1, 294

Form of Regression: $\log_{10}\left(\frac{P}{D}\right) = -.0591 + .7299\log_{10}V + .0276ST + .0037CV$

RMS Deviation: 11%

for $V > 45$ km/sec

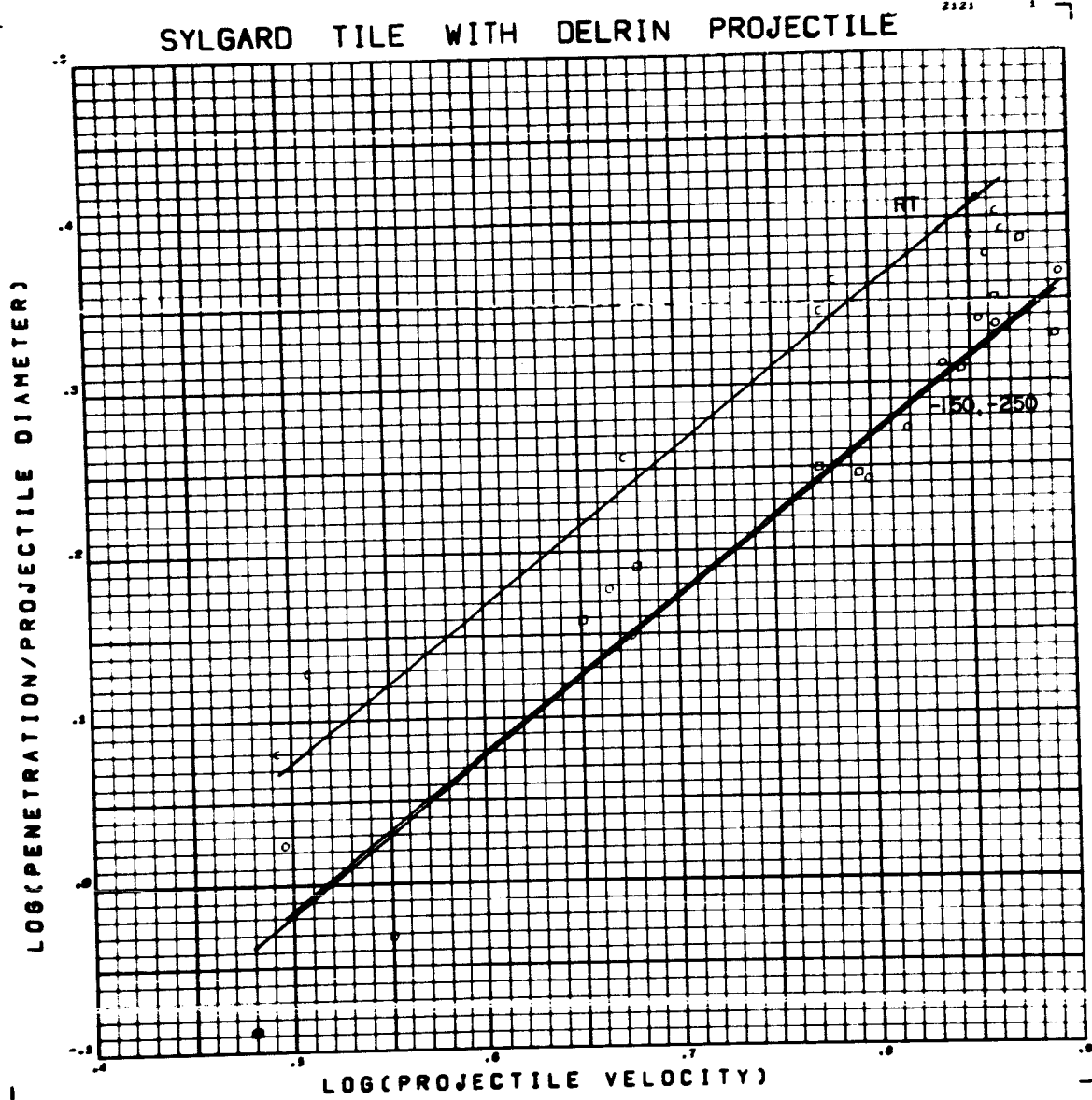


Figure G29 Log Reduced Penetration versus Log Velocity for Delrin

Projectiles on Sylgard 325 Tile

Data Points Skipped: 187, 211 R2

Form of Regression: $\log_{10}\left(\frac{P}{D}\right) = -.4614 + .9498 \log_{10} V + .0918 ST - .0289 CV$

RMS Deviation: 7 %

SYLGARD TILE WITH DELRIN PROJECTILE

2121

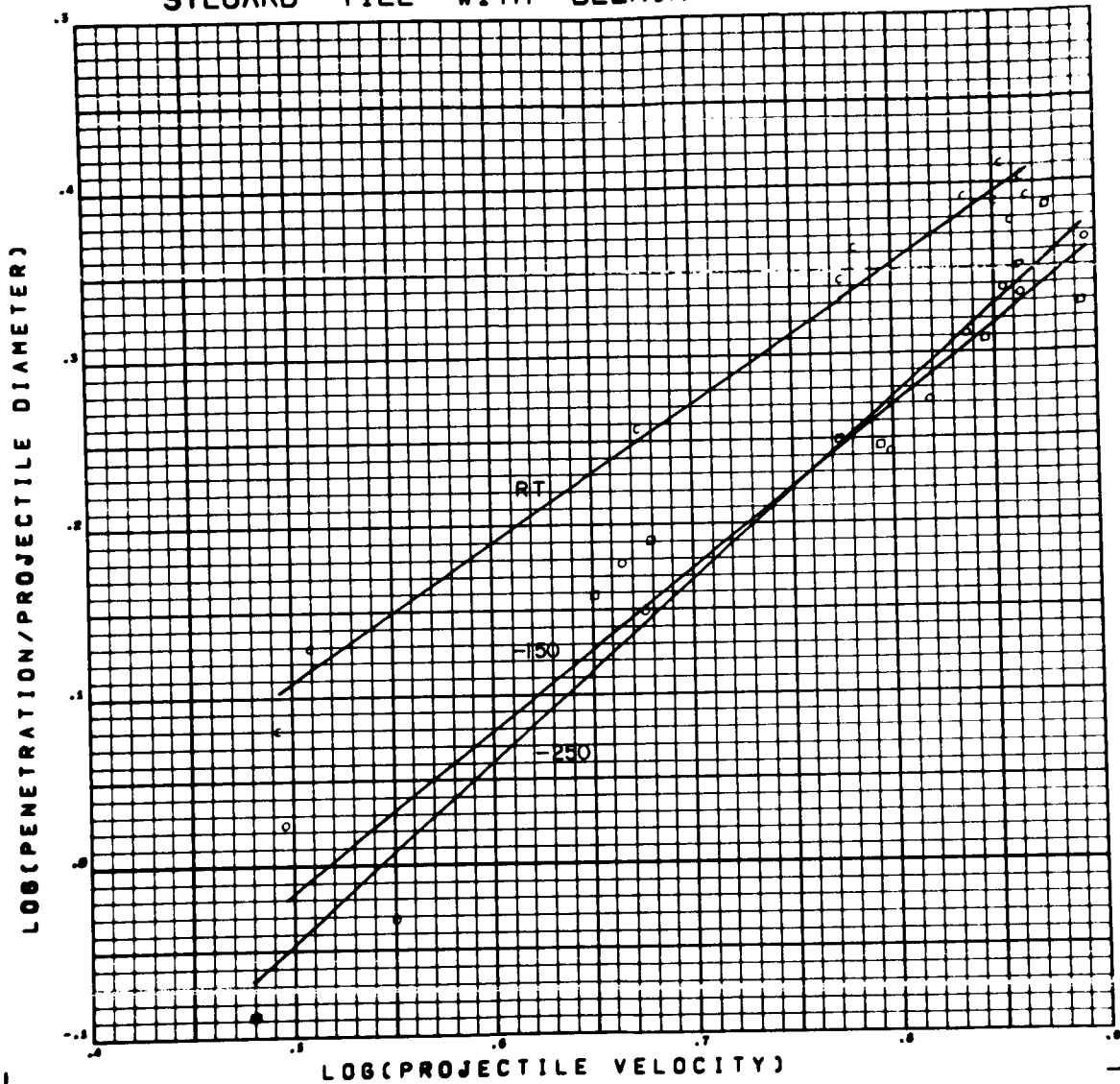


Figure G30 Log Reduced Penetration versus Log Velocity for Delrin

Projectiles on Sylgard 325 Tile

Data Points Skipped: 187, 211 R2

Form of Regression: $\log_{10} \left(\frac{P}{D} \right) = -0.4571 + .9456 \log_{10} V + .2788 ST - .0348 CV$

RMS Deviation: 6% $-.2500 ST \cdot \log_{10} V + .0065 CV \cdot \log_{10} V$

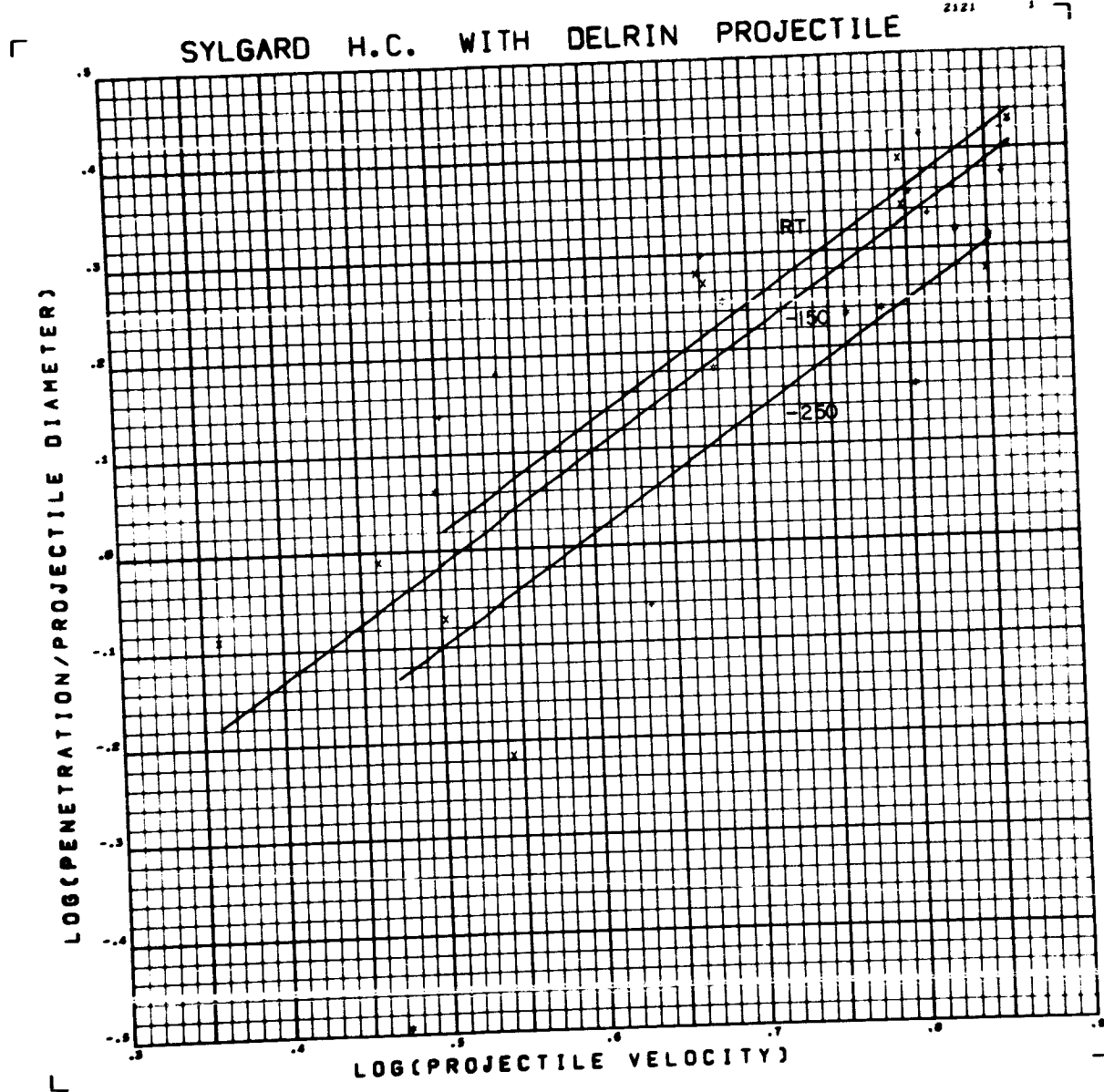


Figure G31 Log Reduced Penetration versus Log Velocity for Delrin

Projectiles on Sylgard 325 HC

Data Points Skipped: 197, 209, 209 R1, 210

Form of Regression: $\log_{10}\left(\frac{P}{D}\right) = -7.6115 + 1.157 \log_{10} V + .1161 ST + .0176 CV$

RMS Deviation: 32%

SYLGARD H.C. WITH DELRIN PROJECTILE

2121

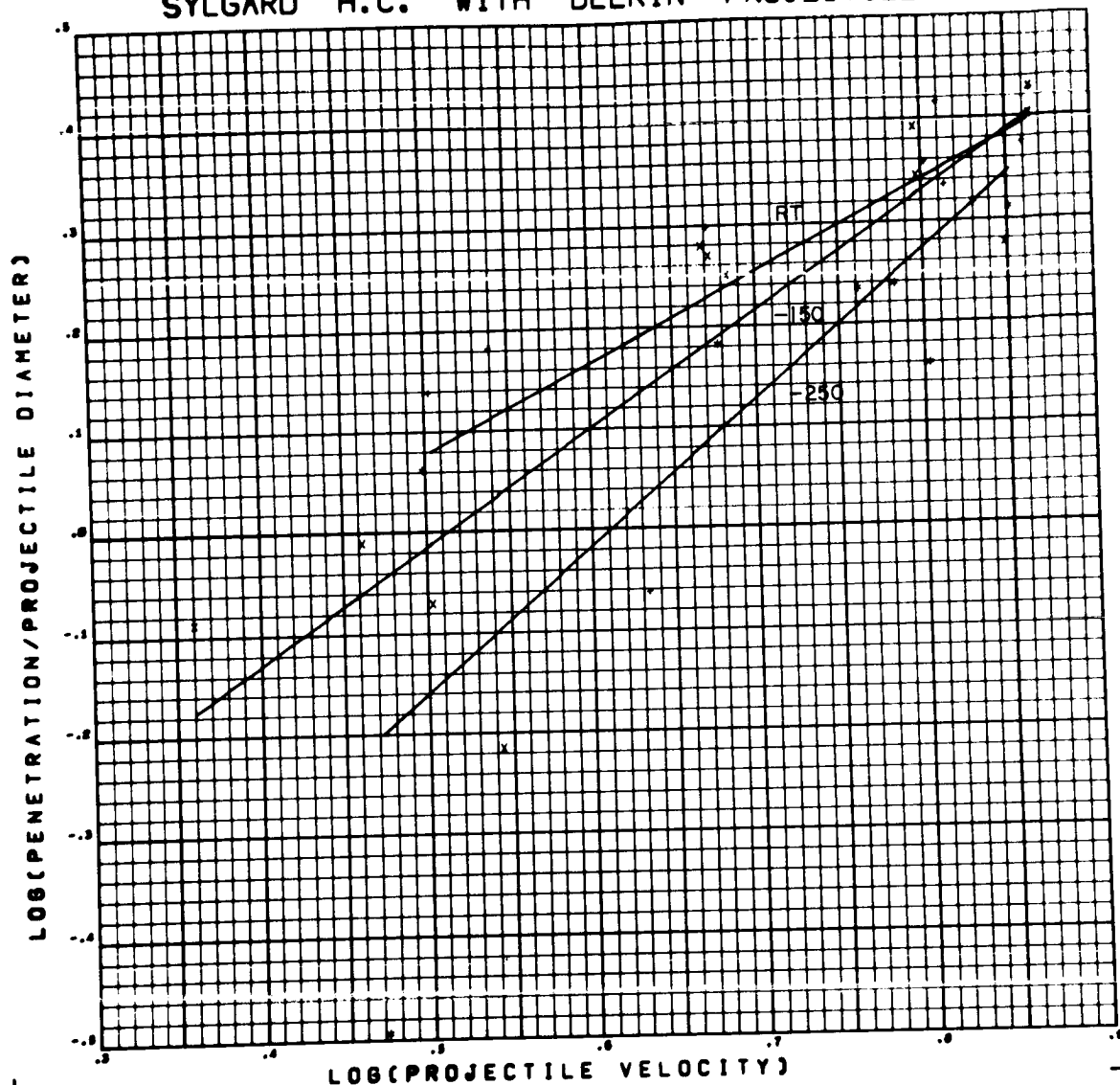


Figure G32 Log Reduced Penetration versus Log Velocity for Delrin

Projectiles on Sylgard 325 HC

Data Points Skipped: 197, 209, 209A1, 210

$$\text{Form of Regression: } \log_{10}\left(\frac{P}{D}\right) = -.6116 + 1.159 \log_{10} V + .5176 ST + .0219 CV \\ - .5618 ST \cdot \log_{10} V - .0084 CV \cdot \log_{10} V$$

RMS Deviation: 31%

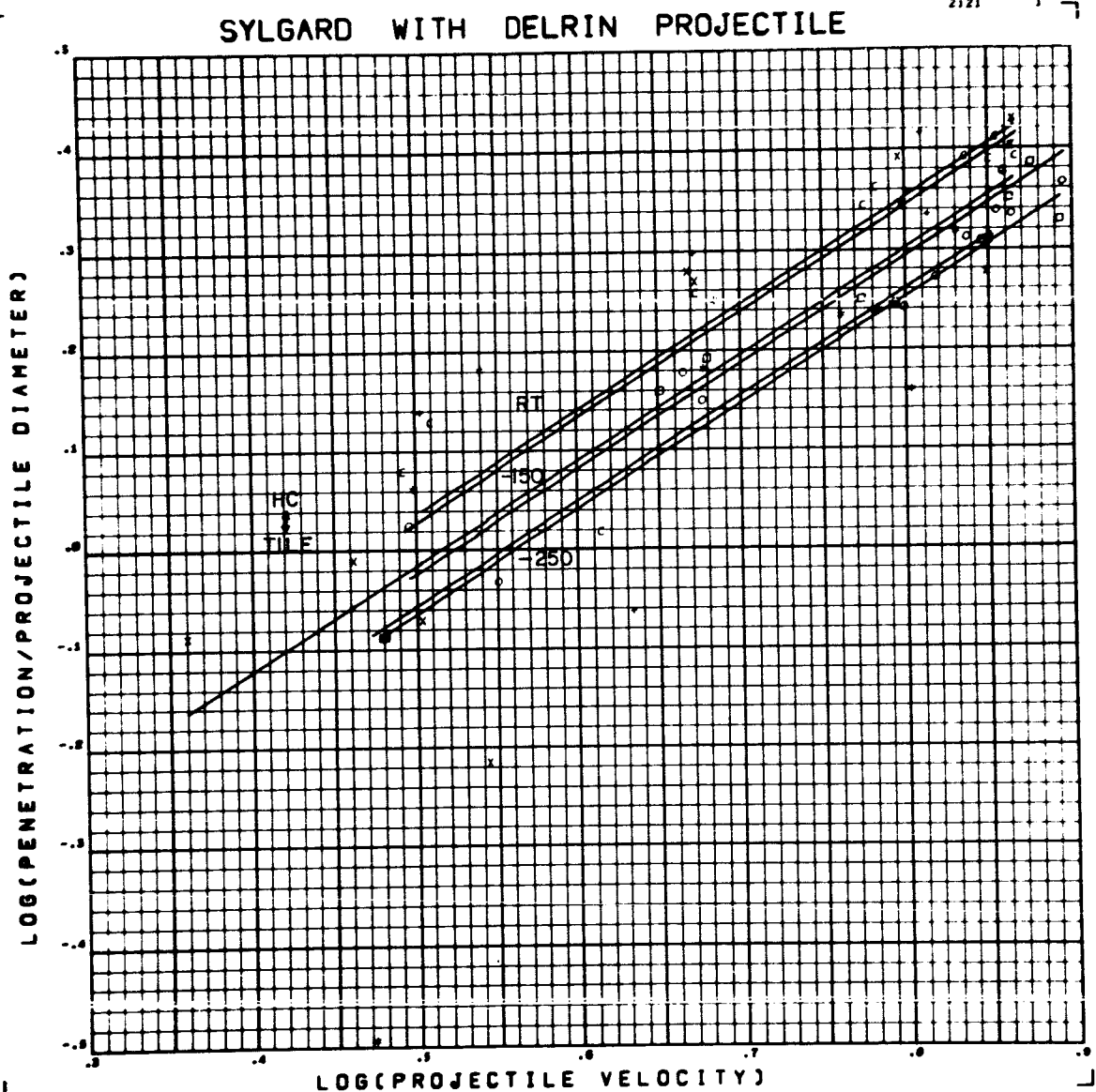


Figure G33 Log Reduced Penetration versus Log Velocity for Delrin

Projectiles on Sylgard 325

Data Points Skipped: 197, 209, 209 R1, 210

Form of Regression: $\log_{10} \left(\frac{P}{D} \right) = -0.5450 + 1.058 \log_{10} V + 0.0917 ST - 0.0034 CV$
 $+ 0.0081 H$

RMS Deviation: 2.3%

SYLGARD WITH DELRIN PROJECTILE

2121

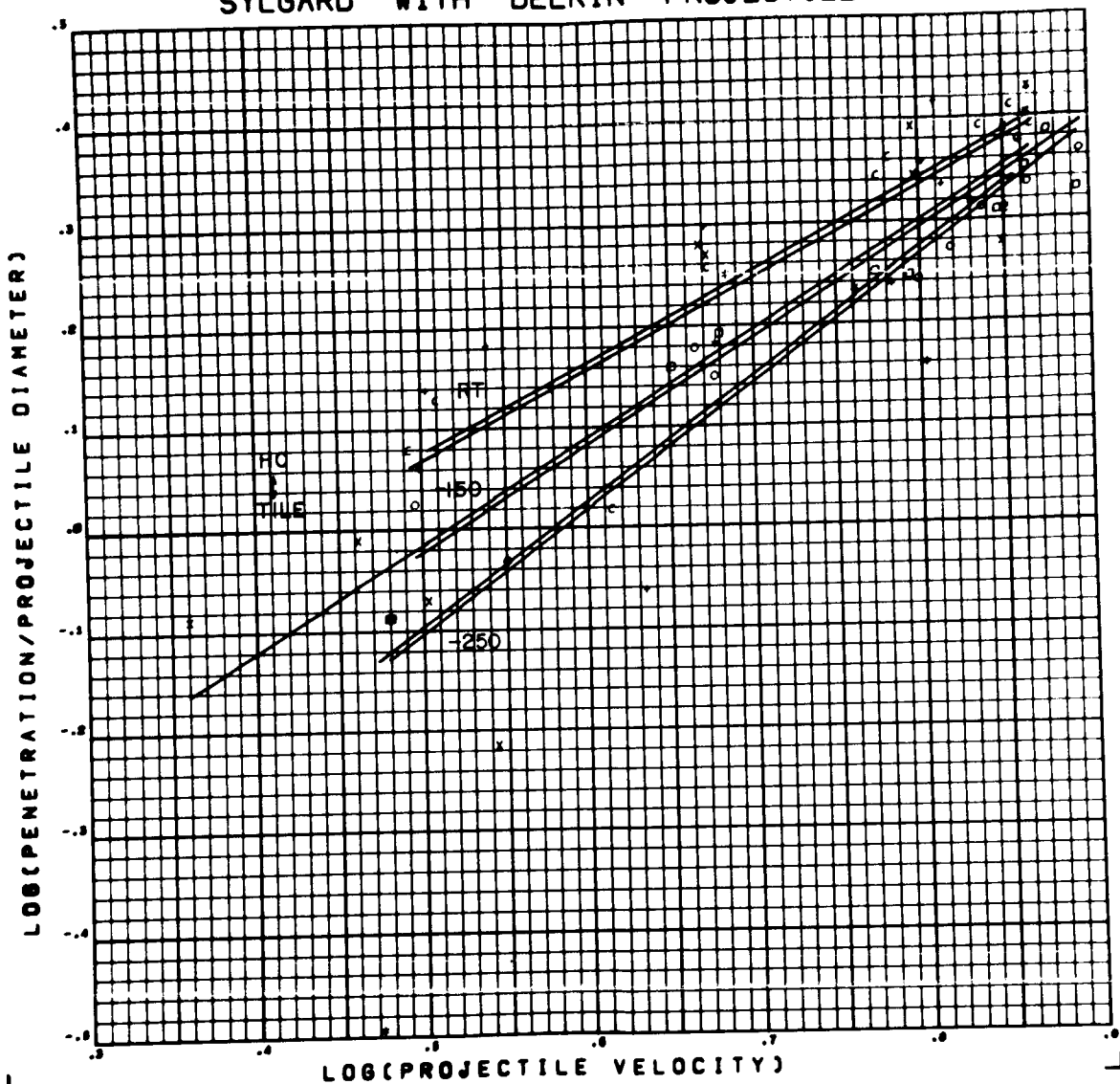


Figure G34 Log Reduced Penetration versus Log Velocity for Delrin

Projectiles on Sylgard 325

Data Points Skipped: 197, 209, 209 R1, 210

Form of Regression: $\log_{10}\left(\frac{P}{D}\right) = -0.5453 + 1.060 \log_{10} V - 0.3445 ST - 0.0007 CV$

RMS Deviation: 22 %

$-0.3456 ST / \log_{10} V - 0.0073 CV \cdot \log_{10} V + 0.0074 H$

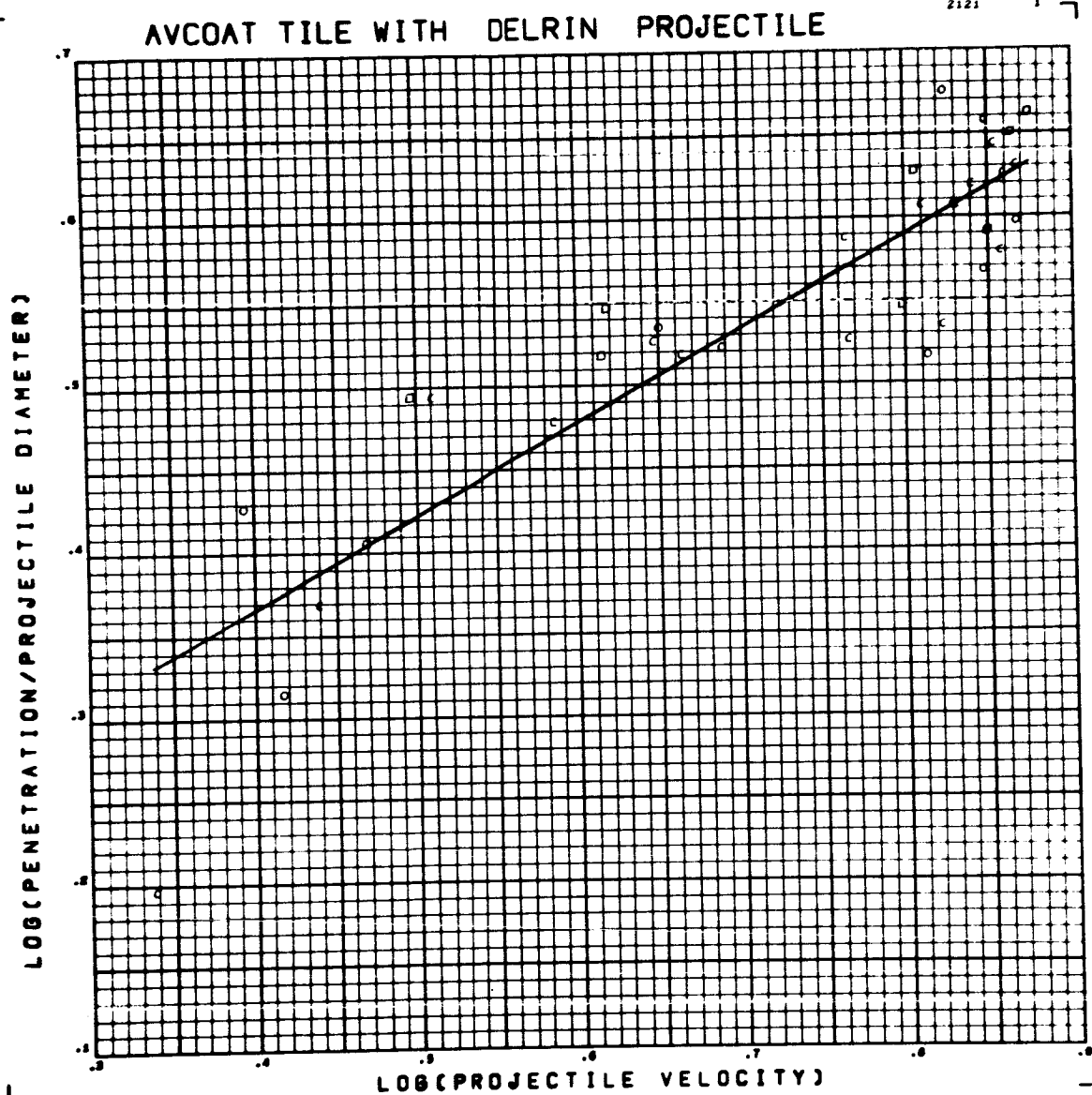


Figure G35 Log Reduced Penetration versus Log Velocity for Delrin

Projectiles on Avcoat 5026 Tile

Data Points Skipped: *none*

Form of Regression: $\log_{10} \left(\frac{P}{D} \right) = .1424 + .5600 \log_{10} V$

RMS Deviation: 11 %

AVCOAT H.C. WITH DELRIN PROJECTILE

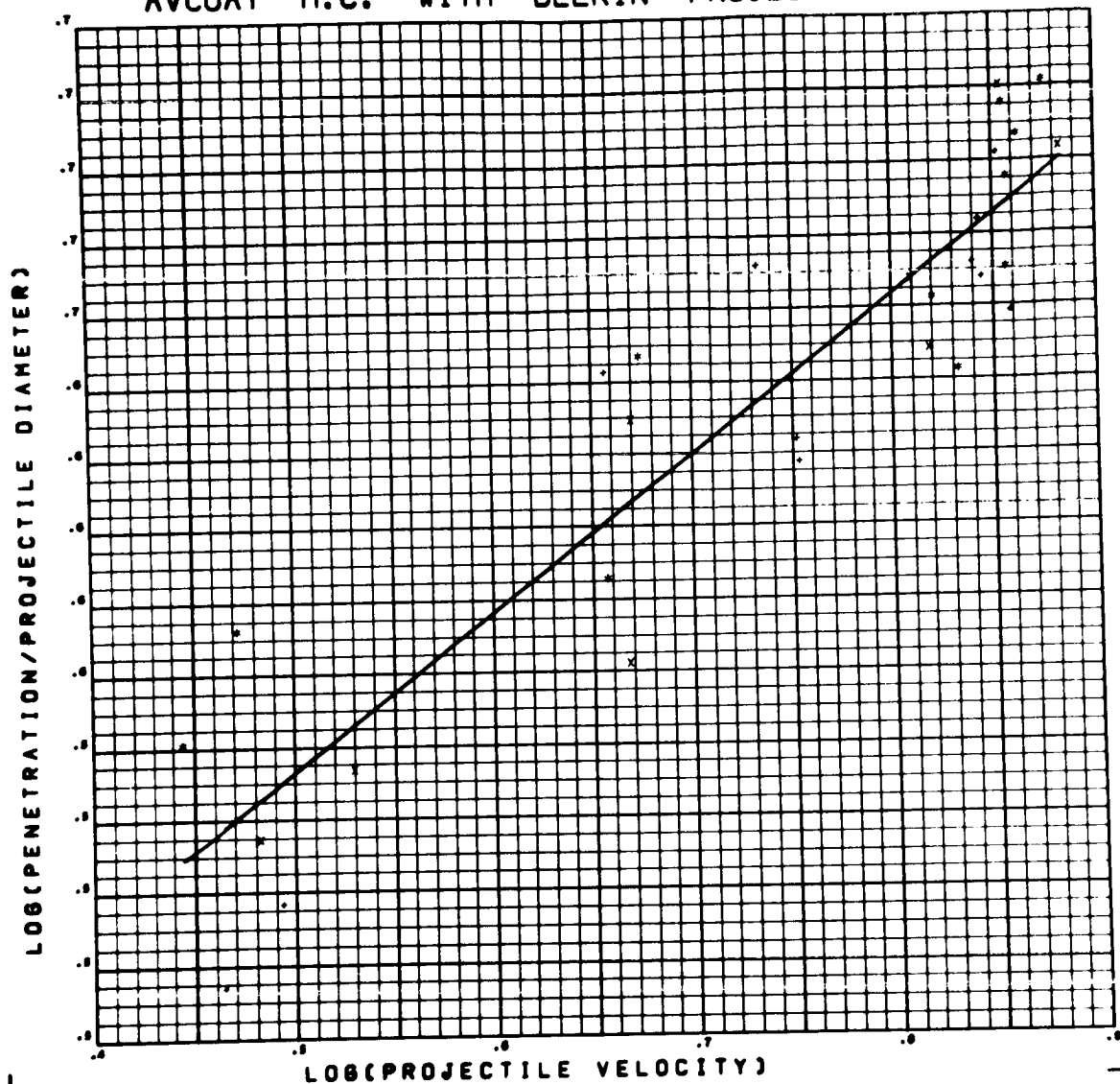


Figure G36 Log Reduced Penetration versus Log Velocity for Delrin

Projectiles on Avcoat 5026 HC

Data Points Skipped: 13, 37 R3, 38 R2

Form of Regression: $\log_{10} \left(\frac{P}{D} \right) = .3553 + .4356 \log_{10} V$

RMS Deviation: 7 %

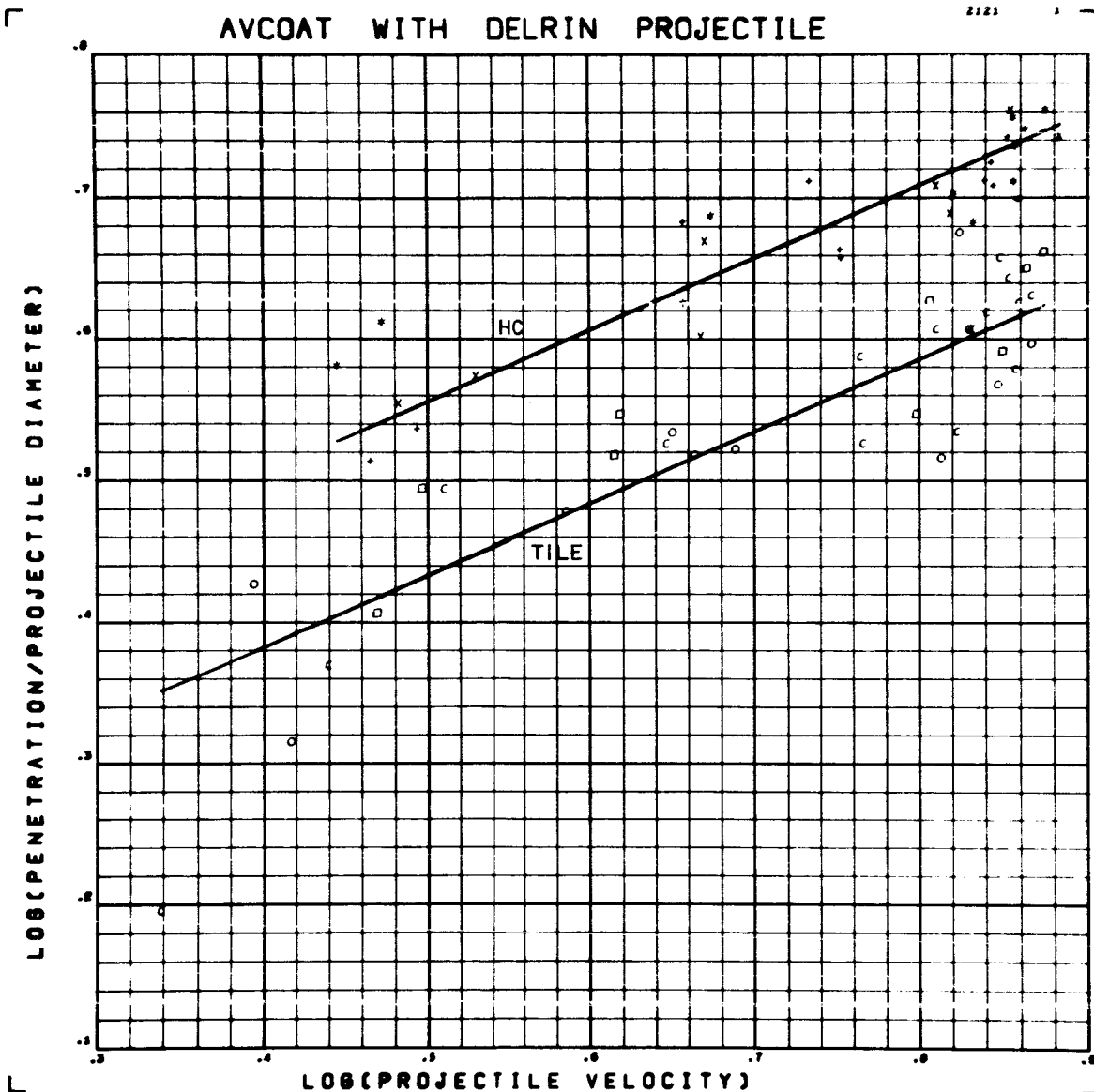


Figure G37 Log Reduced Penetration versus Log Velocity for Delrin

Projectiles on Avcoat 5026

Data Points Skipped: 13, 37 R3, 38 R2

Form of Regression: $\log_{10} \left(\frac{P}{D} \right) = .2396 + .5097 \log_{10} V + .1226 H$

RMS Deviation: 10%

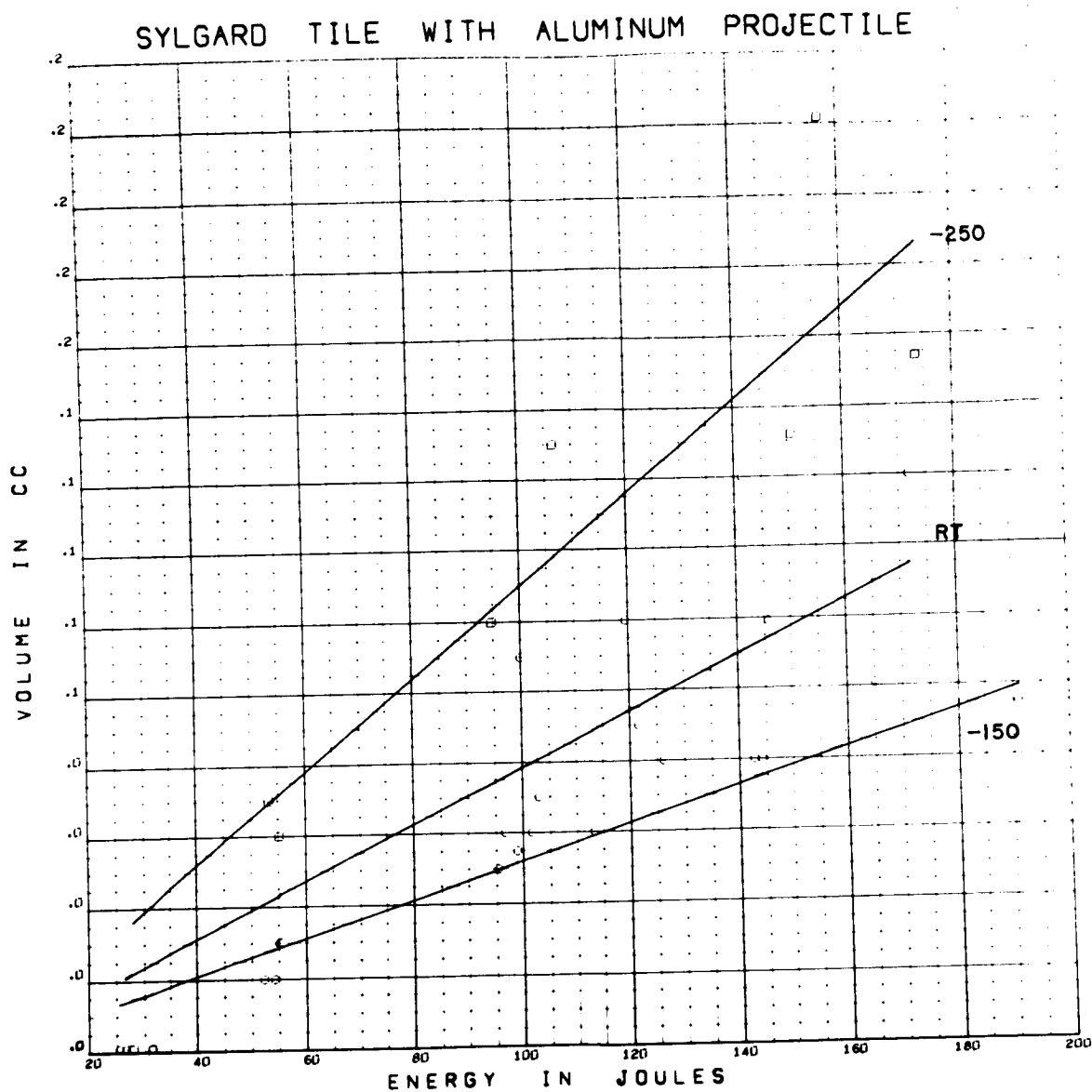


Figure G38 Volume versus Energy for Aluminum Projectiles on Sylgard 325 Tile

Data Points Skipped: 283 R2, 300

Form of Regression: $V = (.8695 - .5174 \cdot ST - .3480 \cdot CV) \cdot 10^{-3} E$

RMS Deviation: .023 cc

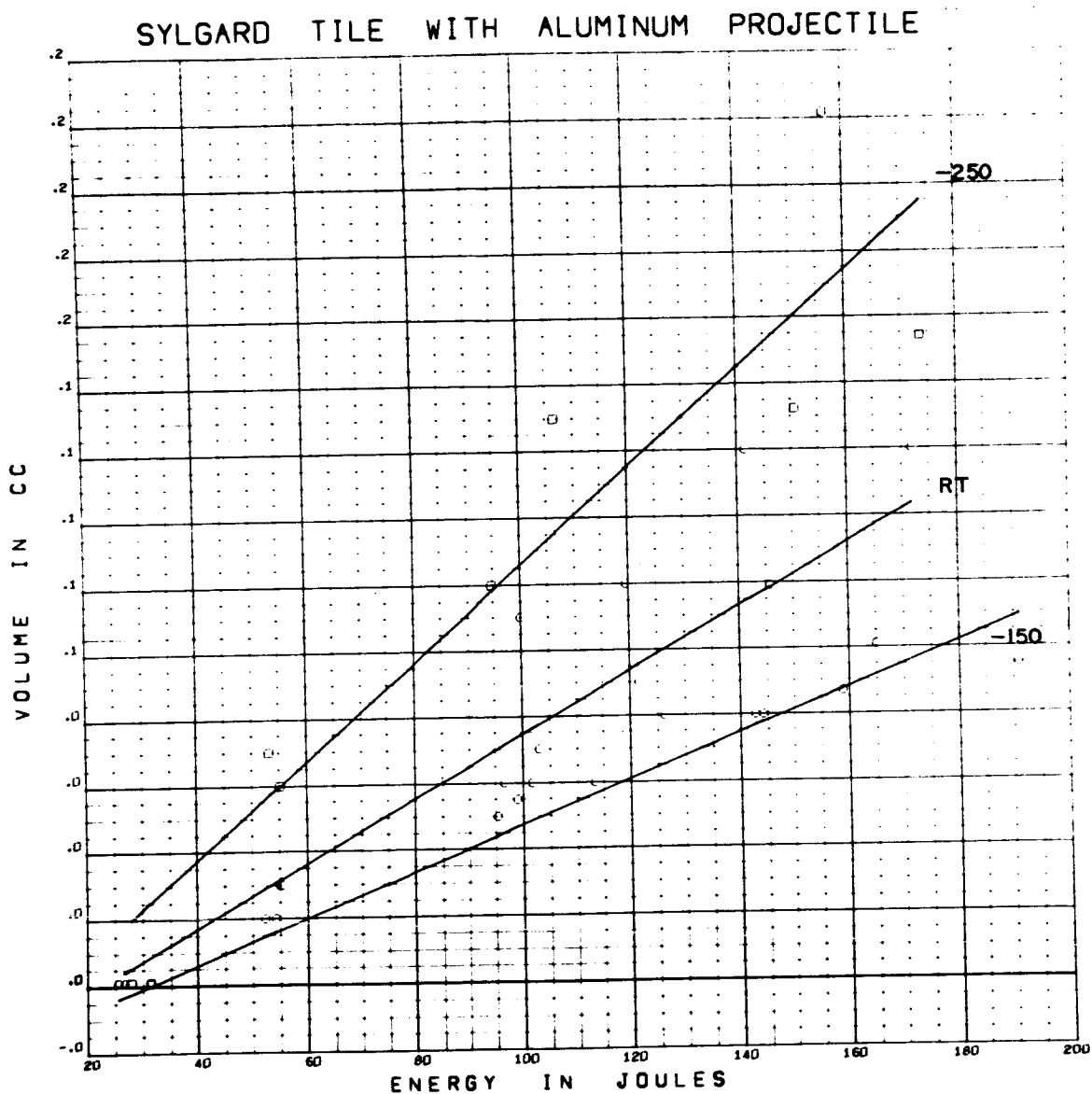


Figure G39 Volume versus Energy for Aluminum Projectiles on Sylgard 325 Tile

Data Points Skipped: 283 R2, 300

Form of Regression: $V = (1.040 - .5144 \cdot ST - .3542 \cdot CV) \cdot 10^{-3} E - .0214$

RMS Deviation: .021 cc

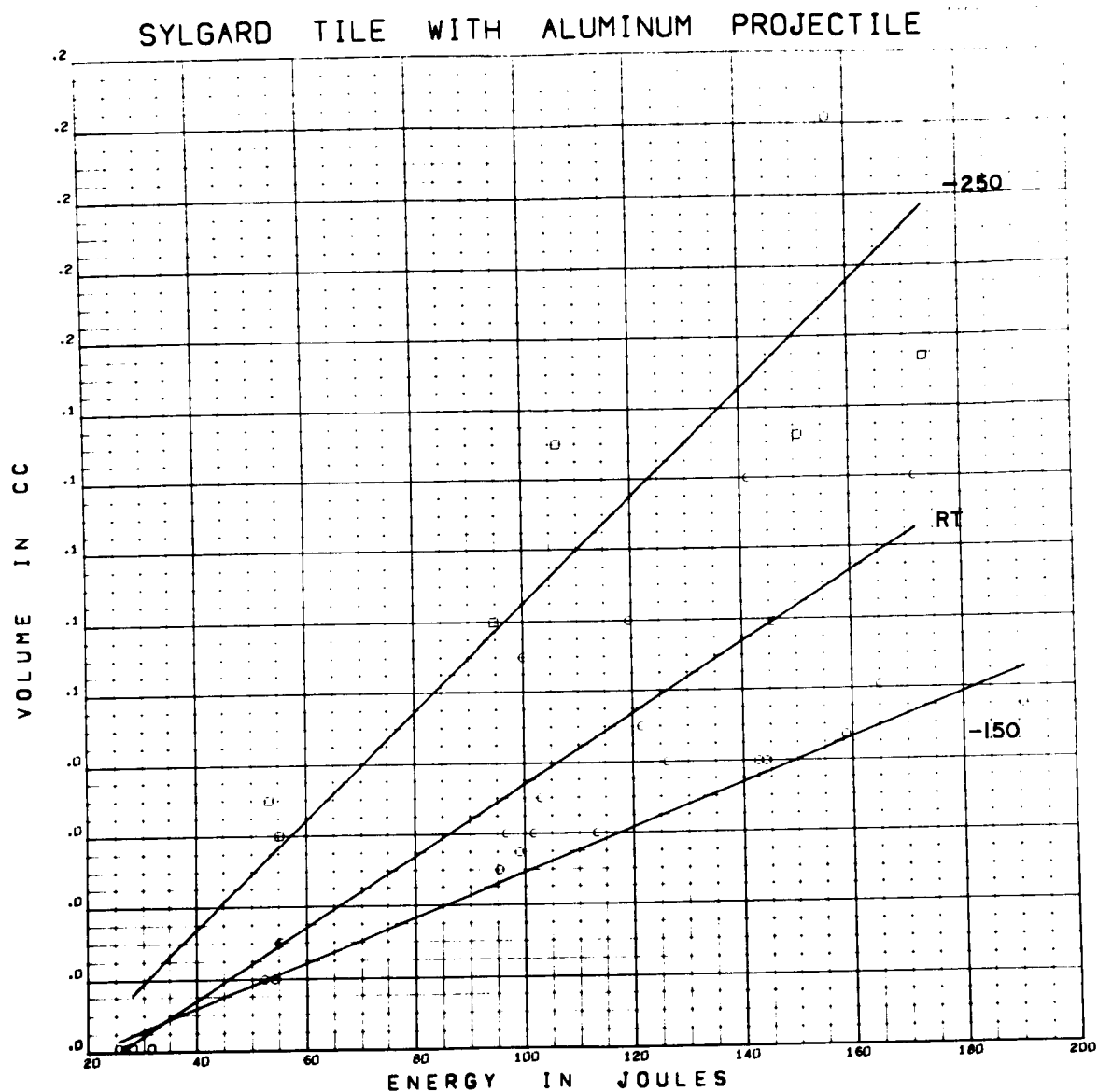


Figure G40 Volume versus Energy for Aluminum Projectiles on Sylgard 325 Tile

Data Points Skipped: 283 R2, 300

Form of Regression: $V = (1.043 - .5221 \cdot ST - .4234 \cdot CV) \cdot 10^{-3} E^{-.0215}$

RMS Deviation: .021 CC

+ .0010 ST + .0018 CV

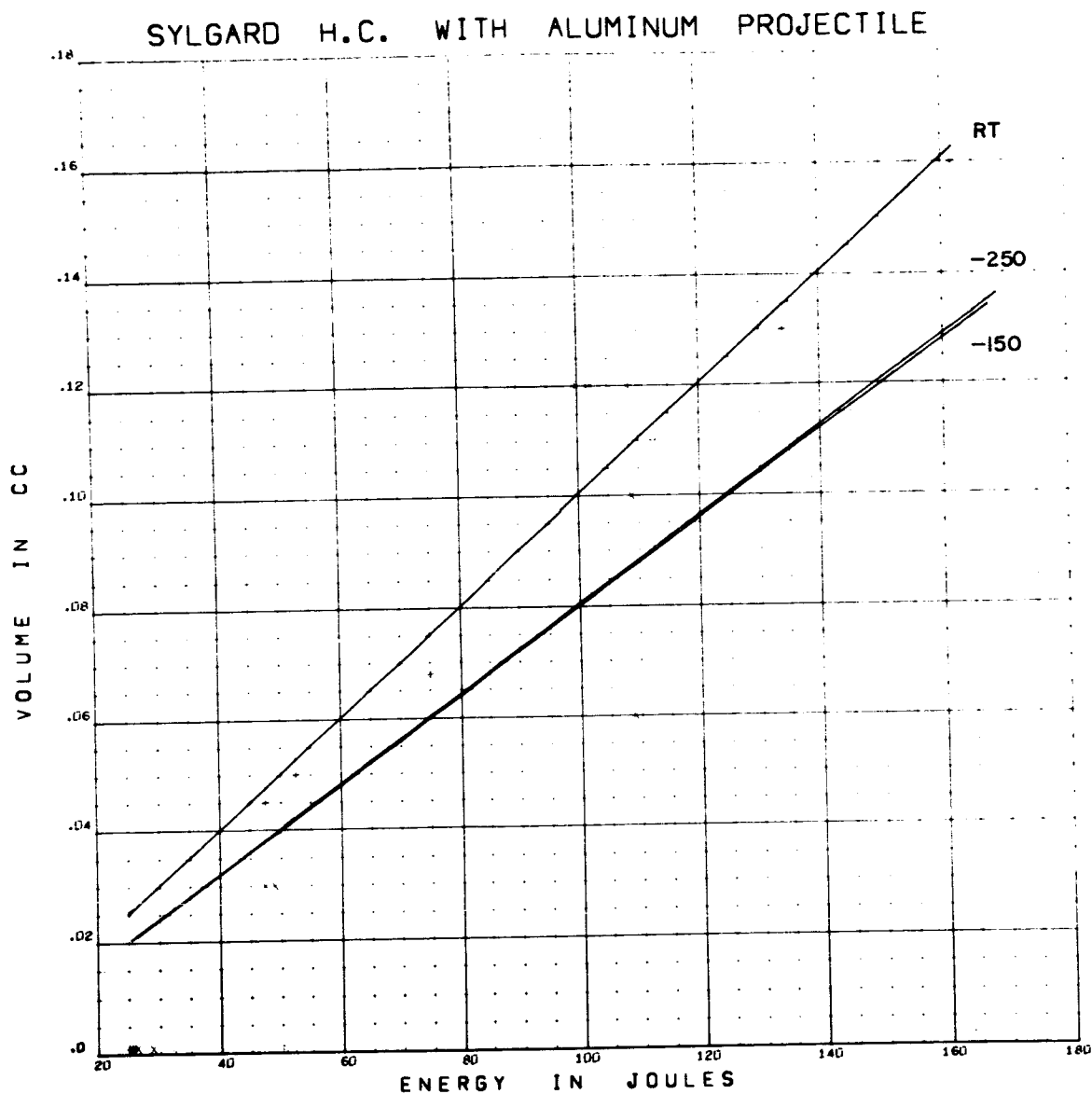


Figure G41 Volume versus Energy for Aluminum Projectiles on Sylgard 325 HC

Data Points Skipped: 280 R1, 289 R1, 289 R2, 290 R1, 294

Form of Regression: $V = (.8707 + .1988 ST - .0698 CV) \cdot 10^{-3} E$

RMS Deviation: .023 cc

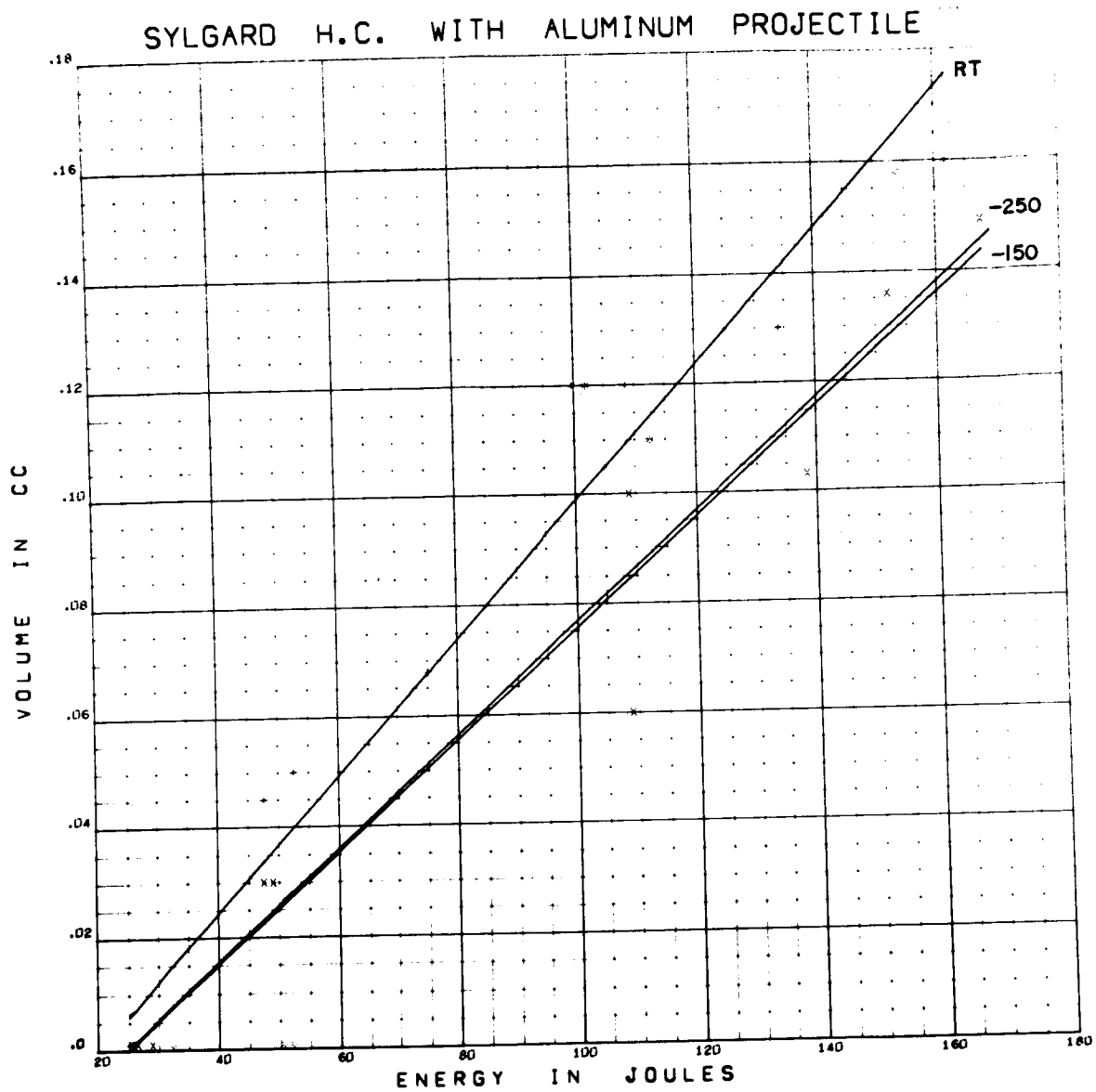


Figure G42 Volume versus Energy for Aluminum Projectiles on Sylgard 325 HC
 Data Points Skipped: 280 R1, 289 R1, 289 R2, 290 R1, 294
 Form of Regression: $V = (1.089 + .22115T - .0811CV) \cdot 10^{-3} E - .0251$
 RMS Deviation: .0186 cc

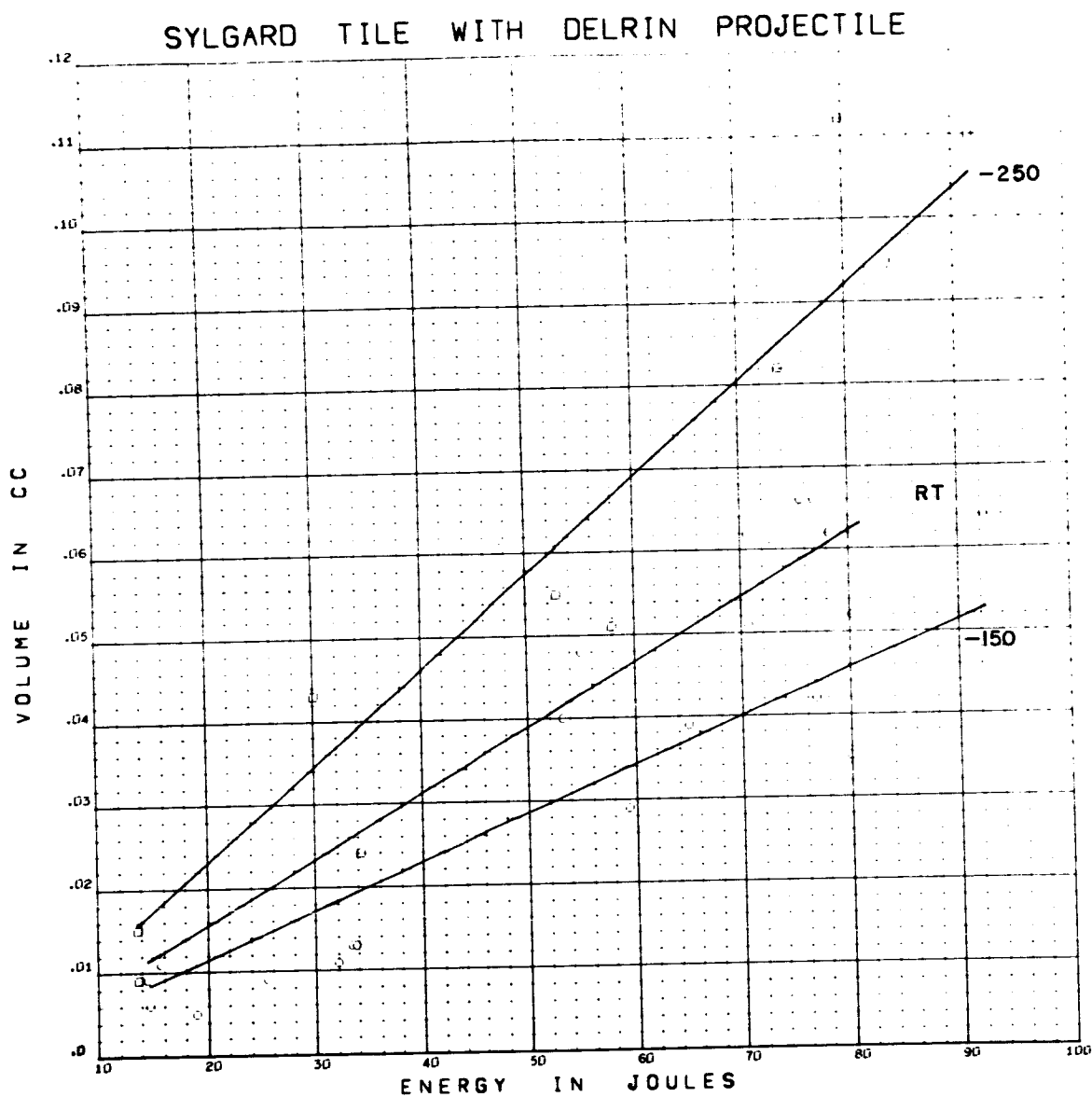


Figure G43 Volume versus Energy for Delrin Projectiles on Sylgard 325 Tile

Data Points Skipped: none

Form of Regression: $V = (.8341 - .3727ST - .2624CV) \cdot 10^{-3}E$

RMS Deviation: .0084 cc

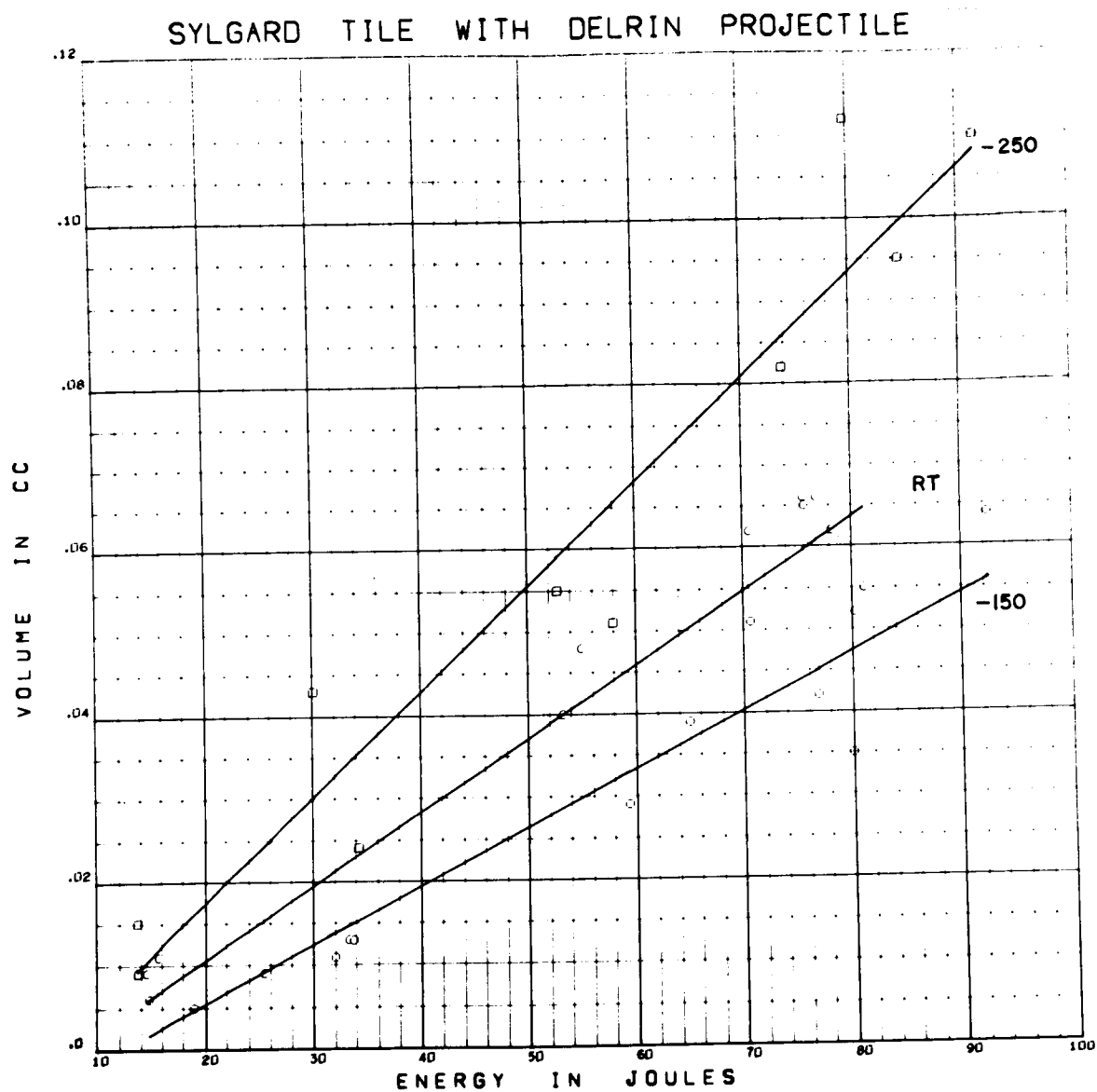


Figure G44 Volume versus Energy for Delrin Projectiles on Sylgard 325 Tile

Data Points Skipped: none

Form of Regression: $V = (.9509 - .3854ST - .2511CV) \cdot 10^{-3}E$

RMS Deviation: .0077 cc $-.0078 + .00089ST - .00071CV$

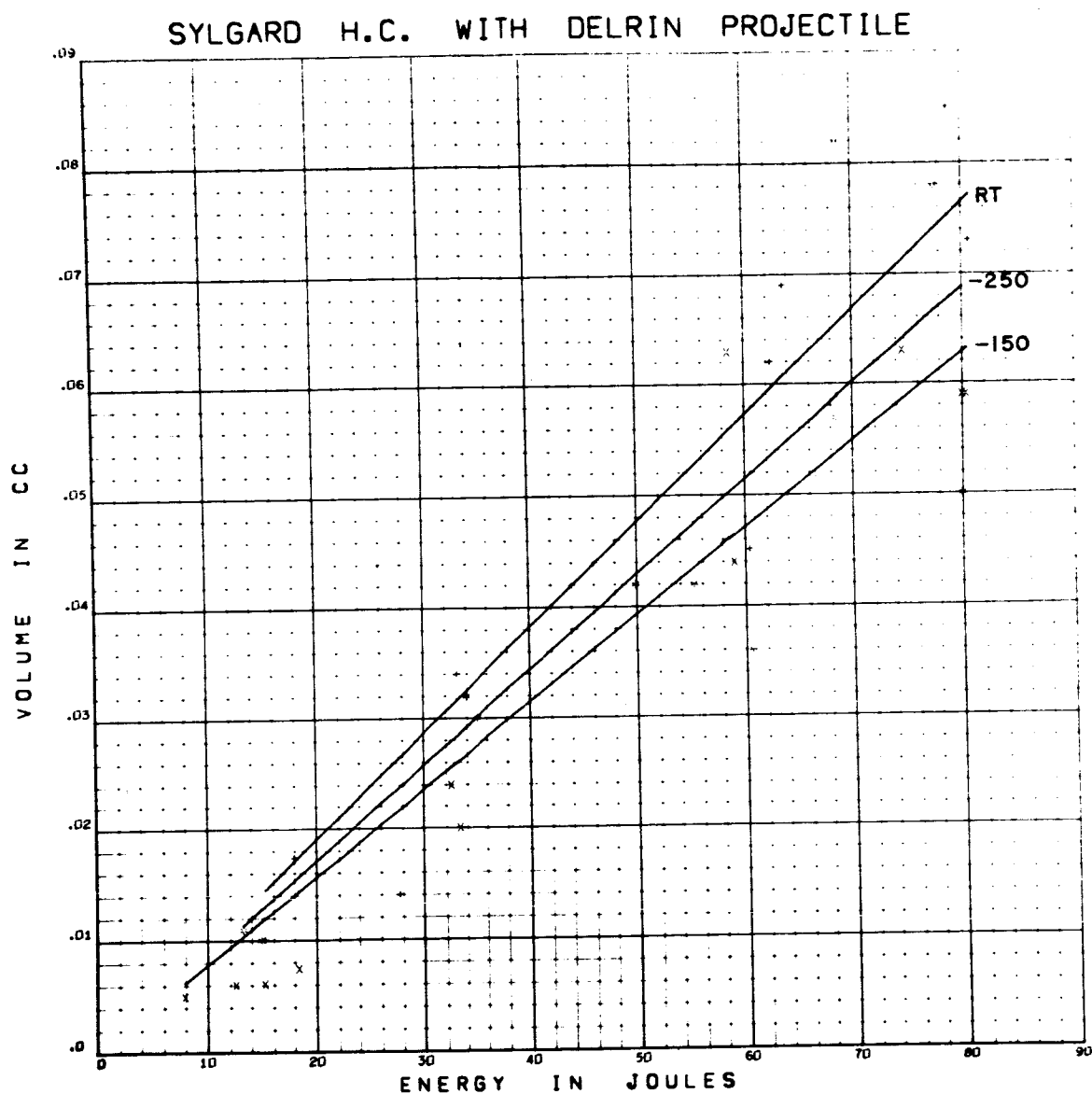


Figure G45 Volume versus Energy for Delrin Projectiles on Sylgard 325 HC

Data Points Skipped: 209 R1

Form of Regression: $V = (.8670 + .0956 ST - .0809 CV) \cdot 10^{-3} E$

RMS Deviation: .0087 cc

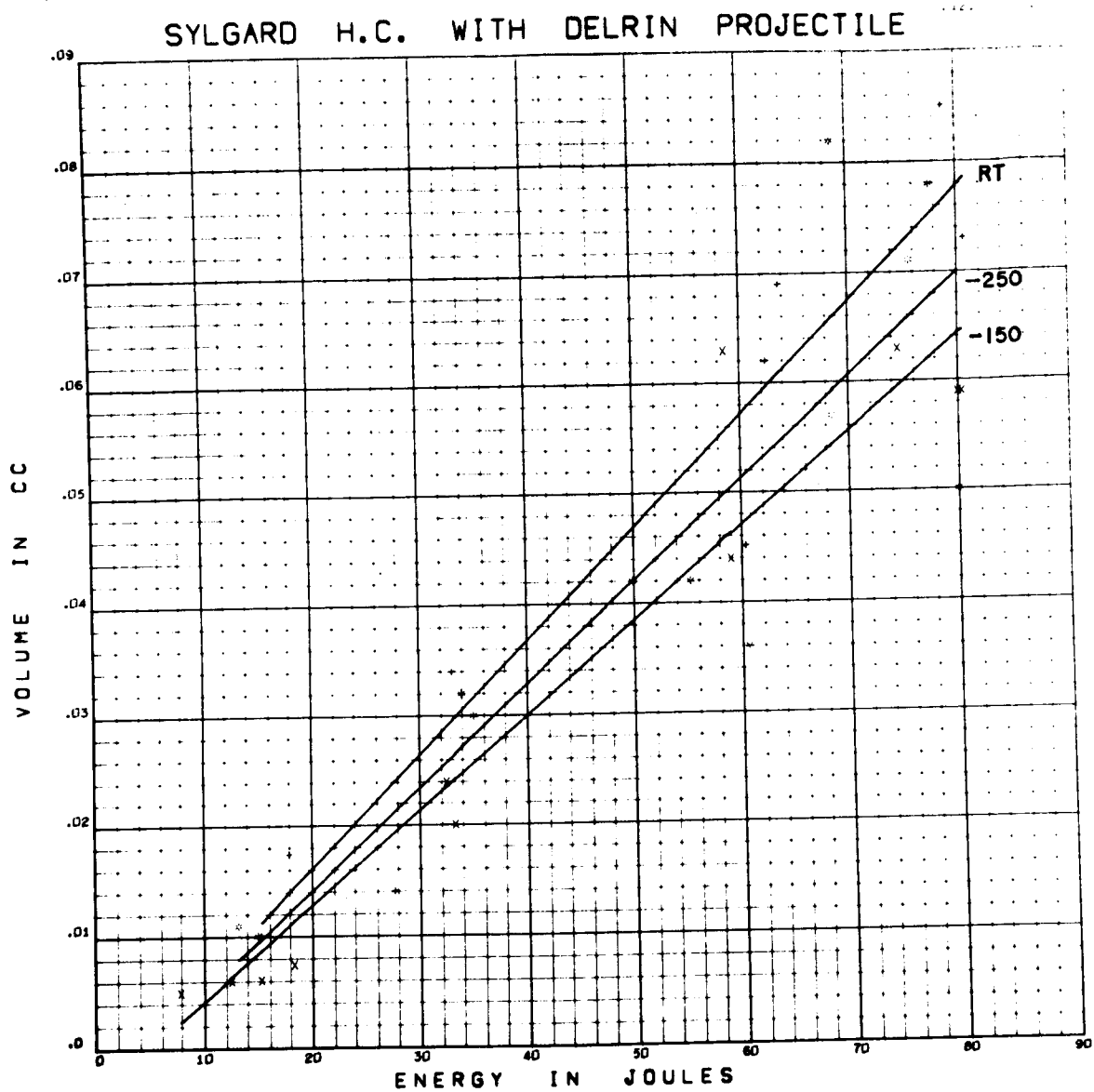


Figure G46 Volume versus Energy for Delrin Projectiles on Sylgard 325 HC

Data Points Skipped: 209 R1

Form of Regression: $V = (.9380 + .0975 ST - .0796 CV) \cdot 10^{-3} E$

RMS Deviation: .0085 cc

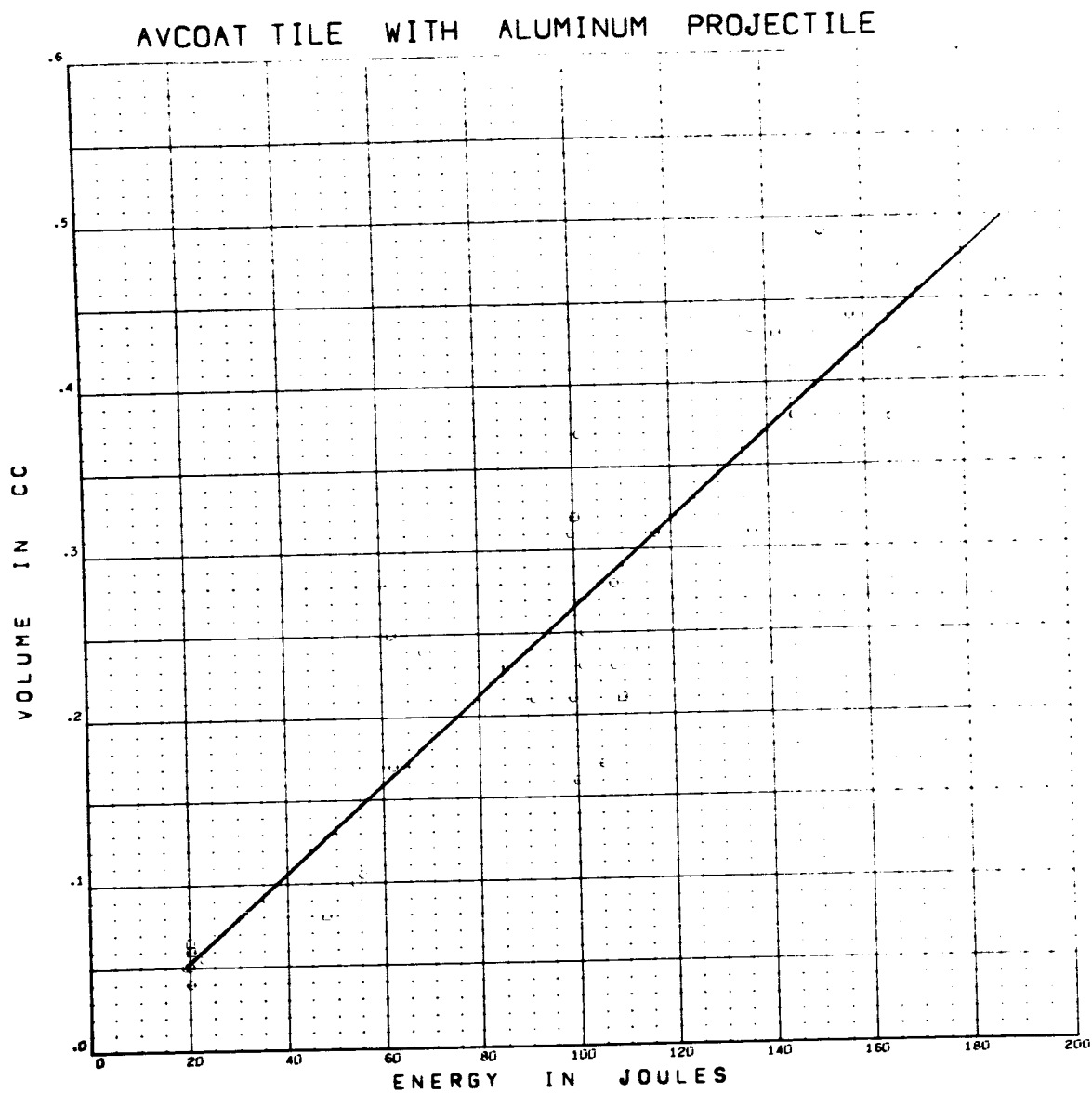


Figure G47 Volume versus Energy for Aluminum Projectiles on Avcoat 5026 Tile

Data Points Skipped: 132, 116

Form of Regression: $V = 2.656 \times 10^{-3} E$

RMS Deviation: .057 cc

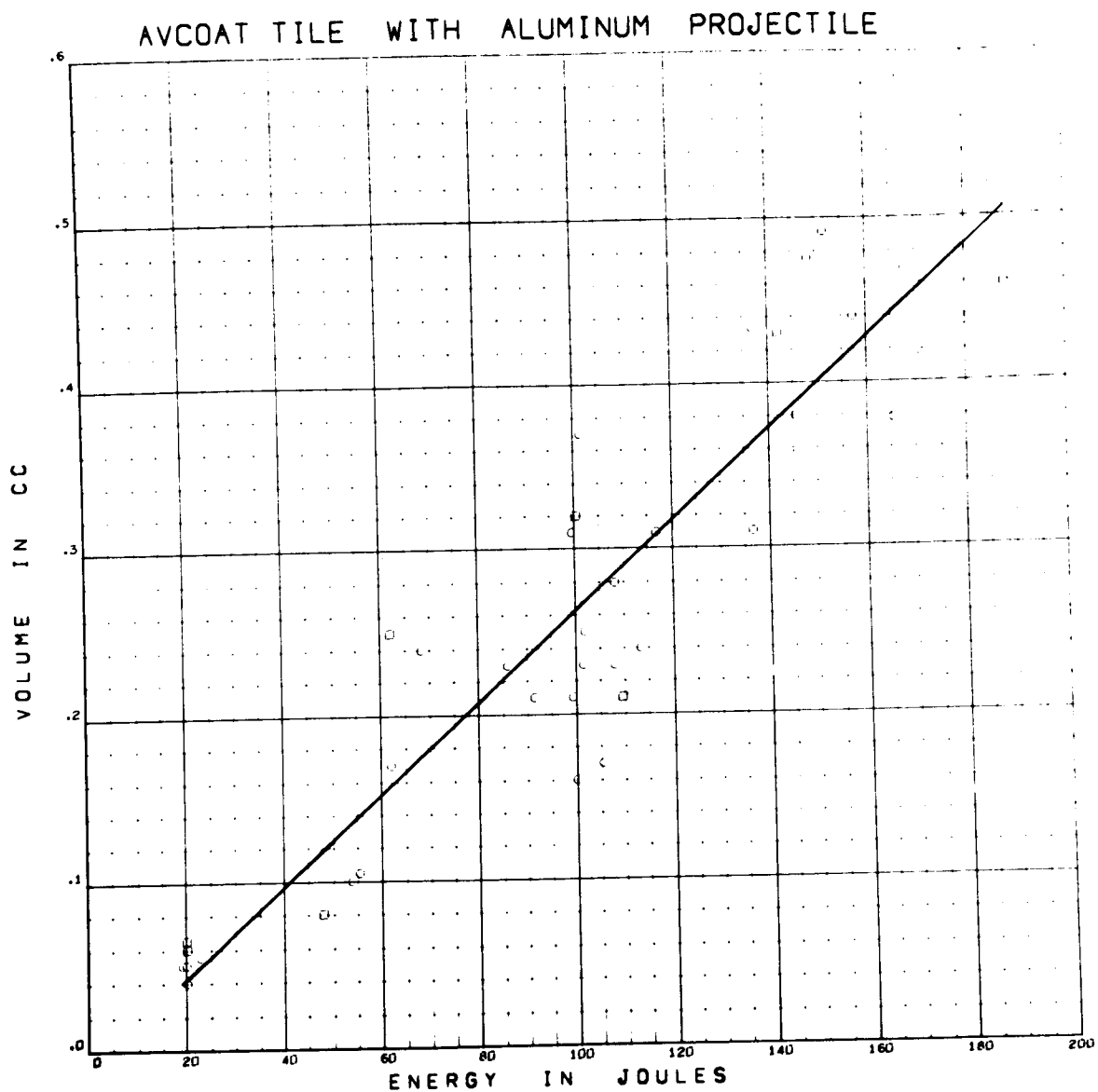


Figure G48 Volume versus Energy for Aluminum Projectiles on Avcoat 5026 Tile

Data Points Skipped: 132, 116

Form of Regression: $V = 2.759 \times 10^{-3} E - .0129$

RMS Deviation: .057 cc

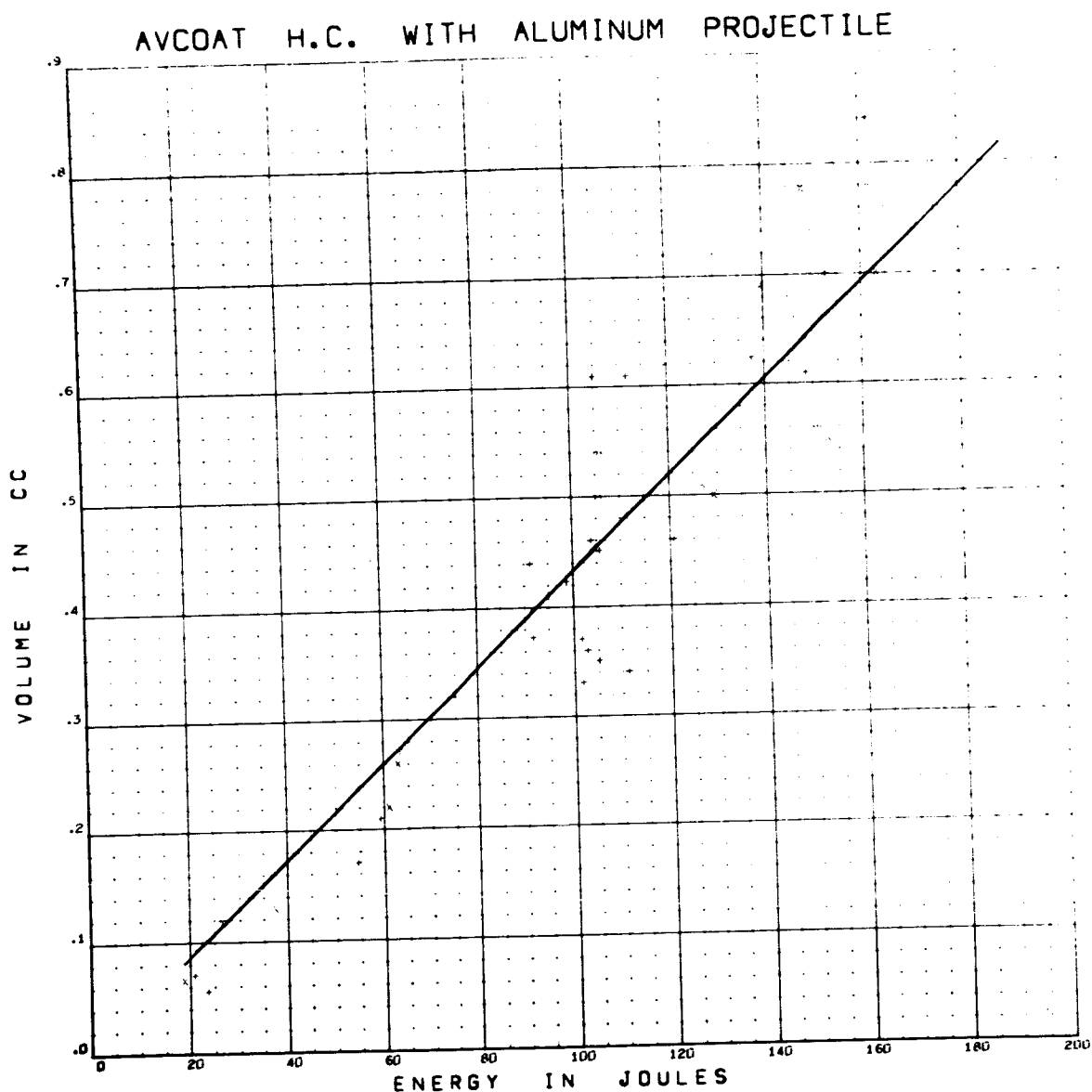


Figure G49 Volume versus Energy for Aluminum Projectiles on Avcoat 5026 HC

Data Points Skipped: 122 R1

Form of Regression: $V = 4.331 \times 10^{-3} E$

RMS Deviation: .074 cc

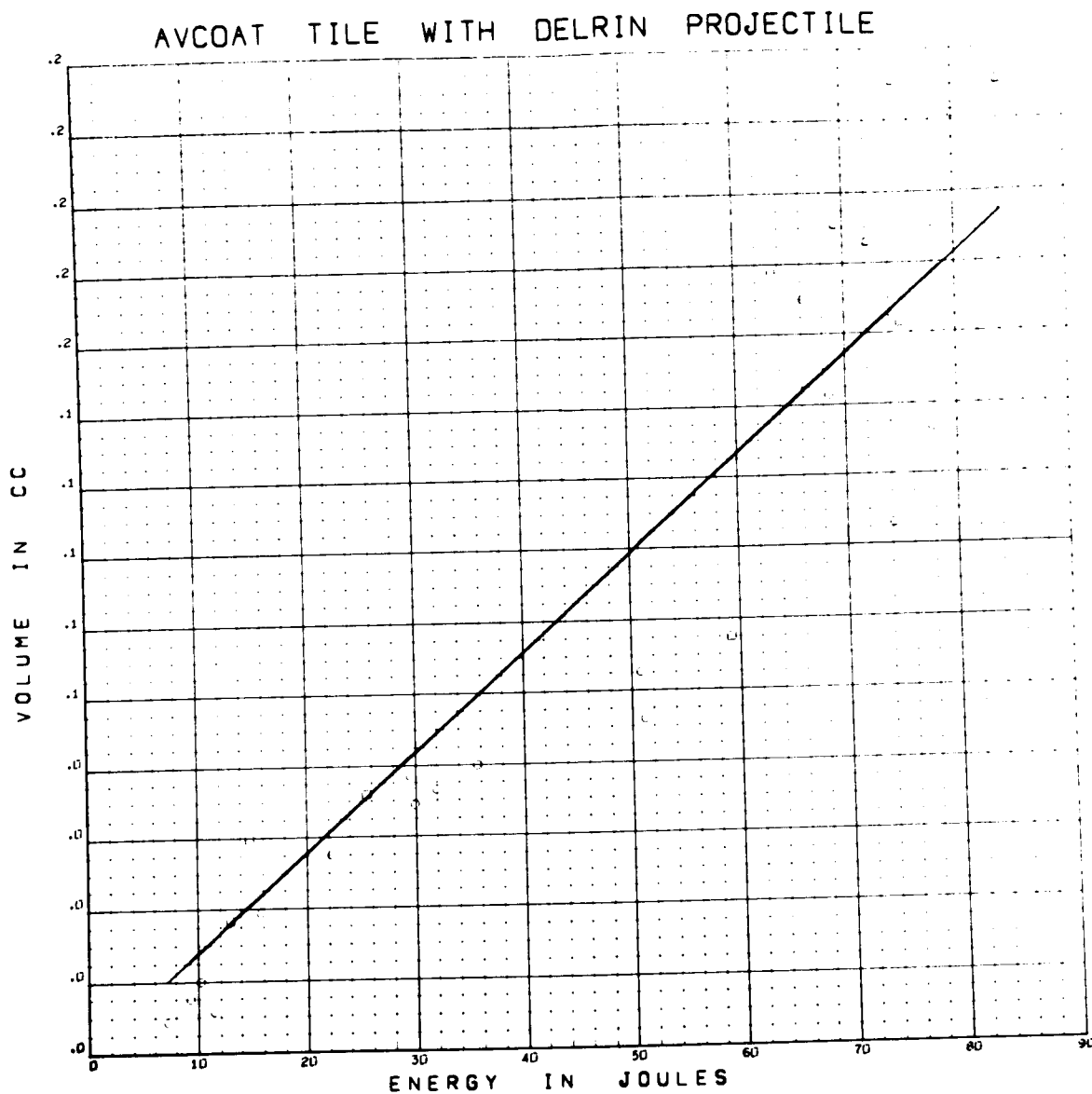


Figure G50 Volume versus Energy for Delrin Projectiles on Avcoat 5026 Tile

Data Points Skipped: 24, 31 R1, 33, 36, 44 R1, 45

Form of Regression: $V = 2.785 \times 10^{-3} E$

RMS Deviation: .03/cc

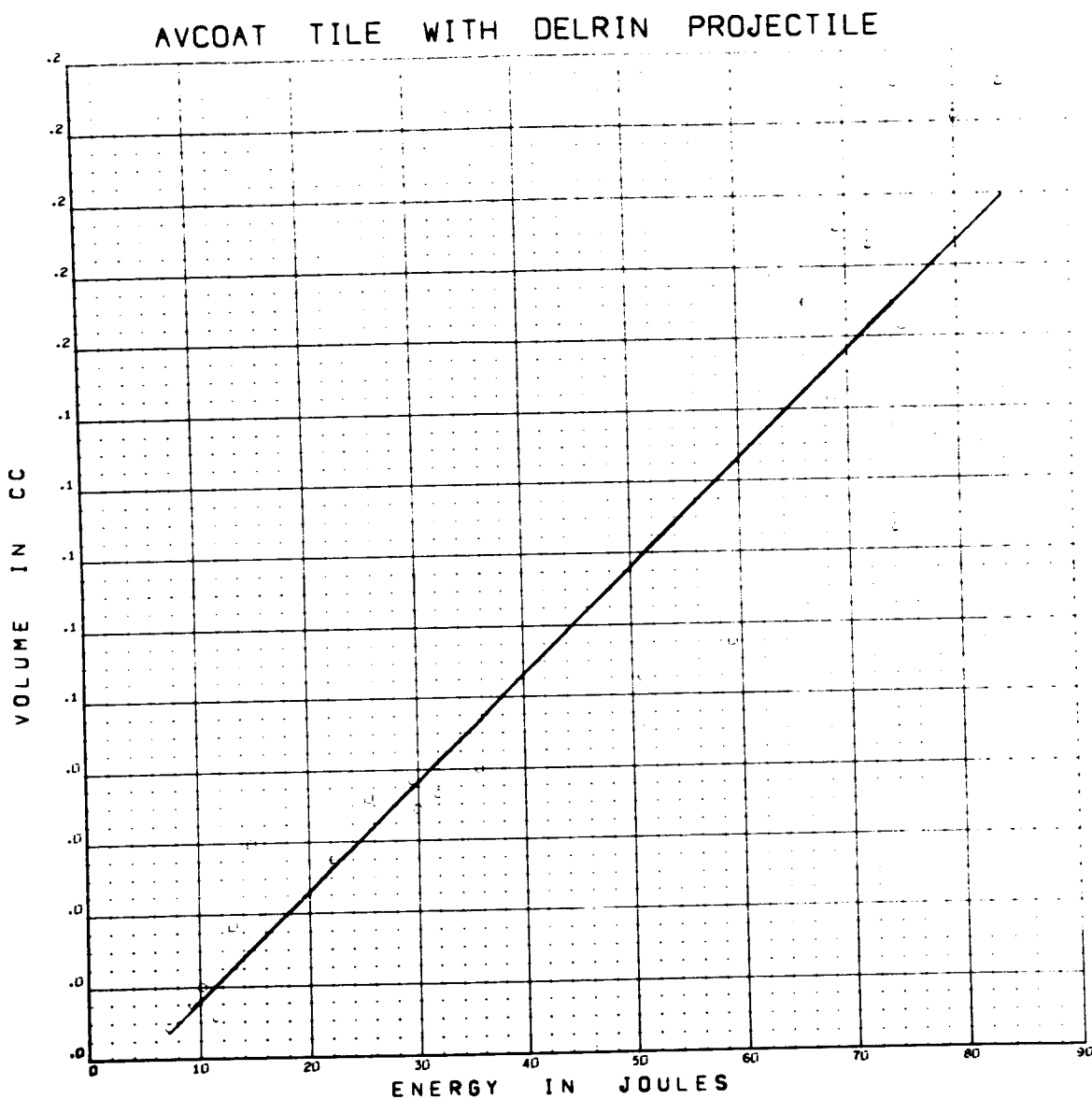


Figure G51 Volume versus Energy for Delrin Projectiles on Avcoat 5026 Tile

Data Points Skipped: 24, 31 R1, 33, 36, 44 R1, 45

Form of Regression: $V = 3.015 \times 10^{-3} E - 0.0142$

RMS Deviation: .030 CC

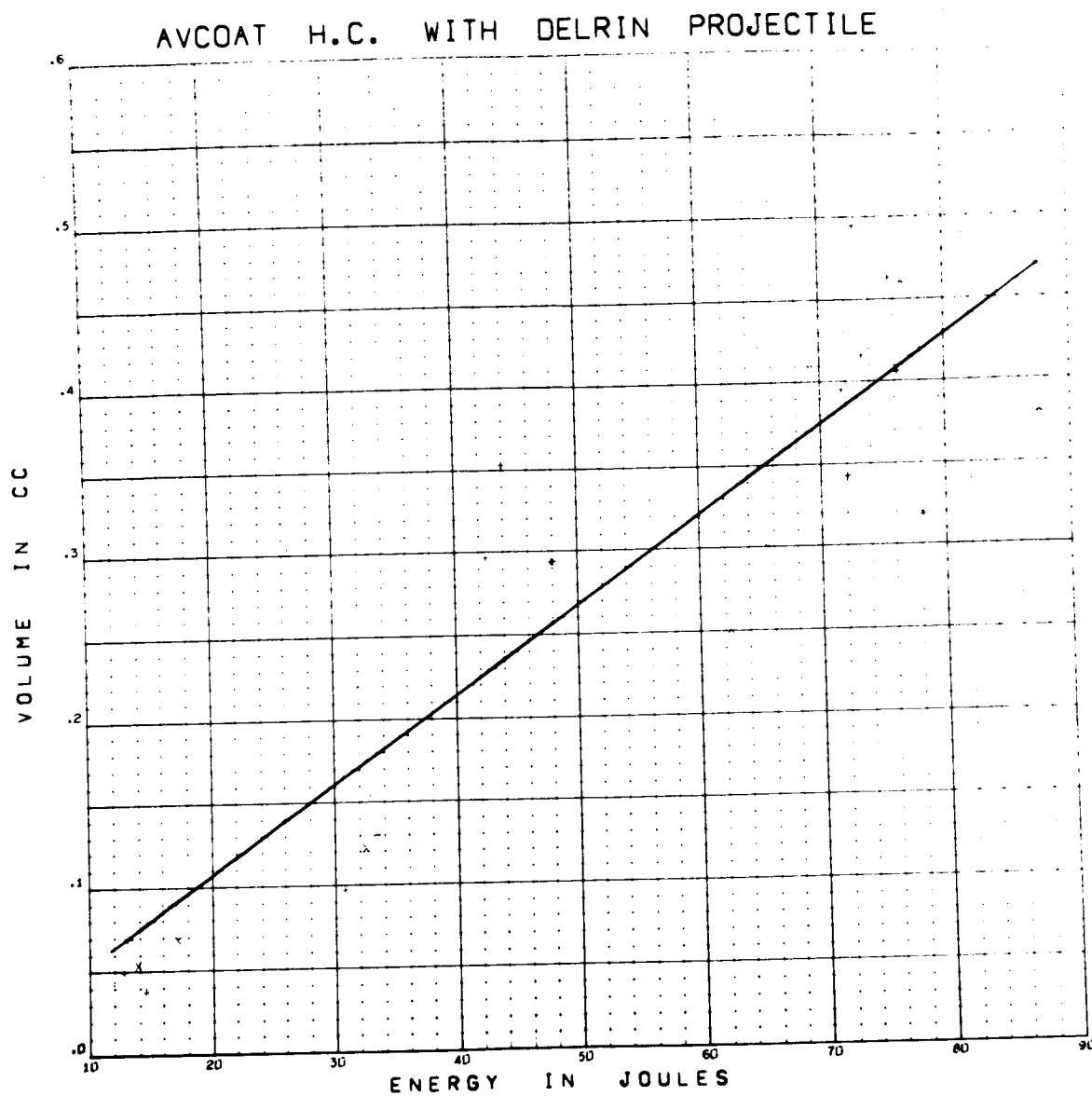


Figure G52 Volume versus Energy for Delrin Projectiles on Avcoat 5026 HC

Data Points Skipped: none

Form of Regression: $V = 5.362 \times 10^{-3} E$

RMS Deviation: .055 cc

APPENDIX H

REGRESSION FORMS

H. 1 INTRODUCTION

It is the purpose of this appendix to give supplementary explanatory information concerning the form of the regression information included with each graph in Appendices D-G.

H. 2 UNITS

The following units were used consistently in all regressions:

linear dimensions	cm
volume, v	cc
velocity, V	km/sec
energy, E	joules
density, ρ	gm/cc
momentum, M	gm cm/sec

The RMS deviation is given in units of the parameter for a linear plot and in percent for a log plot.

H. 3 REGRESSION TERMS

Most of the regression terms used are self-explanatory, but a few, described below, are not.

H. 3. 1 Temperature Variation

When temperature variation was allowed, three degrees of freedom were given to the three temperatures. One term is included in the constant; the other two terms were linear and quadratic in the temperature points, and were:

ST = 0.5 for room temperature targets

0 for -150° F targets

-0.5 for -250° F targets

CV = -0.5 for room temperature targets

1.0 for -150° F targets

-0.5 for -250° F targets

If one thinks of the temperature used in this study as successive points,
 $t_n, t_1 = -250^\circ\text{F}, t_2 = -150^\circ\text{F}, t_3 = \text{RT}$, then

$$\text{ST} = 1/2 (n-2)$$

$$\text{CV} = 1 - 1.5 (n-2)^2$$

ST is linear in n , and CV is quadratic in n .

H. 3. 2 Structure Variation

The following function was used to allow for honeycomb effects:

$H = +0.5$ if the target is honeycomb

-0.5 if the target is tile

H. 3. 3 Transition Region Terms

To permit meaningful fits for data on penetration by aluminum projectiles, a term was used which is linear in velocity in the transition region and zero above. This term had the effect of decoupling the transition region data from the fits. The regression form listed with the graph gives only the form above the transition region.

H. 4 REGRESSIONS NOT PLOTTED

Those regressions which gave meaningful results and which contain projectile variation as an independent variable are given below. Regressions with projectile variation could not be plotted with the existing program.

H. 4. 1 Crater Diameter in Sylgard

$$\begin{aligned} \log_{10} \left(\frac{d}{D} \right) = & 0.39586 + 0.9076 \log_{10} (V) \\ & + 0.0900 \text{ ST} - 0.0184 \text{ CV} \\ & - 0.0197 H + 0.382 \log_{10} \rho_p \end{aligned}$$

RMS deviation: 13 percent

Data Points Skipped: 209 R2

H. 4. 2 Crater Diameter in Avcoat

$$\log_{10} \left(\frac{d}{D} \right) = 0.7123 + 0.9215 \log_{10} V + 0.03581 H \\ + 0.2324 \rho_p$$

RMS deviation: 9 percent

Data points skipped: 29, 30, 37, R3, 116

H. 4. 3 Penetration in Sylgard

For $V > 0.45$ units/ μ sec

Slope $\left(\frac{\partial \log p}{\partial \log v} \right)$ independent of temperature

$$\log_{10} \left(\frac{P}{D} \right) = 0.3068 + 0.9459 \log_{10} V + 0.06857 ST \\ - 0.006938 CV + 0.01490 H + 0.7871 \log_{10} \rho_p$$

RMS deviation: 19 percent

Data points skipped: 197, 209, 209 R1, 210, 280 R1, 293 R1, 294

For slope dependent on temperature:

$$\log_{10} \left(\frac{P}{D} \right) = 0.3629 + 0.9529 \log_{10} V - 0.03308 ST \\ - 0.0130 CV - 0.3715 ST \cdot \log_{10} V \\ - 0.1522 CV \cdot \log_{10} V + 0.01537 H \\ + 0.7943 \log_{10} \rho_p$$

RMS deviation: 18 percent

Data points skipped: 197, 209, 209 R1, 210, 280 R1, 293 R1, 294

H. 4. 4 Penetration in Avcoat

for $V > 0.6$ cm/ μ sec

$$\log_{10} \left(\frac{P}{D} \right) = 0.6634 + 0.5109 \log_{10} V + 0.1144 H \\ + 0.5544 \log_{10} \rho_p$$

RMS deviation: 10 percent

Data points skipped: 13, 37 R3, 38 R2, 89, 110 R8, 110 R9, 116, 116 R2, 116 R3, 122, 122 R1, 132